FURTHER STUDIES ON FLOW DISTRIBUTION ON DISTILLATION SIEVE TRAYS

A THESIS SUBMITTED

BY

CHIMEREZE OKORIE CHIMA B.Sc. M.Sc.

A candidate for the degree of

Doctor of Philosophy

DEPARTMENT OF CHEMICAL ENGINEERING

AND

APPLIED CHEMISTRY

ASTON UNIVERSITY

MARCH 2002

CERTIFICATE

ASTON UNIVERSITY

FURTHER STUDIES ON FLOW DISTRIBUTION ON DISTILLATION SIEVE TRAYS

A Thesis submitted by
Chimereze Okorie Chima B.Sc. M.Sc.
A candidate for the degree of Doctor of Philosophy
March 2002

THESIS SUMMARY

The thesis describes experimental work on the possibility of using deflection baffles in conventional distillation trays as flow straightening devices, with the view of enhancing tray efficiency. The mode of operation is based on deflecting part of the liquid momentum from the centre of the tray to the segment regions in order to drive stagnating liquid at the edges forward. The first part of the work was a detailed investigation into the two-phase flow patterns produced on a conventional sieve tray having 1 mm hole size perforations. The data provide a check on some earlier work and extend the range of the existing databank, particularly to conditions more typical of industrial operation. A critical survey of data collected on trays with different hole sizes (Hine, 1990; Chambers, 1993; Fenwick, 1996; this work) showed that the hole diameter has a significant influence on the flow regime, the size of the stagnant regions and the hydraulic and mass transfer performance.

Five modified tray topologies were created with different configurations of baffles and tested extensively in the 2.44 m diameter air-water pilot distillation simulator for their efficacy in achieving uniform flow across the tray and for their impact on tray loading capacity and mass transfer efficiency. Special attention was given to the calibration of the over 100 temperature probes used in measuring the water temperature across the tray on which the heat and mass transfer analogy is based. In addition to normal tray capacity experiments, higher weir load experiments were conducted using a 'half-tray' mode in order to extend the range of data to conditions more typical of industrial operation.

The modified trays show superior flow characteristics compared to the conventional tray in terms of the ability to replenish the zones of exceptionally low temperatures and high residence times at the edges of the tray, to lower the bulk liquid gradient and to achieve a more uniform flow across the tray. These superior flow abilities, however, tend to diminish with increasing weir load because of the increasing tendency for the liquid to jump over the barriers instead of flowing over them. The modified tray topologies showed no tendency to cause undue limitation to tray loading capacity. Although the improvement in the efficiency of a single tray over that of the conventional tray was moderate and in some cases marginal, the multiplier effect in a multiple tray column situation would be significant (Porter et al., 1972). These results are in good agreement with an associated CFD studies (Fischer, 1999) carried out by partners in the **A**dvanced **S**tudies **i**n **D**istillation consortium.

It is concluded that deflection baffles can be used in a conventional distillation sieve tray to achieve better liquid flow distribution and obtain enhanced mass transfer efficiency, without undermining the tray loading capacity. Unlike any other controlled-flow tray whose mechanical complexity impose stringent manufacturing and installation tolerances, the baffled-tray models are simple to design, manufacture and install and thus provide an economic method of retrofitting badly performing sieve trays both in terms of downtime and fabrication.

Keywords: DISTILLATION, SIEVE TRAYS, FLOW PATTERNS, CONTROLLED FLOW, MESH, TRAY EFFICIENCY, MASS TRANSFER.

Dedication

Dedicated to the Memory of my Beloved Brother and Friend, Paul-Anoke.

Acknowledgements

I would like to express my gratitude to the following:-

My supervisor, Dr. J. D. Jenkins, for his guidance and stimulating ideas throughout the course of my research.

Dr. J. P. Fletcher for his assistance with the adaptation of the computer programs.

The workshop technicians and secretarial staff of CEAC department for their support and assistance throughout the period of this research.

The Advanced Studies in Distillation (ASID) Consortium for their sponsorship of this work and the wealth of information made available to me by the industrial and academic members of the consortium.

And finally, to my friends and family for their prayers and support throughout the research.

Table of Contents

List of Figures

List of Tables

Nomenclature

a	Interfacial mass transfer area	$[m^2m^{-3}]$
A_B	Active area of tray	$[m^2]$
A_D	Downcomer area	$[m^2]$
A_T	Column cross-sectional area	$[m^2]$
A_f	Fractional hole area	$[m^2]$
CPI	Chemical and process industries	[-]
C_{air}	Specific heat of air	$kJ\ kg^{-1}K^{-1}]$
C_P	Specific heat of moist air	$[kJ\ (kg\ dry\ air)^{-1}K^{-1}]$
C_W	Specific heat of water	$[kJ\ kg^{-1}K^{-1}]$
C_s	Load factor = $u_s\ [\rho_V/(\rho_L - \rho_V)]^{0.5}$	$[m\ s^{-1}]$
Cf	Capacity factor	$[m\ s^{-1}]$
C_{SB}	Capacity factor based on bubbling area	$[m\ s^{-1}]$
d_h	Hole diameter	[m]
E_{mv}	Murphree vapour tray efficiency	[-]
E_O	Overall column efficiency	[-]
E_{og}	Murphree vapour point efficiency	[-]
F	Flooding factor in tray design	[-]
F_{lv}	Flow parameter = $L/G.(\rho_V/\rho_L)^{0.5}$	[-]
g	Acceleration due to gravity	$[m\ s^{-2}]$
G	Total air (vapour) mass flowrate	$[kg\ s^{-1}]$
h_{cl}	Height of clear liquid	[m of H_2O]
h_{DT}	Dry tray pressure drop	[m of H_2O]
h_R	Residual pressure drop	[m of H_2O]
h_{wT}	Wet tray pressure drop	[m of H_2O]
h_f	Froth height	[m]
h_R	Residual pressure drop	[m of liquid]
h_w	Weir height	[m]
h_{ow}	Height of liquid crest over weir	[m]
H	Enthalpy of Vapour	$[kJ\ kg^{-1}]$
H^*	Saturation Enthalpy of Vapour	$[kJ\ kg^{-1}]$
H_{fg}	Latent Heat of Vapourisation	$[kJ\ kg^{-1}]$

H_{air}	Humidity of Unsaturated Air	[kg moisture/kg dry air]
H^*	Humidity of Saturated Air	[kg moisture/kg dry air]
P	Hole pitch	[-]
Pe	Peclet number	[-]
PRT	Platinum resistance thermometer	[-]
k_y	Film Mass Transfer Coefficient in Vapour Phase	[kmol $s^{-1}m^{-1}$]
L	Total Liquid mass flowrate	[kg s^{-1}]
m	Slope of the Equilibrium Line	[-]
N	Number of Pools	[-]
N	Mass Transfer rate of the more Volatile Component	[kmol $s^{-1}m^{-2}$]
N_A	Number of actual trays	[-]
N_T	Number of theoretical trays	[-]
q	Volumetric Liquid Flowrate	[m^3s^{-1}]
Q	Heat Transfer Rate	[kJ $s^{-1}m^{-2}$]
Q_L	Liquid volumetric flowrate	[m^3s^{-1}]
Q_G	Vapour volumetric flowrate	[m^3s^{-1}]
T	Temperature	[^oC]
T_R	Reduced Temperature	[-]
U_{DF}	Downcomer velocity of vapour-liquid Mixture	[m s^{-1}]
u_h	Gas hole velocity	[m s^{-1}]
u_s	superficial gas velocity	[m s^{-1}]
W	Weir length	[m]
x_n	Composition of liquid leaving stage n	[kmol kg^{-1}]
x	Liquid concentration	[-]
x_n^*	Composition of liquid in equilibrium with vapour composition y_n	[kmol kg^{-1}]
$\overline{x}_n$	Average composition of liquid leaving stage n	[kmol kg^{-1}]

$\overline{x}_{n+1}$	Average composition of liquid leaving stage n+1	[kmol kg^{-1}]
y_n	Composition of vapour leaving stage n	[kmol kg^{-1}]
y_{n-1}	Composition of vapour leaving stage n-1	[kmol kg^{-1}]
y^*	Composition of vapour in equilibrium with liquid composition x_n	[kmol kg^{-1}]
$\overline{y}_n$	Average composition of vapour leaving stage n	[kmol kg^{-1}]
$\overline{y}_{n-1}$	Average composition of vapour leaving stage n-1	[kmol kg^{-1}]
α	Relative volatility	[-]
ε	Gas holdup fraction	
λ	Ratio of gradient of equilibrium line to operating line	[-]
ρ_G	Gas density	[kg m^{-3}]
ρ_V	Vapour density	[kg m^{-3}]
ρ_F	Froth density	[kg m^{-3}]
ρ_L	Liquid density	[kg m^{-3}]
σ	Surface tension	[N m^{-1}]
α	Relative volatility of a binary mixture	[-]
λ	Ratio of gradient of equilibrium line to operating line (= mG/L)	[-]
ρ_L	Liquid density	[kg m^{-3}]
ρ_V	Vapour density	[kg m^{-3}]

CHAPTER ONE

Introduction

Distillation is recognised as a major and versatile unit operation that has a huge impact on the energy and financial costs of many industrial processes. It is often likened to the motor industry because it is a business technology that is continually being driven by market and more recently environmental forces in which research and development play key roles. The notion that distillation has reached its full stature and therefore lacks potential for further improvement is not born out by the constant innovation that takes place in the field or by the continuing need to understand fully all the fundamental issues that are involved in the operation. Hardly any decade has passed since the 1920s without a major break through or innovation in distillation technology brought about by research and development (Darton, 1992; Porter, 1995; Kunesh et al., 1995).

From small beginnings in the mists of history when it originated as a technique to produce liquors from plant or animal substrates, distillation has indeed developed into a workhorse of the chemical and process industries (CPI). It is estimated that distillation accounts for about 3% of the world energy consumption, with 95% of all separations in the CPI carried out by distillation and 4% of all crude oil burnt to provide the energy required to refine it into desirable products (Mix et al. 1980; Humphrey and Seibert, 1992). This large energy consumption is a major economic and environmental drawback in the application of distillation technology. Ironically, the same challenges have been the major incentives for sustained research and development in the area.

Although conventional distillation does not offer a high thermodynamic efficiency, it is commonly favoured over other separation technologies because of reliability, simplicity and often lower capital cost process (Humphrey and Seibert, 1992). However, unstable energy costs and increasing environmental tax burdens are constant reminders that radical and new energy efficient and environmental friendly distillation technology will be required in the future to sustain the advantages that has made it the preferred choice over alternative separation techniques in the fluid separation field. It is envisaged that in the near future, the operation of a badly performing tray will no longer be judged on economics alone but also by environmental burdens that are associated with a badly performing tray.

One area that has been known to be a major source of inefficiency and poor energy utilisation in conventional distillation trays is the nature of liquid distribution on the tray. Since this was discovered in the 1930s (Kirschbaum, 1934), considerable work has been done to unravel the two-phase flow behaviour on distillation trays (Lewis, 1936; Gerster, 1958; Porter et al., 1972; Bell and Solari, 1974; Sohlo and Kouri, 1982; Yu et al., 1990, 1991), resulting in the common recognition that the pattern of flow is complex and far from the "ideal-uniform-plug" flow behaviour that was assumed in the past. In fact, it is now widely accepted that nonuniform (maldistributed) flow is a characteristic feature of conventional cross flow trays, except perhaps those of very small diameter. However, the many differing approaches to be found in the literature for modelling the flow nonuniformities reflects a degree of uncertainty that still exist in the understanding of the mechanisms driving them. Although several works (Porter et al., 1972; Bell and Solari, 1974) also support the view that maldistributed flow across conventional trays has serious consequences for performance no generalised understanding exist on how to improve the flow behaviour and enhance efficiency.

The thrust of this work is the investigation of the potential use of deflection baffles as flow straightening devices in conventional distillation trays. The incentive to study this was to assess the possibility of diverting part of the liquid momentum from the centre of the tray to the sides in order to drive stagnating liquid at the edges forward. The experiments were conducted on a 2.44 m diameter air-water simulator from which a realistic simulation of the tray hydraulics, similar to that which is obtained in practice is to be expected. In all, five controlled-flow tray topologies were created with different configurations of baffles, studied and tested extensively for their efficacy in mitigating the flow maldistribution obtained in conventional trays.

The first step in the investigation was to establish the flow distribution on the unmodified conventional sieve tray, having a 10% free area and 1 mm hole size perforations, to serve as a control model on which to measure the performance of the baffled trays. The efficacy of trays fitted with deflection baffles in mitigating the flow maldistribution on the tray was then investigated using a variety of experimental techniques to assess the distinctive tray hydraulics and mass transfer performance. The results of the investigations provide

validation for the associated CFD studies (Fischer, 1999) carried out by partners in the Advanced Studies in Distillation Consortium.

This work forms part of an existing long term project (Hine, 1990; Chambers, 1993; Fenwick, 1996; Khan, 1998) conducted on a commercial size test rig to establish the flow patterns on various hole size trays, covering the wide range used in the industry from air separation to application in chemical and petrochemical industries. The project started with the design and construction of the 2.44 m diameter pilot column and a limited experimental work on the 1.0 mm hole diameter tray (Hine, 1990). The work was extended to the 6.35 mm hole diameter tray (Chambers, 1993), after fundamental modifications to the original air distribution system, and then to 12.7 mm hole trays (Fenwick, 1996). The current work on the 1 mm hole diameter tray is based on the same air distribution system as the experiments on the 6.35 and 12.7 mm hole diameter trays. This provides a basis for a critical analysis of the data collected on 1, 6.35 and 12.7 mm hole diameter trays, in order to determine the effect of hole size on the operation of a sieve tray. Additionally, experiments were carried out on a 'half-tray' to simulate distillation at higher weir loadings in order to extend the range of the existing databank.

The presentation of the thesis starts with a brief review of the literature information in chapter 2 to put the research into perspective. After the literature review, chosen for evidence of the existence and effect of liquid maldistribution on distillation trays, a description of the experimental apparatus is presented in chapter 3, chapter 4 provides a detailed discussion of the techniques and procedures used in the experimental programme. The following chapters present the results of the experiments alongside their discussions before the summary in the last two chapters of the thesis.

CHAPTER TWO

Background and Literature Survey

2.1 Introduction

The origin of distillation dates back several centuries, to the small-scale production of crude liquors by ancient civilisations, but it is only over the last eighty years that it has enjoyed scientific development, corresponding with the establishment of the petrochemical industry that relies heavily on the separation of organic chemicals. Initial research was confined to the delineation of the operating limits of the column because of the problems associated with the scale of operation. During this period, only a very limited amount of test data was available, and distillation technology was advanced mainly by means of empirical models, which were used to correlate existing experience (Porter and Jenkins, 1979). The 1970's, however, witnessed the publication of an increased amount of test data in the open literature and this has led to a better insight into the phenomena that control distillation column operation. As a result, a new generation of experimental, theoretical and, more recently, computational models have emerged, that help to give light on the nature and behaviour of two-phase flows on distillation trays and in other contacting devices.

This chapter presents a brief overview of the literature information necessary to put the research presented in this thesis into perspective. The topics covered are broken down into the following five headings:

(i) Distillation sieve trays.

(ii) Conventional tray capacity design procedure.

(iii) Two-phase flow regimes on sieve trays.

(iv) Flow control devices.

(v) Investigative Techniques for determining liquid flow-patterns on trays.

2.2 Distillation Sieve Trays

A distillation column can be designed with random packing, structured packing, or various tray configurations. A sieve-tray distillation column uses the least complicated tray design and the tray is simply a horizontal plate perforated with small holes. Usually, they are of cross – flow type and thus are provided with downcomers. Hole size and arrangement are varied depending upon the service and the design preference (Van Winkle, 1967). In general the holes are sized so that the pressure drop of the vapour passing through them is somewhat greater than the head of liquid on the tray. The arrangement of the holes may be on a triangular or square pitch as shown in Figure 2.1. The ratio of the hole pitch to the hole diameter is a geometric function of the fractional hole area and the hole pattern and can be calculated from the relation:

$$A_f = K_p\left(\frac{d_h}{P}\right)^2 \qquad \ldots. 2.1$$

where $K_p = 0.905$ for an equilateral triangular pitch, and $K_p = 0.785$ for a square pitch. Hole pitch, P, is the centre-to-centre hole spacing while fractional hole area, A_f, is the ratio of the total area of the tray holes to the tray bubbling area (bubbling area being column area less areas of unperforated regions such as downcomers, downcomer seal, and large calming zones). Typical values for the fractional hole area on commercial sieve trays usually range from 5% to 15%, while hole sizes range from 3 mm to 12.5 mm (Norman, 1961).

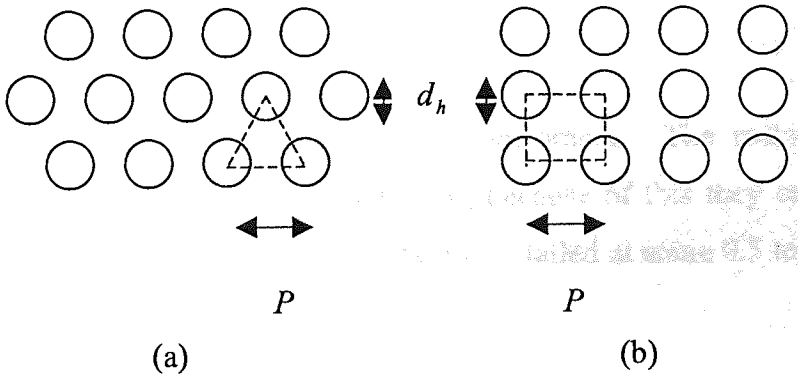

Fig. 2.1: Hole arrangement of sieve trays (a) Triangular (b) Square

There are a variety of sieve trays in commercial use. The overall objective is to maximise vapour-liquid contact and throughput with minimum pressure drop, weeping, and entrainment. Some types of commercial sieve trays are shown in Figures 2.2-2.5 (Wijn E. F, http://www.euronet.nl/users/wijnef/public_html/TrEffDis.html#traytype).

2.2.1 Conventional Downcomer Tray

This is the most common type of tray layout, which can have a single pass for the liquid over the tray or multiple passes. The example shown in Figure 2.2 has two passes for the liquid flowing over the tray. The liquid enters the tray from the downcomer(s) of the tray above and is aerated with vapour rising from the tray below to form froth on the tray. The froth flows across the tray and over the weir into the downcomer, where the vapour is disengaged from the liquid.

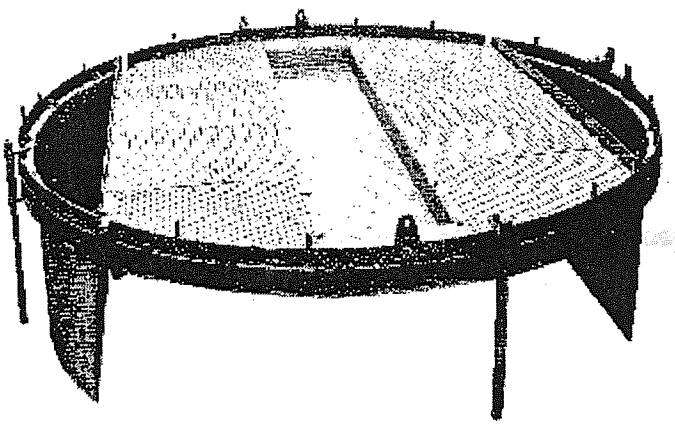

Fig. 2.2: Conventional Downcomer Tray.

2.2.2 Shell Calming-Section Tray

The 'Calming Sections' are a special type of downcomers. The rectangularly shaped 'Calming Sections' are relatively narrow and short, because of this they can be distributed more easily across the tray area. Typically, they are installed at some 0.5 to 2.5 CS's/sq.mtr, depending on liquid load.

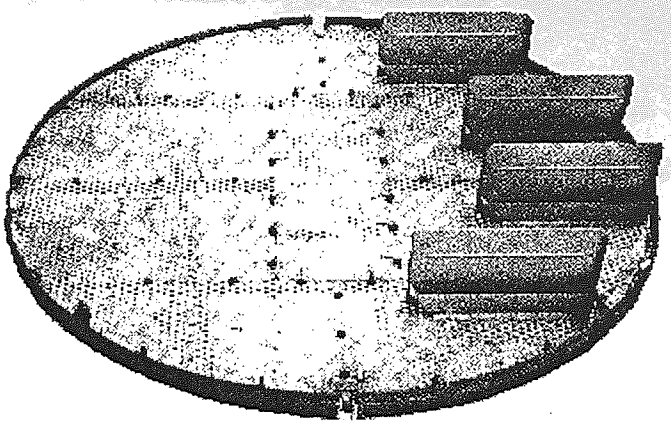

Fig. 2.3: Shell Calming-Section Tray.

2.2.3 Shell HiFi Tray

This layout was developed for use at high liquid loadings (high flowparameters, hence: HiFi). Several narrow and long downcomers run in parallel across one-half of the column diameter. The other half of the column contains another set of parallel downcomers, which are placed at intermediate positions with respect to the downcomers on the first half. On subsequent trays, these tray halves will be mirror images. As these 'HiFi'-downcomers are placed in parallel, the flow path lengths are uniform, although they may be short.

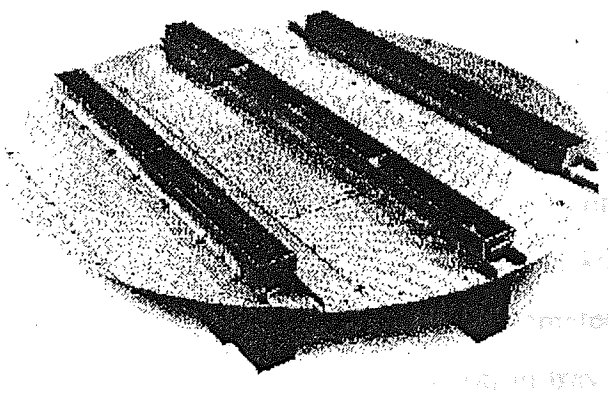

Fig. 2.4: Shell HiFi Tray.

2.2.4 UOP Multiple Downcomer Tray (MD-tray)

This tray layout was originally developed by Union Carbide and later Union Carbide transferred its tray technolgy to UOP, which is actively developing and marketing these trays nowadays. More recently, they have introduced Enhanced Capacity and Enhanced Efficiency versions of the original MD-layout (which is shown). Here, the downcomers on subsequent trays are rotated by an angle of 90 degrees. This downcomer rotation forces the liquid to flow across the tray in a 90 degrees turn, as well.

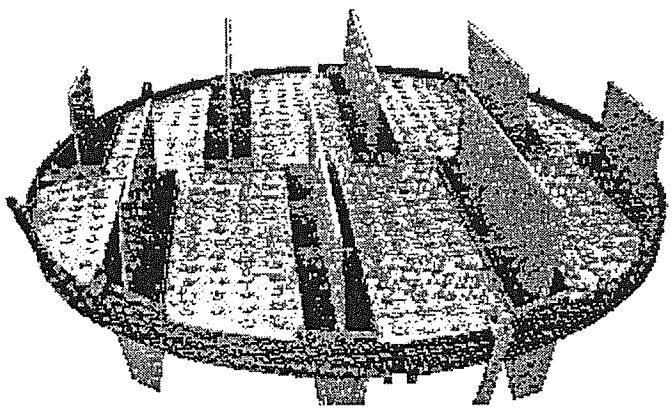

Fig. 2.5: UOP Multiple Downcomer Tray (MD-tray).

2.3 Conventional Tray Capacity Design

A complete distillation tray-column design is measured principally against two sets of criteria. These are the ability to carry out the separation function required, at the specified throughput and the capacity to run profitably. To ensure economic success, cost is generally used to optimise the design, with minimum cost usually taken as the optimum cost. In practice, the use of minimum hardware or column diameter will normally translate to minimum capital cost. Thus, the overall consideration in tray column design is to achieve the maximum vapour and liquid loading through the smallest possible column, without compromising the separation efficiency. The conventional design methodology to achieve this optimum sizing of tray columns is presented below.

2.3.1 Background Approach to Design

The conventional method of designing trays for a given hydraulic duty is based on empirical observation of tray flooding (Locket, 1986; Kister, 1992). The major consideration is to achieve a given vapour and liquid loading through the smallest possible column. The sizing procedure is a trial-and-error calculation where a preliminary design is set, and then refined by checking against the performance correlations until an "adequate and balanced" design is achieved. The objective is to arrive at an optimum combination of tray bubbling area, downcomer area and the number of passes on a tray in order to minimise the column diameter, and hence costs for a given separation duty.

It is worth noting that tray design, like most engineering design, is a combination of theory and practice. The design methods use semi-empirical correlatons derived from fundamental research work combined with practical examples obtained from the operation of commercial columns. With certain systems, traditional flooding correlations consistently predict higher flood points than those actually experienced. To allow for this discrepancy, a derating or system factor S may be applied to reduce the "flood factor", F. S is purely an empirical factor and usually set at 1.0, but can be as low as 0.5 (Locket, 1986). For example, a high-pressure depropanizer distillation column is derated by a factor of 0.9. The overall effect of the S factor is that a larger diameter column is required for the same hydraulic duty. This emphasises the empirical nature of tray design methods. The steps set out below are only an outline procedure and do not represent a complete guide for tray capacity design. Reference should be made to technical manuals or standard texts.

2.3.2 Stepwise Procedure for Tray Capacity Design

Step 1: Establish the necessary information. The crucial information required for optimum sizing of tray columns are the vapour and liquid mass flow rates and the density ratio between the two phases. These factors are used to relate practical experience of flooding to design values and are usually correlated as:

$$\text{Load factor, } C_S = u_s\left(\frac{\rho_V}{\rho_L - \rho_V}\right)^{0.5} \text{ and} \qquad \ldots. 2.2$$

Flow parameter, $F_{lv} = \frac{L}{G}\left(\frac{\rho_V}{\rho_L}\right)^{0.5}$ 2.3

Step 2: The turndown, exit weir height and hole area and diameter should be fixed based on experience in similar applications. Except in fouling and vacuum conditions, typical values for a sieve tray are: turndown, 60-70 percent of full loading; weir height, 40 to 50 mm; fractional hole area and hole size, 5-10 percent and 4.5 to 6.5 mm respectively (Sinnott, 1993; Locket, 1986; Kister, 1992). Larger holes sizes are desirable in operations where fouling or corrosion is likely to occur and lower weir heights are recommended to reduce pressure drop in vacuum operations. Lower turndown can be achieved but at the expense of pressure drop and often of increased tray spacing. Also, increasing the weir height will increase the tray efficiency but at the expense of pressure drop.

Step 3: Estimate the column diameter based on flooding consideration. A correlation such as those of Fair (1961) or Porter and Jenkins (1979) may be used. The flooding condition fixes the upper limit of vapour velocity and a value of 80 to 85 percent of the flooding velocity is usually recommended for design. Porter and Jenkins made use of a total flows chart based on 80% flood, from which the column diameter could be obtained directly.

The column cross-sectional area, A_T can then be calculated, $D = 2.\left(\frac{A_T}{\pi}\right)^{0.5}$

Step 4: Split the column into its three functional zones; the active area for mixing vapour and liquid, the downcomer area for moving liquid from one contacting tray to another and disengaging vapour from the liquid, and the vapour space between trays for separating the vapour from the liquid. The total flows chart (Porter and Jenkins, 1979) is based on a tray spacing of 0.6 m and this should be assumed if no previous experience exists. The downcomer area is calculated from the relation, $A_D = Q_L/U_{DF}.F$, where F is the flood factor. It is the usual practice to calculate the downcomer velocity at the fraction of flood from the following correlations and to use the lowest value as the design value,

$U_{DF} = 0.17$ m/s; $U_{DF} = 0.007(\rho_L - \rho v)^{0.5}$ m/s;

$U_{DF} = 0.008[T.S.(\ (\rho_L - \rho v)^{0.5})]$ m/s where T.S = Tray Spacing - m 2.4

The tray bubbling area A_B, can be obtained by difference, that is, $A_B = A_T - 2A_D$

Also, the bubbling area load factor, C_{SB} may be obtained from the following relation:

$$C_{SB} = u_{SB}\left(\frac{\rho_V}{\rho_L - \rho_V}\right)^{0.5} = \frac{G}{A_B[\rho_V(\rho_L - \rho_V)]^{0.5}} \quad \text{.... 2.5}$$

Step 5: Specify the weir load at the calculated values of A_T and A_D. The weir load is defined as the flow rate per unit length of weir, thus, $q/b = Q_L/F.b.N$, where N is the number of passes and b ($\geq 0.6D_T$) is a geometrical function of A_T and A_D. The limit for b is an empirical one, which is used to prevent liquid channelling and associated loss in efficiency.

Step 6: Using the jet flooding curve shown in Figure 2.6, identify C_{SBf} at the weir load q/b and calculate the vapour fractional flood.

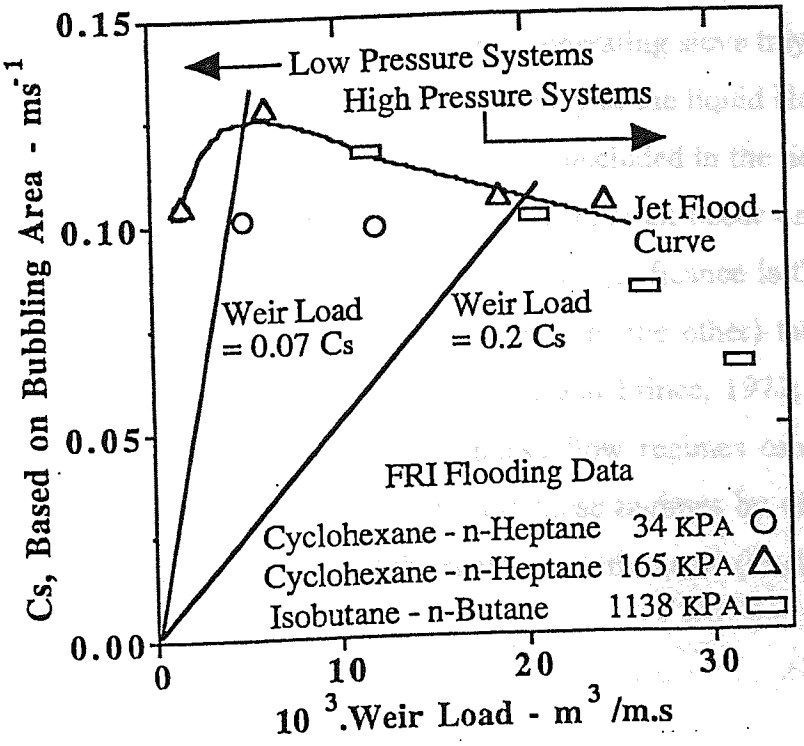

Fig. 2.6: Maximum capacity for an FRI sieve tray as an jet flood versus weir load plot

Step 7: Alter the design to produce the same fraction of flood for the bubbling area and downcomer. Compare this fraction of flood with that specified, and readjust the design until the specification is satisfied. For example, if the weir load is high, increase the number of passes by increasing the total weir length, b, which at the same time results in a slight decrease in A_B and an increase in C_{SB}. The overall aim at this stage is to achieve a balanced design by adjusting A_D and b in order to modify A_B so as to produce the same percent flood both in the downcomer and on the tray bubbling area. If necessary alter the column diameter and repeat the above steps until a balanced design is achieved.

2.4 Two-Phase Flow Regimes on Sieve Trays

The flow regime is the nature of the vapour-liquid dispersion on the tray and as with two-phase flow in closed channels, the flow on a sieve tray can be characterised by the amount of each phase in the dispersion and how they flow past each other. The type of flow regime on an operating tray is important because it dictates the hydrodynamic behaviour of the two-phase flow. Also, evidence exists where tray efficiency has been improved by designing the tray to operate in a more appropriate regime (Porter, Safekourdi and Lockett, 1977; Raper et al., 1984).

The structure of the vapour-liquid dispersion on an operating sieve tray ranges from those of a slightly aerated liquid having almost the same density as the liquid alone to those of a foam mass containing relatively large quantities of vapour occluded in the liquid, having a density much less than the liquid alone. The full spectrum may all occur on the same tray under different liquid and vapour flow rates. Of particular significance is the condition at which the phase inversion (the transition from one regime to the other) takes place (Porter and Wong, 1969; Burgess and Robinson, 1969; Payne and Prince, 1977; Pinczewski and Fell, 1972; Prince et al., 1979). In all, five two-phase flow regimes can be identified in tray distillation operation. Different authors describe these regimes by different names but the general characteristics and properties of the regimes are the same (Lockett, 1986; Zuiderweg, 1982).

2.4.1 The Bubble Flow regime

The bubble flow regime is uncommon in industrial applications but can be observed in bench-scale and pilot columns at relatively low gas velocities and thick liquid layers (Wallis, 1969; Abdell-aal, Stites and Holland, 1996). The regime is characterised by a clear liquid surface and fully submerged discrete bubbles. The bubble population has a wide size distribution as a result of a dynamic equilibrium between break up and coalescence involved in the chaotic turbulent motion. The bubbly liquid flows over the outlet weir into the downcomer where degassing takes place, a process that causes an upflow of gas out of the downcomer and may interfere with the downflow of liquid. The two-phase dispersion sitting in the downcomer usually has two strata, that is, a clear bottom layer with an upper bubbly layer. The bubble flow regime is a liquid continuous regime. A schematic diagram of the two-phase regime is shown in Figure 2.7a (Kister, 1992).

2.4.2 The Foaming Flow Regime

The foaming or cellular foam regime is also rarely observed in commercial applications and like the bubbly regime occurs at low gas velocities and thick liquid layers (Calderbank and Rennie, 1962; Calderbank, 1975; Ho, Muller and Prince, 1969; Steiner, Hunkeler and Hartland, 1977). The difference with the bubbly flow regime is caused by inhibition of bubble coalescence, as break up of liquid films in between the bubbles is retarded by the presence of surface tension gradients, very fine solids, or a high liquid viscosity. The bubbles distorted to polyhedra rise unbroken to the top of the dispersion, resulting in a structure of typical foam with fairly stable liquid lamella in between bubbles of various sizes. This leads to an increased residence time of the gas in the dispersion, thus giving rise to a high gas content. The foamy liquid falling over the outlet weir into the downcomer takes along a large amount of gas, as a result of the inhibited bubble coalescence and hampered degassing. A much larger amount of gas now becomes available from the degassing process in the downcomer, giving rise to a larger upflow of gas out of the downcomer, which can interfere even more strongly with the volumetricly enlarged foamy liquid. Thus leading to earlier inducement of choking phenomena and hence premature flooding of the downcomer.

The two-phase dispersion sitting in the downcomer again has two strata, but their relative contributions differ. The upper bubbly (foamy) layer is enlarged, as an enlarged gas flow has to be separated, while the separation takes more time as well. Very small bubbles may not separate at all and can be carried under the downcomer lower edge, with the liquid leaving the downcomer exit. A schematic diagram of the two-phase regime is shown in Figure 2.7b.

2.4.3 The Froth Flow Regime

The froth regime is the most common operating regime in distillation practice and is some times referred to as the "mixed" or "sandwiched" regime, as it is intermediate to both the bubbly regime and the spray regime (Hofhuis and Zuiderweg, 1979; Prado, Johnson and Fair, 1987). In the structure of this two-phase dispersion, these regimes can still be identified: the bubbly regime in the bottom layer and the spray regime in the upper layer. Often, an approximately uniform intermediate layer is present as well. The dispersion is very chaotic and full of fluctuations of many sizes and frequency scales. The 'bubbly' size distribution is even wider than in the bubbly flow regime, as now large clusters of bubbles or even 'slugs' (large voids) of non uniform shape can be seen rising at high velocity through the two phase layers. As the gas velocity increases, jetting begins to replace bubbling in some holes. When jetting becomes the dominant mechanism, the dispersion changes from froth to spray. Prado, Johnson and Fair (1987) showed that this change is gradual and that the transition from froth to spray does not take place until jetting replaces bubbling in at least 45 percent of the tray holes. The liquid flow passing into the downcomer entrance is composed of a part contributed by drops thrown over the weir (out of the spray layer) and a part contributed by a disintegrating bubbly liquid flowing over it (out of the liquid continuous bottom layer). Their relative contributions vary, depending on the operating conditions and the specifics of the outlet weir geometry. Again, the dispersion in the downcomer has a two-layered structure, with a bubbly upper layer and a fairly clear liquid layer at the bottom. A schematic diagram of the two-phase regime is shown in Figure 2.7c.

2.4.4 The Spray Flow Regime

The spray regime frequently occurs in industrial practice and is produced at relatively high gas velocities and thin liquid layers (Porter and Wong, 1969). The regime is gas phase continuous and is characterised by random movement of droplets at the surface and partially submerged jets or bubbles at the bottom. The high velocity of the gas flowing out the perforations in the tray floor atomises the liquid and accelerates the droplets upward. The droplet population has a wide size distribution and a fraction of the very smallest droplets is dragged along by the gas flow and carried away to the next higher tray, as droplet entrainment (or carry over). The liquid passes into the downcomer entrance by splashing over the outlet weir. Hence a cloud of droplets rains down in and impacts on the liquid surface in the downcomer. On impact some gas is entrained and bubbles forming from entrained gas are dragged down for some distance, before they escape the impacting liquid flow and rise up and separate. A schematic diagram of the two-phase regime is shown in Figure 2.7d.

2.4.5 The Emulsion Flow Regime

The emulsion flow regime occurs at high liquid loads, usually corresponding to high-pressure operations where the shearing action of the high velocity liquid bends the gas bubbles as they emerge from the orifices. The emulsion regime is a uniform mixture in which the vapour is emulsified as small bubbles within the liquid. Here, the liquid phase is considered to be continuous while the gas phase is in fine dispersion (Hofhuis and Zuiderweg, 1979). A schematic diagram of the two-phase regime is shown in Figure 2.7e.

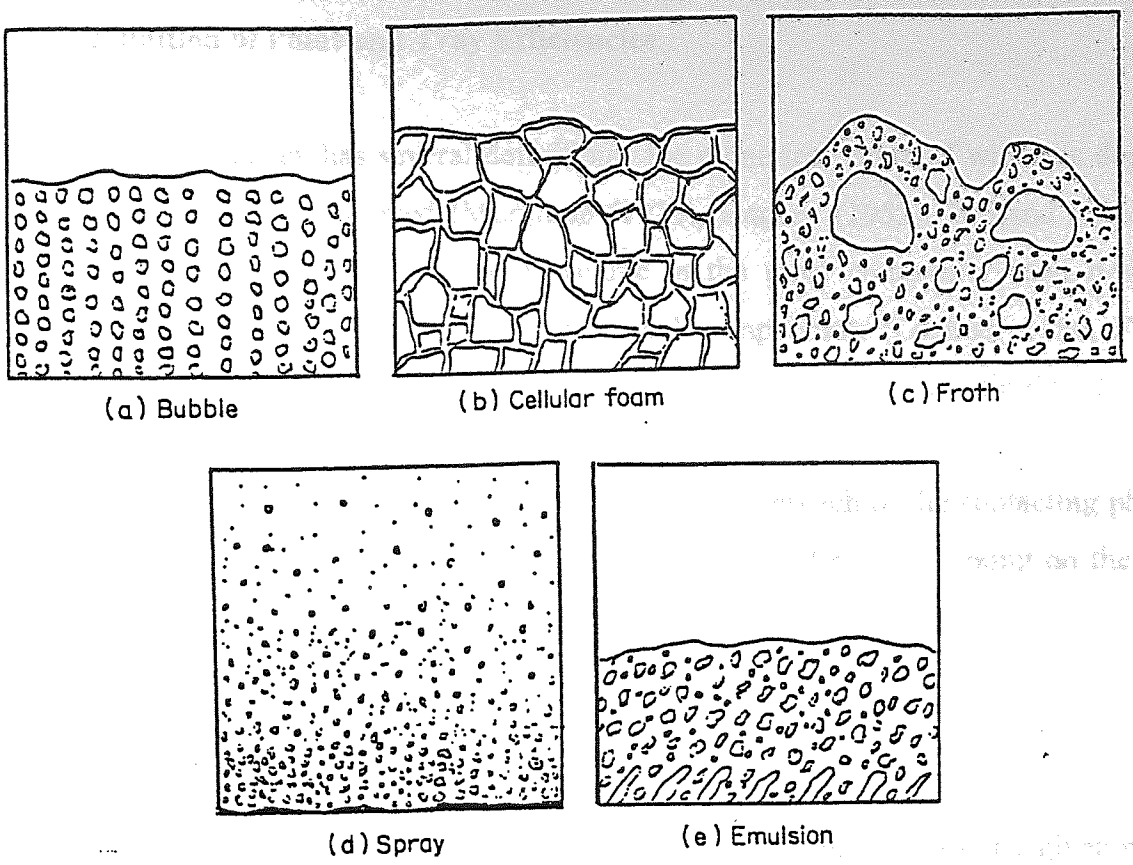

Fig. 2.7: Common Flow Regimes on Distillation Trays

2.5 Modelling of Tray efficiency

Sieve tray-column designs are based on the assumption that each sieve tray is a theoretical one or the so-called ideal tray on which vapour and liquid are completely mixed with the result that the vapour and liquid exit streams are in equilibrium. This is not the true representation of the condition on a tray. There is a limited amount of contact time between liquid and vapour so that only a fractional approach to equilibrium is actually achieved. Although the transport processes between the phases are complex, this approach to equilibrium can be defined by an efficiency term - the tray efficiency. While the number of theoretical trays can be calculated accurately with modern computer methods, the method for predicting tray efficiency does not always give satisfactory results. The ability to estimate tray efficiency is very important, since tray efficiency is used to convert the number of theoretical trays to actual trays ($E_o = N_T / N_A$) and the savings in the capital and operation costs may be remarkable.

2.5.1 Definition of Point and Tray Efficiencies

The term tray efficiency has several definitions, the numerical value of which is dependent on the figure of merit employed (Murphree (1925), Hausen (1953), Holland (1963), and Standart (1965)). The definition by Murphree is the most commonly used despite its limitations with respect to accuracy in numerical computation (Lockett, 1986, Fletcher, 1987).

The Murphree concept of efficiency is a measure of the approach of the contacting phases to a state of maximum separation or equilibrium and can be defined for a point on the tray or for the entire tray based upon the liquid or the vapour composition.

Murphree Point Efficiency

Consider a general tray n, numbered from the bottom of the column. At any given point on the tray, the mass transfer achieved between the liquid and the vapour entering and leaving that point relative to the equilibrium state is defined as the point efficiency, E_{og}. In terms of vapour composition

$$E_{og} = \frac{y_n - y_{n-1}}{y_n^* - y_{n-1}} \qquad \ldots. 2.6$$

where y_n and y_{n-1} are the compositions of the vapour leaving and entering the given point respectively and y_n^* is the composition of the vapour which would be in equilibrium with the liquid of composition, x_n at that point.

Murphree Tray Efficiency

The over-all tray efficiency, E_{mv}, is the ratio of the actual change in the average vapour composition to the change that would occur if the vapour and liquid leaving the tray were in equilibrium with one another. In terms of vapour composition this can be represented as,

$$E_{mv} = \frac{\bar{y}_n - \bar{y}_{n-1}}{y_n^* - \bar{y}_{n-1}} \qquad \ldots. 2.7$$

where $\bar{y}_n$ and $\bar{y}_{n-1}$ are the average vapour composition leaving and entering the tray respectively and y_n^* is the average vapour composition which would be in equilibrium with the liquid leaving tray n with average composition $\bar{x}_n$.

For liquid phase controlled mass transfer systems, the Murphree tray efficiency based on the liquid composition, E_{ml}, may be preferred. In terms of liquid compositions

$$E_{ml} = \frac{\bar{x}_n - \bar{x}_{n+1}}{x_n^* - \bar{x}_{n+1}} \qquad \ldots. 2.8$$

where $\bar{x}_n$ and $\bar{x}_{n+1}$ are the average compositions of the liquid leaving and entering the tray respectively and x_n^* is the composition of the liquid which would be in equilibrium with the vapour actually leaving the tray with average composition, $\bar{y}_n$.

Based on their definitions, the liquid and vapour efficiencies can be converted from one to the other: if the gradient of the operating line is constant and the equilibrium line is also straight over the composition range involved, such that

$$y_n^* = m\bar{x}_n + b \qquad \ldots. 2.9$$

and $$\bar{y}_n = mx_n^* + b \qquad \ldots. 2.10$$

then it can be shown that

$$E_{ml} = \frac{\lambda E_{mv}}{1 + (\lambda - 1) E_{mv}} \qquad \ldots. 2.11$$

where λ is the ratio of the slope of the equilibrium line to the slope of the operating line.

2.5.2 Tray Efficiency Models

The literature contains several conceptual representation of tray functioning from which mathematical models are based for the prediction of tray efficiency (Murphree, 1925; Kirschbaum, 1934; Lewis, 1936; Gautreaux and O'Connell, 1955, Gerster, 1958; Porter et al., 1972). The main factors that affect the magnitude of tray efficiency are rates of mass transfer in the gas and liquid phases, degree of mixing in the dispersion, and the magnitude of the liquid entrainment between trays (AIChE, 1958). These factors depend in turn upon the physical properties of the vapour-liquid system, the design of the tray, and the hydrodynamics of vapour and liquid flows. In the development of a tray efficiency model, the most difficult step is the mathematical representation of the degree of mixing and the type of flow pattern that take place on the tray. Accordingly, tray models are arbitrarily classified according to the type of mixing concept or flow-structure they adopt. Generally, three different types of models can be identified in the literature and are reviewed here as:

(i) Completely mixed model.

(ii) Plug flow model.

(iii) Intermediate model.

Completely Mixed Model

In the early modelling of tray behaviour it was generally assumed that the action of rising vapour was sufficient to mix completely the froth on the tray such that a uniform liquid composition is achieved. If this were the case, then the liquid composition at any point will be the same as that of the liquid leaving the tray. For a completely mixed tray the point and tray efficiency becomes identical ($E_{og} = E_{mv}$), under uniform vapour flow.

Experimental evidence did not, however, support the assumption of a completely mixed tray. Even at high superficial vapour velocities significant liquid concentration gradients were reported on a tray of only few inches in diameter (Kirschbaum, 1934). This observation was to lead to the development of alternative models.

Plug Flow Model

Since the assumption of a perfectly mixed tray proved to be poor and lead to incorrect implications regarding tray efficiency, Lewis (1936) proposed that the liquid crossed the tray in a plug flow fashion. With the aid of simplifying assumptions he obtained equations that showed the tray efficiency resulting from various conditions of flow. His equations have been widely used and are the basis for most of the analysis between point efficiency and overall tray efficiency. The model is applied to a rectangular tray and has three analytical cases, usually referred to as cases I, II and III, the flow schemes of which are depicted in Figure 2.8. In general, Lewis theory demonstrates that in the absence of perfect mixing, the tray efficiency, as ordinarily defined, becomes higher than the point efficiency and in favourable circumstances may exceed 100%. However, the enhancement of the tray efficiency over the point efficiency on an actual tray is expected to be less than predicted due to liquid and vapour nonuniformities and liquid mixing. The tray efficiency is greater when the liquid flowed parallel (case II) than in opposite (case III) direction as it descends from tray to tray.

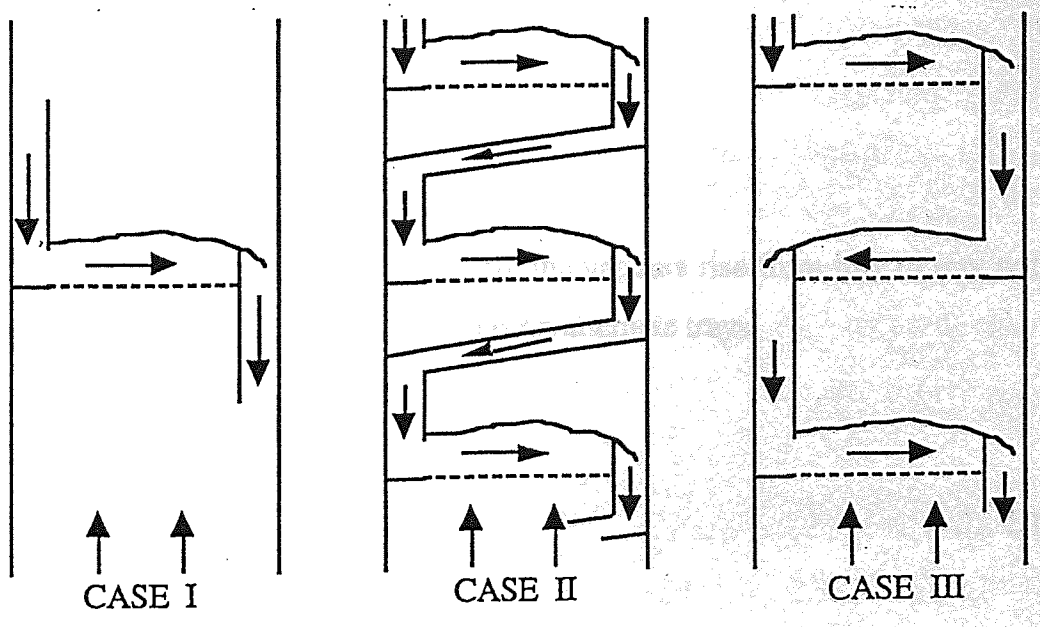

Fig. 2.8 Representation of the flow schemes for the three cases of the Lewis models

Lewis Case I

The first case describes the tray efficiency where the vapour enters the tray completely mixed and the direction of liquid flow on successive trays is inconsequential. The resulting equation is:

$$E_{mv} = \frac{\exp(\lambda E_{og}) - 1}{\lambda} \qquad \text{.... 2.12}$$

Lewis Case II

Lewis case II describes the tray efficiency where the vapour rises from tray to tray without mixing and liquid flows in the same direction on all trays. The relationship between the tray efficiency and the point efficiency is as follows:

$$E_{mv} = \frac{\alpha - 1}{\lambda - 1} \qquad \text{.... 2.13}$$

$$\text{where } \lambda = \left[\frac{1}{E_{og}} + \frac{1}{\alpha - 1}\right] \ln\alpha \qquad \text{.... 2.14}$$

Here α is the relative volatility.

Lewis Case III

Lewis case III describes the tray efficiency where the vapours rise from tray to tray without mixing and the liquid flows in opposite directions on alternate trays.
The resulting equation is:

$$E_{mv} = \frac{\alpha - 1}{\lambda - 1} \qquad \text{.... 2.15}$$

where, if $\alpha < 1$,

$$\lambda=\left[\frac{\alpha^2-(1-E_{og})^2}{E_{og}^{\ 2}(1-\alpha^2)}\right]^{0.5}\cos^{-1}\left[1\frac{(1-\alpha)(\alpha-1+E_{og})}{\alpha(2-E_{og})}\right] \quad \ldots. 2.16$$

and if $\alpha>1$,

$$\lambda=\left[\frac{\alpha^2-(1-E_{og})^2}{E_{og}^{\ 2}(\alpha^2-1)}\right]^{0.5}\cosh^{-1}\left[1+\frac{(\alpha-1)(\alpha-1+E_{og})}{\alpha(2-E_{og})}\right] \quad \ldots. 2.17$$

Intermediate Models

The assumption of a completely mixed or plug flow dispersion does not accurately represent the reality of what takes place between the liquid and vapour on an active distillation tray. The various intermediate models are the most realistic and ambitious of the tray efficiency models as they try to give appropriate quantitative value to the degree of mixing on the tray, rather than use inaccurate simplifications. The intermediate models can also be called the partially mixed models, as they are intermediate to both the completely mixed and plug flow models. They exist in two major types, those based on a mixed pool theory and those based on eddy diffusion theory.

Series of Mixed Pools (SMP)

The mixed pool model is the first departure from the limiting cases of completely mixed and plug flow trays. The idea was mooted by Kirschbaum (1948) but extended mathematically by Gautreaux and O'Connell (1955) who derived an expression for the tray efficiency. In the SMP model, the liquid on the tray is divided into a number of hypothetical pools, each consisting of completely mixed liquid. The liquid moved from pool to pool, changing composition as it crosses the tray, and for a series of n pools the relationship between E_{mv} and E_{og} is given by:

$$\frac{E_{mv}}{E_{og}}=\frac{1}{\lambda E_{og}}\left[\left(1+\frac{\lambda E_{og}}{n}\right)^n-1\right] \quad \ldots. 2.18$$

The number of pools, n, represents the degree of mixing in the liquid. For a completely mixed tray, n = 1, the tray efficiency simply reduces to the point efficiency, i.e, $E_{mv} = E_{og}$. For the other limiting case of plug flow, $n = \infty$, equation (2.18) reduces to the well-known Lewis case I. A major drawback in the model is that it is difficult to quantify n under various conditions of mixing. However, Ashley and Heselden (1970) have obtained numerical solutions for Lewis' cases II and III, using this concept.

Backmixing imposed on plug flow

Another approach to the problem of liquid mixing on distillation trays is based on the supposition that mixing takes place by an eddy-diffusion mechanism. This was pioneered by Gerster et al. (1955 and 1958) and has since found wide application in the methodology for estimating tray efficiency. There are several generations of this model (AIChE, 1958; Porter et al., 1972; Bell and Solarin, 1974; Biddulph, 1975; Sohlo and Kouri, 1982; Chan and Fair, 1984; Yu et al., 1990), some of which allow for eddy diffusion in two directions on the tray. Detailed below is the AIChE method for the imposition of eddy diffusion mechanism on liquid plug flow for the purpose of predicting distillation tray efficiency. The procedure was the direct offshoot of the pioneering work by Gerster and is based upon the modern interpretation of the two-resistance film theory. All the correlations used are as recommended in the AIChE design manual.

The method requires a number of user's supplied values, these and the nomenclature used in the method are given below for convenience. It must be noted that the system of units used is the American system.

Q_l	liquid flowrate	[gpm]
Q_v	vapour flowrate	$[ft^3s^{-1}]$
W	average width of liquid flow	[in]
A	active area	$[ft^2]$
D_l	liquid molar diffusivity	$[ft^2hr^{-1}]$
h_w	weir height	[in]

d_c	bubble cap diameter	[in]
Δ	liquid gradient across tray	[in liquid]
λ	slope of the equilibrium line divided by slope of the operating line	[-]
ρ_l and ρ_v	liquid and vapour densities	[lbft^{-3}]

Step 1: calculate the liquid phase resistance to mass transfer, N_l [-]

$$N_l = 103(D_l)^{0.5}(0.26F + 0.15)\theta_l \quad \text{.... 2.19}$$

where $$\theta_l = \frac{37.4 h_{cl} A}{Q_l} \quad \text{.... 2.20}$$

$$h_{cl} = \frac{103 + 11.8 h_w - 40.5F + 1.25\frac{Q_l}{W}}{\rho_l} \quad \text{.... 2.21}$$

$$F = U_s(\rho_g)^{0.5} \quad \text{.... 2.22}$$

and $$U_s = \frac{Q_v}{A} \quad \text{.... 2.23}$$

Step 2: Calculate the vapour phase resistance to mass transfer, N_g [-]

$$N_g = \left[\frac{\rho_g D_g}{\mu_g}\right]^{0.5}\left(0.776 + 0.116 h_w - 0.290F + 0.0217\frac{Q_l}{W} + 0.200\Delta\right) \quad \text{.... 2.24}$$

Step 3: Combine the liquid and vapour phase resistances to obtain a value for the overall mass transfer resistance, N_{og} [-],

$$\frac{1}{N_{og}} = \frac{1}{N_g} + \frac{\lambda}{N_l} \quad \text{.... 2.25}$$

Step 4: The point efficiency is calculated from the overall mass transfer resistance,

$$E_{og} = 1 - \exp(-0.434\, N_{og}) \qquad \text{.... 2.26}$$

Step 5: Calculate the eddy diffusivity coefficient, D_e [$ft^2 s^{-1}$],

$$D_e = [1 + 0.044(d_c - 3)]^2 \left[0.0124 + 0.015 h_w + 0.017 U_s + 0.0025 \frac{Q_l}{W} \right]^2 \qquad \text{.... 2.27}$$

Step 6: Calculate the Peclet number, Pe [-]

$$Pe = \frac{Z_l^{\,2}}{D_e \theta_l} \qquad \text{.... 2.28}$$

then,
$$\frac{E_{mv}}{E_{og}} = \frac{1 - e^{-[\eta + (Pe)]}}{[\eta + (Pe)]\left[1 + \frac{\eta + (Pe)}{\eta}\right]} \cdot \frac{e^{\eta} - 1}{\eta\left[1 + \frac{\eta}{\eta + (Pe)}\right]} \qquad \text{.... 2.29}$$

where
$$\eta = \left(\frac{Pe}{2}\right)\left(\sqrt{1 + \frac{4\lambda E_{og}}{(Pe)}} - 1\right) \qquad \text{.... 2.30}$$

Step 7: As the mathematical relationship (equation. 2.29) between E_{mv}, E_{og}, λ and (Pe) is fairly complex and somewhat cumbersome to use, the Murphree tray efficiency may be found graphically knowing the values of λE_{og} and Pe. See AIChE (1958).

2.5 .3 Hypothetical Liquid Flow Patterns

Apart from liquid mixing the other phenomenon that is of central importance in the modelling of tray efficiency is the liquid flow pattern. That is the manner in which the liquid crosses the tray from inlet to outlet. Ideal flow is taken to mean the uniform unidirectional movement of liquid from the tray inlet to outlet, where lines of constant residence time (RT) would be parallel to the outlet weir. Deviations from this behaviour are characterised as non-ideal liquid flow or liquid maldistribution. In this case, the liquid flow is non-uniform and multidirectional due to velocity gradients across the tray, arising from hydraulic imbalances or from flow path of different lengths due to the tray geometry.

The effect of these flow non-uniformities on tray efficiency has been widely studied, with the consensus that liquid flow maldistribution has a significant detrimental effect on the efficiency of large diameter trays (Porter et al., 1972; Bell 1972).

Several hypothetical liquid flow patterns have been proposed to explain these effects among which are the stagnant regions and the retrograde flow models.

Stagnant Regions Model

The stagnant regions model (SRM) was developed by Porter et al. (1972), based on results of a photographic study of froth behaviour on a 1.2 m diameter tray. The liquid entering the tray section flows directly across a rectangular zone (region I) delineated by the shortest route between the inlet and outlet weirs, and the diverging and converging tray sections (region II) at the edges of the tray were considered macroscopically stagnant. A schematic diagram of the stagnant regions model is shown in Figure 2.9.

Eddy diffusion is assumed to be the only mechanism by which exchange of material between the dead liquid zones (region II) and main flow zone (region I) take place. For large diameter columns (>5 ft) diffusional mixing was considered ineffectual in maintaining fresh liquid in the stagnant regions, with the result that only a fraction of the efficiency achievable under ideal flow conditions is realised. The reduction in efficiency is expected to be even more drastic in a multi-tray situation where stagnant regions would be stacked above each other, and where, without vapour mixing between trays, the vapour passing through the successive stagnant regions would pass up the column unrectified.

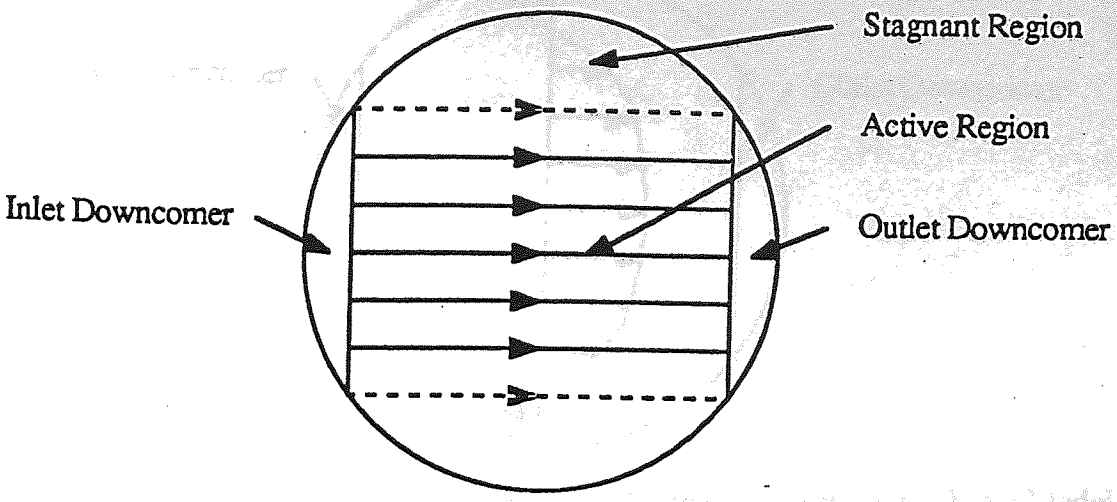

Fig. 2.9: Hypothetical Flow Pattern: Schematic Diagram of the Stagnant Regions Model.

Retrograde Flow Model

The retrograde flow model was proposed by Bell (1972) based upon fibre-optic studies carried out on a 2.44 m diameter air-water test tray. Measurement of concentration profiles showed the expected gradual concentration changes in the direction of the liquid flow in the middle part of the tray; however in the tray segments outside the "weir to weir" area retrograde concentration profile was observed. These results also matched the residence time distribution on the tray where lines of constant residence time revealed closed loops adjacent to the tray wall. The explanation of the closed isolines was for reverse or retrograde flow to be occurring at the sides of the tray, with high-speed flow down the centre of the tray between the weirs. It was found that these profiles are caused by a lack of spreading of the liquid flow issuing from the downcomer, and from the contraction of the flow towards the outflow weir.

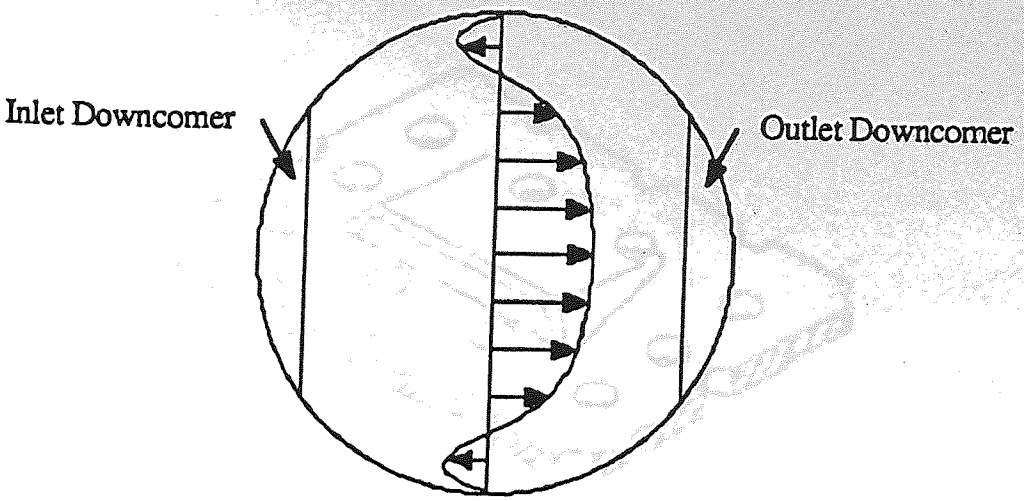

Fig. 2.10: Hypothetical Flow Pattern: Schematic Diagram of the Retrograde Flow Model.

2.6 Flow Control Devices

The tendency for various types of flow nonuniformities to increase as tray diameter increases has been well established and several previous works support the view that liquid flow pattern on distillation trays is of importance in determining tray efficiency (Porter et al., 1972; Bell 1972). In particular, liquid channelling is thought to be the major contributor to the fall-off (or even failure) in tray efficiency as column diameter increased and several methods have been suggested whereby the gas and liquid flows on the tray can be controlled to mitigate these problems. Some of the techniques employed include modifying the tray area, downcomer area or the weir shape in order to obtain better liquid distribution.

2.6.1 The Slotted Sieve Tray

The use of slots to straighten and improve the liquid flow pattern on sieve trays was developed by UOP Processing Equipment Group (formerly Union Carbide) as patented by Williams and Yendall (1963 and 1968), Matsh (1973) and Kirkpatrick and Weiler (1978). This tray has angled slots punched at various points to deflect some of the vapour and use the horizontal momentum to drive the liquid across. A typical slot design is shown in Figure 2.11.

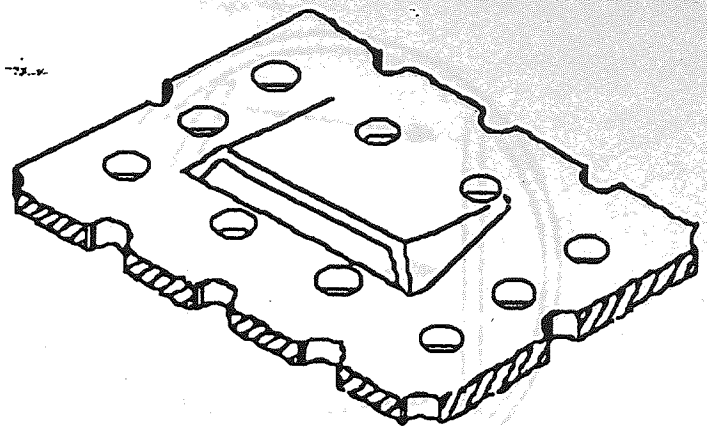

Fig. 2.11: Single Slot as used on Sieve Trays.

2.6.2 The FRI Downcomer

The use of varying and notched downcomer clearance design to improve liquid flow distribution was developed by Fractionation Research Incorporated (FRI) as patented by Keller (1973). The FRI Downcomer has a variable clearance along the length of the inlet weir such that the gap size at the ends of the weir is higher than at the centre, to allow preferential liquid flow. The outlet weir is made of carefully distributed notches, also to allow for a preferential liquid flow off the tray at certain positions along its length. The drawback of this design is that the modification is specific for particular flow rates and may not work well for general design conditions.

2.6.3 The Swept-back Downcomer

The swept-back or winged downcomer design is a patent of BOC Group (Levin, 1986), see Figure 2.12. The winged weir increases the weir length to diameter ratio, with the result that the flow path lengths from all positions along the inlet weir are made more uniform. This arrangement coupled with a varying hole density is expected to provide sufficient liquid momentum at the sides of the tray to mitigate the development of non-forward liquid flows at the sides of the tray.

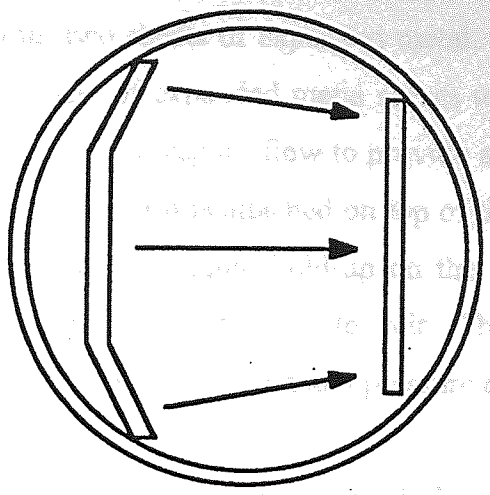

Fig. 2.12: Winged Downcomer.

2.6.4 The Inclined Counter-Current Contact Tray

The slanting of the tray deck in the direction of liquid flow has been reported to minimise the maldistribution of liquid flow on distillation trays (Monovyan and Gaivanskii, 1980). However, the use of forward tilting tray may lead to reduced liquid residence time and encourage vapour channelling with increased possibility of vapour collapse at some sections of the tray. Hine (1990) proposed the use of inclined counter-current tray as a solution to the problems in the 'inclined only' tray. It is expected that the opposing movement of the gas and liquid will improve liquid residence time and reduce hydraulic gradient on the tray. Figure 2.13 presents a sketch of the inclined counter-current tray arrangement.

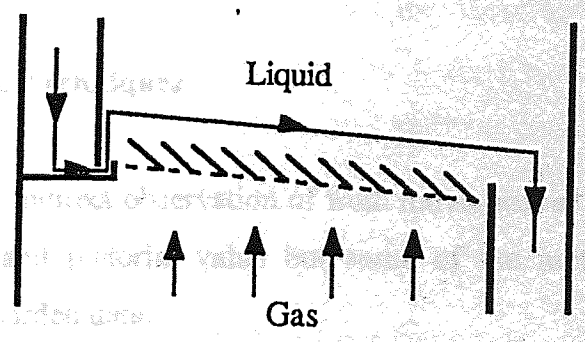

Fig. 2.13: Sketch of Inclined Counter-Current Tray.

2.6.5 Double Expanded Metal (BOC) Tray

The double expanded metal tray is another patent design of BOC Group (Biddulph et al., 1990). The tray is formed from two sheets of expanded metal, one with fine slots and the other a course grid. The fine sheet of expanded metal serves to support the biphase, with slots aligned in such a way as to use the vapour flow to provide additional momentum to the liquid cross flow. The second coarse grid is attached on top of the lower sheet of expanded metal and serves to maintain a uniform liquid hold-up on the tray and induce prolonged vapour-liquid contact time by acting as an intermediate weir. The design was for cryogenic distillation of air, which requires a low tray spacing and pressure drop.

2.7 Investigative Techniques for Determining Liquid Flow Patterns on Trays

The study of liquid flow distribution on distillation trays has proceeded over a considerable period of time, leading to the establishment of various experimental techniques for the investigation of the liquid flow patterns across the tray. The following investigative techniques are reviewed below:

(i) Flow visualisation techniques.

(ii) Measurement of residence time distribution.

(iii) Water-cooling technique

(iv) Direct froth velocity measurement.

(v) Applications of computerised fluid dynamics.

2.7.1 Flow Visualisation Techniques

This involves the direct or indirect observation of froth movement as it flows across tray. It is mainly of qualitative and pictorial value but some of the methods have options of quantitative analysis of recorded data.

Dye on Tray Techniques

The use of coloured dye to monitor liquid flow on experimental trays was a highly popular technique among many researchers (Weiler et al., 1971, 1973; Aleksandrov and Vybronov, 1971; Porter et al., 1972; Solari et al., 1982). Essentially two versions of the technique are used. These are the pulsed and continuos injection techniques. The continuous technique is generally used to demonstrate the presence of flow non-uniformities over the tray while the pulsed version is favoured to obtain raw data for constructing residence time distributions. In the continuous version, dye is continuously injected onto the tray until the biphase is completely coloured. The dye injection is then stopped and the removal of dye by clear liquid entering the tray is monitored visually or by an overhead video camera. The areas where the dye remains longest are interpreted as areas of extended residence times. One disadvantage of this version is that it consumes large volume of liquid, since the coloured liquid cannot be recycled. In the pulsed version a pulse of dye is injected perpendicular to the flow path length and its movement is monitored using an overhead video camera or sampled periodically. The variation of dye concentration in the tray effluent is determined as a function of time. The concentration versus time plots, usually expressed in dimensionless form, yields the RTD of the dye on the test tray.

Floating Balls and Camera

The use of floating balls and a camera is another visual technique to show the presence of non-uniform liquid flow. Deviations from ideal liquid flow have been illustrated by observing the motion of semi-buoyant table tennis balls on open channel water flume (Porter et al., 1972; Lim et al., 1974; Lockett and Safekourdi, 1976; Sohlo and Kinnunen, 1977). The cine-photographs of the experiment showed that the liquid exhibited the tendency to flow directly across a rectangular path delineated by the shortest route between the inlet and outlet weirs while the liquid at the edges of the tray showed tendency towards slow and reverse movement.

Direction Flow-Pointer Technique

The direction flow-pointer technique is a novel technique that was devised by Hine (1990) for investigating the flow pattern of a bubbly mixture on sieve trays. It is based on the same principle as the wind vane, and leads to a quick and clear visual indication of the flow direction at different points on the tray. Several of such flow vanes can be used to monitor the direction of flow at strategic positions on the tray. This can be monitored visually or by an overhead video camera and has been used to study the conditions that induce or favour non-ideal flow on trays (Chambers, 1993; Fenwick, 1996).

2.7.2 Measurement of Residence Time Distribution

Fibre Optic Technique

The use of fibre optic technique for flow distribution studies was pioneered by Bell (1972a, 1972b) using an n-haxane/toluene system on a 2.44 m diameter sieve tray. The technique is based on the use of fibre-optic probes to detect the presence of a fluorescent tracer that has a rapid activation and decay time. The procedure involves the injection of a pulse of fluorescent dye at a point or points on a tray and monitoring its progress across the tray using an array of fibre optic probes strategically placed over the tray area. The residence time and variance of the dye residence obtained from fluorescent responses of the dye at each point on the tray are used to construct a residence time distribution over the entire tray and estimate localised mixing at each point. The technique has the advantage that it can be used in real columns processing hazardous mixtures.

Salt Tracer (Conductivity) Technique

This is similar to the fibre optic technique except that sodium chloride is used in place of a rapid decaying fluorescent material to complement the change from optic probe to conductivity probe. This technique was extensively used by Yu et al. (1982, 1986, 1990) as published in a series of research papers to validate his mathematical models where liquid velocity, liquid concentration and diffusional mixing change in two dimensions instead of one.

2.7.3 Water-cooling Technique

The water-cooling technique makes use of the analogy between heat and mass transfer as applied to the cooling of hot water by rising air current in a crossflow fashion. The heat transfer is monitored by an array of temperature probes and lines of constant temperatures are constructed. Lines of constant temperatures are interpreted as lines of constant residence time and the regions with lower temperatures are those of extended residence times. The water cooling technique is a powerful tool for the investigation of liquid flow patterns and their effects on mass transfer. Stichlmair et al. (1973 and 1987) first used the technique to investigate the effect of tray out-of-levelness as well as changes in tray downcomers. Porter et al. (1982) extended the technique to enable the calculation of Murphree-based thermal efficiencies, a procedure repeated by his co-workers (Enjugu, 1986; Ani, 1988; Porter et al. 1987).

2.7.4 Direct Froth Velocity Measurement

Direct froth velocity measurement was developed by Biddulph and Bultitude (1990) and relies on the fact that the momentum of the froth introduces a strain into a flat titanium probe installed in the froth. A network of strain gauges is used to convert the strain into an electrical signal, the magnitude of which is dependent on the froth velocity. Appropriate calibration data are used to convert the electrical signal into froth velocity measurements.

2.7.5 Application of Computerised Fluid Dynamics

Computational Fluid Dynamics, CFD, uses the numerical solution of the governing equations which describe fluid flow, the set of the Navier-Stokes equations to solve for detailed flow lines, velocity gradients, pressure gradients and enthalpy throughout a complex physical system. The attraction of the approach is twofold. Firstly, the desire to be able to model physical fluid phenomena that cannot be easily simulated or measured with a physical experiment, for example, where the equipment used is much too large to be the subject of experimental investigations. Secondly, the desire to be able to investigate physical fluid systems more cost-effectively and more rapidly than with experimental procedures.

CFD is now applied to almost every branch of fluid dynamics and has experienced great success in such areas as heat-transfer, fluid mixing, combustion and reactor equipment design. However, only limited application has been made in the area of mass-transfer equipment and separation equipment design where there is much interest in the possibility of predicting flow patterns by computational fluid dynamics. If this could be done it would be possible to develop new and improved shapes of column internals with greater confidence. Also, apart from impacting positively on design by shortening lead times from research to final plant design, it can help to enhance energy and separation efficiency.

CHAPTER THREE

Description of the Apparatus

3.1 Introduction

This chapter presents a full description of the test facility used for the experimental programme reported in this thesis, including the error analysis associated with the measuring instruments. The procedures for data acquisition and processing are contained in Chapter 4.

The heart of the pilot facility is a 2.44 m diameter air-water distillation simulator. The ancillary units include the pumping and heating and exchange systems as well as the circuitry for air and water supply. Other minor peripheral units include the measuring and recording instrumentation.

3.2 Overall Test Facility

A schematic diagram of the overall test facility is shown in Figure 3.1. The commercial scale pilot plant incorporates a 2.44 m diameter aluminium and steel column, a 150 HP air fan, two 0.5 MW process heaters and a steam top-up facility. The overall design specifications of the ancillary units are summarised in Table 3.1. The test facility is equipped for the direct observation and recording of liquid flow patterns, the measurement of concentration profiles and mass transfer efficiency in the form of temperature profiles and thermal point and tray efficiencies, and the measurement of clear liquid height variation on the test tray.

The procedures used in the design and construction of the facility are given elsewhere (Hine, 1990). An up-to-date description of the facility now follows.

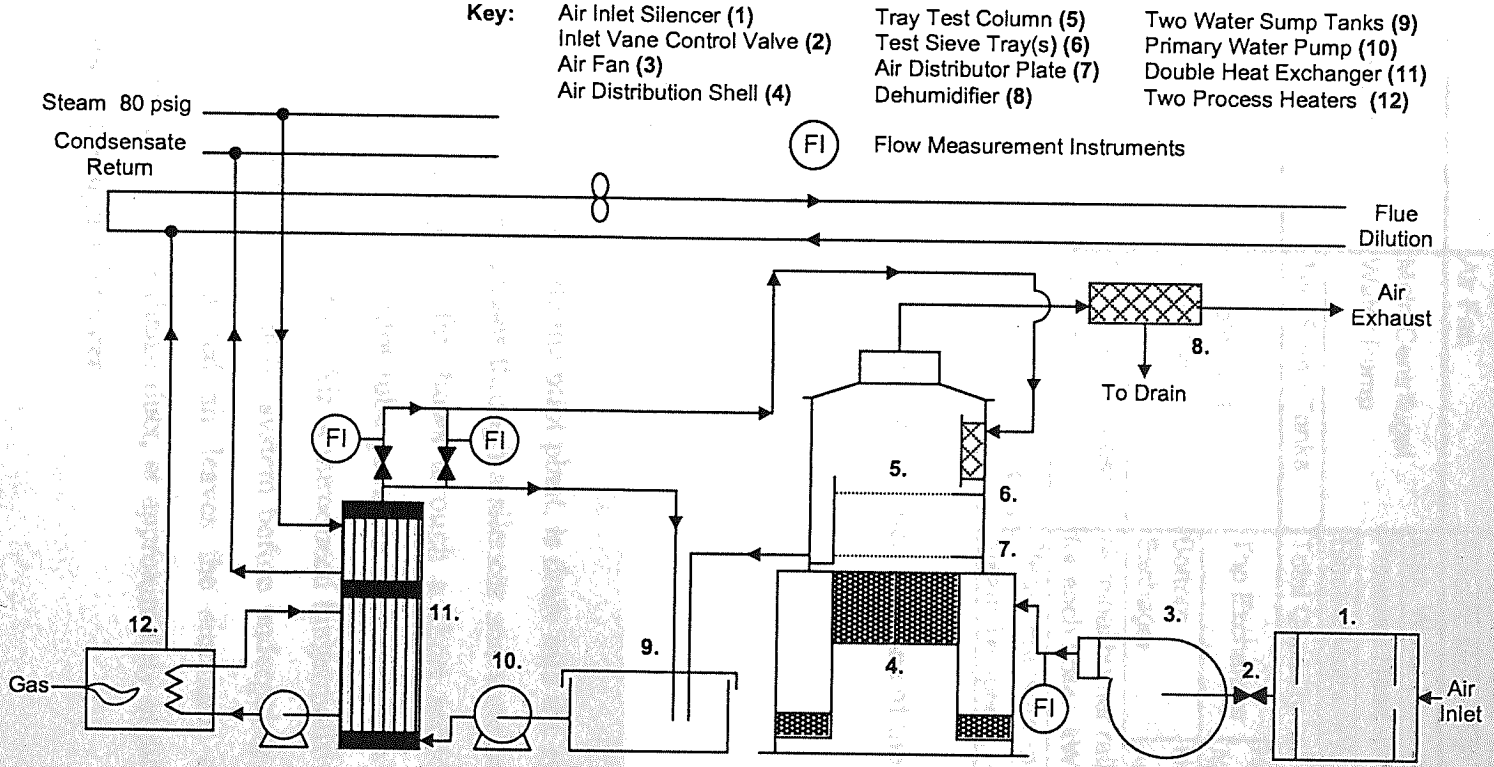

Fig. 3.1: Process flow sheet of the Aston distillation simulator

Ancillary Unitts		Design Specifications		
Air Equipment	Number 48 "Minstral Backward Inclined" Air Fan	Max. Air Flow-rate -m^3s^{-1}		14.38
		Pressure Head -mH_2O		0.51
		Electric Motor -HP		150
Water Equipment	Main Centrifugal Water Pump	Max. Water Flow-rate -m^3s^{-1}		0.055
		Pressure Head -mH_2O		12.75
		Electric Motor -kW		15.00
	Two Sump Tanks	Total Capacity -m^3		5.45
Heating Equipment	Double Heat Exchanger	Top Exchanger	Heat Transfer Area -m^2	3.37
		Bottom Exchager	Heat Transfer Area -m^2	10.22
	Gas-Fired Process Heaters	Nominal burner rating for each boiler -kW		500
	Steam Top-up Supply	Steam Pressure -psig		80.0
		Steam Temperature -°C		162.0

Table 3.1: Summary of the design specifications of the ancillary units

3.3 The Air and Water Circuits

The Air Circuit

Unsaturated ambient air, outside the pilot plant, is draw into the system through a protective grill, at floor level. The air passes through a silencer and vane control valve to the inlet of the fan. The air leaving the fan flows through a short section of rectangular ducting containing an array of fifteen pitot tube pressure sensors which are linked to an air flow meter, and then into the simulator. Air is introduced tangentially into the simulator column where it passes through a distribution system before undergoing a cross-flow contact with water on the test tray. Saturated air leaves the simulator column (into the outside atmosphere) through the top exhaust duct, at approximately eight metres above the ground level after passing through a demister.

The Water Circuit

The water circuit consists of two 2.7 m^3 storage tanks linked in series, a double heat exchanger, a main 15 kW centrifugal pump, and a high grade PVC pipe network capable of withstanding high water temperatures of up to 75°C. Water is pumped to the top of a 1.0 m

liquid distribution bed at the inlet downcomer of the simulator column from the sump tanks, through the double heat exchanger and one of two flow meters, each meter being calibrated for a particular flow-rate range. The first exchanger heats the water by counter-current contact with hot water, the hot water being supplied in a closed cycle from two gas-fired process heaters. The second exchanger further heats the water by condensing steam from the departmental generator. The tray column is of the conventional one pass downcomer type and water leaving the inlet downcomer flows directly across the tray, where it is contacted with vertically rising air, over the outlet weir and then through the outlet downomer back to the sump tanks. A water top-up line supplied fresh water to the sump tanks to account for evaporative loses in the column.

3.3.1 Maximum Air and Water Flows

The specifications for the air and water throughputs were based on conventional tray hydraulic-capacity design procedure as outlined in section 2.3. The tray flooding curve which was used to determine the maximum flow throughputs of the air and water is shown in Figure 3.2 (Hine, 1990).

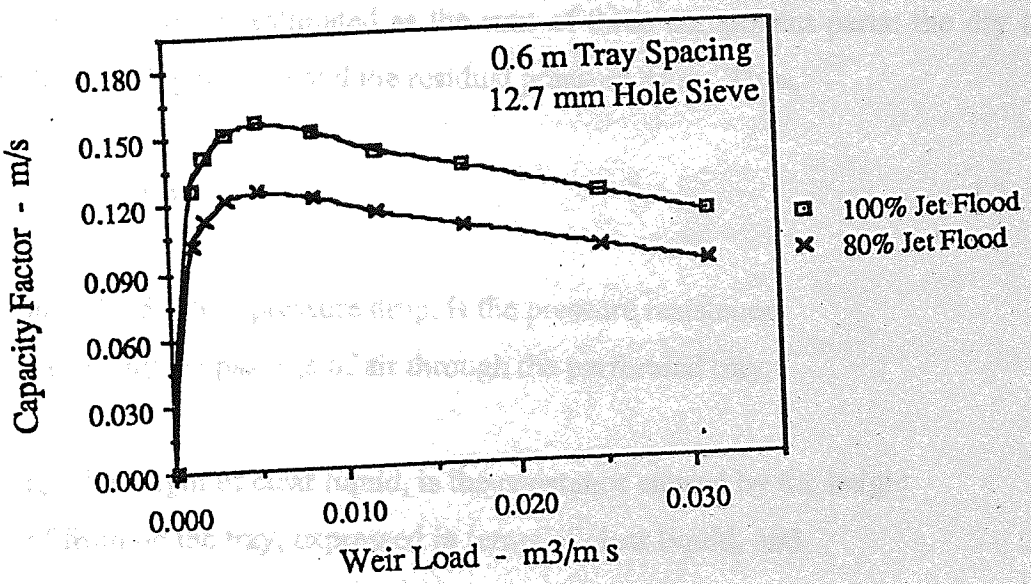

Fig. 3.2 Tray Flooding Curve used to determine the air and water throughputs

The capacity factor, C_f, is defined as,

$$C_f = \frac{Q_G}{A_b}\left(\frac{\rho_G}{\rho_L - \rho_L}\right)^{0.5} \quad \ldots.3.1$$

The maximum value of the capacity factor, C_f, from the 80% jet flooding curve is 0.12 m s^{-1}. Using equation 3.1 and given that D = 2.44 m, W = 1.50 m, A_b = 4.189 m^2, ρ_L = 1000 kg m^{-3}, the maximum air flow rate, $Q_G(max)$, is 14.38 m^3s^{-1}.

Similarly, the maximum value of the weir load, (Q_L/W), is 0.03 $m^3m^{-1}s^{-1}$. Using equation 3.2 and given the same conditions, the maximum water flow, $Q_L(max)$, is 0.045 m^3s^{-1}.

$$Q_L = \left[\frac{Q_L}{W}\right]W \quad \ldots.3.2$$

In order to specify the duty for a fan, it is necessary to estimate not only the air throughput but also the pressure head resistance against the direction of flow. The pressure head resistance is usually called the system pressure drop and is estimated by the summation of the individual pressure resistances around the system. The total pressure drop across an operating sieve tray column is estimated as the sum of three component parts: the dry tray pressure drop, the clear liquid head and the residual pressure drop. Thus,

$$h_{WT} = h_{DT} + h_{cl} + h_R \quad \ldots.3.3$$

where h_{DT}, the dry tray pressure drop, is the pressure resistance caused by the passage of air through the perforated tray,

h_{cl}, the height of clear liquid, is the resistance caused by the height of froth on the tray, expressed in terms of clear liquid, and

h_R, the residual pressure drop, is the pressure resistance due to gas-liquid momentum transfer processes.

Based on the forgoing, the maximum wet tray pressure drop for the air-water column was estimated to be 0.37 m of water (Hine, 1990).

The Air fan and Water Pump

The final specification for the air fan was to deliver 14.38 m^3s^{-1} of air against a resistance of 0.51 m of H_2O. The extra pressure capacity was to take account of other system pressure drops, terms of which include for the inlet silencer, the air flow meter, the air distributor and other loses due to flow contractions and expansions. The fan is a number 48 "Mistral Backward Inclined" type with a rotary impeller blade driven by a 150 HP electric motor via a fan belt.

The final specification of the water pump was to deliver $5.5x10^{-2}$ m^3s^{-1} of water against a head of 12.75 m of H_2O. The head value takes into account the vertical height of rise, the friction due to expansions, contractions and fittings and the head loss due to the water passage through the double heat exchanger. The chosen pump was an in-line centrifugal pump with a 15 kW electric motor.

3.4 The Heating Circuits

Since the experimental investigations involve the use of various air and water throughputs, ranging from very low to very high flow-rates, the heating duty was designed to be variable. It was expected that the heat removed from the water, for any given air flow rate, would be greatest at high weir loads (Ani, 1988) and the heat capacity required for the maximum water loading on the 2.44 m diameter simulator was calculated to be 1.2 MW (Hine, 1990). Thus, a flexible heat source of two 0.50 MW gas-fired process heaters and a steam top-up supply were used to supply the simulator with the required heat load.

3.4.1 The Process Heaters

The varying heat load of the simulator required a flexible supply of source heat, and so two smaller gas-fired process heaters were used as the primary source of heat to the process water, as opposed to a single large one. One or both process heaters can be operated on-line

according to the heating duty required. The nominal rating of each burner is 0.5 MW, however, when burner efficiency and heat transfer efficiency within the process heater are taken into account, the actual efficiency of a process heater is only 80%, only 0.4 MW is available. The hot water generated is pumped in a closed loop system from the heaters to the first stage of the double heat exchanger using a secondary pump. Flue gases, produced from the process heaters, are diluted with fresh, ambient air, using a flue pipe and extractor fan system, and discharged to the outside atmosphere at a height of 8 m above ground level.

3.4.2 The Steam Supply

Steam at 80 psig is supplied from the departmental utilities generator to the second stage of the double heat exchanger through a 100 mm I.D lagged steam line. The condensate is returned back to the generator for recycle, through a condensate line. The steam injection into the heat exchanger is controlled using a steam pressure regulator. The purpose of the steam is to provide a high-grade top-up heat source, for a good fast response to the continuous removal of heat from the system and to achieve a steady state operation.

3.4.3 The Double Heat Exchanger

The heat exchanger is in two parts, the bottom water-water exchanger and the top condensing steam-water exchanger. Because the primary heating load is produced in the process heaters, the heat transfer area, 10.22 m^2, of the bottom water-water exchanger is much greater than that of the top steam-water exchanger, 3.37 m^2. The function of the double heat exchanger is to transfer heat from the process heaters and the steam line to the main water circuit. Water is pumped through the bottom section of the exchanger where it is heated by a counter current flow of hot water from the process heaters, in a closed loop cycle. At the top section of the exchanger the water undergoes further heating and fine-tuning before entering the simulator column through one of two flow meters.

3.5 The 2.44 Metre Diameter Simulator Column

The 2.44 m diameter air-water simulator column has three main sections. These are the annular base of the column, comprising the air inlet and air distribution system; the middle

contacting test section, containing the test tray, together with the supports and downcomer arrangements; and the top section which supports the video recorder and directs the air to the exhaust ducting. A schematic diagram of the simulator column is shown in Figure 3.2.

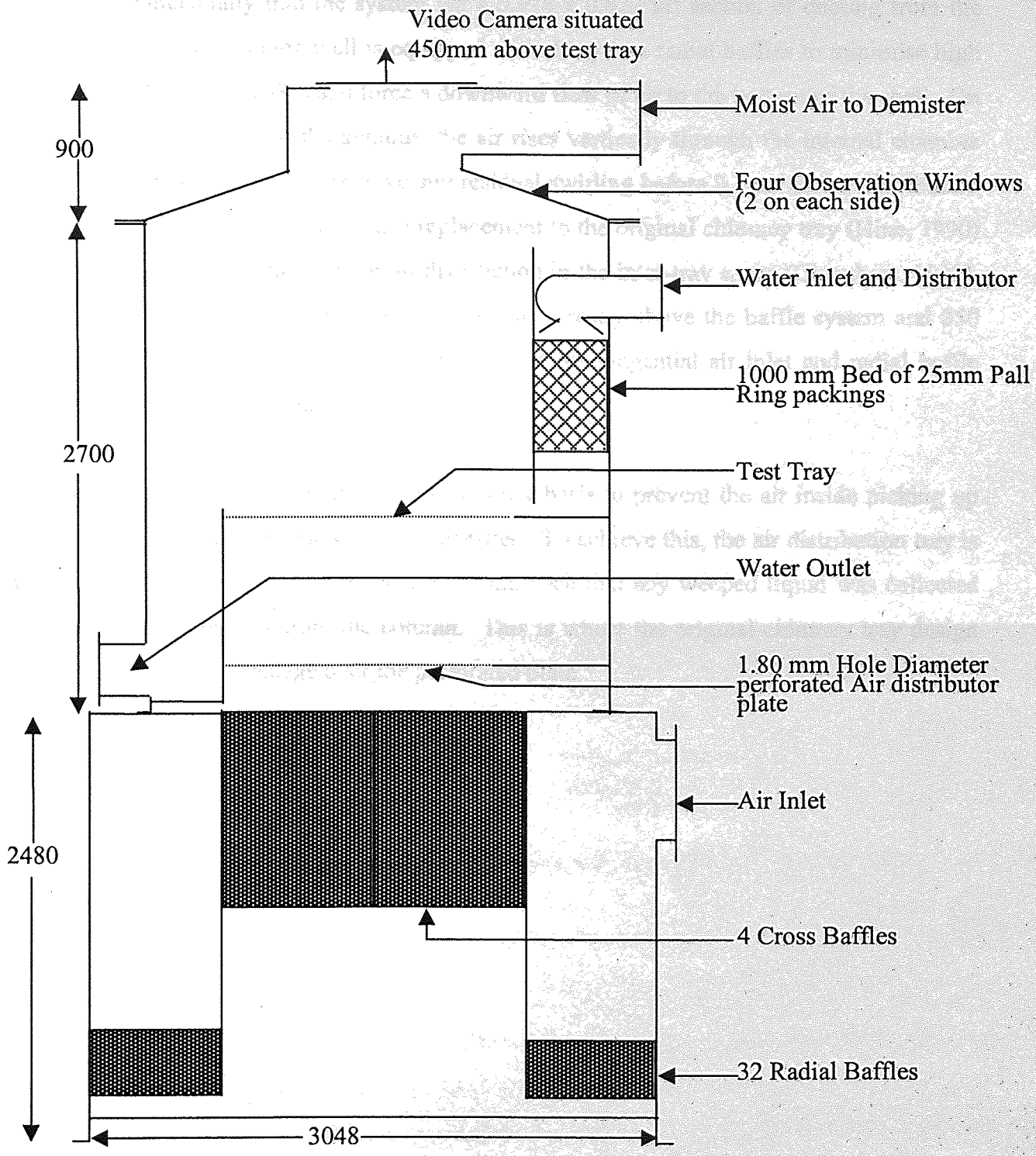

Fig. 3.3 Schematic Diagram of the 2.44 m Diameter Simulator

3.5.1 The Air Distribution Shell

The air distribution shell is the bottom and annular section of the column from where air is introduced tangentially into the system via a 0.978 x 0.622 m^2 section of ducting from the supply fan. The distributor shell is equipped with thirty-two radial baffles to minimise high velocity swirling (Ali, 1984) and force a downward flow of air to the bottom of the shell. On discharge at the bottom of the annulus, the air rises vertically through the internal chamber where four large cross baffles remove any residual swirling before it reaches the distribution sieve plate. The distribution plate is a replacement to the original chimney tray (Hine, 1990) which was found to produce a poor air distribution in the inter-tray space (Chambers, 1993). The 1.80 mm hole diameter distribution plate sits directly above the baffle system and 850 mm below the test tray. A schematic diagram of the tangential air inlet and radial baffle system is shown in Figure 3.3.

It is important that the distributor works on a dry basis to prevent the air inside picking up any moisture and thereby changing its properties. To achieve this, the air distribution tray is equipped with a drainage pipe in each quadrant, such that any weeped liquid was collected and discharged promptly from the column. This is where the original chimney tray design with 128 risers has advantage over the perforated plate.

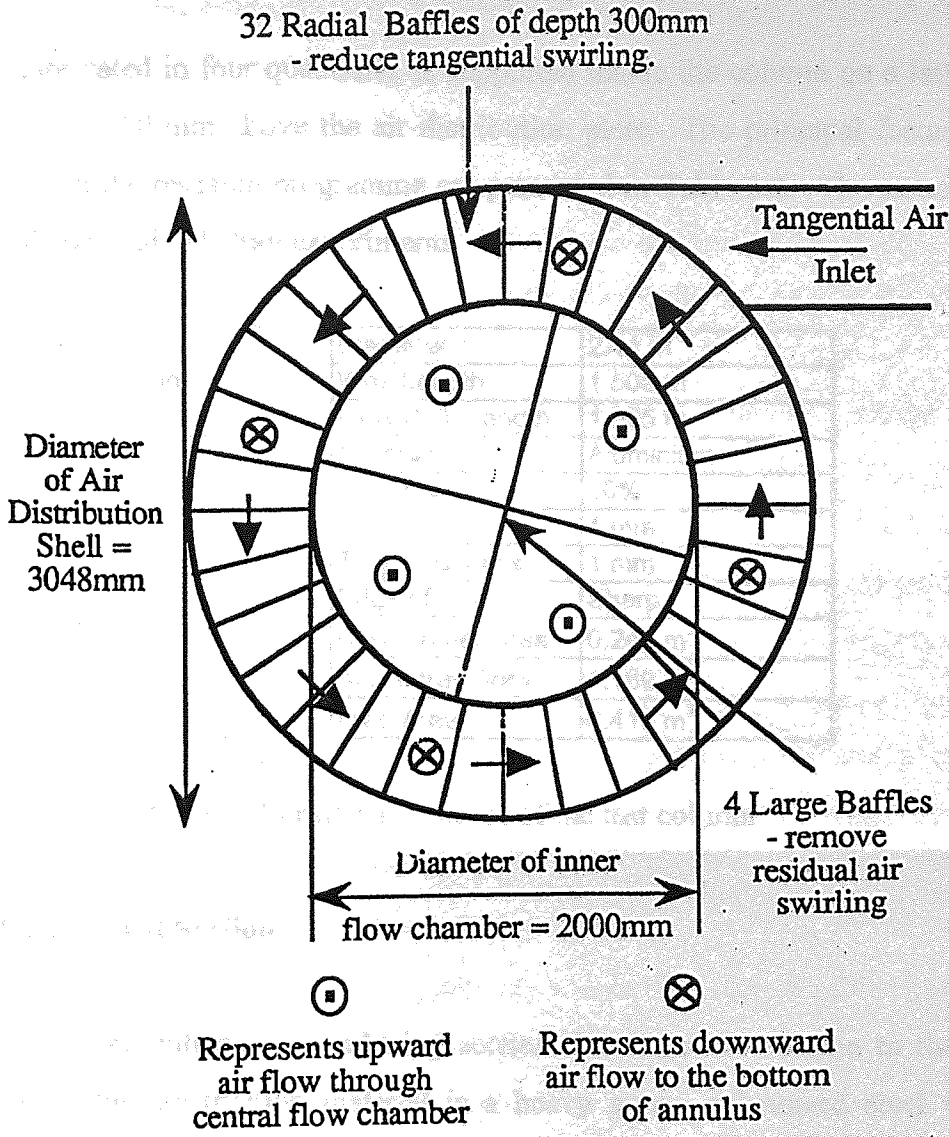

Fig. 3.4 Schematic diagram of the tangential air inlet and distribution system

3.5.2 The Test Column

The 2.44 m diameter test section of the column is of the conventional cross-flow, one-pass downcomer type. The column shell is fabricated from an aluminium sheet of thickness 6.35 mm and contains a number of access windows for easy access to the interior of the column as well as for making direct experimental observation. The inlet downcomer of the column contains the liquid distribution system, which is a 1.0 m packed bed of 25 mm Pall rings, held at a clearance height of 600 mm above the underflow plate. The inlet gap clearance and outlet weir height are adjustable; the inlet gap clearance can be set at varying heights using

an adjustable aluminium plate and the height of the outlet weir can be fixed at 0, 10, 20 and 50 mm using specially made angle aluminium strips.

The test tray, fabricated in four quadrants, is supported inside the column on a lattice beam framework situated 850 mm above the air distribution plate. The principal features of the test tray (s) used in the research programme are presented in Table 3.2. The same tray was used for the full-tray and half-tray experiments.

Column	Diameter	2.44 m
	Weir Length	1.500 m
	Flow Path Length	1.925 m
Tray	Material	Aluminium
	Free Area	10%
	Hole Diameter	1 mm
	Tray Thickness	1 mm
	Edge of Hole	Sharp
Areas	Downcomer Area	0.243 m^2
	Active tray Area	4.189 m^2
	Free Area	0.419 m^2

Table 3.2 Principal features of the test column

3.5.3 The Air Exhaust Section

The top section of the column is a reducing section that links the column to the exhaust ducting system. The construction material is a heavy gauge galvanised steel with four transparent observation windows, and the top of the section is equipped to support a video camera, 4.5 m above the test tray, to record or display flow patterns on a monitor at ground level.

3.6 Modification of the Simulator Column for Half-tray Experiments

In addition to normal tray capacity experiments, higher weir loading experiments were conducted on a half-tray, in order to extend the range of data and also study the flow pattern behaviour at conditions that were deemed to be more relevant to industrial practice. To perform the experiments based on a half tray, it was necessary to alter the test section of the simulator column. A 12 mm thick PVC dividing wall was used to partition the test section

into two similar halves, with the dividing wall extending the full height of the downcomers and rising 0.6 m above the test tray and over the outlet weir to the end of the column wall. The entire liquid flow was diverted to one half of the test section to achieve a "double liquid capacity" tray simulator, with a semicircular flow path. Complete sealing of the partition was achieved using extendible angle brackets, rubber strips and silicone sealant.

It was obvious that the above modifications will introduce serious air distribution problems during simulation experiments. Even on a normal tray the tendency for vapour channelling because of slight out-of-levelness of the tray or simple hydraulic gradient on the tray has been well documented (Lockett and Augustyniak, 1991). The half-tray design is further complicated by the complete absence of liquid flow on one side of the tray, which will inevitably induce air channelling through the inactive half and probably lead to a fluctuating vapour collapse on the active half. A number of methods for mitigating these problems and achieving an even air distribution were considered, but there seemed to be only two realistic options open to our resources. One was to blank off the inactive tray section completely and the other was to use hydrostatic pressure to introduce liquid from the active half to the inactive half and then maintain a hydrostatic equilibrium between both compartments, while no water is allowed to flow off the inactive tray section.

Option one was rejected on the ground of poor air distribution due to convergence of the airflow beneath the test tray. The airflow was vertical for a circular tray but when a contraction in the effective flow area was introduced, the streamlines of the airflow converged, leading to poor air distribution and additional pressure drop that was not provided for in the design. Option two was therefore adopted, but not without its difficulties and limitations. First, the downcomer of the inactive section was blocked at the outlet weir to prevent water outflow. Then a series of trial experiments were done to determine the appropriate number and size of holes to be made on the dividing wall, such that water flow through them will not disturb the flow pattern on the test side of the tray and also ensure a rapid attainment of hydrostatic equilibrium between both halves. In the end, a total of twelve holes, each 6 mm in diameter and 5 cm from the tray floor, were spaced evenly on the dividing wall, from the inlet downcomer under flow to the outlet weir.

In order to check that even air distribution was achieved, the superficial air velocity above the froth on both halves of the tray was measured. Since the air velocity was a mere 1.0-2.4 m s^{-1}, pitot-static tubes, which were installed at symmetrical positions on either sides of the divide - corresponding to the centre of the flow path and 0.5 m from the side of the column, was used as the measuring device. The air velocity measurements above both sides of the compartments did not indicate any change in airflow in switching from half tray mode to full tray mode.

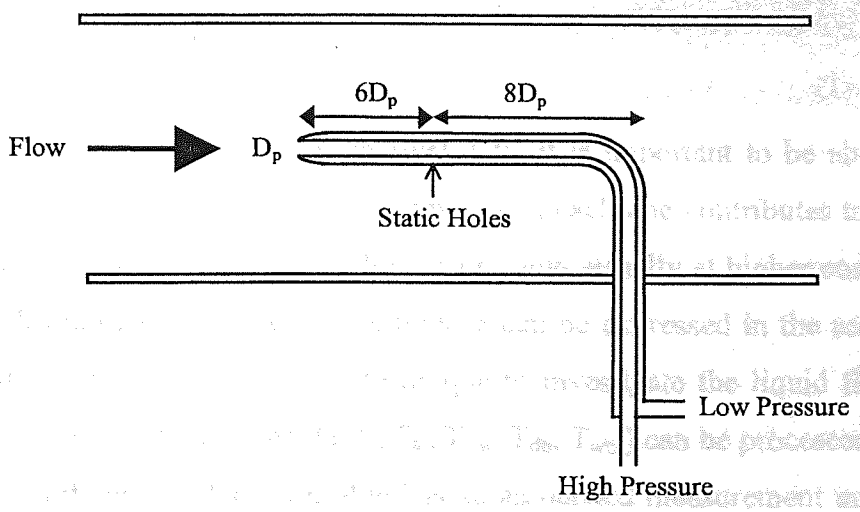

Fig. 3.5 Pitot tube arrangement for superficial velocity measurement

The positive x co-ordinate (inlet-outlet, LHS) was chosen as the test side for the experimental programme. The choice was informed by practical considerations such as position of the observation window and instrumentation for measurement.

To establish further the integrity of the experiments, temperature and clear liquid height measurements were made across the full tray, at steady state. Results showed that there was only negligible exchange of material between both compartments after hydrostatic equilibrium had been attained. The small exchange of material was because of fluctuations in the clear liquid height due to the liquid and gas momentum. For the same reason, the clear liquid height on the inactive side was marginally higher than that on the active side. It was judged that the experiments on the half tray had about the same order of integrity as those on the full tray.

3.7 Measurement Instrumentation

The important variables measured in the course of the experiments were classified either as a system variable or an operating variable. The air and water flow rates constitute the operating variables while the air enthalpy and humidity and air and water temperatures make up the system variables. The other physical properties of the air-water system, such as density and viscosity were assumed to be constant at all conditions of the experiments.

3.7.1 Measures of Error

In any experiment which rests on numerical data, it is important to be able to "audit" the experimental uncertainties and determine how much each one contributes to the final result, in order to draw valid conclusions. A low error value, usually at higher costs in equipment, is generally desirable so that greater confidence can be expressed in the results. Now, one advantage of using the water-cooling technique to investigate the liquid flow pattern on a tray is that the measured variables (G, L, T_{in}, T_{out}, T_{db}, T_{wb},) can be processed to calculate the Murphree tray efficiency. Each variable has an associated measurement uncertainty (error) due to instrumental limitations, which were used to calculate the final consequential uncertainty in the efficiency value. Knowing the sensitivity of the efficiency to each of the measured variables, the following error specifications for the operating and system variables were allowed in the instrumentation (Hine, 1990):

Air Flow Rate	2.0%	Air Temperatures	0.5°C
Liquid Flow Rate	0.5%	Water Temperatures	0.02°C

The specifications yielded a Murphree tray efficiency that was within an error range of 2.1%. This was deemed to be acceptable in view of the scale of the apparatus being used. The specifications are based on the condition that measurements were made at steady state. Thus, any variations in the measured variables with time must be taken into account in any final error analysis.

3.7.2 Measurement Equipment

The above error specifications were used to determine the choice of suitable measuring devices for the instrumentation.

The Air Flowmeter

The air flowmeter consisted of a network of fifteen impact and static pitot pressure sensors, distributed uniformly, at centres of equal area, over the cross section of the ducting between the air fan and simulator column. Flow profile irregularities were reduced by use of shrouds around the pitot sensors and by honeycomb flow straighteners, located upstream of the flow sensors. The pitot sensor array is interconnected to provide a representative average differential pressure that is proportional to the air velocity in accordance with classical Bernouli theory. The differential pressure is measured using an inclined micromanometer with an accuracy of ± 0.005 mm of H_2O. For differential pressures of between 3.19 and 57.92 mm of H_2O, the corresponding superficial air velocities lies in the range 0.7 and 3.0 ms^{-1}.

The Water Flowmeters

Two separate flow meters were used to measure the water flow rate because of the wide range of flow rates used in the experiments. For normal operation and the higher flow rates an electromagnetic flow meter was used, and for lower flow rates, which accounted for less than 5% of operation, an orifice plate rotameter was used. An electromagnetic flow meter has no moving parts and causes no disturbance to flow. The system is a compact, volumetric liquid flow-measuring device in which a transducing method is employed, such that the conduction properties of liquid are used to produce an induced voltage on passing through a magnetic field. The amplitude of the voltage thus produced is directly proportional to the average flow velocity of the fluid. The water flow rate is calibrated in milliamps, and for a given flow rate, the corresponding current output is shown on a digital display unit. The meter has an accuracy of 0.5% and is capable of measuring water flow rates of between 0.009 and 0.090 m^3s^{-1}.

The orifice plate rotameter was used to measure low water flow rates because the electromagnetic flow meter requires a critical velocity of fluid through the sensor. The orifice plate was used to measure low water loadings, up to 0.009 m^3s^{-1}, with accuracy in the order of 2 to 3%. This is slightly higher than the specification in the error analysis, but deemed acceptable because it was used in less than 5% of the operation.

The Resistance Thermometers

In order to obtain accurate water temperature measurements across the tray, an array of platinum resistance thermometers interfaced with a data logging system were used. A full description of the technique and the data logging procedure are contained in chapter 4.

CHAPTER FOUR

Data Acquisition Procedure

4.1 Introduction

The air-water distillation simulator is a unique and flexible pilot apparatus, suitably adapted to the investigation of two-phase flow patterns on a scale that is immediately relevant to industrial practice. The apparatus incorporates a number of experimental techniques, including capabilities for direct observation and video recording, using flow pointers or water soluble dye technique; mass transfer and flow pattern studies, using the water cooling technique; and measurement of clear liquid height variation across the tray, using water manometers. This chapter describes each technique in detail, together with the experimental procedures used in the data gathering and processing. The results from these procedures will provide the basis for the discussion and analysis of results in subsequent chapters. A step by step instruction on the safe start up, operation and shutdown of the test facility is contained in Appendix 1.

4.2 Dyed Tray Experiments

The dyed tray technique is an established technique and has been used differently by several workers for flow pattern studies (Weiler et al., 1973; Porter et al., 1972; Ani, 1988). In this work, the coloured dye and camera recording approach was used to gather mainly pictorial and qualitative information about the controlling flow phenomena that affect the performance of distillation trays.

4.2.1 Experimental Procedure

The mode adopted in the experimental programme was that of continuous dye injection mode, where water-soluble dye (potassium permanganate solution) was continuously released along the length of the inlet weir until the entire phase is completely and uniformly coloured. The progress of the dye as it is washed away by clear liquid, was then monitored by a video camera mounted 4.5 m above the test tray. Apart from the traditionally qualitative inferences derivable from this mode of dyed tray studies, the video images were

analysed using the UTHSCSA image tool program (developed at the University of Texas Health Science Centre at San Antonio, Texas and available from the Internet by anonymous FTP: htt://www.hensa.micros.ac.uk) to give semi-quantitative results. Full details of the video image analysis and results are presented in chapter 5.

4.3 Heat Transfer Experiments by Water Cooling

The water cooling experiments are used to simulate the effect of liquid flow pattern on the mass transfer process by feeding hot water on to a cross-flow tray and cooling it by air forced through the perforations. The progress of the heat transfer is observed by an array of temperature measuring devices. The recorded temperature data are processed and the analogy between mass transfer and heat transfer is used to relate the temperature profiles to concentration profiles found in practical distillation operation. Temperature profiles can also be interpreted in terms of enthalpy driving forces to calculate thermal point and tray efficiencies.

4.3.1 Temperature Data Collection

The water cooling technique involves the monitoring of the water temperature at various locations on the tray. In principle, the more the number of temperature measurement points, the better the precision of the generated pattern of temperatures, due to interpolation over a smaller distance. In this work, temperature measurements are made at over 100 points on the tray and it is desirable that the measurements are made simultaneously. In practice, this was done by means of a data-logging device, which collected all the temperature data over a short but finite period of time, of the order of one to two seconds.

Temperature Measurement Technique

The temperature measurements were carried out using mainly platinum resistance thermometers, interfaced with a computer-based data logging system. The choice of the device was based primarily on the need to meet the error specification of 0.02°C in the error analysis.

Resistance thermometry is based on the principle that the electrical resistance of a conductor varies according to its temperature. Due to high accuracy of the technique, the resistance of the external lead-wires connecting the sensor to the source of power must also be taken into account. To compensate for this, a four lead-wire arrangement, in a current/voltage measuring mode was used in the circuitry. Figure 4.1 shows the typical circuit for the four-wire configuration.

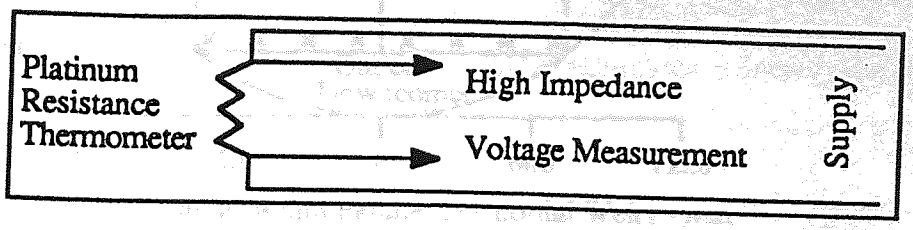

Fig. 4.1 Circuit arrangement for the Platinum Resistance Thermometers

The resistance thermometer was housed inside the tip of a stainless steel probe of length 300 mm and diameter 3 mm. The four lead-wires were individually covered before being cased in a PVC coating, to provide the final protection against moisture. The measurable resistance range for each PRT correspond to a temperature range of -10 to 55°C.

In addition to the PRTs, two stand alone mercury in a bulb thermometers were used to carry out few temperature measurements to determine the wet bulb temperature of the air during the experimental programme.

Mounting of the Platinum Resistance Thermometers

To obtain a precise temperature field over the whole tray, 118 PRTs were mounted on to the tray deck as shown in Figure 4.2. Four PRTs were placed 50 mm to the rear of the inlet downcomer, 108 were positioned on a 200 mm square pitch configuration across the active tray area, four beneath the test tray, and two at the bottom of the outlet downcomer. The exact co-ordinates of the PRT probes on the tray are presented in Appendix 3.

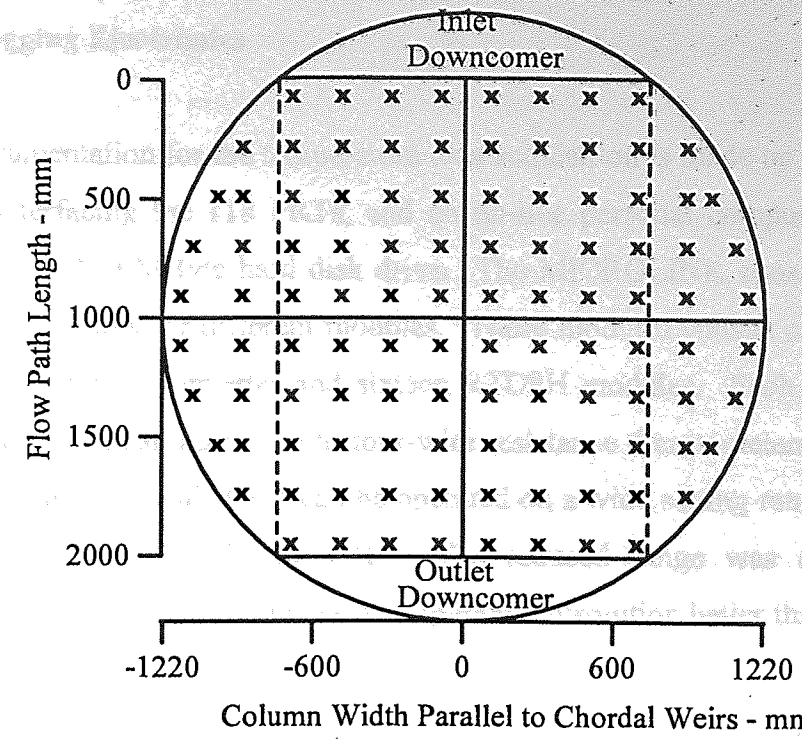

Fig. 4.2 Arrangement of temperature probes on the 1 mm hole tray.

Apart from the four probes in the downcomer and the four beneath the tray, each of the PRTs was mounted onto the tray deck from beneath by means of a rubber grommet and a water shroud as shown in Figure 4.3. Water shroud was incorporated into the PRT arrangement to guarantee the probe was surrounded by water only and therefore prevent any premature cooling effect the rising air might have on the bare probe.

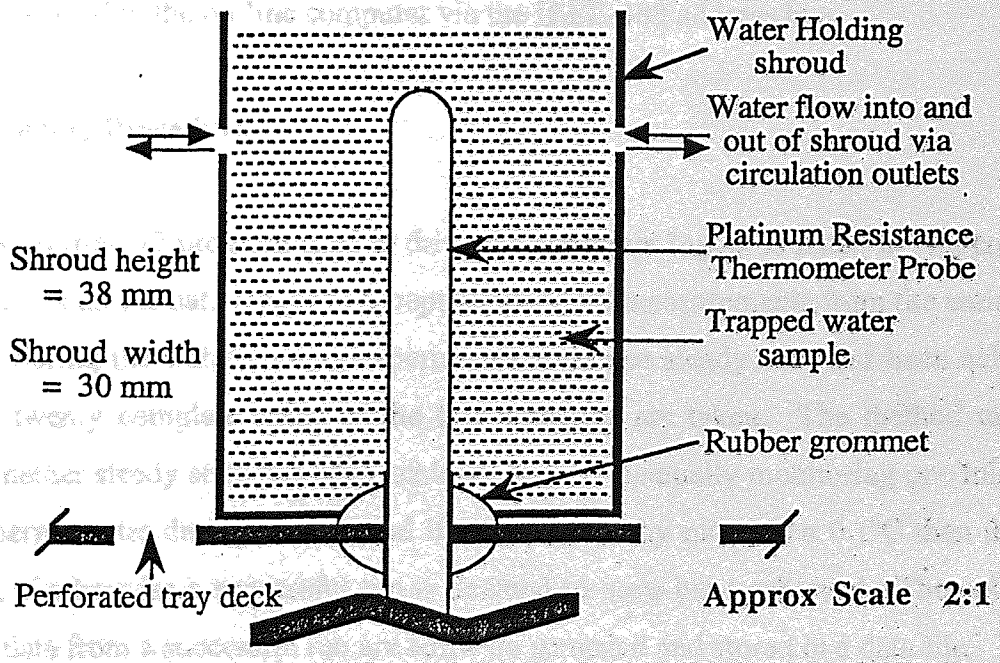

Fig. 4.3 Thermometer mounting technique using rubber grommet and shroud

Data Logging Electronics

The instrumentation for the temperature data acquisition is made up of a MICROLINK data-logger, interfacing the 118 PRTs, and an on-line personal computer (model number ESP 9228) with a 130 MByte hard disk drive. The MICROLINK consists of a mainframe unit with eighteen slots for different modules. These modules consist of a high-speed clock, an analogue to digital converter and sixteen RTD8H modules. Each RTD8H is an analogue input device that can accept eight four-wire resistance thermometers (PRTs), or channels as they are commonly called and can be operated on a wide setting range of 200°C to 900°C or a reduced range of 10°C to 55°C. The reduced range was adopted throughout the experimental programme and gave a temperature resolution better than 0.02°C, as required in the error analysis.

The high-speed clock allows the interface to make rapid data acquisition at equally spaced time intervals between channels. As the time delay for each analogue to digital (A-D) conversion between each channel is one millisecond, a complete scan of the 120 usable channels takes 1.2 seconds, which seemed reasonably close to instantaneous.

The A-D converter is a twelve-bit analogue to digital converter, which implies that any measured value after conversion has a resolution of 2^{-12} of the full-scale range. The A-D converter changes the analogue signals from the RTD8H input module to a digital output signal that is relayed to the on-line computer via the IEEE-488 address bus.

The Data Logging Procedure

The modified Fortran 77 program used to drive the computer logger is listed in Appendix 2. The program sets up the data logger to accept temperature measurements from the entire 118 PRTs in use during the water cooling experiments and once steady state has been achieved on the tray, twenty complete scans of the thermometers are taken. The method used to determine whether steady state has been achieved was by manually monitoring one inlet and one outlet thermometer during the run and if either varied by more than 0.1°C then the run was aborted, if otherwise a successful run is deemed to have been achieved. The collected temperature data from a successful run are software screened and stored in a data file.

The software screening consists of searching the collected data for rogue data and if found the erroneous value is made void, by replacement with a default value of 99.9.

It was the practice to apply corrections to the measured temperature values in situ, by linear interpolation between calibrated temperature points, before the data are logged and saved in the computer. But, because of the remarkably superior contour lines obtained when a new calibration was applied, the program was modified so that the correction can be applied externally, to take advantage of any such future improvement in calibration and also to be able to apply any one calibration to the historical data. Figure 4.4 shows the actual calibrated and averaged temperature data from a particular run. It is on these calibrated and averaged data that further downstream processing and calculations are based.

4.3.2 Recalibration of the Thermometers

Platinum resistance thermometers are sensitive and reproducible instruments. They are also rugged and capable of withstanding different environmental conditions, however, recalibration is often considered necessary after a reasonable time of use as there is, in many applications, risk of contamination, evaporation and possibility of strains being introduced into the wires. These risks were confirmed when, with all the thermometers were connected to the interface and computer, the measured temperatures (calibrated) varied within one degree, even though all the probes were in the same temperature environment. Some of the PRTs even showed readings that were clearly outside the temperature bracket and as such were taken to be dud. There are also uncertainties about the way in which the PRTs were previously calibrated. As such recalibration or standardisation of the measured temperatures was required.

The following procedure has been developed for the recalibration and standardisation of the 118 PRTs used by the data logger system for temperature measurements across the tray surface during the water cooling experiments:

Since the primary purpose of the calibration is to calibrate individually each of the PRTs used for data acquisition, it is essential to have a means of ensuring that the sensing elements of the PRTs are at the same temperature during calibration. For this purpose, a cylindrical

block of Dural of 10 cm OD and 15 cm height was used. Twenty-nine holes were drilled symmetrically within a radius of 6 cm from the centre of the block, to serve as pockets for the PRTs. A maximum of 29 PRTs can be inserted in the block at a time for calibration. To ensure isothermal conditions in the block, a tightly fitting copper coil was wound round the block and connected to a thermostatic water bath. This apparatus is suitably encased to allow continuous circulation of water round the block and its easy insulation. To ensure as far as possible isothermal conditions and to prevent heat losses, the entire circuit and block were well lagged and a booster pump incorporated for high-speed circulation of water round the block.

A test run for the calibration of the PRTs was carried out with twenty PRTs distributed at every symmetry position on the block. Repetitive scanning was done close to 1, 18, 30, 40 and 45°C. Results of the different tests suggested that the calibration block was very effective in providing an isothermal environment for the PRTs. One PRT among the twenty used for the exercise proved to be dud, by showing readings that were consistently well outside the temperature bracket. It was also observed that when moving from one temperature to another the readings all moved together (except for the dud PRT that maintained same reading at all temperatures), suggesting a highly uniform temperature profile. For conditions close to ambient, the water flow was stopped but this made no significant difference to the temperature distribution, again suggesting a virtually constant temperature profile across the block. This assumption was checked and confirmed by using a sensitive stand-alone PRT (with a precision of $\pm$ 0.01K) that was inserted into each pocket in turn.

After commissioning the kit, a similar method was used for the calibration of the rest of the PRTs. The mercury thermometers were standardised with the PRTs by calibration in a standard water bath, using one of the PRTs as reference.

Air Velocity (m/s)	1.500
Weir Load ($cm^3cm^{-1}s^{-1}$)	150.0
Dew Point (deg C)	17.10
Column Diameter (m)	2.44
Weir Length (m)	1.50
Free Area (%)	10.0
Outlet Weir height (m)	0.050
Inlet Weir Gap m)	0.050
Hole Diameter (m)	0.001

Temperature Data Information

First row = Four inlet temperature values

10 row x 12 column matrix = 108 temperature readings over tray area

12th row = Two outlet temperature values

13th row = Three inlet air temperatues

				99.99	43.20	42.93	43.44				
		42.58	42.02	42.27	42.68	42.08	41.66	42.30	41.13		
	40.61	41.59	41.45	99.99	41.18	42.31	99.99	41.41	42.15	38.63	
38.73	38.89	41.22	40.19	41.05	41.79	40.61	40.98	40.60	99.99	37.87	36.51
35.83	38.56	39.49	39.05	99.99	40.74	40.99	39.65	39.38	39.55	37.14	35.16
34.22	37.14	38.96	38.04	39.11	40.19	39.86	39.13	38.82	37.88	36.67	34.35
33.86	36.29	37.25	37.03	38.48	39.84	40.43	38.69	37.98	37.17	34.46	33.70
33.29	32.80	37.09	36.70	38.44	39.54	39.58	38.45	36.62	36.70	34.41	32.99
-5.81	31.75	35.75	34.86	37.74	39.08	38.75	38.05	36.53	35.20	32.63	32.54
	32.42	34.62	35.47	35.66	38.71	37.85	36.59	35.46	33.52	31.59	
		32.60	34.09	99.99	37.68	36.94	99.99	33.86	32.03		
					33.96	38.55					
					18.19	18.42	18.17				

Fig. 4.4 Example of Collected Temperature Data

4.3.3 Temperature Contour Processing

During the water cooling experiments, the manual control over the heat supply only allowed for the inlet water temperature to be held constant during a particular experimental run, but not for an entire set of experiments. Also, the inlet air condition varied from day to day, giving different dry and wet bulb temperatures. In order to present the temperature profile graphically, the raw temperature data was first converted into reduced temperature data so that results from different experiments can be compared on a like basis. Reduced temperature, T_r, at a particular point is defined as:

$$T_r = \frac{T - T_{wb}}{T_{in} - T_{wb}} \qquad \ldots.4.1$$

where T, T_{in}, and T_{wb} are the measured water temperature at a given point, inlet water temperature, and the wet bulb temperature of the inlet air respectively. By definition, the entering air wet bulb temperature is the minimum temperature that can be exhibited by a simple air-water system. The water entering the tray has a reduced temperature of 1.0, and the water leaving the tray has a reduced temperature lying between 1.0 and 0.0.

The software package used for the temperature contour processing is the UNIRAS suit of plotting routines. This was held on a VAX CLUSTER main frame computer where two and three-dimensional displays are generated as shown in Figure 4.5. A full description of the process and the calculation procedure involved is contained in the UNIRAS instruction manual. The computer coding used to perform the interpolation and plotting procedure is listed in Appendix 3.

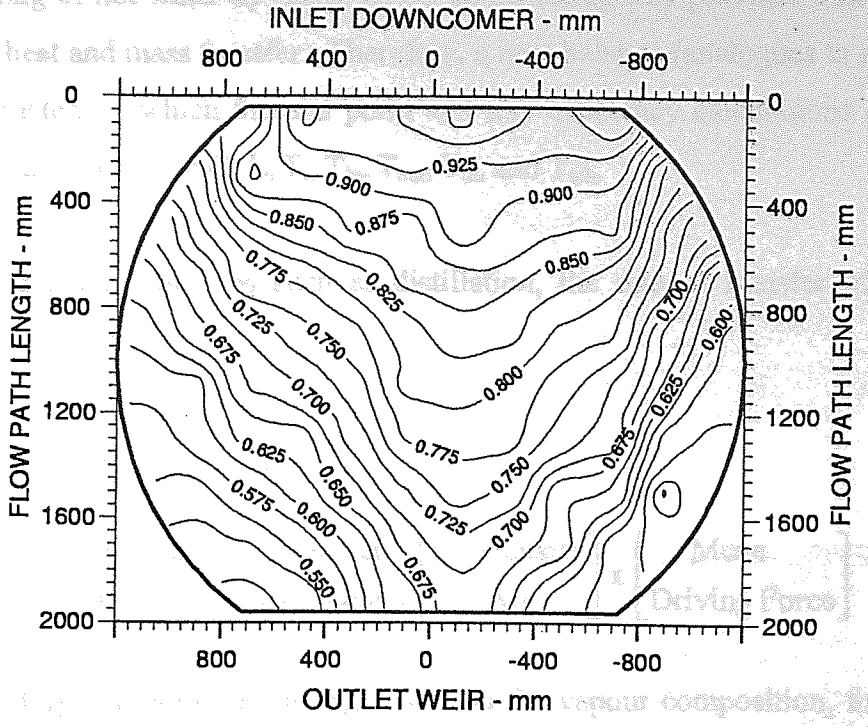

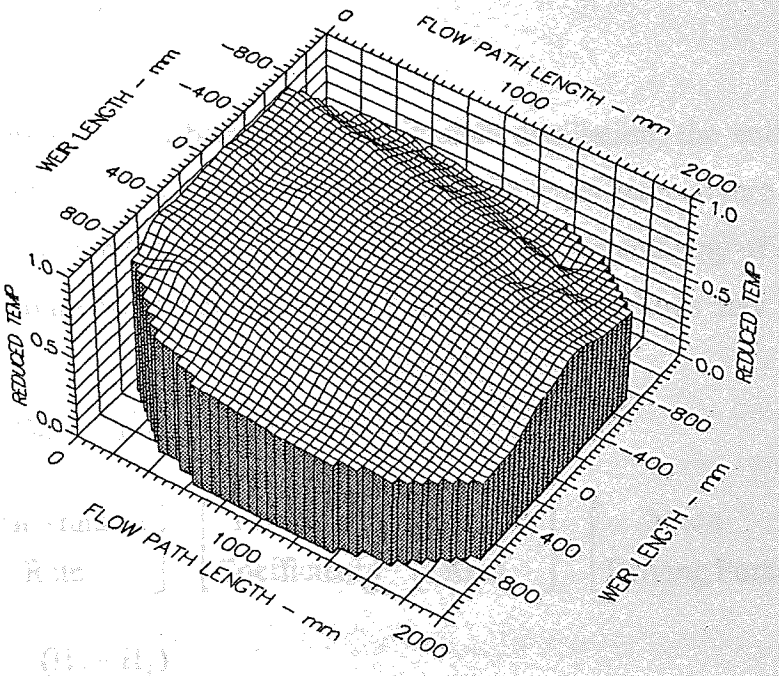

Fig. 4.5 Examples of a 2 and 3D temperature profile diagram

4.3.4 Calculation of Thermal Efficiencies

The cooling of hot water by rising air on an operating tray provides a model for an analogy between heat and mass transfer. Therefore, a heat balance (analogues to a mass balance) can be constructed on which thermal point and tray efficiency calculations can be based. The measured quantities are G, L, T_i, T_{in}, T_{out}, T_{db} and T_{wb}.

In mass transfer processes such as distillation, the rate of transfer of the more volatile component, is given by:

$$dN = Gdy = k_y a(y - y_i) = Ldx \qquad \ldots.4.2$$

$$\text{i.e,} \quad \begin{bmatrix}\text{Mass Transfer}\\ \text{Rate}\end{bmatrix} = \begin{bmatrix}\text{Transfer}\\ \text{Coefficient}\end{bmatrix} \text{x} \begin{bmatrix}\text{Transfer}\\ \text{Area}\end{bmatrix} \text{x} \begin{bmatrix}\text{Mean}\\ \text{Driving Force}\end{bmatrix}$$

and the Murphree point efficiency, based on the vapour composition, for such a process is given by:

$$E_{og} = \frac{y_2 - y_1}{y^* - y_1} \qquad \ldots.4.3$$

Where water-cooling is being used to simulate distillation, the enthalpy of the air (H) is analogous to the vapour concentration (y) and the water temperature (T) is analogous to the liquid concentration (x). The equilibrium line relates the enthalpy of air saturated with water vapour (H^*) to the water temperature. Thus the above equations may be rewritten as:

$$Q = GdH = k'_y a(H - H^*) = LdT \qquad \ldots.4.4$$

$$\text{i.e} \quad \begin{bmatrix}\text{Heat Transfer}\\ \text{Rate}\end{bmatrix} = \begin{bmatrix}\text{Transfer}\\ \text{Coefficient}\end{bmatrix} \text{x} \begin{bmatrix}\text{Transfer}\\ \text{Area}\end{bmatrix} \text{x} \begin{bmatrix}\text{Mean}\\ \text{Driving Force}\end{bmatrix}$$

$$E_{og} = \frac{(H_2 - H_1)}{(\overline{H}^* - H_1)} \qquad \ldots. 4.5$$

$$E_{mv} = \frac{(H_2 - H_1)}{(H^*_{out} - H_1)} \qquad \ldots. 4.6$$

where $$\overline{H}^* = \frac{1}{A}\int H^* . dA \qquad \ldots. 4.7$$

The definition of the point efficiency, E_{og}, is based on the assumption that it is constant at all points on the tray. Clearly, the rate at which water is being cooled must equal the rate at which air is being heated. Thus, from the overall heat balance at steady state:

$$H_2 = \frac{L}{G} C_p (T_{in} - T_{out}) + H_1 \qquad \ldots.4.8$$

H_1 and H^* are calculated from psychrometric data tables using the following relationships:

$$H^* = C_{air}\, x\, T + H^*[(C_w\, x\, T) + H_{fg}] \qquad \ldots.4.9$$

$$H_1 = C_{air}\, x\, T + H_{air}[(C_w\, x\, T) + H_{fg}] \qquad \ldots.4.10$$

The Fortran computer program developed by Hine (1990) and updated to perform the efficiency calculations is presented in Appendix 4.

4.4 Measurement of Height of Clear Liquid

The flow pattern on an operating distillation tray can be considered to constitute three component parts: the flow direction, the flow velocity and the flow depth, each combining to give the overall flow pattern. It is important therefore, while investigating the flow patterns, to give an indication of the flow depth and variation over the tray area. It is generally assumed that in order to overcome frictional resistance to froth passage and maintain flow across the tray that a froth gradient must exist between the inlet and outlet downcomers, such that the froth height is greatest at the inlet and least at the outlet. In practice however, the contacting of vapour and liquid on a distillation sieve plate is often a violent mixture without a distinct or sharp upper surface. As such, direct measurement of froth height is difficult. Instead the pressure drop between the tray floor, the froth or spray dispersion and the space above is measured from which effective froth height or height of clear liquid is evaluated.

The clear liquid height or liquid hold-up on a tray is defined as the height to which the aerated mass would collapse in the absence of vapour flow, that is, the liquid depth on a tray when the vapour supply is stopped to eliminate foam build-up (bubbling action) and the formation of liquid droplets above it.

4.4.1 Measurement Technique

An established method of measuring the height of clear liquid on an air-water test tray is to connect a manometer, filled with water, to a pressure tapping mounted flush on the tray floor as shown in Figure 4.5.

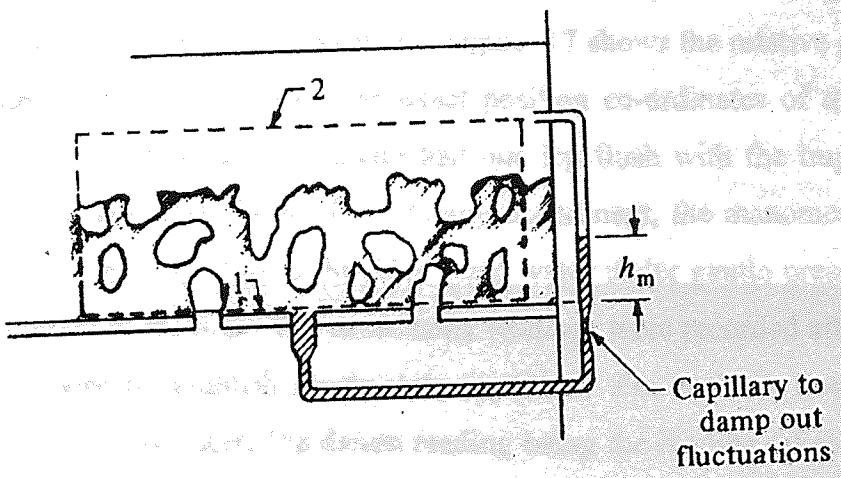

Fig. 4.6 Manometer set up for measuring clear liquid height

According to Thomas and Haq (1976) and Locket (1986), the clear liquid height, h_{cl}, can be related to the manometer reading, h_m, through a vertical momentum balance between the tray floor and the surface of the aerated bed, so that:

$$h_{cl} = h_m + \frac{u_s \rho_G (u_h - u_s)}{\rho_L g} - \frac{2\sigma}{\rho_L g r_m} \qquad \ldots. 4.11$$

The additional terms are added to account for the momentum head of the vapour leaving the holes and the capillary rise in the tube. The correction terms can be eliminated from the equation by relating manometer readings to a datum level. Datum readings are measured by

operating the tray with no liquid at the corresponding air flowrates. By subtracting datum values from the actual readings, obtained with a liquid head on the tray, the clear liquid height is obtained without the need to correct for capillary rise and gas momentum effects. Datum readings constitute "zero" height of clear liquid.

The manometer technique has been verified by comparing h_{cl} measured by manometer against integrated froth density profiles obtained by γ-ray absorption (Prince et al. 1979) and against h_{cl} fixed by using a measured amount of liquid on a tray with no liquid cross flow (Davies and Porter, 1965).

4.4.2 Experimental Procedure

The clear liquid height on the tray was determined using the average of thirty-six manometers mounted flush with the tray floor. Figure 4.7 shows the relative positions of the manometer tappings on the tray floor, the exact position co-ordinates of the tappings are contained in Appendix 5. Each manometer had one leg flush with the tray floor and the other projecting into the atmosphere. Prior to any experiment, the manometers were filled with water and the lines purged of air bubbles using water under gentle pressure, from a T-junction at the middle of the line. The manometer readings were recorded after a reasonable time had been allowed to establish steady state condition. For each air flow-rate, a datum and an actual reading were taken, the datum reading being the reading taken in the absence of water flow and thus zero liquid hold-up. The clear liquid height was evaluated by subtracting the datum readings from the actual readings.

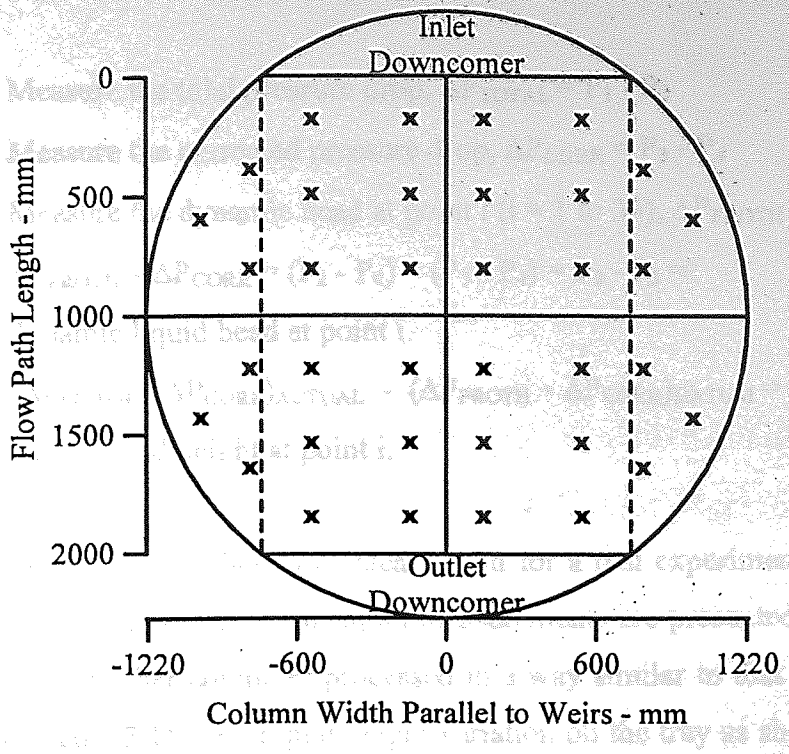

Fig. 4.7 Position of manometer tappings across the test tray

The analytical framework on which the calculation of the clear liquid height at a given point is depicted in Figure 4.8.

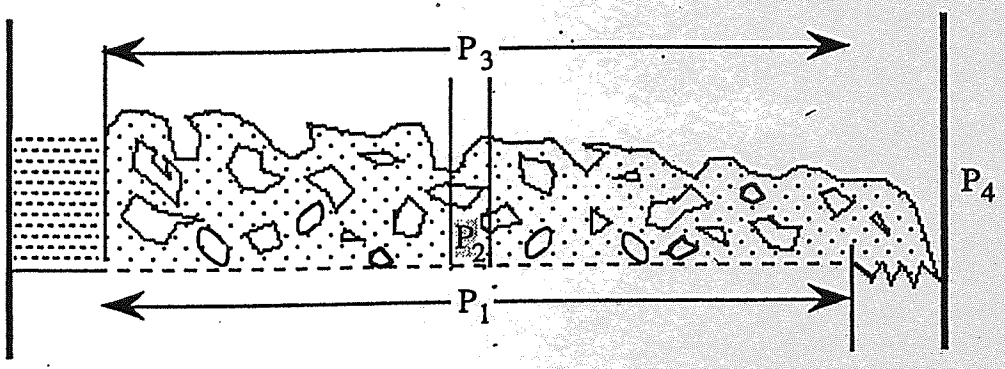

Fig. 4.8 Pressure diagram for the calculation of height of clear liquid

P_1- Pressure below test tray. $\Delta P_{TOTAL} = P_1 - P_3$

P_2- Pressure above test tray. $\Delta P_{CORR} = P_3 - P_4$

P_3- Pressure above the froth. $\Delta P_{DRY} = P_1 - P_2$

P_4- Atmospheric pressure

The above experimental procedure can be summarised in a five-step procedure as follows:

Step 1: Measure the total pressure drop, $\Delta P_{TOTAL} = P_1 - P_3$

Step 2: Measure the corrected pressure drop, $\Delta P_{CORR} = P_3 - P_4$

Step 3: Measure the dynamic head at point i (i = 1 to 36), $\Delta P_{FROTH} = P_2 - P_4$

Step 4: $\Delta P_{FROTH} - \Delta P_{CORR} = (P_2 - P_4) = (P_3 - P_4) = P_2 - P_3 =$ dynamic liquid head at point i.

Step 5: $(\Delta P_{FROTH} - \Delta P_{CORR})_{ACTUAL} - (\Delta P_{FROTH} - \Delta P_{CORR})_{DATUM} =$ clear liquid height at point i.

An example of point-to-point height of clear liquid for a real experimental run is shown in Figure 4.9. The full data for the clear liquid measurements are presented in Appendices 12-14. The results are further computer processed in a way similar to that of 3-D temperature profiles to generated a 3-D clear liquid height variation on the tray as shown in Figure 4.10. The program used to perform this task is listed in Appendix 5.

Superficial Air velocity 1.0 ms^{-1}
Weir Load 25 $cm^3cm^{-1}s^{-1}$

	30	25	23	23		
24					22	
	28	28	21	25		
21						20
	26	28	21	23	19	
	25	22	18	23	22	
17						15
	24	23	19	21		
20					22	
	16	16	26	24		

Figure 4.9 An Example of Collected Liquid Hold-up Data

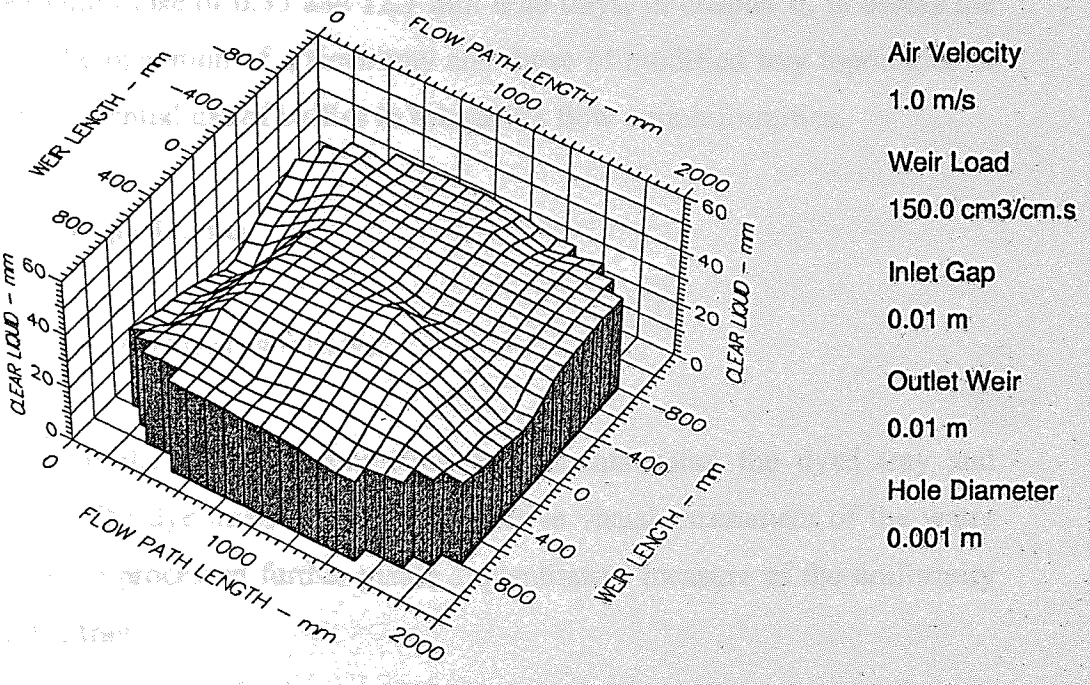

Fig. 4.10 An example of 3D profile of clear liquid height

CHAPTER FIVE

Investigations into the Gas-Liquid Flow Patterns on a Conventional Sieve Tray with 1 mm Holes

5.1 Introduction

The contacting of vapour and liquid on a conventional distillation sieve tray produces a chaotic mixture in which the mechanism of liquid cross-flow is complex and poorly understood. Although several works (Porter et al., 1972; Bell and Solari, 1974) support the view that the cross-flow pattern is generally nonuniform and multidirectional, the many differing approaches to be found in the literature for modelling the flow nonuniformities reflects a degree of uncertainty in the understanding of the mechanisms driving them. This chapter is concerned with the identification of air-water flow patterns on a commercial size sieve tray with 1 mm hole diameter perforations using the dye tracing and temperature profiling techniques. The measured tray efficiency and clear liquid height are used to evaluate the effect of flow patterns on tray mass transfer and hydraulic performances. The results are compared with those of 6.35 and 12.7 mm hole trays, in chapter 6, to assess the effect of hole size on the operation of a sieve tray and those of modified tray topologies in chapter 7, to assess the potential use of baffles in mitigating flow nonuniformities.

5.2 Programme of Experiments

The programme of experiments was as follows:

a) Direct observation of the air-water contacting experiments using the dyed tray and camera technique. The dye images provide qualitative visual assessment of the water flow pattern and when processed further yields a quantitative measure of the uniformity in dye spread on the tray.

b) Investigations into the effect of air-water flow-patterns on the clear liquid head profiles across the tray using an array of water manometers. This will provide comprehensive

clear liquid hold-up data and give an indication of the overall liquid distribution on the tray and the backup in the downcomer.

c) Investigations into the effect of the biphase flow-pattern on mass transfer using the water-cooling technique. The water temperature profiles across the tray are analogous to concentration profiles and when interpreted in terms of enthalpy-driving forces permit the calculation of thermal point and tray efficiencies. The temperature isotherms will complement the dye tracing and clear liquid height results to reveal the overall liquid flow behaviour.

d) Use of new approaches and rig adaptations (half-tray experiments) to extend investigations to higher liquid loads, to study the flow patterns at near flooding conditions.

5.3 Investigation by Direct Observation

Direct observation of the flow-patterns during air-water contacting experiments was aided by the use of coloured dye (potassium permanganate) and camera technique. Although the coloured dye and camera technique is an effective visual method of assessing air-water interactions on a distillation test tray, difficulties can arise due to lack of clarity of the dye in the highly agitated mixture. In this study, a novel approach to image analysis is used (Fischer, 1998) to isolate the dye images from grey images generated from the video recording of the dye movement during air-water contacting experiments. The experimental procedure used in the study has been described in chapter 4.

5.3.1 Results and Discussion

Many dye tracer runs were recorded on video and the images processing was carried out by Fischer (1999). The raw images from the videotape, digitised and converted from colour to 256 grey levels, were normalised for variable camera lighting intensity in order to remove the effect of camera automatic adjustment to different brightness in the field of view. Figure 5.1 presents a series of normalised images taken from the video recording of the air-water dye tracer studies carried out at a liquid loading of 50 $cm^3cm^{-1}s^{-1}$ and superficial air velocity

of 0.8 ms^{-1}, consistent with the froth regime. The images were sampled at time, t = 5, 10, 20, 25, 30 and 40 seconds, where time t = 0 represents the time the dye injection was stopped and only clear water entered the tray. In order to highlight the dye traces, the images were separated into pixels of pure black and white by subtracting background images from the normalised images and setting a nominal grey level threshold limit of 249. Background images were generated by operating the tray normally but without the injection of dye, at the corresponding air and water flowrates. This is carried out in practice by recording the surface of the dispersion just before dye was introduced. The binary images are presented in Figure 5.2. The tray centreline is considered to be a mirror-axis of symmetry and slight deviations from perfect symmetry along the centreline in the images are attributed to slight out of levelness in the tray and limitations in the imaging procedure. An ideal flow is one that provides for an even and steady dye subsidence across the tray.

It is difficult to construct an accurate pictorial view of the liquid flow patterns from the dye images presented in Figures 5.1 and 5.2 alone. However, it is evident from the series of dye shots in Figure 5.2 that the section of the tray between the chordal downcomers is being replenished with fresh water at a faster rate than the segmented regions adjacent to the walls. Even after 40 seconds when virtually all the dye in the central portion of the tray had subsided, substantial dye traces can still be found around the edges of the tray near the walls. In some cases the dye seemed trapped adjacent to the walls for a prolonged period of time. The dye distribution suggests that the liquid residence time increased almost radially from the inlet, with the tendency for the liquid to flow preferentially between the chordal weirs and to pool adjacent to the walls.

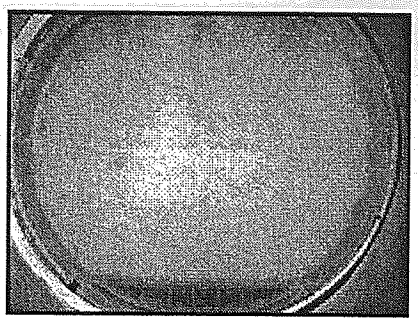

5 Seconds

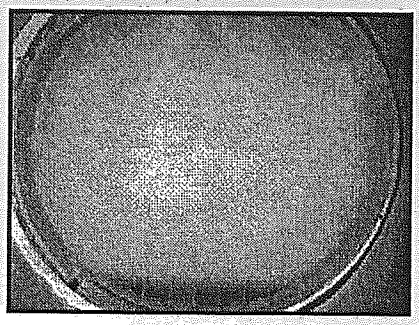

10 Seconds

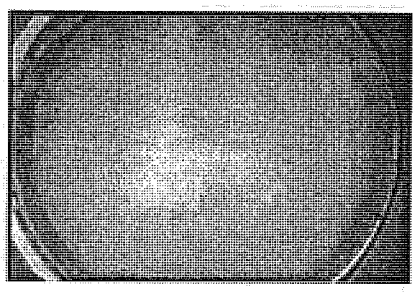

20 Seconds

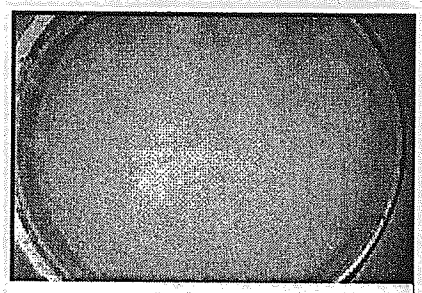

25 Seconds

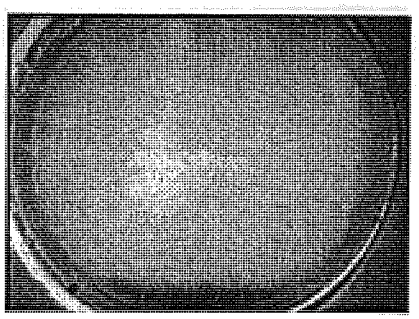

30 Seconds

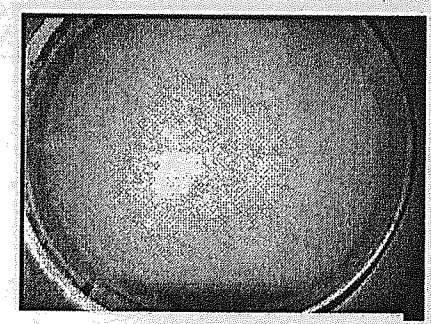

40 Seconds

Figure 5.1 Normalised Dye Traces at Weir Loading of 50 $cm^3cm^{-1}s^{-1}$ and Superficial Air Velocity of 0.8 $m\ s^{-1}$

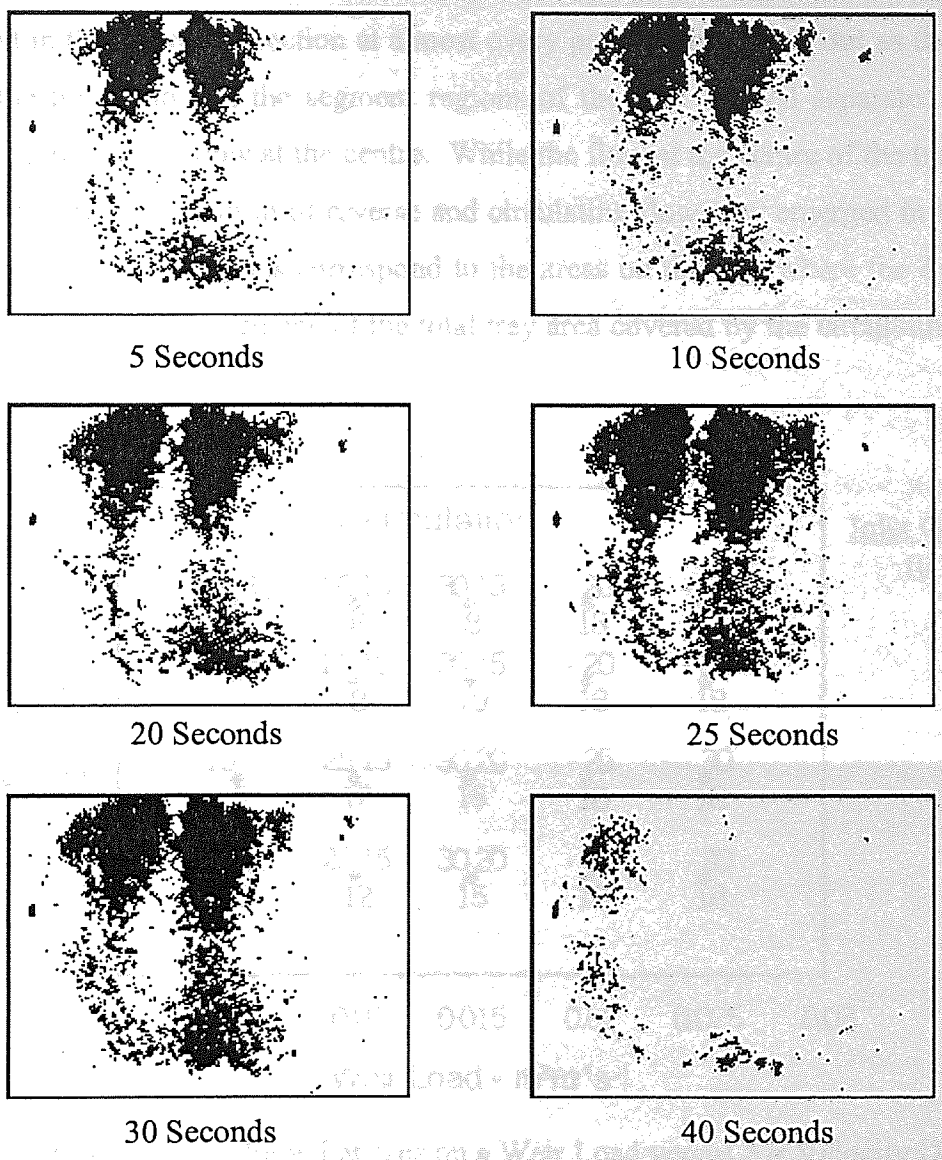

Figure 5.2 Binary Dye Images at Weir Loading of 50 $cm^3cm^{-1}s^{-1}$ and Superficial Air Velocity of 0.8 $m\ s^{-1}$

The effects of various experimental variables on the flow patterns are not clearly discernible from the dye images. However, a direct visual observation of the functioning dyed tray revealed that changes in the liquid flowrate caused different flow patterns to develop over the tray area. At low water flowrates, below 50 $cm^3cm^{-1}s^{-1}$, the bulk liquid flow appeared uniform and in the forward direction at almost every point on the tray. But as the water rate increased the liquid flow at the segment regions of the tray seemed separated and out of synchronisation with the flow at the centre. While the flow at the centre of the tray remained in forward direction some form of reverse and circulating flow now emerged in the segment regions. The circulating regions correspond to the areas on the tray where the dye appeared trapped. The estimated percentage of the total tray area covered by the circulating regions is set out in Figure 5.3.

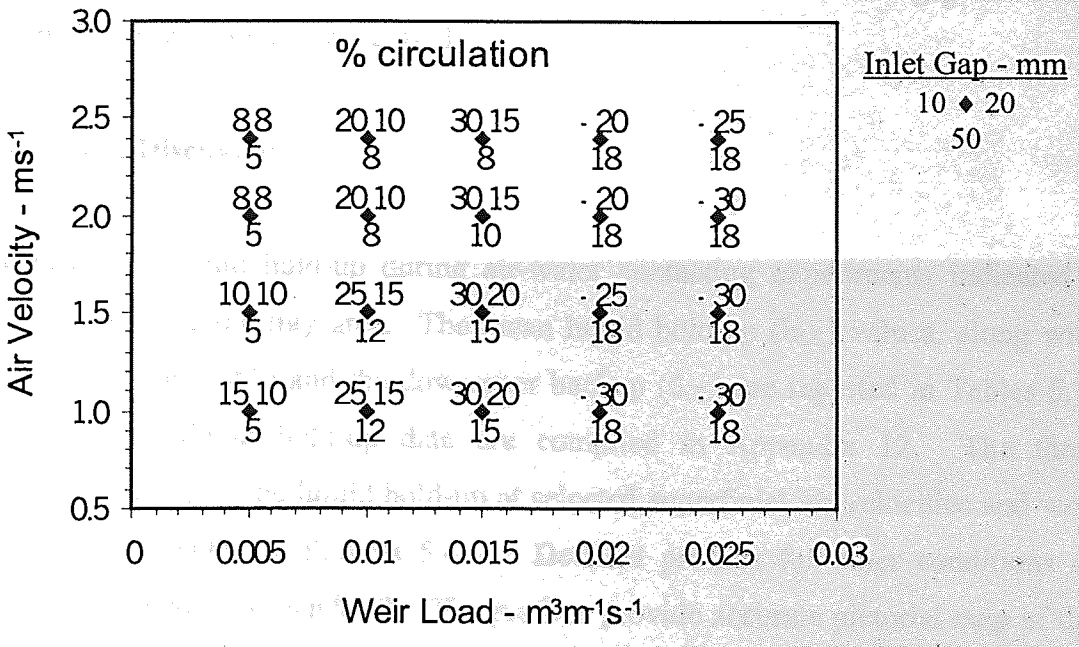

Figure 5.3 Summary of Flow Patterns on a Weir Load versus Air Velocity Diagram

It is important to state that the tool used in the dye image analysis is still a developing one (Fischer, 1999) and the procedure may not have yielded exact representative traces of the dye images across the tray. One inherent shortcoming in the procedure is that the video camera only captures the top surface of the froth and the dye concentration below the surface is unaccounted for. On a number of occasions, some images seemed anomalous to the trend with the time period because a greater quantity of dye becomes exposed to the camera.

Nevertheless, the technique is very helpful as a qualitative and comparative tool, an advantage used to compare the performance of different tray topologies in chapter 7. The binary image sampled at 40 seconds provides a fair pictorial representation of the results of direct visual observation of the distribution on the functioning tray.

5.4 Investigation by Liquid Head Measurements

The clear liquid height on the tray was determined using the average of thirty-six manometers mounted flush with the tray floor. The liquid backup in the inlet downcomer was also monitored during every run. The water flowrate, expressed as a weir loading, was varied between 2.5×10^{-3} and 3.5×10^{-2} $m^3 m^{-1} s^{-1}$ and the superficial air velocity was in the range of 0.5 to 2.4 m s^{-1}. Experiments involving water flowrates beyond 2.0×10^{-2} $m^3 m^{-1} s^{-1}$ were carried out on a "half-tray" (section 3.6). All combinations of the inlet gap and outlet weir heights of 10, 20 and 50 mm were used.

5.4.1 Results and Discussion

Measurements of the liquid hold-up during air-water contacting experiments indicated a significant variation over the tray area. The mean liquid hold-up (h_{CL}) values, along with their standard deviations (Std.) and the dowcomer backup (d_{CL}) are reported in Tables 5.1-5.3, the actual point liquid hold-up data are compiled in Appendix 12. The three dimensional, 3D, profiles of the liquid hold-up at selected superficial air velocities and weir configurations are presented in Figures 5.4a-l. Detailed profiles for other conditions of experiment are presented in Appendix 9. The profiles provide accurate pictorial map of the overall liquid distribution and the hydraulic imbalances on the operating tray. The results are discussed in terms of the individual effects of the air and water flowrates, the inlet gap and height of the outlet weir. The experimental liquid hold-ups are compared with those predicted with the correlations of Stichlmair (1978) and Bennett et al. (1983), presented in Tables 5.4 and 5.5, respectively.

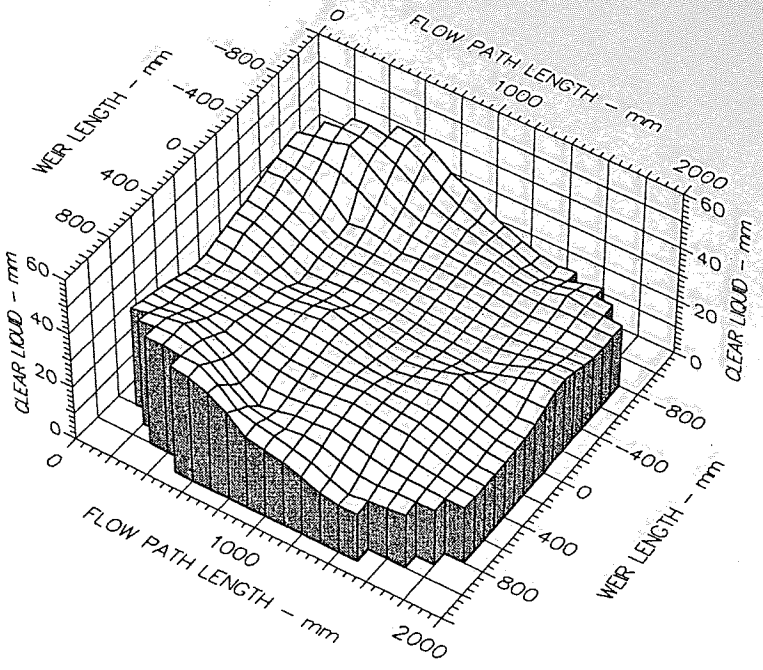

Air Velocity
0.800 m/s

Weir Load
25.0 cm3/cm.s

Inlet Gap
0.020 m

Outlet Weir
0.020 m

Hole Diameter
0.001 m

Fig.5.4a Surface of Clear Liquid Hold-up
Superficial Air velocity 0.8 m/s

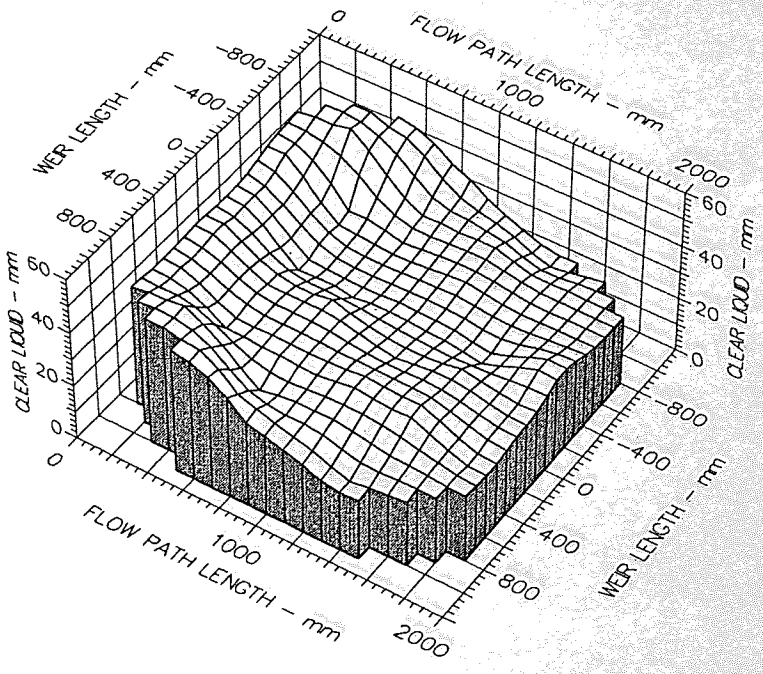

Air Velocity
0.8 m/s

Weir Load
50.0 cm3/cm.s

Inlet Gap
0.02 m

Outlet Weir
0.02 m

Hole Diameter
0.001 m

Fig.5.4b Surface of Clear Liquid Hold-up
Superficial Air velocity 0.8 m/s

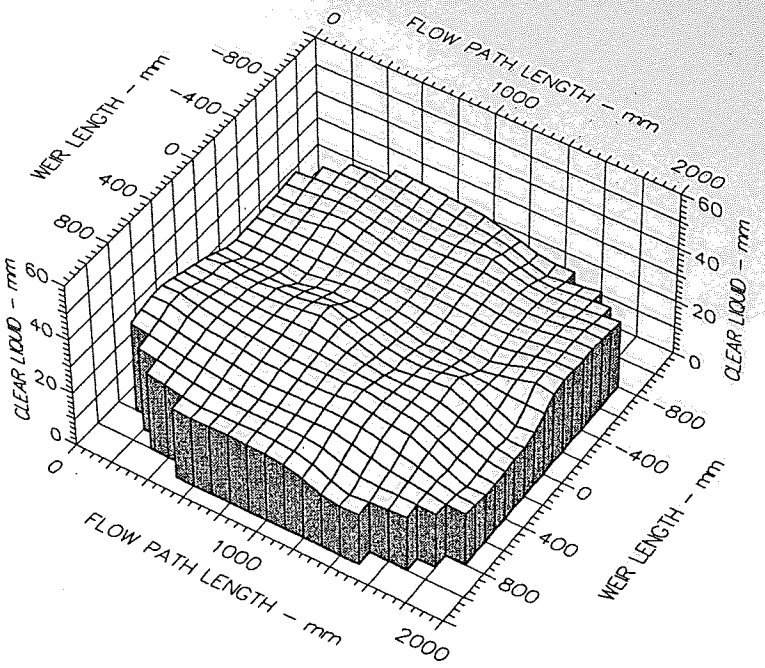

Air Velocity
1.000 m/s

Weir Load
50.0 cm3/cm.s

Inlet Gap
0.010 m

Outlet Weir
0.010 m

Hole Diameter
0.001 m

Fig.5.4c Surface of Clear Liquid Hold-up
Superficial Air velocity 1.0 m/s

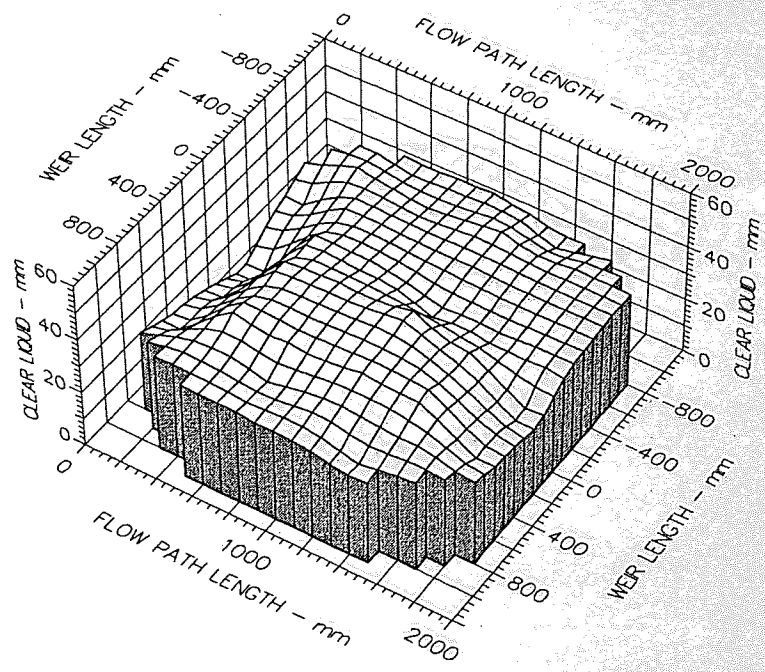

Air Velocity
1.0 m/s

Weir Load
150.0 cm3/cm.s

Inlet Gap
0.01 m

Outlet Weir
0.01 m

Hole Diameter
0.001 m

Fig.5.4d Surface of Clear Liquid Hold-up
Superficial Air velocity 1.0 m/s

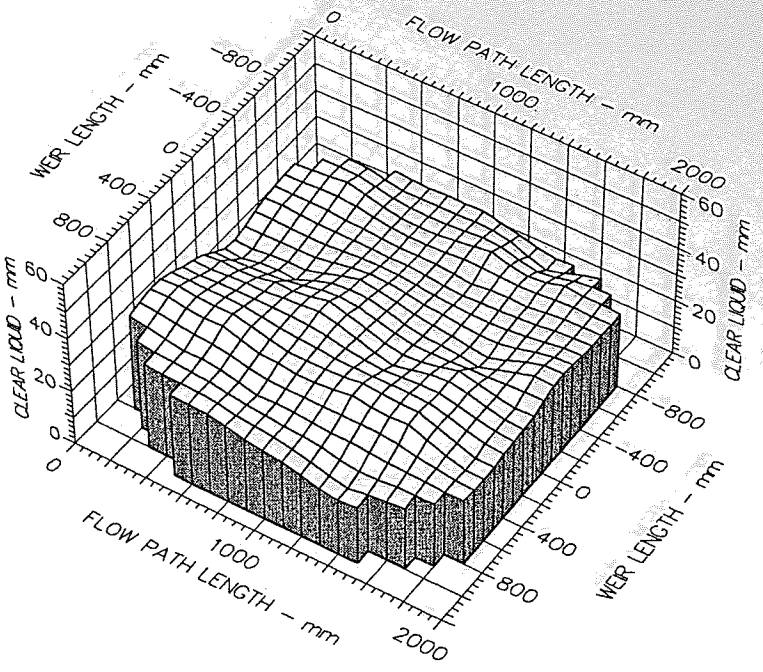

Air Velocity
1.000 m/s

Weir Load
50.0 cm3/cm.s

Inlet Gap
0.020 m

Outlet Weir
0.020 m

Hole Diameter
0.001 m

Fig.5.4e Surface of Clear Liquid Hold-up
Superficial Air velocity 1.0 m/s

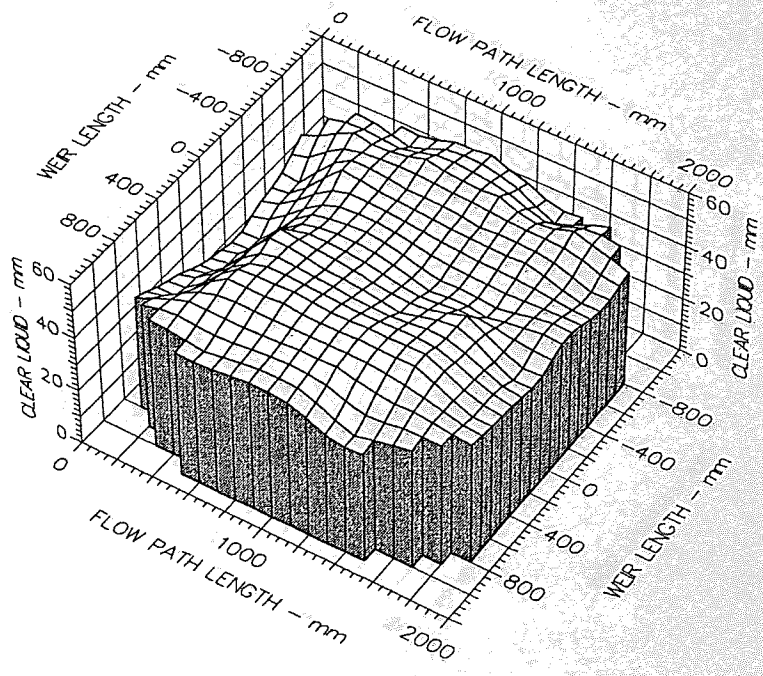

Air Velocity
1.0 m/s

Weir Load
200.0 cm3/cm.s

Inlet Gap
0.02 m

Outlet Weir
0.02 m

Hole Diameter
0.001 m

Fig.5.4f Surface of Clear Liquid Hold-up
Superficial Air velocity 1.0 m/s

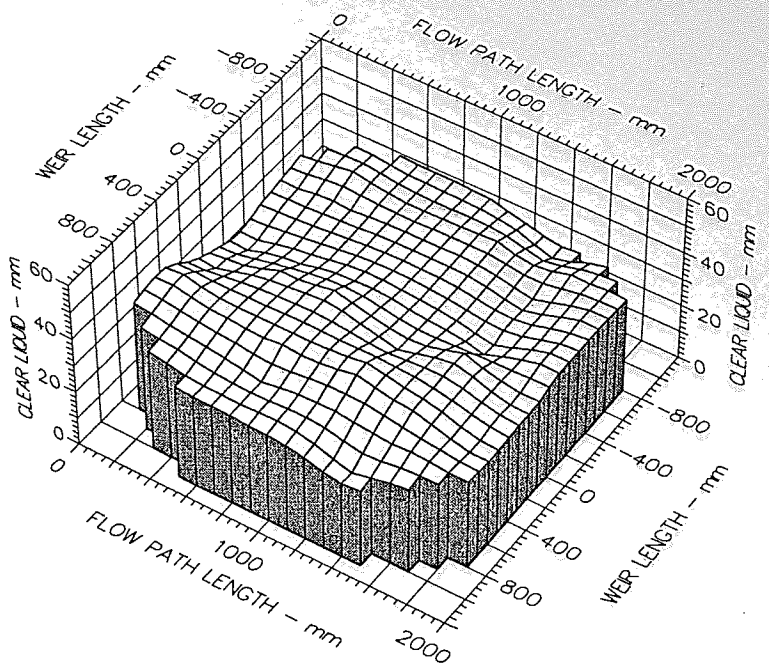

Air Velocity
1.000 m/s

Weir Load
50.0 cm3/cm.s

Inlet Gap
0.050 m

Outlet Weir
0.050 m

Hole Diameter
0.001 m

Fig.5.4g Surface of Clear Liquid Hold-up
Superficial Air velocity 1.0 m/s

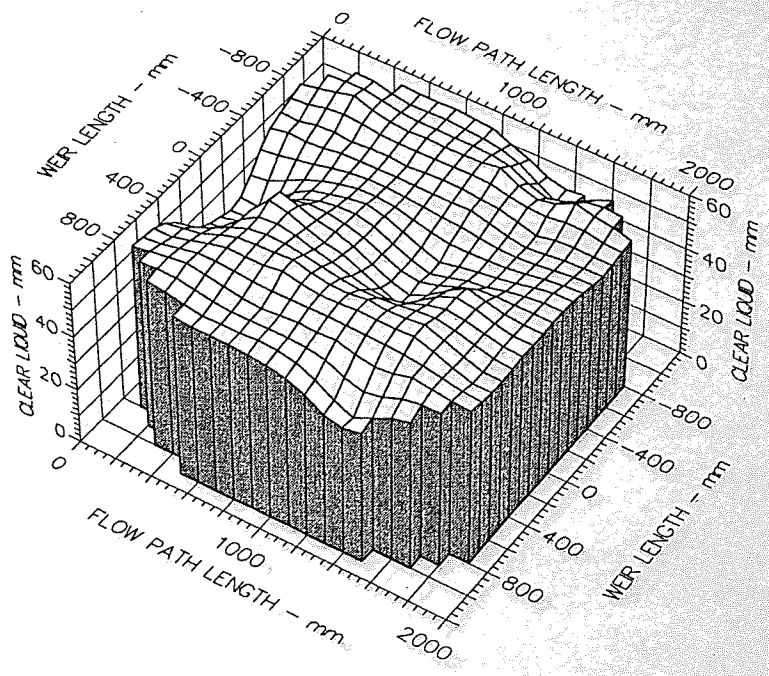

Air Velocity
1.0 m/s

Weir Load
200.0 cm3/cm.s

Inlet Gap
0.05 m

Outlet Weir
0.05 m

Hole Diameter
0.001 m

Fig.5.4h Surface of Clear Liquid Hold-up
Superficial Air velocity 1.0 m/s

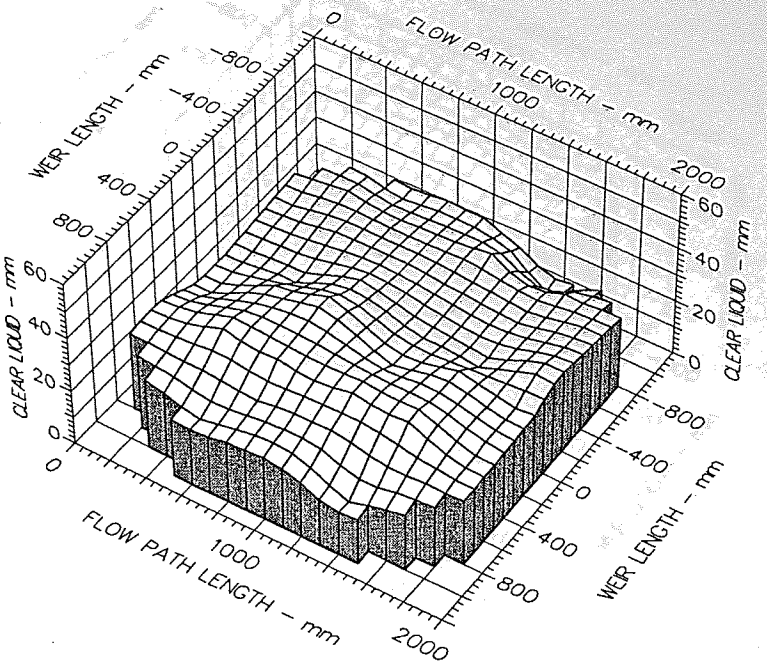

Air Velocity
2.000 m/s

Weir Load
50.0 cm3/cm.s

Inlet Gap
0.050 m

Outlet Weir
0.050 m

Hole Diameter
0.001 m

Fig.5.4i Surface of Clear Liquid Hold-up
Superficial Air velocity 2.0 m/s

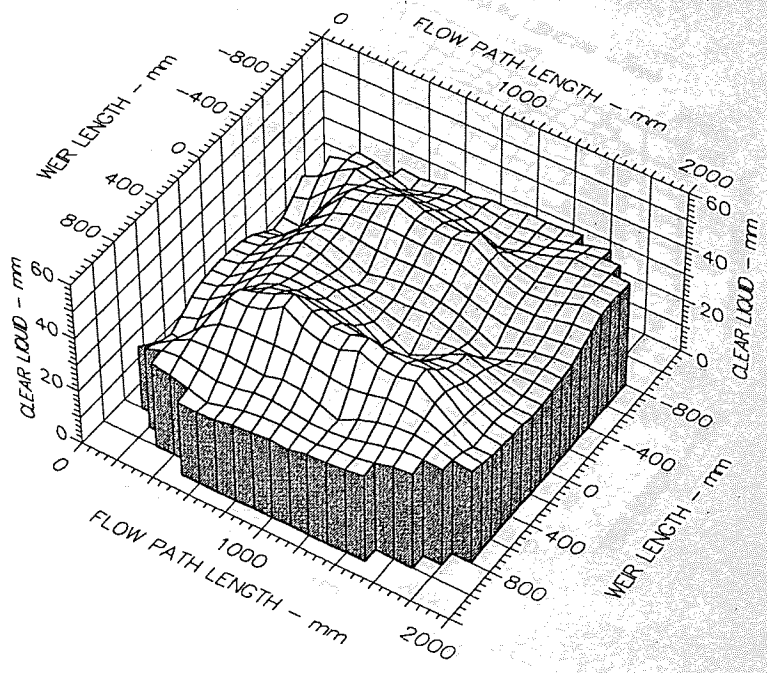

Air Velocity
2.0 m/s

Weir Load
200.0 cm3/cm.s

Inlet Gap
0.05 m

Outlet Weir
0.05 m

Hole Diameter
0.001 m

Fig.5.4j Surface of Clear Liquid Hold-up
Superficial Air velocity 2.0 m/s

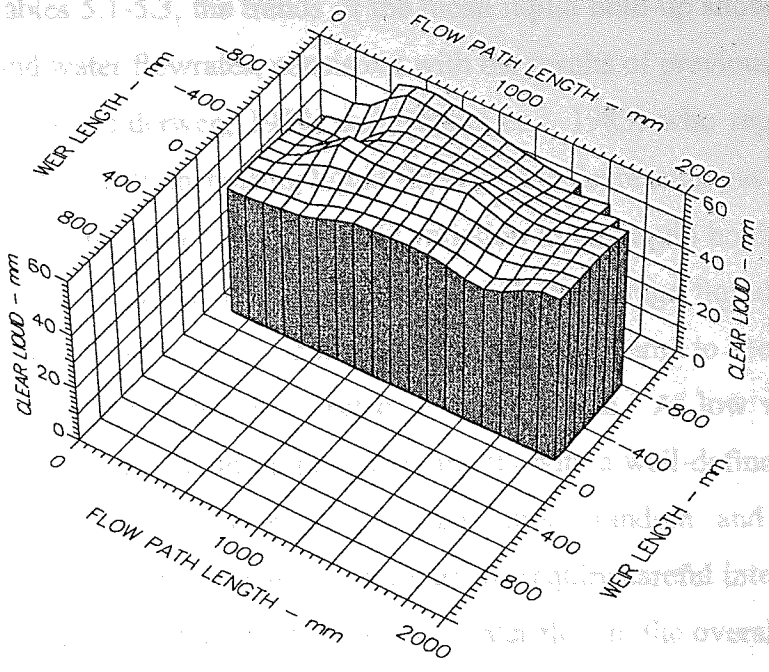

Air Velocity
2.000 m/s

Weir Load
300.0 cm3/cm.s

Inlet Gap
0.050 m

Outlet Weir
0.050 m

Hole Diameter
0.001 m

Fig.5.4k Surface of Clear Liquid Hold-up
Superficial Air velocity 2.0 m/s

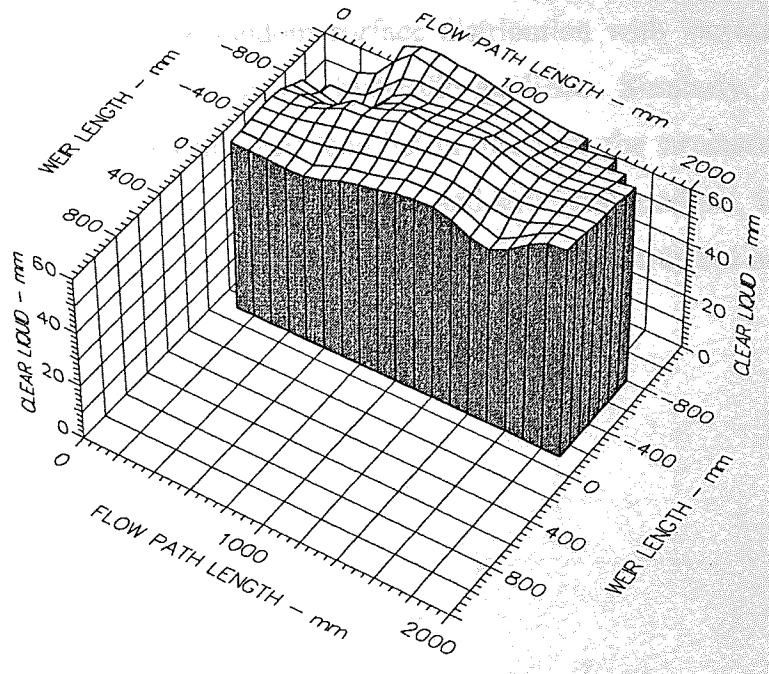

Air Velocity
2.0 m/s

Weir Load
350.0 cm3/cm.s

Inlet Gap
0.05 m

Outlet Weir
0.05 m

Hole Diameter
0.001 m

Fig.5.4l Surface of Clear Liquid Hold-up
Superficial Air velocity 2.0 m/s

Effect of the Air and Water Flowrates

From Tables 5.1-5.3, the trends of the mean liquid hold-up show contrasting dependence on the air and water flowrates, consistent with the results of previous workers (Stichlmair, 1978; Hofhuis and Zuiderweg, 1979; and Bennet et l, 1983) who reported increase in the mean liquid hold-up with increasing liquid flowrate and decreasing gas flowrate. Additionally, this work gives a measure of the possible variation in the liquid hold-up in terms of the standard deviation of thirty-six point measurements, if an average liquid hold-up value is assumed. The standard deviation of the mean liquid hold-up seems to increase with increasing water and air flowrates. This is reflected in the 3D plots. At low water and air flowrates, the surface of the liquid hold-up profile is smooth with a well-defined liquid gradient, but as the flowrates increased, the surface became more random and uneven without a 'clear-distinctive' gradient on the tray. These trends require careful interpretation in order to isolate the individual contribution of the air and water flow to the overall liquid hold-up profile. As expected, the hydraulic gradient on the tray tends to increase with increasing water flowrate and decrease with increasing air flowrate, resulting in steeper profiles as the water flowrate increased and flatter profiles as the air flowrate increased. However, the fluctuating imbalances and eddies due to air agitation is not lost on the surface of the liquid hold-up which assumes more random surface distribution with increasing air flowrate despite an overall flatter structure in the hydraulic gradient. Similarly, the surface imbalances also increase with increasing weir load but in this case, the structural gradient increases as well. These two effects, i.e. smooth surface and structural gradient, tend to offset and mask each other on a direct visual observation of the functioning tray but are reflected clearly in the 3D plots.

Inlet Gap - 10mm		UMD Tray								
Outlet Weir - mm		10			20			50		
Air Velocity - ms^{-1}		1	1.5	2	1	1.5	2	1	1.5	2
Water Load - $cm^3cm^{-1}s^{-1}$	Average Height Of Clear Liquid - mm									
25	h_{CL}	22.3	18.9	17.2	23.6	22.0	18.6	31.6	28.6	22.5
	Std.	3.6	3.4	4.2	3.3	3.6	4.7	3.8	4.3	5.3
	d_{CL}	26.0	22.2	25.3	32.0	29.8	31.5	42.3	44.0	47.2
50	h_{CL}	26.3	22.3	18.7	28.6	25.7	20.6	34.7	32.6	26.5
	Std.	4.2	4.3	5.2	3.8	4.2	5.8	4.3	4.6	5.7
	d_{CL}	43.2	39.0	42.2	49.5	48.2	54.8	66.0	64.5	67.7
75	h_{CL}	29.1	26.3	20.9	31.2	29.4	22.3	40.5	34.1	28.9
	Std.	4.3	4.1	5.1	3.6	4.2	5.1	5.5	5.3	5.4
	d_{CL}	76.5	80.0	83.7	81.3	87.2	90.2	98.5	102.7	101.5
100	h_{CL}	31.5	28.1	22.1	33.9	31.6	23.5	42.1	36.8	31.2
	Std.	4.5	4.8	5.9	4.6	4.9	5.5	5.3	5.9	5.5
	d_{CL}	111.0	110.3	121.5	116.7	116.7	124.8	132.7	139.3	141.2
150	h_{CL}	33.8	31.2	25.6	36.0	33.1	26.4	45.3	40.6	32.9
	Std.	6.3	6.1	6.2	6.2	6.2	6.3	6.7	7.3	6.5
	d_{CL}	199.3	208.7	220.8	204.0	211.3	220.3	219.3	222.7	233.2

Table 5.1 Mean Height of Clear Liquid Data - 10 mm Inlet Gap

Inlet Gap - 20mm		UMD Tray								
Outlet Weir - mm		10			20			50		
Air Velocity - ms^{-1}		1	1.5	2	1	1.5	2	1	1.5	2
Water Load - $cm^3cm^{-1}s^{-1}$	Average Height Of Clear Liquid - mm									
25	h_{CL}	22.4	21.4	17.0	24.9	22.8	17.7	31.3	29.1	22.5
	Std.	3.8	3.8	4.0	3.7	3.5	4.9	4.1	3.4	5.4
	d_{CL}	26.7	22.8	23.0	28.3	25.2	25.2	42.0	36.5	37.8
50	h_{CL}	26.4	24.7	18.8	28.4	25.5	20.8	34.0	31.9	26.9
	Std.	4.1	3.7	5.4	4.1	4.0	5.3	5.1	4.1	6.1
	d_{CL}	36.7	32.2	32.5	36.8	32.7	34.7	53.7	46.5	51.7
100	h_{CL}	32.5	29.3	20.9	33.9	31.9	24.1	42.8	35.6	31.6
	Std.	4.4	4.6	5.4	3.8	4.7	5.7	9.3	5.4	5.4
	d_{CL}	70.3	70.3	76.5	68.5	69.7	74.7	89.8	86.7	87.7
150	h_{CL}	35.3	33.0	26.2	37.0	33.8	26.7	46.3	40.2	32.0
	Std.	5.3	6.3	6.0	5.5	6.4	6.5	5.8	6.7	6.0
	d_{CL}	110.0	107.5	118.3	105.5	107.0	115.7	125.0	122.0	127.3
200	h_{CL}	44.0	38.0	29.9	45.4	44.1	29.5	52.7	47.0	34.0
	Std.	6.4	7.5	6.8	6.7	6.9	7.0	6.9	7.2	6.5
	d_{CL}	163.2	161.2	179.2	147.0	157.0	169.5	164.7	165.8	170.3

Table 5.2 Mean Height of Clear Liquid Data - 20 mm Inlet Gap

Inlet Gap - 50mm		UMD Tray								
Outlet Weir - mm		10			20			50		
Air Velocity - ms^{-1}		1	1.5	2	1	1.5	2	1	1.5	2
Water Load - $cm^3cm^{-1}s^{-1}$	Average Height Of Clear Liquid - mm									
25	h_{CL}	22.7	21.0	17.2	23.9	22.1	17.8	31.7	28.4	22.4
	Std.	3.8	3.4	4.6	3.5	3.8	5.7	3.7	4.3	5.4
	d_{CL}	23.7	22.5	20.5	29.7	29.3	26.0	45.7	37.2	41.0
50	h_{CL}	26.3	24.0	18.8	28.1	26.3	20.8	34.4	32.5	26.8
	Std.	3.9	3.9	5.2	3.9	4.3	5.5	3.8	4.2	5.0
	d_{CL}	30.7	28.5	27.5	35.7	36.7	33.2	52.7	43.7	49.7
100	h_{CL}	32.8	29.8	21.9	34.3	33.3	23.6	42.3	36.9	31.0
	Std.	5.1	5.0	5.4	5.3	4.9	5.6	8.3	5.1	6.3
	d_{CL}	47.3	46.5	43.5	48.5	51.7	45.7	67.0	57.3	65.0
150	h_{CL}	36.1	33.4	26.1	37.1	37.1	26.8	45.5	40.2	32.6
	Std.	5.8	6.2	6.6	5.5	6.3	6.3	6.7	6.4	7.5
	d_{CL}	58.3	58.7	58.5	58.3	60.0	56.7	76.0	73.7	76.2
200	h_{CL}	44.5	37.5	28.9	46.0	44.4	28.7	57.2	53.9	35.4
	Std.	6.1	7.0	6.7	7.5	10.2	5.9	6.5	6.6	8.7
	d_{CL}	82.3	79.7	79.5	88.3	87.8	82.7	95.2	98.3	98.0

Table 5.3a Mean Height of Clear Liquid Data - 50 mm Inlet Gap

Inlet Gap - 50mm		UMD Tray		
Outlet Weir - mm		50		
Air Velocity - ms^{-1}		1.5	2	2.4
Water Load - $cm^3cm^{-1}s^{-1}$	Average Height Of Clear Liquid - mm			
250	h_{CL}	59.7	46.5	39.9
	Std.	6.1	6.7	6.2
	d_{CL}	105.7	104.2	109.8
300	h_{CL}	70.1	55.4	46.4
	Std.	6.7	5.6	5.7
	d_{CL}	137.3	145.2	153.7
350	h_{CL}	73.3	69.7	57.3
	Std.	5.8	6.4	6.6
	d_{CL}	168.0	192.5	199.8

Table 5.3b Mean Height of Clear Liquid Data - 50 mm Inlet Gap

The trends of the mean liquid hold-up and the downcomer backup with the water flowrate are demonstrated in Figures 5.5 and 5.7, respectively. Figure 5.6 is the variation in the standard deviation of the thirty-six point measurements with water flowrate.

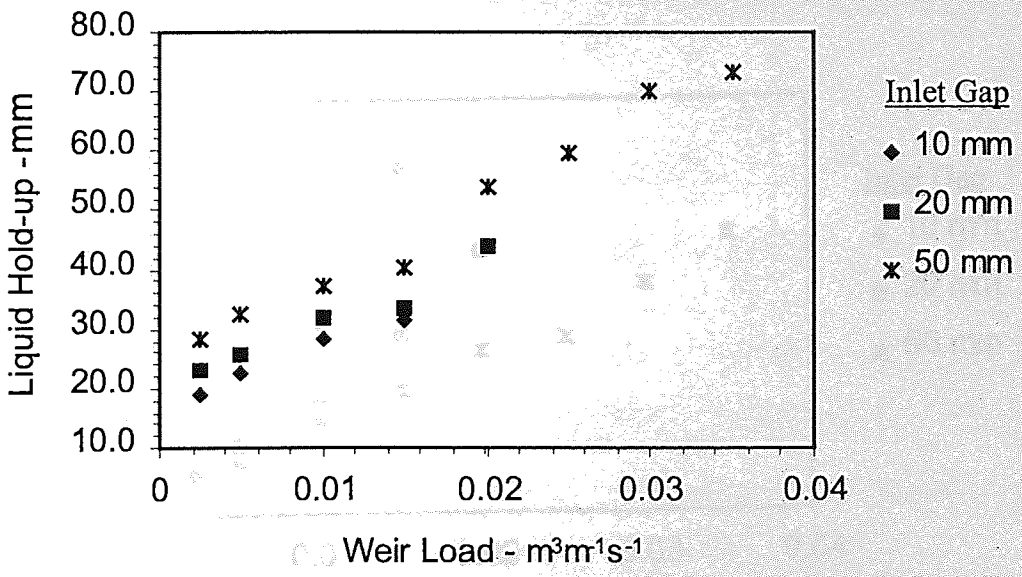

Figure 5.5 Graph of Measured Liquid Hold-up against Weir Load

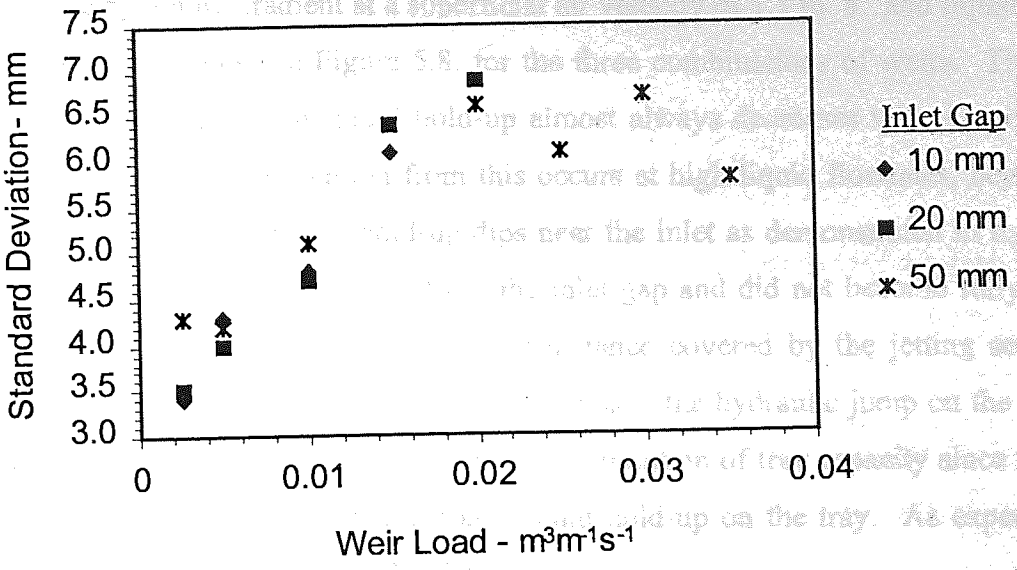

Figure 5.6 Graph of the Standard Deviation of the Thirty-six Manometer point Measurements against Weir Load

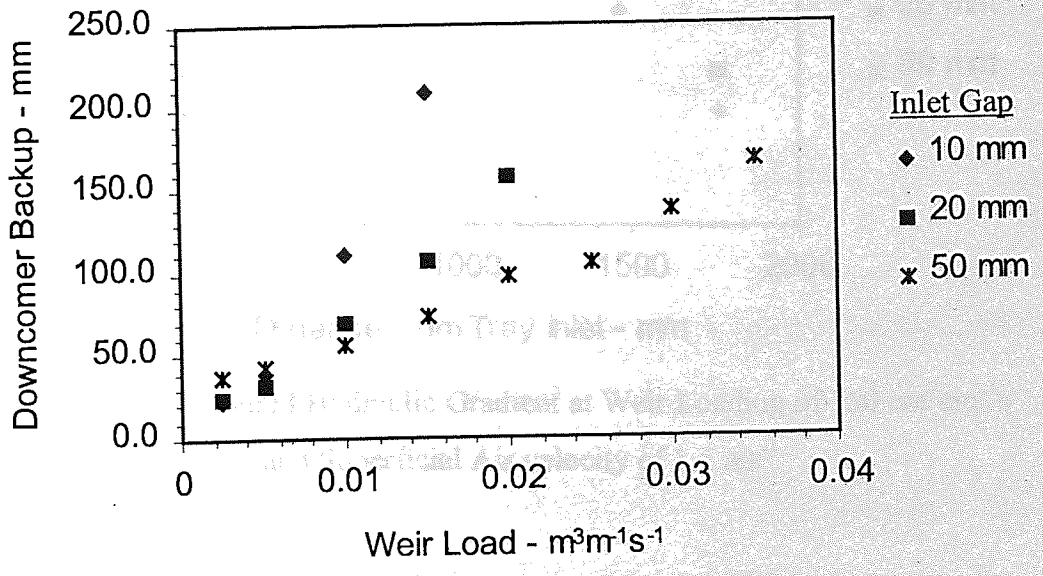

Figure 5.7 Graph of the Measured Inlet Downcomer Backup against Weir Load

The Hydraulic Gradient

The hydraulic gradient under various loading conditions was estimated by means of the series of clear liquid head tappings along the centreline of the 2.44-m long air-water simulator. The hydraulic gradient at a superficial air velocity of 1.5 $m^{-1}s^{-1}$ and liquid loading of 150 $cm^3cm^{-1}s^{-1}$ is shown in Figure 5.8, for the three combinations of weirs. The figure illustrates clearly that the clear liquid hold-up almost always decreases with distance from the inlet downcomer. The exception from this occurs at high liquid flowrates, beyond 100 $cm^3cm^{-1}s^{-1}$, where the clear liquid hold-up dips near the inlet as demonstrated in the figure. In these cases the liquid seemed to jet from the inlet gap and did not become fully aerated until after some distance from the inlet. The distance covered by the jetting seemed to decrease with increasing inlet gap. At high liquid loads, the hydraulic jump on the tray can cause premature tray flooding and therefore undue limitation of tray capacity since the peak of the jump is much higher than the average liquid hold-up on the tray. As expected, the gradient shows an increase with weir height.

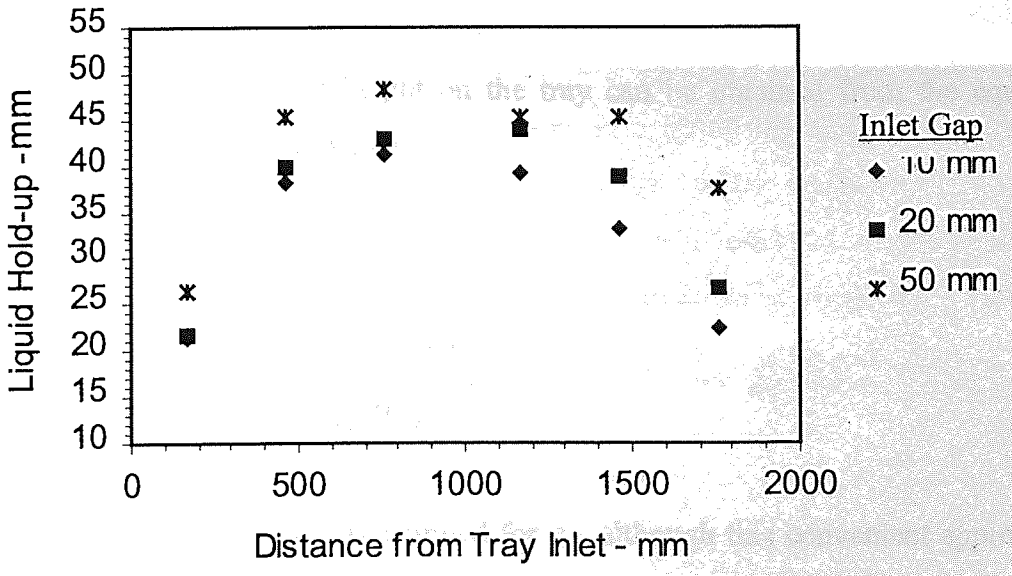

Figure 5.8 Measured Hydraulic Gradient at Weir Loading of 150 $cm^3cm^{-1}s$ and Superficial Air velocity of 1.5 ms^{-1}

Effect of the inlet Gap and Outlet Weir

The inlet gap and outlet weir height play very dominant roles in setting the liquid entrance velocity and froth height, respectively. The liquid hold-up increased steadily with the weir height. The surface profiles at low inlet gaps, where the liquid entrance velocity is high, are generally smoother than at high gaps where the velocity is low.

Predictive Models of Height of Clear Liquid

Several correlations exist in the literature for the prediction of the height of clear liquid on the tray, many of which are based on the Francis's weir equation (Francis, 1883), including those of Cowell (1979), Stichlmair (1978) and Bennett et al. (1983). The final equation over the weir is given by

$$h_{ow} = \frac{1.04}{C_d^{0.67} g^{0.33}} \left(\frac{Q_L}{(1-\varepsilon_w)W} \right)^{0.67} \quad \ldots. 5.1$$

An estimate of the clear liquid height on the tray can be obtained from the equation by making use of the following equations:

$$h_{cl} = (1-\varepsilon)h_f = (1-\varepsilon)(h_w + h_{ow}) \quad \ldots. 5.2$$

$$h_{cl} = (1-\varepsilon)\left[h_w + \frac{0.49}{C_d^{0.67}} \left(\frac{Q_L}{(1-\varepsilon_w)W} \right)^{0.67} \right] \quad \ldots. 5.3$$

For most practical purposes, ε is substituted for ε_w although this convenient approximation tends to lead to an underestimation of the height of clear liquid, h_{cl}. This approach was adopted by Colwell (1979) who proposed

$$h_{cl} = (1-\varepsilon)\left[h_w + \frac{0.49K}{C_d^{0.67}} \left(\frac{Q_L}{(1-\varepsilon)W} \right)^{0.67} \right] \quad \ldots. 5.4$$

Colwell's equation has been verified for the froth regime, with k = 1.49, using data from a wide variety of systems (Lockett, 1986). The weir coefficient, C_d is given as

$$C_d = 0.61 + 0.08\frac{h_{ow}}{h_w} \quad \text{when } \frac{h_{ow}}{h_w} \leq 8.14 \qquad \ldots. 5.5$$

and

$$C_d = 1.06\left(1 + \frac{h_{ow}}{h_w}\right)^{1.5} \quad \text{when } \frac{h_{ow}}{h_w} > 8.14 \qquad \ldots. 5.6$$

where

$$h_{ow} = \frac{h_{cl}}{1-\varepsilon} - h_w \qquad \ldots. 5.7$$

The calculation procedure is iterative as the method for obtaining ε also involves h_{cl}.

In the mixed froth and spray regimes, some of the liquid is projected over the weir as drops rather than flowing over as a liquid phase continuos dispersion and this tends to increase h_{cl} above the value given in equation 5.3. Although Colwell's correlation is restricted to the froth regime, the correction factor k is included to account for the liquid that is projected over the weir as drops rather than flowing over as a liquid phase continuos dispersion. Stichlmair (1978) argued that only gas velocities in excess of the single bubble rise velocity u_b are significant in causing drop projections over the weir and used an additional term to account for the drop projections over the weir. His equation can be written as

$$h_{cl} = (1-\varepsilon)\left[h_w + \frac{0.49}{C_d^{0.67}}\left(\frac{Q_L}{(1-\varepsilon)W}\right)^{0.67} + \frac{125(u_s - u_b)^2 \rho_G}{g(\rho_L - \rho_G)\varepsilon^2}\right] \qquad \ldots. 5.8$$

where $$u_b = 1.55\left[\frac{\sigma(\rho_L - \rho_G)g}{\rho_L^2}\right]^{0.25} \cdot \left(\frac{\rho_G}{\rho_L}\right)^{1/24} \qquad \ldots. 5.9$$

and $C_d = 0.67$.

A more recent correlation due to Bennett et al. (1983), is given by

$$h_{cl}=\alpha_e\left[h_w+C\left(\frac{Q_L}{W\alpha_e}\right)^{0.67}\right] \quad \ldots. 5.10$$

where

$$\alpha_e=\exp\left[-12.55\left(u_s\left(\frac{\rho_G}{\rho_L-\rho_G}\right)^{0.5}\right)^{0.91}\right] \quad \ldots. 5.11$$

and

$$C=0.50+0.438\exp(-137.8h_w) \quad \ldots. 5.12$$

The clear liquid height predicted with the correlations of Stichlmair (1978) and Bennett et al., (1983) are reported in Tables 5.4 and 5.5 respectively. It is noteworthy that the Bennett et al. model predicts higher clear liquid height for a 10 mm weir than for a 20 mm weir at high liquid loading. Figures 5.9-5.11 compare the experimental liquid hold-ups with the ones predicted from the correlations of Stichlimer (model 1) and Bennett et al. (model 2). The experimental values match well with those of predictive models, especially at high weir heights. The liquid hold-ups were averaged for various air velocities so that a general representative plot could be made against the water load.

Model		Stichlmair (1978)											
Weir Height - mm		10				20				50			
Air Velocity - ms^{-1}		1	1.5	2	2.4	1	1.5	2	2.4	1	1.5	2	2.4
Water Load - $cm^3cm^{-1}s^{-1}$	Predicted Height Of Clear Liquid - mm												
25	h_{CL}	17.4	15.0	12.7	8.8	19.9	18.1	14.4	9.6	27.4	22.9	17.2	11.0
50	h_{CL}	22.0	19.0	16.0	11.4	24.5	22.0	17.7	12.2	32.0	26.9	20.5	13.5
75	h_{CL}	25.8	22.3	18.8	13.6	28.4	25.4	20.5	14.4	35.9	30.2	23.2	15.7
100	h_{CL}	29.3	25.3	21.2	15.5	31.8	28.4	23.0	16.3	39.4	33.2	25.7	17.7
150	h_{CL}	35.4	30.6	25.6	19.0	38.0	33.7	27.4	19.8	45.5	38.5	30.1	21.1
200	h_{CL}	40.9	35.4	29.6	22.1	43.5	38.4	31.3	22.9	51.0	43.3	34.1	24.2
250	h_{CL}	46.0	39.7	33.2	24.9	48.5	42.8	34.9	25.7	56.1	47.6	37.7	27.0
300	h_{CL}	50.7	43.8	36.6	27.6	53.3	46.9	38.3	28.4	60.8	51.7	41.1	29.7
350	h_{CL}	55.2	47.7	39.8	30.1	57.7	50.7	41.5	30.9	65.3	55.6	44.3	32.2

Table 5.4 Predicted Height of Clear Liquid Data using the Stichlmair Model

Model		Bennett et al. (1983)											
Weir Height - mm		10				20				50			
Air Velocity - ms^{-1}		1	1.5	2	2.4	1	1.5	2	2.4	1	1.5	2	2.4
Water Load - $cm^3cm^{-1}s^{-1}$	Predicted Height Of Clear Liquid - mm												
25	h_{CL}	14.6	12.5	10.9	9.8	18.9	15.6	13.1	11.5	35.0	28.0	22.6	19.2
50	h_{CL}	19.9	17.4	15.4	14.0	23.5	19.9	17.0	15.2	39.4	32.0	26.3	22.7
75	h_{CL}	24.4	21.6	19.2	17.6	27.4	23.5	20.3	18.2	43.1	35.4	29.4	25.6
100	h_{CL}	28.5	25.3	22.6	20.7	30.9	26.6	23.2	21.0	46.4	38.4	32.2	28.2
150	h_{CL}	35.6	31.8	28.6	26.4	37.1	32.3	28.5	25.9	52.3	43.8	37.1	32.8
200	h_{CL}	42.0	37.7	34.0	31.4	42.6	37.4	33.1	30.2	57.5	48.6	41.6	37.0
250	h_{CL}	47.9	43.1	38.9	36.1	47.7	42.0	37.4	34.2	62.3	53.0	45.6	40.8
300	h_{CL}	53.4	48.1	43.6	40.4	52.4	46.4	41.4	38.0	66.9	57.1	49.4	44.3
350	h_{CL}	58.6	52.9	48.0	44.5	57.0	50.5	45.2	41.5	71.1	61.1	53.0	47.7

Table 5.5 Predicted Height of Clear Liquid Data using the Bennett et al. Model

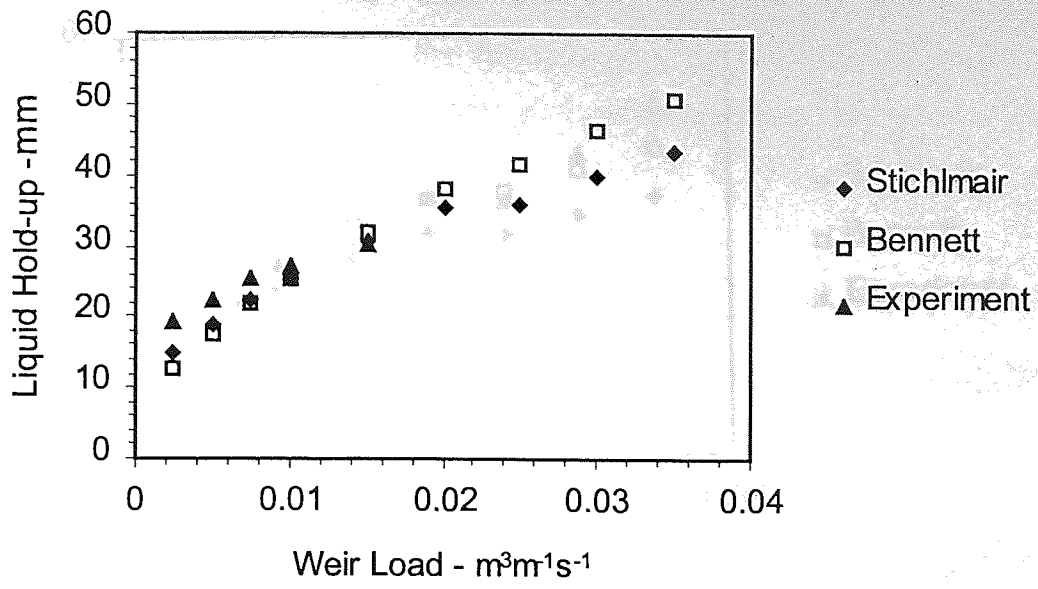

Figure 5.9 Graph of Measured and Predicted Liquid Hold-ups against Weir Load - 10 mm Weir Height

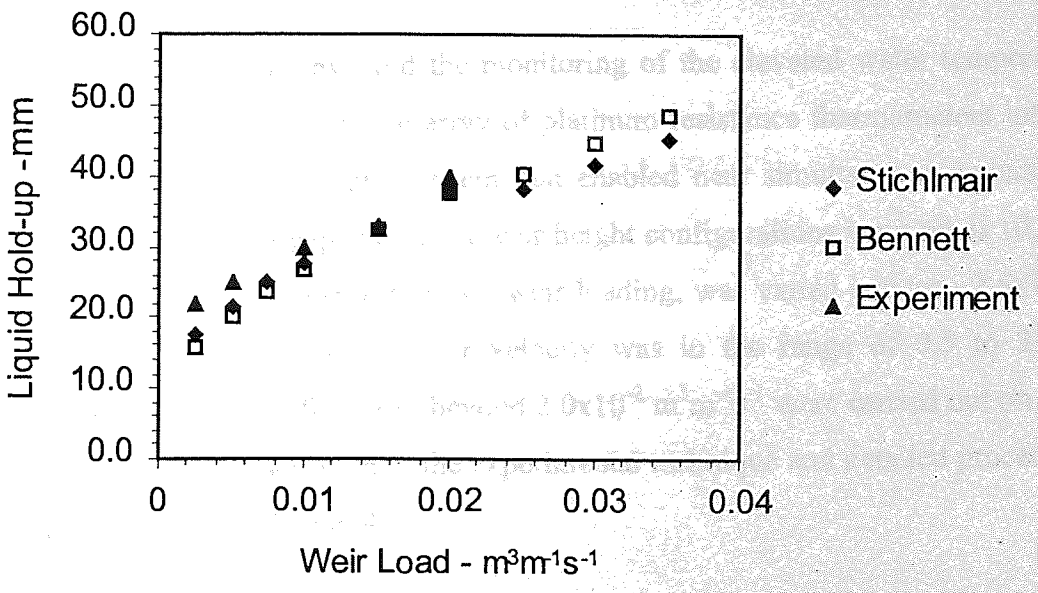

Figure 5.10 Graph of Measured and Predicted Liquid Hold-ups against Weir Load - 20 mm Weir Height

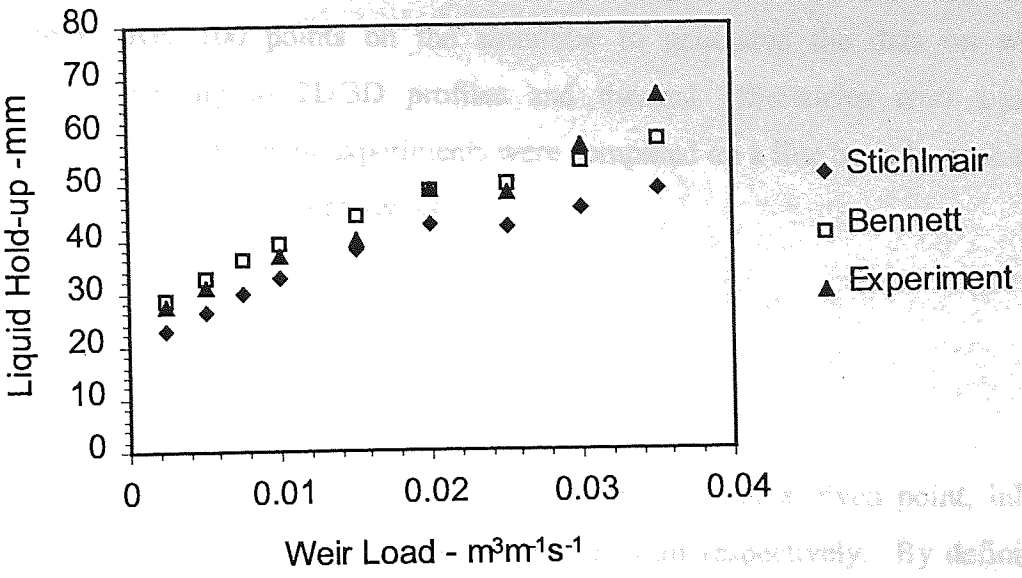

Figure 5.11 Graph of Measured and Predicted Liquid Hold-ups against Weir Load - 50 mm Weir Height

5.5 Investigation by Water-cooling Technique

The water cooling technique involved the monitoring of the elevated water temperature at various locations on the tray using an array of platinum resistance thermometers interfaced with a computer-based data logging system that enabled near simultaneous acquisition of data at all points. The inlet gap and outlet weir height configurations were set at 10, 20 and 50 mm. The water flowrate, expressed as a weir loading, was varied between 2.5×10^{-3} and 3.5×10^{-2} $m^3m^{-1}s^{-1}$ and the superficial air velocity was in the range of 0.5 to 2.4 ms^{-1}. Experiments involving water flowrates beyond 2.0×10^{-2} $m^3m^{-1}s^{-1}$ were carried out on a "half-tray" (section 3.6). Full description of the experimental technique and detailed procedure has already been dealt with in chapter 4.

5.5.1 Results and Discussion

Measurements of the air and water temperatures during air-water contacting experiments were made at over 100 points on the simulator to generated the data on which the downstream processing to 2D/3D profiles and thermal efficiencies were based. The temperature data from different experiments were compared on a like basis by making use of the reduced temperature term, defined as

$$T_r = \frac{T - T_{wb}}{T_{in} - T_{wb}} \qquad \ldots.4.1$$

where T, T_{in}, and T_{wb} are the measured water temperature at a given point, inlet water temperature, and the wet bulb temperature of the inlet air respectively. By definition, the entering air wet bulb temperature is the minimum temperature that can be exhibited by a simple air-water system. The water entering the tray has a reduced temperature of 1.0, and the water leaving the tray has a reduced temperature lying between 1.0 and 0.0. The water temperatures are analogous to concentration profiles and areas with low temperatures are interpreted as areas with high residence-times and vice versa.

The Temperature Profiles

Representative reduced temperature isotherms at various superficial air velocities and liquid loadings are presented in Figures 5.12a-l. More complete isotherms for other conditions of experiment are compiled in Appendix 6. Generally, lines of constant reduced temperature enter the tray parallel to the downcomers in line with the definition of reduced temperature that restricts the value at the inlet gap to unity. But progressively down the flow path length the temperature, reduced or actual, begins to tail off, with steep gradients between the segment regions and the centre of the tray.

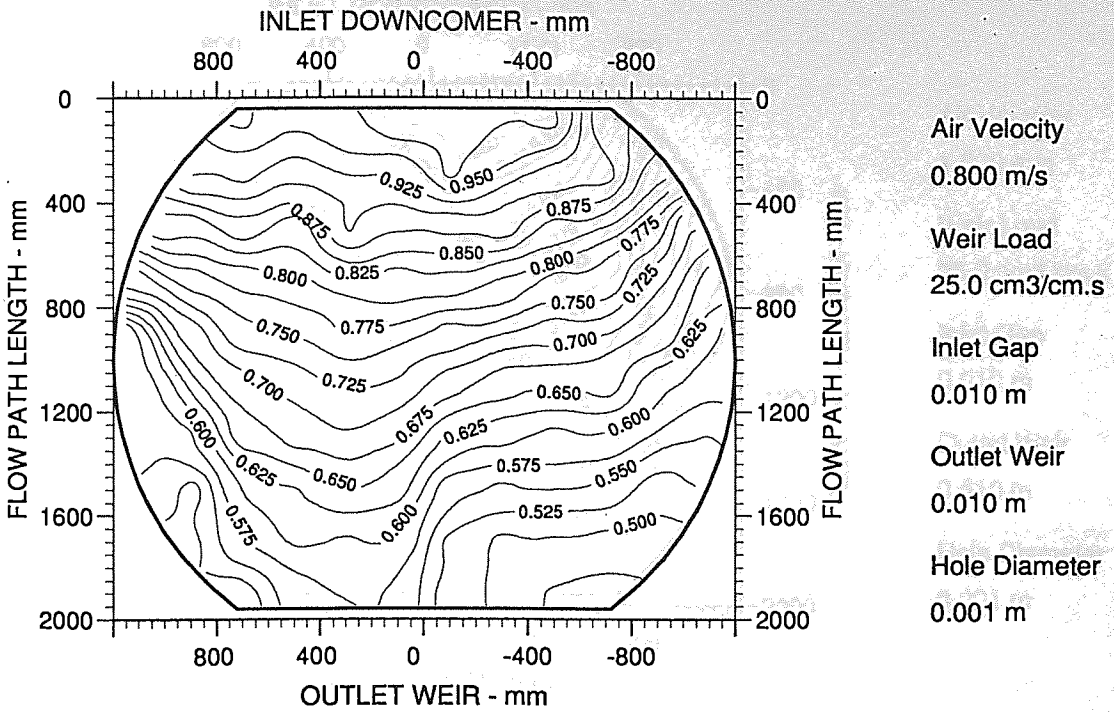

Fig. 5.12a Two-dimensional reduced temperature isotherms

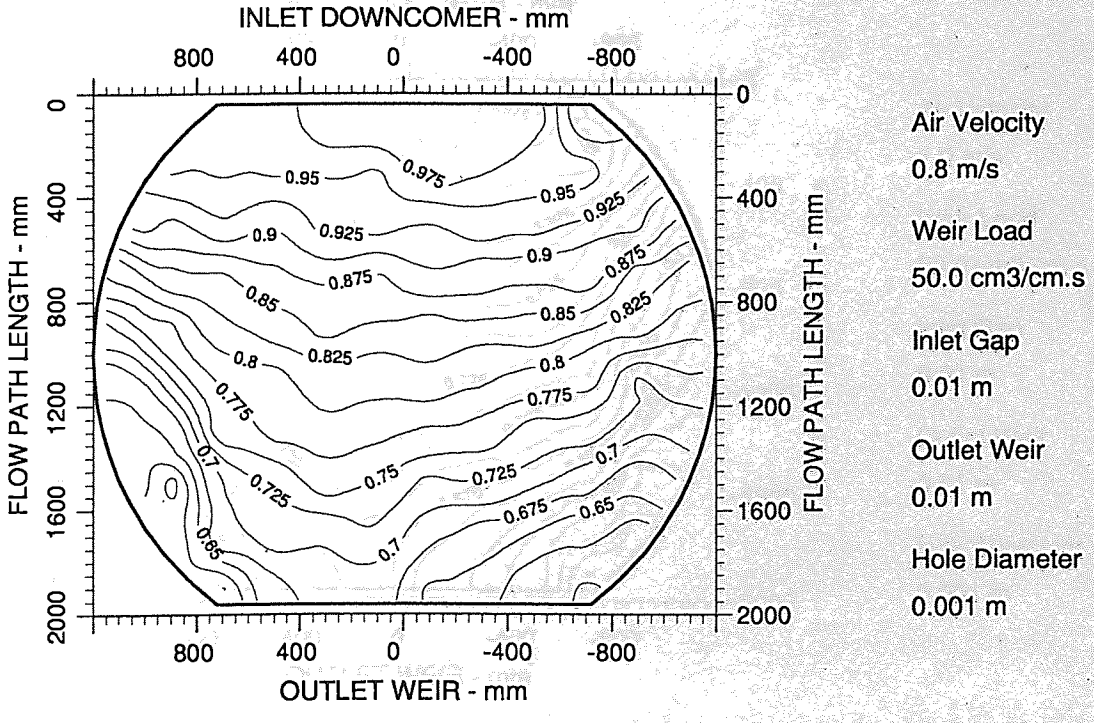

Fig. 5.12b Two-dimensional reduced temperature isotherms

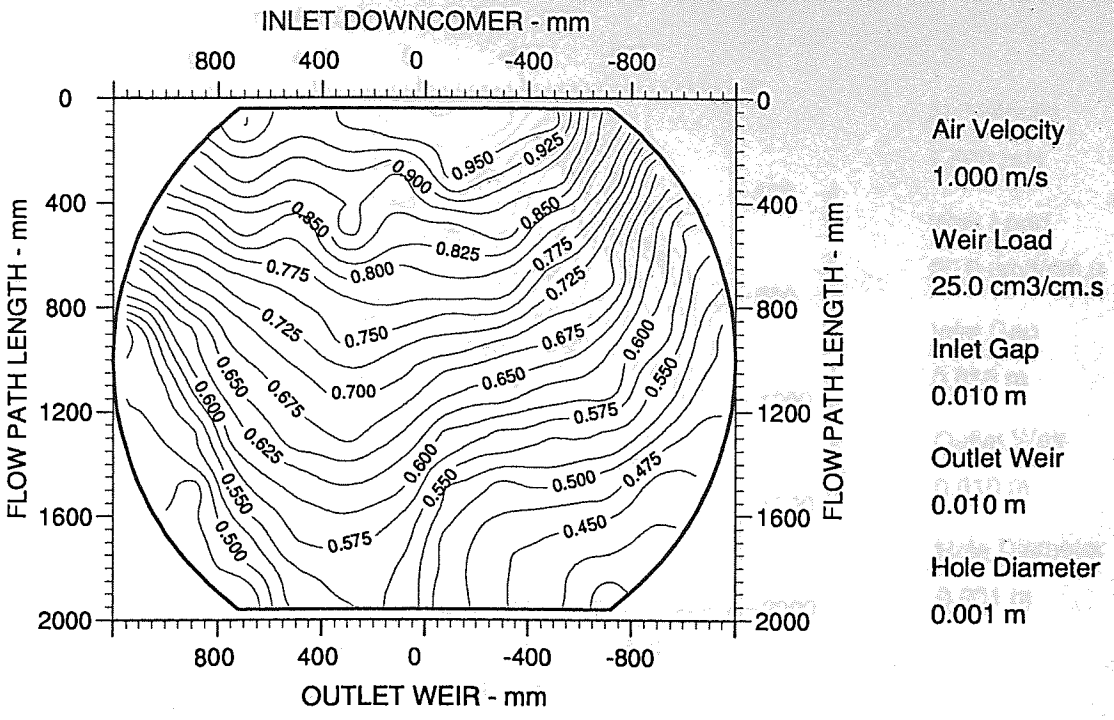

Fig. 5.12c Two-dimensional reduced temperature isotherms

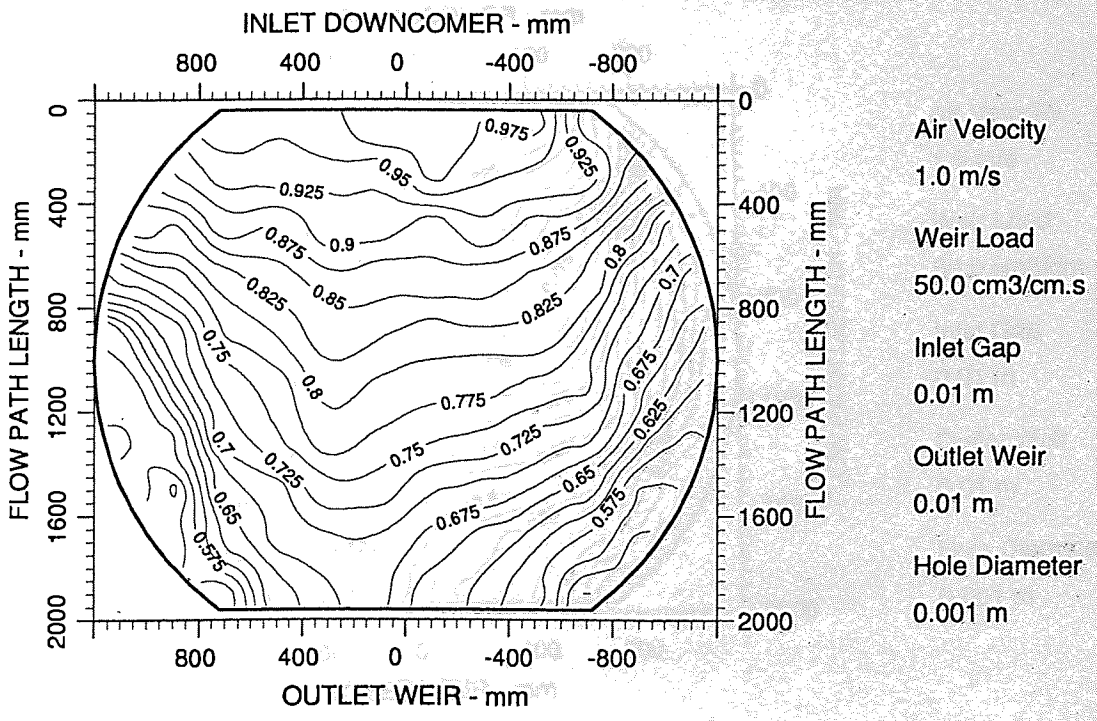

Fig. 5.12d Two-dimensional reduced temperature isotherms

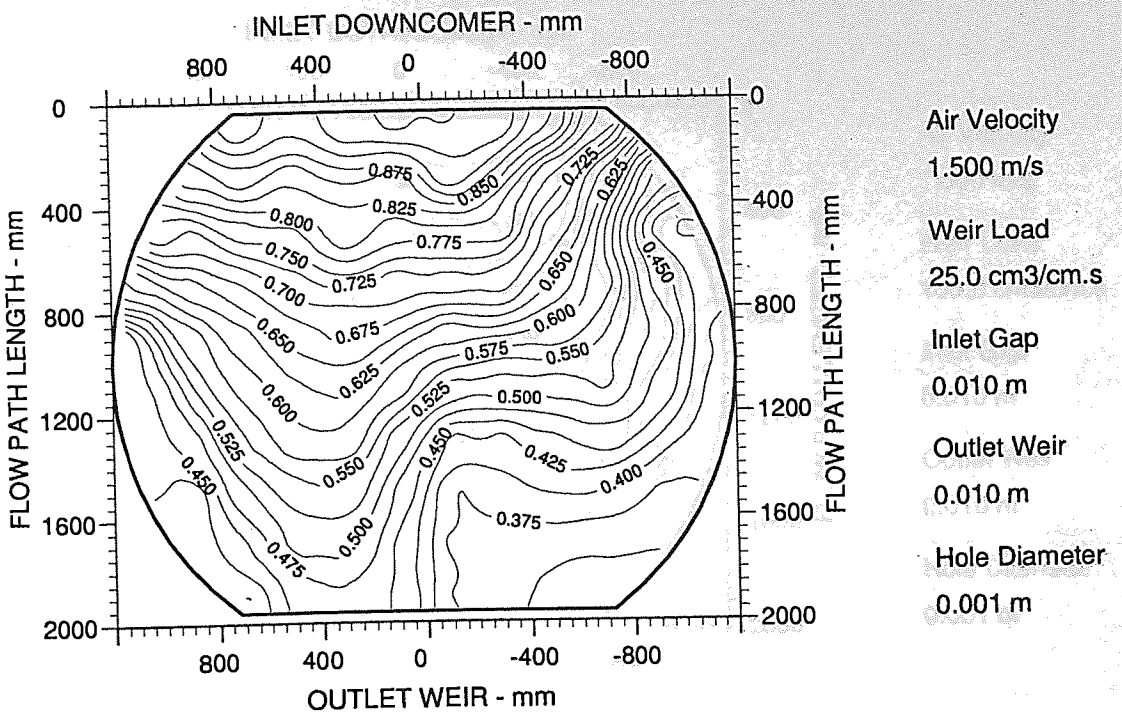

Fig. 5.12e Two-dimensional reduced temperature isotherms

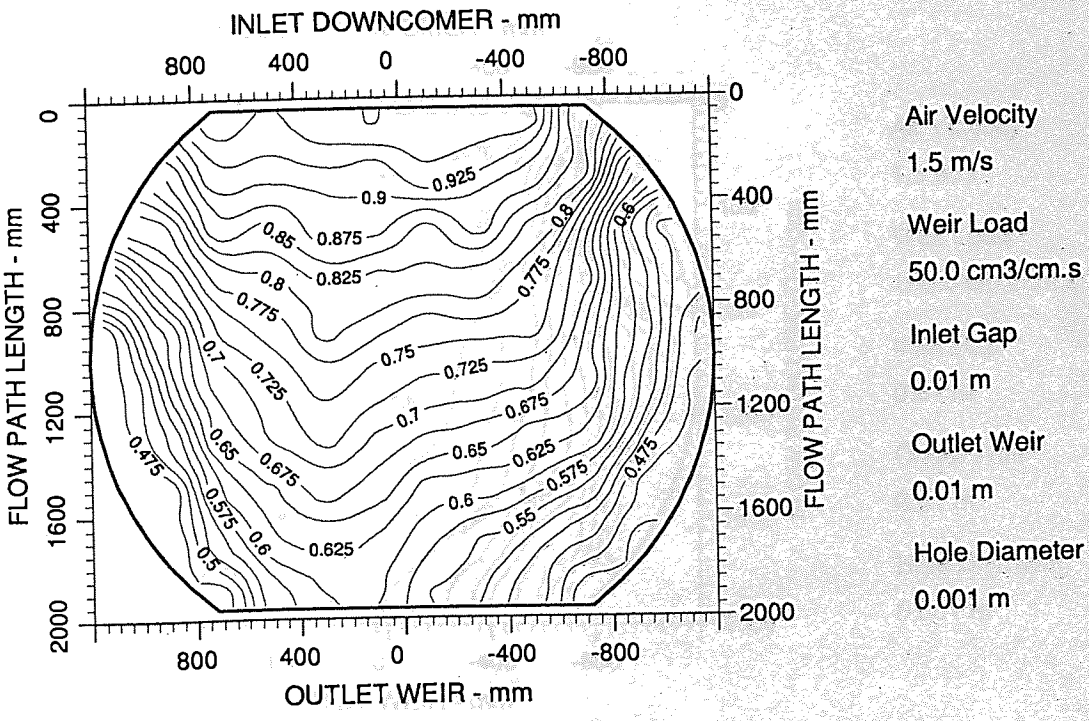

Fig. 5.12f Two-dimensional reduced temperature isotherms

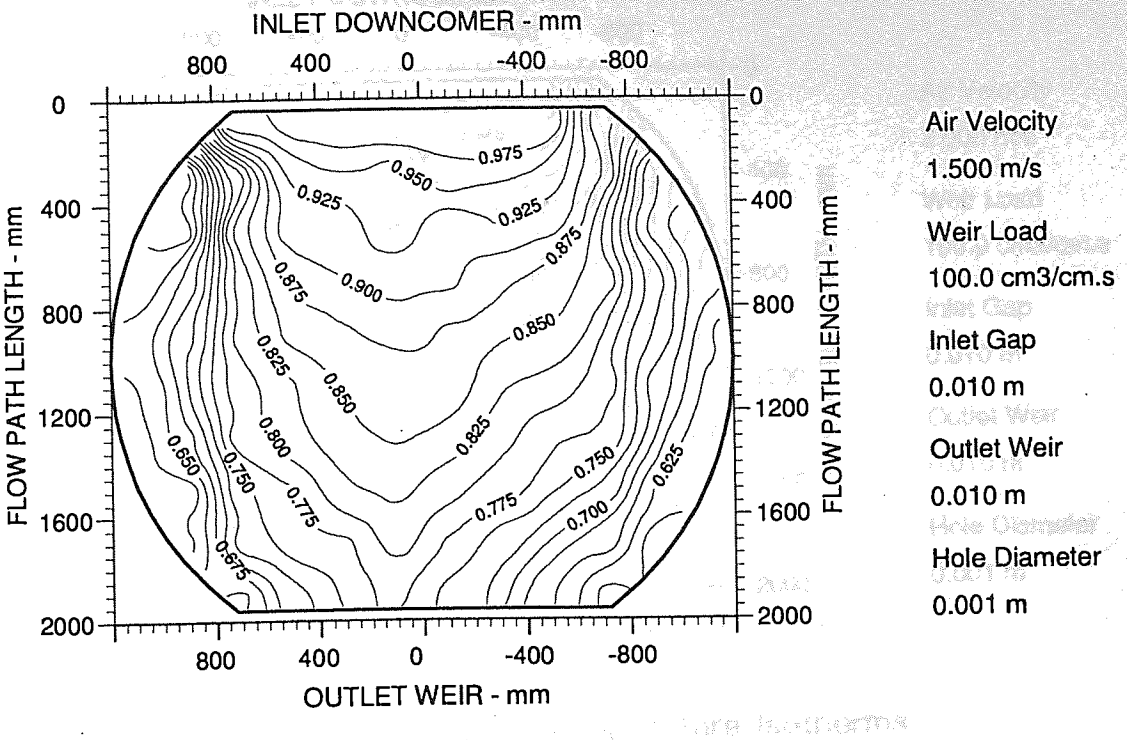

Fig. 5.12g Two-dimensional reduced temperature isotherms

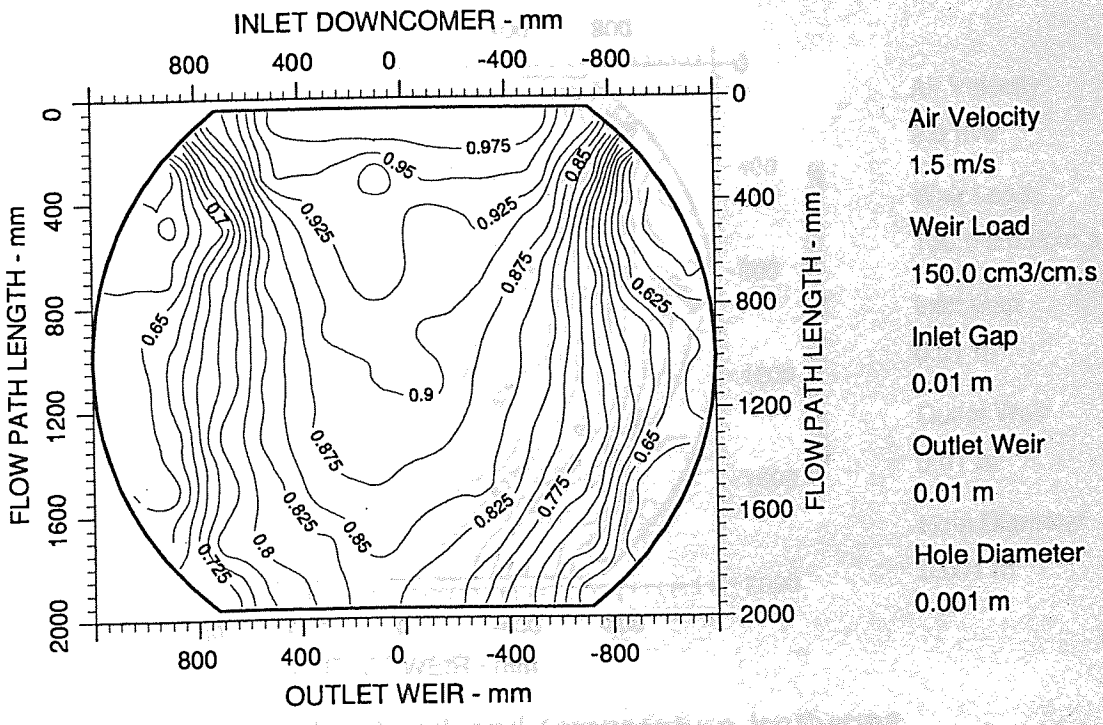

Fig. 5.12h Two-dimensional reduced temperature isotherms

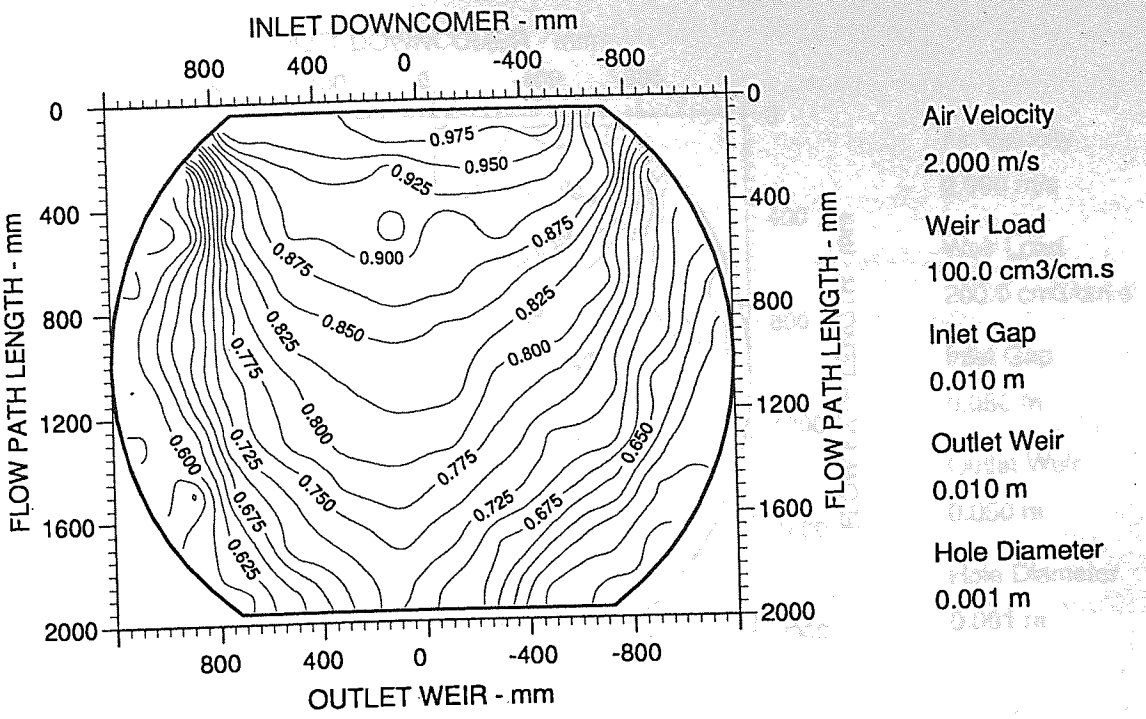

Fig. 5.12i Two-dimensional reduced temperature isotherms

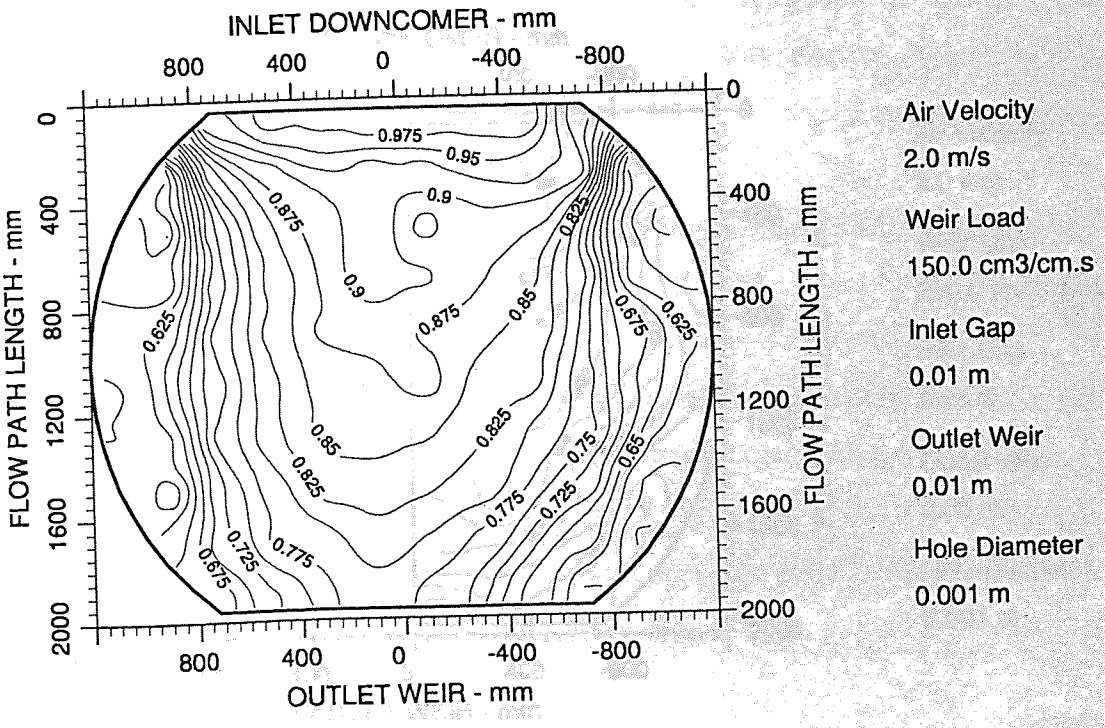

Fig. 5.12j Two-dimensional reduced temperature isotherms

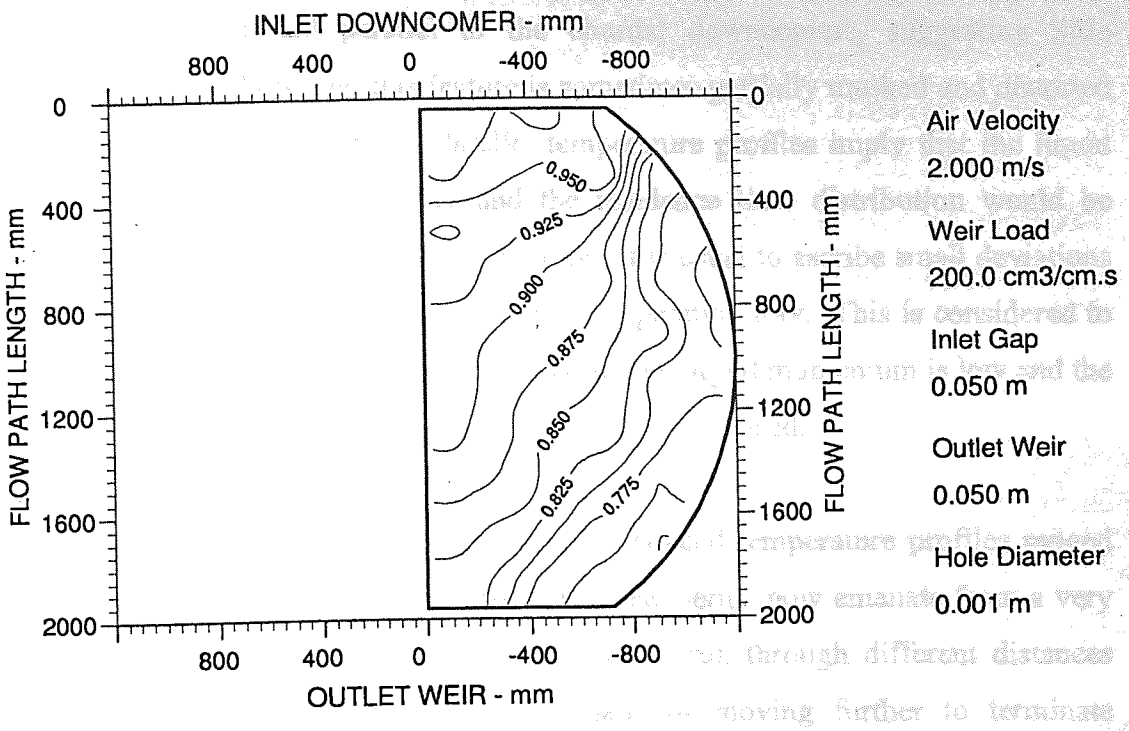

Fig. 5.12k Two-dimensional reduced temperature isotherms

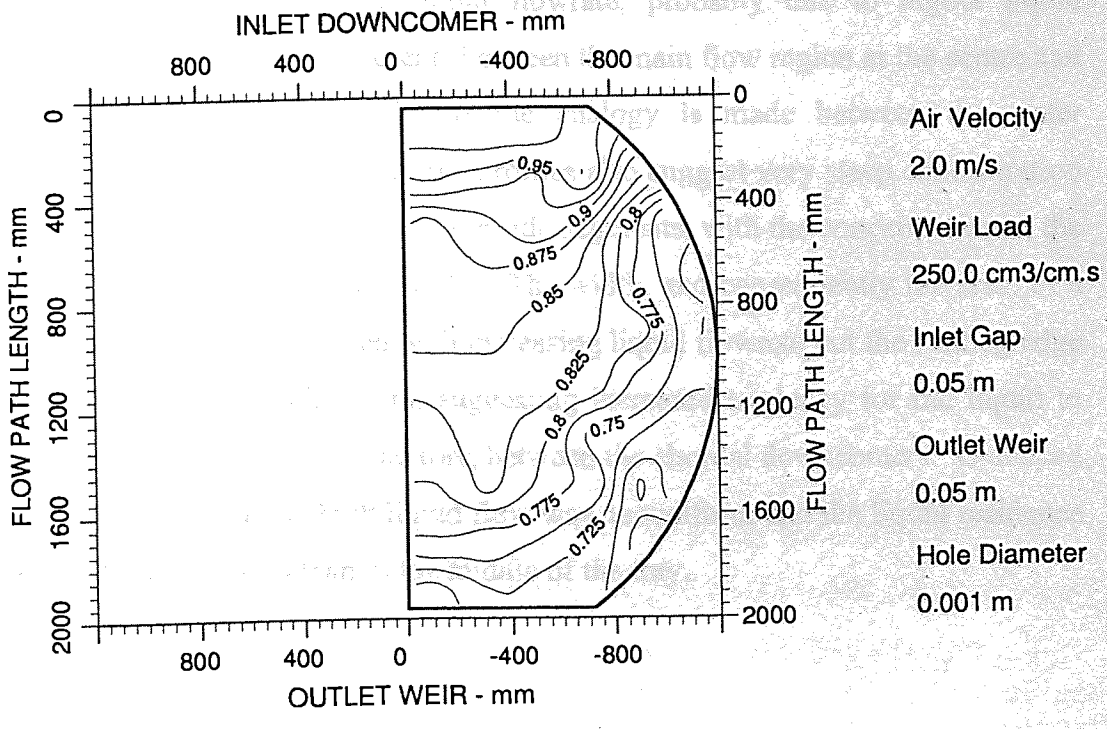

Fig. 5.12l Two-dimensional reduced temperature isotherms

Effect of the Water Flowrate

At low water flowrates, less than 50 $cm^3cm^{-1}s^{-1}$ - where the froth height is low, two features are apparent in the temperature profiles. Firstly, the temperature profiles are slightly out of symmetry along the mirror-axis of symmetry. Secondly, the isotherms over most of the tray are approximately straight and parallel to the chordal downcomers, suggesting little deviations from plug flow, however, this feature is sometimes partially masked and distorted by the skewed nature of the isotherms. Parallel temperature profiles imply that the liquid flow was largely uniform across the tray and the residence time distribution would be similar, both at the sides and in the middle of the tray. It is usual to ascribe small deviations from perfect symmetry to slight out of levelness in the operating tray. This is considered to be the case in this instance because at low liquid loading the liquid momentum is low and the hydraulic imbalance due to slight out of levelness is most pronounced.

As the water flowrate and froth height increased, the reduced temperature profiles ranged from slight-to-severe U-shaped isotherms. Most of the isotherms now emanate from a very low temperature region at the edges of the inlet gap and run through different distances before either joining together to complete a U-shape or moving further to terminate independently at the outlet weir. The remaining isotherms form closed loops of exceptionally low temperatures with the column walls. The symmetry of the profiles improved dramatically with increasing liquid flowrate, probably due to higher liquid momentum, but steeper temperature gradients between the main flow region at the centre and the cooler side regions were recorded. If the analogy is made between the water temperatures and the liquid concentrations, the profiles also suggest very steep concentration gradients between the middle of the tray and the side segments, with the concentration at the segments being much lower than in the middle. The width, and consequently the area, of a continuous U-shaped isotherm decreased with increasing liquid flowrate but the leading edge travels further down the flow path length, suggesting increased tendency for the liquid to flow preferentially down the middle of the tray, between the chordal downcomers. U-shaped temperature profiles imply that the bulk liquid flow was nonuniform and the liquid residence time would be greater at the sides than in the middle of the tray.

It is expected that the temperature, actual or reduced, will decrease in the direction of the outlet weir, but exceptionally low temperatures were recorded at the edges of the inlet gap and outlet weir adjacent to the walls. This type of distribution cannot be explained by the fact that the liquid flow path lengths at the tray segments are longer than at the middle of the tray. A more plausible explanation is the separation of liquid flow at the corner of the inlet gap, which induced some form of 'reverse-circulating' flows at the segment areas of the tray adjacent to the walls. This observation has been made before (Hine, 1990 and Biddulph, 1994) and is supported by the results of the dyed tray studies which revealed circulating flow regions at the segment regions of the tray where the liquid appeared trapped for prolonged period of time. The Slow movement of fluid elements out of these separated and circulating flow regions is responsible for the formation of the virtually dead liquid zones of exceptionally low temperatures. It is remarkable that the evidence of liquid flow separation, that is, U-shaped temperature profiles begins to emerge at 50 $cm^3cm^{-1}s^{-1}$, similar to what was observed in the dyed tray studies. This type of flow pattern approximates the stagnant regions model of Porter et al. (1972) whose analysis showed that the presence of dead liquid zones are particularly damaging to the mass transfer efficiency of a multiple tray column. In this studies water temperatures at the circulating regions are reduced even below that leaving the tray. This implies that the enthalpy change of the air passing through the circulating regions will be much reduced and a similar form of bypassing may be expected to occur in real distillation tray operation.

Effect of the Air Flowrate

The effect of the air flowrate on the liquid flow pattern is not clearly discernible from the temperature profiles but seemed to inhibit the onset of flow separation such that it occurred at higher weir loads and with smaller gaps under the inlet downcomer.

Effect of the Inlet Gap and Outlet Weir

The temperature profiles at different configurations of the inlet gap and outlet weir shows that U-shaped profiles are more reinforced at low inlet gaps and high outlet weirs. At low gaps and high outlet weirs, the steepest temperature gradients between the main flow region at the middle of the tray and the cooler side regions were recorded.

However, the positions of the low temperature isotherms adjoining the walls tend to remain fairly the same, indicating little change in overall pattern. This suggests that high inlet gaps and low outlet weir heights may be more favourable to achieving an even liquid distribution on the tray. This should however be put along side the influence of the operating liquid load. At low liquid loads, the inlet gap and outlet weir have very little effect on the flow pattern developed on the tray but play increasing roles as the liquid load increased.

The Tray Efficiency

The procedure used in calculating the point and tray efficiencies have been discussed in chapter 4 and the computer programme used to execute the process is contained in Appendix 4. The efficiencies along with the enhancement ratios are presented in Tables 5.6, 5.7, and 5.8 for inlet gaps of 10, 20 and 50 mm respectively. To supplement the tables, Figures 5.13-5.16 are presented to show how the point efficiency, tray efficiency and the enhancement ratio vary with the water weir load.

Inlet Gap - 10 mm		UMD TRAY								
Outlet Weir - mm		10			20			50		
Air Velocity - ms^{-1}		1	1.5	2	1	1.5	2	1	1.5	2
Water Load - $cm^3cm^{-1}s^{-1}$	Efficieny - %									
25	E_{mv}	94	93	87	105	101	91	117	103	98
	E_{og}	58	50	47	62	57	50	69	59	56
	E_{mv} / E_{og}	1.62	1.86	1.86	1.7	1.78	1.81	1.7	1.74	1.74
50	E_{mv}	101	99	91	101	99	97	113	107	104
	E_{og}	72	64	57	73	68	62	80	71	65
	E_{mv} / E_{og}	1.41	1.55	1.6	1.39	1.46	1.56	1.41	1.51	1.6
75	E_{mv}	104	103	99	103	103	101	118	111	106
	E_{og}	79	74	69	79	75	72	87	81	74
	E_{mv} / E_{og}	1.32	1.4	1.44	1.3	1.37	1.4	1.36	1.38	1.44
100	E_{mv}	98	95	93	99	95	99	110	103	100
	E_{og}	81	76	72	82	78	74	91	84	78
	E_{mv} / E_{og}	1.2	1.26	1.3	1.2	1.23	1.33	1.21	1.22	1.28
150	E_{mv}	97	94	94	97	92	91	102	100	101
	E_{og}	90	84	81	91	84	78	96	90	85
	E_{mv} / E_{og}	1.08	1.11	1.17	1.07	1.09	1.16	1.07	1.11	1.19

Table 5.6 Measured Murphree Efficiency Data - 10 mm Inlet Gap

Inlet Gap - 20 mm		UMD TRAY								
Outlet Weir - mm		10			20			50		
Air Velocity - ms^{-1}		1	1.5	2	1	1.5	2	1	1.5	2
Water Load - $cm^3cm^{-1}s^{-1}$	Efficieny - %									
25	E_{mv}	82	80	74	90	84	81	93	92	85
	E_{og}	52	46	42	56	49	47	60	55	51
	E_{mv} / E_{og}	1.59	1.73	1.76	1.61	1.69	1.73	1.56	1.68	1.67
50	E_{mv}	88	84	85	94	94	94	107	104	96
	E_{og}	64	58	55	68	62	60	79	70	63
	E_{mv} / E_{og}	1.37	1.44	1.53	1.38	1.51	1.57	1.36	1.48	1.52
100	E_{mv}	90	88	84	100	97	97	110	102	99
	E_{og}	73	70	67	80	77	73	87	82	75
	E_{mv} / E_{og}	1.24	1.26	1.26	1.25	1.25	1.34	1.26	1.24	1.32
150	E_{mv}	93	91	92	100	93	95	101	98	95
	E_{og}	81	78	77	87	81	78	90	86	79
	E_{mv} / E_{og}	1.14	1.17	1.2	1.15	1.15	1.23	1.12	1.15	1.2
200	E_{mv}	95	93	93	104	92	97	99	98	94
	E_{og}	86	83	82	94	85	84	91	87	82
	E_{mv} / E_{og}	1.11	1.12	1.14	1.11	1.08	1.15	1.09	1.12	1.15

Table 5.7 Measured Murphree Efficiency Data - 20 mm Inlet Gap

Inlet Gap - 50 mm		UMD TRAY								
Outlet Weir - mm		10			20			50		
Air Velocity - ms^{-1}		1	1.5	2	1	1.5	2	1	1.5	2
Water Load - $cm^3cm^{-1}s^{-1}$	Efficieny - %									
25	E_{mv}	86	76	71	87	82	73	87	87	76
	E_{og}	50	45	40	52	47	44	55	49	48
	E_{mv} / E_{og}	1.7	1.68	1.76	1.67	1.75	1.66	1.57	1.76	1.59
50	E_{mv}	89	85	80	90	90	89	96	92	90
	E_{og}	64	57	52	66	59	56	73	67	64
	E_{mv} / E_{og}	1.4	1.5	1.53	1.36	1.53	1.58	1.32	1.38	1.4
100	E_{mv}	96	91	85	102	93	86	101	104	93
	E_{og}	77	71	64	79	72	66	88	83	74
	E_{mv} / E_{og}	1.24	1.28	1.32	1.3	1.3	1.3	1.15	1.25	1.26
150	E_{mv}	101	99	91	99	101	94	106	105	101
	E_{og}	84	81	73	83	81	74	92	89	84
	E_{mv} / E_{og}	1.2	1.22	1.24	1.19	1.24	1.27	1.15	1.18	1.21
200	E_{mv}	106	103	97	101	102	99	105	105	101
	E_{og}	93	90	83	89	87	82	94	93	88
	E_{mv} / E_{og}	1.14	1.15	1.17	1.13	1.17	1.21	1.11	1.13	1.15

Table 5.8a Measured Murphree Efficiency Data - 50 mm Inlet Gap

Inlet Gap - 50 mm		UMD TRAY		
Outlet Weir - mm		50		
Air Velocity - ms^{-1}		1	1.5	2
Water Load - $cm^3cm^{-1}s^{-1}$	Efficieny - %			
250	E_{mv}	94	101	102
	E_{og}	92	94	91
	E_{mv} / E_{og}	1.03	1.07	1.12
300	E_{mv}	97	99	102
	E_{og}	96	95	94
	E_{mv} / E_{og}	1.01	1.04	1.08
350	E_{mv}	101	101	103
	E_{og}	94	97	97
	E_{mv} / E_{og}	1.07	1.03	1.07

Table 5.8b Measured Murphree Efficiency Data - 50 mm Inlet Gap

Figure 5.13 shows how the Murphree point efficiency varies with the weir load. At low weir loading of 25 $cm^3cm^{-1}s^{-1}$, the measured point efficiency was 49 %, but this value rises up rapidly to 83 % as the weir load increases to 100 $cm^3cm^{-1}s^{-1}$, and then to 93% at weir load of 200 $cm^3cm^{-1}s^{-1}$. Further increase in weir load lead to only marginal increase in the point efficiency, the maximum point efficiency measured being 97 % at weir load of 350 $cm^3cm^{-1}s^{-1}$. In principle the point efficiency is calculated independent of the liquid flow pattern and the increase in the point efficiency with weir load is tied down to the increase in the clear liquid height as the weir load increased. This is further confirmed by comparing the point efficiencies at different outlet weir heights which shows that the point efficiency increased consistently with outlet weir height. The outlet weir height has already been established to set the amount of clear liquid on the operating tray.

Figures 5.14 shows how the Murphree tray efficiency varies with weir load. The measured tray efficiency was 87 % at 25 $cm^3cm^{-1}s^{-1}$, rising to a maximum of 104 % at 100 $cm^3cm^{-1}s^{-1}$ and then decreasing gradually to 99 %, at 300 $cm^3cm^{-1}s^{-1}$. This trend of the Murphree tray efficiency is somewhat similar to that of the point efficiency, with a few notable exceptions tied down to the influence of flow patterns on the tray efficiency. While the point efficiency increased continuously with the weir load, the tray efficiency increases up to a maximum value and then begins to level off gradually with weir load. The levelling off being more pronounced at low inlet gaps and outlet weir heights. The trend of the Murphree tray efficiency with weir load is compared with that of the point efficiency in Figure 5.15.

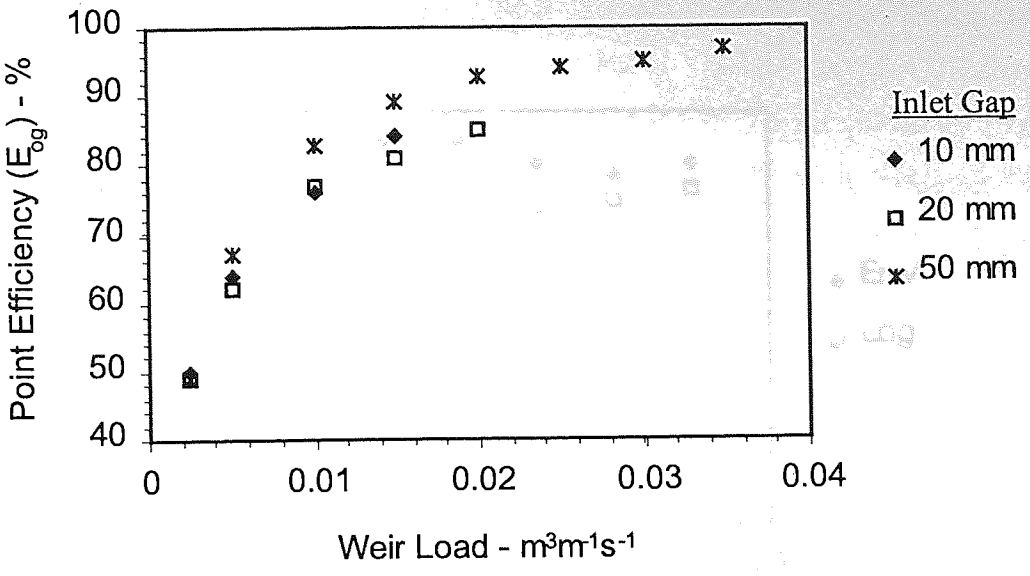

Figure 5.13 Graph of Measured Point Efficiency against Weir Load

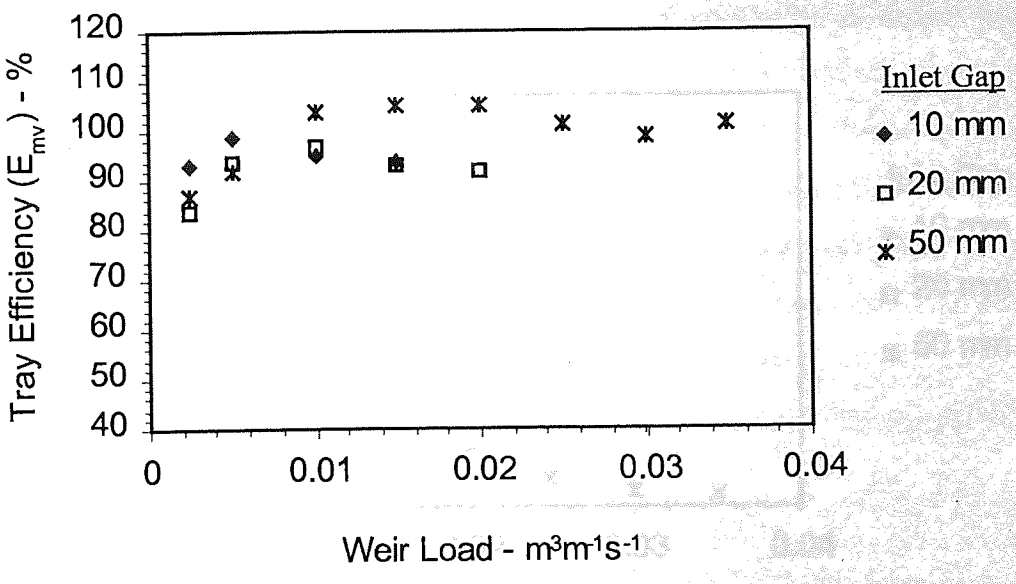

Figure 5.14 Graph of Measured Tray Efficiency against Weir Load

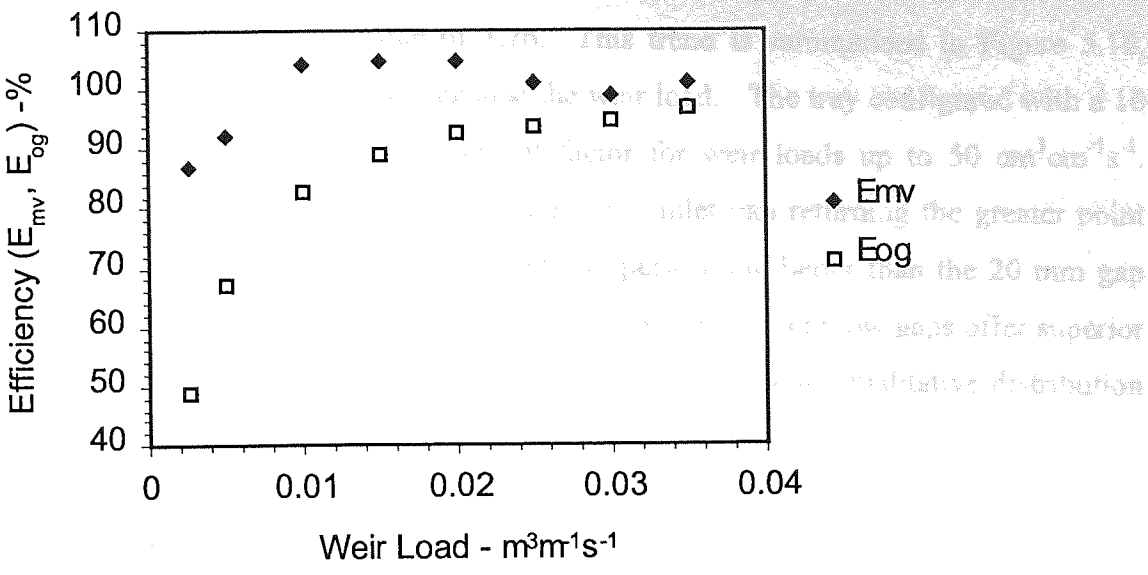

Figure 5.15 Graph of Measured Point and Tray efficiency against Weir Load

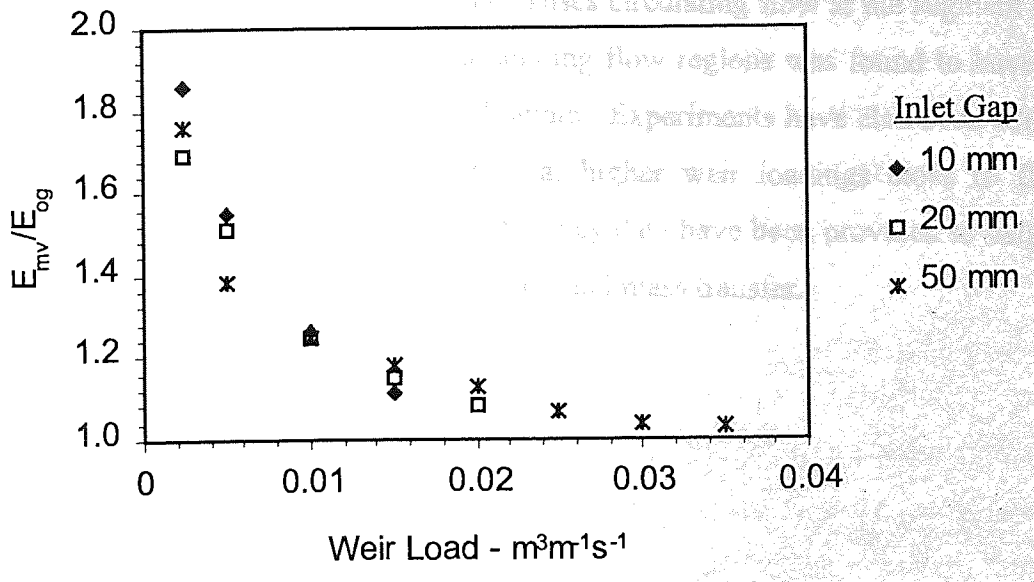

Figure 5.16 Graph of Measured Enhancement Ratio against Weir Load

The lowest tray efficiency of 87% was recorded at the lowest weir load of 25 $cm^3cm^{-1}s^{-1}$, however, this low tray efficiency was combined with a low point efficiency of 49%. The result of the low tray efficiency and even lower point efficiency is a high enhancement factor for the point efficiency of 1.76. Although the tray efficiency rises as the weir load increases from 25 $cm^3cm^{-1}s^{-1}$, the point efficiency also rises but at a steeper rate and the enhancement factor falls from the maximum value of 1.76. This trend is summarised in Figure 5.16, where the enhancement ratio is plotted against the weir load. The tray configured with a 10 mm inlet gap gives the greatest enhancement factor for weir loads up to 50 $cm^3cm^{-1}s^{-1}$. Increasing the weir load further will lead to the larger inlet gap returning the greater point efficiency enhancements, with the 50 mm inlet gap performing better than the 20 mm gap than the 10 mm gap. This could be related to the flow patterns where low gaps offer superior flow characteristics at low weir loads and the larger gaps give better qualitative distribution at the higher water loadings.

5.6 Conclusions

An experimental study on a 2.44 m diameter air-water distillation simulator has produced results which provide further valuable insight into the nature of liquid flow distribution on sieve trays. The investigation supports the view that the separation of liquid flow at the corner of the inlet gap is the major factor that causes circulating flow at the segment regions of the tray. The severity and size of the circulating flow regions was found to have strong dependence on the inlet gap and the liquid flowrate. Experiments have also been conducted on a 'half-tray mode' to simulate distillation at higher weir loadings close to flooding conditions and valuable liquid hold-up and efficiency data have been provided to help in the evaluation of theoretical models of tray hydraulics and mass transfer.

CHAPTER SIX

The Effect of Hole Size on the Operation of a Sieve Tray

6.1 Introduction

This chapter presents a comparative analysis of the data collected on three identical trays with the same free area of 10% but different hole-sizes of 1.0, 6.35, and 12.7 mm. The results of the investigations on the 1.0 mm hole diameter tray have been reported in chapter 5, the data for the 6.35 and 12.7 mm hole diameter trays are from the works of Chambers (1993) and Fenwick (1996) respectively. All three studies were conducted on the same column with exactly the same air and water distribution using similar experimental techniques and procedures.

6.2 The Operating Flow Regime

Perhaps the best point to start an assessment of the effect of hole-size on the tray operation is to determine the operating flow regime the perforation size imposed on the trays at the different operating conditions used in the experimental programme. The type of flow regime on an operating tray is important because it dictates the hydrodynamic behaviour of the two-phase flow and of particular significance is the condition at which the phase inversion, that is, the transition from one regime to the other takes place. Since most commercial distillation columns operate either in the froth or spray regime, the transition line between these regimes is used to categorise the flow on the three trays broadly into either froth or spray regime.

The transition from froth to spray is deemed to take place when a substantial proportion of the gas completely penetrates the dispersion as jets. This definition is a loose one since the proportion of holes carrying jets which completely penetrate the froth at the froth-to-spray transition is open to dispute and difficult to measure (Lockett 1981). Among the several correlations in the literature for the determination of the transition from froth to spray regime, equation 6.1, proposed by Lockett (1981) based on data from several studies, has been adopted for this analysis.

$$\frac{h_{CL}}{d_h} = 2.78.u_h\left(\frac{\rho_G}{\rho_L}\right)^{0.5} \qquad \ldots 6.1$$

Figures 6.1 and 6.2 show the operating flow regimes for the 1 mm and 6.35 and 12.7 mm hole diameter trays, respectively. The dotted line is the transition line from froth to spray regime and each position shown on the graphs represent the real condition of experiment. It is clear that the operation of the 1 mm hole diameter tray was well into the froth regime and only a very small percentage of the operation entered the spray regime in the case of the 12.7 mm hole diameter tray. The operation of the 6.35 mm hole diameter tray is sandwiched between those of the 1 and 12.7 mm hole trays but still entirely within the froth regime. Although the figures were plotted for a weir setting of 10 mm, it is reasonable to assume that the pattern is not too different at the other settings used in the experiments, since higher weir settings lead to higher clear liquid hold-up which tend to favour froth operation. It is therefore safe to conclude that spray is more likely at low clear liquid heights, large hole diameters and gas velocities.

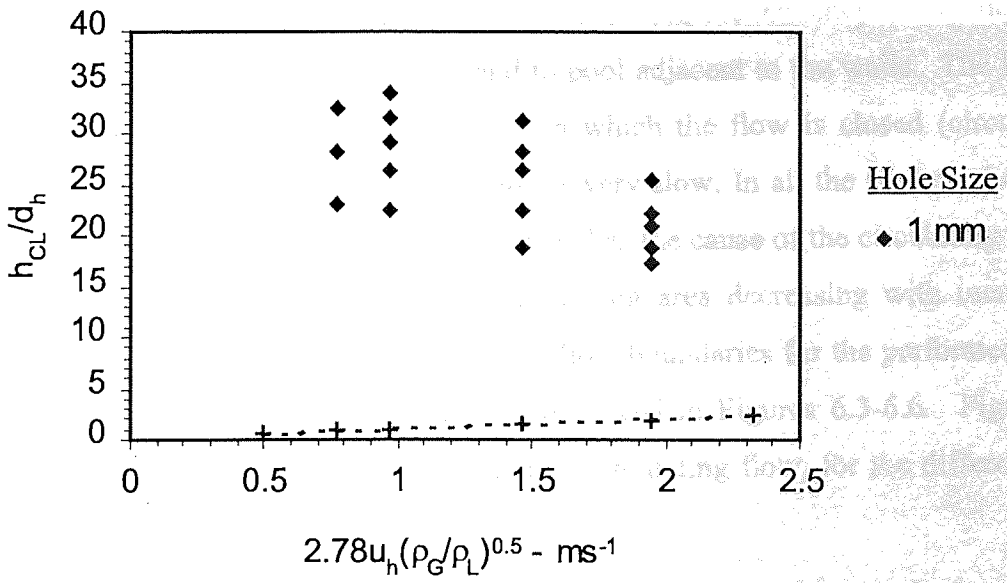

Figure 6.1 Spray-to- froth Transition for the 1 mm Hole-diameter Tray

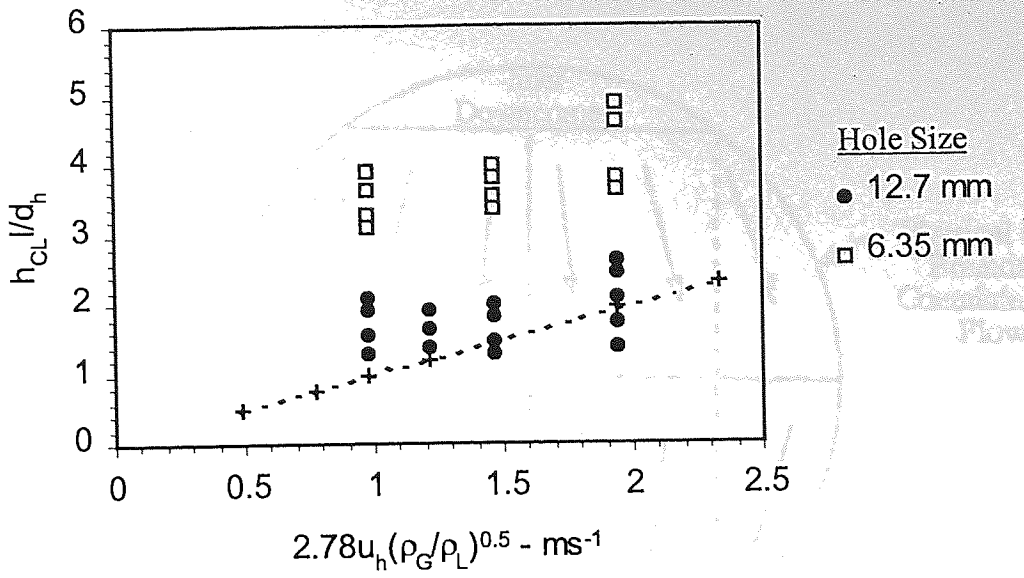

Figure 6.2 Spray-to- froth Transition for the 6.35 and 12.7 mm Hole-diameter Trays

6.3 The Flow Patterns

The two-phase flow patterns described for the various trays are similar to the results of earlier studies (Hine, 1990) on a blank tray which showed the tendency for the liquid to flow preferentially between the chordal weirs and to pool adjacent to the walls. The liquid pools adjacent to the walls originate from regions in which the flow is closed (circulating) and movement of fluid elements out of the region is very slow. In all the studies, the separation of flow at the edges of the inlet gap was identified as the cause of the circulating flows at the tray segment areas, with the size of the circulating area decreasing with increasing hole diameter. The overall shape of the circulating flow boundaries for the perforated trays were similar to that of water-only flow studies reproduced in Figures 6.3-6.6. Figures 6.7-6.9 show the percentage of the tray area containing circulating flow, for the different hole size trays.

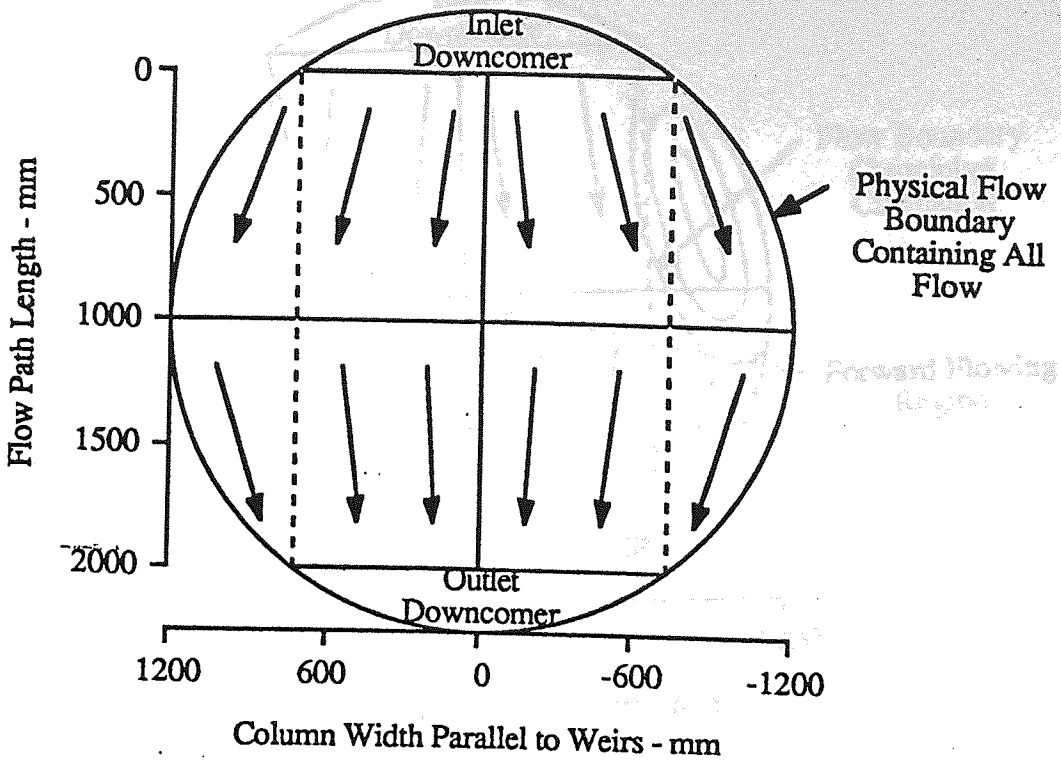

Figure 6.3 Example of 0% Circulation Flow Pattern

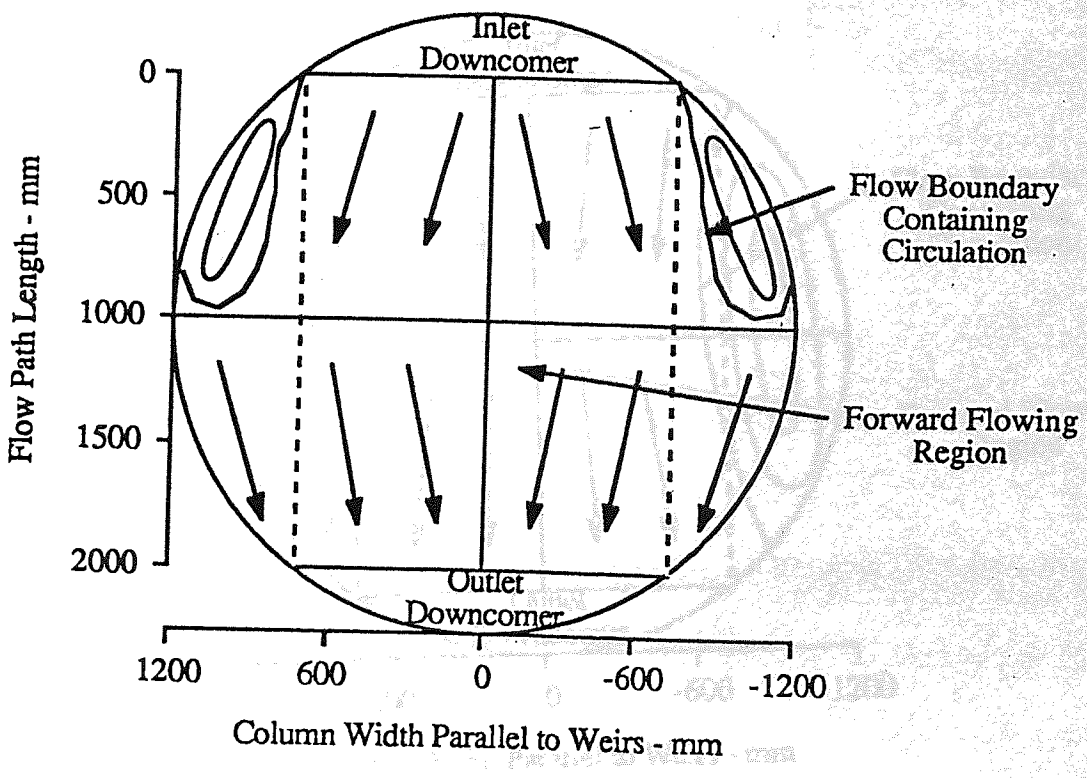

Figure 6.4 Example of 10% Circulation Flow Pattern

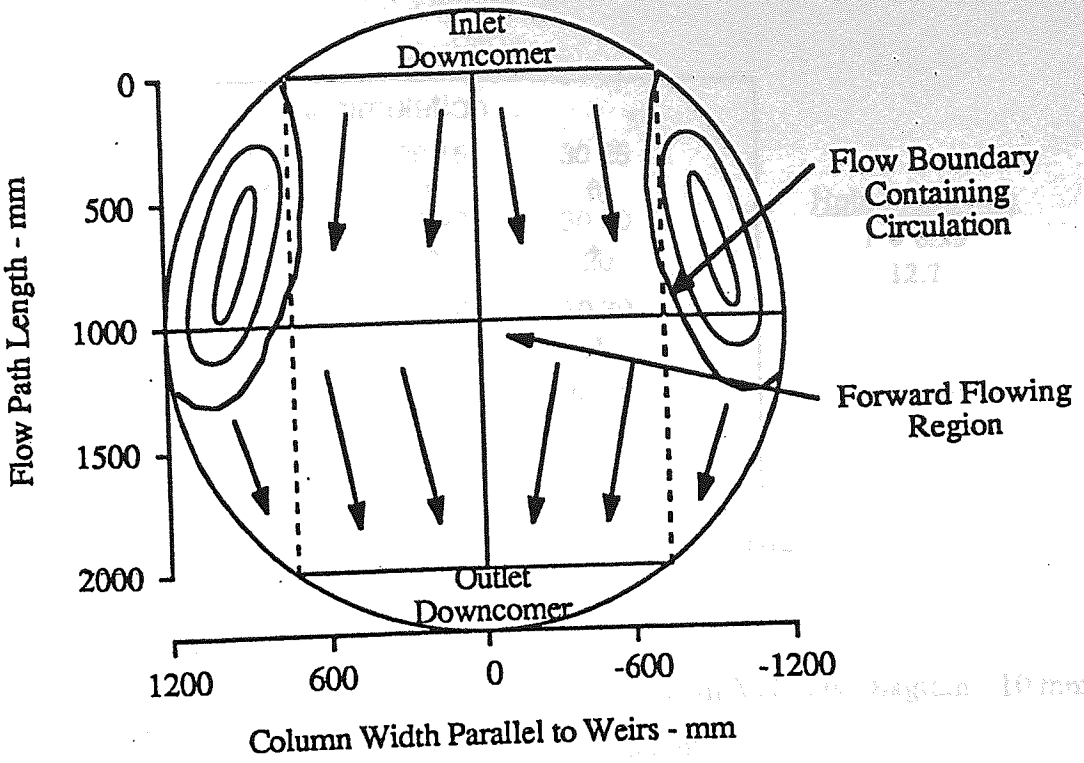

Figure 6.5 Example of 20% Circulation Flow Pattern

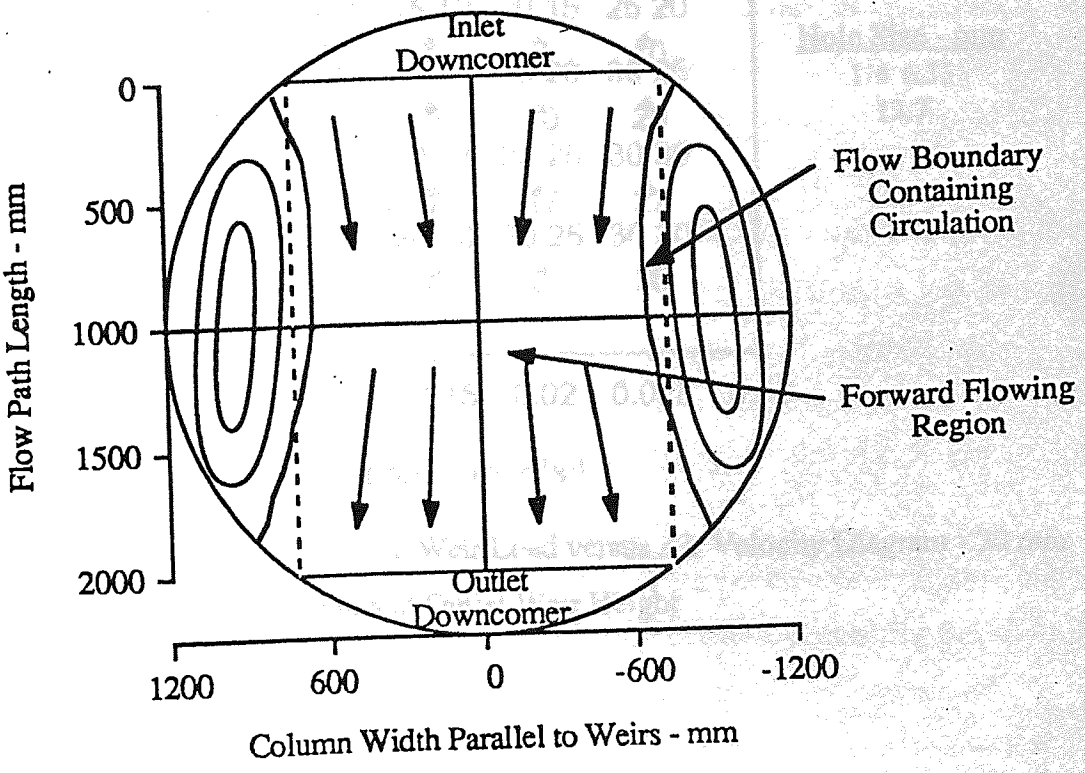

Figure 6.6 Example of 30% Circulation Flow Pattern

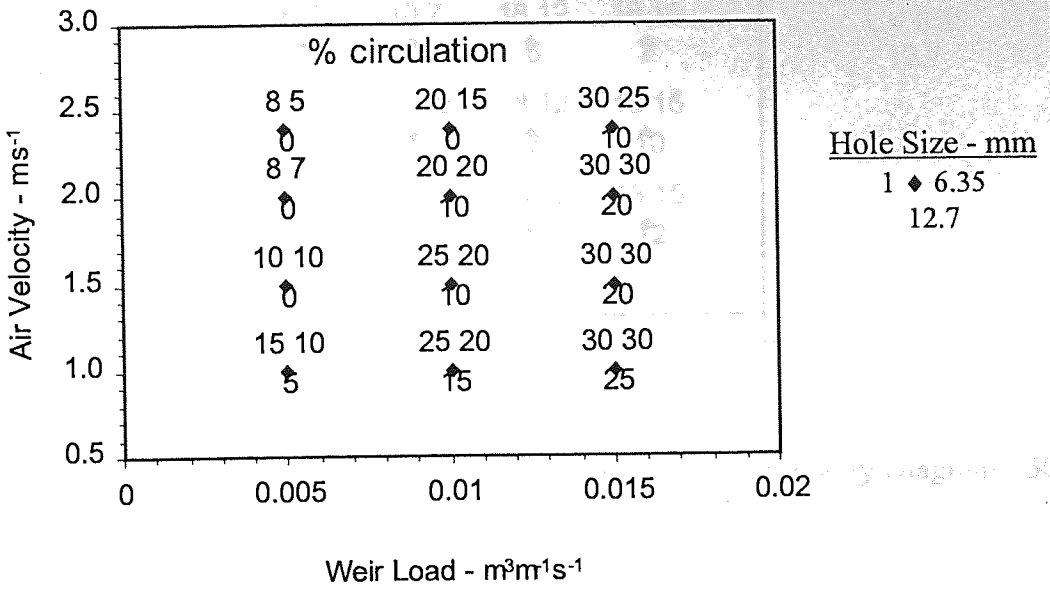

Figure 6.7 Summary of Flow Patterns on a Weir Load versus Air Velocity Diagram - 10 mm Inlet Gap and Outlet Weir Height

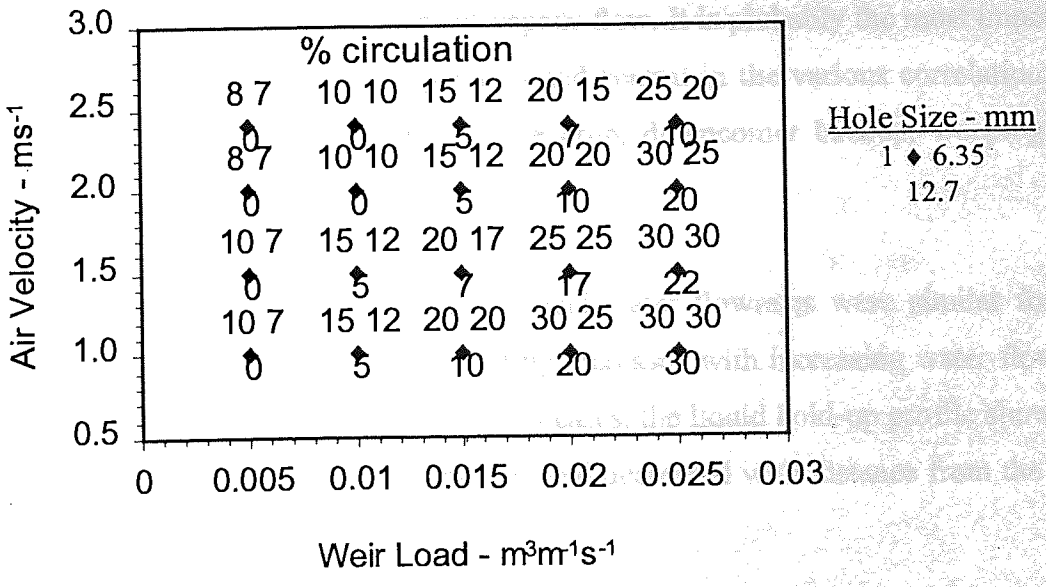

Figure 6.8 Summary of Flow Patterns on a Weir Load versus Air Velocity Diagram - 20 mm Inlet Gap and Outlet Weir Height

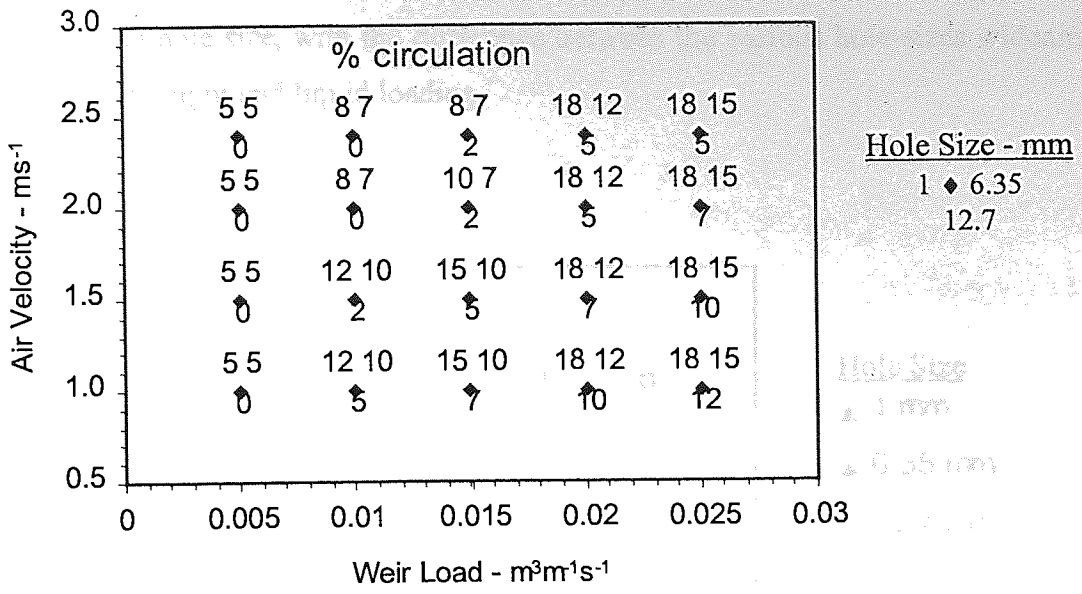

Figure 6.9 Summary of Flow Patterns on a Weir Load versus Air Velocity Diagram - 50 mm Inlet Gap and Outlet Weir Height

6.4 The Clear Liquid Hold-up

The clear liquid height or the liquid hold-up on a distillation tray is the height to which the aerated mass would collapse in the absence of vapour flow. It is probably the most important hydraulic parameter in distillation tray operation and central in the various correlations for estimating the tray efficiency, flooding, pressure drop, downcomer backup, weeping and entrainment factors.

The basic trends of the liquid hold-up with air and water flowrates were similar for the various hole sizes, that is, the mean liquid hold-up increased with increasing water flowrate and decreased with increasing air flowrate. In all cases, the liquid hold-up profile showed a significant but similar variation over the tray area and decreased with distance from the inlet downcomer.

The trends of the mean liquid hold-up with the water flowrate are compared in Figures 6.10-6.12, for the various hole-sizes. The mean liquid hold-up data was averaged for the various air flowrates so that a general representative plot can be made against the water loads. It is reasonable to use this approach because the liquid hold-up variation with the air flowrate is

very small compared with that for the water flowrate. In general, the liquid hold-up increases with decreasing hole size, with the difference between the various hole-sizes widening with increasing weir height and liquid loading.

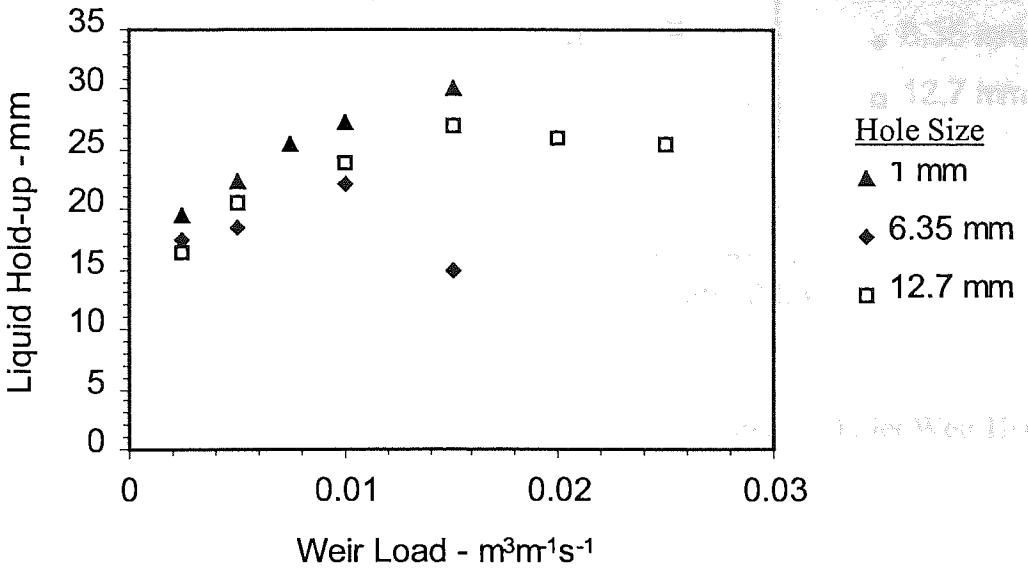

Figure 6. 10 Mean Liquid Hold-up - 10 mm Inlet Gap and Outlet Weir Height

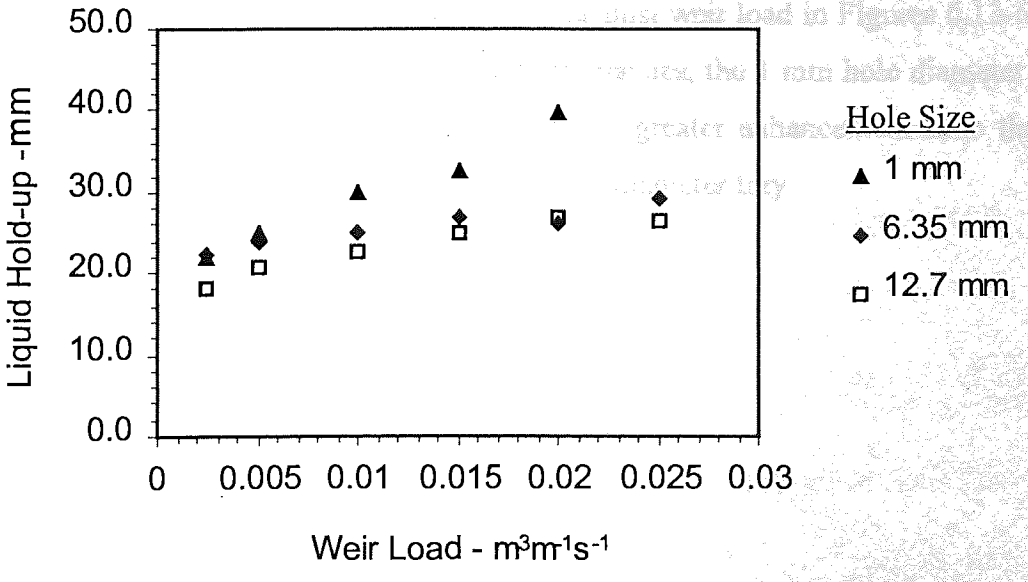

Figure 6. 11 Mean Liquid Hold-up - 20 mm Inlet Gap and Outlet Weir Height

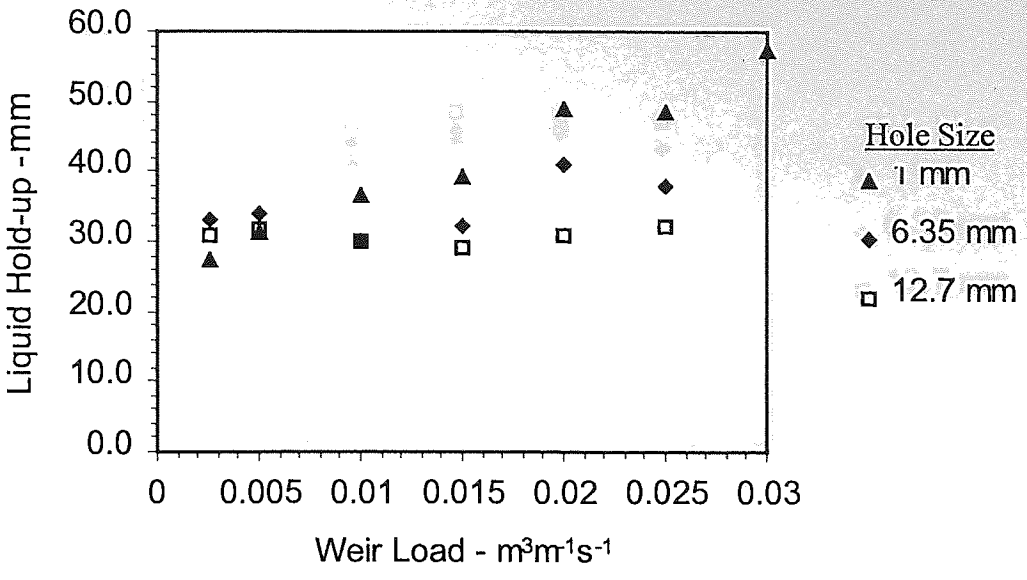

Figure 6. 12 Mean Liquid Hold-up - 50 mm Inlet Gap and Outlet Weir Height

6.5 The Tray Efficiency

The raw data collected for the various hole sizes were processed in identical manner to yield the Murphree point and tray efficiencies. The efficiencies and their enhancement ratios at a superficial air velocity of 1.5 m s^{-1} are plotted against weir load in Figures 6.13-6.15, for the various hole sizes. Despite very close point efficiencies, the 1 mm hole diameter tray nearly always returned greater tray efficiency and hence greater enhancement ratio than the 6.35 mm hole diameter tray and than the 12.7 mm hole diameter tray.

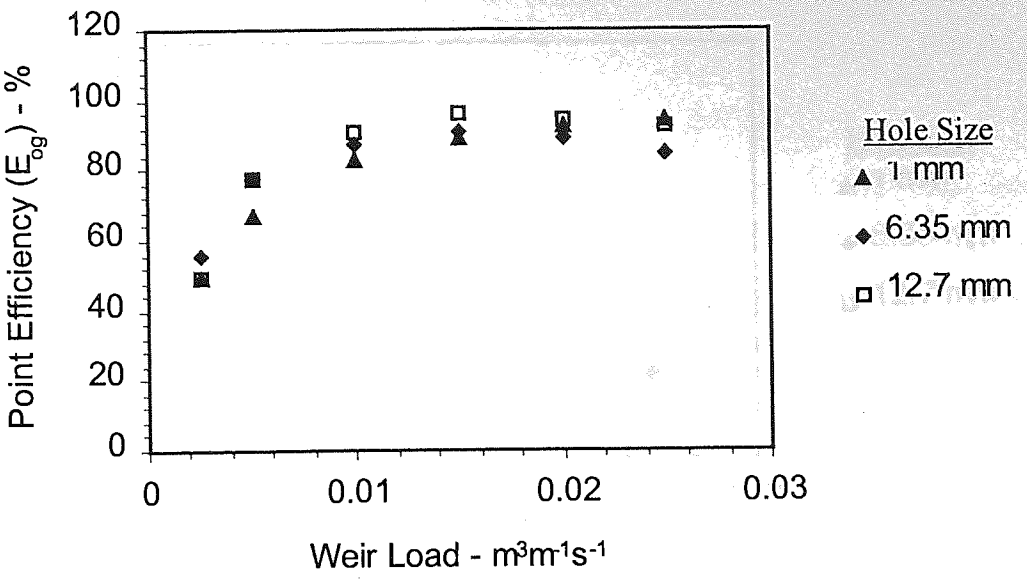

Figure 6.13 Graph of Measured Point Efficiency against Weir Load

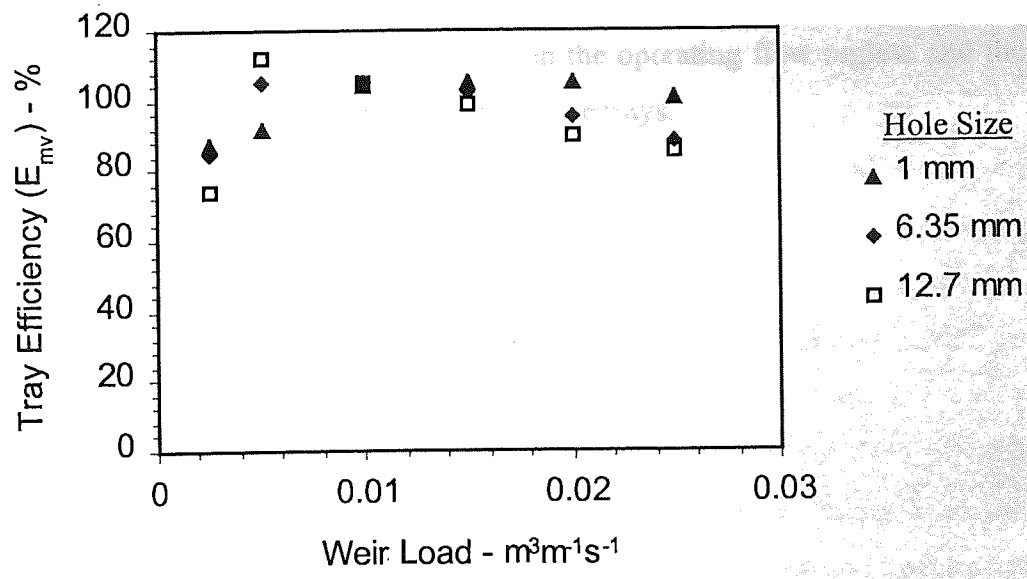

Figure 6.14 Graph of Measured Tray Efficiency against Weir Load

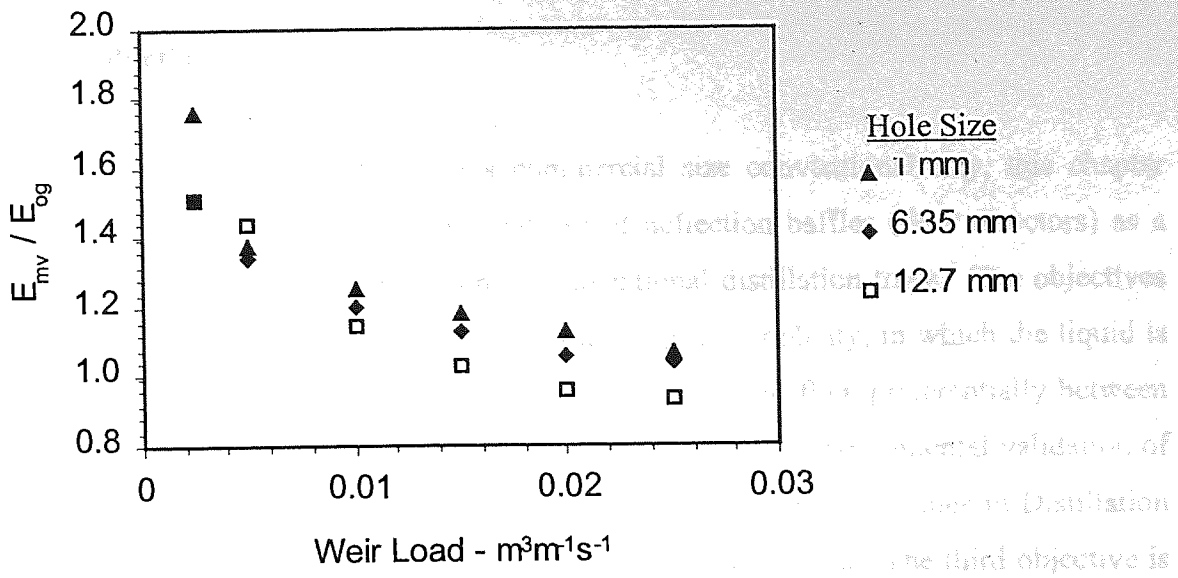

Figure 6.15 Graph of Measured Enhancement Ratio against Weir Load

6.6 Conclusions

The hole diameter has significant influence on the operating flow regime and the hydraulic and mass transfer performance of distillation sieve trays.

CHAPTER SEVEN

Design and Testing of Simple Controlled-flow Trays

7.1 Introduction

Having identified the flow patterns on a commercial size conventional tray, this chapter presents the investigations into the potential use of deflection baffles (flow directors) as a means of mitigating flow maldistribution in conventional distillation trays. The objectives are threefolds. Firstly, to create a tray, without altering its simplicity, in which the liquid is driven positively across at all points, removing the tendency to flow preferentially between the weirs and to 'pool' at the column walls. Secondly, to provide experimental validation of CFD studies (Fischer, 1999) carried out by partners in the Advanced Studies in Distillation Consortium and to extend the same to practical operating conditions. The third objective is to provide some experimental basis for better understanding of the way flow control trays function and in turn better understanding of two-phase flow behaviour on conventional trays to help in better tray design procedure.

7.2 Related work on Flow Directors

Some modelling and limited experimental work have already been conducted under the aegis of the ASID consortium to investigate the potential use of deflection baffles in conventional distillation trays as a liquid flow-straightening device. Single-phase flow calculations made for a series of baffle configurations (Daly, 1997) suggested that placing a baffle at an acute angle to the inlet weir could improve the liquid distribution and achieve a more uniform velocity profile across the tray. The baffles or flow directors as they are also called work by diverting some of the liquid flow at the central portion of the tray to the sides and using the additional momentum to drive stagnant liquid at the walls forward and hence promote better flow distribution.

The effect of baffles on the tray hydraulics was investigated experimentally by Khan (1998) on a rectangular tray using an air-water system. His work also confirmed that it is possible to use part of the liquid momentum at the centre to drive stagnant liquid at the sides forward,

provided that the inlet and outlet weir height combination allow for a fairly even clear liquid height upstream and downstream of the deflection baffle. In a case where the weirs impose a substantially disproportionate clear liquid height upstream and downstream of the baffle, preferential flow of vapour could be induced that might lead to vapour channelling and excessive liquid weeping.

The work started by Daly was extended by Fischer (1999) to two-phase homogeneous and heterogeneous models. The model geometry was generated to match that of the test rig used in the experimental work reported in this thesis. The first step in his modelling process was to establish the flow distribution on the unmodified tray to serve as a control. The optimisation of the flow path was then investigated by introducing obstructions, in the form of flow directors, into the flowpath. Computations were carried out for four differently modified tray topologies and the control. The result of the control study highlights strong recirculation of liquid adjacent to the tray floor and the influence of the outlet weir on the overall liquid flow distribution. The liquid residence time increases almost radially from the inlet, consistent with the stagnant regions model established in the literature (Porter et al., 1972). For the modified tray topologies, the ability of the flow directors to replenish the sectors of the flow domain at the tray walls varies but each exceeded that of the unmodified tray.

Computational drawbacks remain, however. The CFD analysis was only possible at conditions far removed from practice and was limited in the ability to provide direct information on the impact of flow directors on the liquid loading and mass transfer efficiency or what effect hole-size will have on the two-phase flow behaviour. It was therefore desirable to fill the gaps left out in the CFD models and to carry out experimental assessment of the trays' performance at operating conditions that are applicable to the industry. This will provide validation for the models and also quantitative assessment that will help in determining whether superior flow patterns will actually translate to enhanced tray efficiency.

7.3 Programme of Experiments

One aim of this work is to gain thorough knowledge of the distinctive hydraulics of tray-columns fitted with deflection baffles, to help in the procedure of designing optimal flow control trays that will lead to enhanced efficiency without affecting the capacity adversely. Thus, experiments were designed to assess the impact of flow directors on liquid flow patterns, tray loading capacity and mass transfer efficiency.

The programme of experiments was as follows:

a) Investigations into the flow-patterns on conventional trays fitted with deflection baffles, using the dye tracing and temperature profiling techniques. The impact of the baffles on the separated flow regions will be analysed to make qualitative assessment of the ability of the baffles to mitigate circulating flow at the segment regions of the tray.

b) Investigations into the hydraulics of baffled trays by measuring the clear liquid height profile across the tray and in the downcomer. This will provide information about the impact of the baffles on the tray loading-capacity as well as give indication of the overall liquid flow distribution on the tray. The hydraulic gradient on the tray will be analysed to determine whether there is any premature limitation of the tray capacity due to excessive hydraulic jump.

c) Quantitative assessment of the mass transfer performance of the baffled trays using the water cooling technique. The water temperature profiles across the tray are analogous to concentration profiles and when interpreted in terms of enthalpy-driving forces permit the calculation of thermal point and tray efficiencies.

7.4 Experimental Procedure

Five different tray topologies were created with deflection baffles fabricated from 2 mm sheet steel and fitted to the tray floor with steel rivets, each baffle rising 25 mm above the tray floor. Each set of baffle configuration constitutes a tray model, with the angle and shape

of the baffles relative to the flow direction being the main geometrical variables. The designs (Fischer, 1999) are shown in Figures 7.1a-f. Each tray design is assigned an arbitrary name in this way; UMD, for the unmodified tray (control), STR-1, ARC-1, RAB-1, STR-2 and ARC-2, for the modified trays. One advantage of the baffled trays which distinguish them from other controlled-flow trays in the literature is that they are simple to design, manufacture and install and thus provide an economic method of retrofitting sieve trays, both in terms of downtime and fabrication.

Similar experimental techniques and procedures as those used for the flow pattern studies on the unmodified conventional tray (chapter 5) were employed in the study of the modified trays. In all, five tray topologies were studied, built and tested.

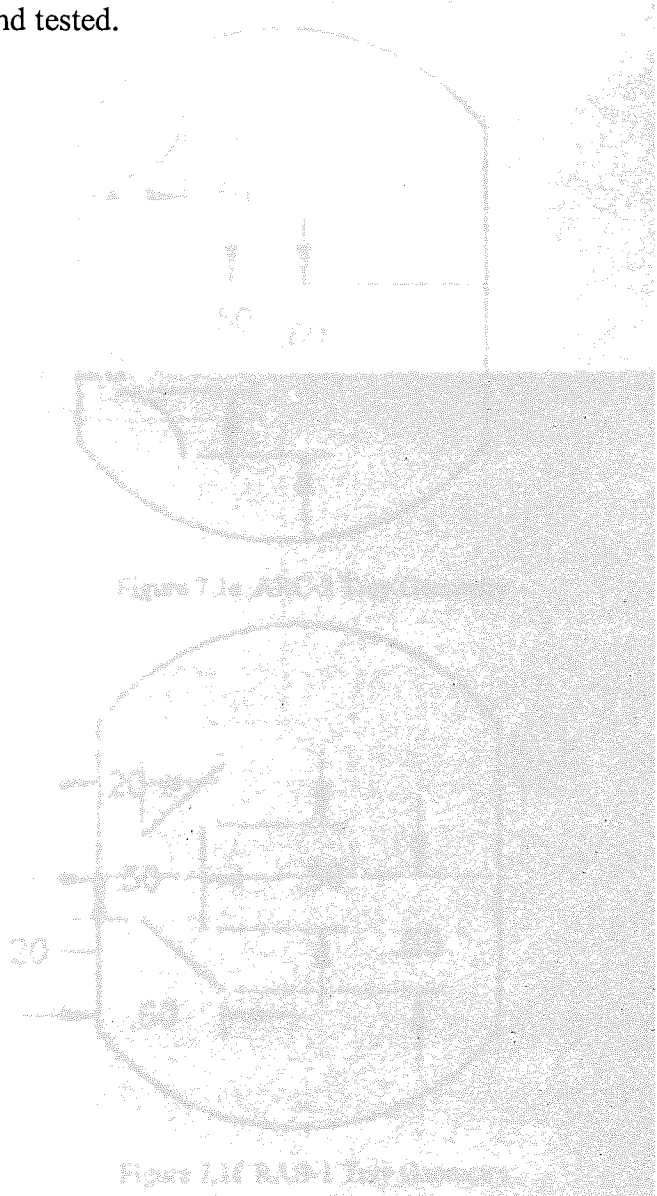

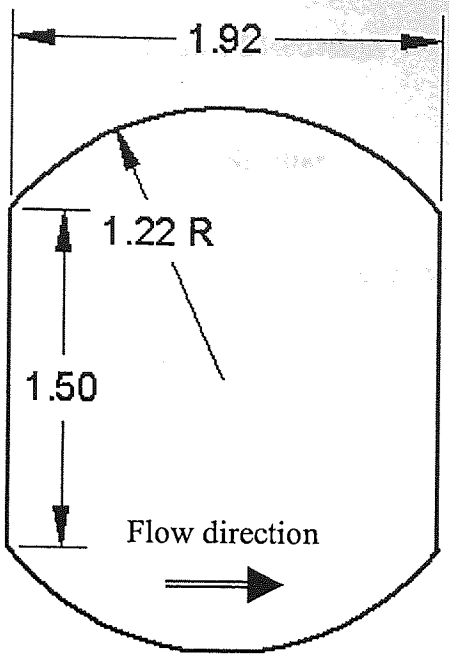

Figure 7.1a UMD Tray Geometry

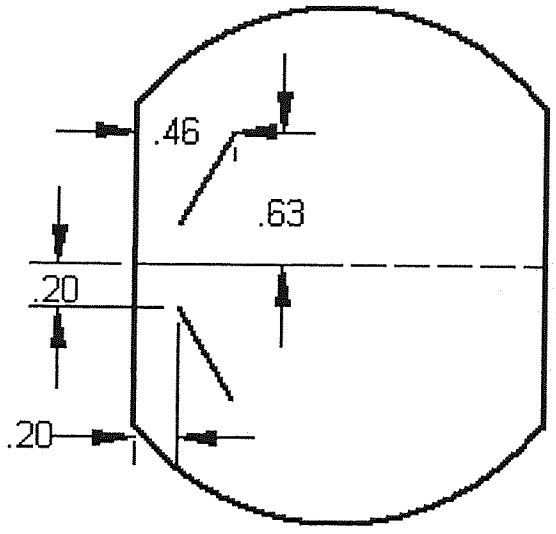

Figure 7.1b STR-1 Tray Geometry

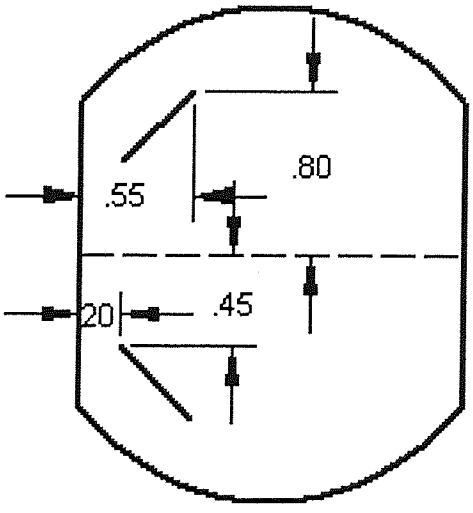

Figure 7.1c STR-2 Tray Geometry

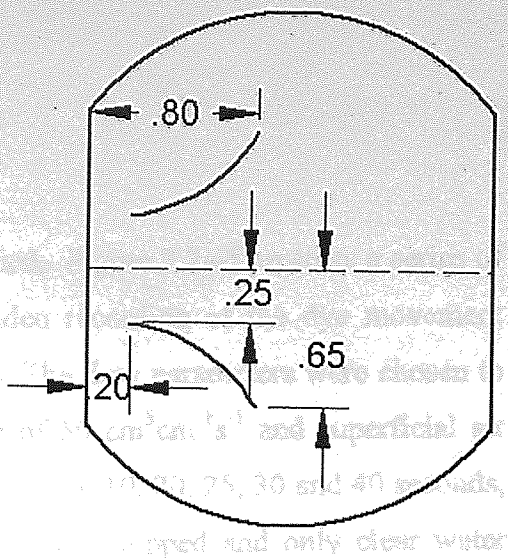

Figure 7.1d ARC-1 Tray Geometry

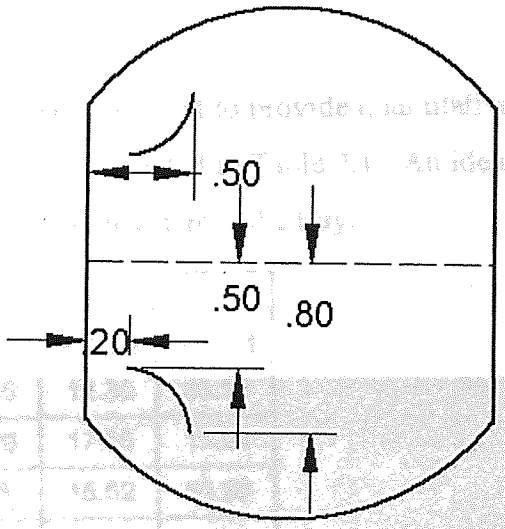

Figure 7.1e ARC-2 Tray Geometry

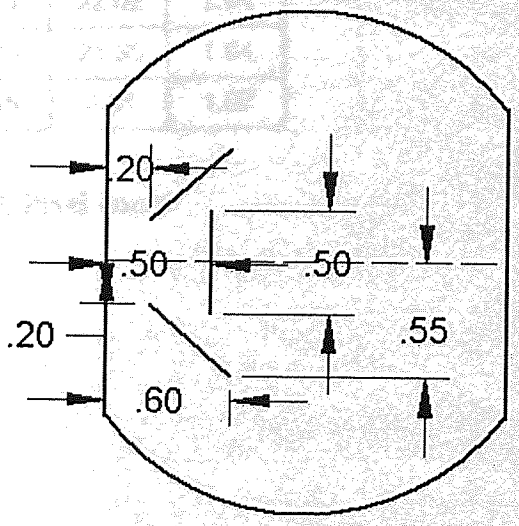

Figure 7.1f RAB-1 Tray Geometry

7.5 Results and Discussion

7.5.1 Dyed Tray Studies

Many dye tracer runs were recorded on video and studied. Figure 7.2a-f presents a series of binary images processed (Fischer, 1999) from the video recording of the dye movement across the tray during air-water contacting experiments. The flow parameters were chosen to be consistent with the froth regime - a liquid loading of 50 $cm^3cm^{-1}s^{-1}$ and superficial air velocity of 0.8 m s^{-1}. The images were sampled at time, t = 5, 10, 20, 25, 30 and 40 seconds, where time t = 0 represents the time the dye injection was stopped and only clear water entered the tray.

The black and white pixels present in each image series were counted to provide quantitative measure of the dye subsidence with time and the results are presented in Table 7.1. An ideal flow is one that provides for a uniform and steady dye subsidence across the tray.

	Tray Type					
Time	UMD	STR-1	STR-2	ARC-1	ARC-2	RAB-1
5	13.30	28.17	32.64	26.45	12.30	33.16
10	16.10	11.52	28.42	12.20	17.50	15.54
15	19.97	5.95	26.31	4.48	15.52	10.98
20	19.78	2.47	27.19	3.08	21.39	6.99
25	26.13	1.39	21.29	1.24	22.02	2.94
30	24.34	0.52	10.59	0.63	23.35	1.64
40	2.92	0.14	4.02	0.15	4.31	1.07

Table 7.1 Percentage black Pixel count

5 Seconds

10 Seconds

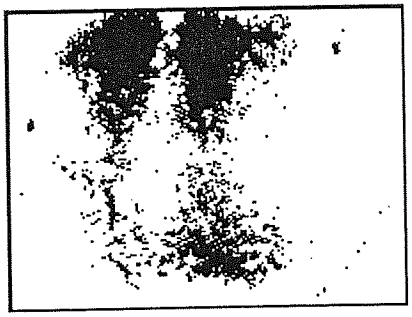

20 Seconds

25 Seconds

30 Seconds

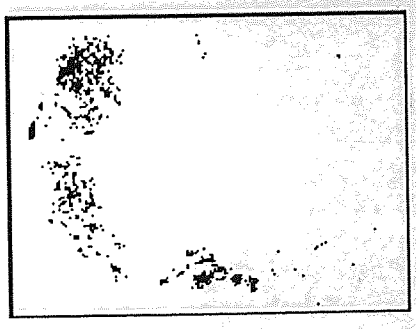

40 Seconds

Figure 7.2a Binary Dye Images for the UMD Tray at Weir Loading of 50 $cm^3cm^{-1}s^{-1}$ and Air Velocity of 0.8 $m\ s^{-1}$

5 Seconds

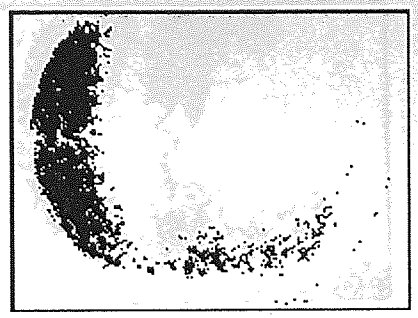

10 Seconds

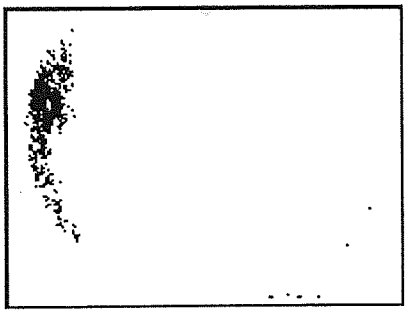

20 Seconds

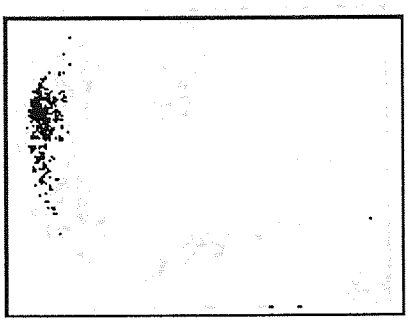

25 Seconds

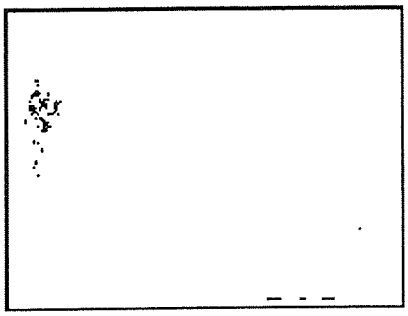

30 Seconds

40 Seconds

Figure 7.2b Binary Dye Images for the STR-1 Tray at Weir Loading of 50 $cm^3cm^{-1}s^{-1}$ and Air Velocity of 0.8 $m\ s^{-1}$

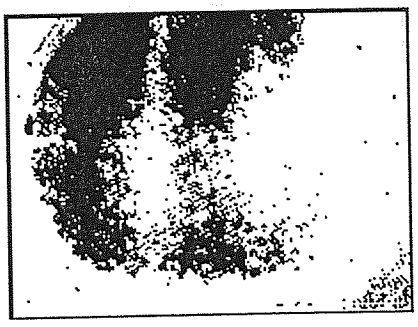

5 Seconds

10 Seconds

20 Seconds

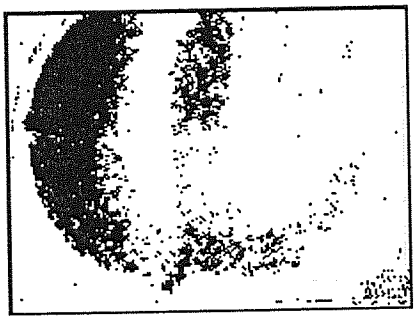

25 Seconds

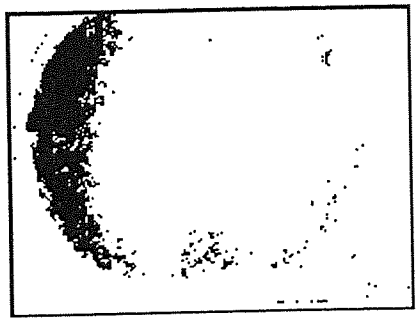

30 Seconds

40 Seconds

Figure 7.2c Binary Dye Images for the STR-2 Tray at Weir Loading of 50 $cm^3cm^{-1}s^{-1}$ and Air Velocity of 0.8 $m\ s^{-1}$

5 Seconds

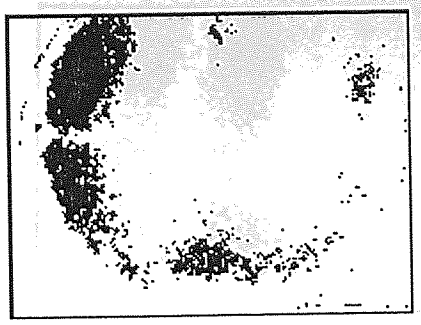

10 Seconds

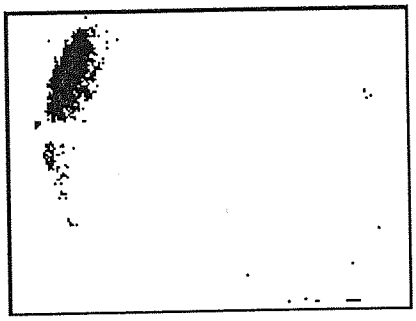

20 Seconds

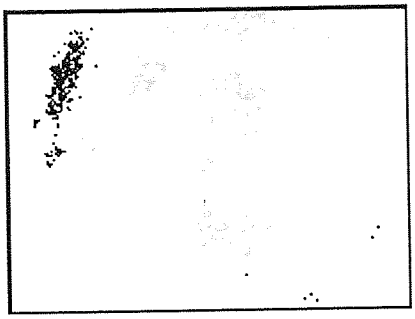

25 Seconds

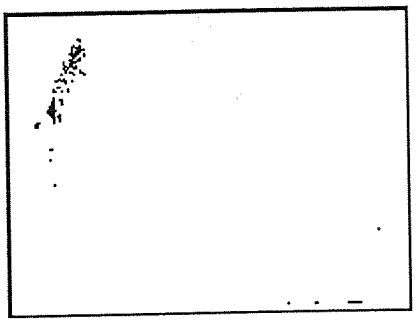

30 Seconds

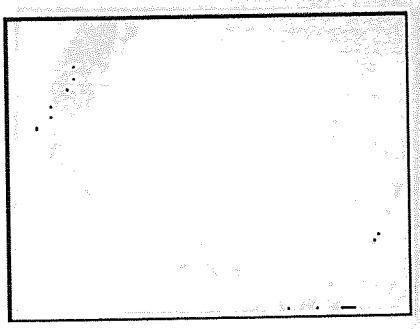

40 Seconds

Figure 7.2d Binary Dye Images for the ARC-1 Tray at Weir Loading of 50 $cm^3cm^{-1}s^{-1}$ and Air Velocity of 0.8 m s^{-1}

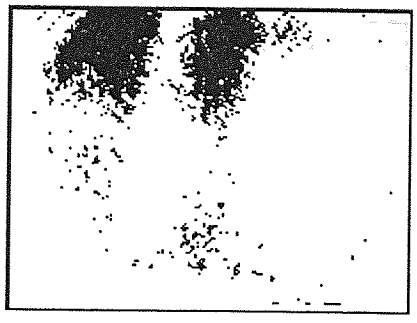

5 Seconds

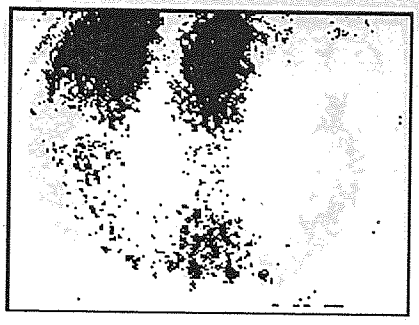

10 Seconds

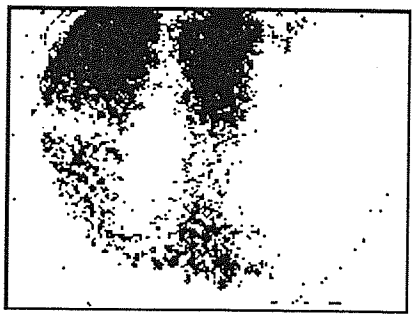

20 Seconds

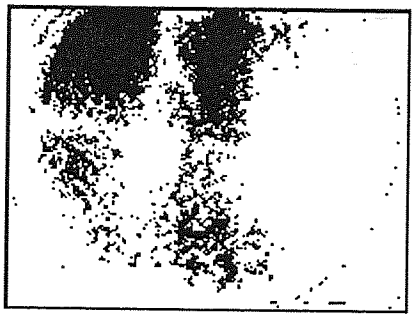

25 Seconds

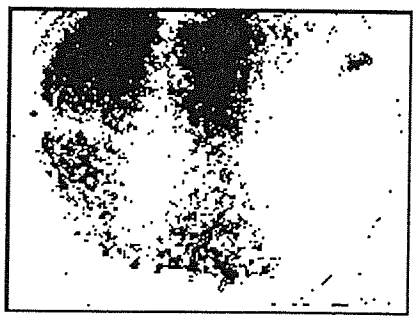

30 Seconds

40 Seconds

Figure 7.2e Binary Dye Images for the ARC-2 Tray at Weir Loading of 50 $cm^3cm^{-1}s^{-1}$ and Air Velocity of 0.8 $m\ s^{-1}$

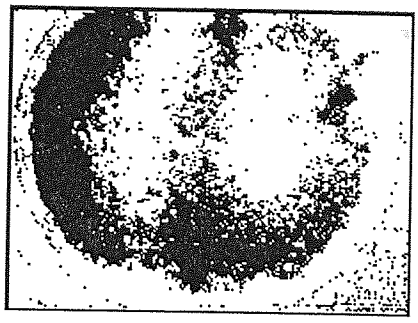

5 Seconds

10 Seconds

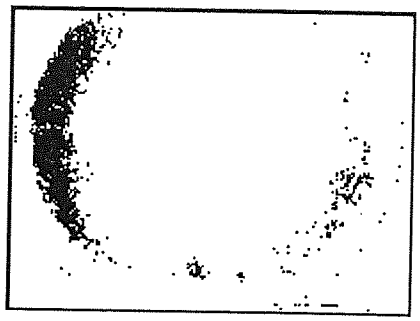

20 Seconds

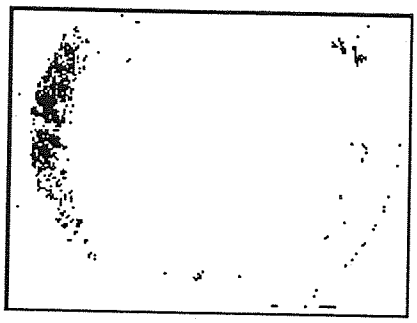

25 Seconds

30 Seconds

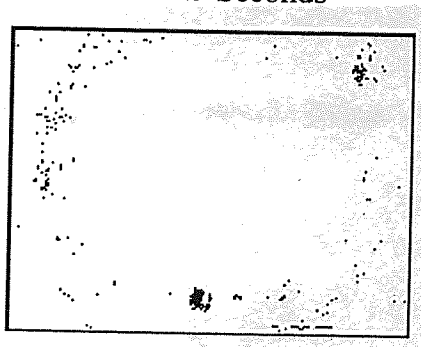

40 Seconds

Figure 7.2f Binary Dye Images for the RAB-1 Tray at Weir Loading of 50 $cm^3cm^{-1}s^{-1}$ and Air Velocity of 0.8 $m\ s^{-1}$

From Table 7.1, the trend of the mean percentage black count seems to reduce steadily with time for the ARC-1, STR-1 and RAB-1 trays. In the case of the UMD (control), ARC-2 and STR-2 trays, the mean percentage black count tend to hold steady before a sudden drop toward the end of the time step. In terms of dye uniformity, the ARC-1, STR-1 and RAB-1 trays showed better uniformity in the dye spread, especially in the ability to replenish the segmented areas adjacent to the walls, than the control. When viewed in terms of the ability to clear the dye on the tray alone, i.e. overall dye reduction with time, the same modified tray topologies offer superior flow characteristics to that offered by the conventional tray. After 20 seconds, STR-1 and ARC-1 trays had reduced the amount of dye on the tray to that achieved by the control after about 40 seconds. RAB-1 arrived at the same level of reduction after about 25 seconds while ARC-2 and STR-2 took longer than 40 seconds to attain the same level of subsidence. These results require careful interpretation. Although residence time, flow pattern and efficiency are intrinsically linked (AIChE, 1958; Porter et al., 1972; Chan and Fair, 182), a quantitative reduction in the net residence time does not equate to a direct improvement in the flow pattern or tray efficiency. However, any device that succeeds in eliminating or diminishing the 'circulating-dead' liquid zones on the tray segments is likely to reduce the net liquid residence time on the tray, improve liquid flow profile and probably tray mass transfer efficiency.

Based on the above results, more detailed experiments were narrowed down to ARC-1 and STR-1 trays.

7.5.2 The Temperature Profiles

Due to the vast number of reduced temperature isotherms obtained only a representative few are presented here for use in the discussion. The detailed temperature isotherms are compiled in Appendices 6, 7 and 8 for the UMD, STR-1 and ARC-1 trays, respectively. The temperature isotherms for all six trays operating at superficial air velocity of 0.8 m s^{-1} and weir load of 50 $cm^3cm^{-1}s^{-1}$ are presented in Figures 7.3a-f. Figures 7.3g-x show the isotherms at 1.0, 1.5 and 2.0 m s^{-1} for UMD, STR-1 and ARC-1 trays.

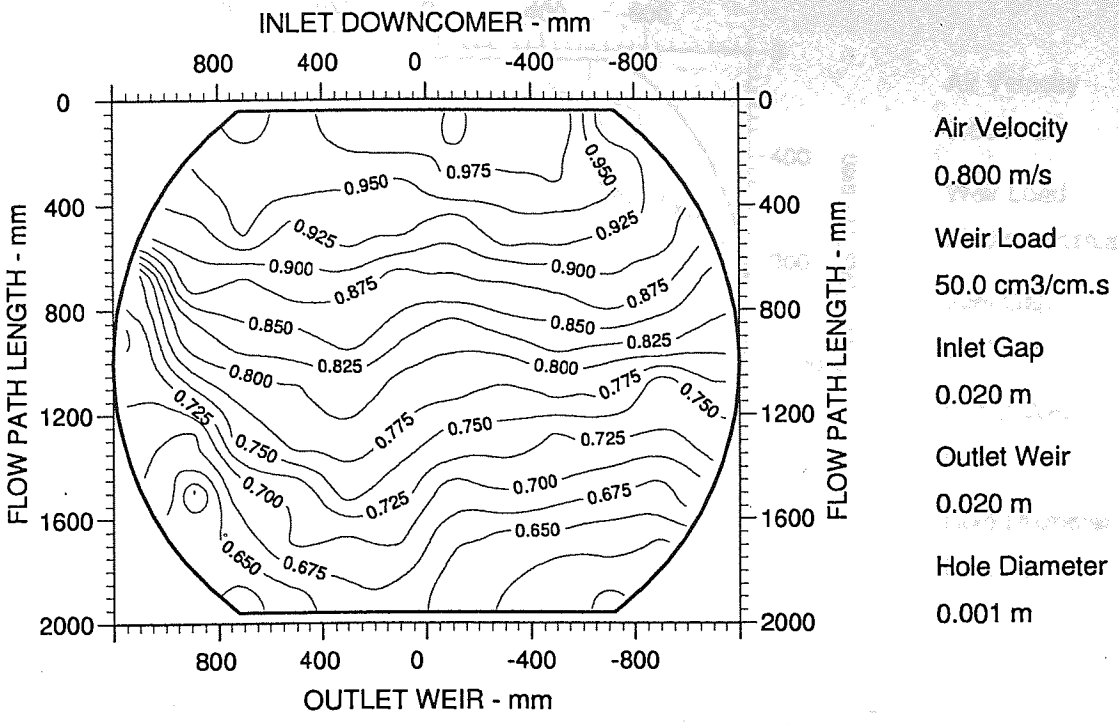

Fig. 7.3a Two-dimensional reduced temperature isotherms
Superficial Air velocity 0.8 m/s - UMD Tray

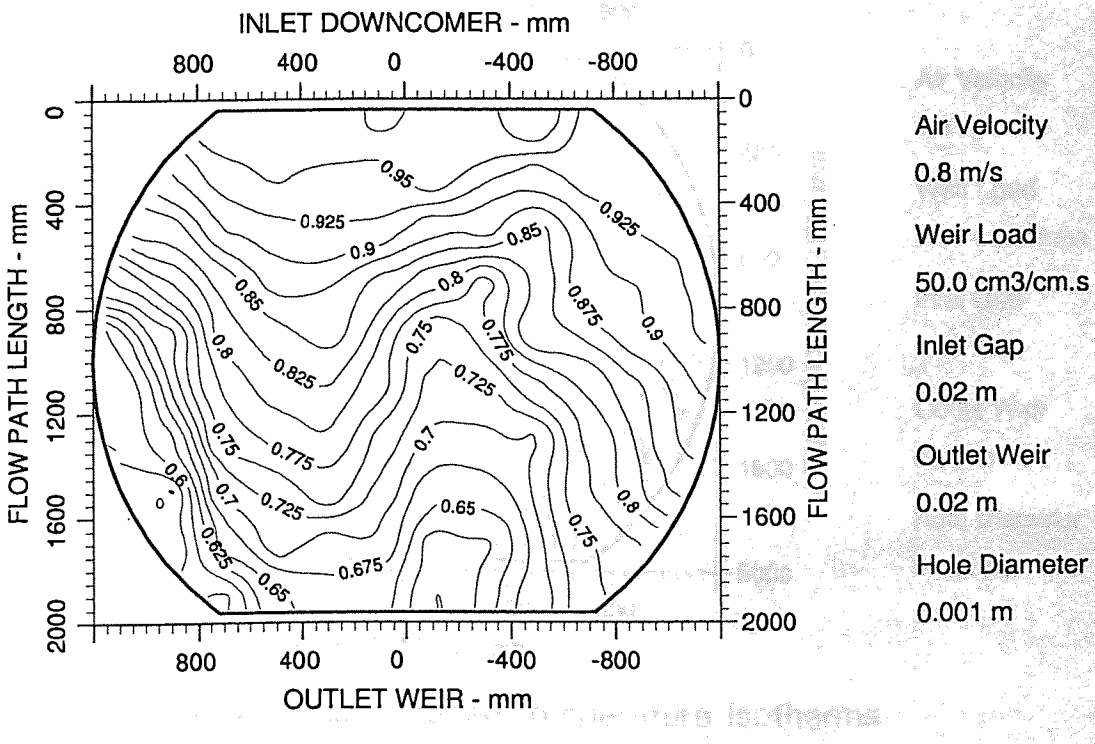

Fig. 7.3b Two-dimensional reduced temperature isotherms
Superficial Air velocity 0.8 m/s - STR-1 Tray

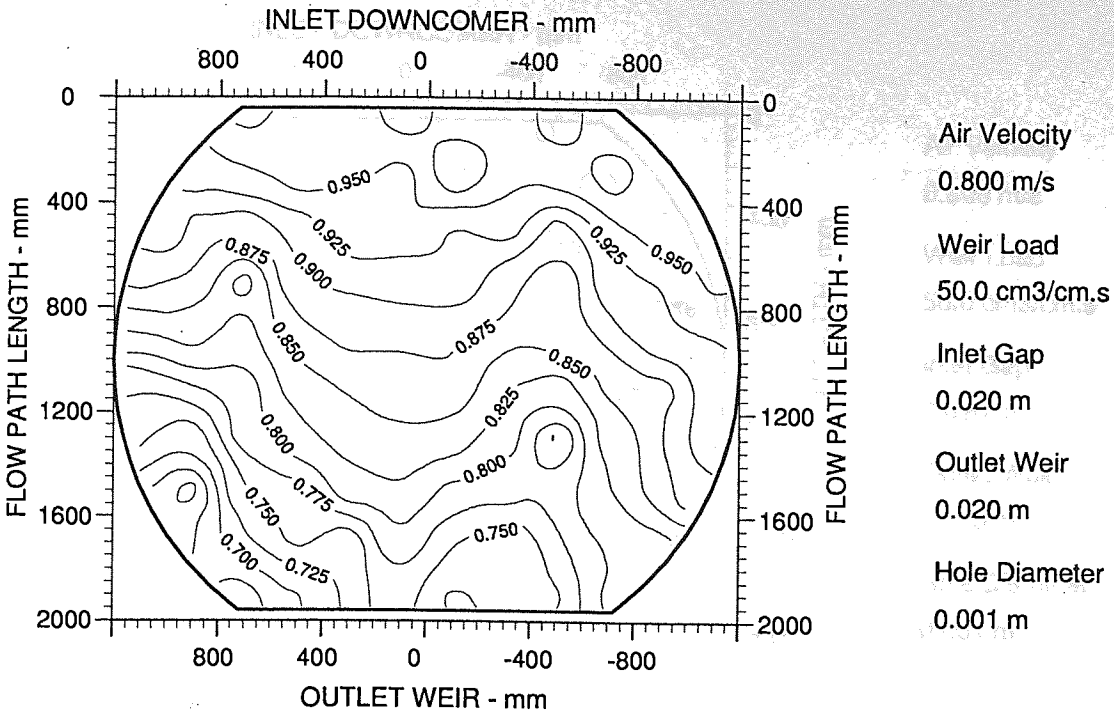

Fig. 7.3c Two-dimensional reduced temperature isotherms
Superficial Air velocity 0.8 m/s - STR-2 Tray

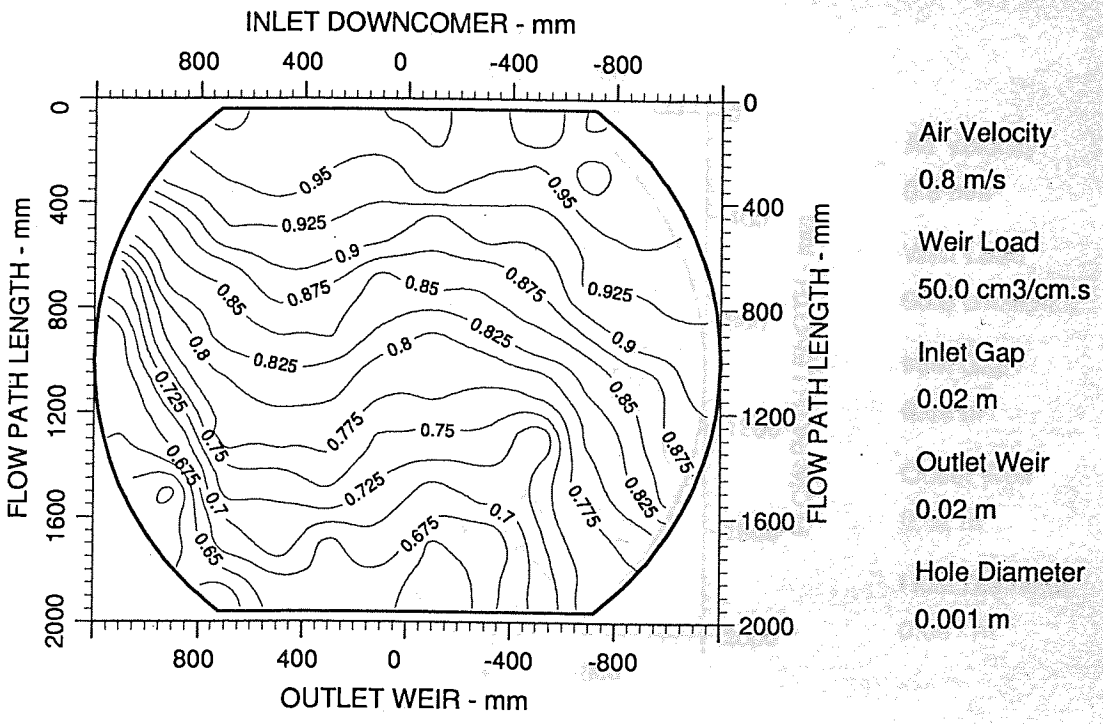

Fig. 7.3d Two-dimensional reduced temperature isotherms
Superficial Air velocity 0.8 m/s - ARC-1 Tray

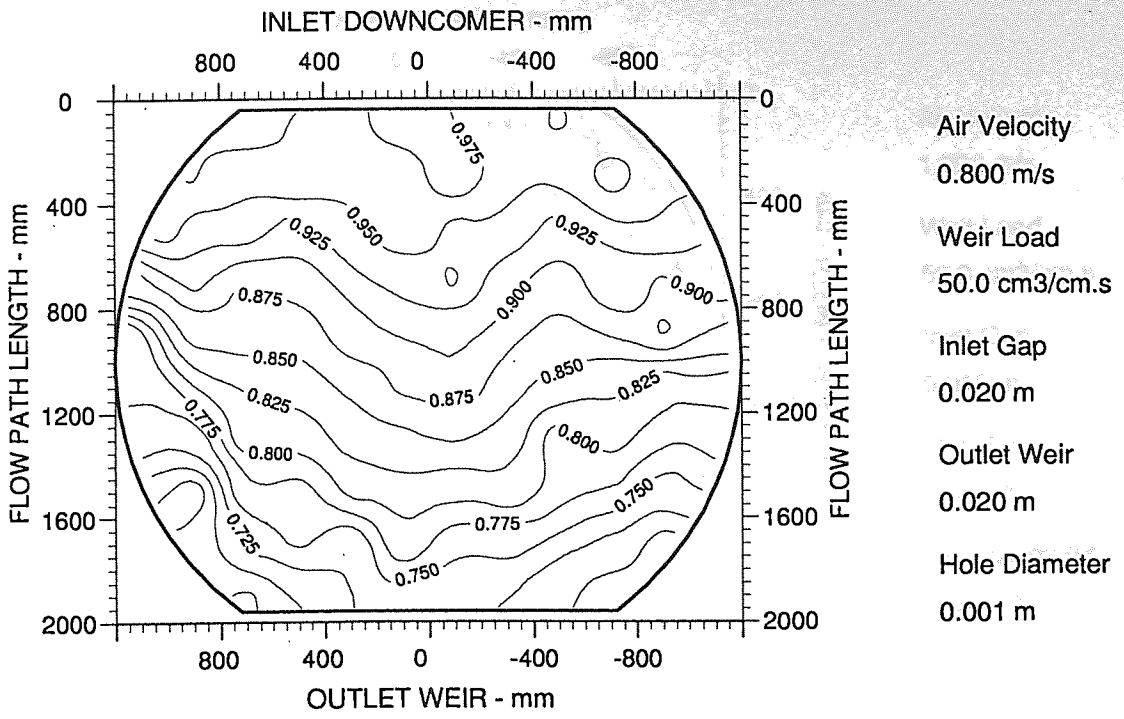

Fig. 7.3e Two-dimensional reduced temperature isotherms
Superficial Air velocity 0.8 m/s - ARC-2 Tray

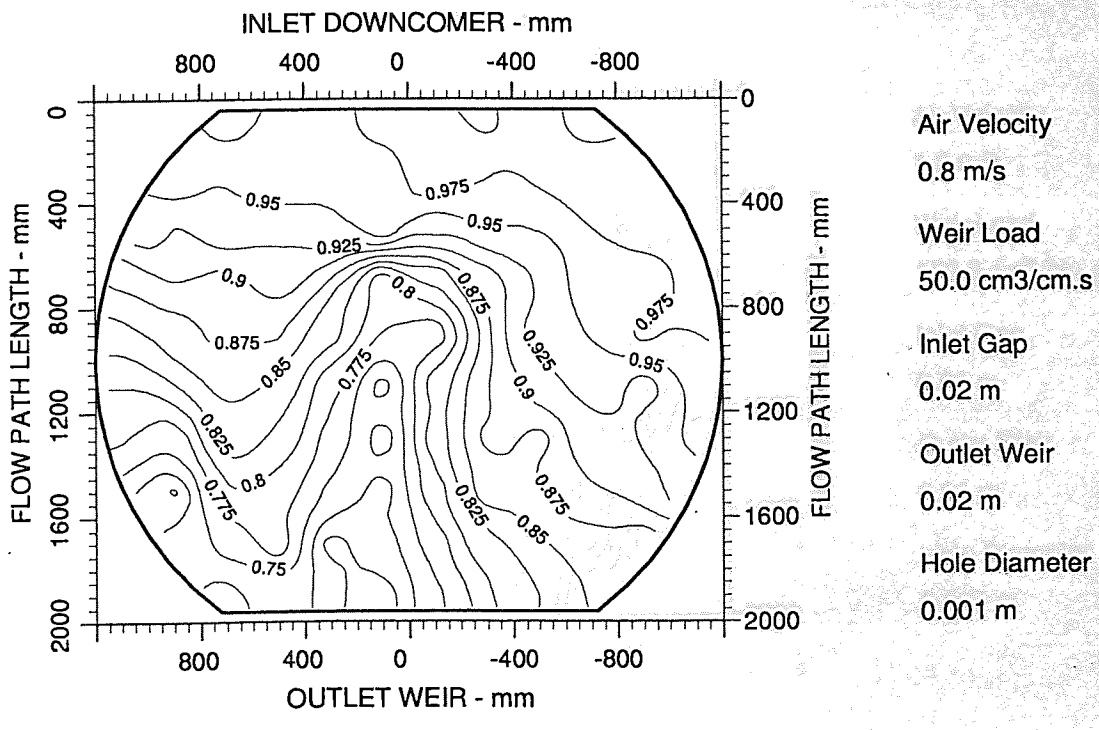

Fig. 7.3f Two-dimensional reduced temperature isotherms
Superficial Air velocity 0.8 m/s - RAB-1 Tray

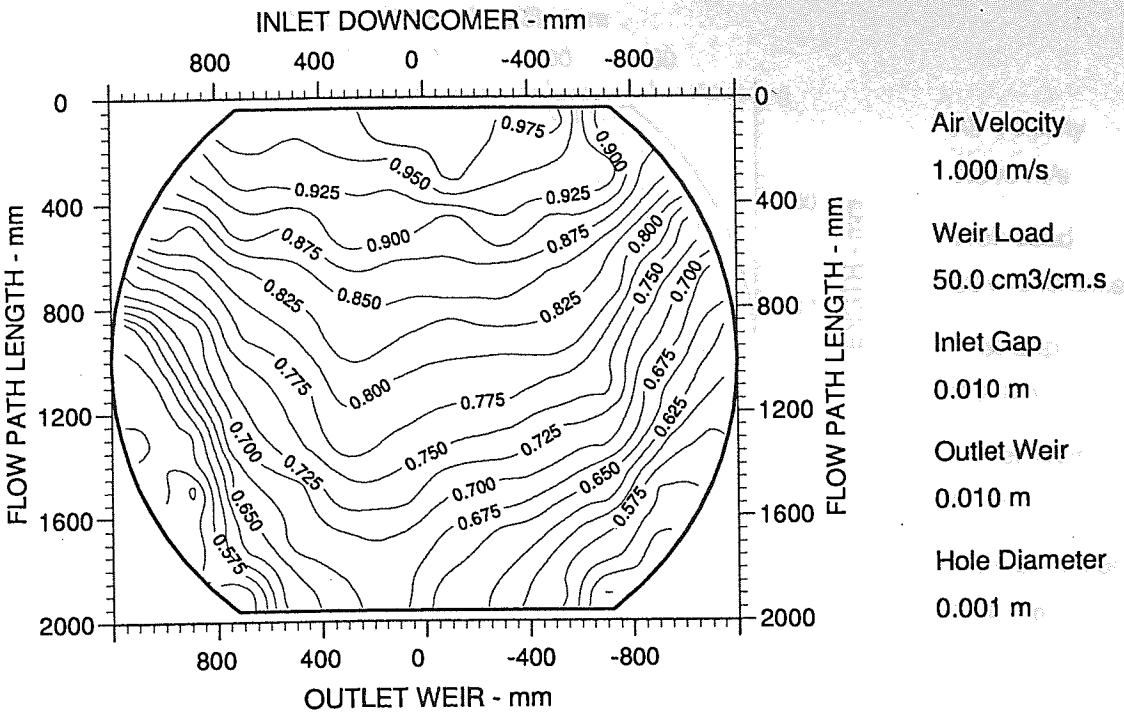

Fig. 7.3g Two-dimensional reduced temperature isotherms
Superficial Air velocity 1.0 m/s - UMD Tray

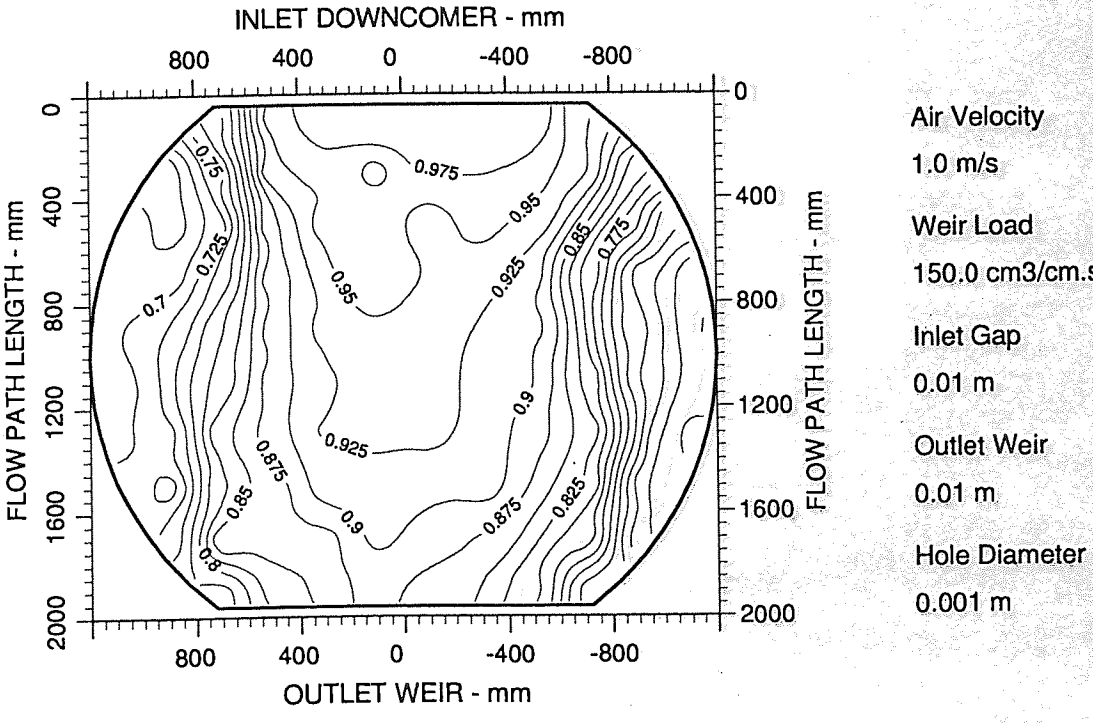

Fig. 7.3h Two-dimensional reduced temperature isotherms
Superficial Air velocity 1.0 m/s - UMD Tray

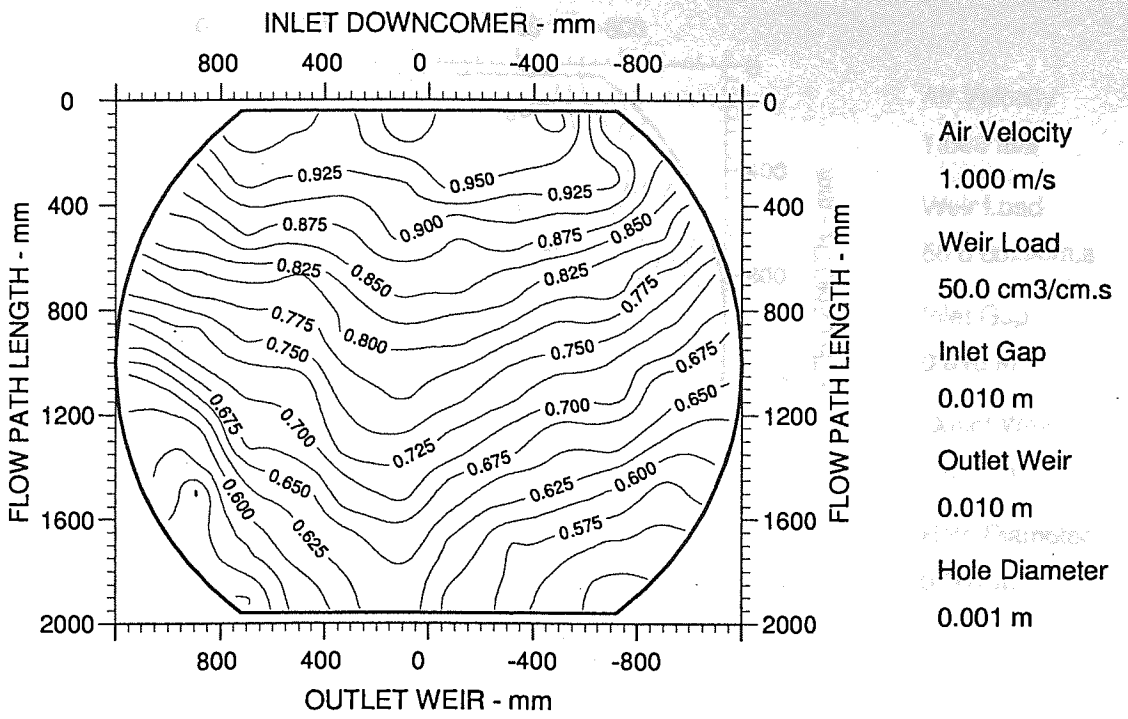

Fig. 7.3i Two-dimensional reduced temperature isotherms
Superficial Air velocity 1.0 m/s - STR-1 Tray

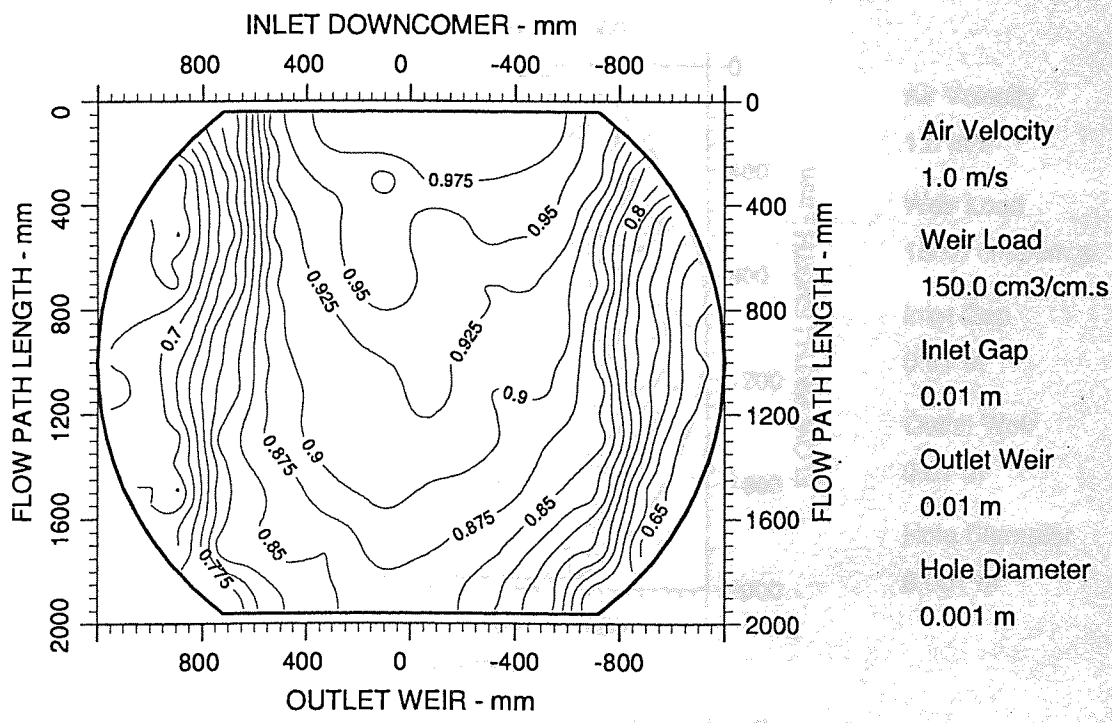

Fig. 7.3j Two-dimensional reduced temperature isotherms
Superficial Air velocity 1.0 m/s - STR-1 Tray

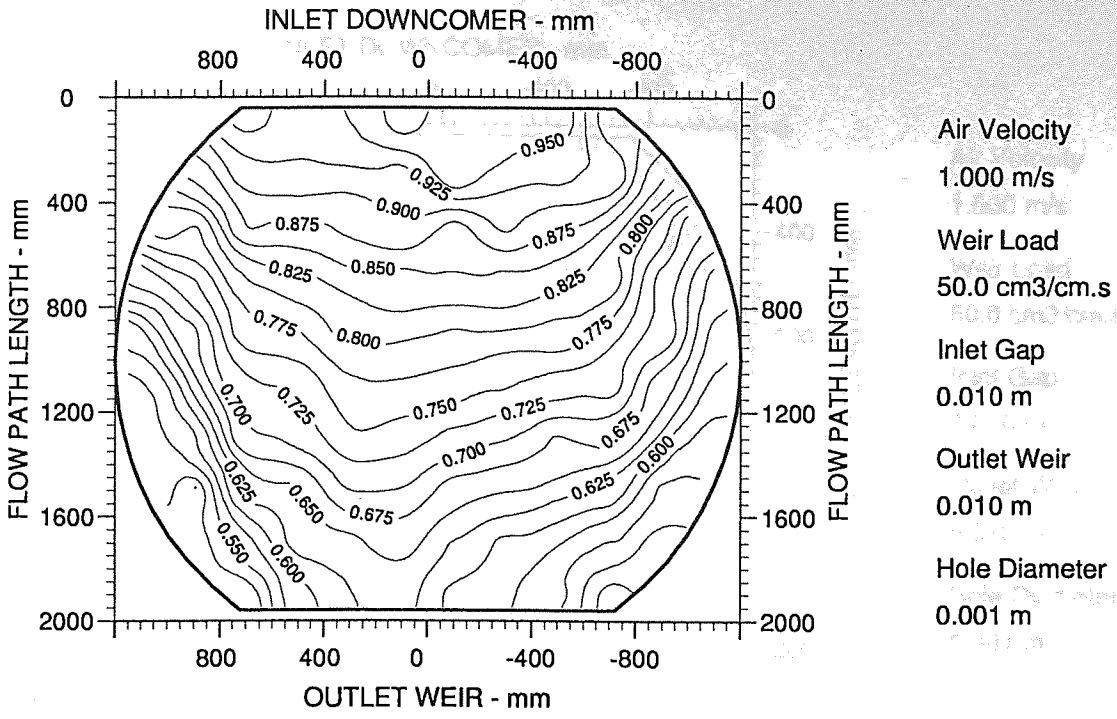

Fig. 7.3k Two-dimensional reduced temperature isotherms
Superficial Air velocity 1.0 m/s - ARC-1 Tray

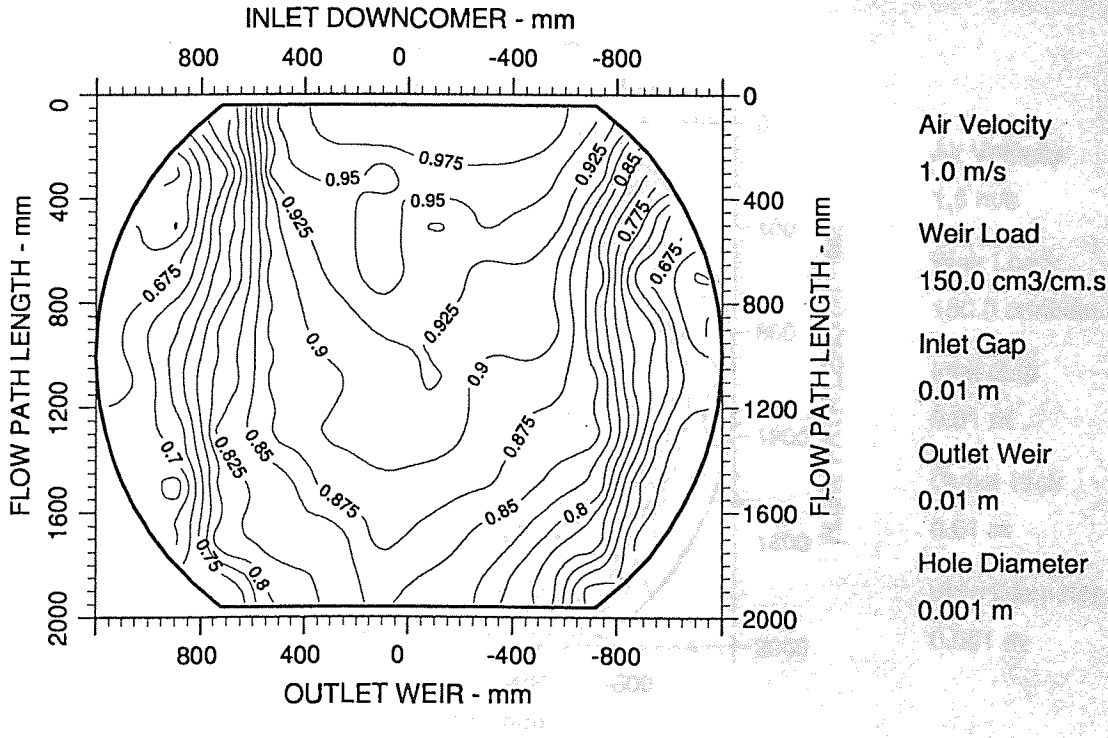

Fig. 7.3l Two-dimensional reduced temperature isotherms
Superficial Air velocity 1.0 m/s - ARC-1 Tray

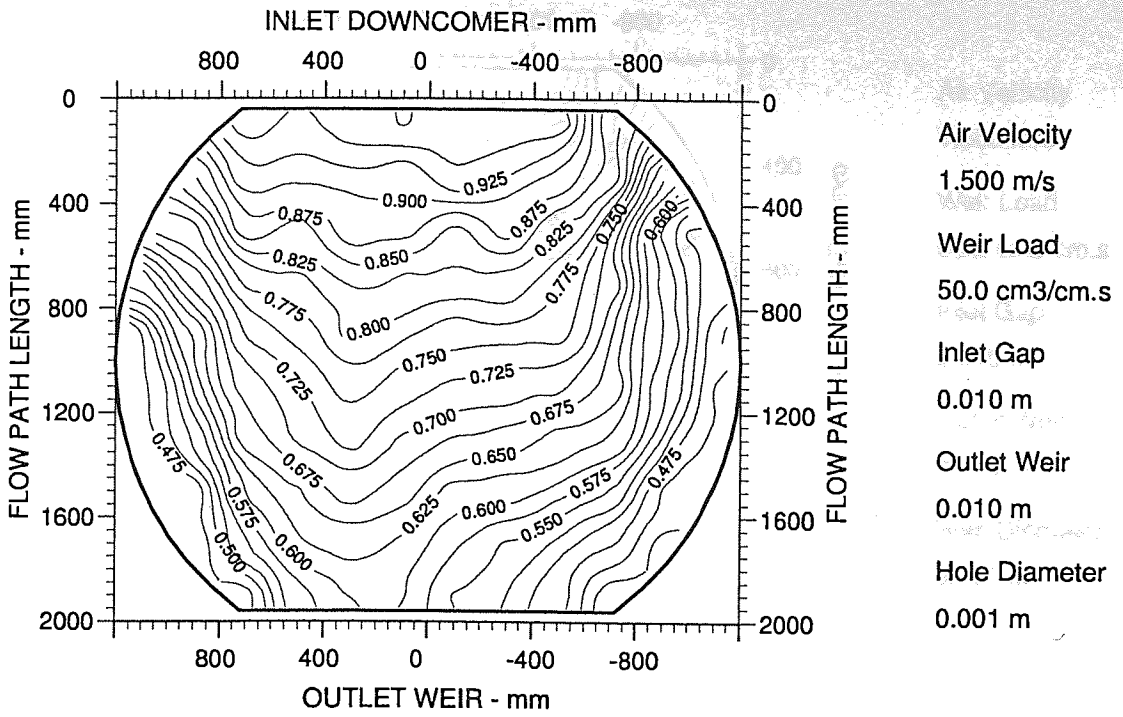

Fig. 7.3m Two-dimensional reduced temperature isotherms
Superficial Air velocity 1.5 m/s - UMD Tray

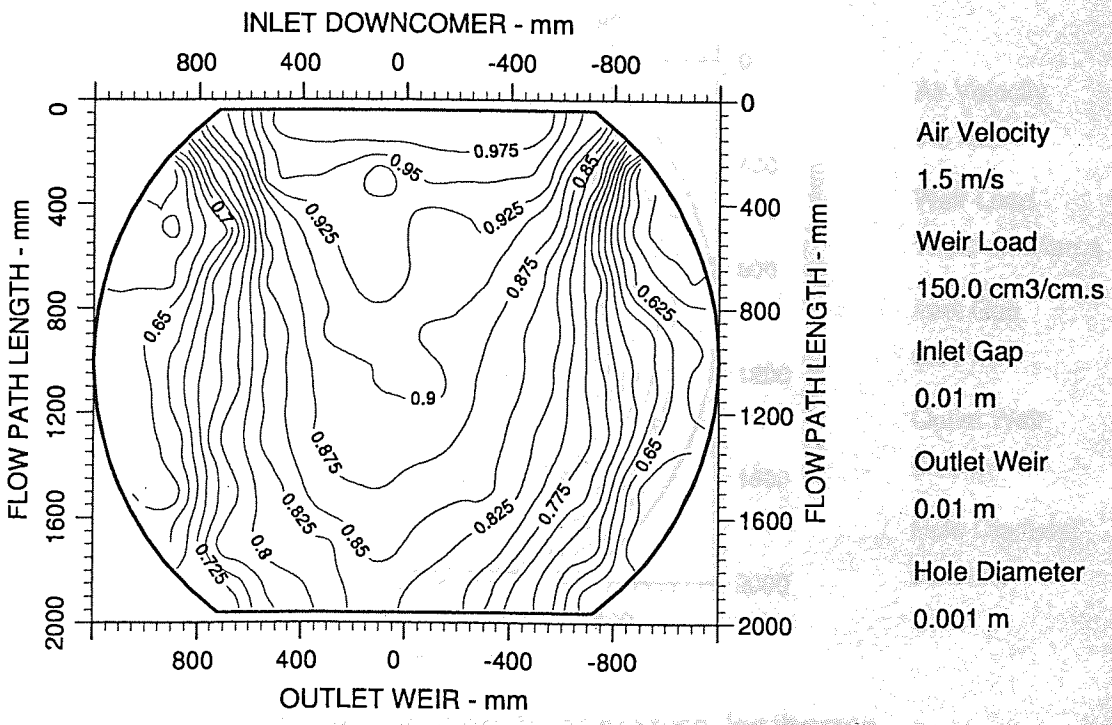

Fig. 7.3n Two-dimensional reduced temperature isotherms
Superficial Air velocity 1.5 m/s - UMD Tray

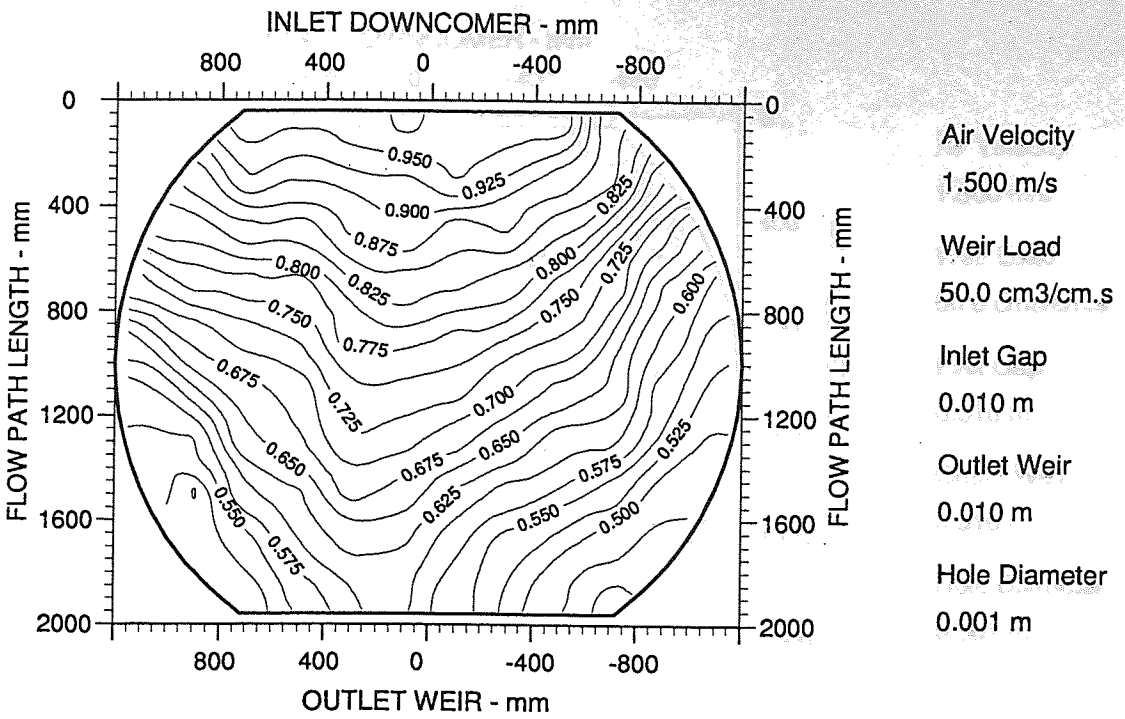

Fig. 7.3o Two-dimensional reduced temperature isotherms
Superficial Air velocity 1.5 m/s - STR-1 Tray

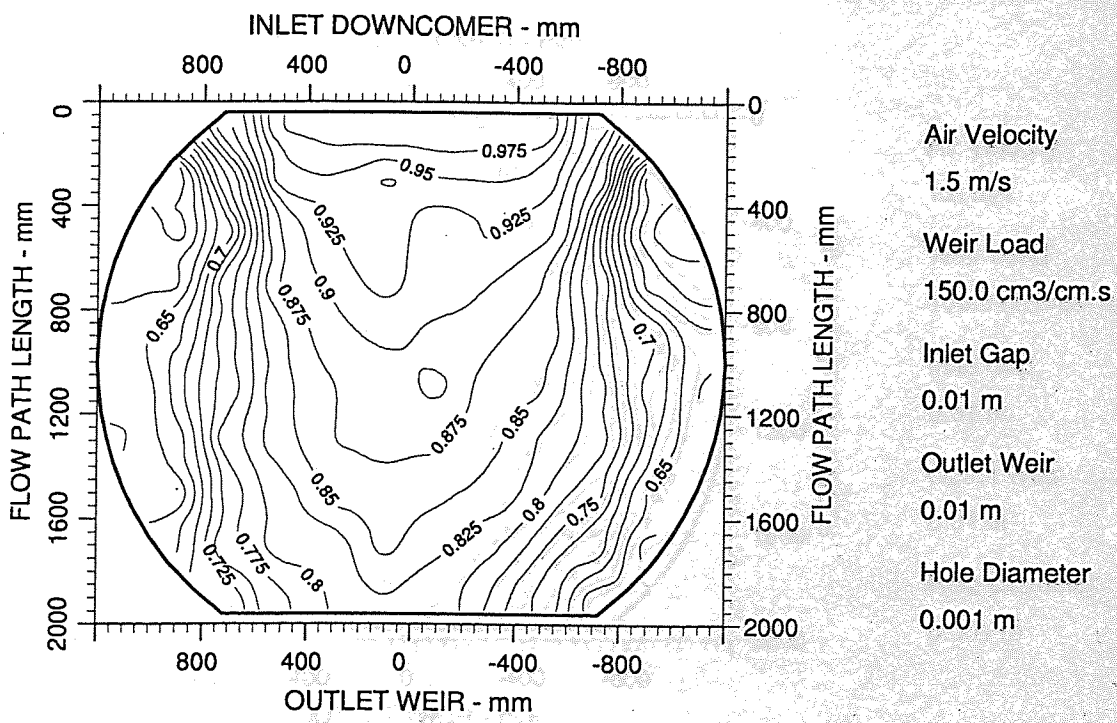

Fig. 7.3p Two-dimensional reduced temperature isotherms
Superficial Air velocity 1.5 m/s - STR-1 Tray

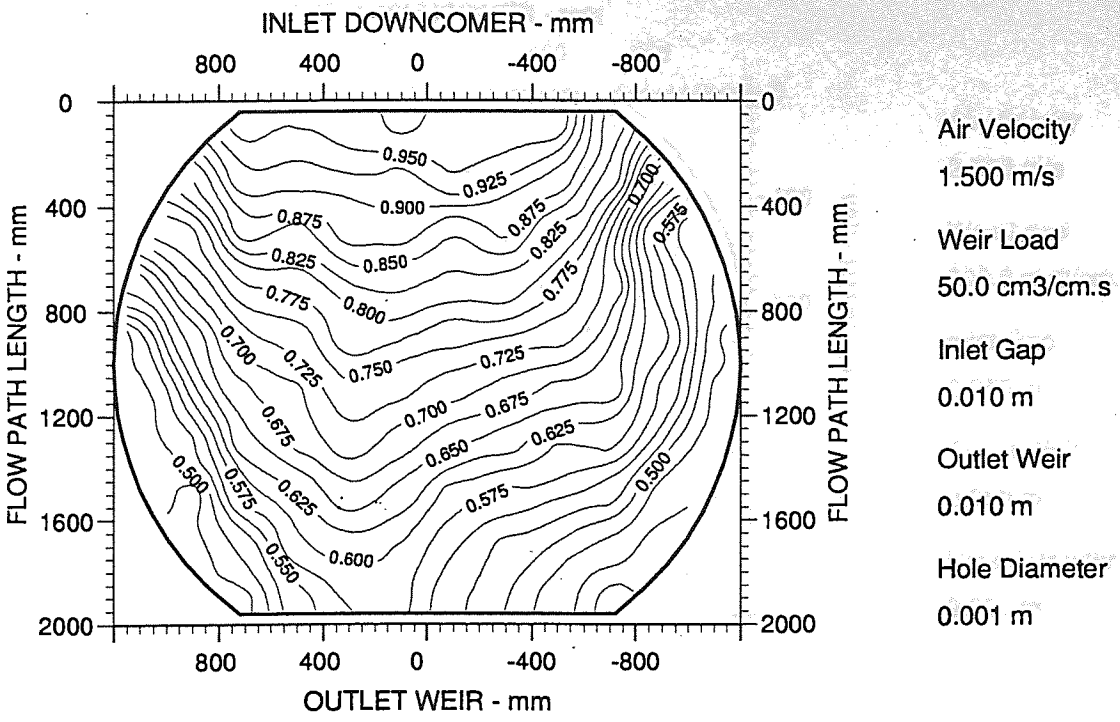

Fig. 7.3q Two-dimensional reduced temperature isotherms
Superficial Air velocity 1.5 m/s - ARC-1 Tray

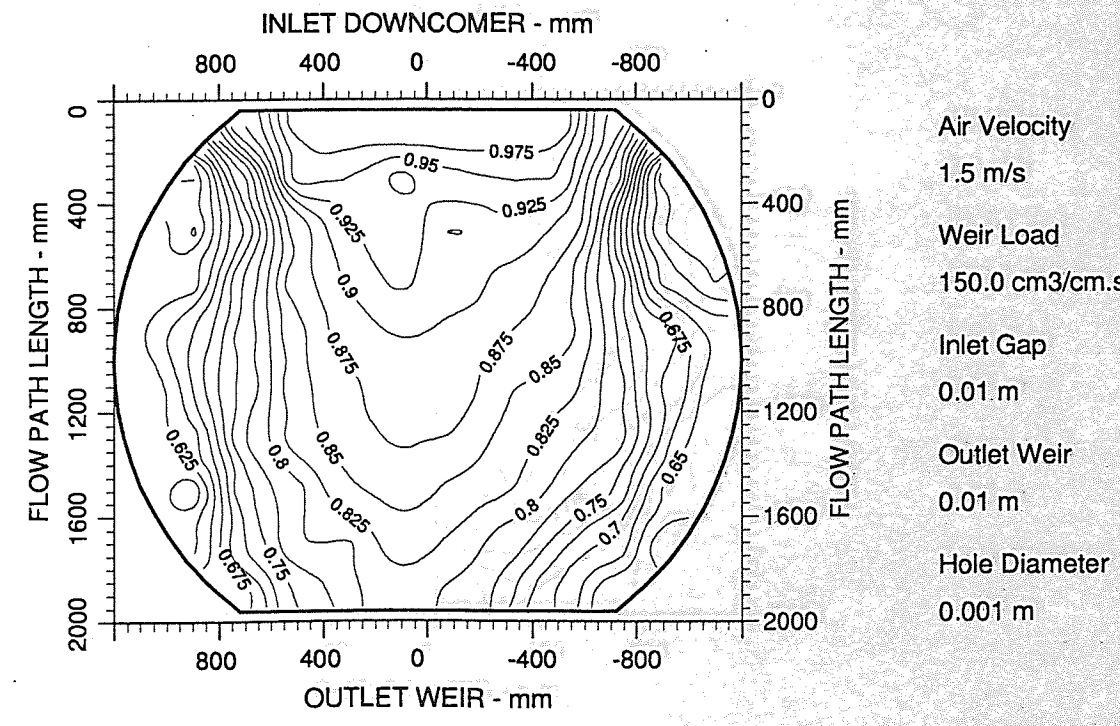

Fig. 7.3r Two-dimensional reduced temperature isotherms
Superficial Air velocity 1.5 m/s - ARC-1 Tray

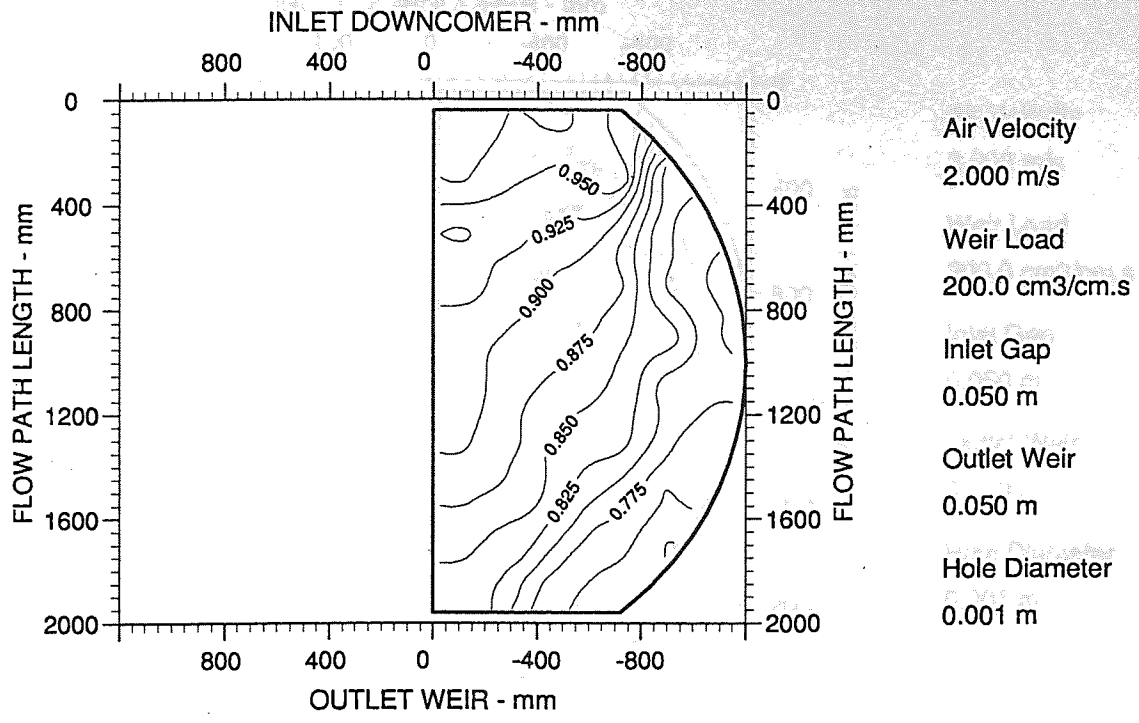

Fig. 7.3s Two-dimensional reduced temperature isotherms
Superficial Air velocity 2.0 m/s - UMD Tray

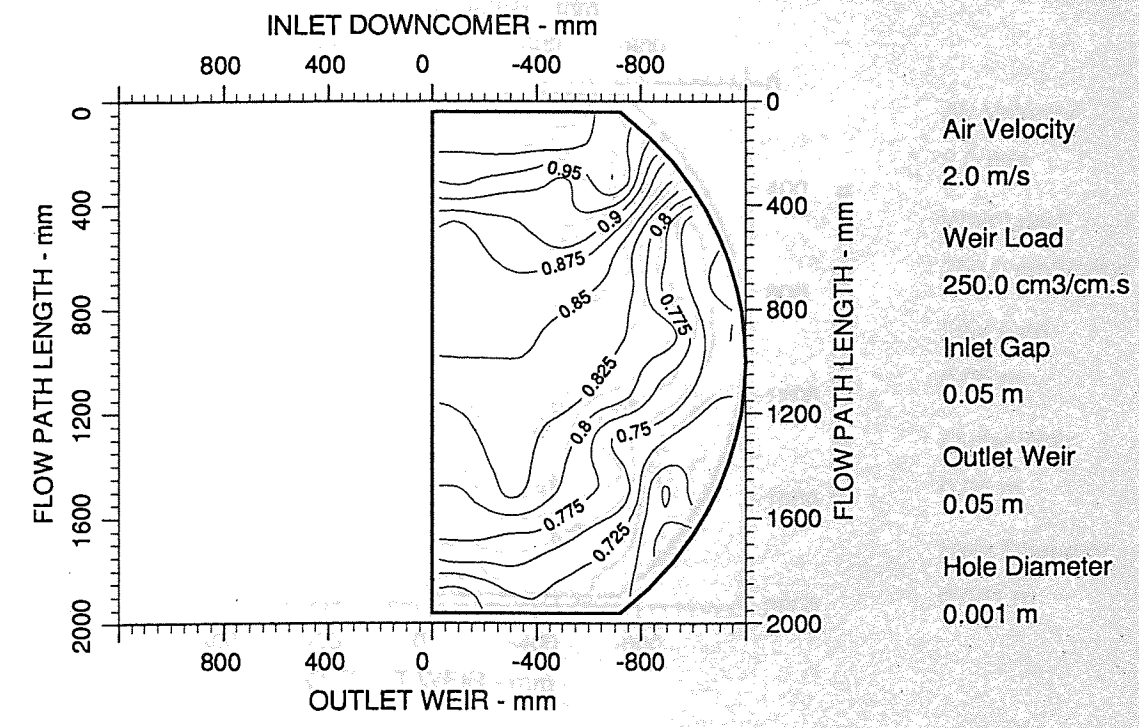

Fig. 7.3t Two-dimensional reduced temperature isotherms
Superficial Air velocity 2.0 m/s - UMD Tray

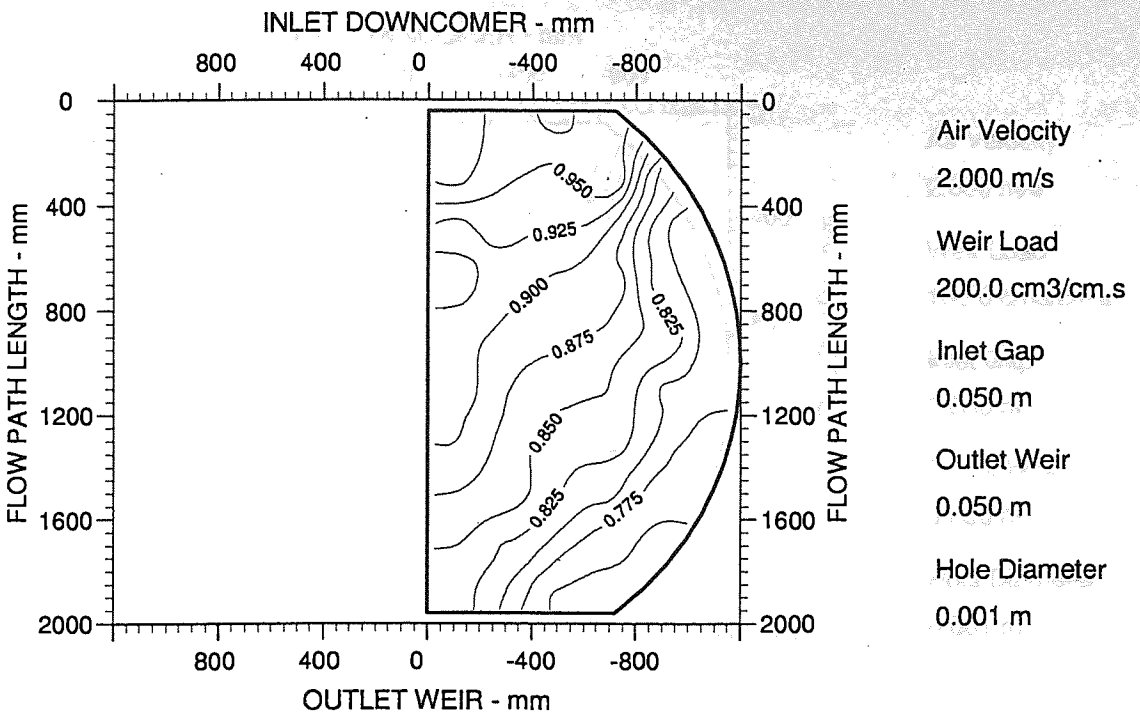

Fig. 7.3u Two-dimensional reduced temperature isotherms
Superficial Air velocity 2.0 m/s - STR-1 Tray

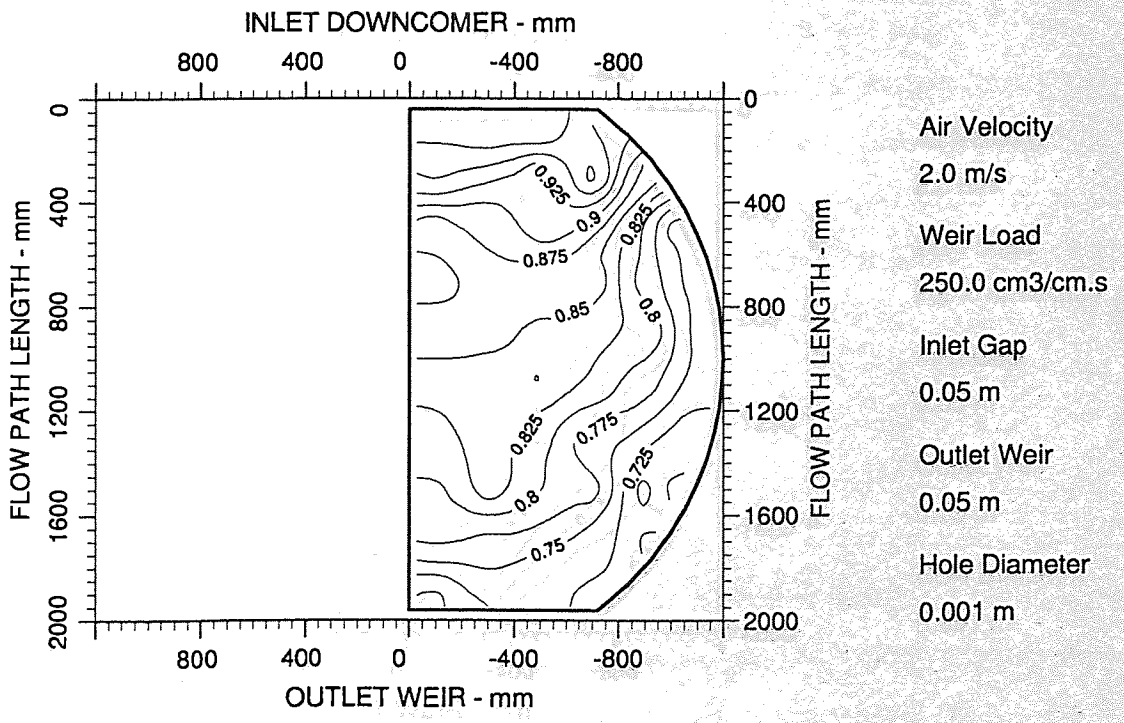

Fig. 7.3V Two-dimensional reduced temperature isotherms
Superficial Air velocity 2.0 m/s - STR-1 Tray

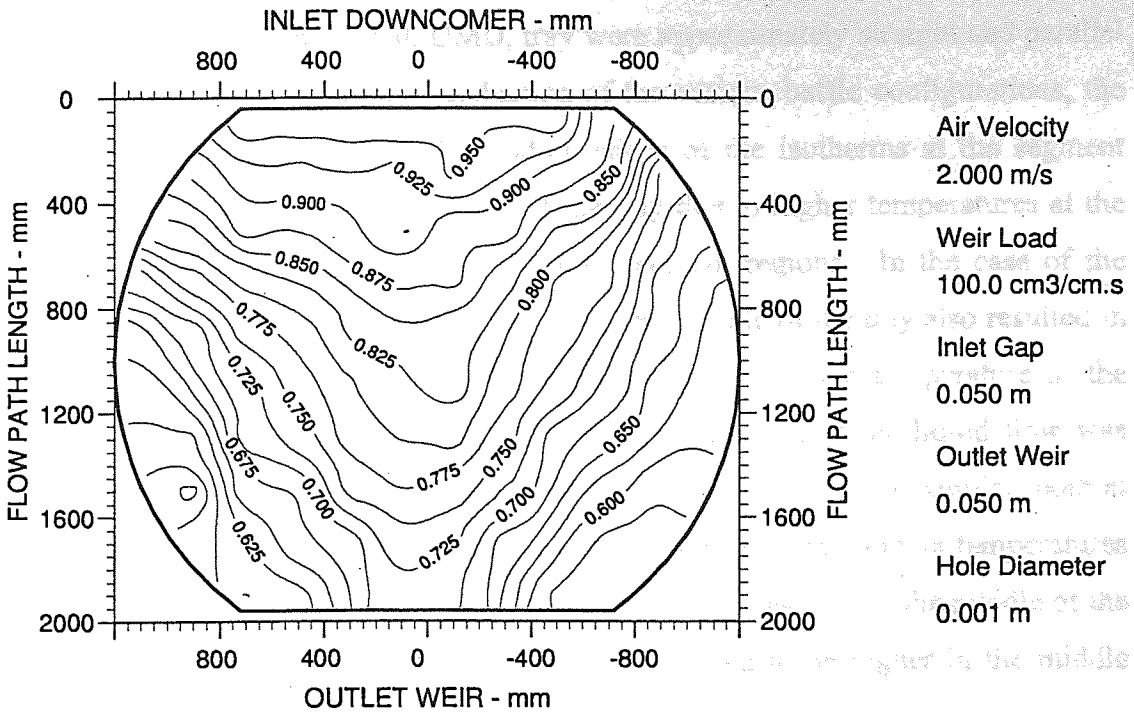

Fig. 7.3w Two-dimensional reduced temperature isotherms
Superficial Air velocity 2.0 m/s - ARC-1 Tray

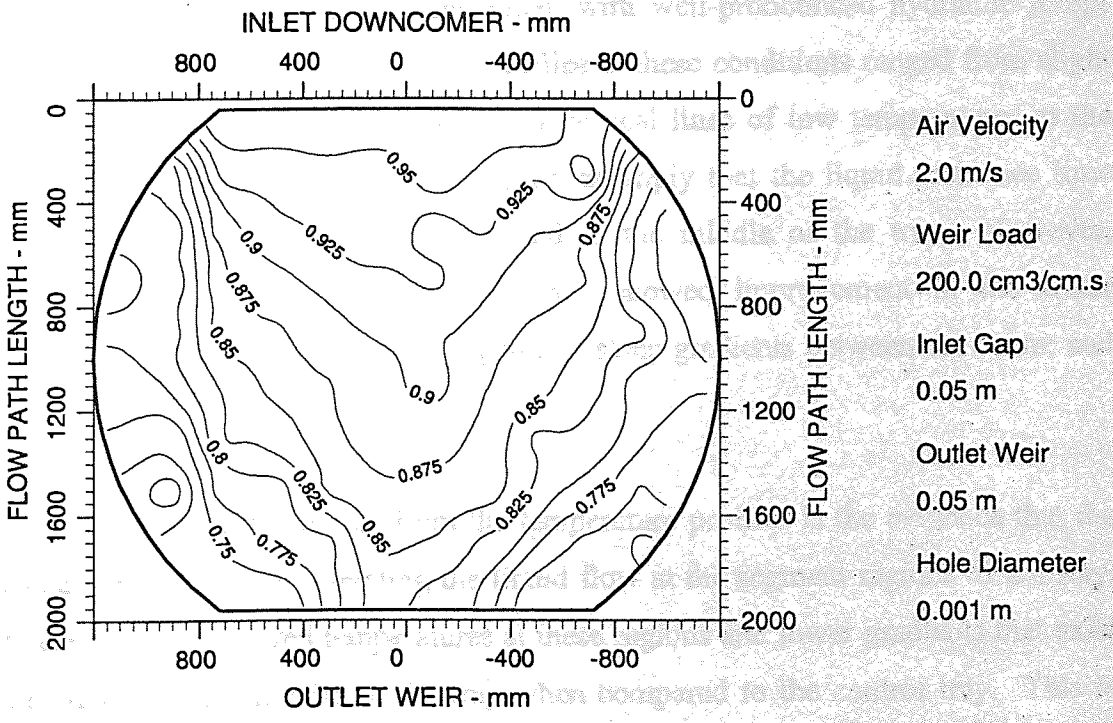

Fix. 7.3x Two-dimensional reduced temperature isotherms
Superficial Air velocity 2.0 m/s - ARC-1 Tray

The profiles at superficial air velocity of 0.8 ms^{-1} and weir load of 50 $cm^3cm^{-1}s^{-1}$ correspond to operation where the bulk liquid movement was relatively calm, continuous and without significant entrance effects. Under this condition where the froth height was also low, the temperature profiles for the unmodified, UMD, tray were approximately straight and parallel to the chordal downcomers. With the introduction of the various baffle configurations, the parallel profiles became distorted, and the leading edges of the isotherms at the segment areas are now ahead of the ones in the middle of the tray due to higher temperatures at the sides. This suggests an accelerated flow at the tray segment regions. In the case of the RAB-1 tray, the direct obstruction of the liquid flow at the middle of the tray also resulted in an inverted profile at the centre with a considerable reduction in the temperature at the centre. The parallel temperature profiles of the UMD tray imply that the liquid flow was largely uniform across the tray and the residence time distribution would be similar, both at the sides and in the middle of the tray. In the case of the modified trays, higher temperatures at the segment regions suggest that the liquid flow faster at the sides than in the middle of the tray. The liquid residence time distribution would be expected to be higher in the middle than at the segment regions.

The temperature profiles at the higher liquid flowrates correspond to operations where the bulk liquid movement was chaotic and separated, with well-pronounced hydraulic jumps immediately after the inlet. The temperature profiles at these conditions ranged from slight to severe U-shaped at the middle of the tray and vertical lines of low temperatures at the segment regions. The U-shaped temperature profiles imply that the liquid residence time distribution would be dissimilar at the sides and in the middle of the tray. However, compared to the control tray, the modified trays showed improvement in the water temperatures at the segment regions, resulting in less steep gradients between the centre and edges of the tray.

One important information to emerge from the temperature profiles is the evidence that the baffled trays are effective in accelerating the liquid flow at the segment regions of the tray. This is reflected in the improved temperatures at these regions and lower gradients that exist between the edges and the middle of the tray when compared to the control tray. This is more pronounced at low liquid flowrates where the baffles actually cause the liquid at the edges of the tray to move faster than in the centre.

7.5.3 The Liquid Hold-up Profiles

As with the case of the temperature profiles, only selected 3D liquid plots are used for the discussion and the detailed plots are compiled in appendices 9, 10 and 11 for the UMD, STR-1 and ARC-1 trays, respectively. The 3D profiles for all six trays operating at superficial air velocity of 0.8 ms^{-1} and weir load of 50 $cm^3cm^{-1}s^{-1}$ are presented in Figures 7.4a-f. Figures 7.4g-x show the profiles at 1.0, 1.5 and 2.0 ms^{-1} for the UMD, STR-1 and ARC-1 trays at various weir loads.

From the continuous surfaces of the liquid hold-ups, almost all the modified trays showed some tendency to flatten the bulk liquid gradient and reduce the accumulation of liquid at the edges of the inlet gap when compared to the control tray. The exception is in the case of the RAB-1 tray where the direct obstruction of the liquid flow at the middle resulted in very steep gradients in the inlet half of the tray. At low water and air flowrates, the ARC trays showed exceptional ability to lower the build up of liquid immediately after the inlet gap.

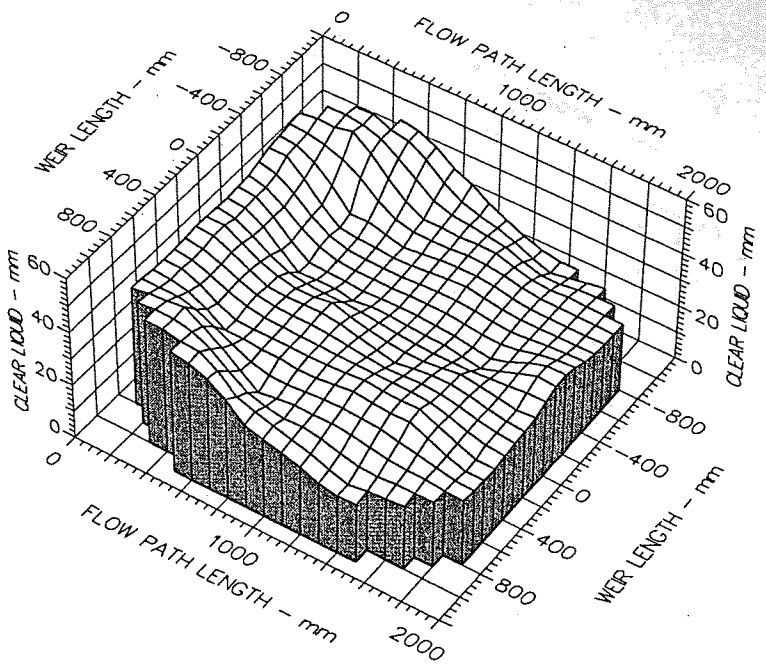

Air Velocity
0.800 m/s

Weir Load
50.0 cm3/cm.s

Inlet Gap
0.020 m

Outlet Weir
0.020 m

Hole Diameter
0.001 m

Fig. 7.4a Surface of Clear Liquid Hold-up
Superficial Air velocity 0.8 m/s - UMD Tray

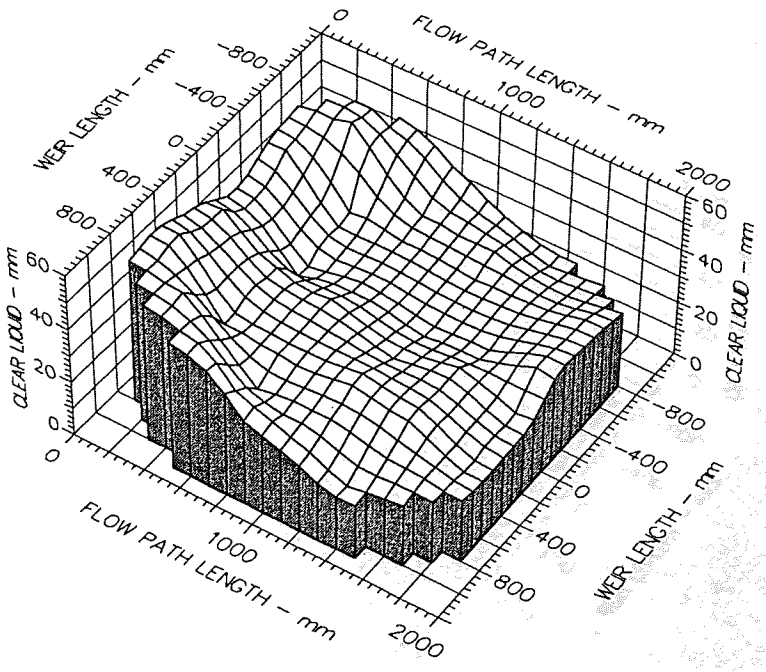

Air Velocity
0.8 m/s

Weir Load
50.0 cm3/cm.s

Inlet Gap
0.02 m

Outlet Weir
0.02 m

Hole Diameter
0.001 m

Fig. 7.4b Surface of Clear Liquid Hold-up
Superficial Air velocity 0.8 m/s - STR-1 Tray

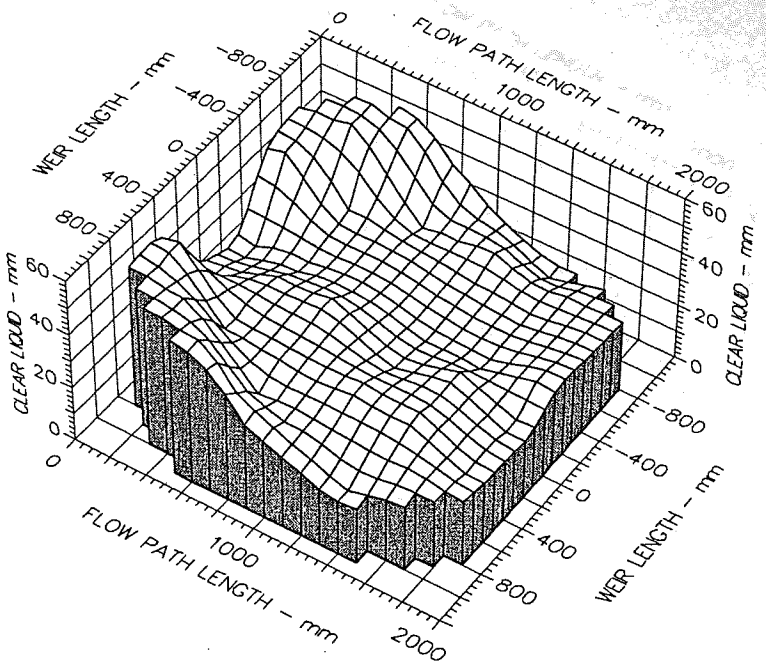

Air Velocity
0.800 m/s

Weir Load
50.0 cm3/cm.s

Inlet Gap
0.020 m

Outlet Weir
0.020 m

Hole Diameter
0.001 m

Fig. 7.4c Surface of Clear Liquid Hold-up
Superficial Air velocity 0.8 m/s - STR-2 Tray

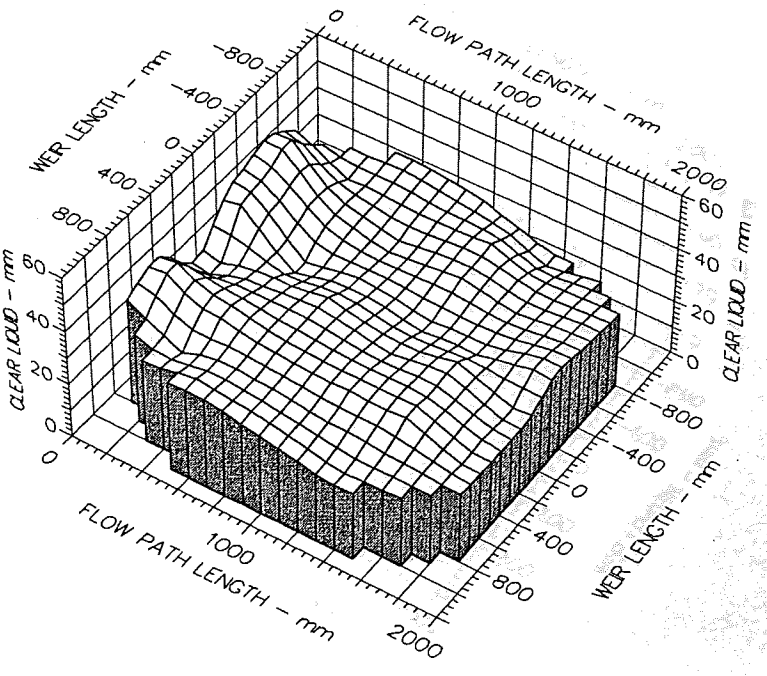

Air Velocity
0.8 m/s

Weir Load
50.0 cm3/cm.s

Inlet Gap
0.02 m

Outlet Weir
0.02 m

Hole Diameter
0.001 m

Fig. 7.4d Surface of Clear Liquid Hold-up
Superficial Air velocity 0.8 m/s - ARC-1 Tray

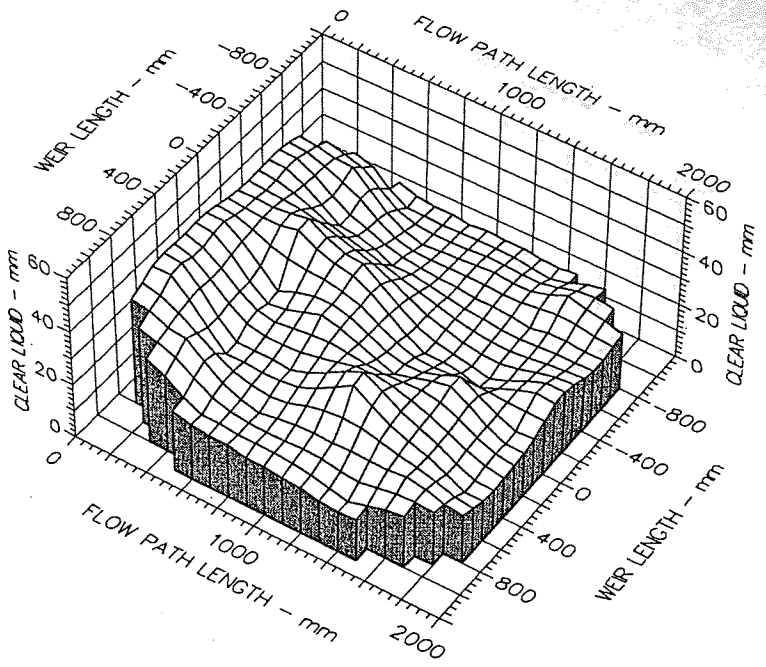

Air Velocity
0.800 m/s

Weir Load
50.0 cm3/cm.s

Inlet Gap
0.020 m

Outlet Weir
0.020 m

Hole Diameter
0.001 m

Fig. 7.4e Surface of Clear Liquid Hold-up
Superficial Air velocity 0.8 m/s - ARC-2 Tray

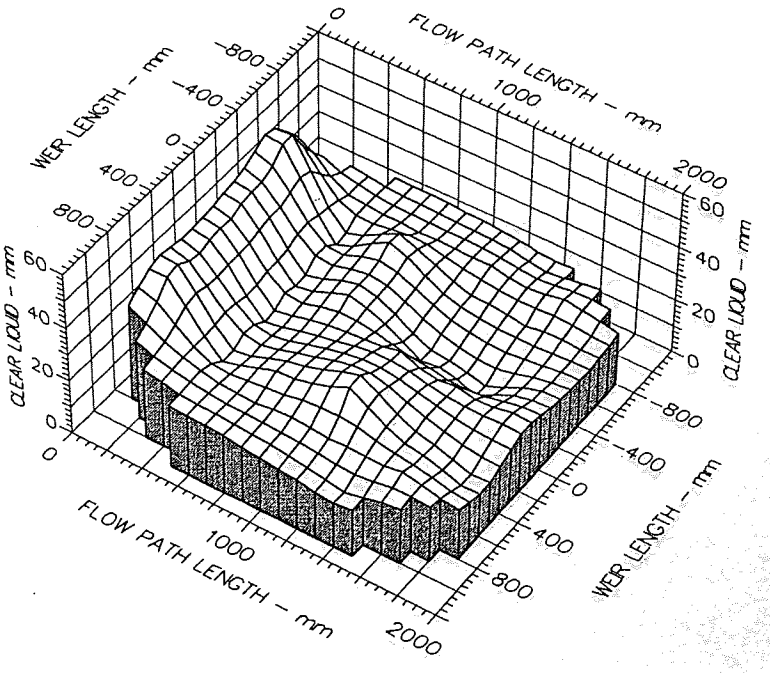

Air Velocity
0.8 m/s

Weir Load
50.0 cm3/cm.s

Inlet Gap
0.02 m

Outlet Weir
0.02 m

Hole Diameter
0.001 m

Fig. 7.4f Surface of Clear Liquid Hold-up
Superficial Air velocity 0.8 m/s - RAB-1 Tray

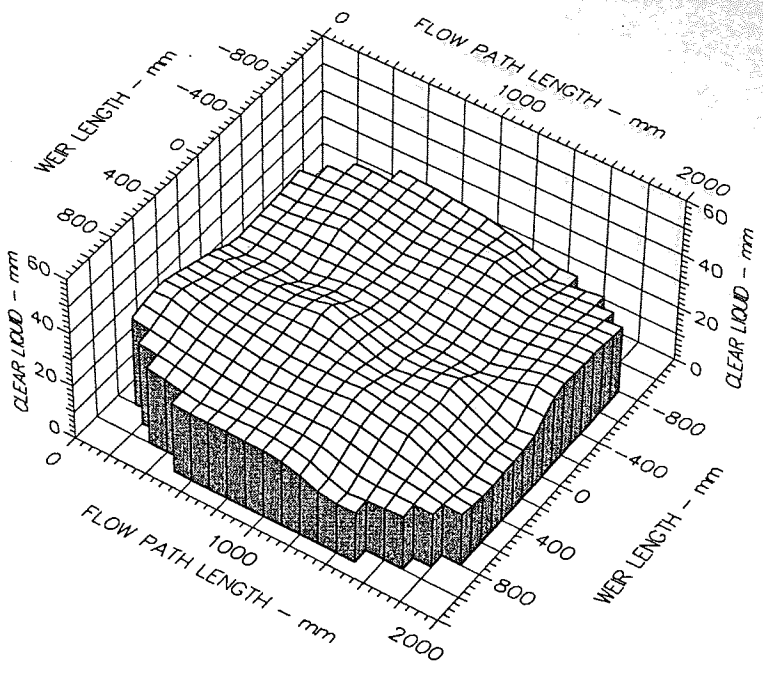

Air Velocity
1.000 m/s

Weir Load
50.0 cm3/cm.s

Inlet Gap
0.010 m

Outlet Weir
0.010 m

Hole Diameter
0.001 m

Fig. 7.4g Surface of Clear Liquid Hold-up
Superficial Air velocity 1.0 m/s - UMD Tray

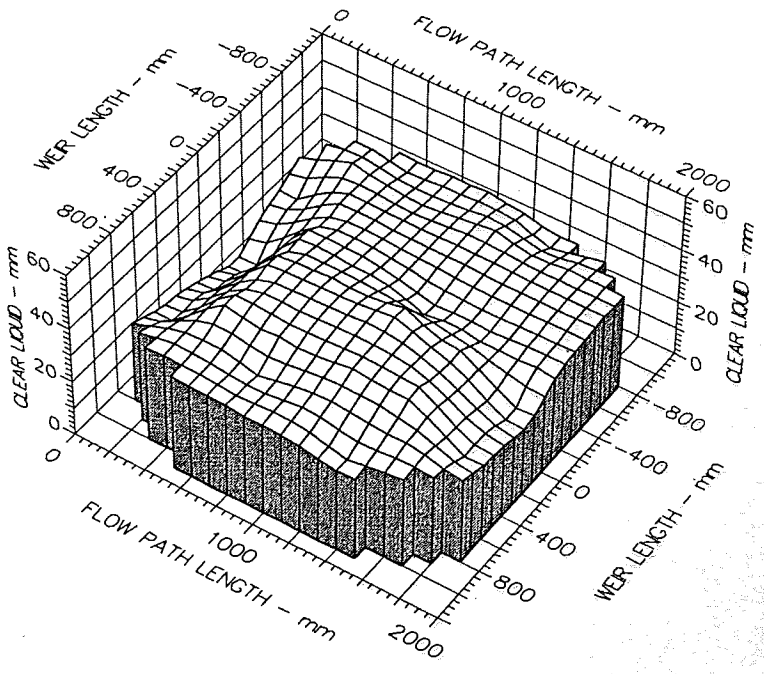

Air Velocity
1.0 m/s

Weir Load
150.0 cm3/cm.s

Inlet Gap
0.01 m

Outlet Weir
0.01 m

Hole Diameter
0.001 m

Fig. 7.4h Surface of Clear Liquid Hold-up
Superficial Air velocity 1.0 m/s - UMD Tray

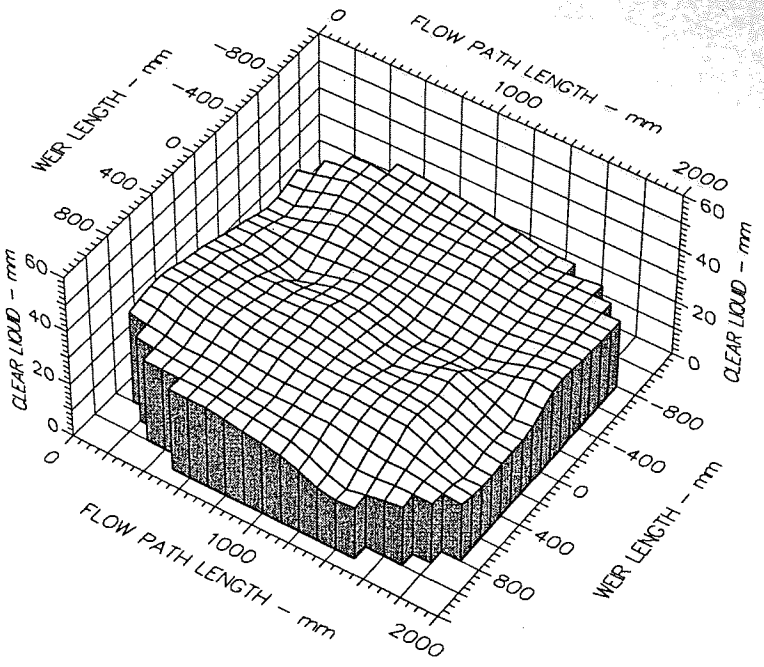

Air Velocity
1.000 m/s

Weir Load
50.0 cm3/cm.s

Inlet Gap
0.010 m

Outlet Weir
0.010 m

Hole Diameter
0.001 m

Fig. 7.4i Surface of Clear Liquid Hold-up
Superficial Air velocity 1.0 m/s - STR-1 Tray

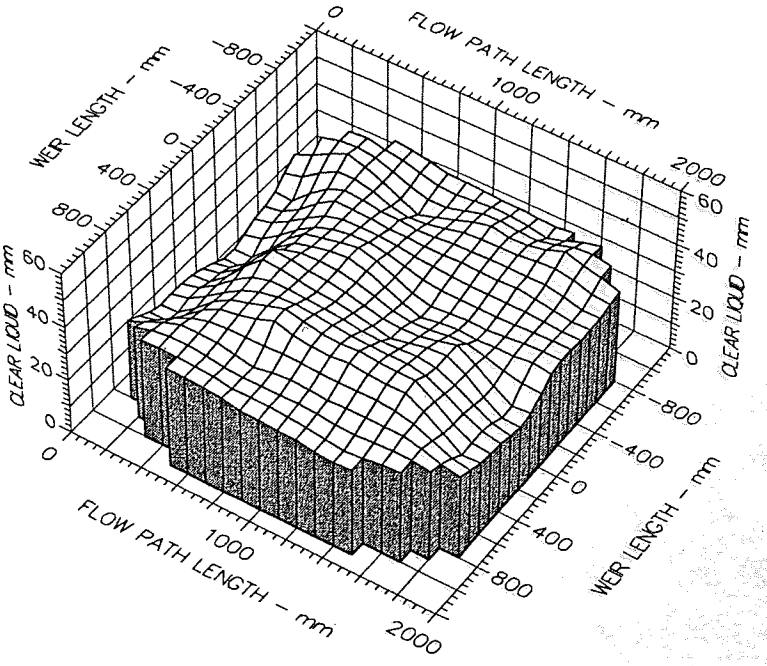

Air Velocity
1.0 m/s

Weir Load
150.0 cm3/cm.s

Inlet Gap
0.01 m

Outlet Weir
0.01 m

Hole Diameter
0.001 m

Fig. 7.4j Surface of Clear Liquid Hold-up
Superficial Air velocity 1.0 m/s - STR-1 Tray

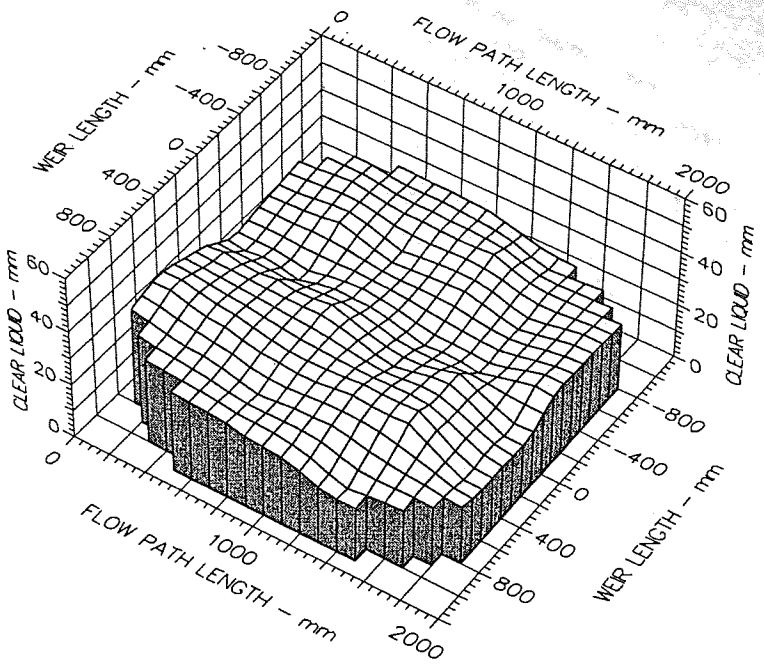

Air Velocity
1.000 m/s

Weir Load
50.0 cm3/cm.s

Inlet Gap
0.010 m

Outlet Weir
0.010 m

Hole Diameter
0.001 m

Fig. 7.4k Surface of Clear Liquid Hold-up
Superficial Air velocity 1.0 m/s - ARC-1 Tray

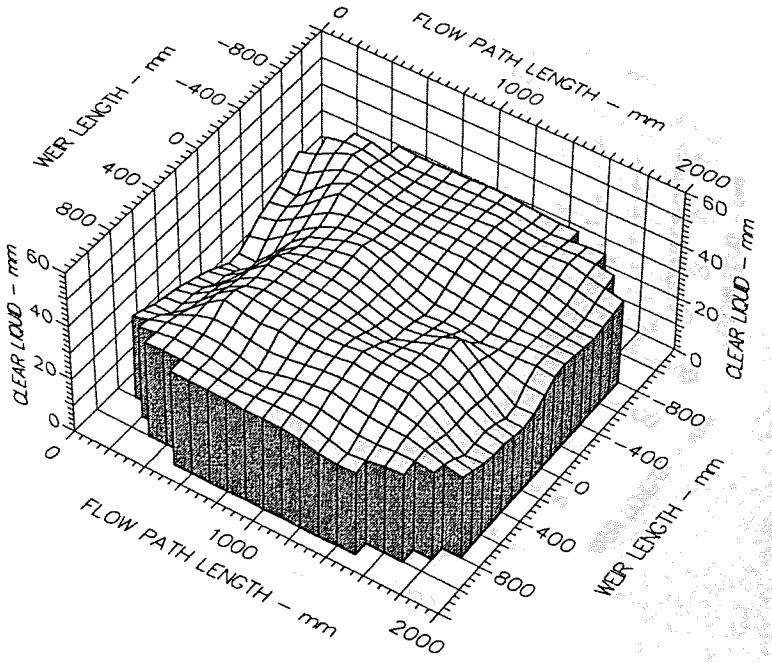

Air Velocity
1.0 m/s

Weir Load
150.0 cm3/cm.s

Inlet Gap
0.01 m

Outlet Weir
0.01 m

Hole Diameter
0.001 m

Fig. 7.4l Surface of Clear Liquid Hold-up
Superficial Air velocity 1.0 m/s - ARC-1 Tray

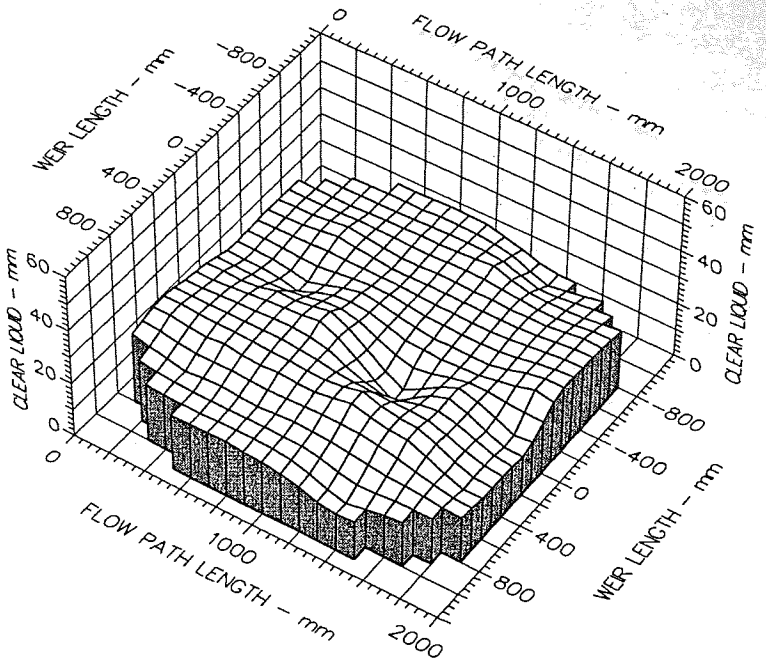

Air Velocity
1.500 m/s

Weir Load
50.0 cm3/cm.s

Inlet Gap
0.010 m

Outlet Weir
0.010 m

Hole Diameter
0.001 m

Fig. 7.4m Surface of Clear Liquid Hold-up
Superficial Air velocity 1.5 m/s - UMD Tray

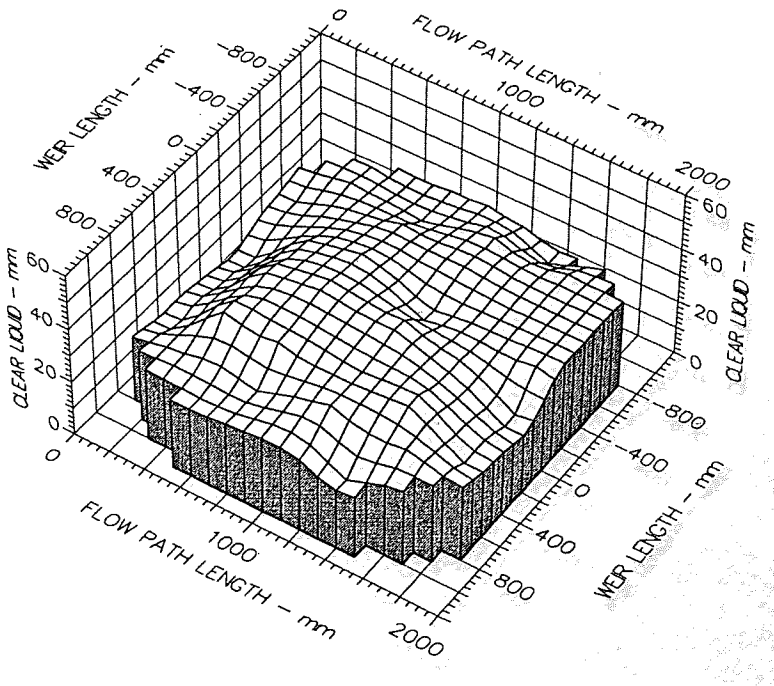

Air Velocity
1.5 m/s

Weir Load
150.0 cm3/cm.s

Inlet Gap
0.01 m

Outlet Weir
0.01 m

Hole Diameter
0.001 m

Fig. 7.4n Surface of Clear Liquid Hold-up
Superficial Air velocity 1.5 m/s - UMD Tray

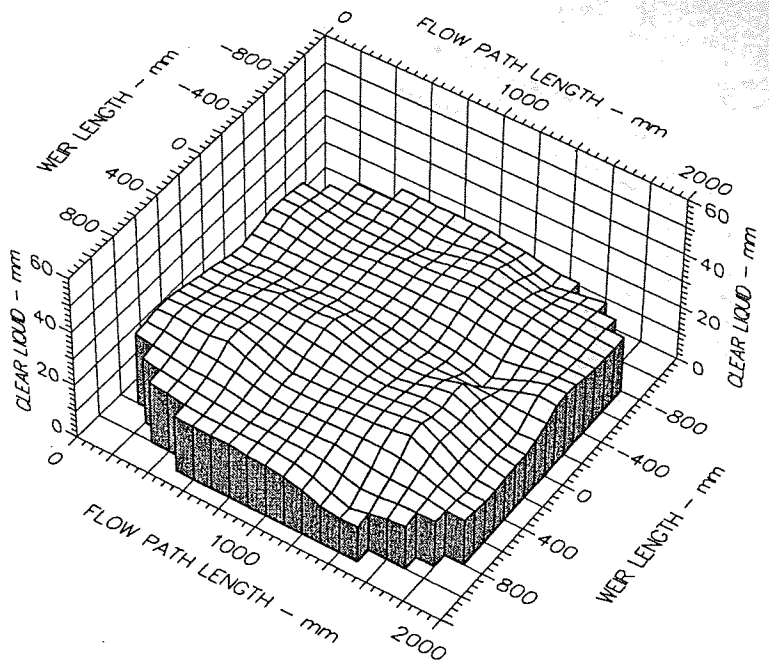

Air Velocity
1.500 m/s

Weir Load
50.0 cm3/cm.s

Inlet Gap
0.010 m

Outlet Weir
0.010 m

Hole Diameter
0.001 m

Fig. 7.4o Surface of Clear Liquid Hold-up
Superficial Air velocity 1.5 m/s - STR-1 Tray

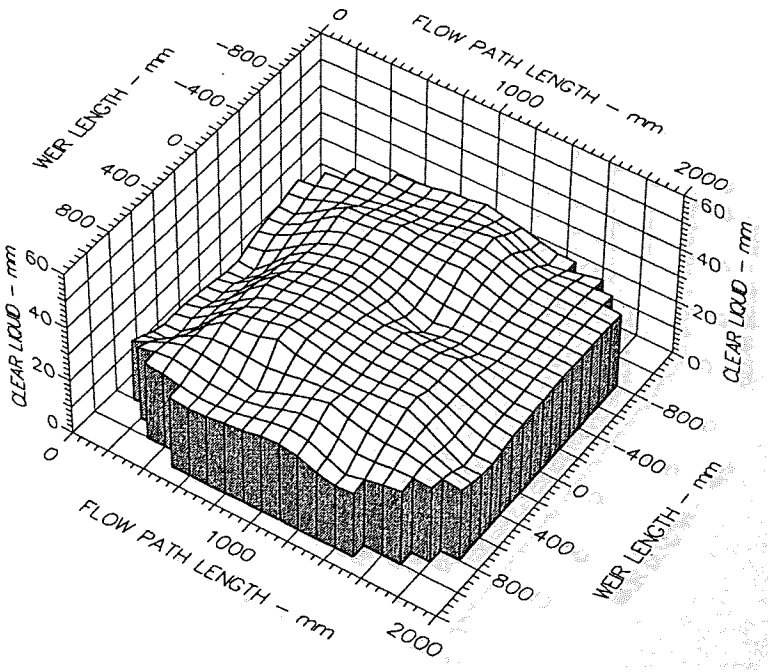

Air Velocity
1.5 m/s

Weir Load
150.0 cm3/cm.s

Inlet Gap
0.01 m

Outlet Weir
0.01 m

Hole Diameter
0.001 m

Fig. 7.4p Surface of Clear Liquid Hold-up
Superficial Air velocity 1.5 m/s - STR-1 Tray

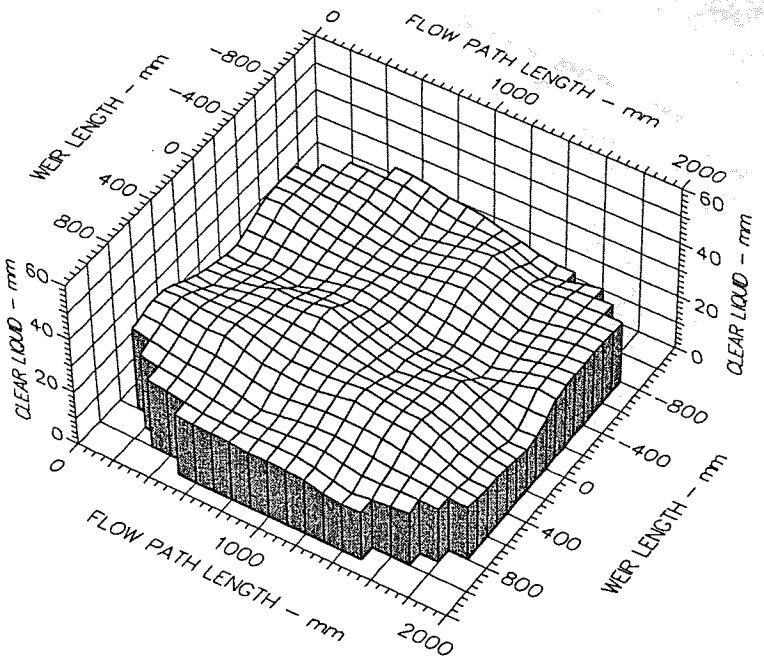

Air Velocity
1.500 m/s
Weir Load
50.0 cm3/cm.s
Inlet Gap
0.010 m
Outlet Weir
0.010 m
Hole Diameter
0.001 m

Fig. 7.4q Surface of Clear Liquid Hold-up
Superficial Air velocity 1.5 m/s - ARC-1 Tray

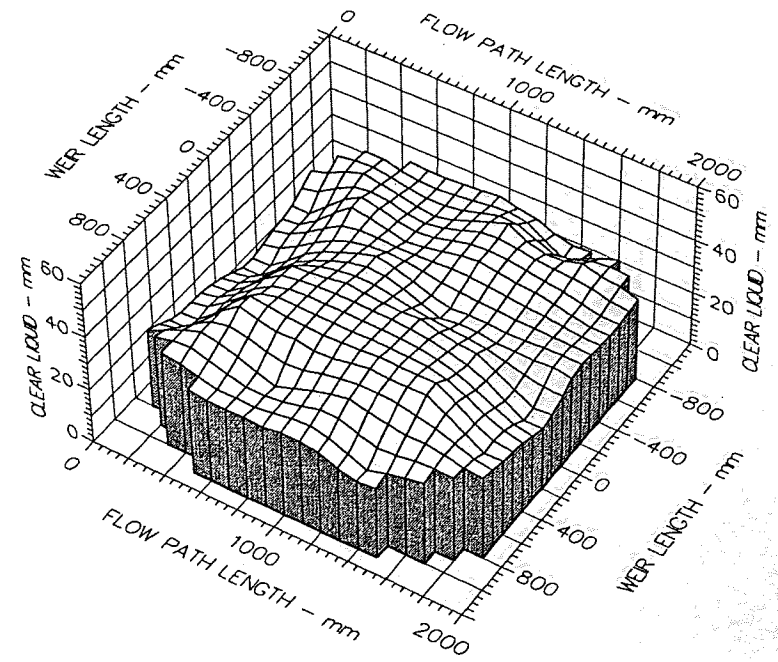

Air Velocity
1.5 m/s
Weir Load
150.0 cm3/cm.s
Inlet Gap
0.01 m
Outlet Weir
0.01 m
Hole Diameter
0.001 m

Fig. 7.4r Surface of Clear Liquid Hold-up
Superficial Air velocity 1.5 m/s - ARC-1 Tray

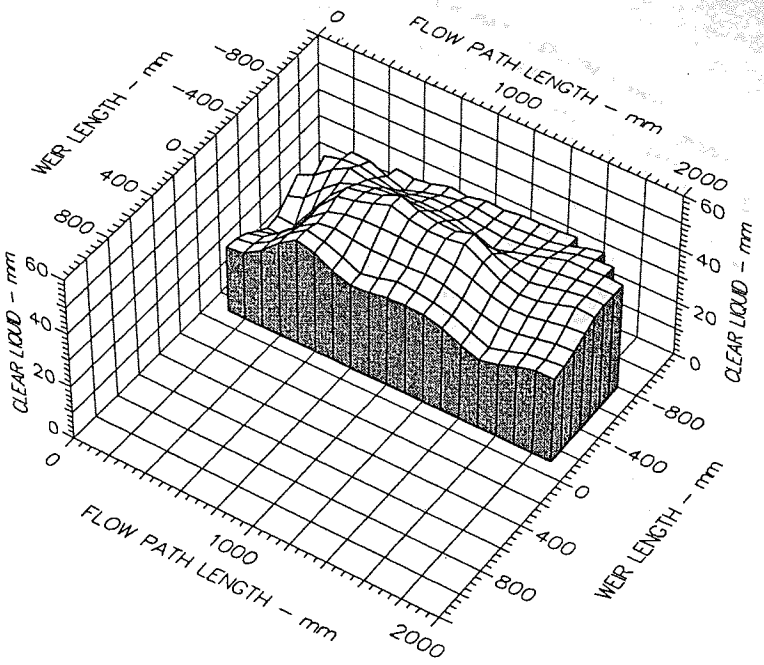

Air Velocity

2.000 m/s

Weir Load

200.0 cm3/cm.s

Inlet Gap

0.050 m

Outlet Weir

0.050 m

Hole Diameter

0.001 m

Fig. 7.4s Surface of Clear Liquid Hold-up
Superficial Air velocity 2.0 m/s - UMD Tray

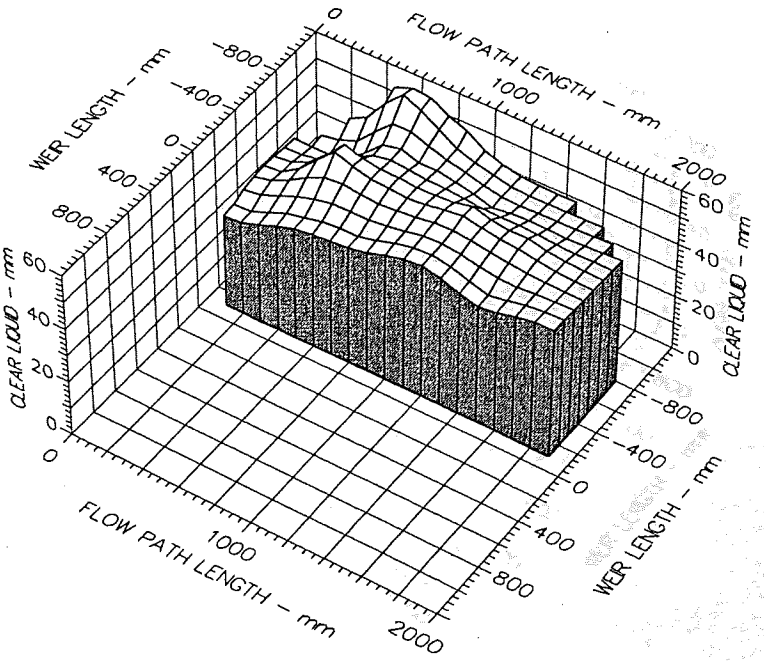

Air Velocity

2.0 m/s

Weir Load

250.0 cm3/cm.s

Inlet Gap

0.05 m

Outlet Weir

0.05 m

Hole Diameter

0.001 m

Fig. 7.4t Surface of Clear Liquid Hold-up
Superficial Air velocity 2.0 m/s - UMD Tray

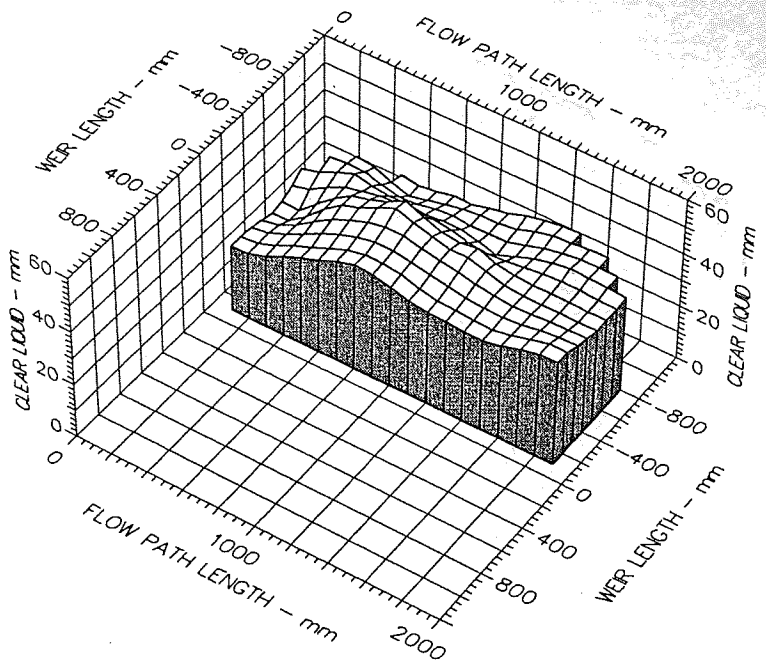

Air Velocity
2.000 m/s

Weir Load
200.0 cm3/cm.s

Inlet Gap
0.050 m

Outlet Weir
0.050 m

Hole Diameter
0.001 m

Fig. 7.4u Surface of Clear Liquid Hold-up
Superficial Air velocity 2.0 m/s - STR-1 Tray

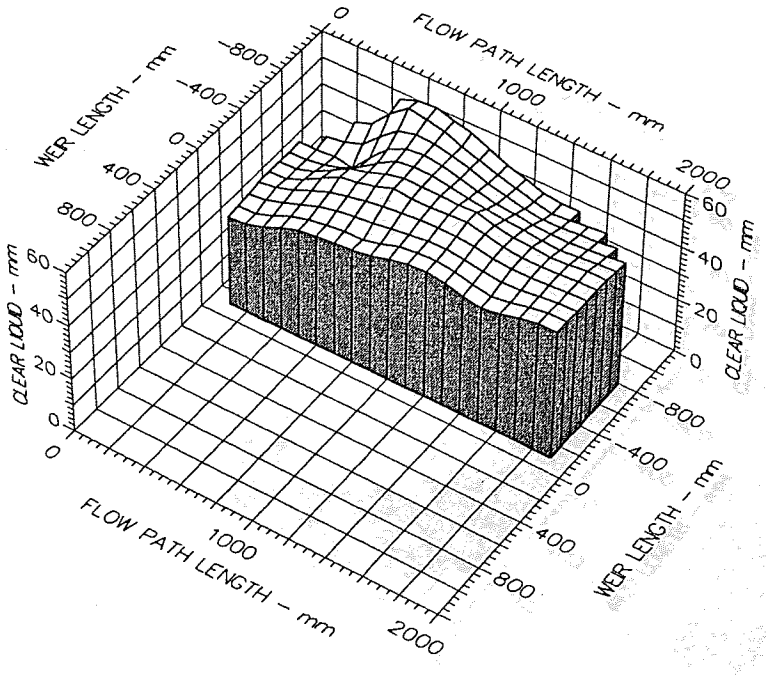

Air Velocity
2.0 m/s

Weir Load
250.0 cm3/cm.s

Inlet Gap
0.05 m

Outlet Weir
0.05 m

Hole Diameter
0.001 m

Fig. 7.4V Surface of Clear Liquid Hold-up
Superficial Air velocity 2.0 m/s - STR-1 Tray

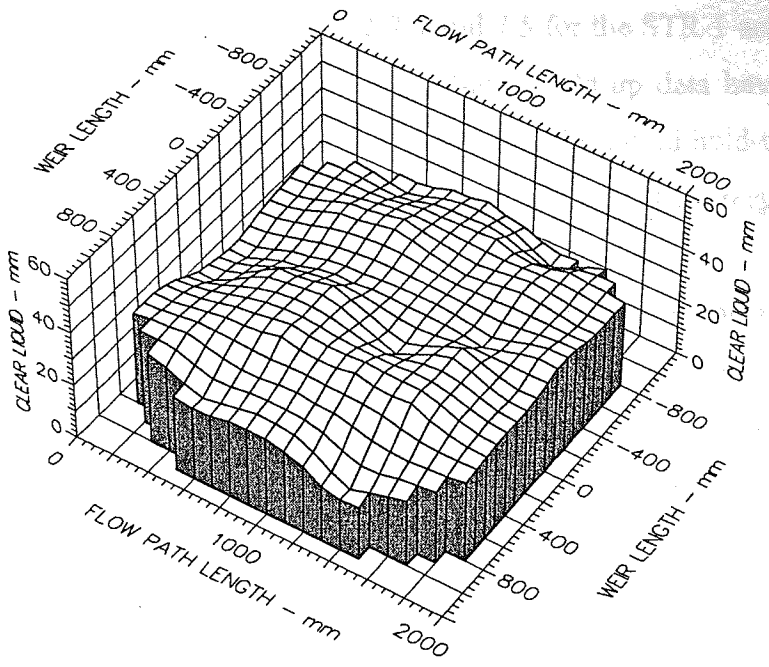

Air Velocity
2.000 m/s
Weir Load
100.0 cm3/cm.s
Inlet Gap
0.050 m
Outlet Weir
0.050 m
Hole Diameter
0.001 m

Fig. 7.4w Surface of Clear Liquid Hold-up
Superficial Air velocity 2.0 m/s - ARC-1 Tray

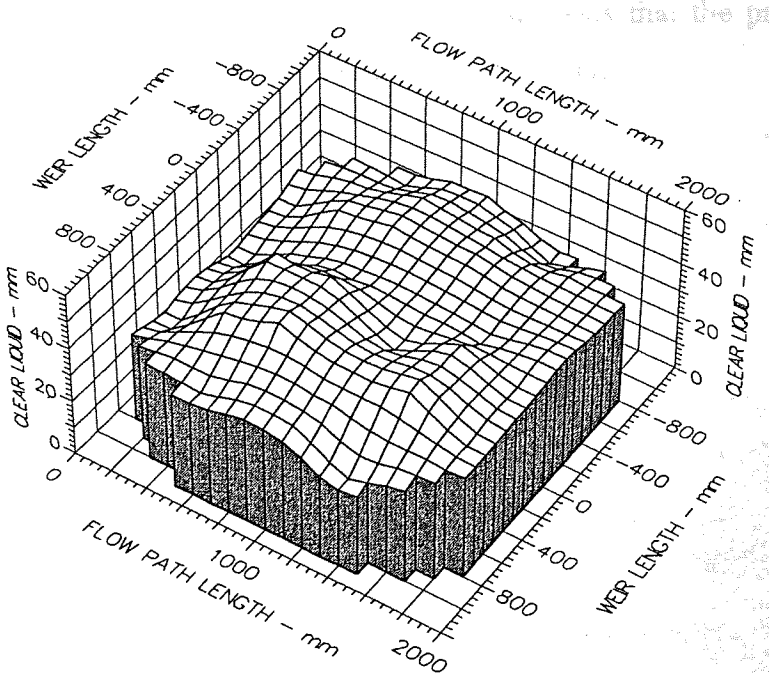

Air Velocity
2.0 m/s
Weir Load
200.0 cm3/cm.s
Inlet Gap
0.05 m
Outlet Weir
0.05 m
Hole Diameter
0.001 m

Fig. 7.4x Surface of Clear Liquid Hold-up
Superficial Air velocity 2.0 m/s - ARC-1 Tray

7.5.4 Numerical Analysis of the Liquid Hold-up

The mean liquid hold-up values, along with their standard deviations and the dowcomer backup are presented in Tables 7.2-7.4 and 7.5 for the STR-1 and ARC-1 trays, respectively. Similar tables of comprehensive mean liquid hold-up data have already been presented in Tables 5.1-5.3 for the UMD tray. The actual point liquid hold-up data for the UMD, STR-1 and ARC-1 trays are compiled in Appendices 12, 13 and 14, respectively.

As with the case of the unmodified tray, the trends of the mean liquid hold-up for the modified trays seem to increase with increasing water flowrate and to decrease with increasing air flowrate. As expected, the downcomer backup increased with increasing water flowrate and decreasing underflow clearance, also similar to the trend exhibited by the control tray.

The liquid hold-up and downcomer backup provide some basis to appraise the effect of the baffles on the tray loading capacity. Figures 7.5-7.7 and 7.8 show respectively how the liquid hold-up and downcomer backup compare for the modified and unmodified trays. The figures show that the downcomer backup and liquid hold-up values are very comparable for the modified and unmodified trays. This suggests that the presence of the baffles is not likely to cause any undue limitation to tray capacity.

Inlet Gap - 10mm		STR-1 Tray								
Outlet Weir - mm		10			20			50		
Air Velocity - ms^{-1}		1	1.5	2	1	1.5	2	1	1.5	2
Water Load - $cm^3cm^{-1}s^{-1}$	Average Height Of Clear Liquid - mm									
25	h_{CL}	22.2	20.6	16.5	23.6	22.6	20.7	32.4	26.5	23.0
	Std.	4.1	4.4	4.6	3.5	3.8	4.4	4.2	4.0	4.9
	d_{CL}	28.8	29.0	26.5	34.8	30.5	33.3	44.2	45.2	46.0
50	h_{CL}	27.2	22.3	18.4	29.9	26.7	21.9	38.2	31.7	26.9
	Std.	4.2	3.9	5.3	4.4	3.7	5.5	4.9	6.9	5.0
	d_{CL}	46.2	43.7	43.5	50.0	48.8	52.8	65.0	71.7	68.8
75	h_{CL}	29.8	24.5	18.8	32.6	27.9	23.6	42.0	37.8	28.6
	Std.	4.3	4.7	5.2	4.3	4.6	5.6	6.5	5.4	5.7
	d_{CL}	80.0	77.3	80.5	83.0	85.7	87.3	97.5	112.3	104.3
100	h_{CL}	32.1	26.4	20.6	34.0	30.1	25.0	43.1	38.8	30.6
	Std.	4.5	5.0	5.9	4.2	5.3	5.8	6.1	6.0	5.6
	d_{CL}	114.2	113.3	119.7	117.0	123.3	125.8	131.8	139.2	142.2
150	h_{CL}	34.0	28.7	22.0	37.7	34.1	28.1	45.6	40.8	32.7
	Std.	6.3	6.2	6.1	5.8	6.7	6.0	5.5	7.0	6.5
	d_{CL}	200.5	207.0	218.0	202.7	209.2	223.8	216.7	225.3	231.3

Table 7.2 Mean Height of Clear Liquid Data - 10 mm Inlet Gap

Inlet Gap - 20mm		STR-1 Tray								
Outlet Weir - mm		10			20			50		
Air Velocity - ms^{-1}		1	1.5	2	1	1.5	2	1	1.5	2
Water Load - $cm^3cm^{-1}s^{-1}$	Average Height Of Clear Liquid - mm									
25	h_{CL}	22.1	20.3	18.9	23.3	22.6	20.5	28.7	26.7	22.8
	Std.	4.1	3.8	4.2	3.7	3.7	5.1	3.8	3.8	5.1
	d_{CL}	27.2	22.2	27.8	30.8	28.0	29.0	36.2	31.3	32.2
50	h_{CL}	28.0	22.8	20.4	28.8	26.6	24.2	37.8	31.9	27.7
	Std.	4.8	4.2	5.0	4.0	4.3	5.2	6.2	3.7	5.6
	d_{CL}	36.2	31.3	37.3	39.8	36.2	38.0	53.5	42.0	43.5
100	h_{CL}	33.8	30.8	24.6	35.4	29.9	27.9	46.6	38.9	32.7
	Std.	4.8	4.9	5.8	4.4	4.9	5.6	11.2	4.5	5.2
	d_{CL}	70.2	70.7	78.0	72.8	74.5	72.5	91.2	82.2	85.0
150	h_{CL}	37.9	34.4	28.6	39.1	34.7	29.6	49.3	40.8	34.4
	Std.	5.9	6.6	6.6	5.7	6.7	6.3	10.0	6.9	6.4
	d_{CL}	114.3	116.3	120.8	115.2	114.5	119.3	132.2	125.7	132.2
200	h_{CL}	44.3	40.9	32.0	45.6	40.8	31.8	57.9	44.3	36.7
	Std.	6.3	7.3	7.0	6.9	6.8	6.4	6.3	6.9	6.8
	d_{CL}	155.7	156.3	174.5	150.5	155.5	165.5	179.2	192.7	199.0

Table 7.3 Mean Height of Clear Liquid Data - 20 mm Inlet Gap

Inlet Gap - 50mm		STR-1 Tray								
Outlet Weir - mm		10			20			50		
Air Velocity - ms^{-1}		1	1.5	2	1	1.5	2	1	1.5	2
Water Load - $cm^3cm^{-1}s^{-1}$	Average Height Of Clear Liquid - mm									
25	h_{CL}	22.6	21.6	18.6	23.6	22.3	20.5	32.3	26.1	24.2
	Std.	3.8	3.6	4.0	3.6	3.7	5.6	3.8	4.4	4.9
	d_{CL}	28.0	24.8	23.0	29.2	28.5	28.3	45.5	40.3	51.3
50	h_{CL}	28.8	24.8	20.6	29.4	26.6	23.8	38.2	31.5	27.6
	Std.	4.1	3.8	5.4	4.1	3.9	5.3	6.8	4.8	5.7
	d_{CL}	33.8	30.7	29.7	34.2	34.3	35.5	54.0	47.5	57.0
100	h_{CL}	34.6	29.2	24.2	35.5	30.2	27.0	46.8	38.3	32.1
	Std.	5.4	5.2	5.7	5.3	4.7	5.3	8.2	5.6	6.2
	d_{CL}	48.5	46.5	46.5	46.5	50.2	50.2	70.5	65.5	72.7
150	h_{CL}	39.2	34.3	28.2	40.3	34.8	29.1	49.1	40.3	34.0
	Std.	6.0	6.2	6.4	5.8	6.1	6.4	5.1	6.4	6.5
	d_{CL}	62.8	63.3	62.0	58.3	59.2	58.3	77.0	78.5	85.8
200	h_{CL}	45.9	40.9	31.6	46.6	41.0	31.7	59.7	44.5	36.6
	Std.	6.4	6.3	6.5	5.7	6.5	6.1	5.9	6.3	7.5
	d_{CL}	95.0	87.5	84.5	92.3	85.5	83.0	99.7	103.8	108.5

Table 7.4a Mean Height of Clear Liquid Data - 50 mm Inlet Gap

ARC-1 Tray										
Inlet Gap / Outlet Weir - mm		10 / 10			20 / 20			50 / 50		
Air Velocity - ms^{-1}		1	1.5	2	1	1.5	2	1	1.5	2
Water Load - $cm^3cm^{-1}s^{-1}$	Average Height Of Clear Liquid - mm									
25	h_{CL}	23.5	20.8	18.9	25.4	23.8	20.1	34.9	32.7	25.1
	Std.	3.8	4.7	4.3	3.4	3.8	5.4	3.7	4.0	5.0
	d_{CL}	27.8	25.5	26.8	30.7	29.5	26.8	45.2	41.2	37.5
50	h_{CL}	27.5	24.4	20.3	29.7	27.8	21.9	39.8	37.9	28.4
	Std.	4.7	4.5	5.1	3.8	3.8	5.3	3.9	4.8	5.2
	d_{CL}	45.0	41.8	42.5	39.5	38.2	36.7	52.7	51.0	43.7
100	h_{CL}	32.1	26.8	23.6	34.7	32.5	24.6	47.7	41.8	32.1
	Std.	4.5	5.1	7.1	4.0	5.1	5.4	9.8	5.8	5.3
	d_{CL}	113.0	117.0	120.8	73.8	82.5	74.3	66.5	62.2	60.5
150	h_{CL}	34.2	32.2	23.9	37.5	33.1	27.0	52.8	45.1	35.0
	Std.	6.3	6.6	6.2	5.8	6.7	6.2	10.8	6.4	6.1
	d_{CL}	195.8	210.5	216.0	114.5	113.0	121.8	73.2	74.0	70.8
200	h_{CL}				44.4	42.3	34.2	61.8	52.5	38.7
	Std.				6.9	7.4	6.8	6.2	6.3	6.3
	d_{CL}				152.7	156.5	161.2	100.7	105.8	94.2

Table 7.5 Mean Height of Clear Liquid Data - 10, 20 and 50 mm Inlet Gaps

Inlet Gap - 50mm		STR-1Tray		
Outlet Weir - mm		50		
Air Velocity - ms^{-1}		1.5	2	2.4
Water Load - $cm^3cm^{-1}s^{-1}$	Average Height Of Clear Liquid - mm			
250	h_{CL}	60.9	45.1	38.4
	Std.	6.9	6.0	8.1
	d_{CL}	111.7	102.2	94.8
300	h_{CL}	71.0	54.5	48.1
	Std.	6.3	5.8	6.5
	d_{CL}	138.5	146.2	139.0
350	h_{CL}	73.6	72.3	55.3
	Std.	6.7	6.0	6.2
	d_{CL}	174.8	196.3	189.5

Table 7.4b Mean Height of Clear Liquid Data - 50 mm Inlet Gap

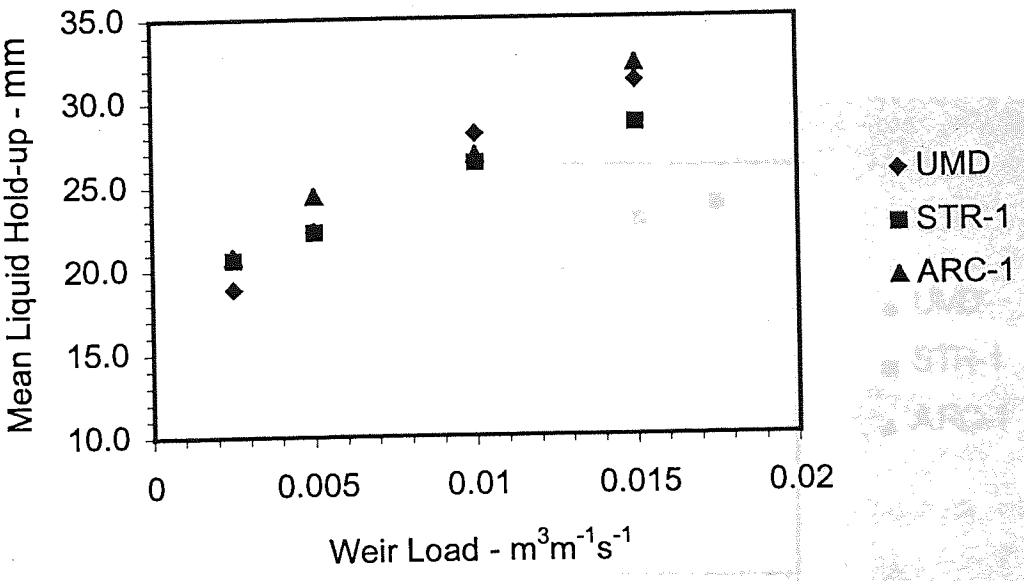

Figure 7.5 Mean Liquid Hold-up - 10 mm Inlet Gap and Outlet Weir Height

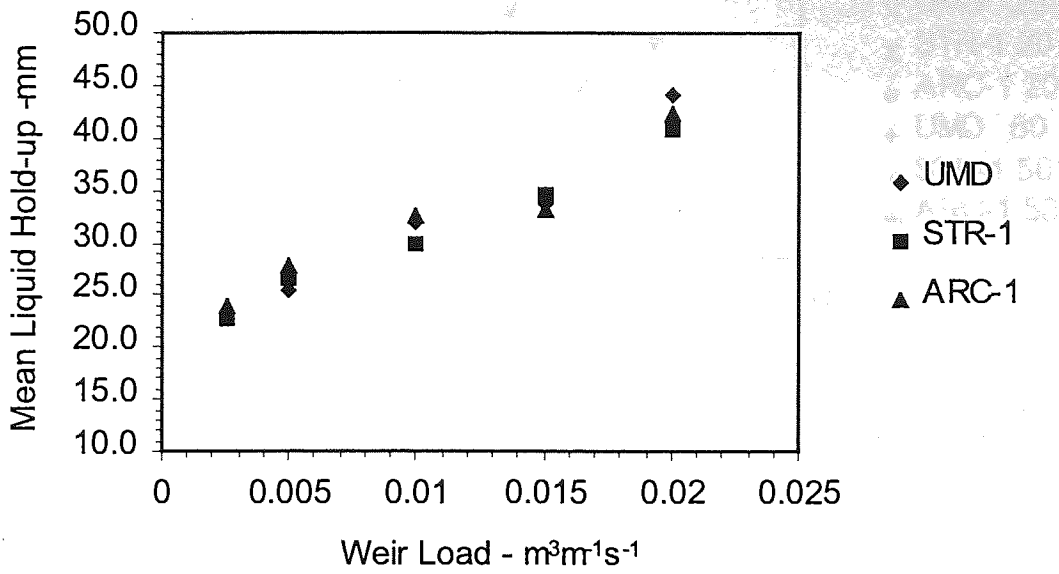

Figure 7.6 Mean Liquid Hold-up - 20 mm Inlet Gap and Outlet Weir Height

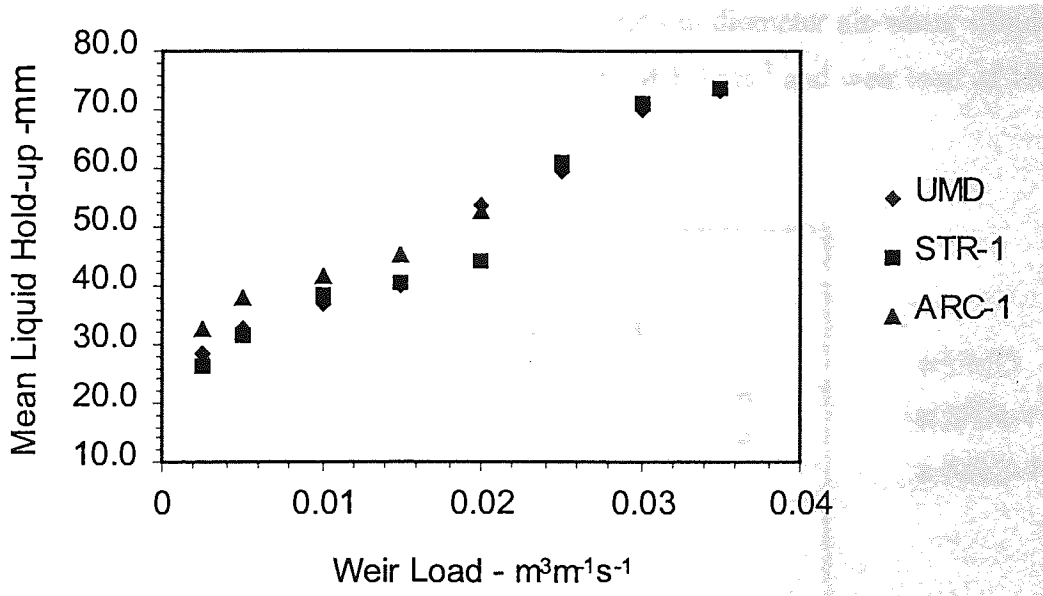

Figure 7.7 Mean Liquid Hold-up - 50 mm Inlet Gap and Outlet Weir Height

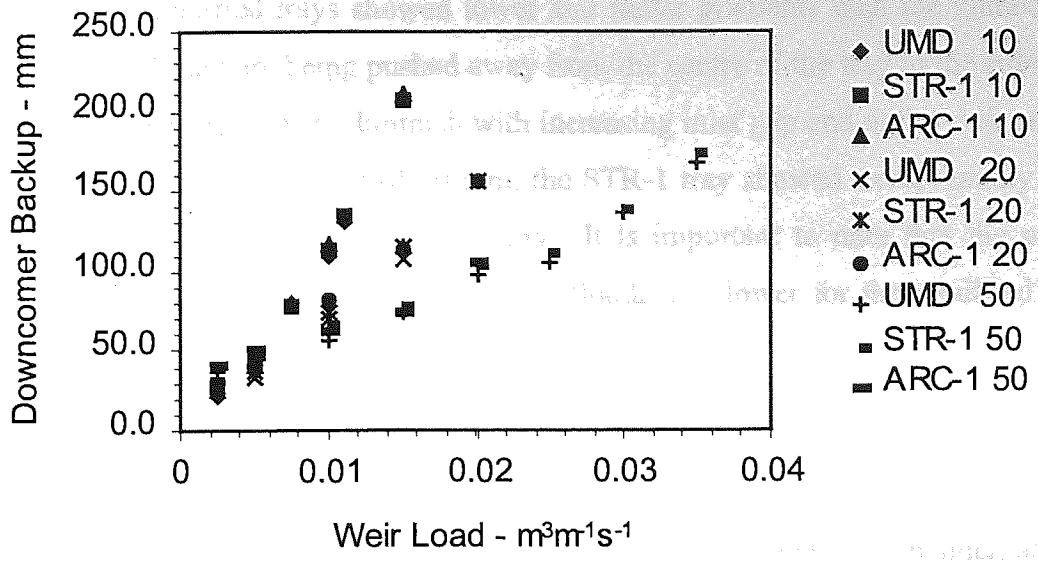

Figure 7.8 Graph of the Measured Inlet Downcomer Backups against Weir Load

Inlet Gap/Outlet Weir = 10, 20, 50 mm

A good illustration of the transfer of part of the liquid momentum from the centre of the tray to the segment areas can be seen in the measurement of the hydraulic gradient along the middle of the tray. The hydraulic gradient was estimated by means of the series of manometer tappings along the centreline of the 2.44 m diameter air-water simulator column. The hydraulic gradients at superficial air velocity of 1.5 ms^{-1} and weir load of 150 $cm^3cm^{-1}s^{-1}$ are shown in figure 7.9.

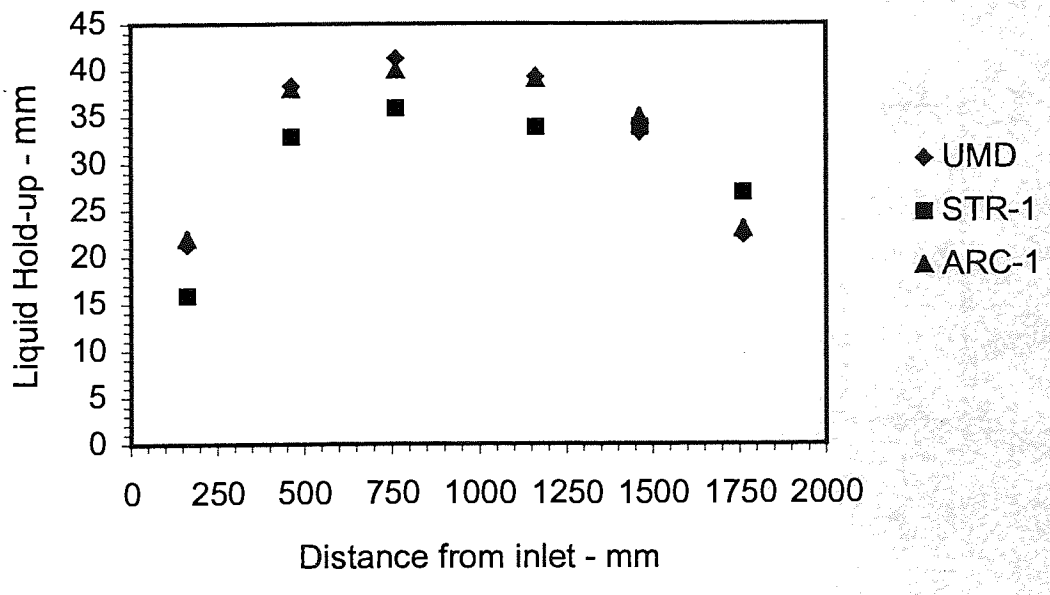

Figure 7.9 Measured Hydraulic Gradients at Weir Loading of 150 $cm^3cm^{-1}s$ and Superficial Air velocity of 1.5 m s^{-1} - 10 mm Inlet Gap and Outlet Weir

Generally, the modified trays showed lower and flatter gradients than the unmodified tray, suggesting that liquid are being pushed away from the centre of the tray to the side segments. This effect, however, tends to diminish with increasing inlet gap and outlet weir settings. At inlet gap and outlet weir height of 10 mm, the STR-1 tray showed exceptionally lower and less steep gradient than the unmodified tray. It is important to note that the peak of the hydraulic jump that tends to cause premature flooding is lower for the modified trays than the control tray.

7.5.5 The Tray Efficiency

The raw data collected for the various trays were processed in identical manner, as discussed in chapter 4, to yield the Murphree point and tray efficiencies. The efficiencies along with the enhancement ratios are presented in Tables 7.6-7.8, and 7.9 for STR-1 and ARC-1 trays, respectively. Similar tables for the UMD tray have been presented in chapter 5, Tables 5.4-5.6.

Inlet Gap - 10 mm		STR-1 TRAY								
Outlet Weir - mm		10			20			50		
Air Velocity - ms^{-1}		1	1.5	2	1	1.5	2	1	1.5	2
Water Load - $cm^3cm^{-1}s^{-1}$	Efficieny - %									
25	E_{mv}	92	84	83	106	113	108	105	103	102
	E_{og}	56	49	45	61	56	53	62	58	55
	E_{mv} / E_{og}	1.65	1.73	1.86	1.74	2.01	2.04	1.67	1.77	1.85
50	E_{mv}	109	99	88	113	114	104	110	104	107
	E_{og}	72	63	55	73	67	61	77	69	65
	E_{mv} / E_{og}	1.52	1.56	1.61	1.55	1.7	1.7	1.43	1.52	1.64
75	E_{mv}	102	98	98	107	106	106	109	113	105
	E_{og}	76	72	68	78	75	72	81	81	75
	E_{mv} / E_{og}	1.34	1.37	1.43	1.37	1.42	1.48	1.34	1.4	1.41
100	E_{mv}	102	90	94	103	102	101	106	109	103
	E_{og}	82	73	72	81	77	75	85	84	78
	E_{mv} / E_{og}	1.25	1.23	1.32	1.26	1.32	1.34	1.25	1.29	1.32
150	E_{mv}	98	93	94	99	94	90	103	103	98
	E_{og}	90	83	79	91	84	77	91	91	82
	E_{mv} / E_{og}	1.09	1.13	1.19	1.09	1.12	1.16	1.13	1.13	1.19

Table 7.6 Measured Murphree Efficiency Data - 10 mm Inlet Gap

Inlet Gap - 20 mm		STR-1 TRAY								
Outlet Weir - mm		10			20			50		
Air Velocity - ms^{-1}		1	1.5	2	1	1.5	2	1	1.5	2
Water Load - $cm^3cm^{-1}s^{-1}$	Efficieny - %									
25	E_{mv}	91	78	73	86	86	82	95	95	89
	E_{og}	52	45	41	54	50	47	56	53	50
	E_{mv} / E_{og}	1.75	1.72	1.78	1.61	1.72	1.74	1.72	1.78	1.78
50	E_{mv}	86	82	75	103	88	92	107	98	91
	E_{og}	61	56	51	70	60	59	74	67	60
	E_{mv} / E_{og}	1.42	1.48	1.48	1.47	1.47	1.57	1.44	1.47	1.5
100	E_{mv}	85	83	81	94	97	94	99	96	96
	E_{og}	68	65	64	76	74	72	79	77	73
	E_{mv} / E_{og}	1.25	1.29	1.27	1.24	1.31	1.31	1.27	1.25	1.31
150	E_{mv}	90	86	88	95	93	95	101	94	94
	E_{og}	75	74	72	82	79	77	85	82	79
	E_{mv} / E_{og}	1.2	1.17	1.22	1.16	1.17	1.23	1.19	1.15	1.2
200	E_{mv}	91	84	87	102	98	101	105	100	99
	E_{og}	79	76	75	90	86	85	92	89	86
	E_{mv} / E_{og}	1.16	1.12	1.16	1.13	1.15	1.19	1.15	1.12	1.16

Table 7.7 Measured Murphree Efficiency Data - 20 mm Inlet Gap

Inlet Gap - 50 mm		STR-1 TRAY								
Outlet Weir - mm		10			20			50		
Air Velocity - ms^{-1}		1	1.5	2	1	1.5	2	1	1.5	2
Water Load - $cm^3cm^{-1}s^{-1}$	Efficieny - %									
25	E_{mv}	82	79	70	86	91	78	90	89	80
	E_{og}	49	45	39	52	49	43	55	52	47
	E_{mv} / E_{og}	1.67	1.74	1.78	1.64	1.86	1.81	1.63	1.71	1.7
50	E_{mv}	94	83	76	89	86	89	106	101	100
	E_{og}	64	56	52	67	59	57	73	67	64
	E_{mv} / E_{og}	1.48	1.47	1.48	1.32	1.46	1.56	1.45	1.5	1.56
100	E_{mv}	98	96	85	101	101	90	105	105	100
	E_{og}	77	72	65	79	75	68	85	82	75
	E_{mv} / E_{og}	1.27	1.32	1.32	1.28	1.34	1.32	1.24	1.28	1.34
150	E_{mv}	102	104	92	100	100	99	112	108	107
	E_{og}	83	82	72	82	81	78	91	89	84
	E_{mv} / E_{og}	1.24	1.26	1.28	1.21	1.23	1.26	1.23	1.22	1.27
200	E_{mv}	106	103	96	104	105	101	111	109	102
	E_{og}	89	88	81	87	90	84	94	93	88
	E_{mv} / E_{og}	1.19	1.17	1.19	1.2	1.17	1.2	1.18	1.13	1.17

Table 7.8a Measured Murphree Efficiency Data - 50 mm Inlet Gap

ARC - 1 TRAY										
Inlet Gap/Outlet Weir - mm		10/10			20/20			50/50		
Air Velocity - ms^{-1}		1	1.5	2	1	1.5	2	1	1.5	2
Water Load - $cm^3cm^{-1}s^{-1}$	Efficieny - %									
25	E_{mv}	97	86	82	87	84	80	89	87	96
	E_{og}	57	50	45	54	50	47	50	44	42
	E_{mv} / E_{og}	1.71	1.72	1.83	1.6	1.69	1.7	1.79	1.98	2.28
50	E_{mv}	107	99	85	98	89	91	97	94	98
	E_{og}	72	64	56	69	61	59	74	68	59
	E_{mv} / E_{og}	1.5	1.56	1.52	1.42	1.43	1.54	1.31	1.38	1.66
100	E_{mv}	98	91	89	100	95	95	106	108	97
	E_{og}	81	74	70	80	76	73	88	84	74
	E_{mv} / E_{og}	1.22	1.23	1.28	1.25	1.25	1.3	1.21	1.29	1.31
150	E_{mv}	101	96	96	97	94	94	105	109	103
	E_{og}	90	84	81	85	81	78	91	89	84
	E_{mv} / E_{og}	1.12	1.14	1.19	1.14	1.16	1.21	1.15	1.22	1.22
200	E_{mv}				103	93	93	104	109	102
	E_{og}				92	83	81	94	92	88
	E_{mv} / E_{og}				1.13	1.12	1.14	1.11	1.19	1.16

Table 7.9 Measured Murphree Efficiency Data - 10, 20, and 50 mm Inlet Gap

Inlet Gap - 50 mm		STR-1 TRAY		
Outlet Weir - mm		50		
Air Velocity - ms^{-1}		1	1.5	2
Water Load - $cm^3cm^{-1}s^{-1}$	Efficieny - %			
250	E_{mv}	103	104	103
	E_{og}	93	95	93
	E_{mv} / E_{og}	1.11	1.09	1.11
300	E_{mv}	102	100	104
	E_{og}	95	95	96
	E_{mv} / E_{og}	1.07	1.05	1.09
350	E_{mv}	104	102	104
	E_{og}	96	97	98
	E_{mv} / E_{og}	1.09	1.04	1.06

Table 7.8b Measured Murphree Efficiency Data - 50 mm Inlet Gap

As with the unmodified tray, the point efficiency increased continuously with the weir load, while the tray efficiency increases up to a maximum value and then begins to tail off gradually with weir load.

Figures 7.10-7.12 show how the point efficiency, tray efficiency and the enhancement ratio compare with the unmodified tray at various water loads and weir heights. Despite almost identical point efficiencies, the modified trays nearly always returned greater tray efficiency than the unmodified tray, although sometimes the difference is marginal. This is reflected more clearly in the enhancement ratio, with the modified trays having superior enhancement factors than the unmodified tray, especially at large weir heights.

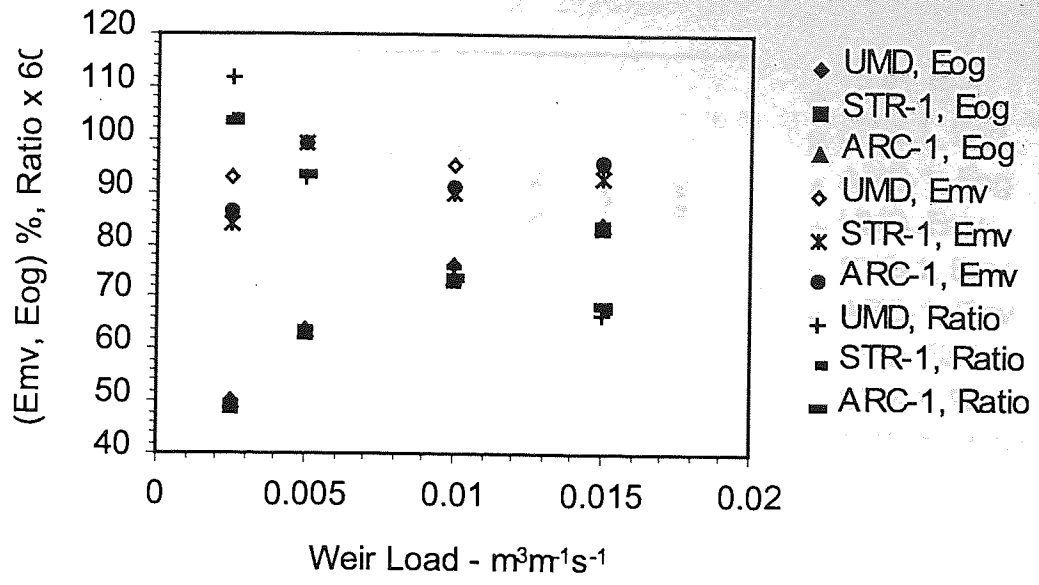

Figure 7.10 Graph of Measured E_{mv}, E_{og} and Enhancement Ratio against Weir Load - 10 mm Inlet Gap and Outlet Weir

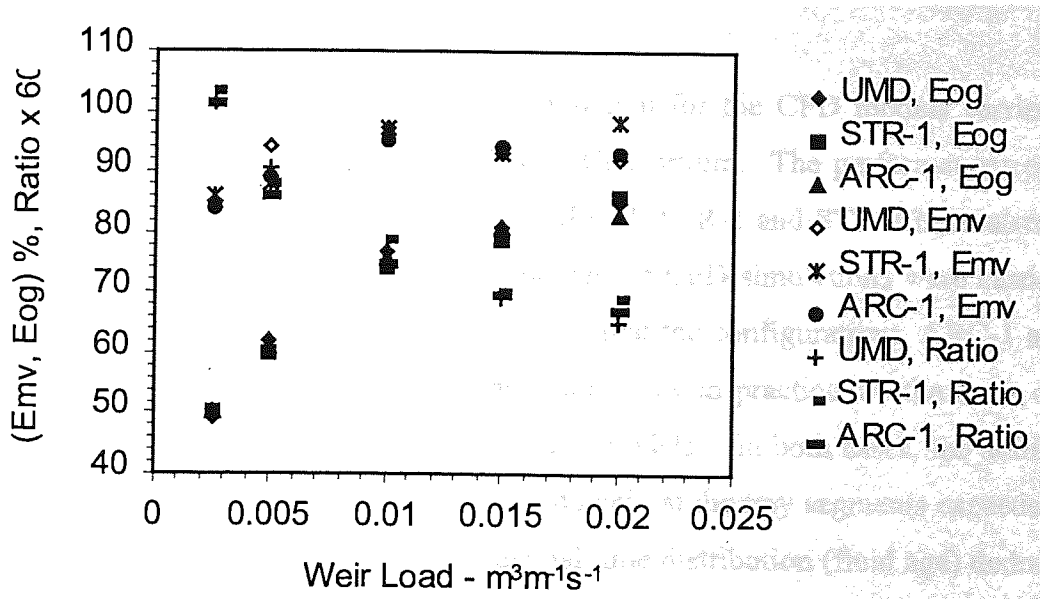

Figure 7.11 Graph of Measured E_{mv}, E_{og} and Enhancement Ratio against Weir Load - 20 mm Inlet Gap and Outlet Weir

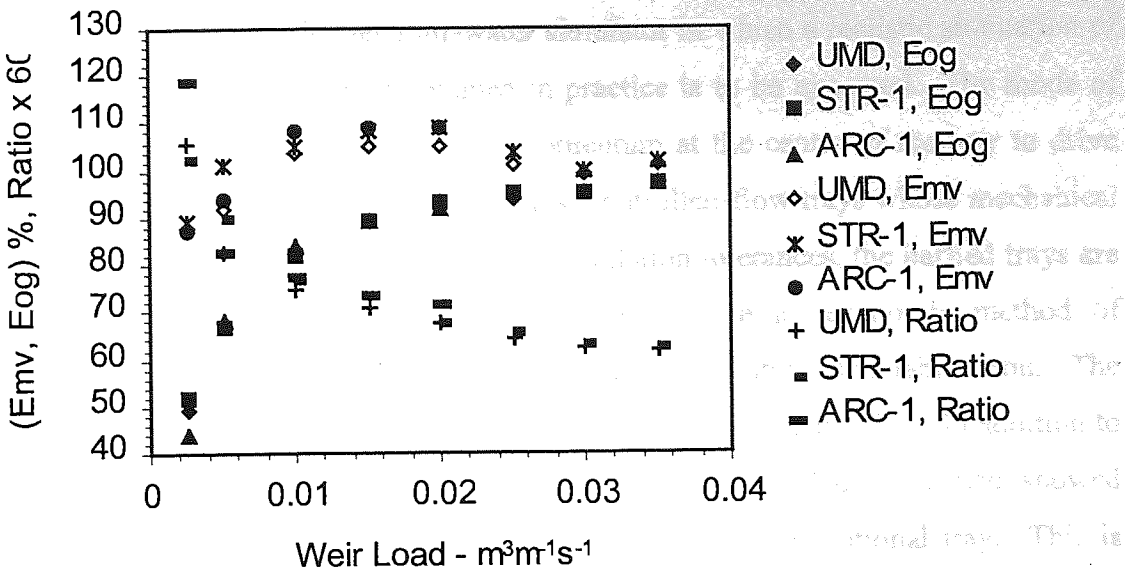

Figure 7.12 Graph of Measured E_{mv}, E_{og} and Enhancement Ratio against Weir Load - 50 mm Inlet Gap and Outlet Weir

7.5.6 Comparison with CFD Model

The results of these investigations provide validation for the CFD models carried out by partners in the Advanced Studies in Distillation Consortium. The performances of four of the modified tray topologies, namely ARC-1, ARC-2, STR-1 and STR-2 have already been studied with a CFD tool (Fischer, 199). Although the CFD simulations were carried out at conditions removed from practice, it is interesting that the configurations, ARC-1 and STR-1, which performed well and better than the control tray in practice are the same ones that showed enhanced flow characteristics in the CFD models. In both cases, the ability of the modified trays to renew the sectors of the flow domain at the tray segments exceeded that of the unmodified tray. Significantly, the residential time distribution (fluid age) deduced from experiments fit well into the pattern generated by the CFD models.

7.6 Conclusions

The principle of using deflection baffles in distillation trays as flow-straightening devices has been investigated on a 2.44 m diameter air-water simulator in which a realistic simulation of the tray hydraulics, similar to what is obtained in practice is to be expected. The mode of operation is based on using part of the liquid momentum at the centre of the tray to drive circulating liquid at the walls forward. Unlike most controlled-flow trays whose mechanical complexity imposes stringent manufacturing and installation tolerances, the baffled trays are simple to design, manufacture and install and thus provide an economic method of retrofitting badly performing sieve trays both in terms of downtime and fabrication. The impact of the baffles on tray loading capacity has been found to be negligible. In addition to providing superior flow characteristics on a single tray, the baffled trays also showed moderate greater enhancement of the point efficiency than the conventional tray. This is expected to have a multiplier effect in a multiple tray column situation (Porter et al., 1972).

CHAPTER 8

Discussion

8.1 Introduction

As already noted, several experimental techniques have been used both to establish the flow patterns on a commercial size sieve tray with 1 mm hole perforations and to investigate the potential use of deflection baffles on such tray as flow straightening devices. The experimental procedures included operating the column in a "half-tray" mode in order to extend the work to very high weir loadings, close to or at flooding conditions. The aim of this chapter is to draw together in summary form the various discussions presented earlier in the thesis.

8.2 The Conventional Sieve Tray

The air-water flow patterns on the 2.44 m diameter test tray were constructed mainly from dye images and temperature profiles generated during the hot-water distillation simulation experiments. In general the flow patterns were characterised by high-speed flow through the centre of the tray and some form of 'pooling' or circulating flow adjacent to the column wall. The separation of water flow at the corner of the inlet gap was identified as the major cause of the circulating flow in the segmental regions at the side of the tray. This was found to develop at a weir loading of between 50 and 80 $cm^3cm^{-1}s^{-1}$ depending on a combination of factors. Of the four variables studied (inlet gap, outlet weir height, weir load and superficial gas velocity), the inlet gap and weir load had the most dominant effects on the developed flow pattern. While the inlet gap seems to serve as a trigger for the separation of flow at the edges of the inlet gap and development of circulation at the wall, the water weir load has the effect of increasing the size of the circulating regions once separation has taken place, a point not noted before in the programme. For an inlet gap setting of 10 mm, the maximum size of circulating flow region of 30% was achieved at a water load of 120 $cm^3cm^{-1}s^{-1}$, a value only attained at a water load of 200 $cm^3cm^{-1}s^{-1}$ for an inlet gap setting of 20 mm. A 30% circulating flow region was never achieved with an inlet gap of 50 mm, even at a water loading of 350 $cm^3cm^{-1}s^{-1}$.

The effect of increasing airflow through the water was to delay the onset of flow separation, such that it only occurred at higher weir loads and smaller gaps under the inlet gap. The outlet weir height seems to increase the tendency for circulating flow at the side regions, although this could not be clearly discerned from the experimental evidences of temperature profiles or the dye traces.

8.3 The Controlled-flow Trays

The principle of using deflection baffles in a conventional sieve tray to improve liquid distribution was investigated by assessing the performance of five tray topologies, using the same techniques that were applied in studying the flow pattern on the unmodified conventional tray. The angle and shape of the baffles relative to the flow direction were the main geometrical variables investigated. The mode of operation, based on driving the liquid across the tray at all points diminishes the tendency for the liquid to channel through the middle and to pool at the wall. With regard to the bulk liquid flow pattern, two tray topologies, STR-1 and ARC-1, performed better than the unmodified conventional one. In those cases, the baffled trays showed greater ability than the unmodified conventional tray to renew the sectors of the tray at the walls.

The liquid hold-up and downcomer backup were used to appraise the effect of the baffles on tray loading capacity. The results showed that the baffles do not contribute to any undue limitation to tray loading capacity. The hydraulic gradient estimated by means of the series of manometer tappings along the centreline of the tray illustrated clearly that the baffles were effective in deflecting liquid momentum to the segmental portion of the tray. This effect, however, tends to diminish with increasing inlet gap and outlet weir settings because at these conditions, most of the liquid tends to jump over the baffles instead of flowing over them. This is a major defect in the current designs because the baffles fall directly under the peak of the clear liquid height, making it less effective at high water loadings where liquid jetting and hydraulic jumps are common.

Figure 8.1 presents a comparative summary of the efficiencies of the unmodified tray (UMD) and the STR-1 tray (modified) at various conditions of experiment, alongside the data points for the 80% flooding curve. Although the improvement in the efficiency of a single modified tray over that of the conventional tray is moderate and in some cases marginal, the multiplier effect in a multiple tray column situation would be significant (Porter et al., 1972). This will in turn translate into significant savings in the capital and operating costs of the column. For example, a 10% improvement in tray efficiency implies that a 100-plate column will require only 90 plates to do the same separation duty at the same reflux ratio, thereby making savings in the capital cost. Alternatively, significant energy savings can be made by operating the at reduced reflux ratio.

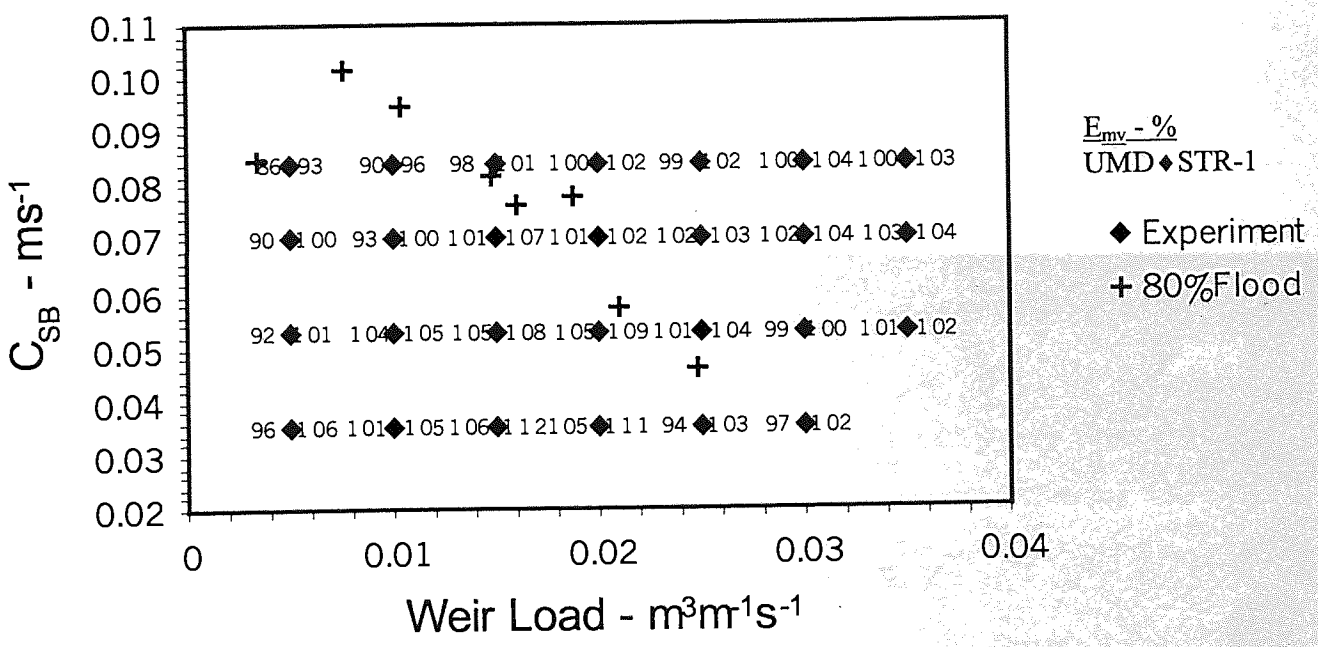

Figure 8.1 Tray Efficiency Plot on the Jet flooding Curve for the UMD and STR-1 Trays

The results of these investigations provide validation for the CFD models carried out by partners in the Advanced Studies in Distillation Consortium. The performances of four of the modified tray topologies, namely ARC-1, ARC-2, STR-1 and STR-2 have already been studied with a CFD tool (Fischer, 199). Although the CFD simulations were carried out at conditions removed from practice, it is interesting that the configurations, ARC-1 and STR-1, which performed well and better than the control tray in practice are the same ones that

showed enhanced flow characteristics using the CFD models. In both cases, the ability of the modified trays to renew the sectors of the flow domain at the tray segments exceeded that of the unmodified tray. Significantly, the residential time distribution (fluid age) deduced from experiments fit well into the pattern generated by the CFD models.

CHAPTER 9

Conclusions

The following conclusions may be drawn from the investigations carried out in this work.

1. The combined techniques of dye tracing, liquid head measurements and temperature profiling provides good data and pictorial view of the liquid flow distribution on a distillation tray from which the flow patterns across the tray can be deduced.

2. The flow pattern on a 2.44 m diameter conventional sieve tray with 1 mm hole diameter perforations has been established. The results have shown clearly that the liquid residence time increases radially from the inlet as a result of the tendency for the liquid to flow preferentially along the centre of the tray, between the chordal weirs and to pool or circulate at the wall. If the analogy is made between the water temperatures and liquid concentrations, the profiles suggest that very steep concentration gradients are to be expected between the middle of the tray and the side segments, with the concentration at the segments being much lower than at the middle.

3. The separation of liquid flow at the ends of the inlet gap was identified as the principal factor that induces circulation flow at the segment regions of the tray, with the chances of flow separation increasing with reducing underflow clearance and increasing weir load.

4. The effect of increasing airflow was to inhibit the onset of flow separation, such that it only occurred at much higher weir loads and with smaller gaps under the inlet downcomer.

5. The principle of using deflection baffles in distillation trays as flow-straightening devices has been investigated on a 2.44 m diameter air-water simulator in which a realistic simulation of the tray hydraulics, similar to that obtained in practice is to be expected. The mode of operation is based on using part of the liquid momentum at the centre of the tray to drive the stagnating liquid at the walls forward.

6. Five controlled-flow tray topologies have been created, studied and tested extensively for their efficacy in mitigating the flow maldistribution obtained on conventional trays. From the five tray topologies studied, two, STR-1 and ARC-1 offered superior flow characteristics than the conventional tray.

7. The impact of the baffles on tray loading capacity has been found to be negligible and do not induce any undue limitation to tray hydraulic capacity.

8. In addition to providing superior flow characteristics on a single tray, the baffled trays also showed moderate greater enhancement of the point efficiency than the conventional tray. The small improvement in the enhancement ratio is expected to have a multiplier effect in a multiple tray column situation.

9. Unlike most controlled-flow trays whose mechanical complexity imposes stringent manufacturing and installation tolerances, one advantage of the baffled trays is that they are simple to design, manufacture and install and thus provide an economic method of retrofitting sieve trays both in terms of downtime and fabrication.

10 It is encouraging that the modified tray topologies, ARC-1 and STR-1, which performed well and better than the control tray in practice are the same ones that showed enhanced flow characteristics in a complementary CFD models (Fischer, 1999), although the CFD simulations were carried out at conditions removed from practice. Significantly, the residential time distribution (fluid age) deduced from experiments fit well into the pattern generated by the CFD models.

Recommendations for Future Work

1. The major area for future work remains the experimental validation and improvement of fluid mechanical theories of open channel two-phase flow so that flow patterns can be predicted from models that work from first principles. If this could be done it would be possible to develop new and improved shapes of column internals with a greater confidence.

2. The results of this work provide a sound basis for the development of more efficient baffled trays that will be effective over a wide range of operating conditions. One defect in the tested designs is that the baffles were placed directly under the crest of the clear liquid height, making it less effective at high weir loadings where liquid jetting and hydraulic jumps are common.

References

AIChE, 1958, Bubble Tray Design Manual, AIChE, New York.

Abdell-aal, H.K., Stites, G.B., Holland, C.D., 1996, AIChE. J., **12** (1)174.

Aleksandrov, A. and Vybronov, V.G., 1971, "Investigation of the hydrodynamic pattern of liquid flow on cross-flow trays", Teor. Osnovy. Kim. Tekh., **5** (2), 339.

Ali, Q. H., 1984, "Gas distribution in shallow large diameter packed beds" PhD Thesis, University of Aston in Birmingham, Birmingham, England.

Ani, C.C., 1988, "Flow patterns, performance and scale-up of distillation trays", PhD Thesis, University of Aston in Birmingham, Birmingham, England.

Ashley, M.J. and Haselden, G.G., 1970, "The calculation of plate efficiency under conditions of finite mixing in both phases in multiplate columns, and the potential advantage of parallel flow", Chem. Engng Sci., **25**, 1665.

Bell, R.L., and Solari, R.B., 1974, "Effect of nonuniform velocity fields and retrograde flow on distillation plate efficiency", AIChE J., **20**,(4), 688.

Bennett, D.L, Agrawal, R. and Cook, P.J., 1983, "New pressure drop correlation for sieve tray distillation columns", AIChE J., **20** (4), 688

Biddulph, M.W., 1975, "Multicomponent distillation simulation-distillation of air", AIChE J., 21(2), 327.

Biddulph, M.W. and Bultitude, D.P., 1990, "Flow characteristics of a small-hole sieve tray", AIChE. J., **36** (12), 1913.

Biddulph, M.W., Kler, S.C. and Lavin, J.T., 1990, "Double-expanded metal distillation tray", US Patent 5091 119.

Burgess, R.G. and Robinson, K., 1969, IChemE Symp. **32** (2) 34.

Calderbank, P.H., 1975, Trans. Inst. Chem. Engrs, **37** 173.

Calderbank, P.H. and Rennie, J., 1962, Trans. Inst. Chem. Engrs., 40, 3.

Chambers, S., 1993, "Flow patterns on sieve trays", PhD Thesis, University of Aston in Birmingham, Birmingham, England.

Chan, H. and Fair, J.R., 1982, AIChE meeting Anaheim, CA, June.

Colwell, C.J., 1979, "Clear liquid height and froth density on sieve trays", Ind. Eng. Chem. Proc. Des. Dev., **23**, 814.

Darton, R.C., 1992, "Distillation and absorption technology: current market and new developments", closing address, IChemE Symp. Ser. No. **128**, A385.

Davies, B., Ali, Z., and Porter, K.E., 1987, "Further observations on the transition between the spray and Bubbly regimes", IChemE symp. Ser., No. 104, B541.

Davies, B.T. and Porter, K.E., (1965), "Some observations of sieve tray froths", Proc. Symp. on Two-phase flow, 21-23 June, University of Exeter, UK, p. F301

Enjugu, B.A., 1986, "Flow patterns and performance of distillation trays", PhD Thesis, University of Aston in Birmingham, Birmingham, England.

Fair, J.R., 1961, "How to predict sieve tray entrainment and flooding", Petro/Chem. Engineer **33**, (10), 45.

Fenwick, K.S., 1996, "Flow patterns on distillation trays", PhD Thesis, University of Aston in Birmingham, Birmingham, England.

Fischer, C.H., 1999, "Numerical modelling of distillation tray hydraulics" PhD Thesis, Bristol University, Bristol, England.

Fletcher, J.P., 1987, A Method for the rigorous calculation of distillation columns using a generalised efficiency model, IChemE Symp. Ser., **104**, A437.

Francis, J.B., 1883, "Lowell hydraulic experiments", 4th edition, Van Nostrand Co., New York.

Gautreaux, M.G., and O'Connell, H.E., 1955, "Effect of length of liquid path on plate efficiency", Chem. Engng. Progr., **51**, 232.

Gerster, J.A., Hill, A.B., Hochgraf, N.N. and Robinson, D.G., 1958, "Tray efficiencies in distillation columns", final report, (University of Delaware, Newark, Del), AIChE., New York.

Hausen, H.F., 1953, "A definition of exchange efficiency of rectifying plates for binary and tenary mixtures", Chem. Ing. Tech. **25**, 595.

Hine, C.J., 1990, "Effect of liquid flow patterns on distillation trays", PhD Thesis, University of Aston in Birmingham, Birmingham, England.
Ho, G. E., Muller, R. L., and Prince, R. G. H., I. Chem. E. Symp. Ser. 32, p. 2:10, 1969

Hofhuis, P.A. and Zuiderweg, F.J., 1979, "Sieve plates: dispersion density and flow regimes", IChemE Symp. Ser. No. 56, 2.2/1-2.2/27.

Holland, C.D., 1963, "Multicomponent distillation", Prentice Hall.

Humphrey, J.L. and Seibert, A.F., 1992, Chem. Engng. Prog., March, pp. 32-41.

Keller, R.D., 1973, "Apparatus for liquid and vapour or gas mass transfer", US Patent 3 729 179

Khan, R.N., 1998, "The use of flow control devices to improve the flow pattern and throughput of sieve trays", PhD Thesis, University of Aston in Birmingham, Birmingham, England.

Kirschbaum, E., 1934, "Efficiency of rectification and appropriate path for liquid flow", Forsch. Gebiete Ingenieur, **5**, 245.

Kirschbaum, E., 1948, "Distillation and rectification", Chemical Publishing Co., New York, 276.

Kirpatrick, R.D. and Weiler, D.W., 1978, "Liquid-gas contacting tray", US Patent 4 101 610.

Kister, H.Z.,1992, "Distillation Design", McGraw-Hill, New York.

Kunesh, J.G., Kister, H.Z., Fair, J.R., "Distillation still towering over other options", Chem. Engng. Prog., October, 1995, pp. 43-54.

Lewis, W.K., 1936, "Rectification of binary mixtures", Ind. Engng. Chem., **28** (1), 399.

Levin, J.T., 1986, "Improvements in distillation trays", UK Patent 2 160 788.

Lim, C.T., Porter, K.E. and Lockett, M.J., 1974, "The effect of liquid channelling on two pass distillation plate efficiency", Trans. IchemE., **52**, 193

Lockett, M.J., 1981, "The froth to spray transition on sieve trays", Trans IChemE, **59**, 26-34

Lockett, M.J., 1986, "Distillation tray fundamentals", Cambridge University Press, Cambridge.

Lockett, M.J. and Augustyniak, J.D., 1991, "On tilted trays", Trans IChemE, **69**, 99.

Lockett, M.J. and Safekourdi, A., 1976, "The effect of the liquid flow pattern on distillation plate efficiency", Chem. Engng. J. **11**, 111.

Matsch, L.C., 1973, "Liquid-gas contact tray", US Patent 3 759498.

Mix, J.E., 1980, Trans IChemE, **55**, 191.

Monovyan, A.K. and Gaivanskii, E.A., 1980, "Investigation of operation of inclined-countercurrent contact tray", Khim. Tekhnol. Topl. Masel, n9, 15.

Murphree, E.V., 1925, "Rectifying column calculations with particular reference to N component mixtures" Ind. Engng. Chem., **17** (7), 747.

Norman, W.S.,1961, "Absorption, distillation and cooling towers", Longmans Green, London.

Payne, G.J. and Prince, R.G.H., 1977, "The relationship between the froth and spray regimes, and the orifice processes occurring on perforated distillation plates", Trans IChemE, **55**, 266.

Pinczewski, W.V. and Fell, C.J.D., 1972, "The transition from froth-to-spray regime on commercially loaded sieve trays", Trans. IChemE, **50**, 102.

Porter, K.E., 1995, "Why research is needed in distillation", Trans. IChemE, **73**, 357

Porter, K.E., Davies, B., Enjugu, B.A and Ani, C.C., 1987, "Investigating the effect of the liquid flow pattern on sieve tray performance by means of the water-cooling technique", IChemE. Symp. Ser., **104**, 569.

Porter, K.E. and Jenkins, J.D., 1979, "The interrelationship between industrial practice and academic research in distillation and absorption", IchemE Symp. Ser., **56**, 5.1/1.

Porter, K.E., Lockett, M.J. and Lim, C.T., 1972, "The effect of liquid channelling on distillation plate efficiency", Trans. IChemE, **50**, 91.

Porter, K.E., Safekourdi, A. and Lockett, M.J., 1977, "Plate efficiency in the spray regime", Trans IChemE, **55**, 190-195.

Porter, K.E. and Wong, P.F.T., 1969, "Transition from spray to bubbling on sieve plates", IChemE, symp. Ser., **32**, 2:22.

Prado, M., Johnson, K. J., and Fair J. R., 1987, Chem. Eng. Prog. **83**(3), 32.

Prince, R.G.H. and Chan, B.K.C., 1965, "The seal point of perforated distillation plates", Trans IChemE, **43,** T49-T55.

Prince, R.G.H, Jones, A.P. and Panic, R.J., 1979, "The froth Spray transition", IChemE symp. Ser., No. **56**, 2.2/27.

Raper, J.A., Pinczewski, W.V. and Fell, C.J.D, 1984, "Liquid passage on sieve trays operating on the spray regime", Chem. Engng. Res. Des., **62**, 111-116.

Sohlo, J. and Kinnunen, S., 1977, Dispersion and flow phenomena on a sieve plate, Trans IChemE, **55**, 71-73.

Sohlo, J. and Kouri, R.J., 1982, "An analysis of enhanced traverse dispersion on distillation plates", Chem. Engng. Sci., **37**,(2), 193.

Solari, R., Saez, E., D'Apollo, I. and Bellet, A., 1982, "Velocity distribution and liquid flow patterns on industrial sieve trays", Chem. Engng. Comm., **13**, 369.

Standart, G., 1965, "Studies on distillation - V", Chem. Engng. Sci. **20**, 611.

Stichlmair, J., 1978, "Grundlagen der dimenionier ung des gaslflussigkeit- Kontaktapparates bodenkolonne" (Weinheim: Verlag Chemie).

Thomas Walter, J. and Haq Mohammad, A., 1976, "Studies of the performance of a sieve tray with 3/8 in. diameter perforations", Ind. Engng. Chem. Proc. Des. Dev., **15**, (4), 509-518.

Wallis G. B., "One-Dimensional Two-phase Flow", McGraw-Hill, New York, 1969.

Weiler, D.W., Bonnett, F.W. and Leavitt, F.W., 1971, "Slotted sieve trays", Chem. Engng. Prog., **67** (9), 86.

Weiler, D.W., Delnicki, W.V. and England, B.L., 1973, "Flow hydraulics of large diameter trays", Chem. Engng. Prog. , **69** (10), 67.

Williams, B. and Yandall, E.F., 1963, "Improvements in and relating to liquid-gas contact tray", GB Patent 941 783.

Williams, B. and Yandall, E.F., 1968, "Apparatus for liquid-gas contacting tray", US Patent 3 417975.

Winkle, M.V., 1967, "Distillation", McGraw-Hill, Inc., New York.

Yu, K.T., 1992, "Some progress of distillation research and industrial applications in China", IchemE. Symposium Series **128**: A139.

Yu, K.T., Huang, J., Li, J.L. and Zhang, Z.T., 1982, "The residence time distributions and effeiencies of large trays", Proceeding of joint meeting of Chemical Engineering, Beijing, China, **2**, 425.

Yu, K.T., Huang, J., Li, J.L. and Zhang, Z.T., 1986, "The residence time profile and plate efficiency for a large tray with single-pass or two-pass liquid flow", J. Chem. Ind. Engng (China), **2**, 151.

Yu, K.T., Huang, J., Li, J.L. and Song, H.H., 1990, "Two-dimensional flow and eddy diffusion on a sieve tray", Chem. Engng. Sci., **45**,(9), 2901.

Zuiderweg, F.J., 1982, "Sieve trays-a view on the state of the art", Chem. Engng. Sci., **37**, (10), 1441.

Appendix 1

Safe Operational Procedure of the Pilot Plant

The procedures for the safe start-up, normal operation, and shutdown of the air-water distillation simulator are set out below.

Start-up Procedure

1. Switch on the main electricity isolator and open the manual gas valves to the process-heaters.
2. Open the air-vent in both water circuits to vent the air in the water circuits and then close it back.
3. Start the circulation pump, in the primary heating circuit, and the flue dilution fan.
4. Start the main water pump, in the secondary water circuit, to circulate water through the double heat exchanger and bypass network from where it is returned back to the sump tanks.
5. Switch on the electrical supply to the gas shutoff valve.
6. Start one or both of the process heaters. This is the primary heating source to the water circuit.
7. Open the steam valve. This is the secondary heating source, which is used as heat top-up supply, for fine tuning the inlet water temperature prior to entering the test tray.
8. When the water in the sump tanks approaches 40°C, start the air fan and set the desired air flow-rate using the mechanical micrometer.
9. Once the water reaches 45°C, set the desired water flow-rate to simulator column, then make any small adjustments to the air flow-rate.
10. Adjust the heating, by manual control of the steam and process heaters, until a steady water temperature is reached.

11. After about ten minutes of steady operation, initiate the manometer and temperature data collection.

Normal Operation

12. Set the new air and water flow-rates and return to instruction 9.

Shutdown Procedure

13. Once the last temperature data collection is complete, close the steam valve and switch off the process heaters, leaving the simulator in operation.

14. Switch off all electrical equipment, apart from the air fan and the two water pumps, and close the manual gas valves.

15. When the water temperature in the sump tanks has cooled down to about 20°C and both sections of the heat exchanger are cool, the water pumps can be shutdown.

16. Five minutes after stopping the water pumps the air fan can be shutdown.

Appendix 2

Source Code for Temperature Data Acquisition

The Fortran 77 computer program, codenamed ZEST.FOR, used to control the acquisition of the temperature data via the Biodata Microlink interface is contained on 3.5", 1.2Mbyte diskette found in the rear cover of the thesis.

Appendix 3

Source Code for Plotting Temperature Profiles and the Coordinates of the PRTs on the Tray

The Fortran 77 computer programs, codenamed 2D3DTBT.FOR (full tray cases) and 2D3DTHLF.FOR ("half-tray" cases), used to generate the temperature contours are contained on 3.5", 1.2Mbyte diskette found in the rear cover of the thesis. The coding calls on routines from the UNIRAS suit of plotting routines.

The coordinates of the PRTs on the tray during the cooling water experiments are present in Figure A3.1

Appendix 4

Source Code for the Calculation of Efficiencies

The Fortran 77 computer programs, codenamed EFFNEW.FOR (full tray cases) and EFFHALF.FOR ("half-tray" cases), used to calculate the point and tray efficiencies are contained on 3.5", 1.2Mbyte diskette found in the rear cover of the thesis.

Appendix 5

Source Code for Plotting Liquid Hold-up Profiles and the Coordinates of the Manometer Tappings on the Tray

The Fortran 77 computer programs, codenamed 3DHCLNEW.FOR (full tray cases) and 3DHCLHLF.FOR ("half-tray" cases), used to generate the three dimensional height of clear liquid surfaces are contained on 3.5", 1.2Mbyte diskette found in the rear cover of the thesis. The coding calls on routines from the UNIRAS suit of plotting routines.

The coordinates of the Manometer tappings on the tray during the cooling water experiments are present in Figure A3.2.

TRAY INLET

(700,-900)(500,-900)(300,-900)(100,-900)(-100,-900)(-300,-900)(-500,-900)(-700,-900)

(900,-700)(700,-700)(500,-700)(300,-700)(100,-700)(-100,-700)(-300,-700)(-500,-700)(-700,-700)(-900,-700)

(1000,-500)(900,-500)(700,-500)(500,-500)(300,-500)(100,-500)(-100,-500)(-300,-500)(-500,-500)(-700,-500)(-900,-500)(-1000,-500)

(1100,-300)(900,-300)(700,-300)(500,-300)(300,-300)(100,-300)(-100,-300)(-300,-300)(-500,-300)(-700,-300)(-900,-300)(-1100,-300)

(1150,-100)(900,-100)(700,-100)(500,-100)(300,-100)(100,-100)(-100,-100)(-300,-100)(-500,-100)(-700,-100)(-900,-100)(-1150,-100)

(1150,100) (900,100) (700,100) (500,100) (300,100) (100,100) (-100,100) (-300,100) (-500,100) (-700,100) (-900,100) (-1150,100)

(1100,300) (900,300) (700,300) (500,300) (300,300) (100,300) (-100,300) (-300,300) (-500,300) (-700,300) (-900,300) (-1100,300)

(1000,500) (900,500) (700,500) (500,500) (300,500) (100,500) (-100,500) (-300,500) (-500,500) (-700,500) (-900,500) (-1000,500)

(900,700) (700,700) (500,700) (300,700) (100,700) (-100,700) (-300,700) (-500,700) (-700,700) (-900,700)

(700,900) (500,900) (300,900) (100,900) (-100,900) (-300,900) (-500,900) (-700,900)

TRAY OUTLET

Fig. A3.1 Coordinates Of The 108 PRTs On The Tray Active Area. The centre of the tray is arbitrarily assigned the coordinates (0,0). The coordinates of the PRTs are listed according to the location of all 108 temperature probes on the tray active area. Measurement towards the outlet downcomer is taken as positive y coordinate.

TRAY INLET

(550,-800) (150,-800) (-150,-800) (-550,-800)

(800,-600) (-800,-600)

(550,-500) (150,-500) (-150,-500) (-550,-500)

(1000,-400) (-1000,-400)

(800,-200) (550,-200) (150,-200) (-150,-200) (-550,-200) (-800,-200)

(800,200) (550,200) (150,200) (-150,200) (-550,200) (-800,200)

(1000,400) (-1000,400)

(550,500) (150,500) (-150,500) (-550,500)

(800,600) (-800,600)

(550,800) (150,800) (-150,800) (-550,800)

TRAY OUTLET

Fig. A3.2 Coordinates Of The 36 Manometer Tappings On The Tray Active Area. The centre of the tray is arbitrarily assigned the coordinates (0,0). The coordinates of the Manometer points are listed according to the location of all the thirty six tapping points on the tray active area. Measurement towards the outlet downcomer is taken as positive y coordinate.

Appendix 6-8

Two-Dimensional Reduced Temperature Isotherm Displays for the UMD, STR-1 and ARC-1 Tray Cases

The appendices contain a full set of the two-dimensional isotherm diagrams to complement the results of the water-cooling experiments in chapter 5 and chapter 7.

Appendix 6

Two-Dimensional Reduced Temperature Isotherm Displays for the UMD Tray Cases

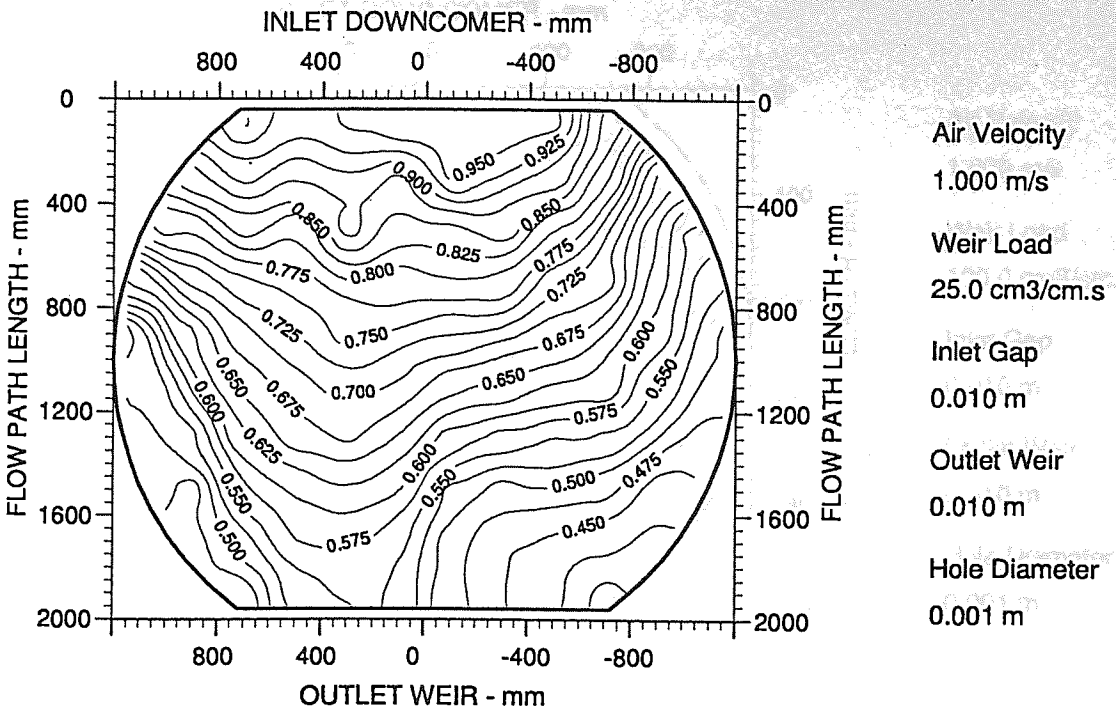

Figure A6.1 Two-dimensional reduced temperature profiles for UMD-tray Emv/Eog 94/58 hCL 22

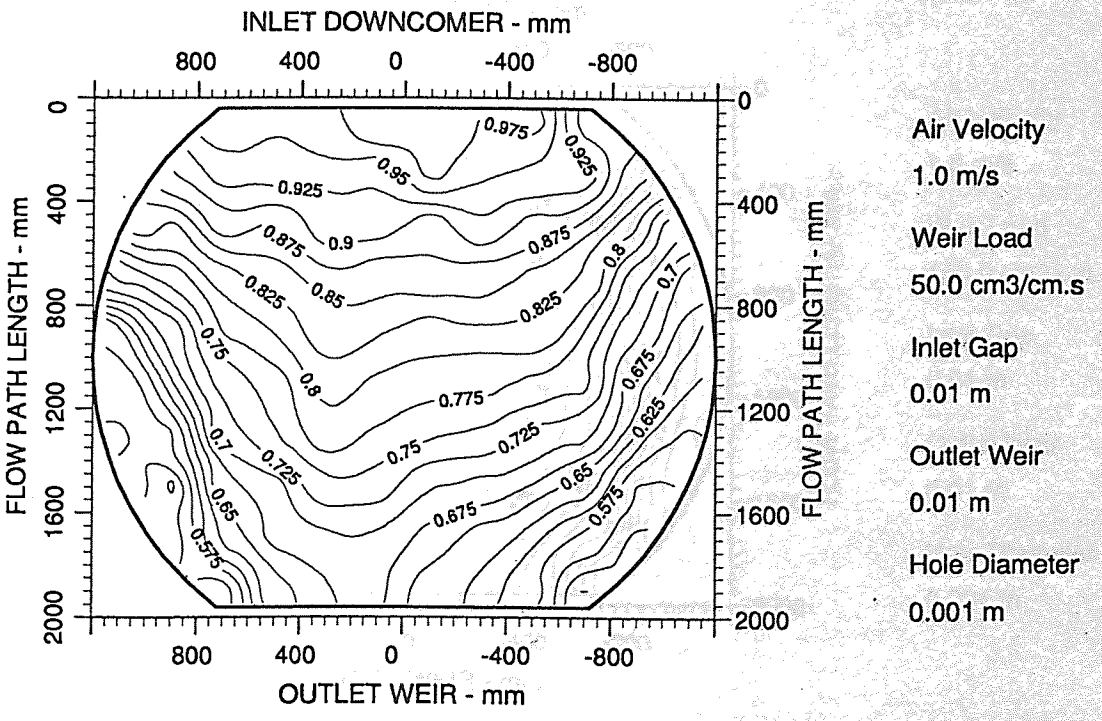

Figure A6.2 Two-dimensional reduced temperature profiles for UMD-tray Emv/Eog 101/72 hCL 26

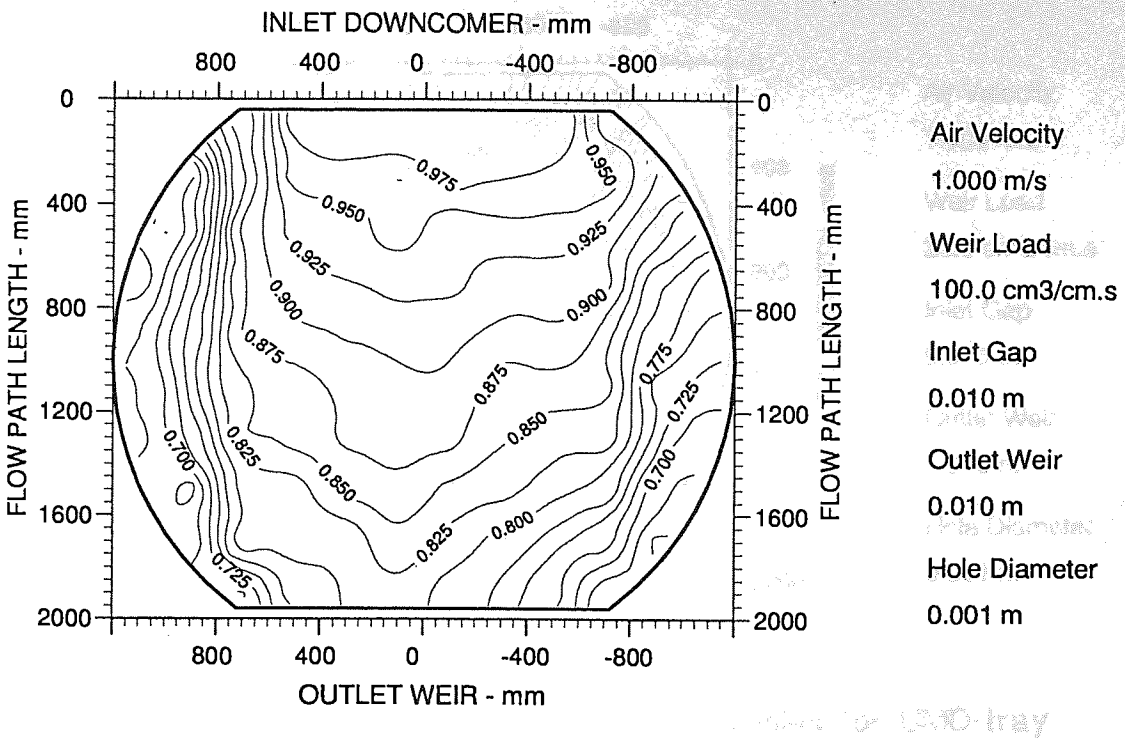

Figure A6.3 Two-dimensional reduced temperature profiles for UMD-tray

Emv/Eog 98/81 hCL 32

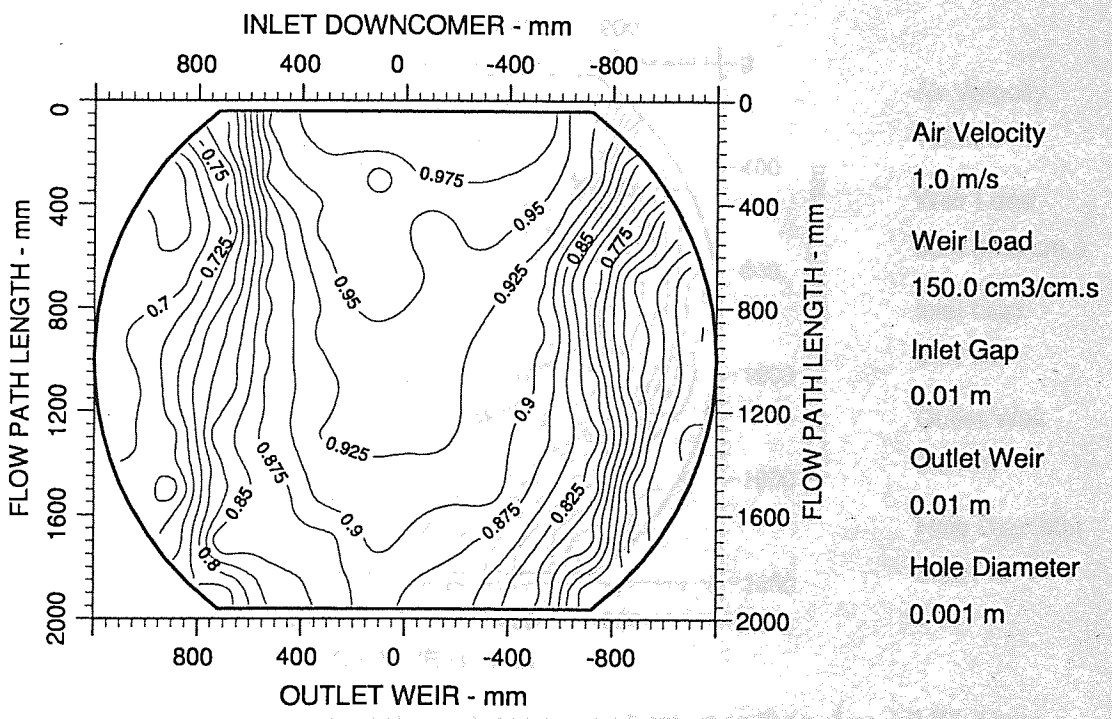

Figure A6.4 Two-dimensionl reduced temperature profiles for UMD-tray

Emv/Eog 97/90 hCL 34

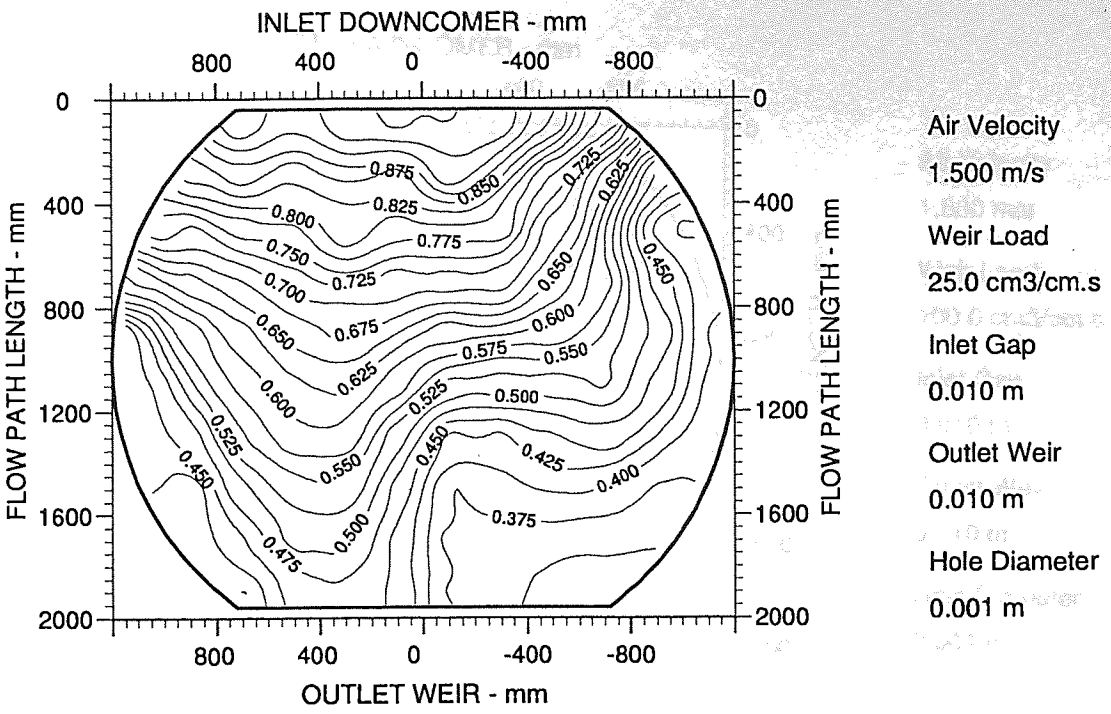

Figure A6.5 Two-dimensionl reduced temperature profiles for UMD-tray

Emv/Eog 93/50 hCL 19

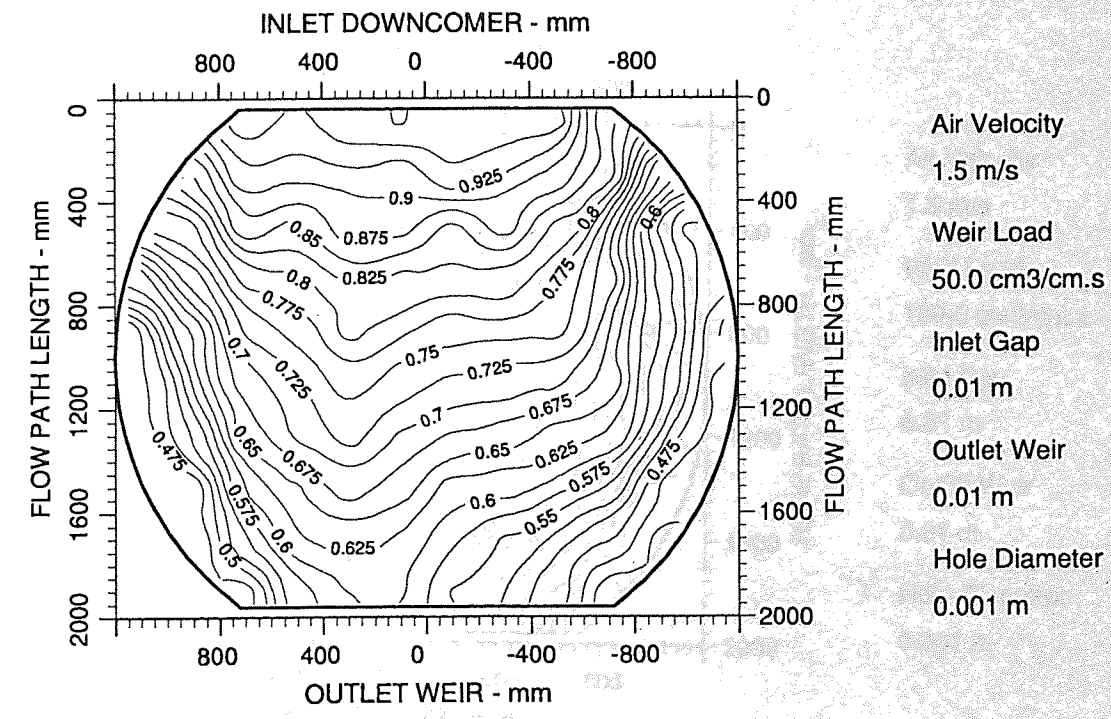

Figure A6.6 Two-dimensionl reduced temperature profiles for UMD-tray

Emv/Eog 99/64 hCL 22

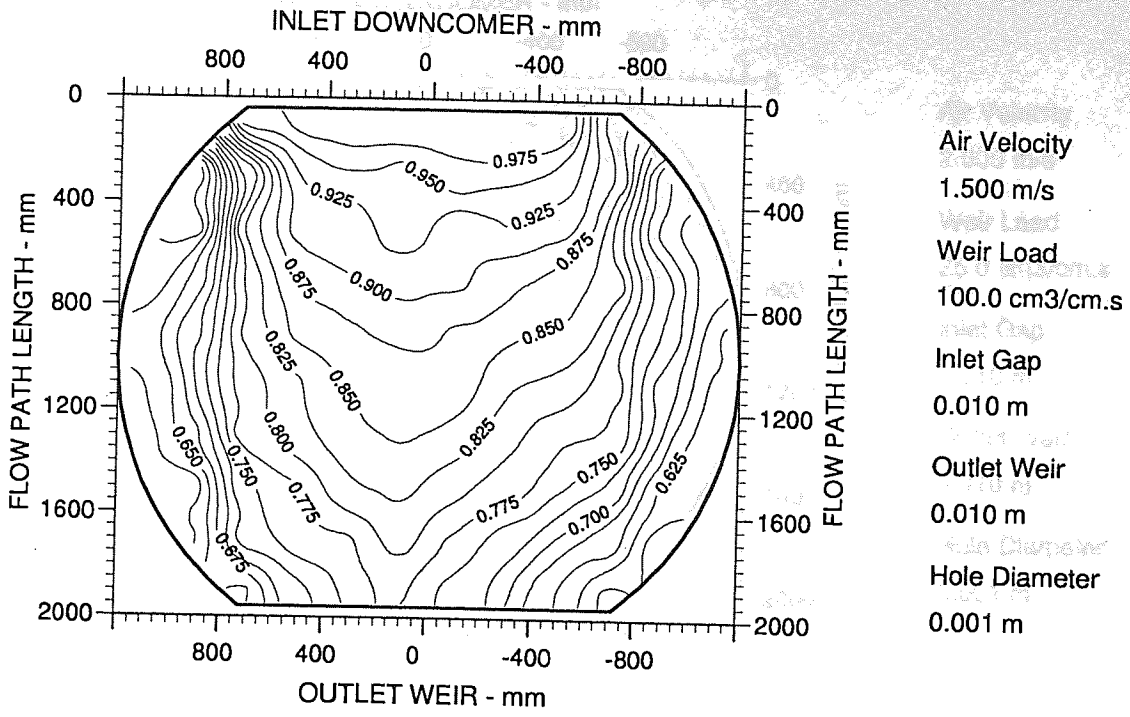

Figure A6.7 Two-dimensionl reduced temperature profiles for UMD-tray
Emv/Eog 95/76 hCL 28

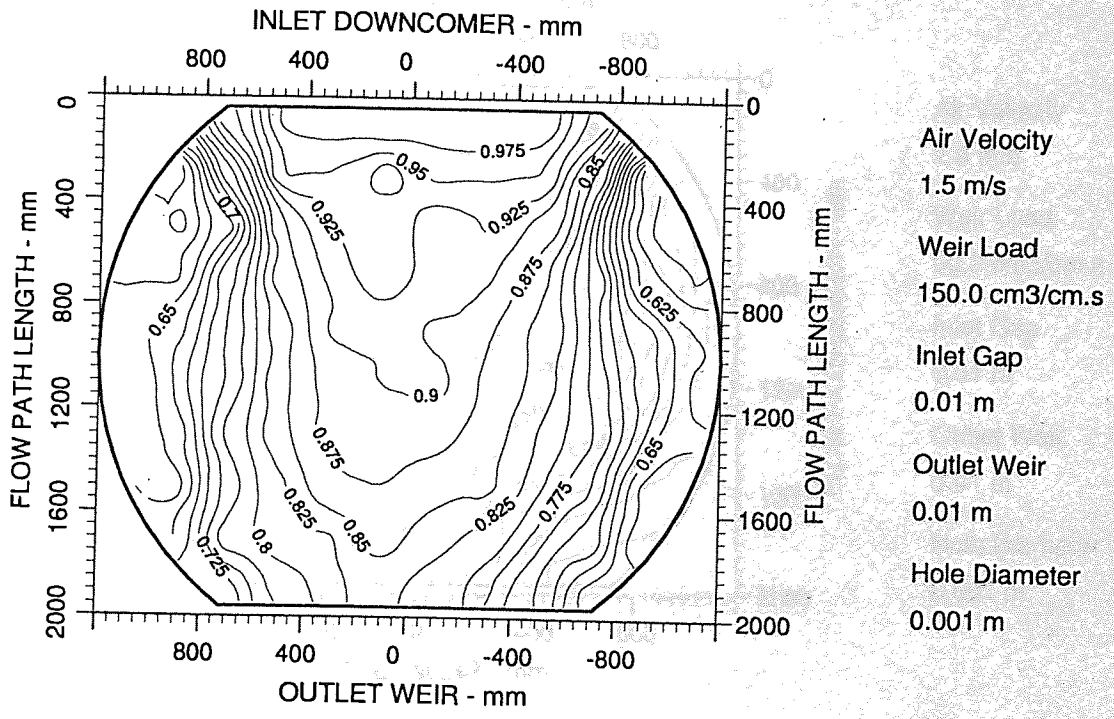

Figure A6.8 Two-dimensionl reduced temperature profiles for UMD-tray
Emv/Eog 94/84 hCL 31

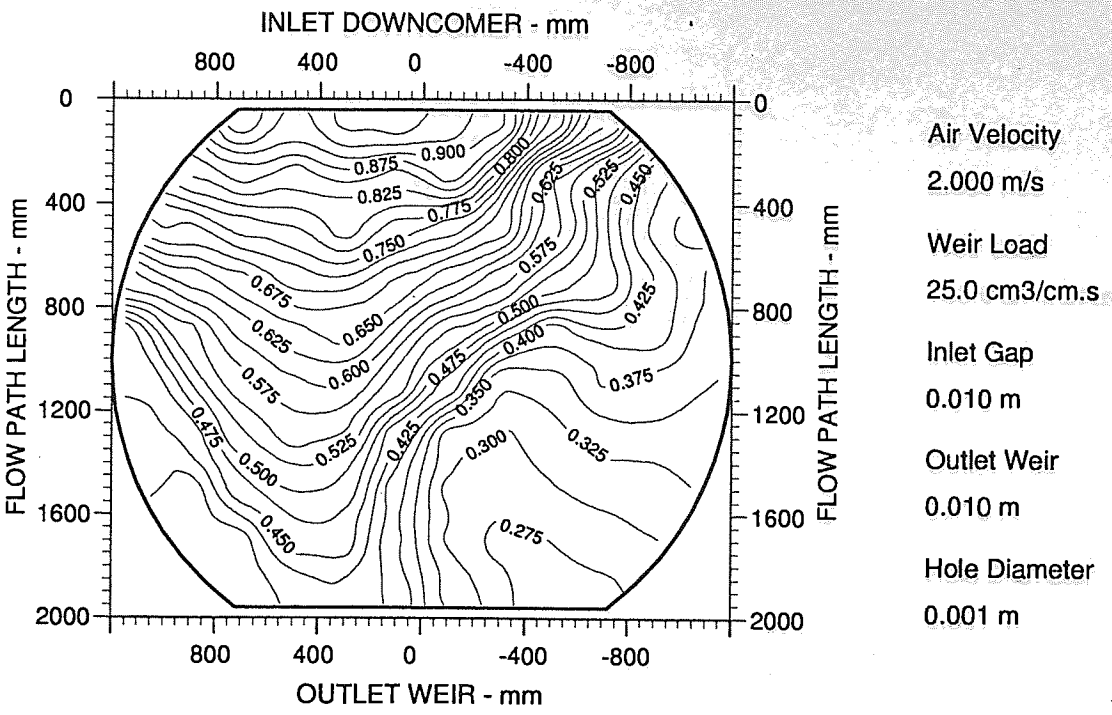

Figure A6.9 Two-dimensionl reduced temperature profiles for UMD-tray
Emv/Eog 87/47 hCL 17

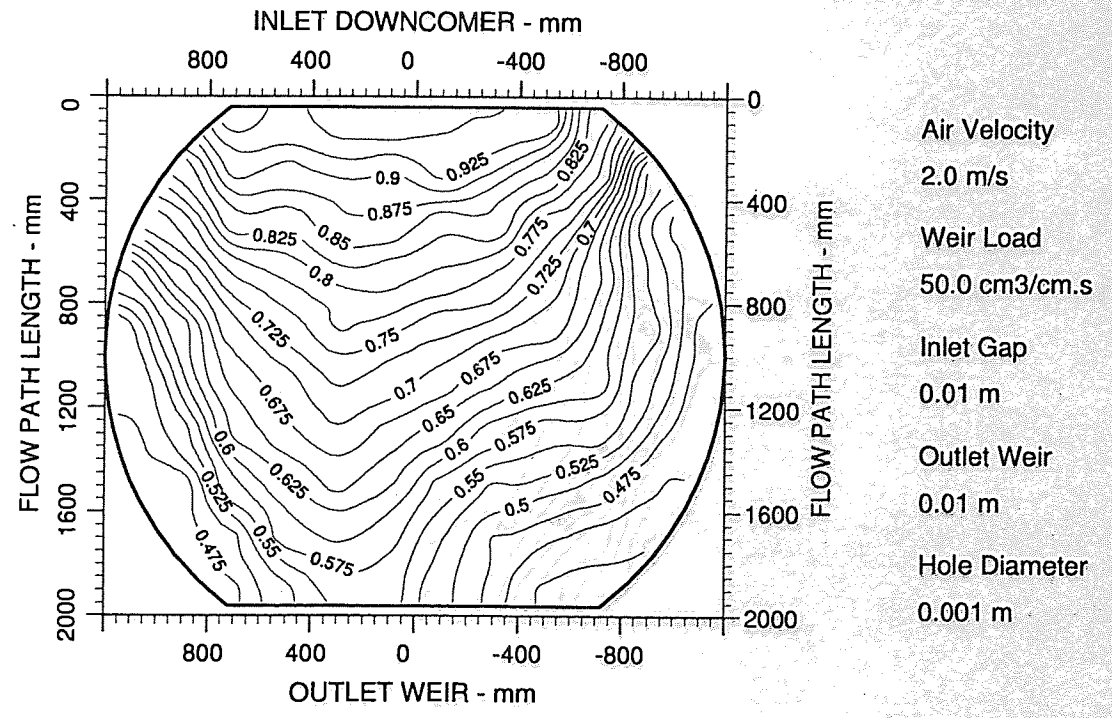

Figure A6.10 Two-dimensionl reduced temperature profiles for UMD-tray
Emv/Eog 91/57 hCL 19

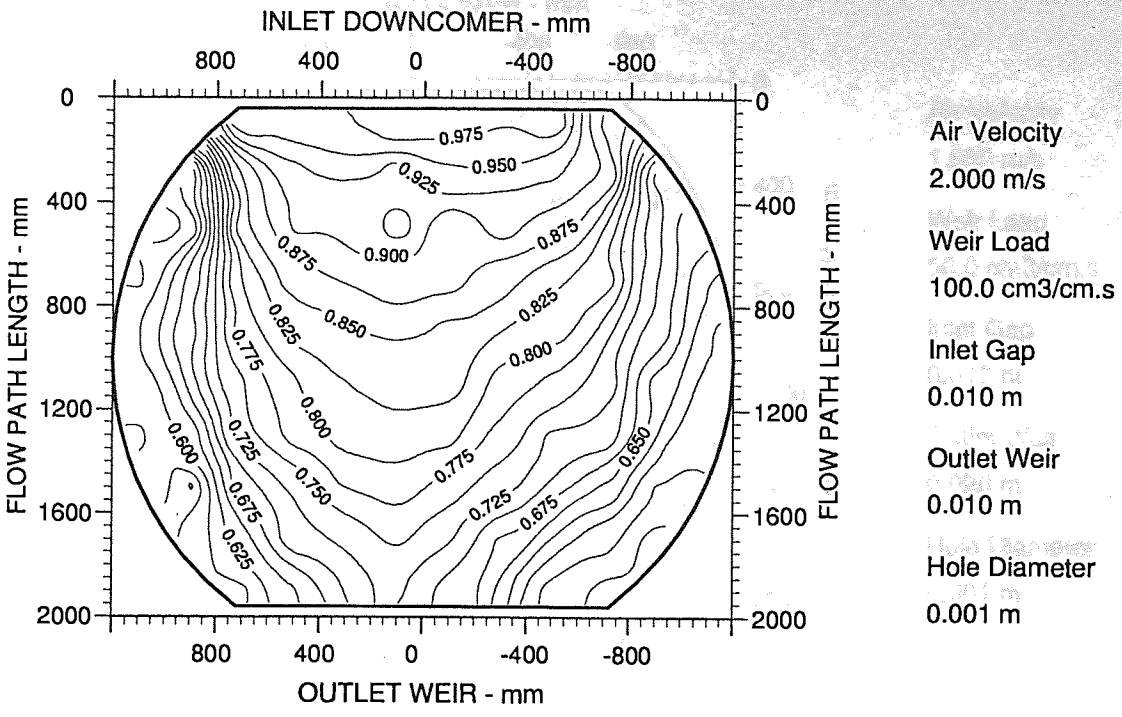

Figure A6.11 Two-dimensionl reduced temperature profiles for UMD-tray
Emv/Eog 93/72 hCL 22

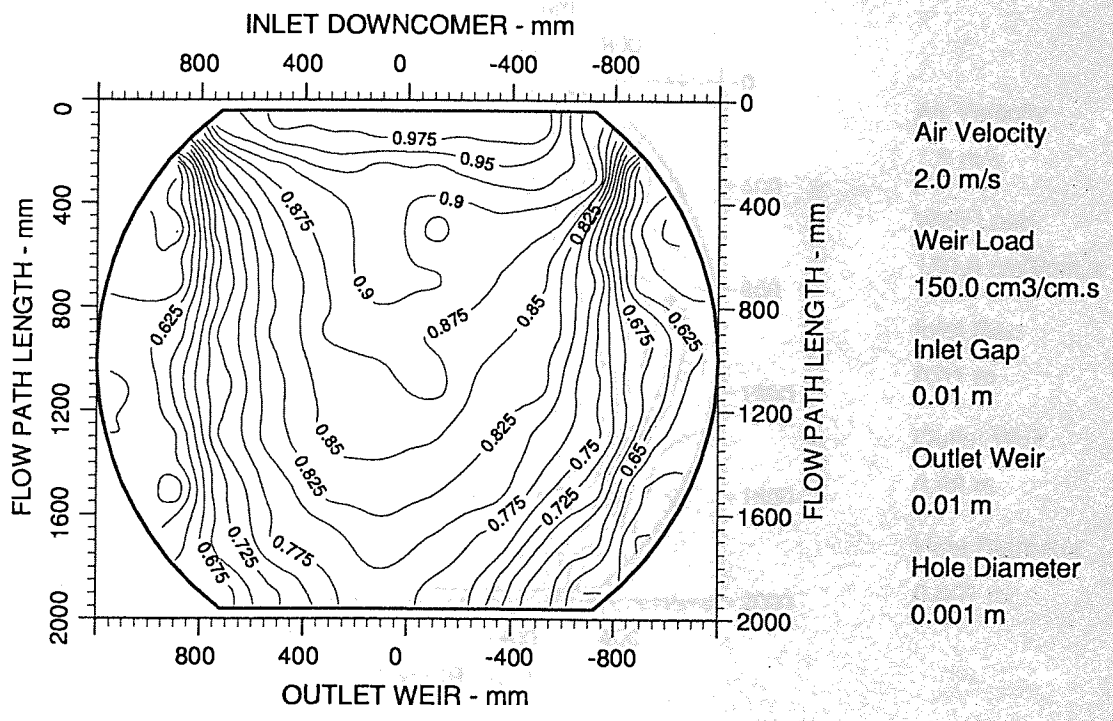

Figure A6.12 Two-dimensionl reduced temperature profiles for UMD-tray
Emv/Eog 94/81 hCL 26

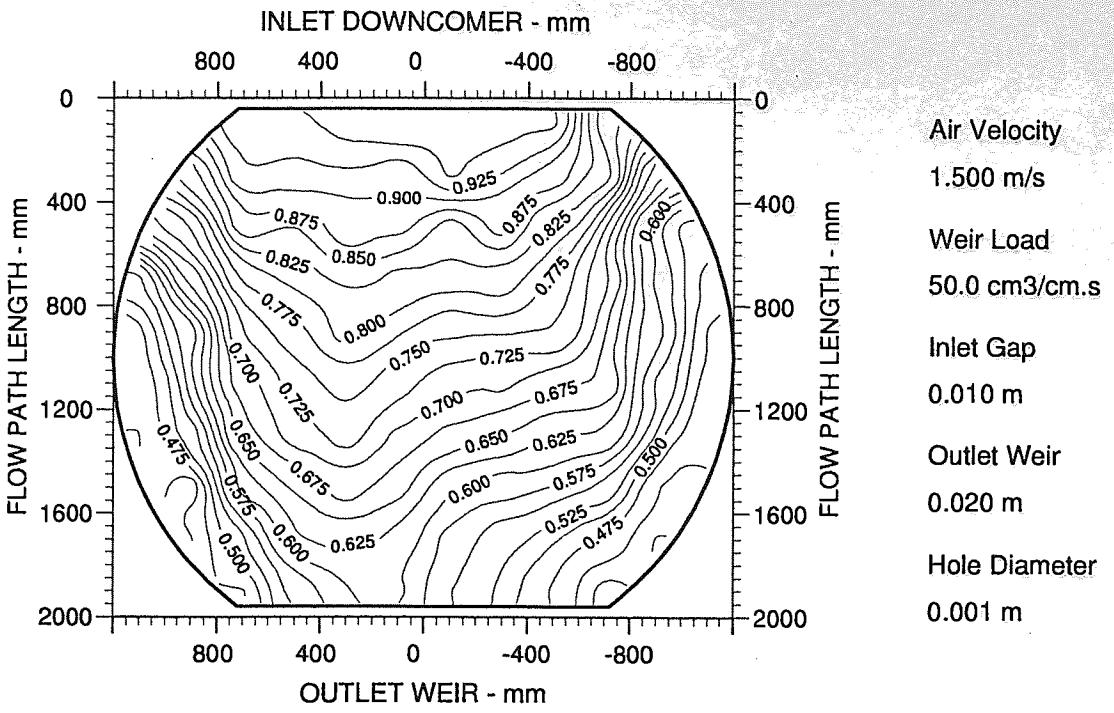

Figure A6.13 Two-dimensionl reduced temperature profiles for UMD-tray
Emv/Eog 98/68 hCL 26

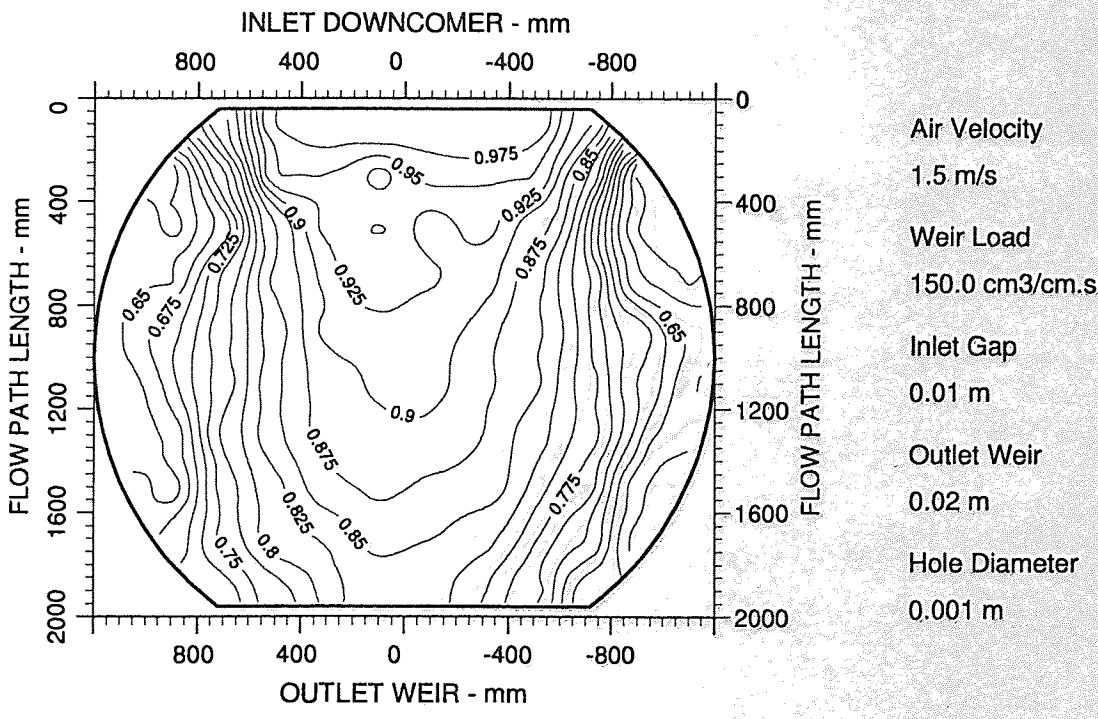

Figure A6.14 Two-dimensionl reduced temperature profiles for UMD-tray
Emv/Eog 92/84 hCL 33

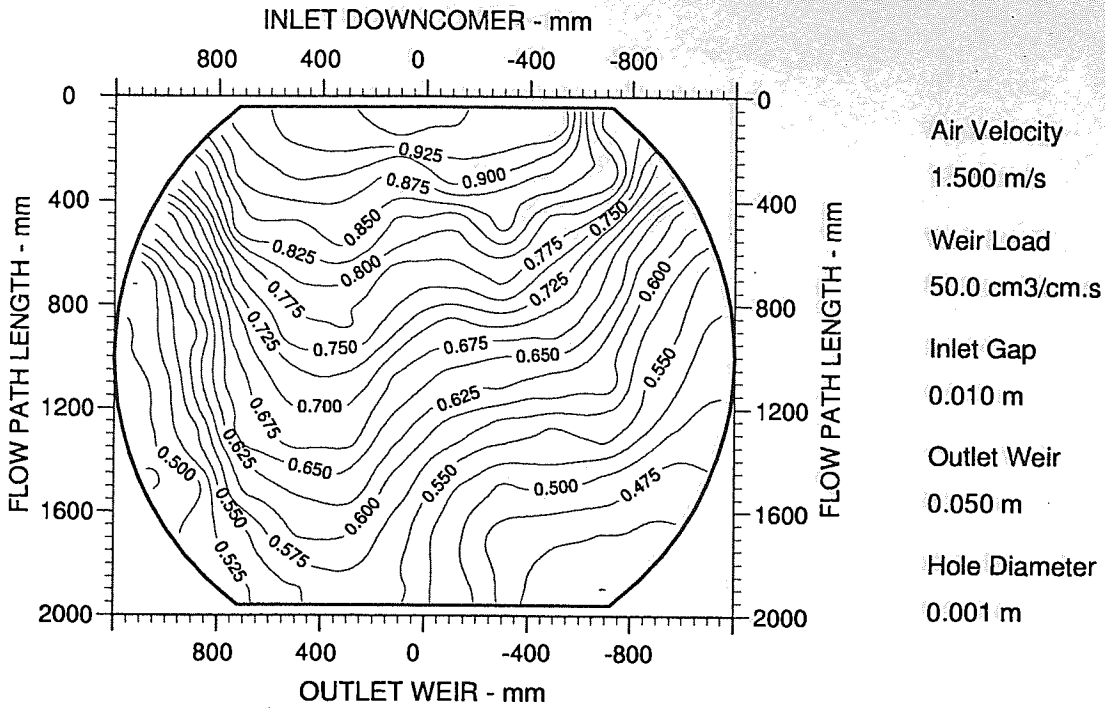

Figure A6.15 Two-dimensionl reduced temperature profiles for UMD-tray
Emv/Eog 107/71 hCL 33

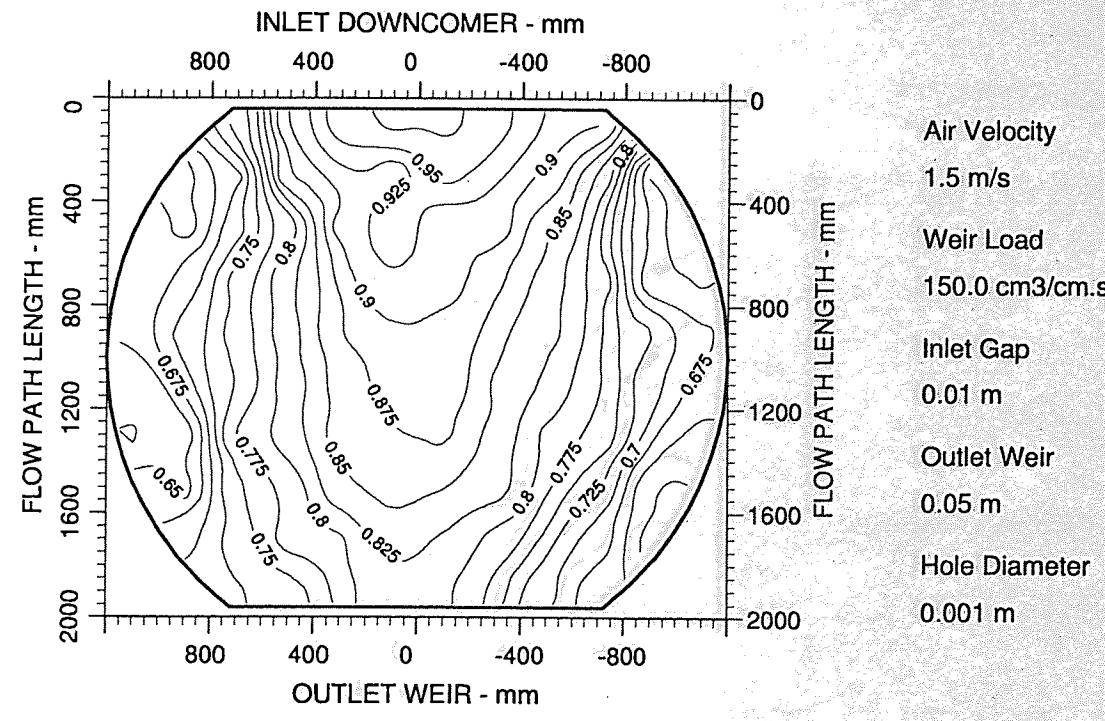

Figure A6.16 Two-dimensionl reduced temperature profiles for UMD-tray
Emv/Eog 100/90 hCL 41

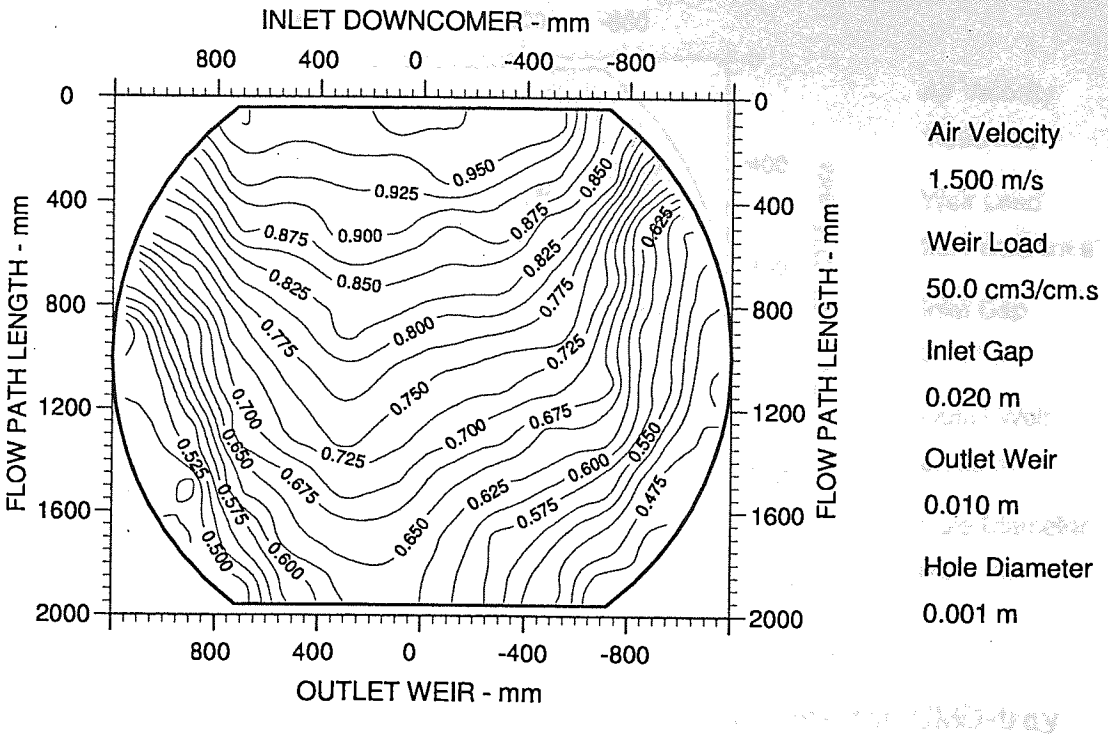

Figure A6.17 Two-dimensionl reduced temperature profiles for UMD-tray
Emv/Eog 84/58 hCL 25

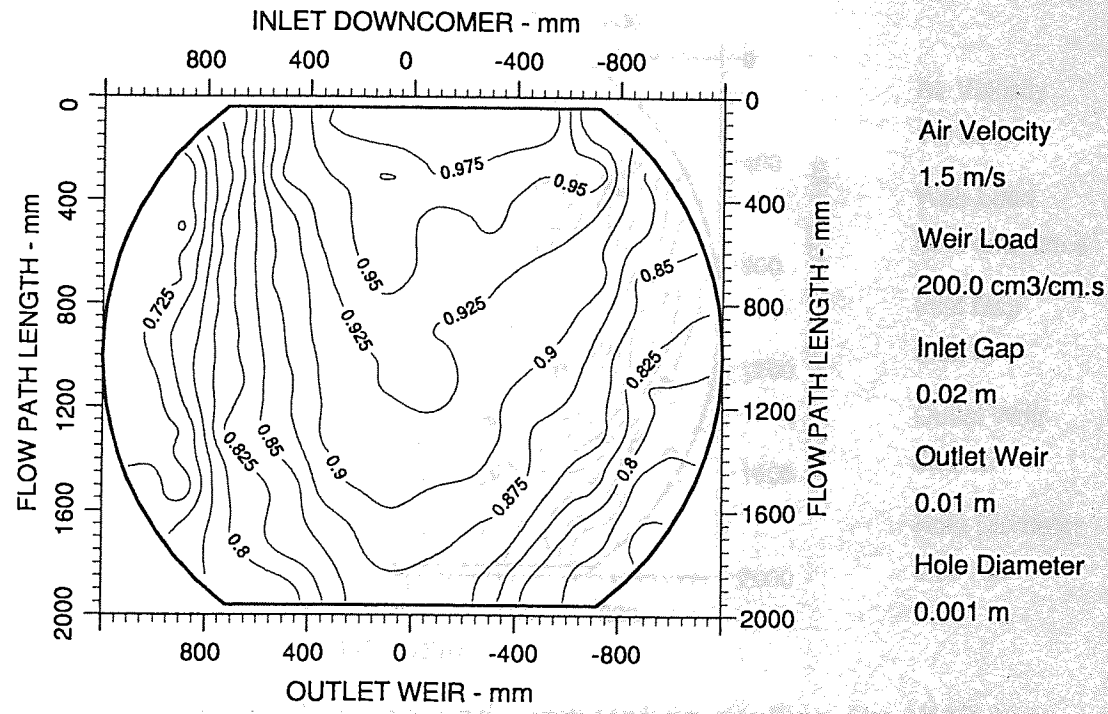

Figure A6.18 Two-dimensionl reduced temperature profiles for UMD-tray
Emv/Eog 93/83 hCL 38

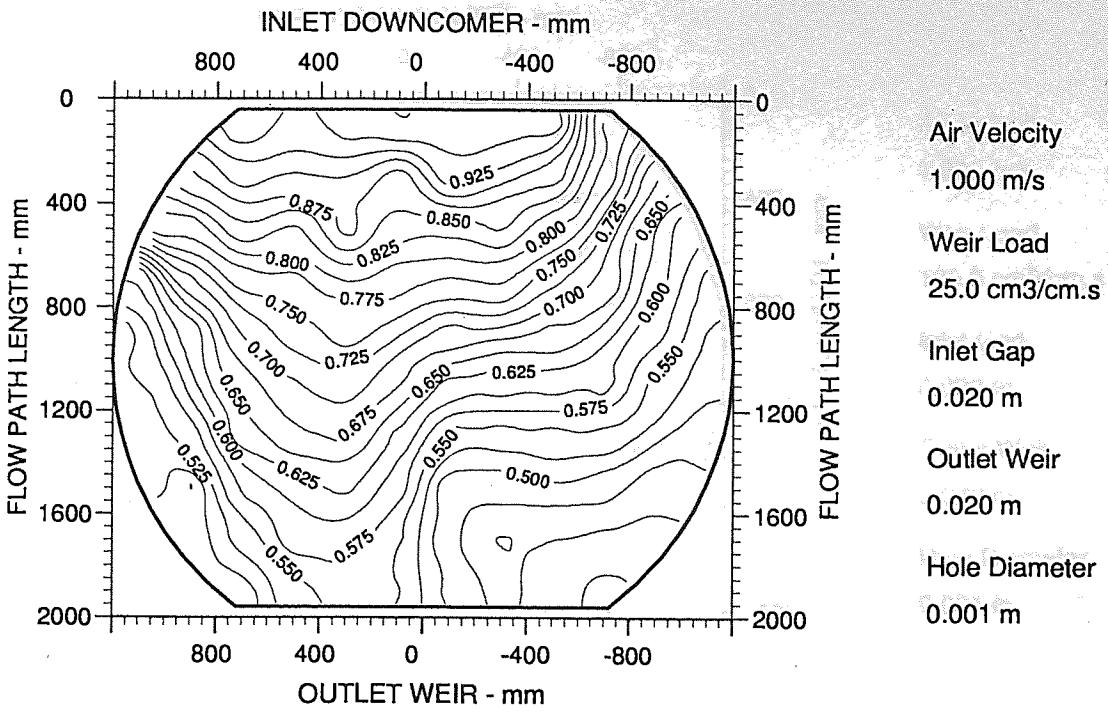

Figure A6.19 Two-dimensionl reduced temperature profiles for UMD-tray
Emv/Eog 90/56 hCL 25

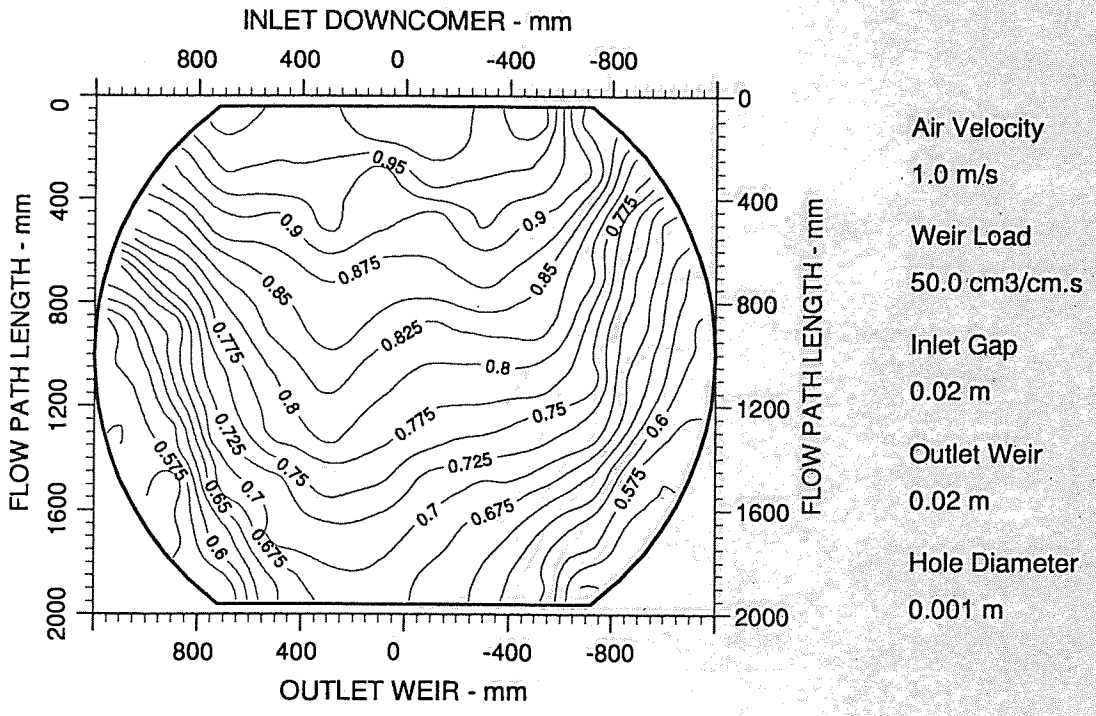

Figure A6.20 Two-dimensionl reduced temperature profiles for UMD-tray
Emv/Eog 94/68 hCL 28

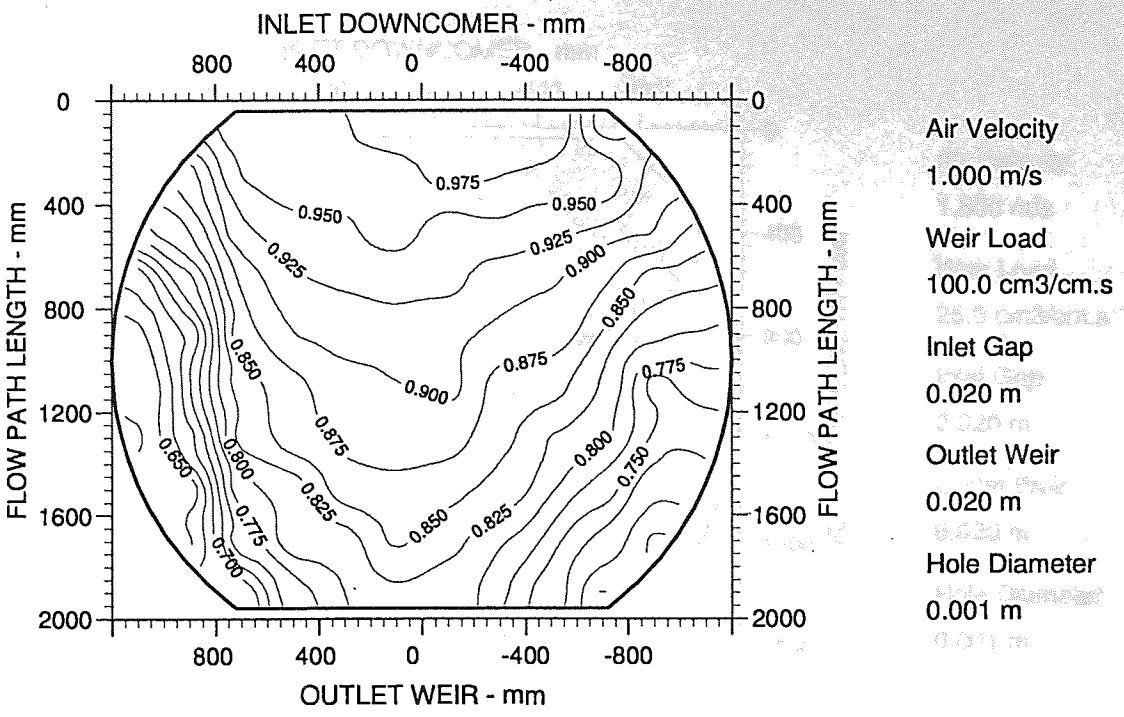

Figure A6.21 Two-dimensionl reduced temperature profiles for UMD-tray

Emv/Eog 100/80 hCL 34

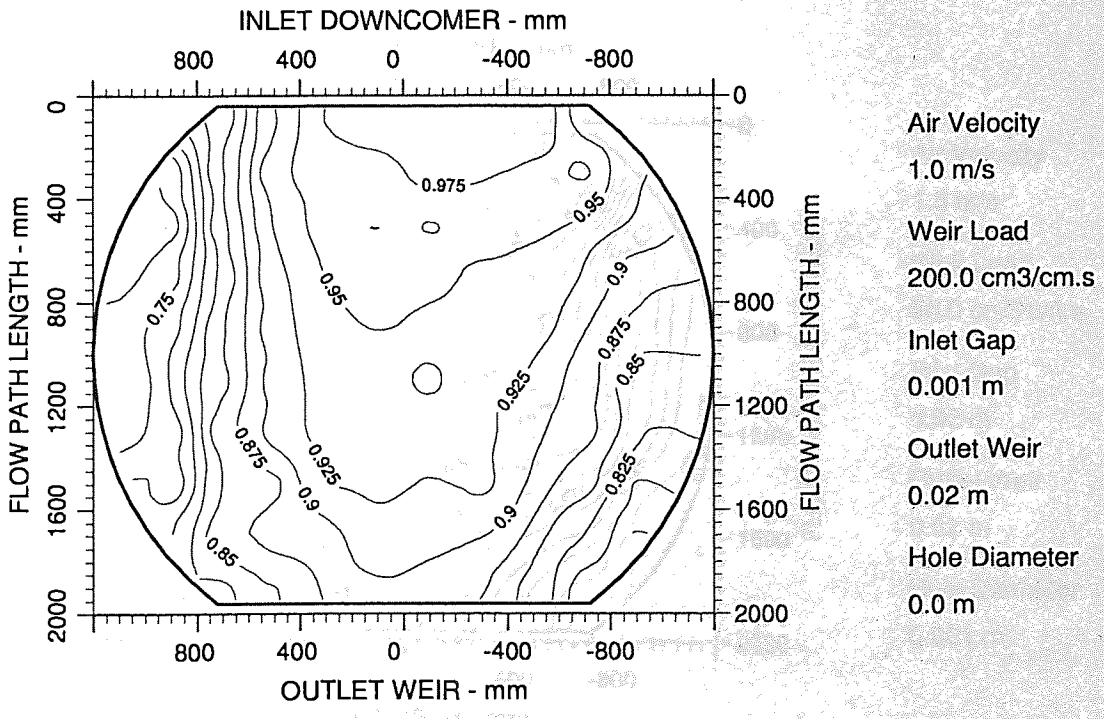

Figure A6.22 Two-dimensionl reduced temperature profiles for UMD-tray

Emv/Eog 104/94 hCL 45

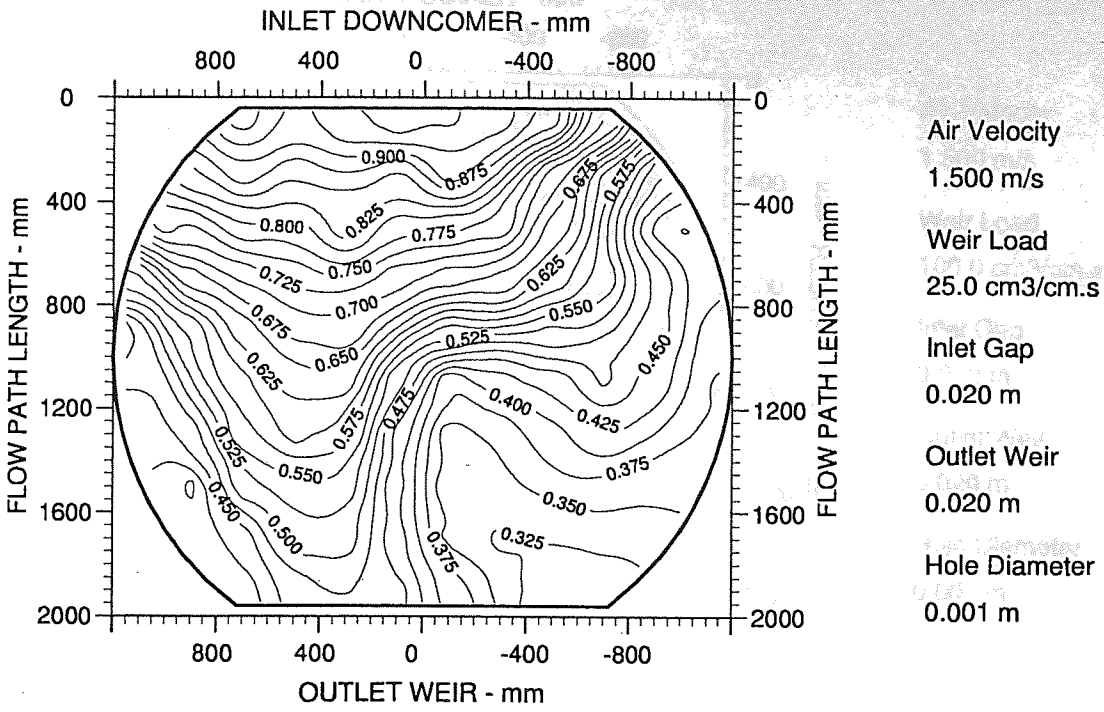

Figure A6.23 Two-dimensionl reduced temperature profiles for UMD-tray
Emv/Eog 84/49 hCL 23

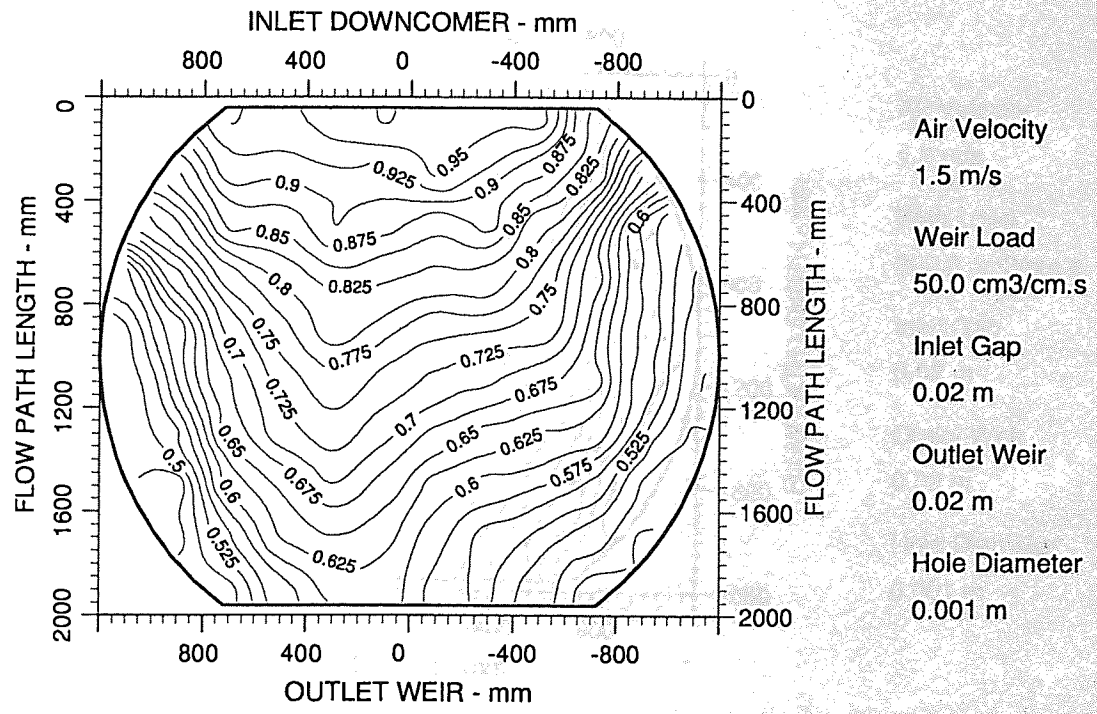

Figure A6.24 Two-dimensionl reduced temperature profiles for UMD-tray
Emv/Eog 94/62 hCL 26

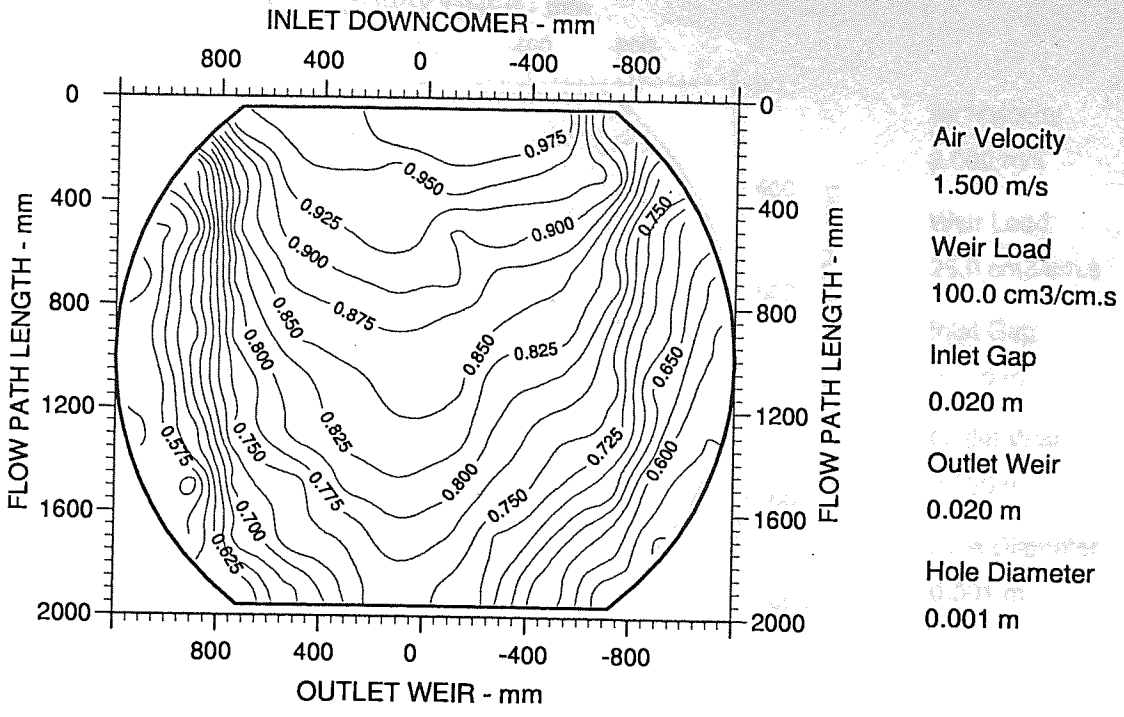

Figure A6.25 Two-dimensionl reduced temperature profiles for UMD-tray
Emv/Eog 97/77 hCL 32

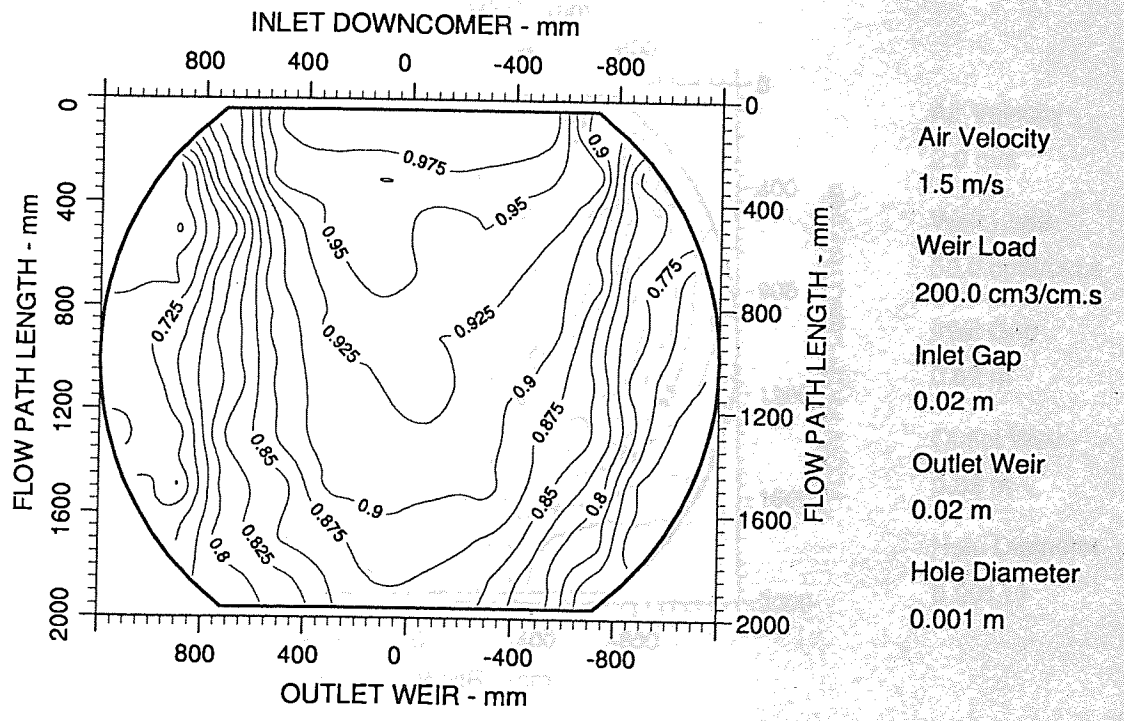

Figure A6.26 Two-dimensionl reduced temperature profiles for UMD-tray
Emv/Eog 92/85 hCL 44

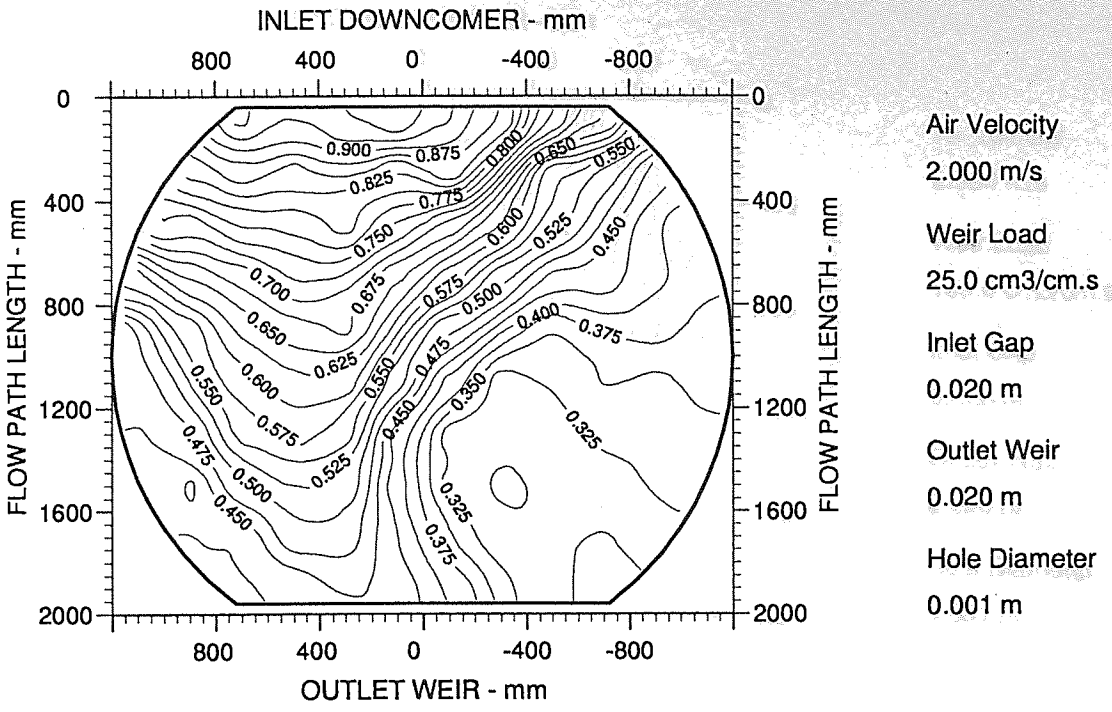

Figure A6.27 Two-dimensionl reduced temperature profiles for UMD-tray

Emv/Eog 81/47 hCL 18

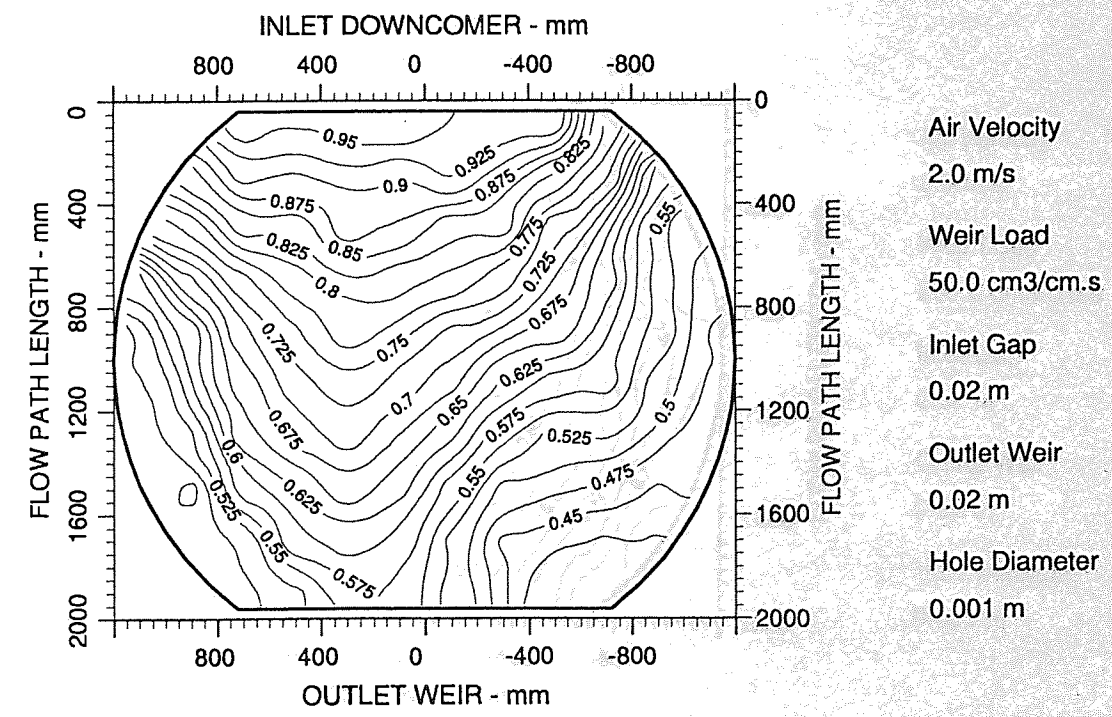

Figure A6.28 Two-dimensionl reduced temperature profiles for UMD-tray

Emv/Eog 94/60 hCL 21

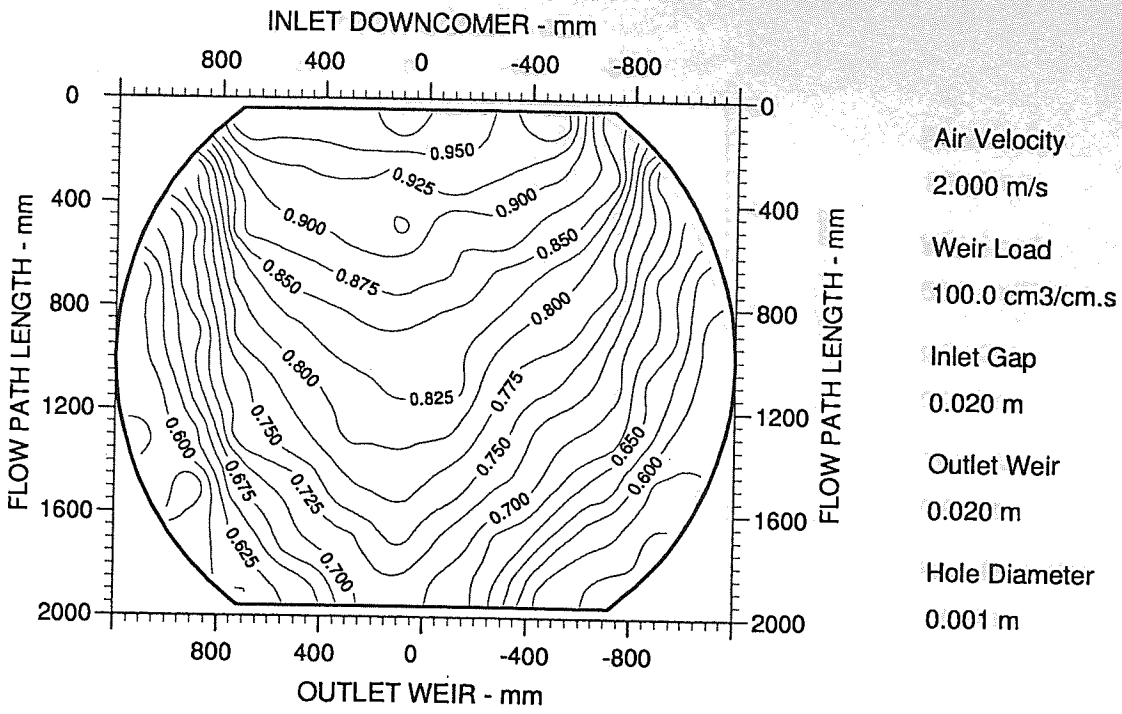

Figure A6.29 Two-dimensionl reduced temperature profiles for UMD-tray Emv/Eog 97/73 hCL 24

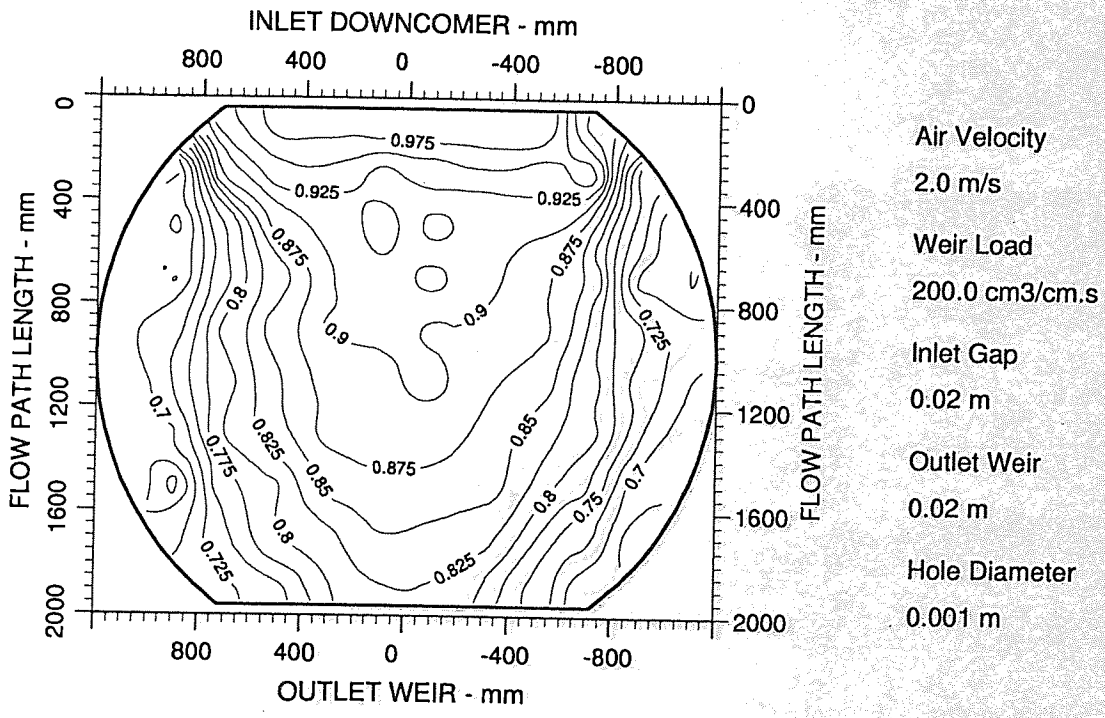

Figure A6.30 Two-dimensionl reduced temperature profiles for UMD-tray Emv/Eog 97/84 hCL 30

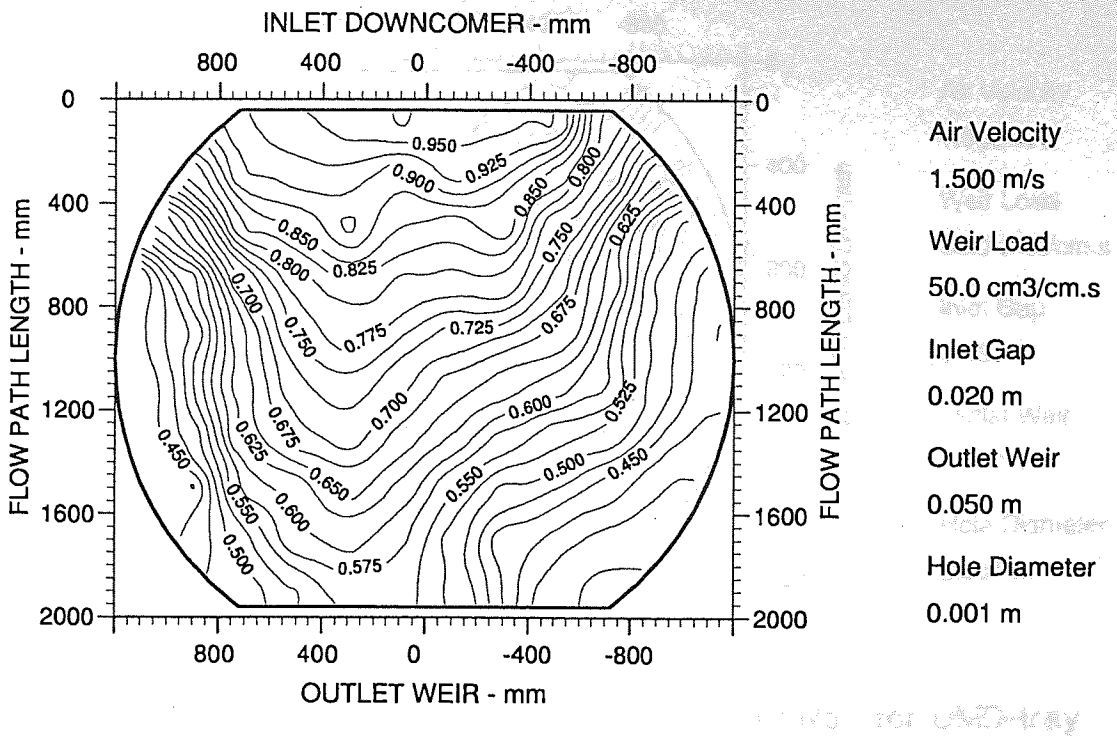

Figure A6.31 Two-dimensionl reduced temperature profiles for UMD-tray

Emv/Eog 104/70 hCL 32

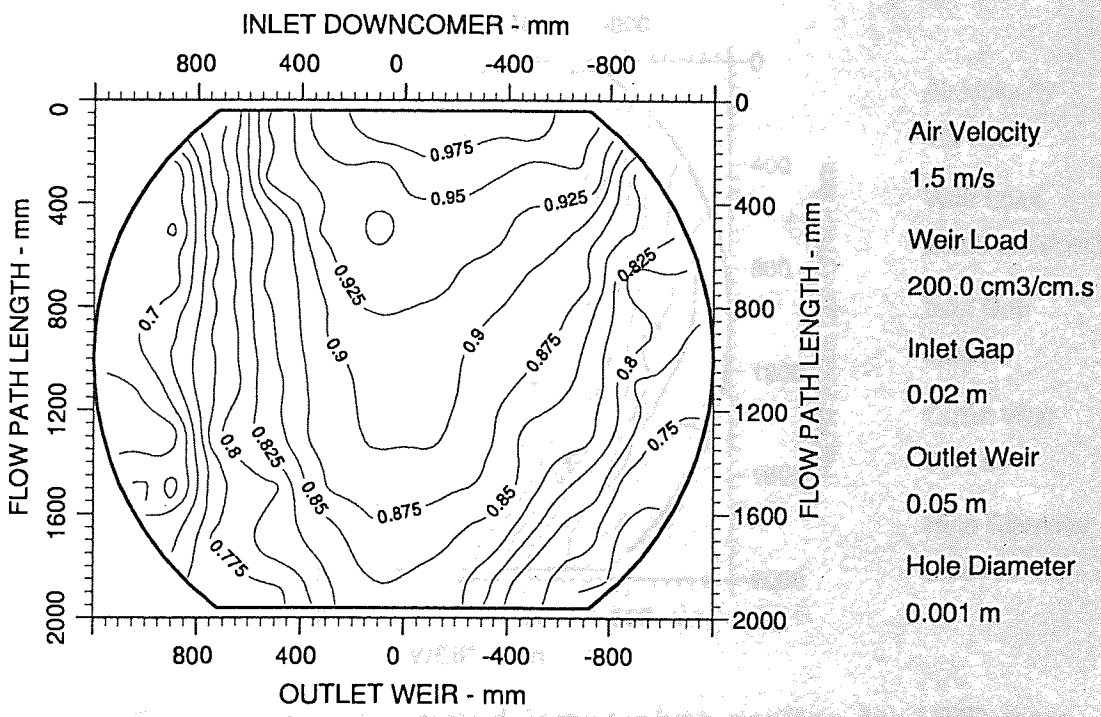

Figure A6.32 Two-dimensionl reduced temperature profiles for UMD-tray

Emv/Eog 98/87 hCL 47

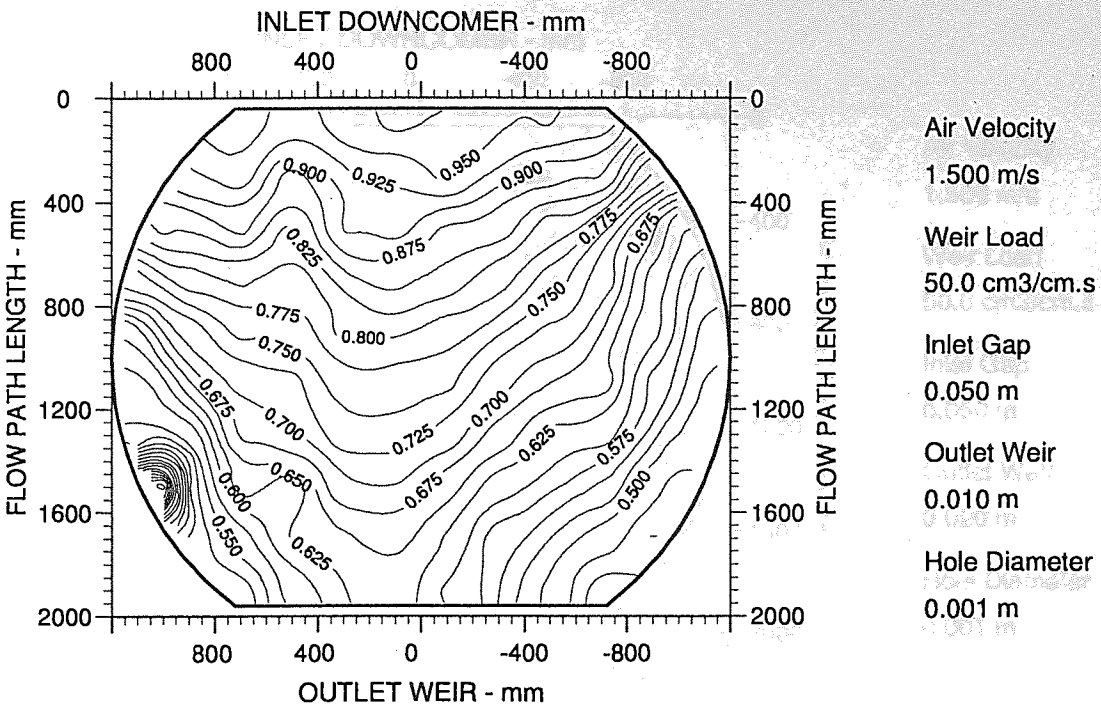

Figure A6.33 Two-dimensionl reduced temperature profiles for UMD-tray
Emv/Eog 85/57 hCL 24

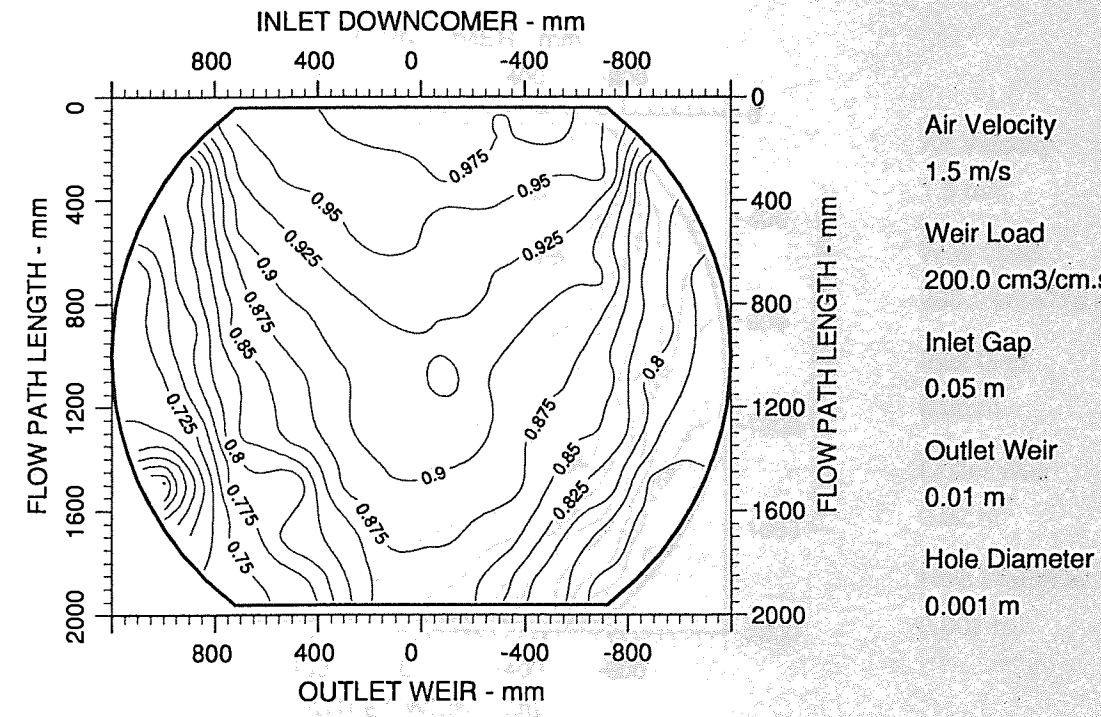

Figure A6.34 Two-dimensionl reduced temperature profiles for UMD-tray
Emv/Eog 103/90 hCL 38

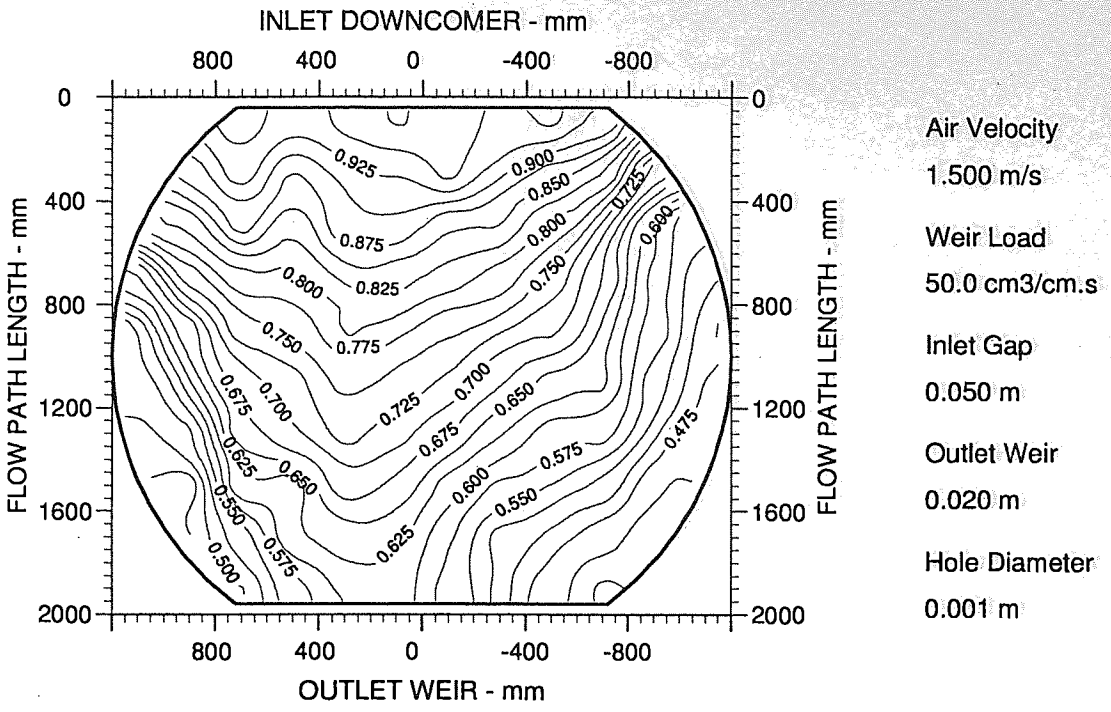

Figure A6.35 Two-dimensionl reduced temperature profiles for UMD-tray
Emv/Eog 90/59 hCL 26

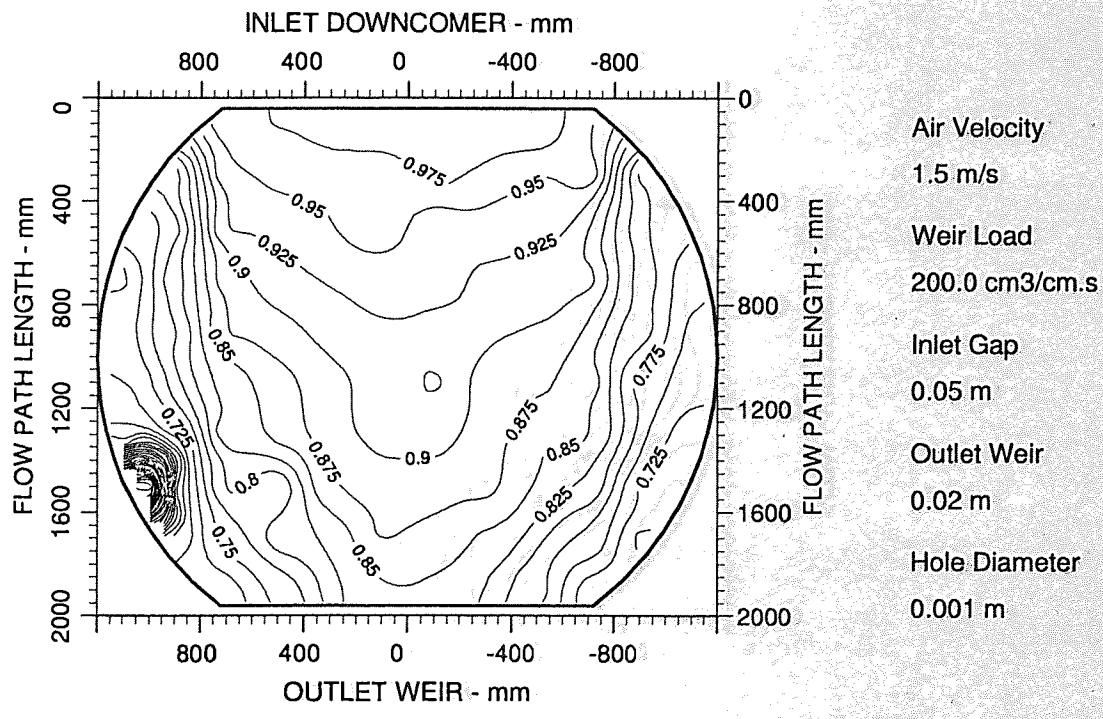

Figure A6.36 Two-dimensionl reduced temperature profiles for UMD-tray
Emv/Eog 102/87 hCL 44

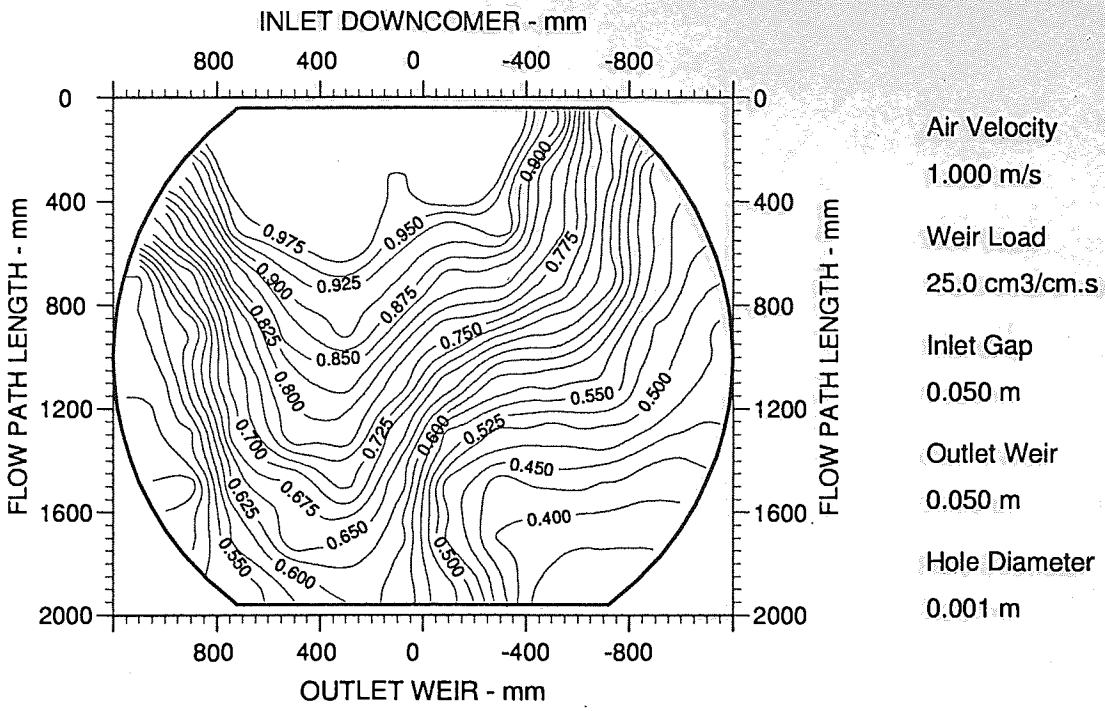

Figure A6.37 Two-dimensionl reduced temperature profiles for UMD-tray

Emv/Eog 87/55 hCL 32

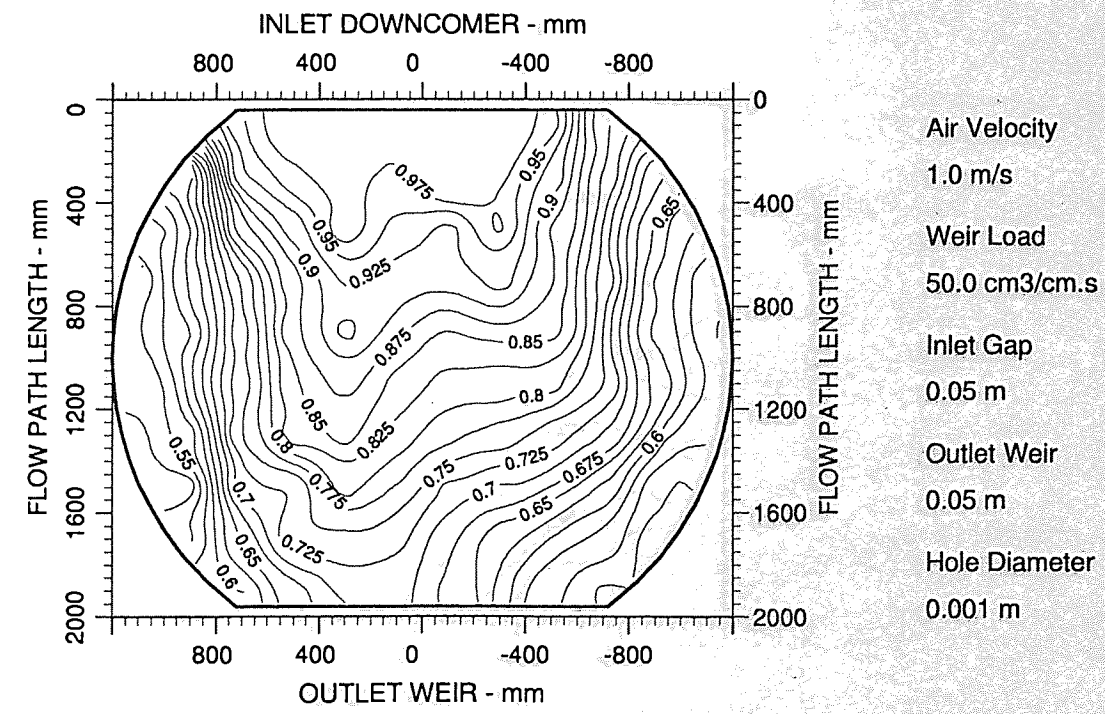

Figure A6.38 Two-dimensionl reduced temperature profiles for UMD-tray

Emv/Eog 96/73 hCL 34

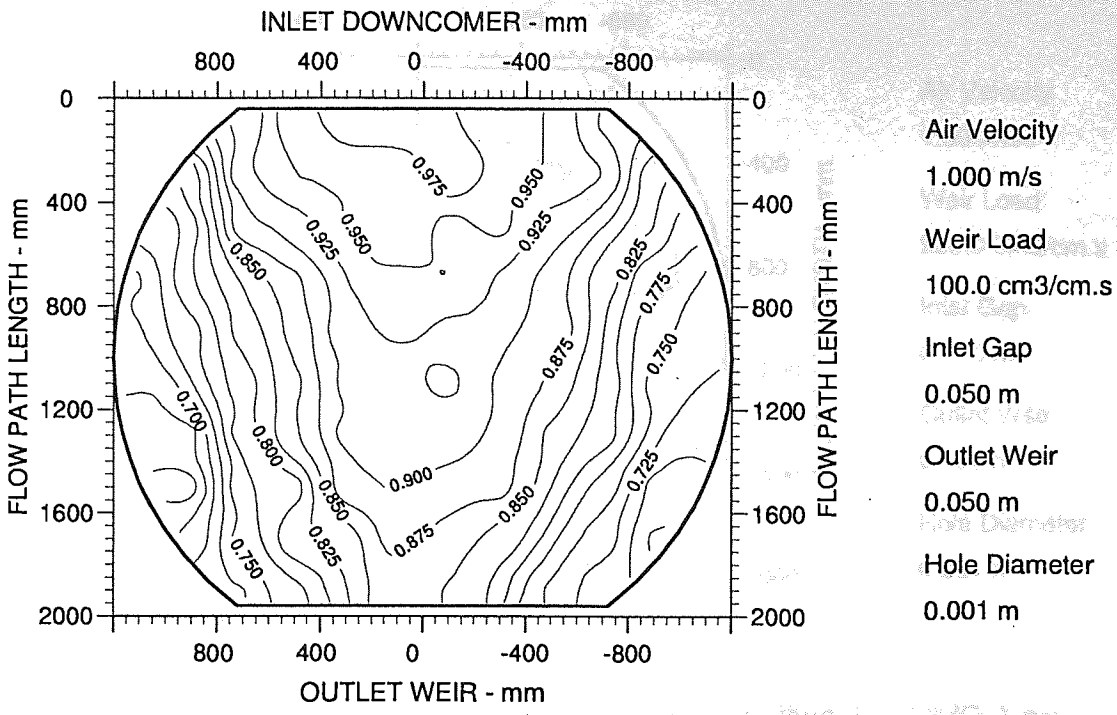

Figure A6.39 Two-dimensionl reduced temperature profiles for UMD-tray
Emv/Eog 101/88 hCL 42

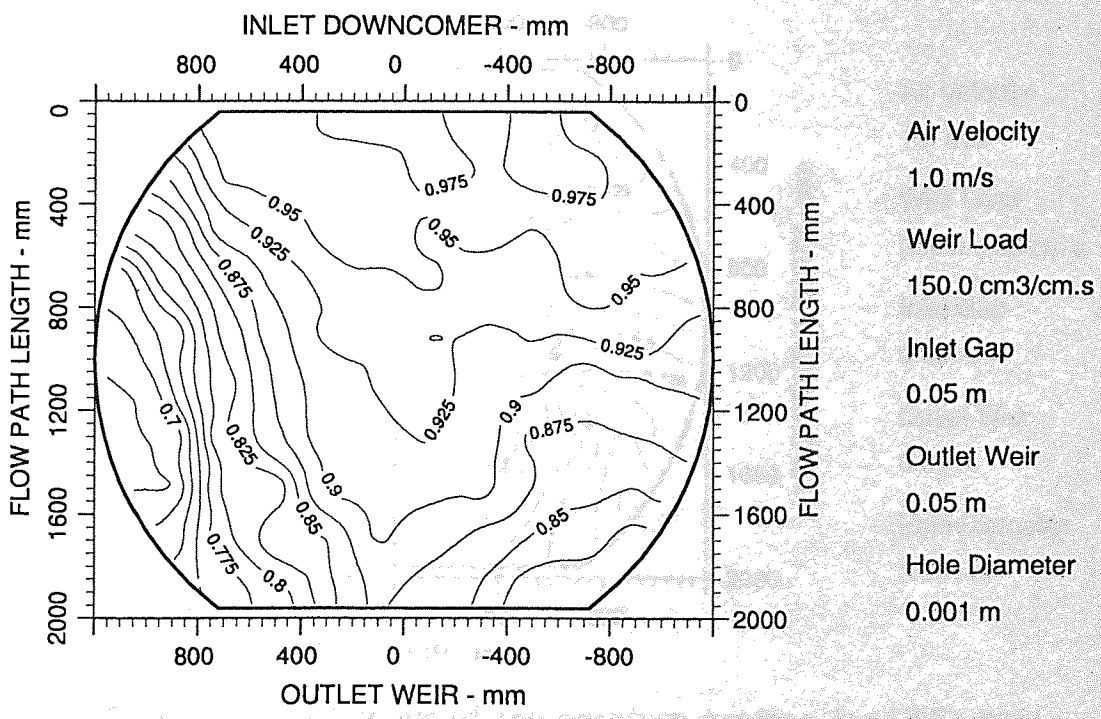

Figure A6.40 Two-dimensionl reduced temperature profiles for UMD-tray
Emv/Eog 106/92 hCL 46

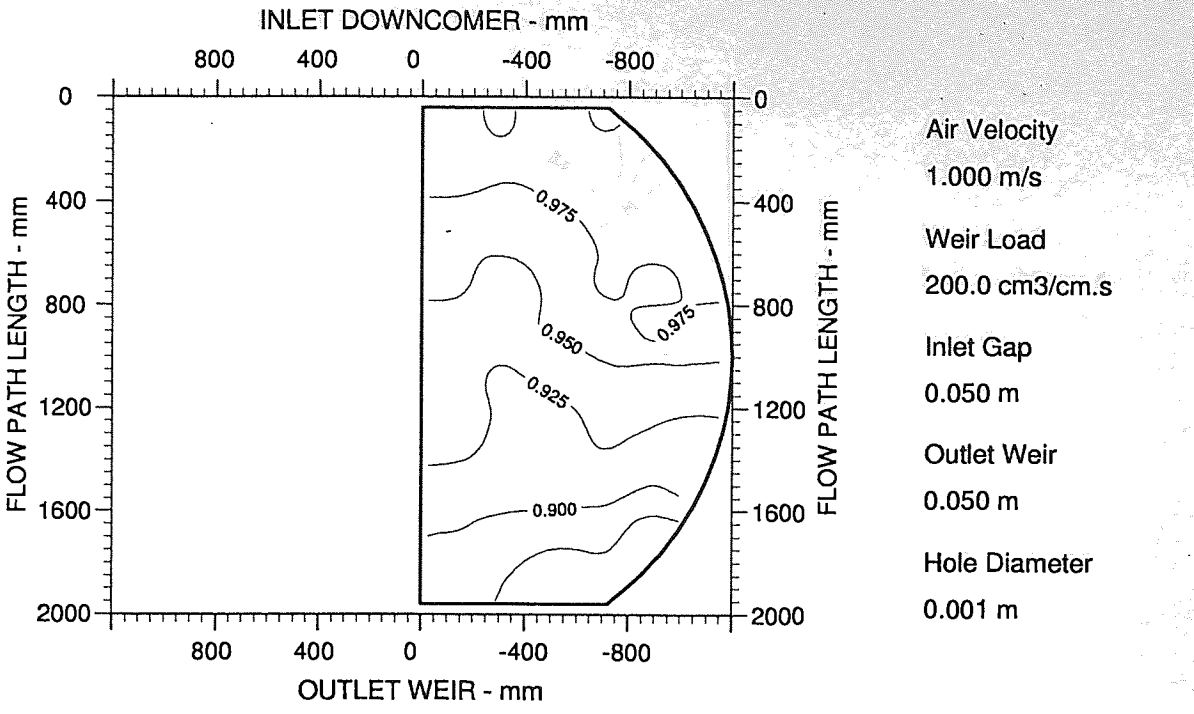

Figure A6.41 Two-dimensionl reduced temperature profiles for UMD-tray Emv/Eog 105/94 hCL 57

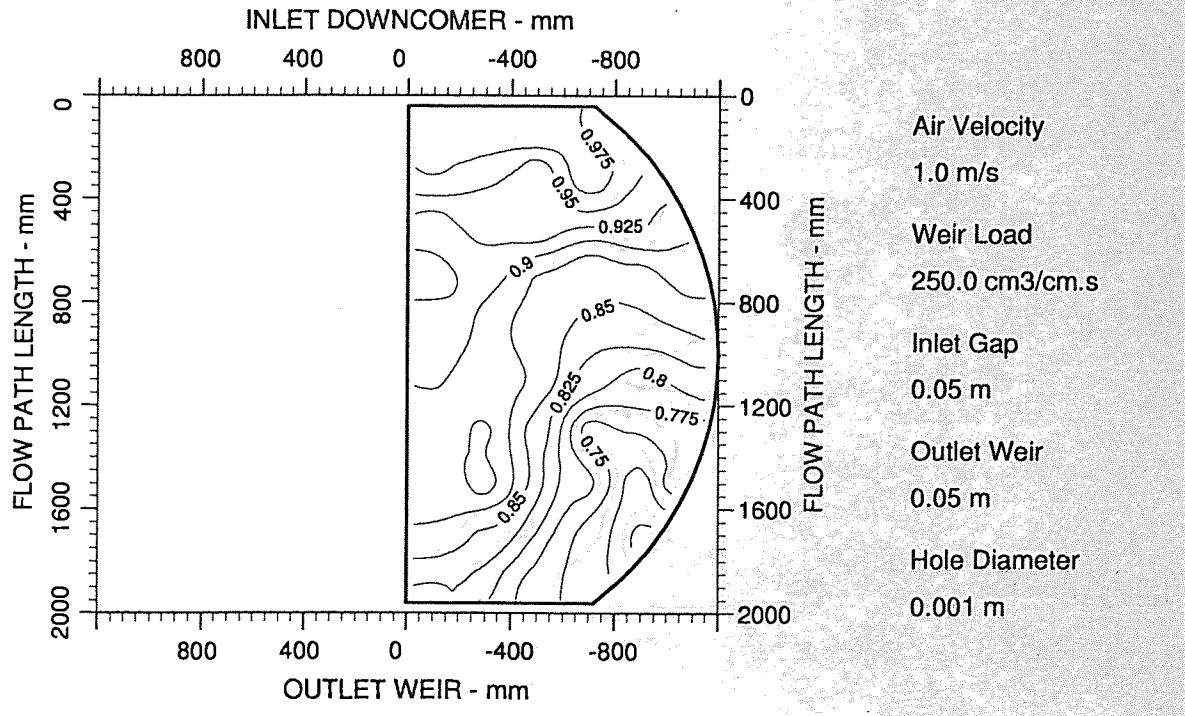

Figure A6.42 Two-dimensionl reduced temperature profiles for UMD-tray Emv/Eog 94/92

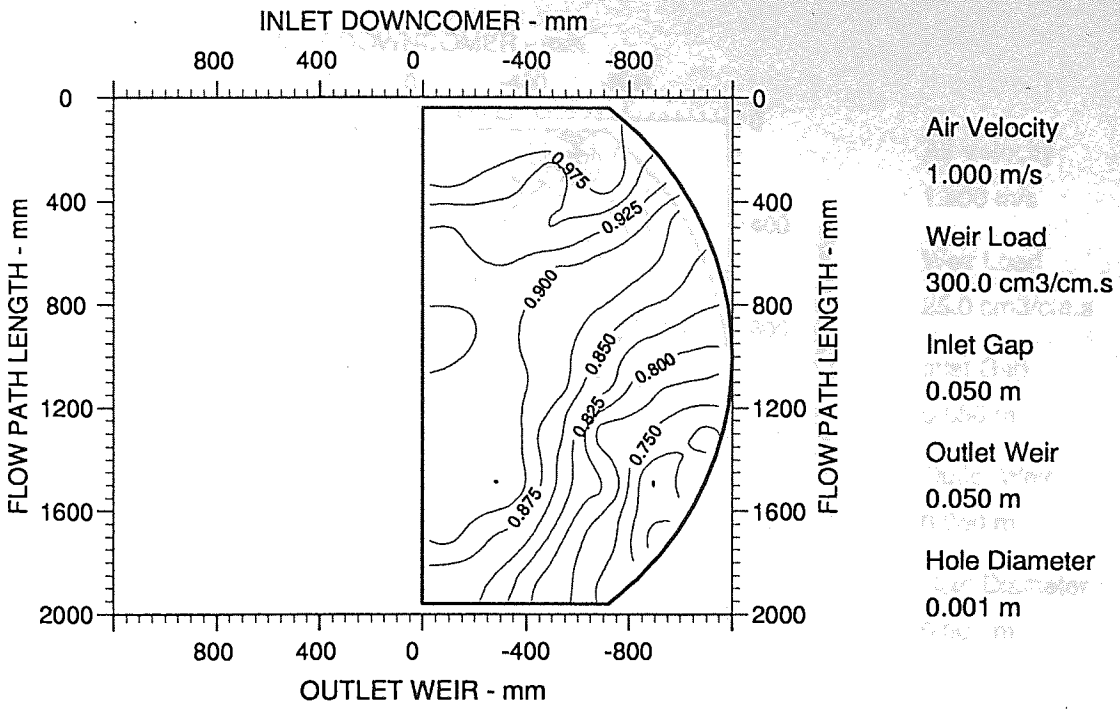

Figure A6.43 Two-dimensionl reduced temperature profiles for UMD-tray Emv/Eog 97/96

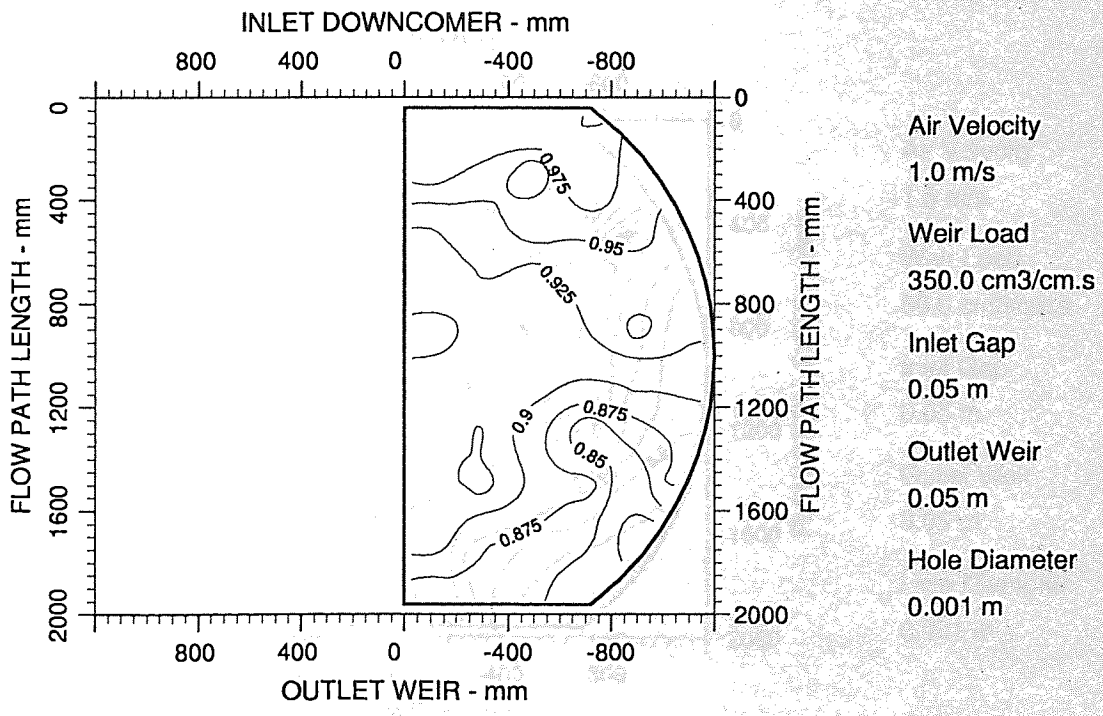

Figure A6.44 Two-dimensionl reduced temperature profiles for UMD-tray Emv/Eog 101/94

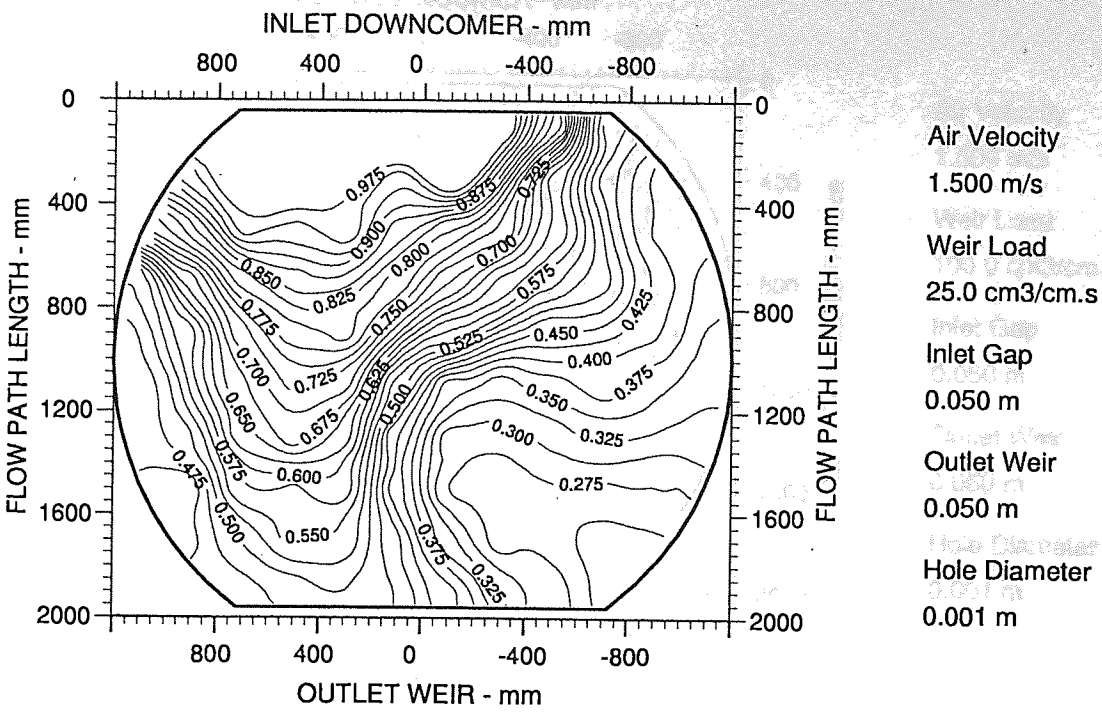

Figure A6.45 Two-dimensionl reduced temperature profiles for UMD-tray
Emv/Eog 87/49 hCL 28

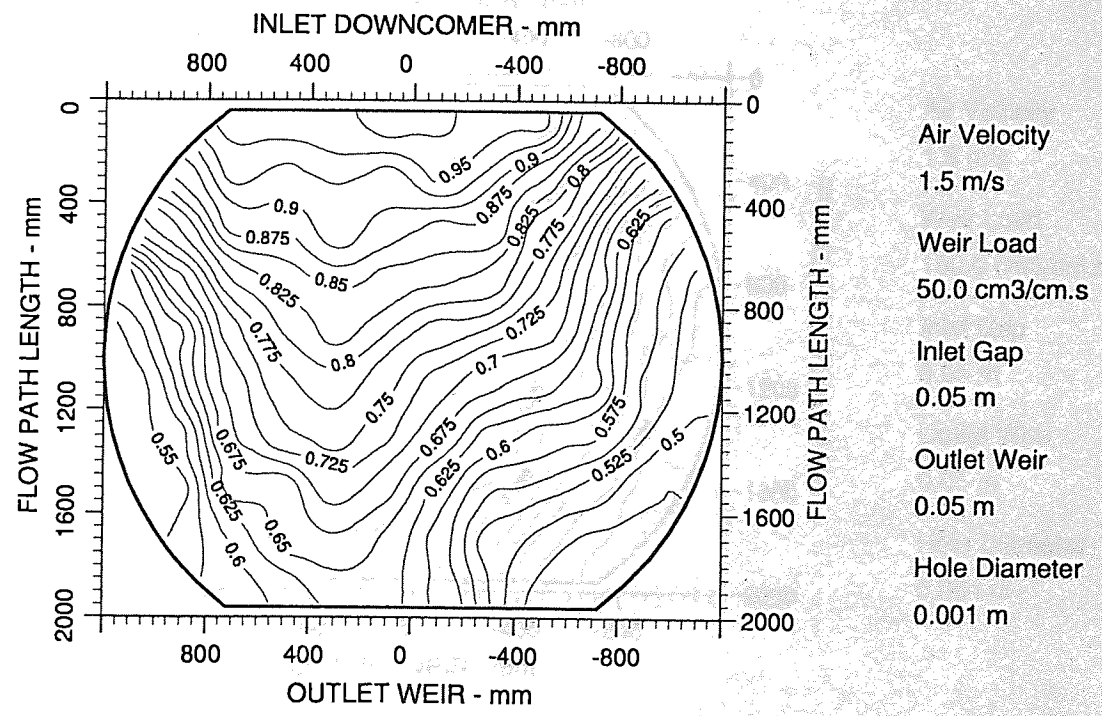

Figure A6.46 Two-dimensionl reduced temperature profiles for UMD-tray
Emv/Eog 92/67 hCL 33

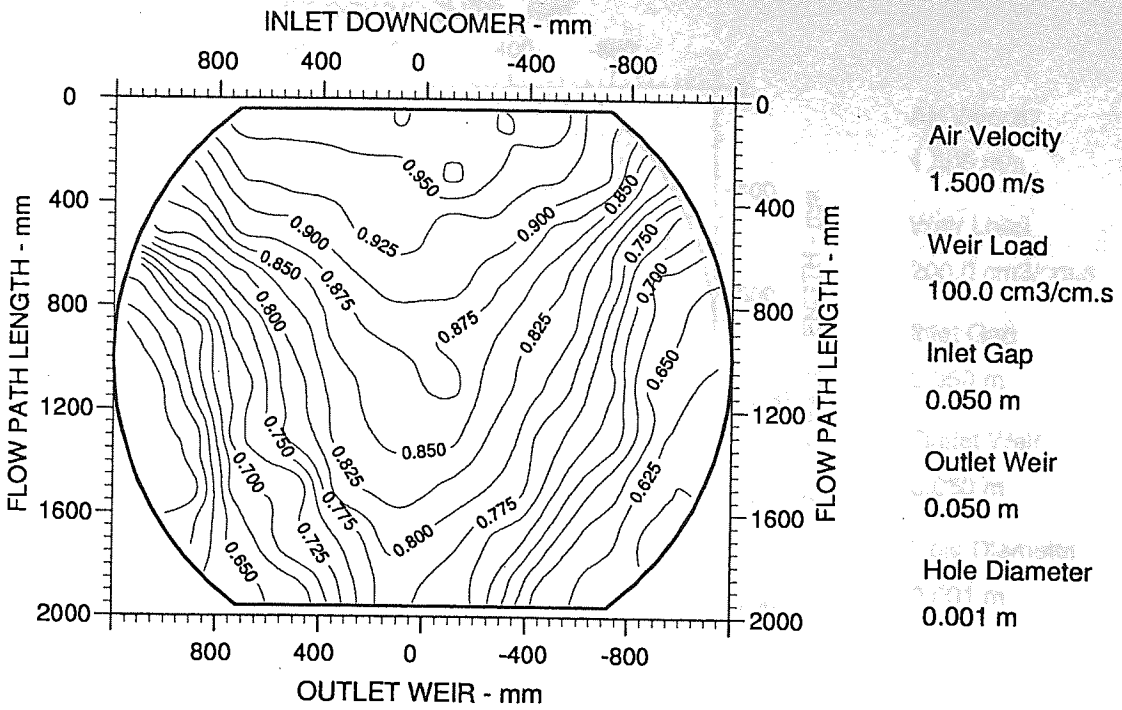

Figure A6.47 Two-dimensionl reduced temperature profiles for UMD-tray
Emv/Eog 104/83 hCL 37

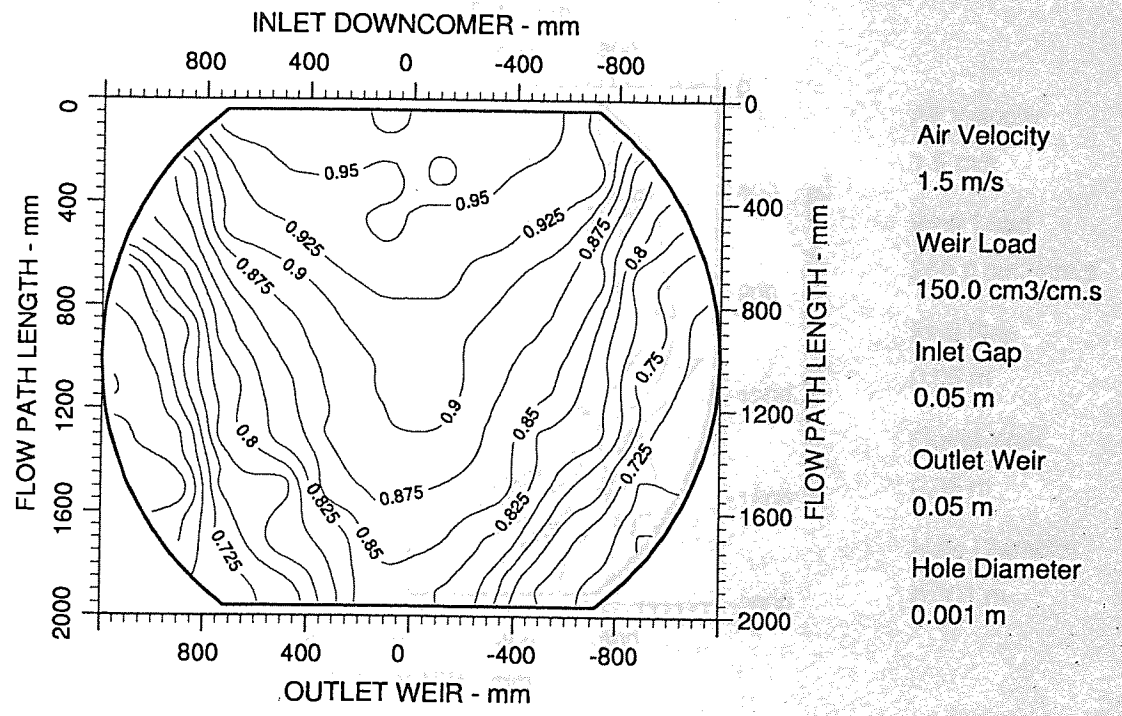

Figure A6.48 Two-dimensionl reduced temperature profiles for UMD-tray
Emv/Eog 105/89 hCL 40

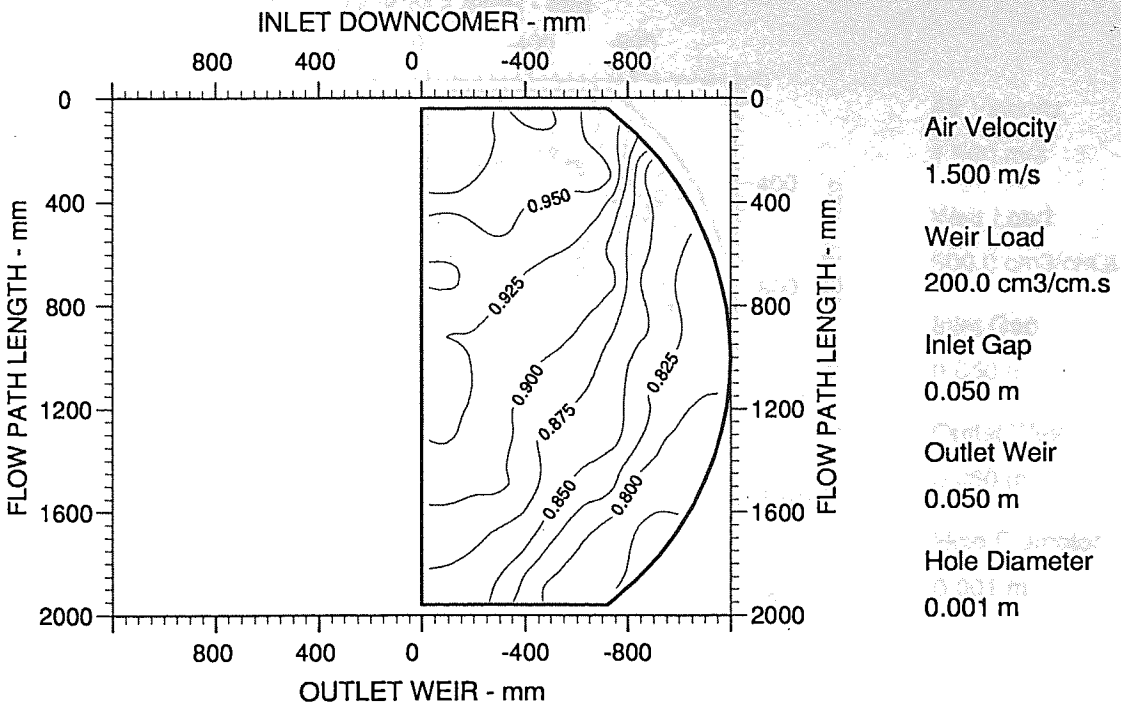

Figure A6.49 Two-dimensionl reduced temperature profiles for UMD-tray

Emv/Eog 105/93 hCL 54

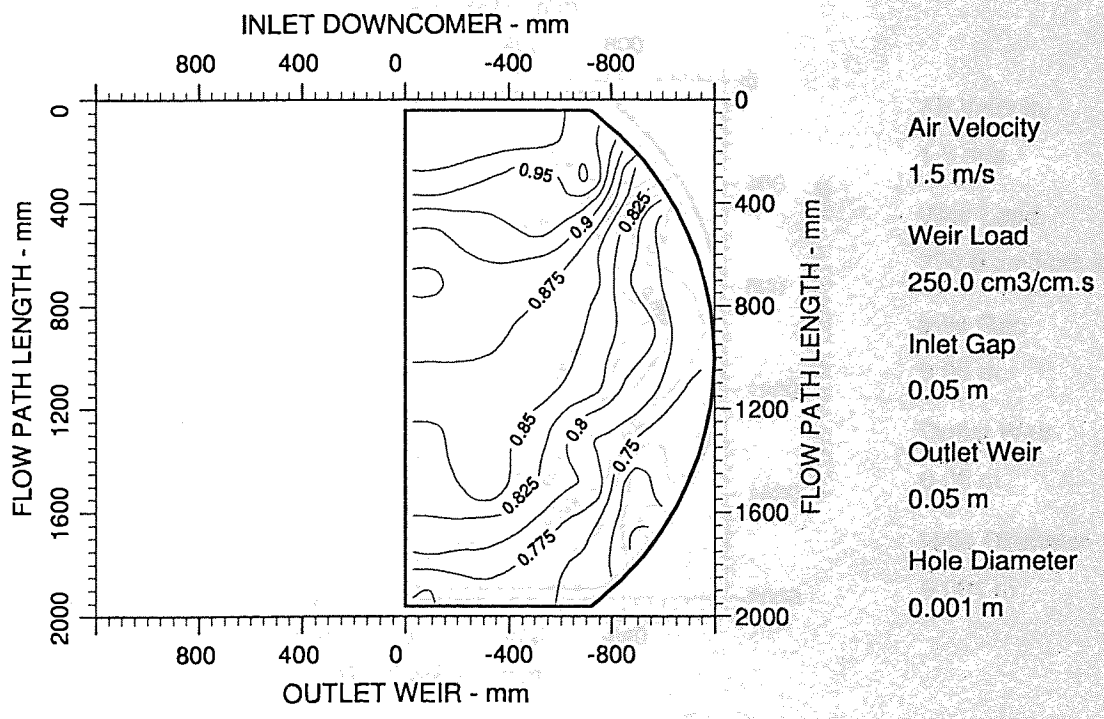

Figure A6.50 Two-dimensionl reduced temperature profiles for UMD-tray

Emv/Eog 101/94 hCL 60

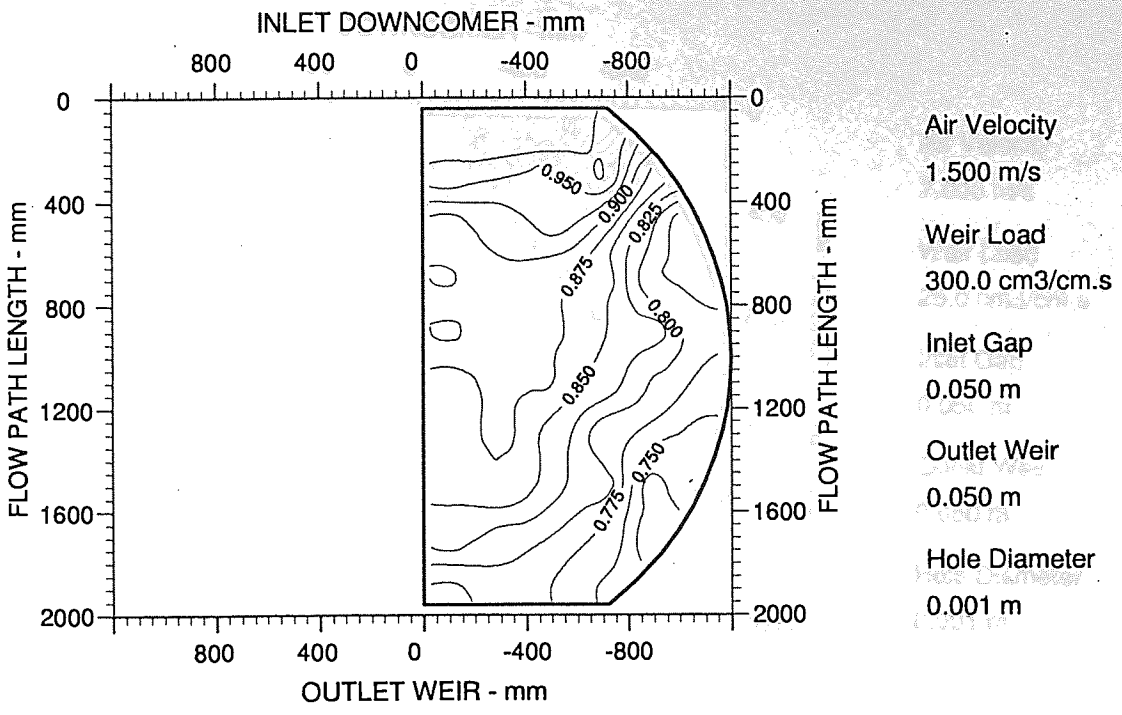

Figure A6.51 Two-dimensionl reduced temperature profiles for UMD-tray

Emv/Eog 99/95 hCL 70

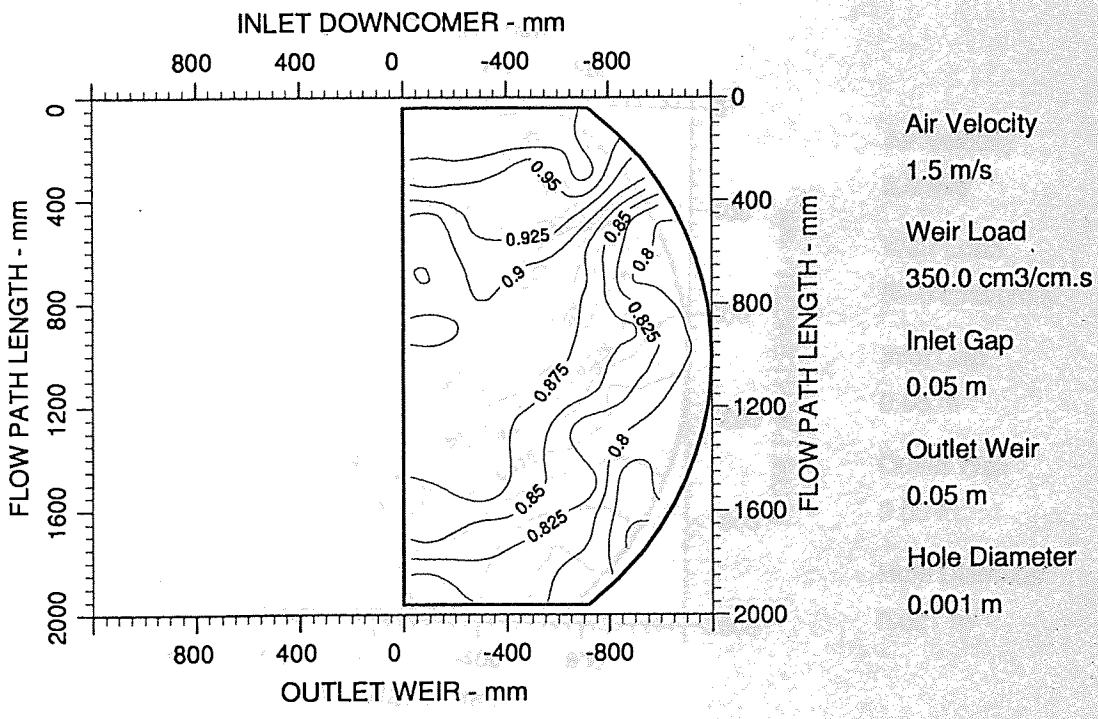

Figure A6.52 Two-dimensionl reduced temperature profiles for UMD-tray

Emv/Eog 101/97 hCL 73

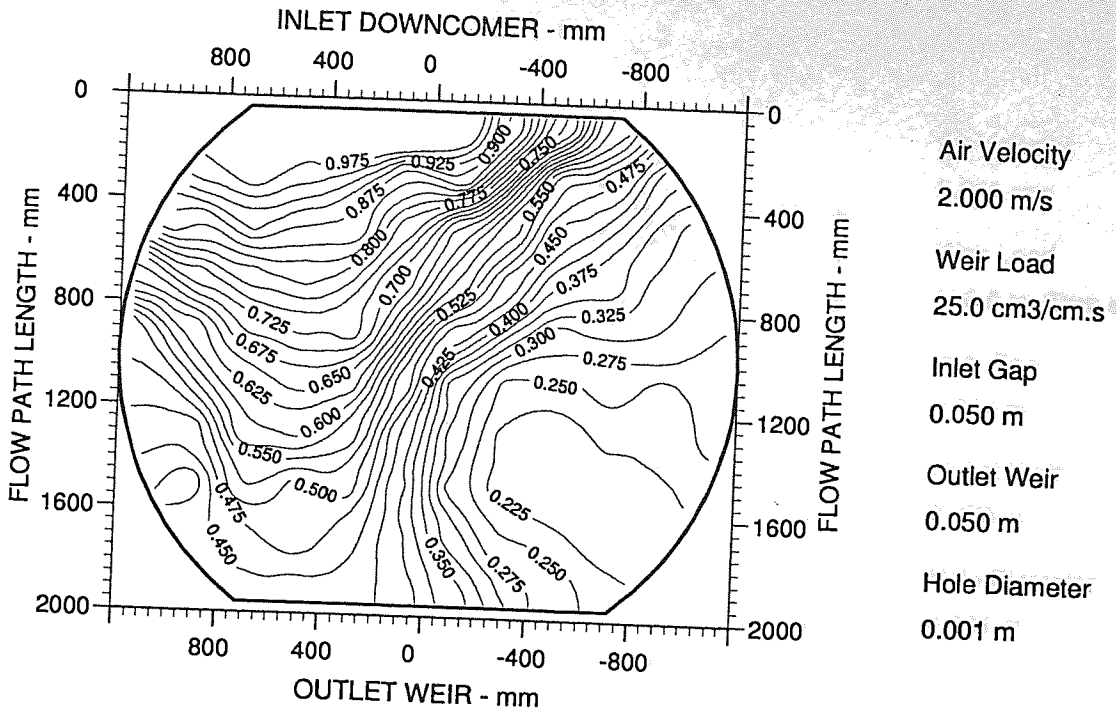

Figure A6.53 Two-dimensionl reduced temperature profiles for UMD-tray
Emv/Eog 76/48 hCL 22

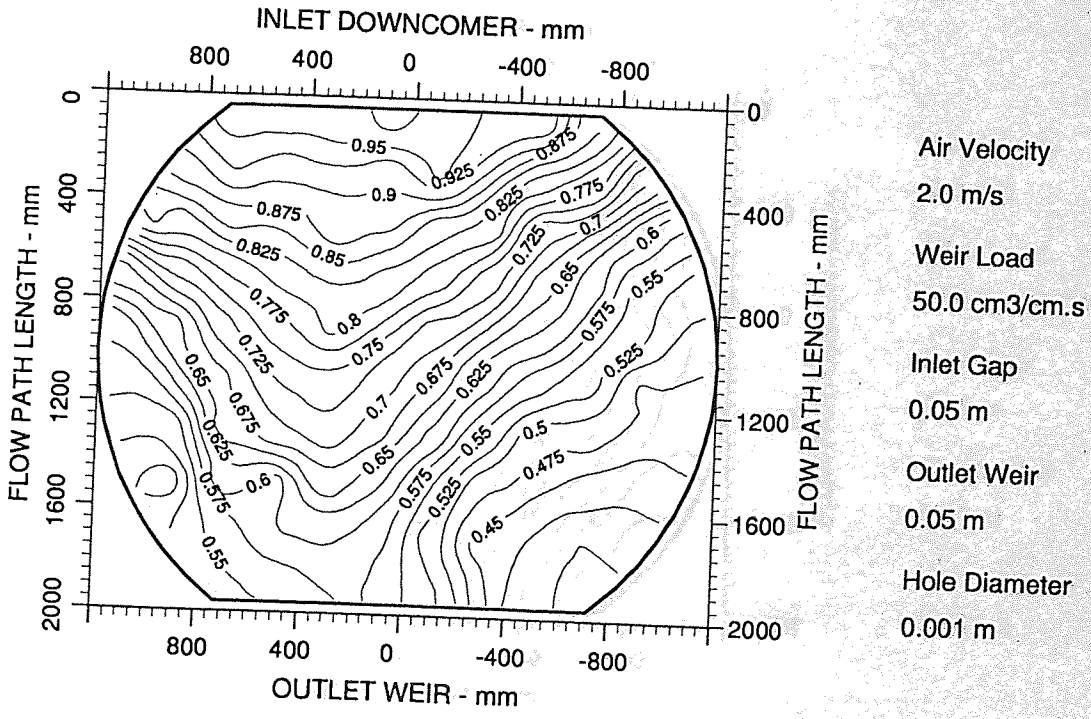

Figure A6.54 Two-dimensionl reduced temperature profiles for UMD-tray
Emv/Eog 90/64 hCL 27

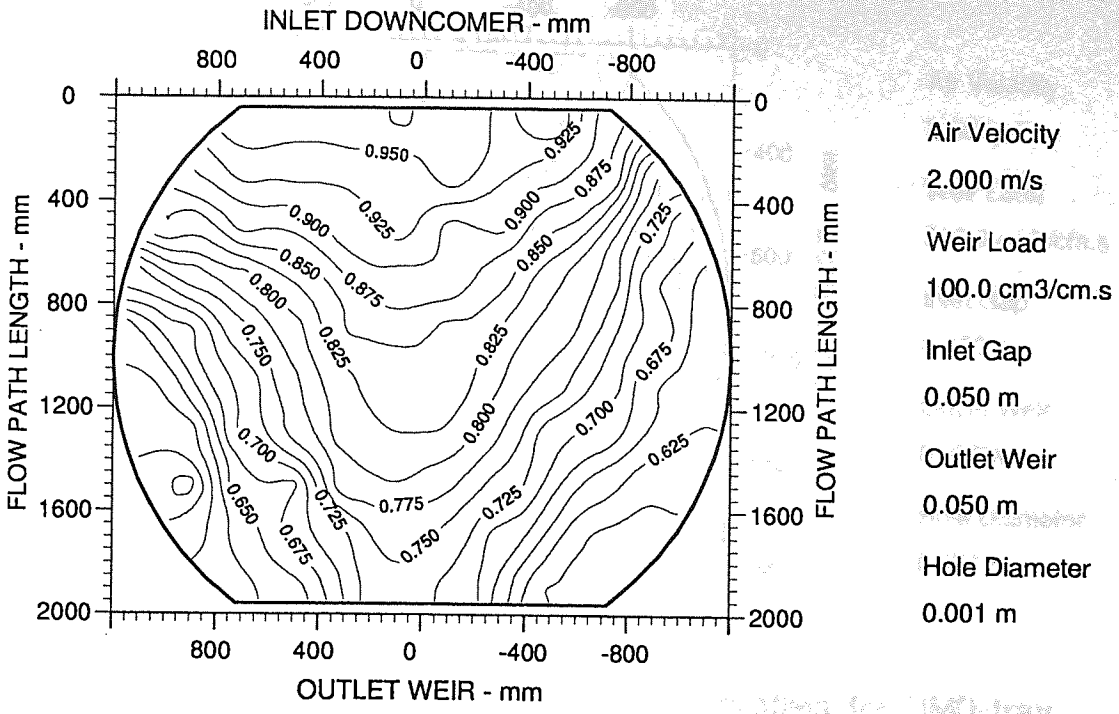

Figure A6.55 Two-dimensionl reduced temperature profiles for UMD-tray

Emv/Eog 93/74 hCL 31

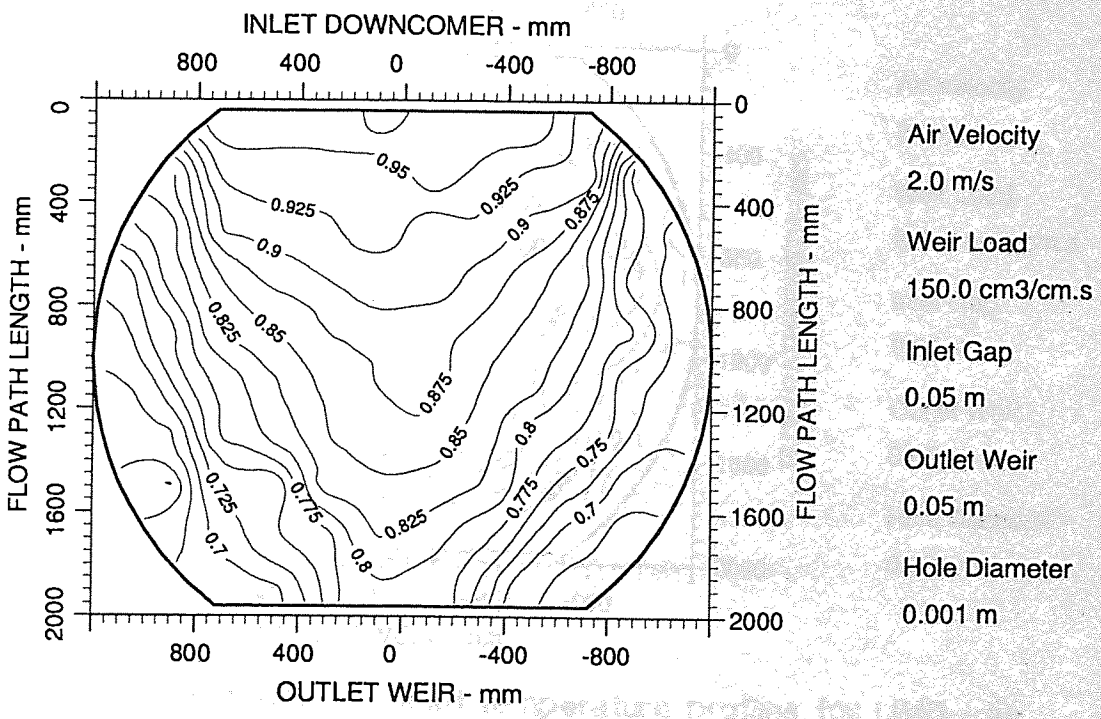

Figure A6.56 Two-dimensionl reduced temperature profiles for UMD-tray

Emv/Eog 101/84 hCL 33

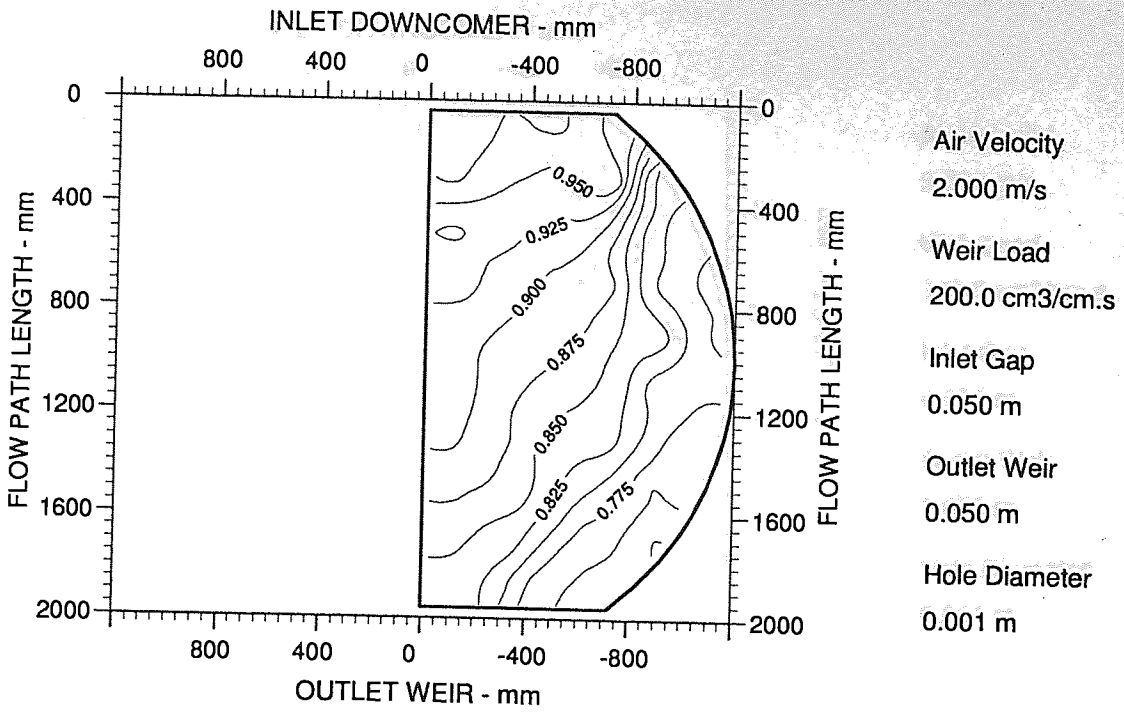

Figure A6.57 Two-dimensionl reduced temperature profiles for UMD-tray
Emv/Eog 101/88 hCL 35

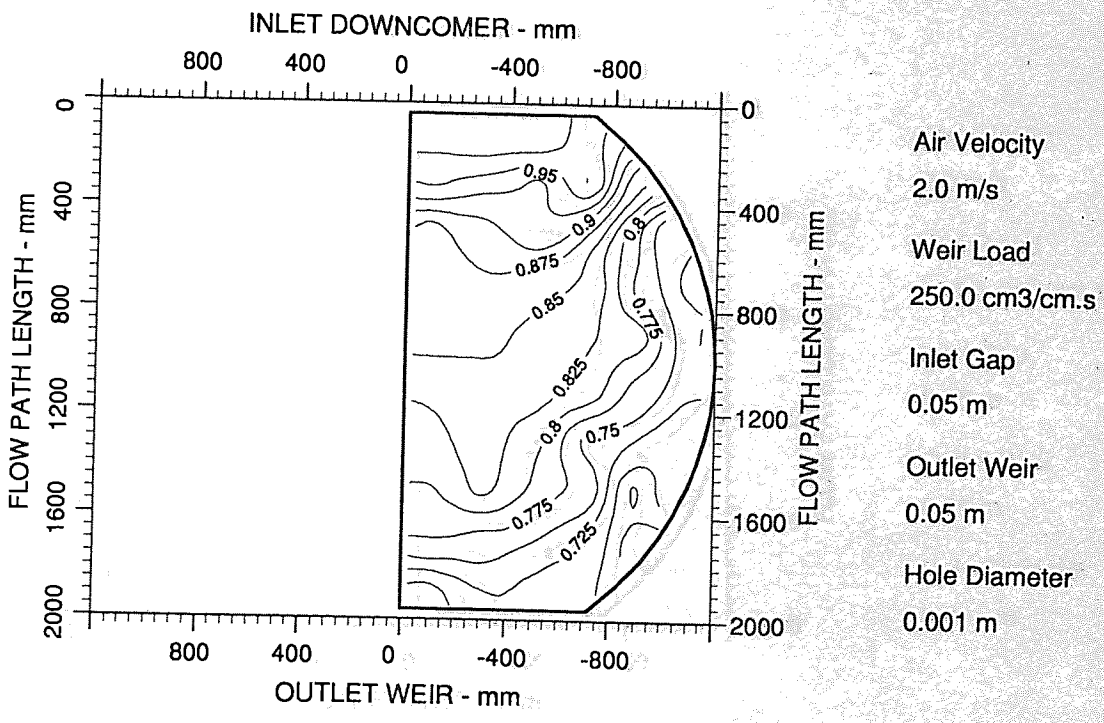

Figure A6.58 Two-dimensionl reduced temperature profiles for UMD-tray
Emv/Eog 102/91 hCL 47

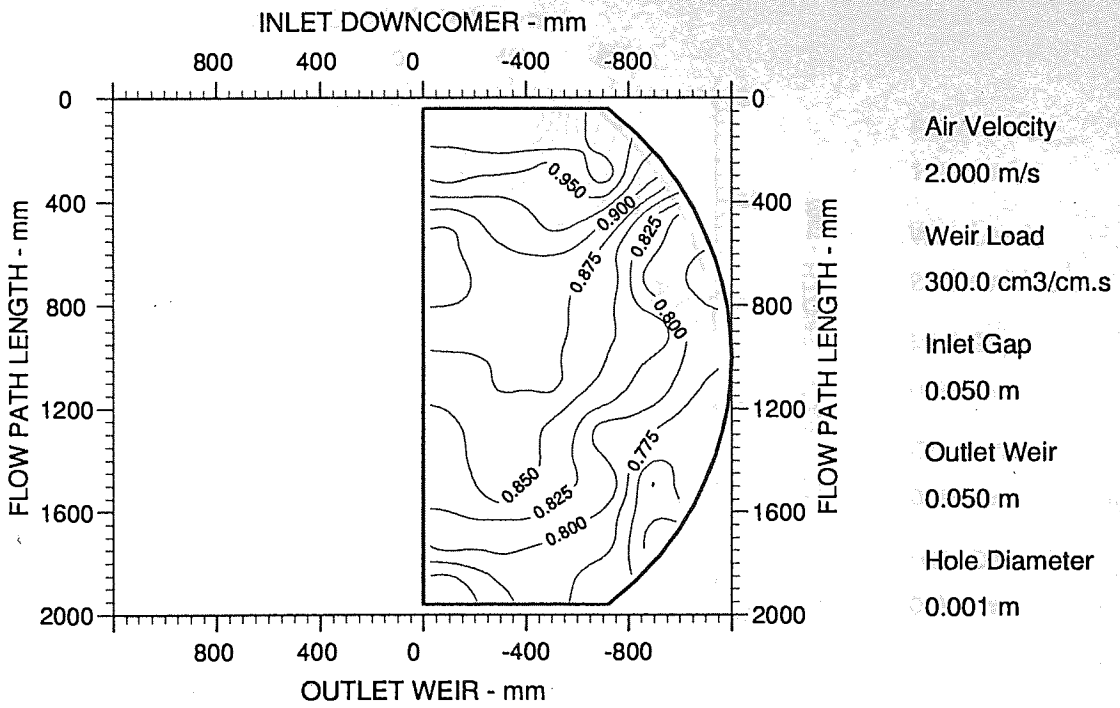

Figure A6.59 Two-dimensionl reduced temperature profiles for UMD-tray
Emv/Eog 102/94 hCL 55

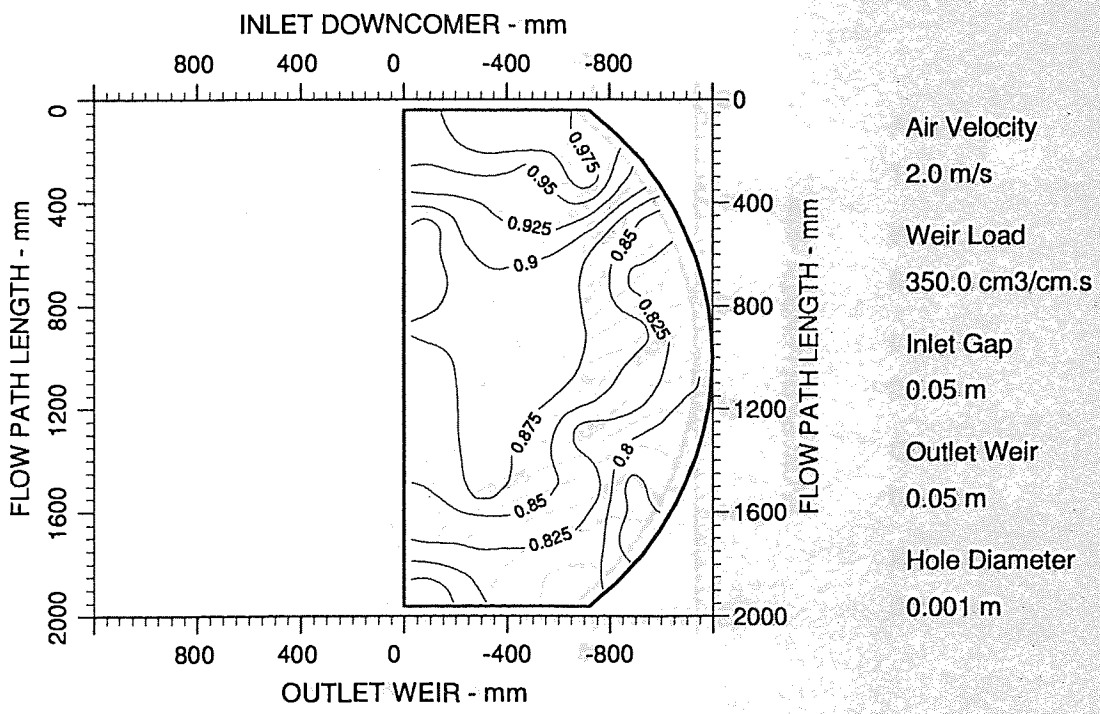

Figure A6.60 Two-dimensionl reduced temperature profiles for UMD-tray
Emv/Eog 103/97 hCL 70

Appendix 7

Two-Dimensional Reduced Temperature Isotherm Displays for the STR-1 Tray Cases

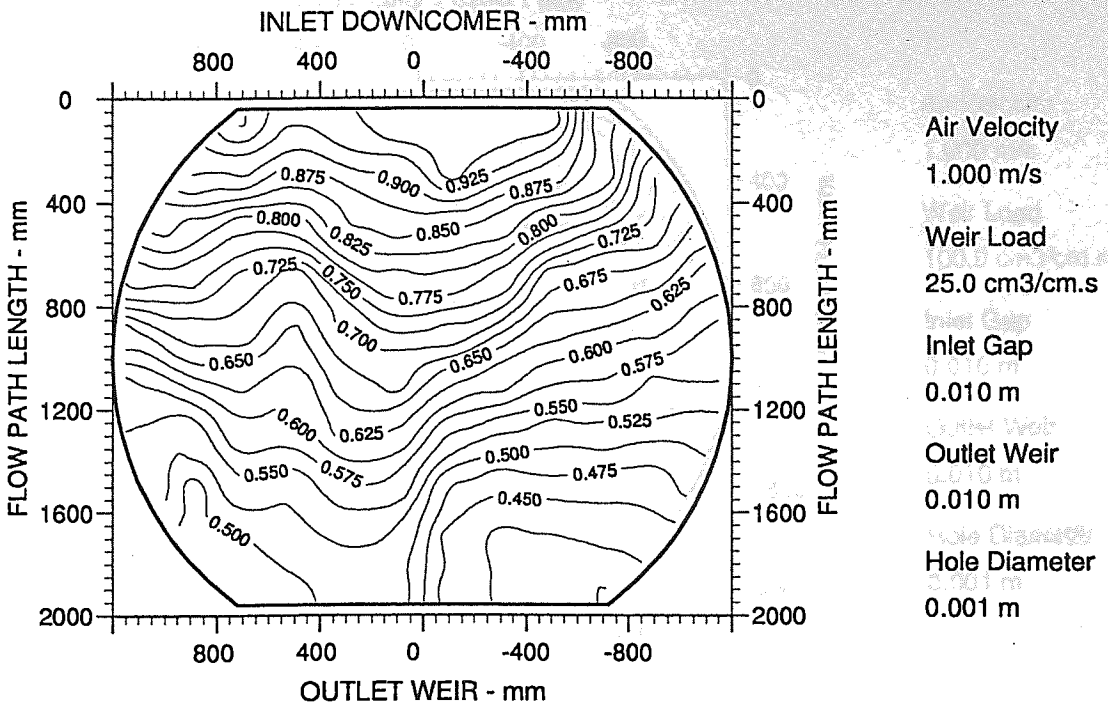

Figure A7.1 Two-dimensionl reduced temperature profiles for STR-1 tray
Emv/Eog 92/56 hCL 22

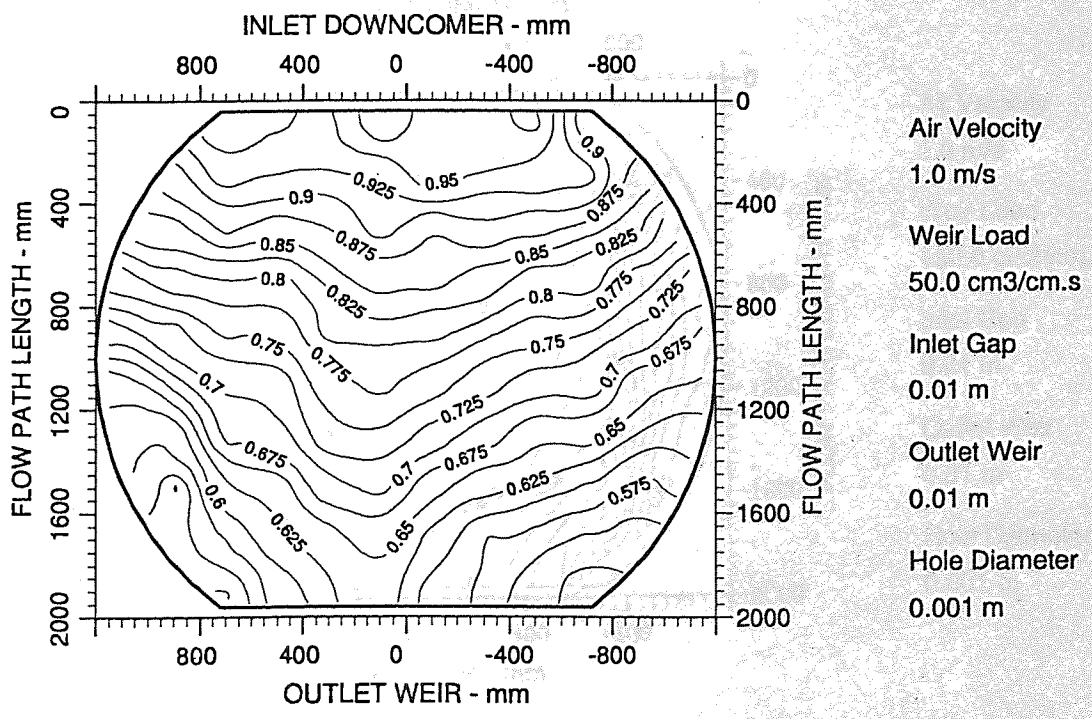

Figure A7.2 Two-dimensionl reduced temperature profiles for STR-1 tray
Emv/Eog 109/72 hCL 27

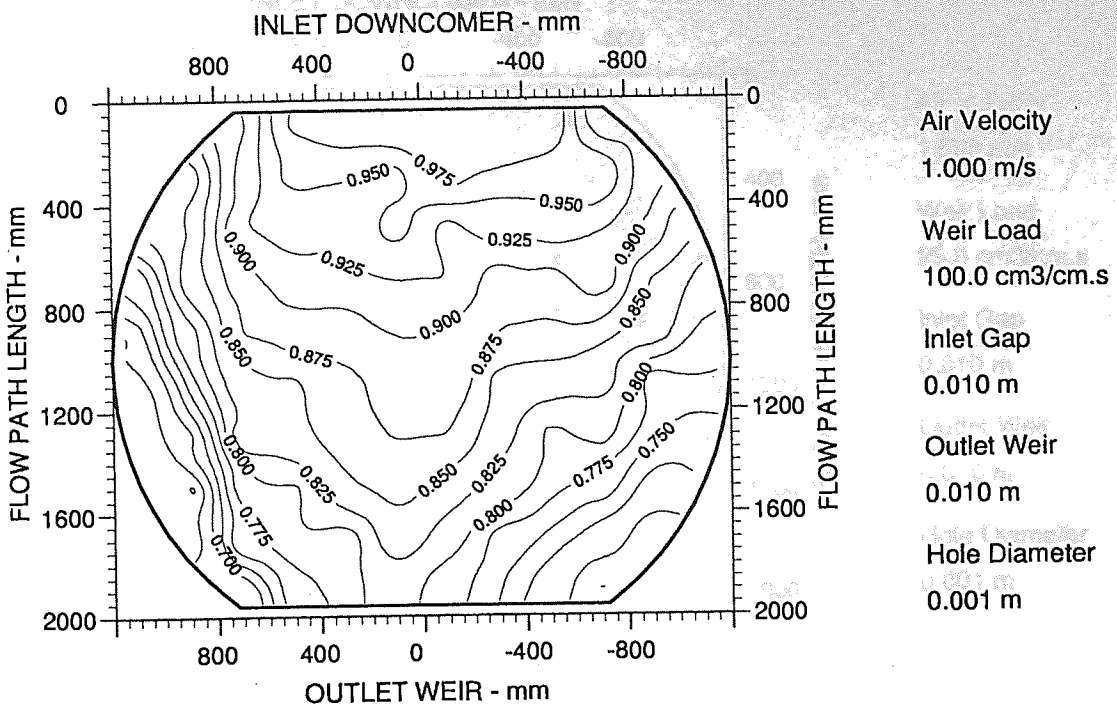

Figure A7.3 Two-dimensionl reduced temperature profiles for STR-1 tray

Emv/Eog 102/82 hCL 32

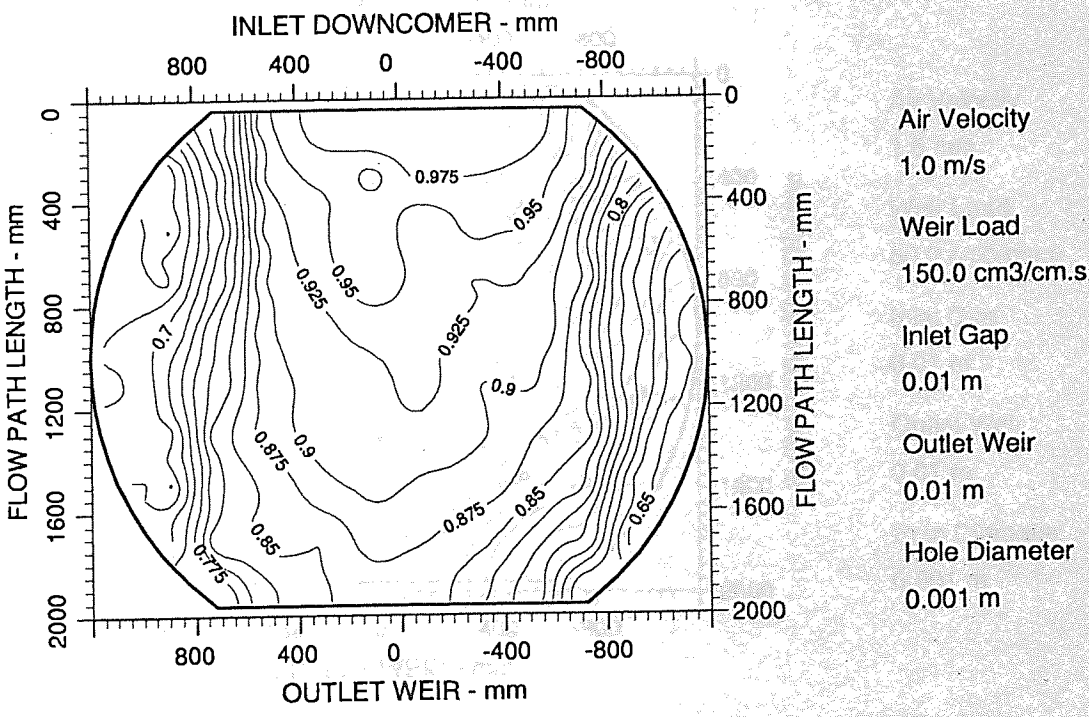

Figure A7.4 Two-dimensionl reduced temperature profiles for STR-1 tray

Emv/Eog 98/90 hCL 34

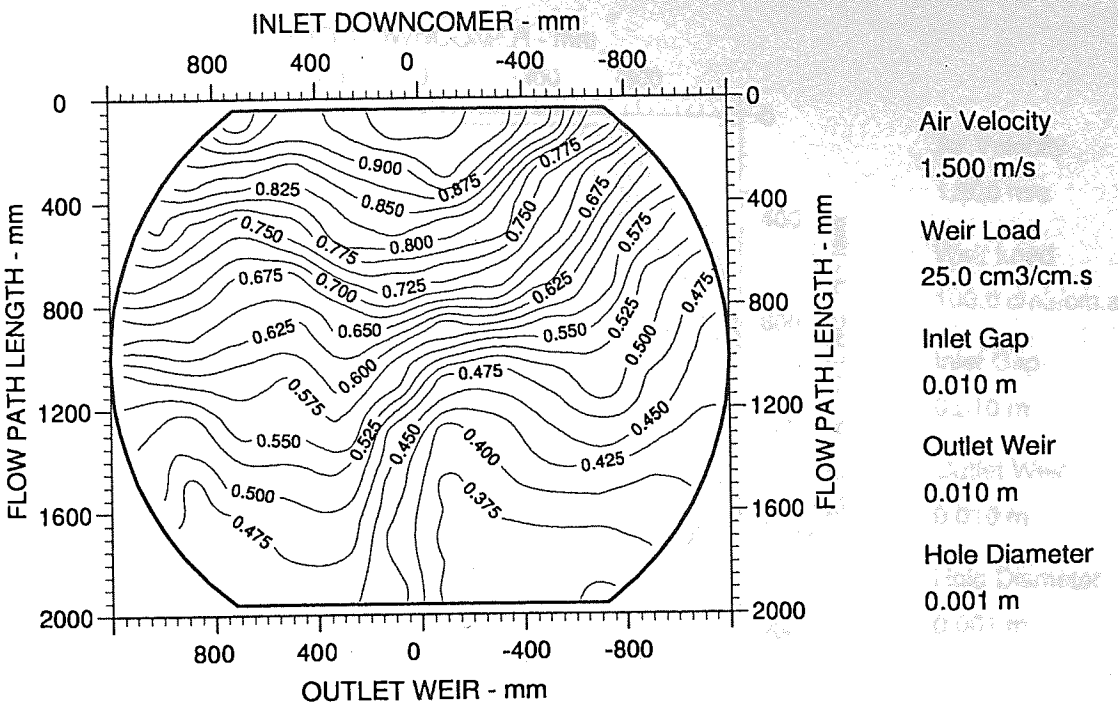

Figure A7.5 Two-dimensionl reduced temperature profiles for STR-1 tray

Emv/Eog 84/49 hCL 21

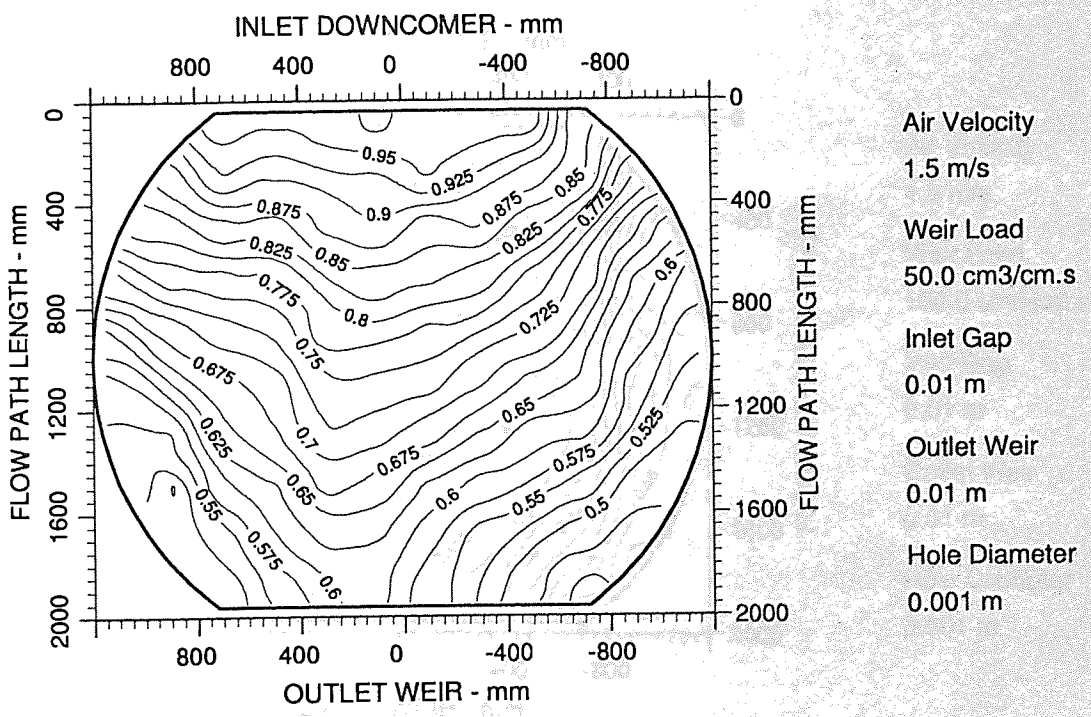

Figure A7.6 Two-dimensionl reduced temperature profiles for STR-1 tray

Emv/Eog 99/63 hCL 22

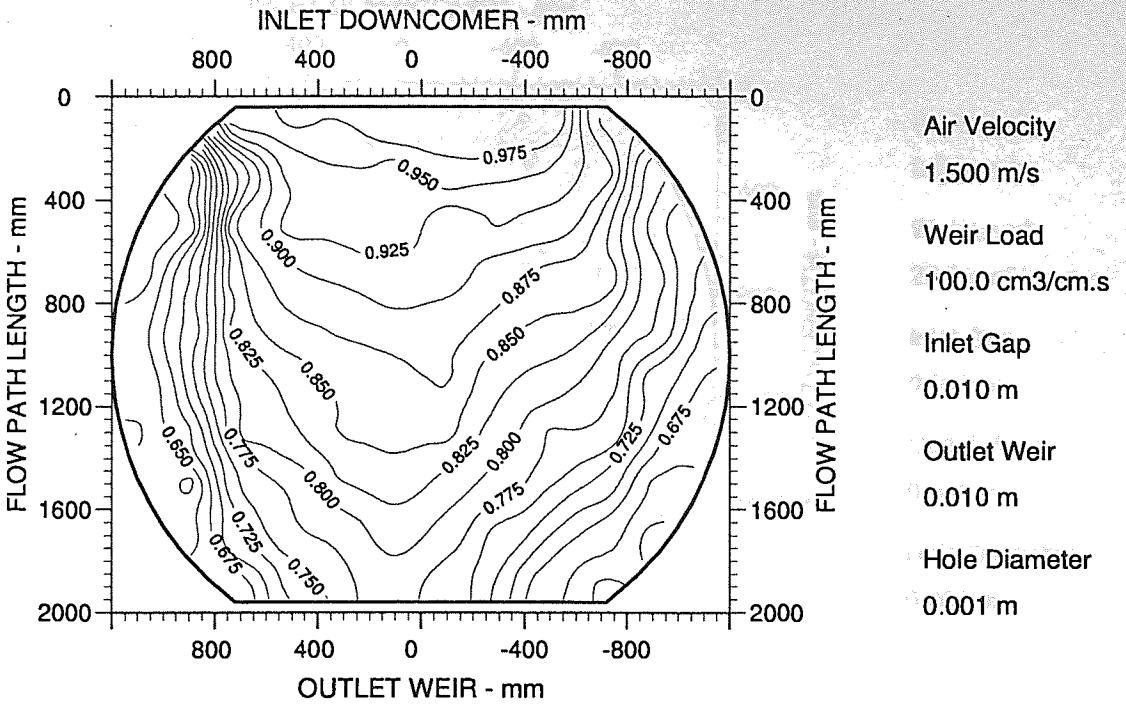

Figure A7.7 Two-dimensionl reduced temperature profiles for STR-1 tray

Emv/Eog 90/73 hCL 26

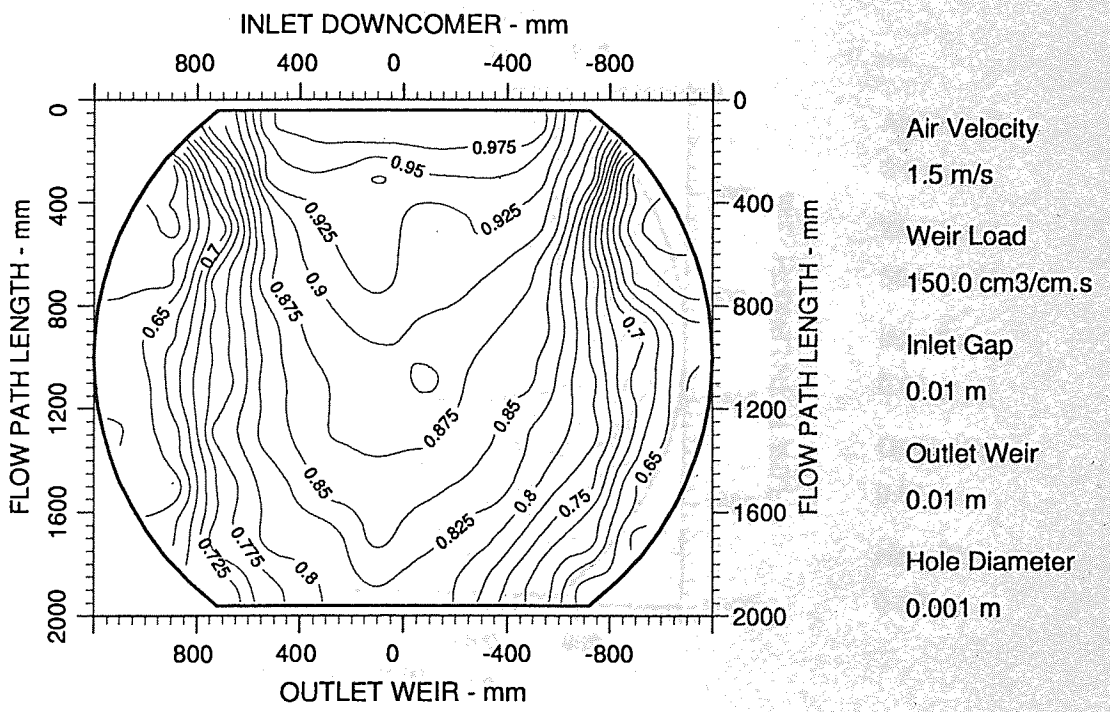

Figure A7.8 Two-dimensionl reduced temperature profiles for STR-1 tray

Emv/Eog 93/83 hCL 29

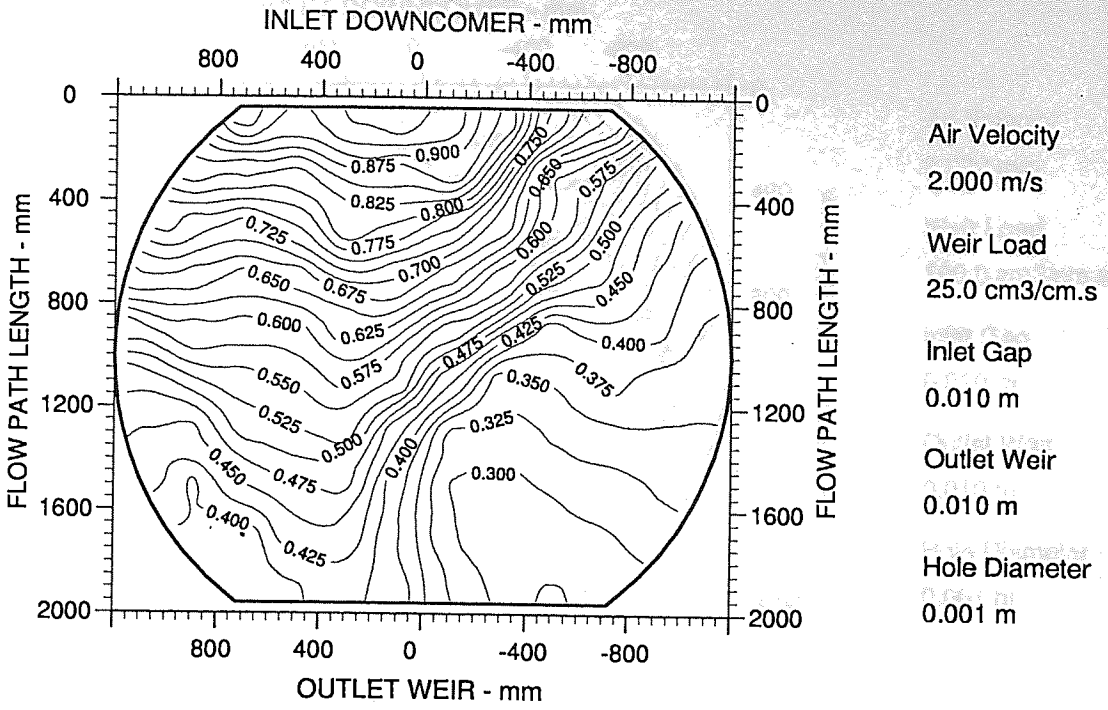

Figure A7.9 Two-dimensionl reduced temperature profiles for STR-1 tray

Emv/Eog 83/45 hCL 17

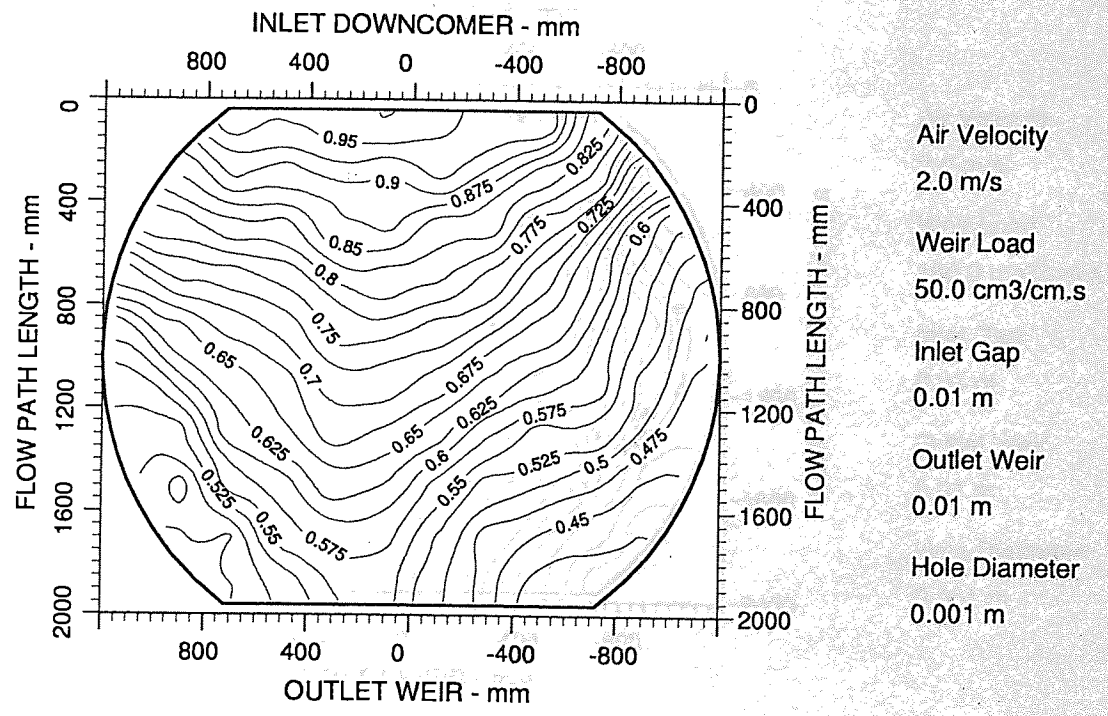

Figure A7.10 Two-dimensionl reduced temperature profiles for STR-1 tray

Emv/Eog 88/55 hCL 18

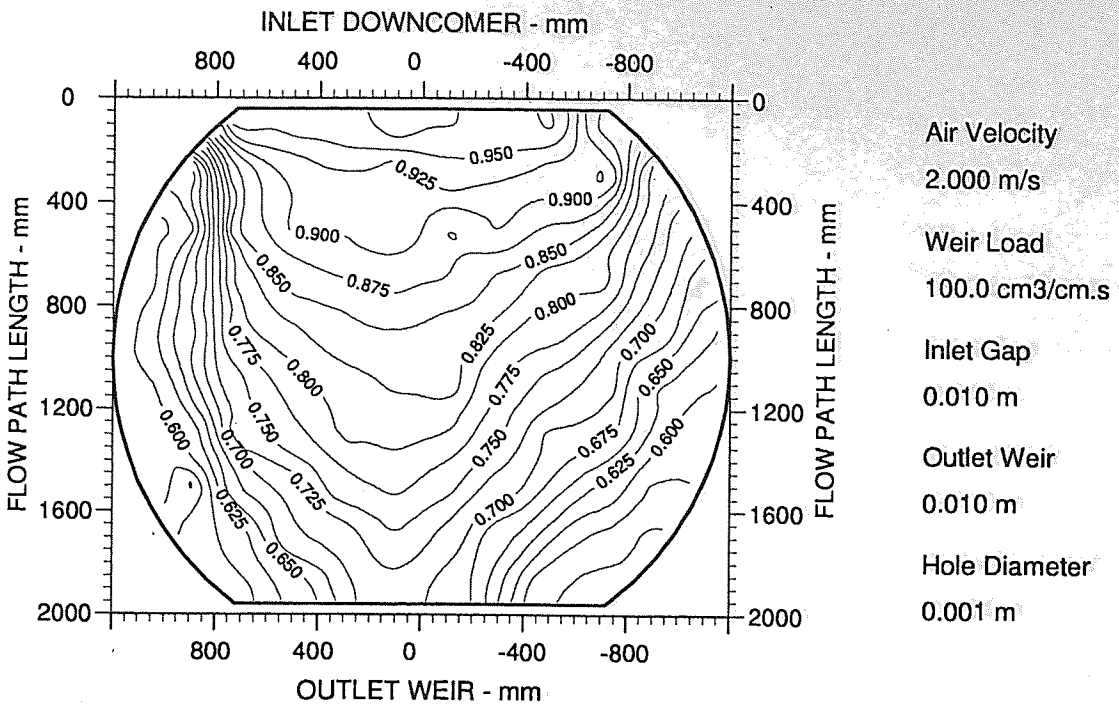

Figure A7.11 Two-dimensionl reduced temperature profiles for STR-1 tray
Emv/Eog 94/72 hCL 21

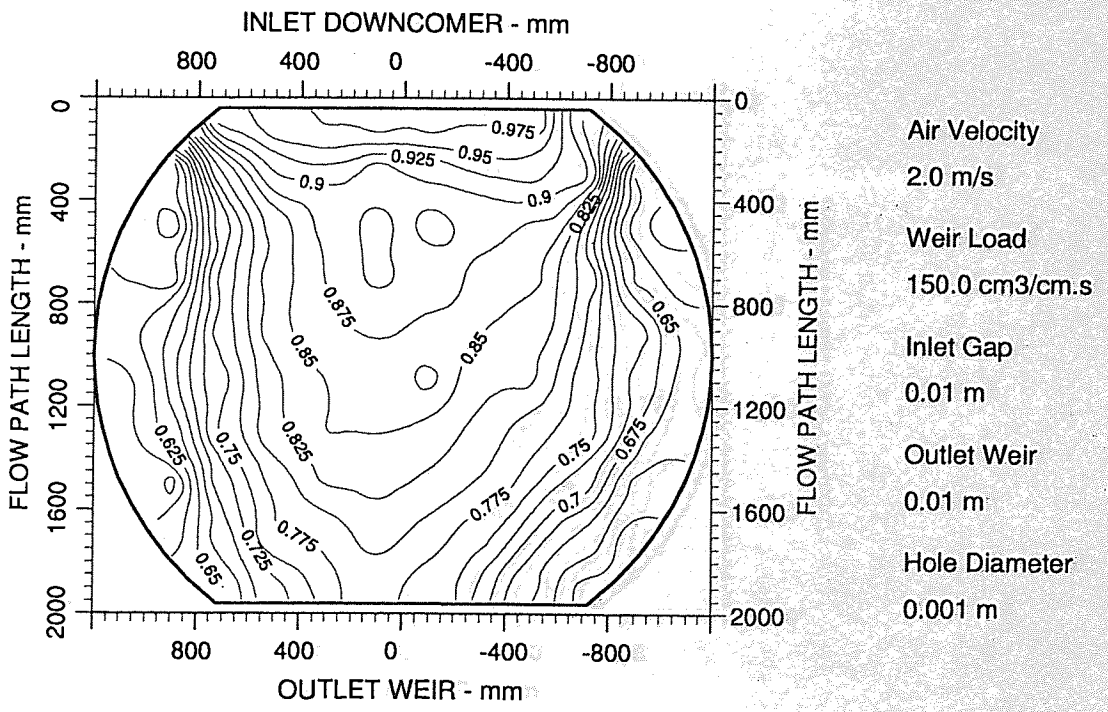

Figure A7.12 Two-dimensionl reduced temperature profiles for STR-1 tray
Emv/Eog 94/79 hCL 22

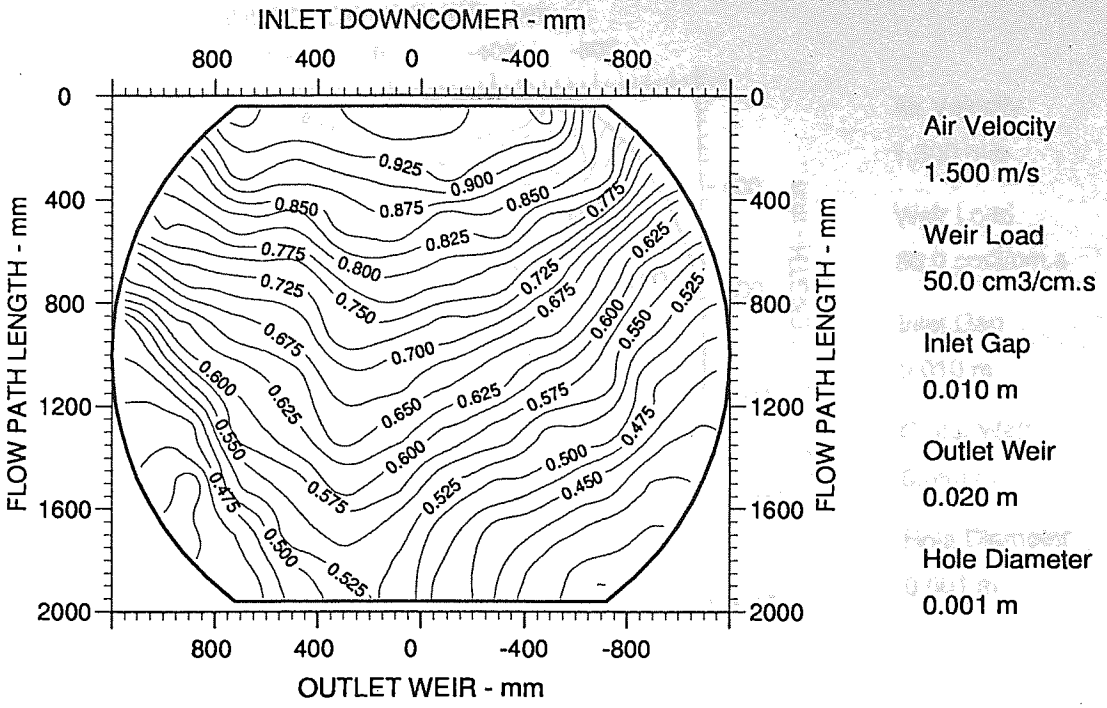

Figure A7.13 Two-dimensionl reduced temperature profiles for STR-1 tray

Emv/Eog 114/67 hCL 23

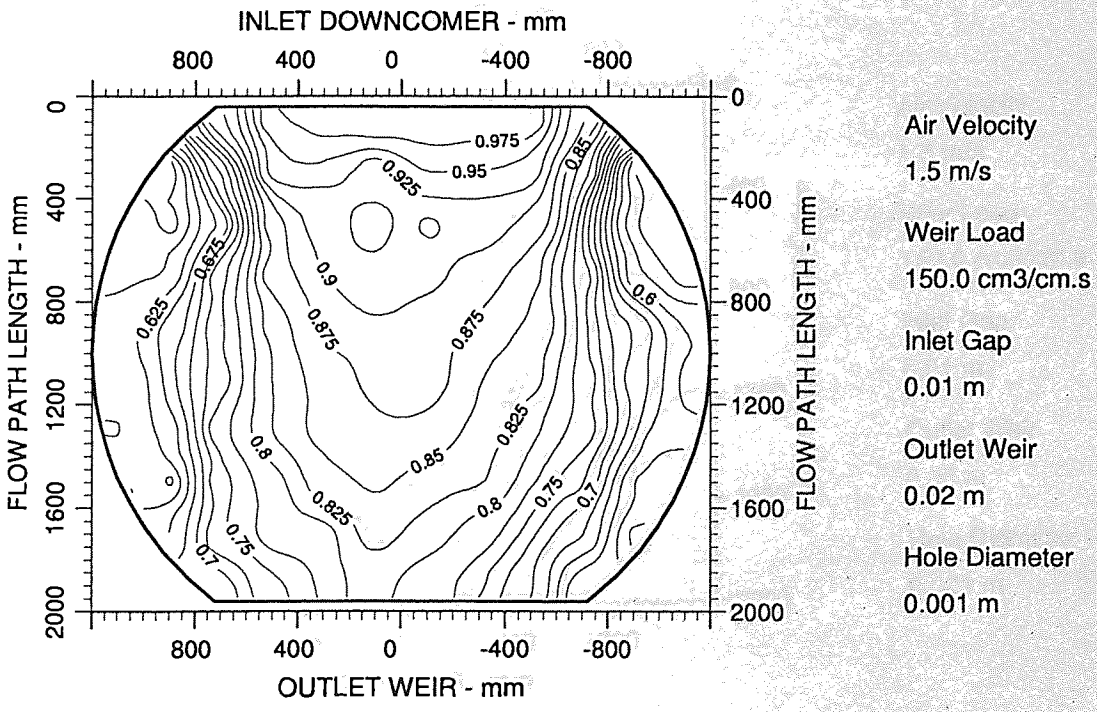

Figure A7.14 Two-dimensionl reduced temperature profiles for STR-1 tray

Emv/Eog 94/84 hCL 34

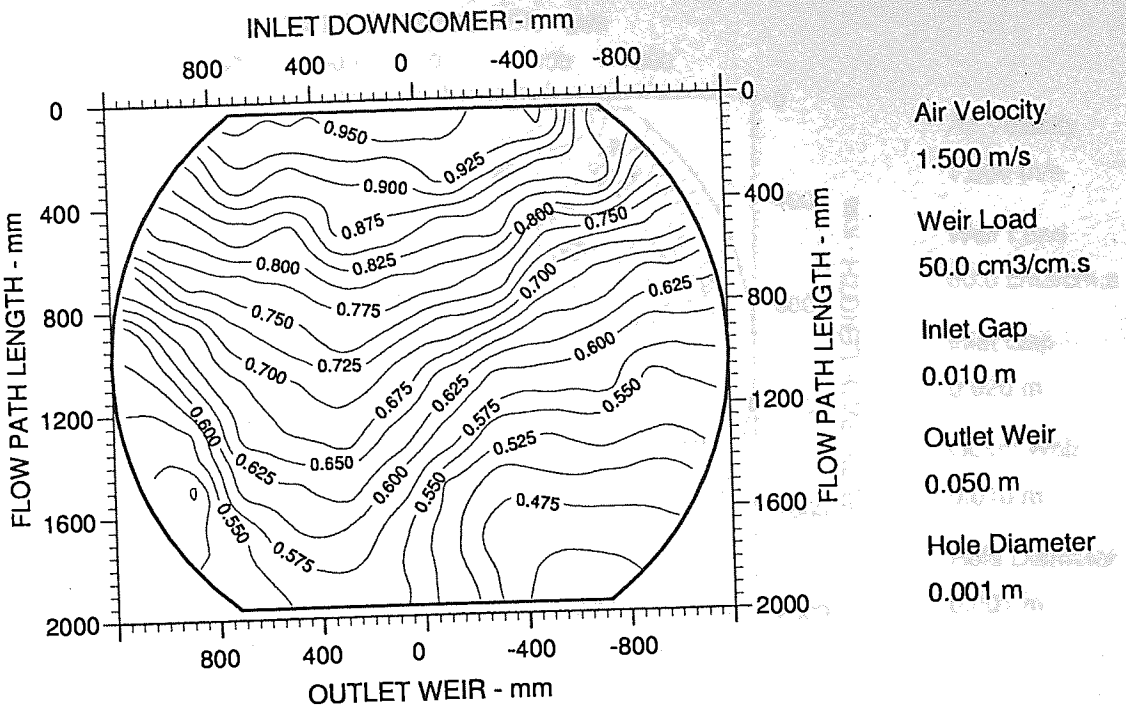

Figure A7.15 Two-dimensionl reduced temperature profiles for STR-1 tray

Emv/Eog 104/69 hCL 32

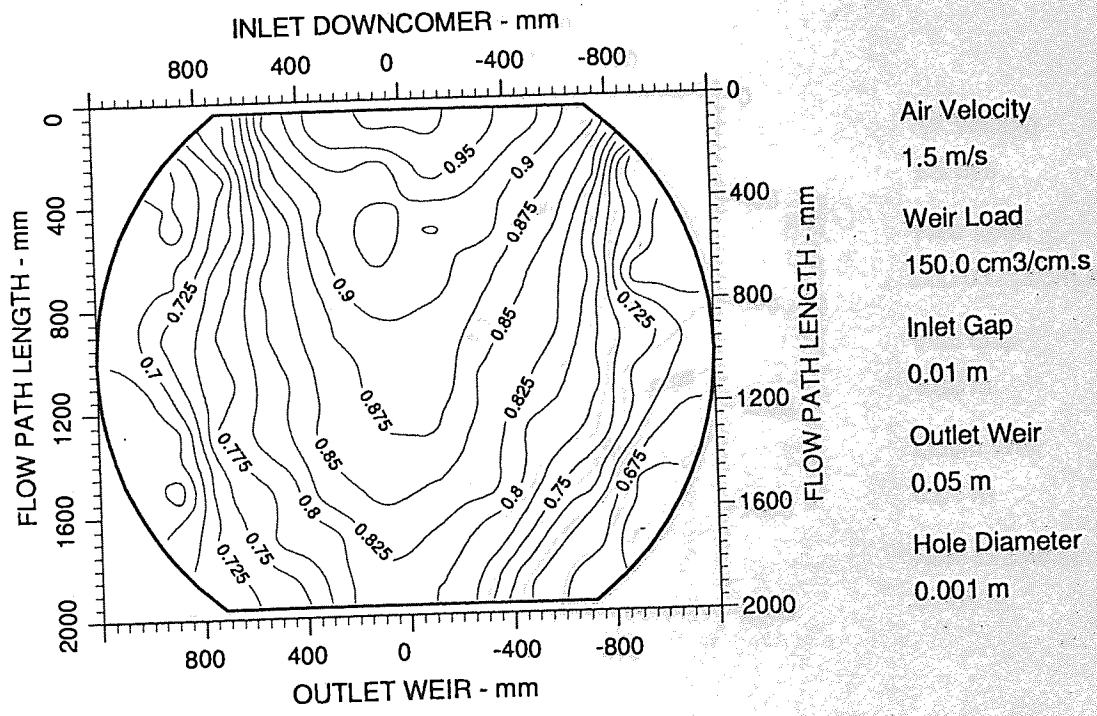

Figure A7.16 Two-dimensionl reduced temperature profiles for STR-1 tray

Emv/Eog 103/91 hCL 41

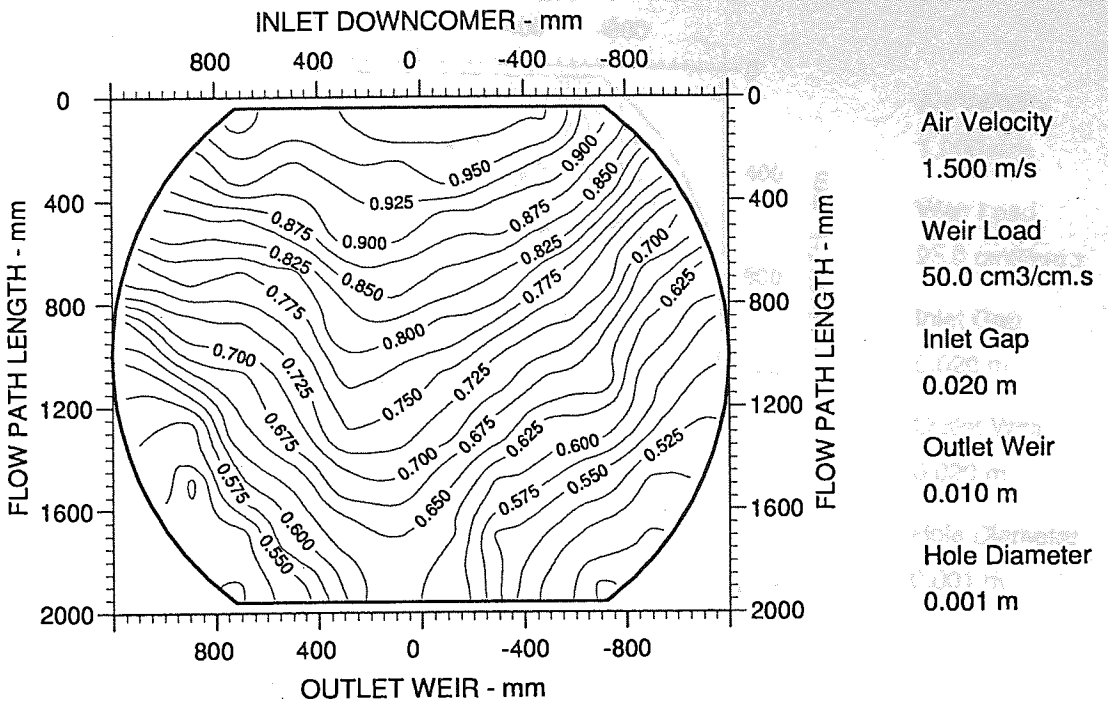

Figure A7.17 Two-dimensionl reduced temperature profiles for STR-1 tray

Emv/Eog 82/56 hCL 23

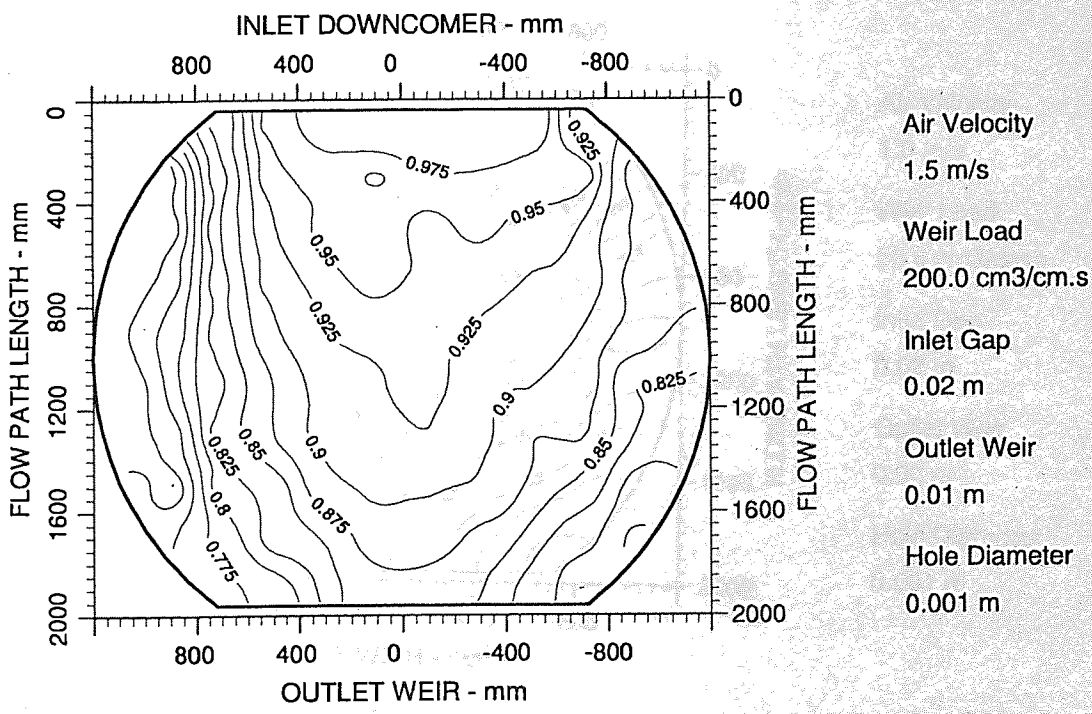

Figure A7.18 Two-dimensionl reduced temperature profiles for STR-1 tray

Emv/Eog 84/76 hCL 41

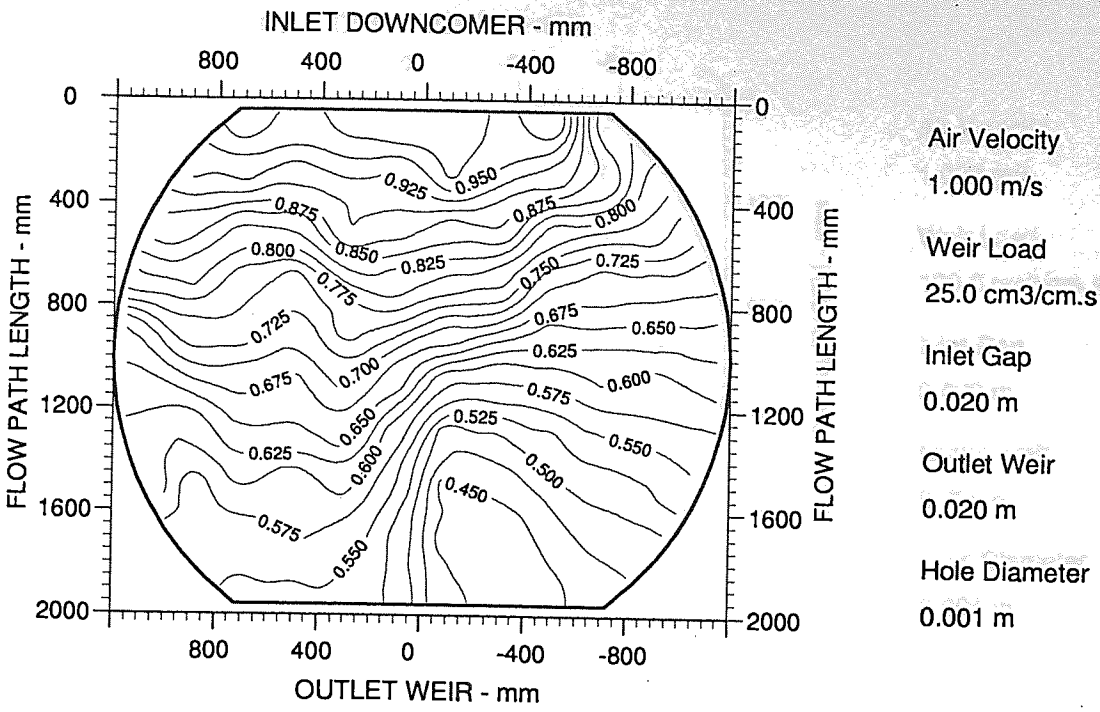

Figure A7.19 Two-dimensionl reduced temperature profiles for STR-1 tray
Emv/Eog 86/54 hCL 23

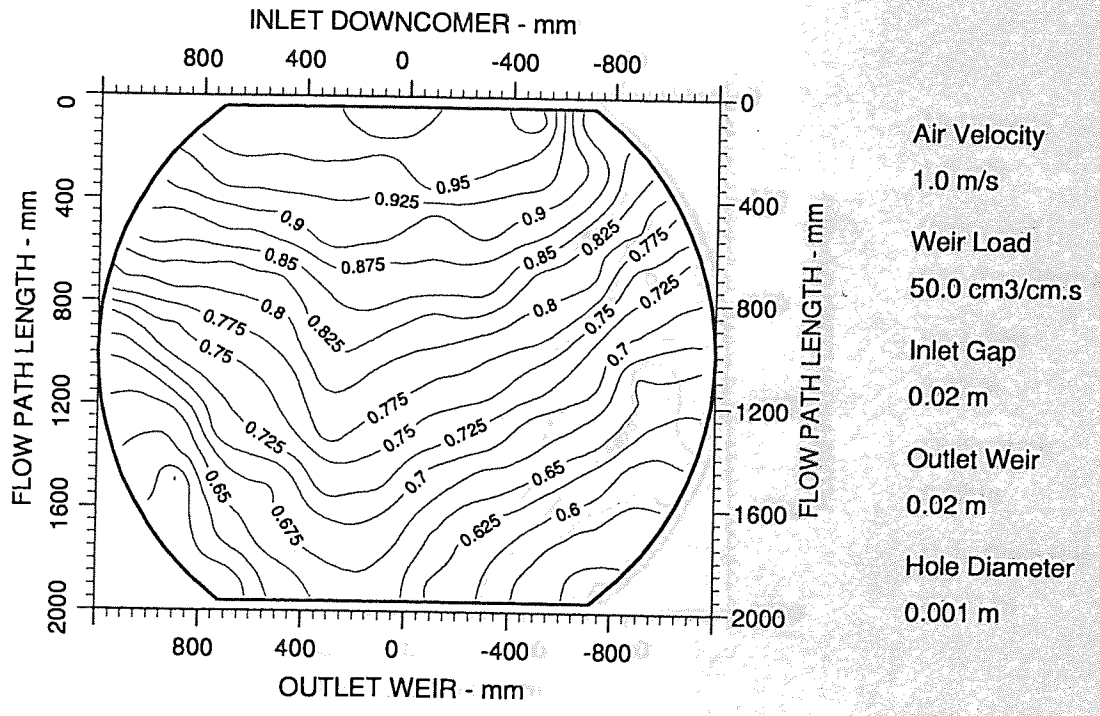

Figure A7.20 Two-dimensionl reduced temperature profiles for STR-1 tray
Emv/Eog 103/70 hCL 29

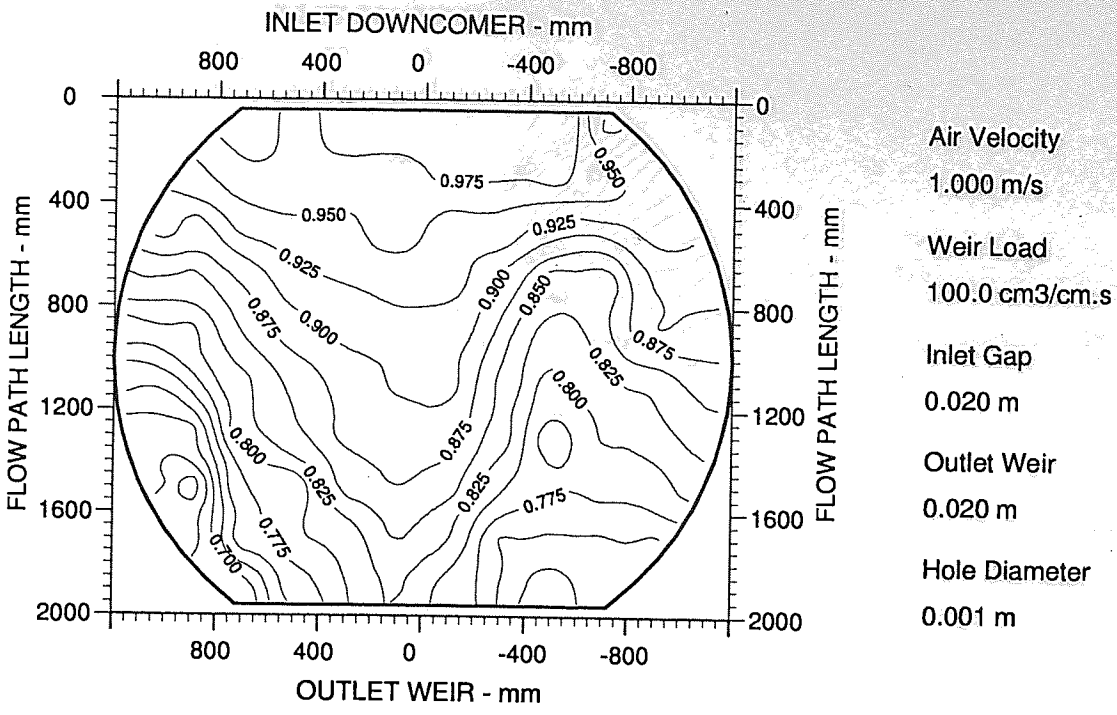

Figure A7.21 Two-dimensionl reduced temperature profiles for STR-1 tray
Emv/Eog 94/76 hCL 35

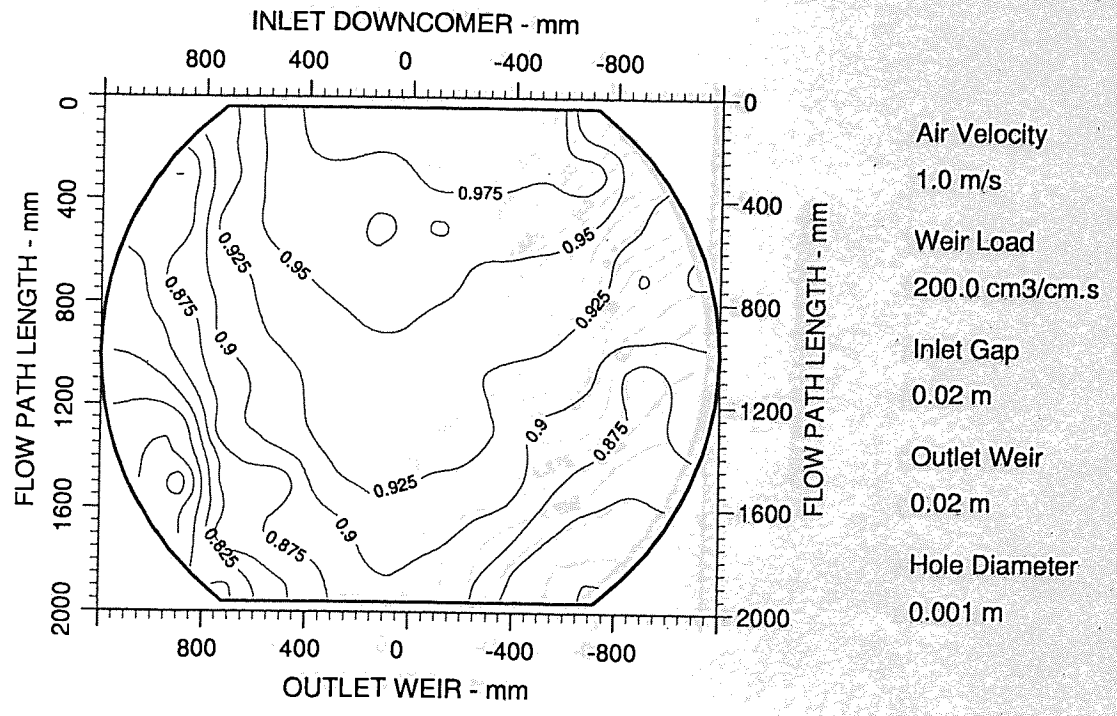

Figure A7.22 Two-dimensionl reduced temperature profiles for STR-1 tray
Emv/Eog 102/90 hCL 46

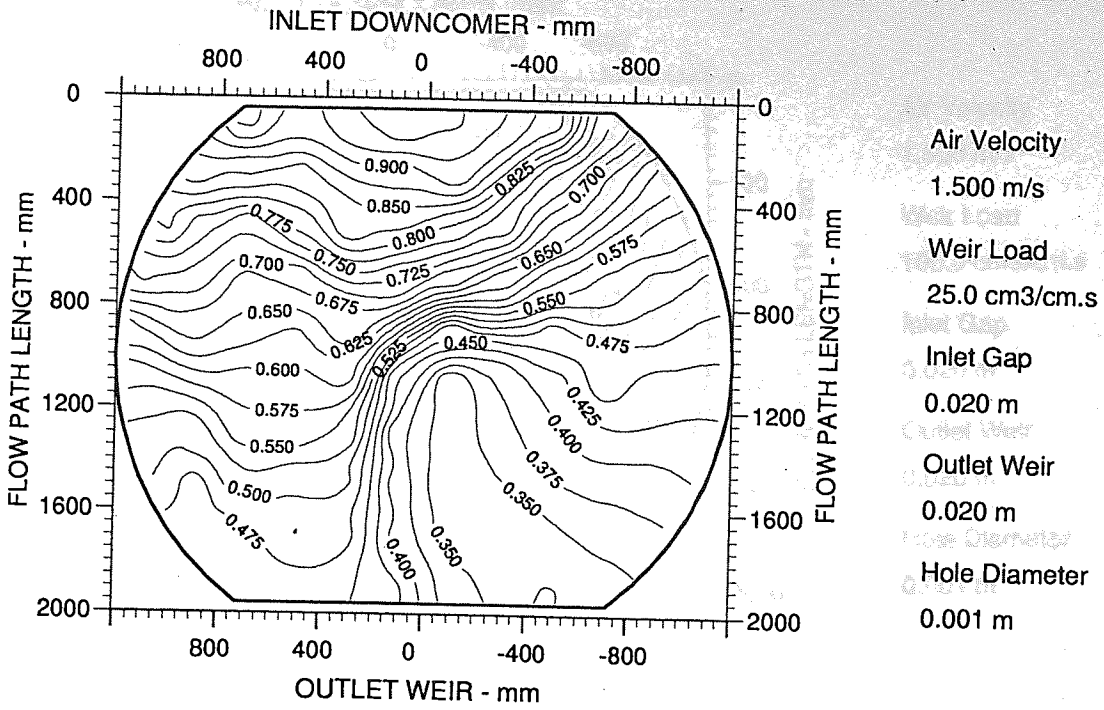

Figure A7.23 Two-dimensionl reduced temperature profiles for STR-1 tray
Emv/Eog 86/50 hCL 23

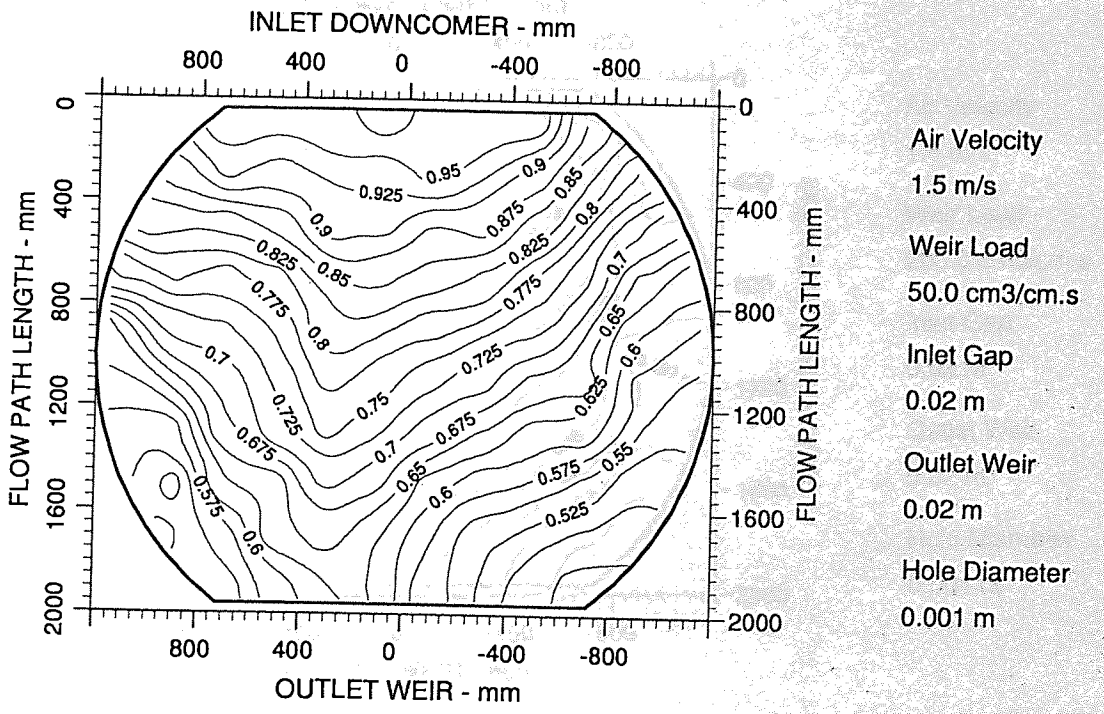

Figure A7.24 Two-dimensionl reduced temperature profiles for STR-1 tray
Emv/Eog 88/60 hCL 27

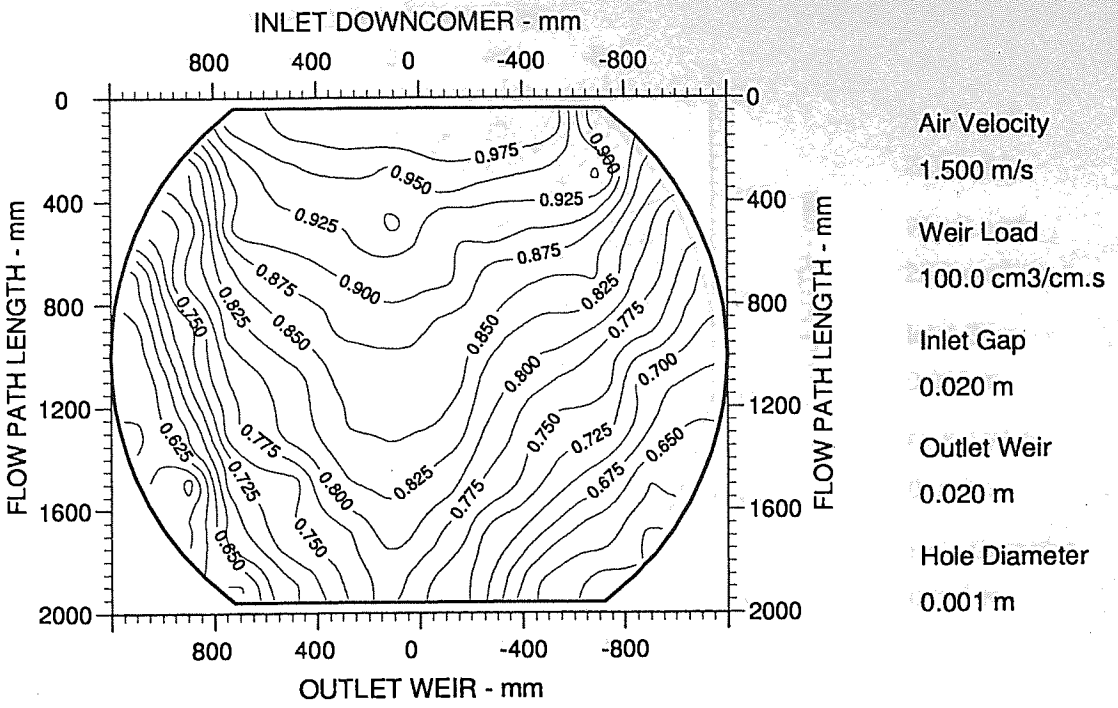

Figure A7.25 Two-dimensionl reduced temperature profiles for STR-1 tray

Emv/Eog 97/74 hCL 30

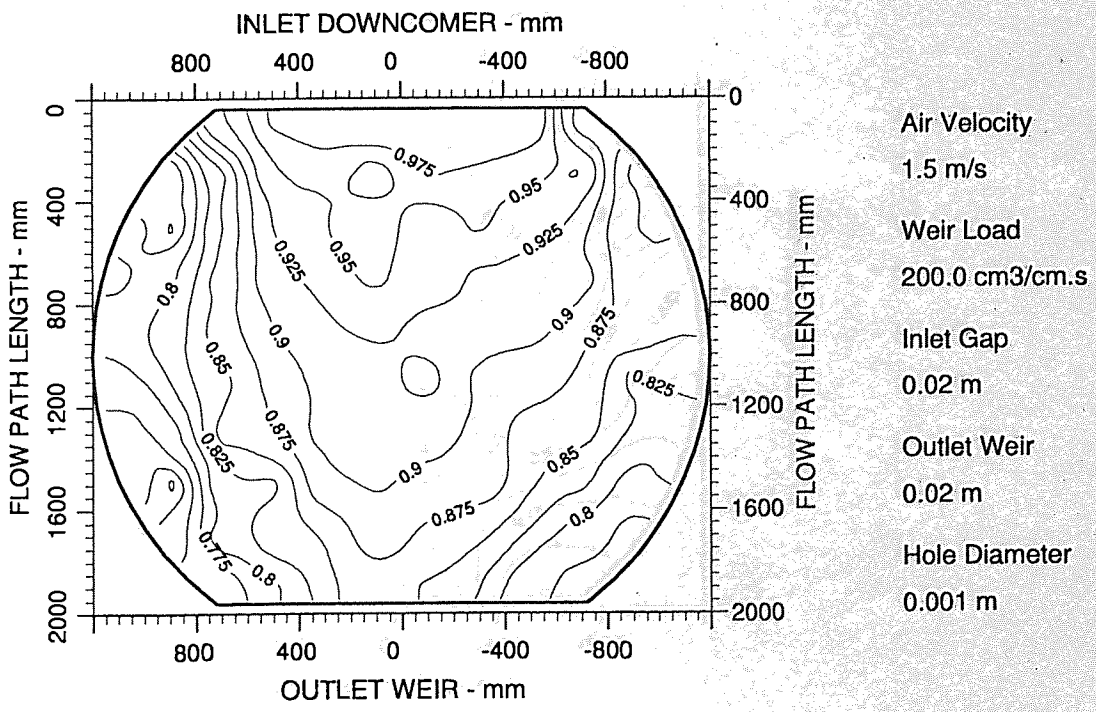

Figure A7.26 Two-dimensionl reduced temperature profiles for STR-1 tray

Emv/Eog 98/86 hCL 41

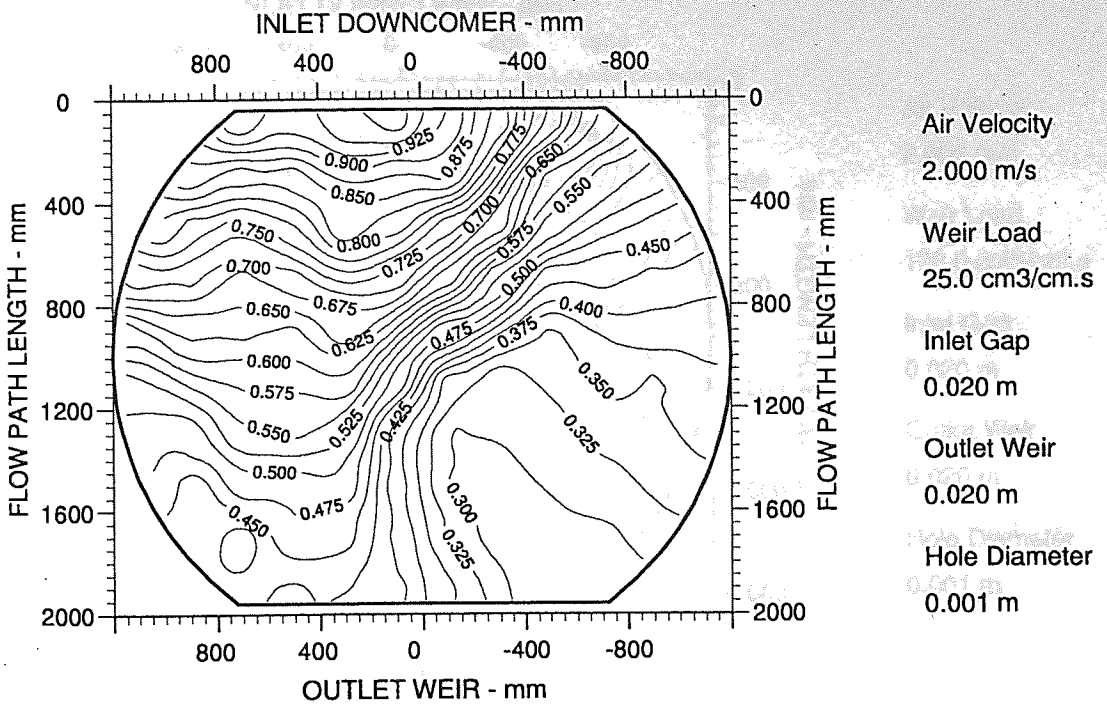

Figure A7.27 Two-dimensionl reduced temperature profiles for STR-1 tray

Emv/Eog 82/47 hCL 21

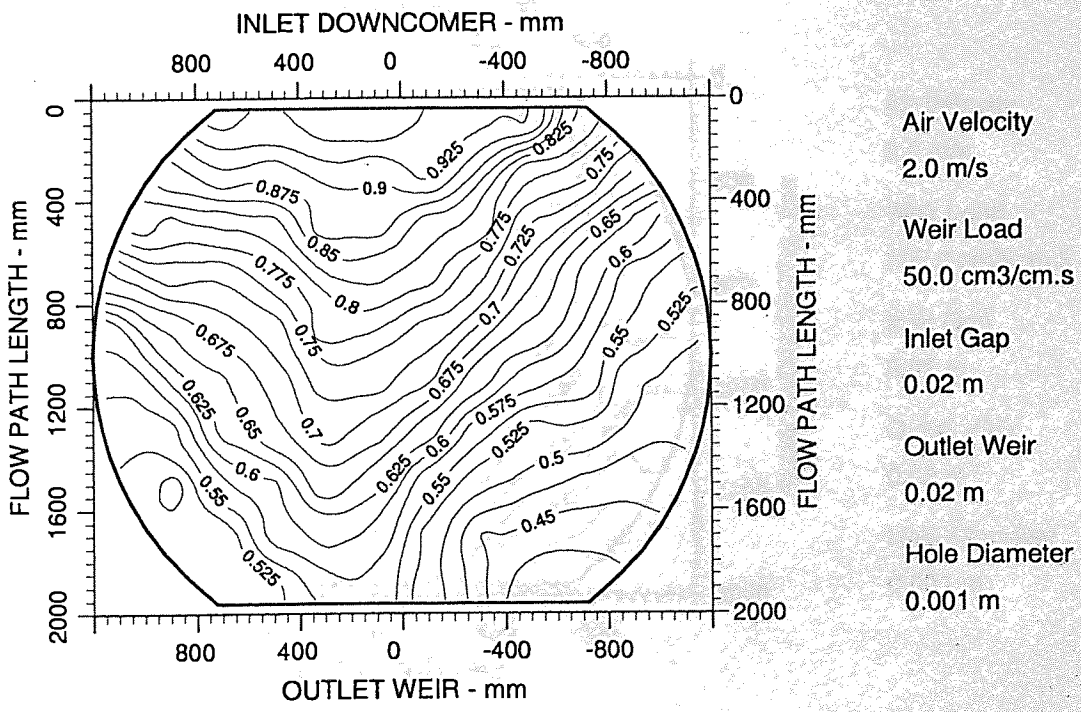

Figure A7.28 Two-dimensionl reduced temperature profiles for STR-1 tray

Emv/Eog 92/59 hCL 24

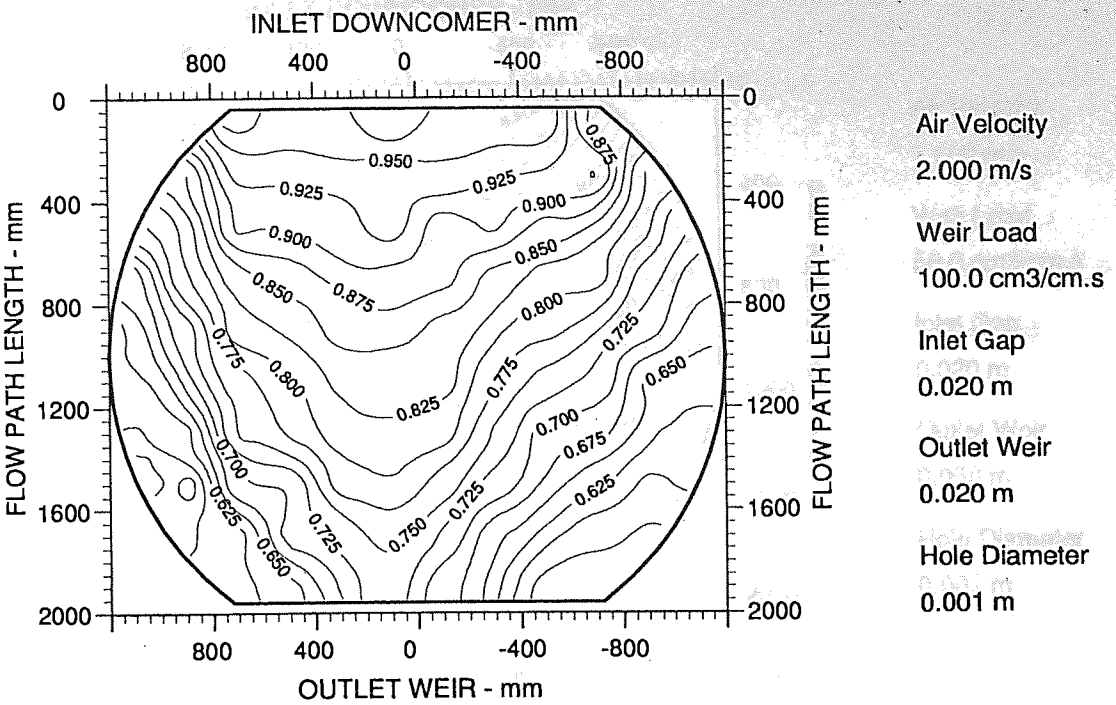

Figure A7.29 Two-dimensionl reduced temperature profiles for STR-1 tray

Emv/Eog 94/72 hCL 28

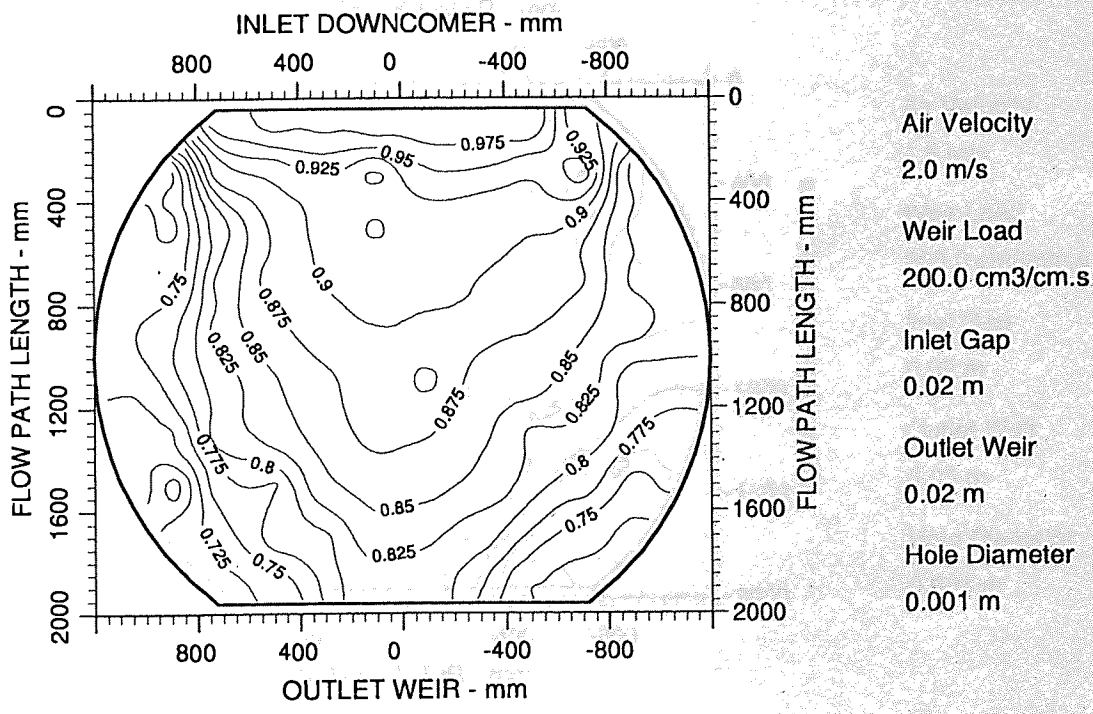

Figure A7.30 Two-dimensionl reduced temperature profiles for STR-1 tray

Emv/Eog 101/85 hCL 32

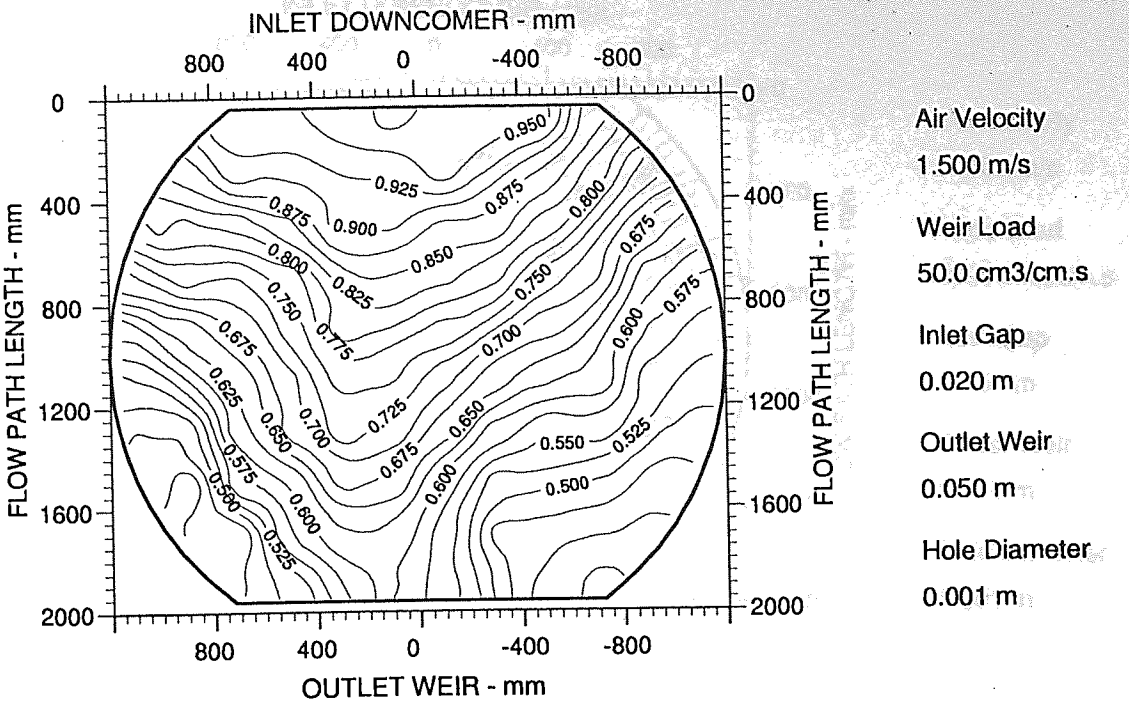

Figure A7.31 Two-dimensionl reduced temperature profiles for STR-1 tray
Emv/Eog 98/67 hCL 32

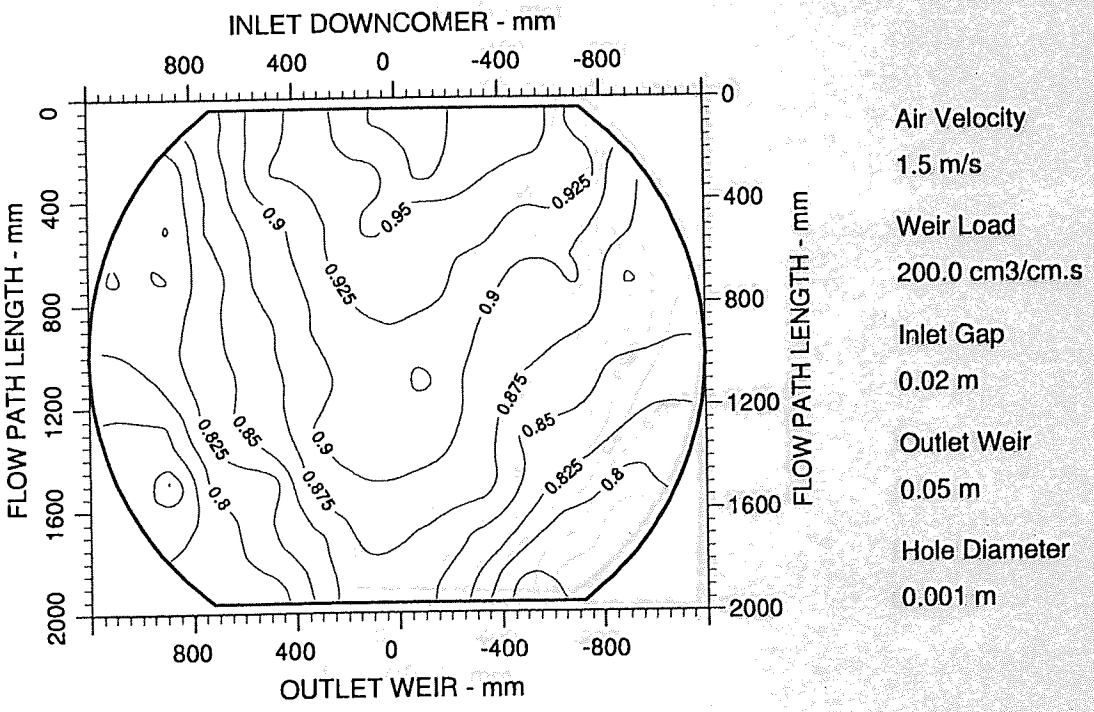

Figure A7.32 Two-dimensionl reduced temperature profiles for STR-1 tray
Emv/Eog 100/89 hCL 44

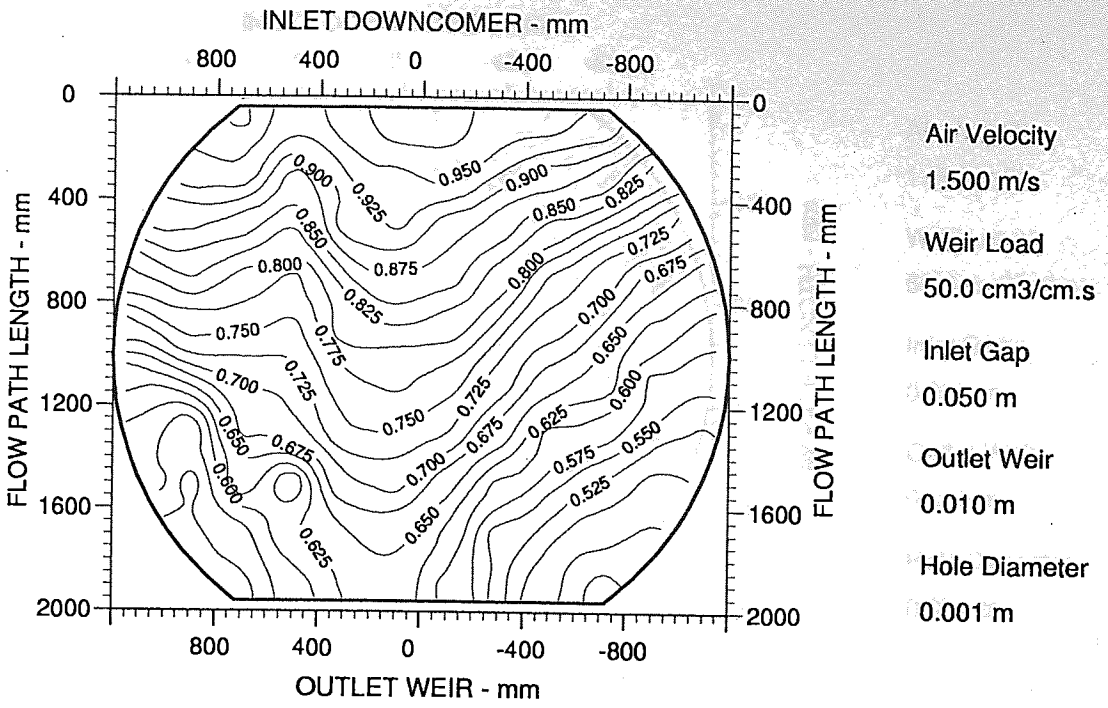

Figure A7.33 Two-dimensionl reduced temperature profiles for STR-1 tray
Emv/Eog 83/56 hCL 25

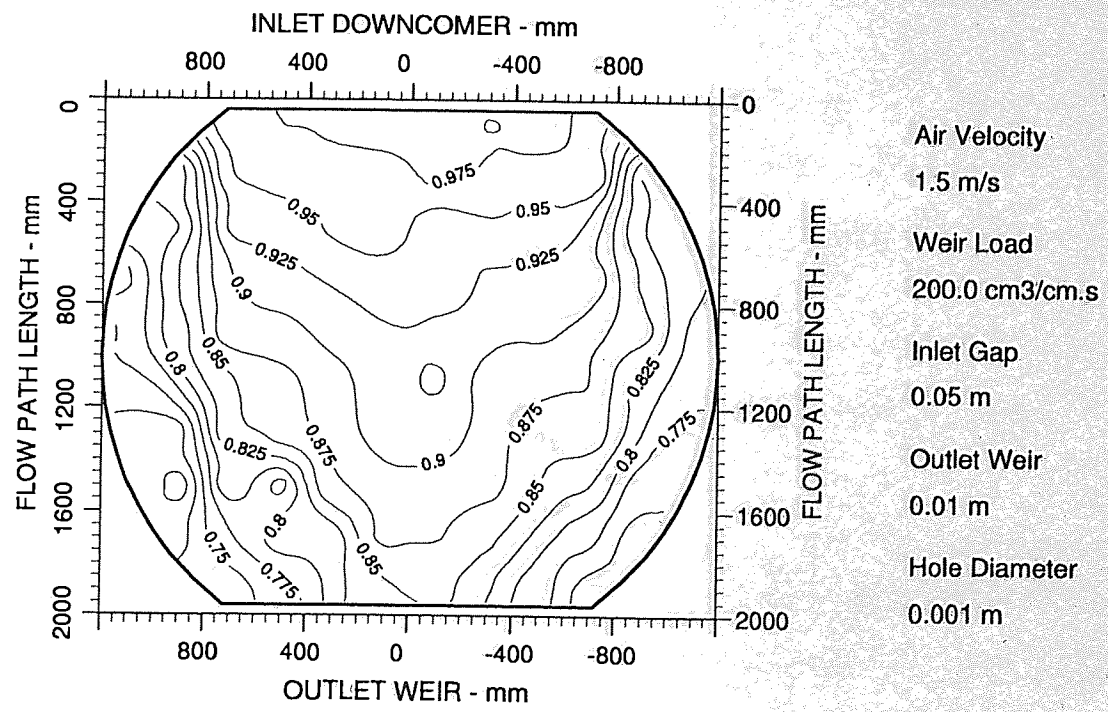

Figure A7.34 Two-dimensionl reduced temperature profiles for STR-1 tray
Emv/Eog 103/88 hCL 41

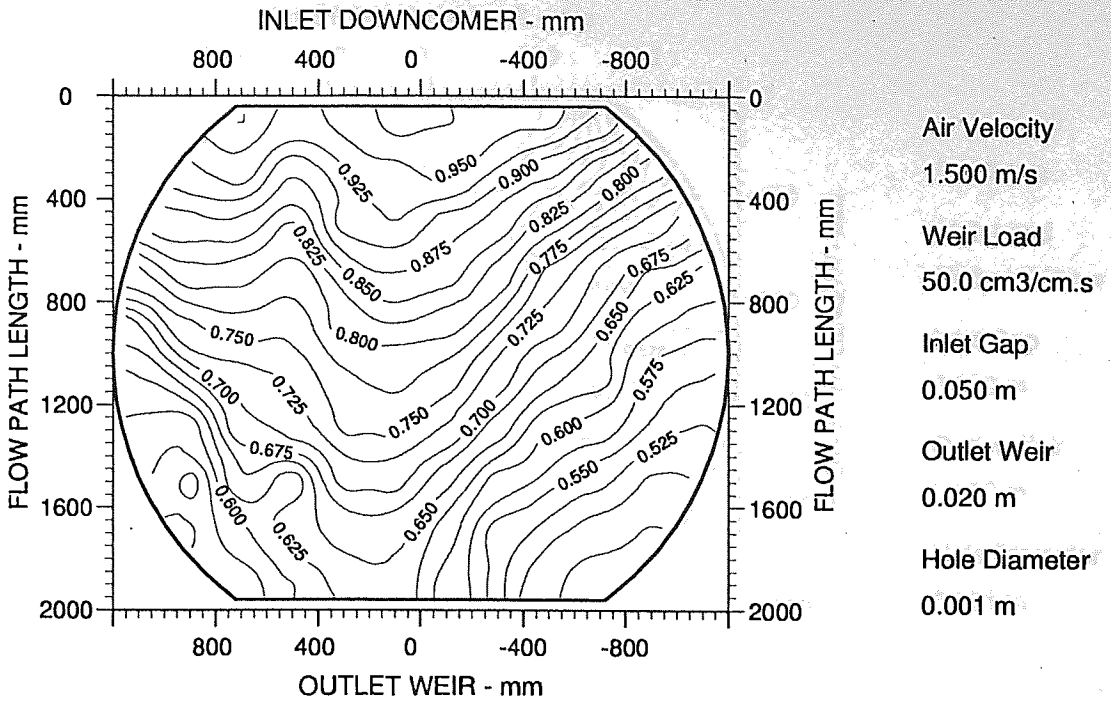

Figure A7.35 Two-dimensionl reduced temperature profiles for STR-1 tray Emv/Eog 86/59 hCL 27

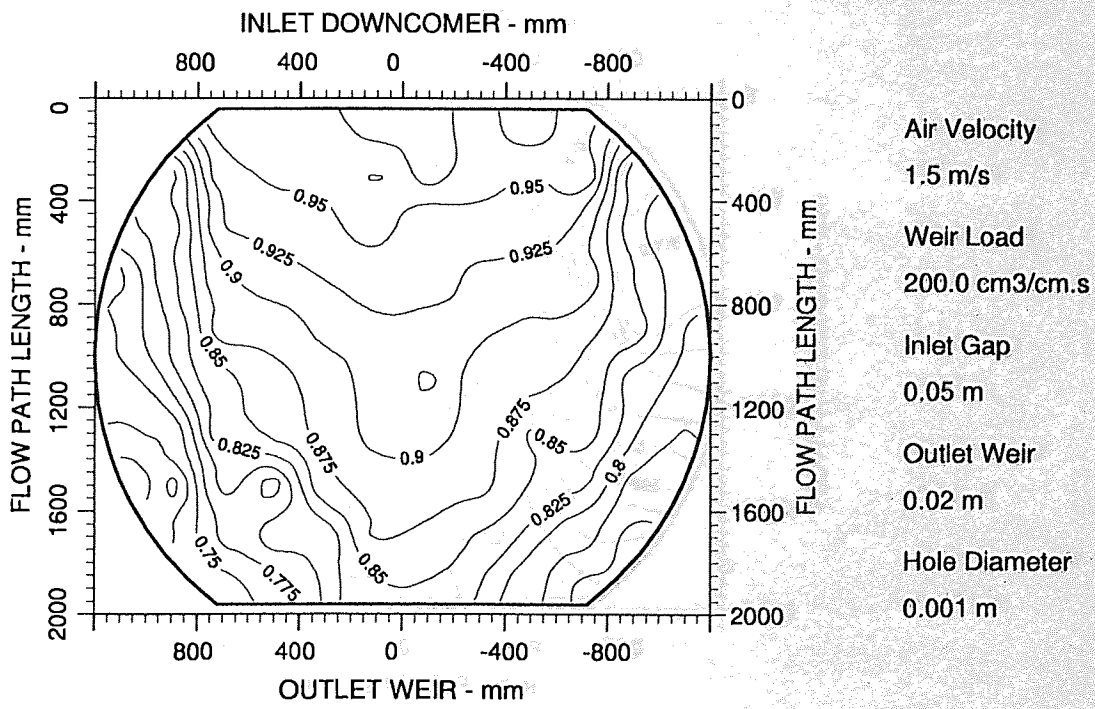

Figure A7.36 Two-dimensionl reduced temperature profiles for STR-1 tray Emv/Eog 105/90 hCL 41

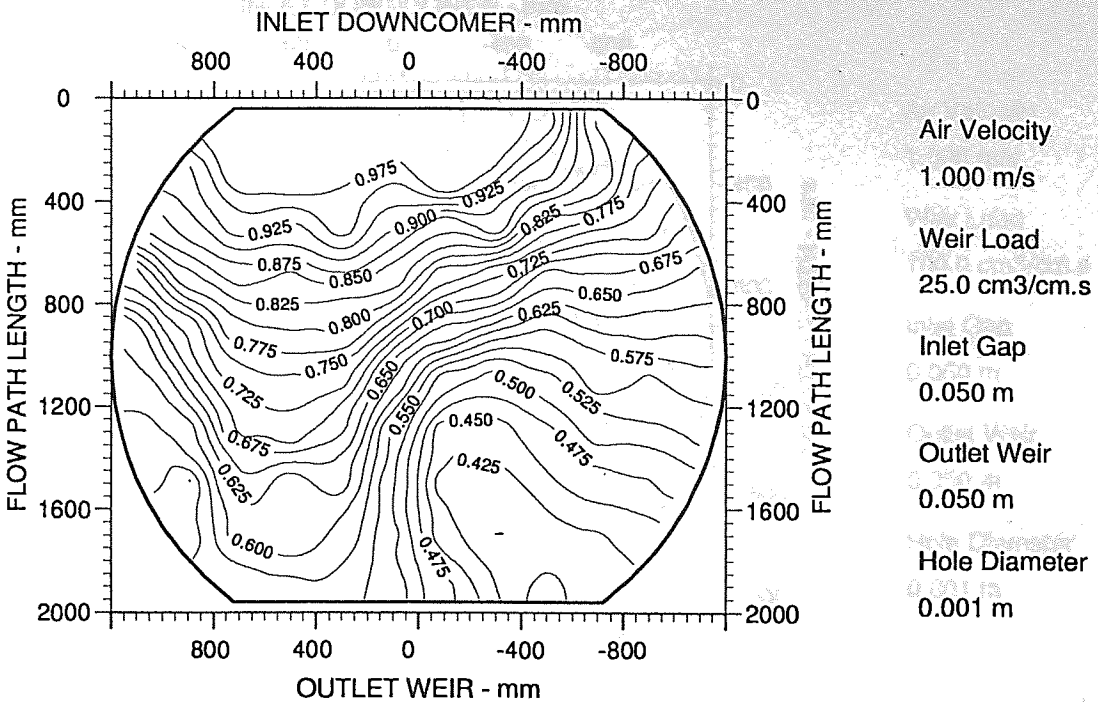

Figure A7.37 Two-dimensionl reduced temperature profiles for STR-1 tray

Emv/Eog 90/55 hCL 32

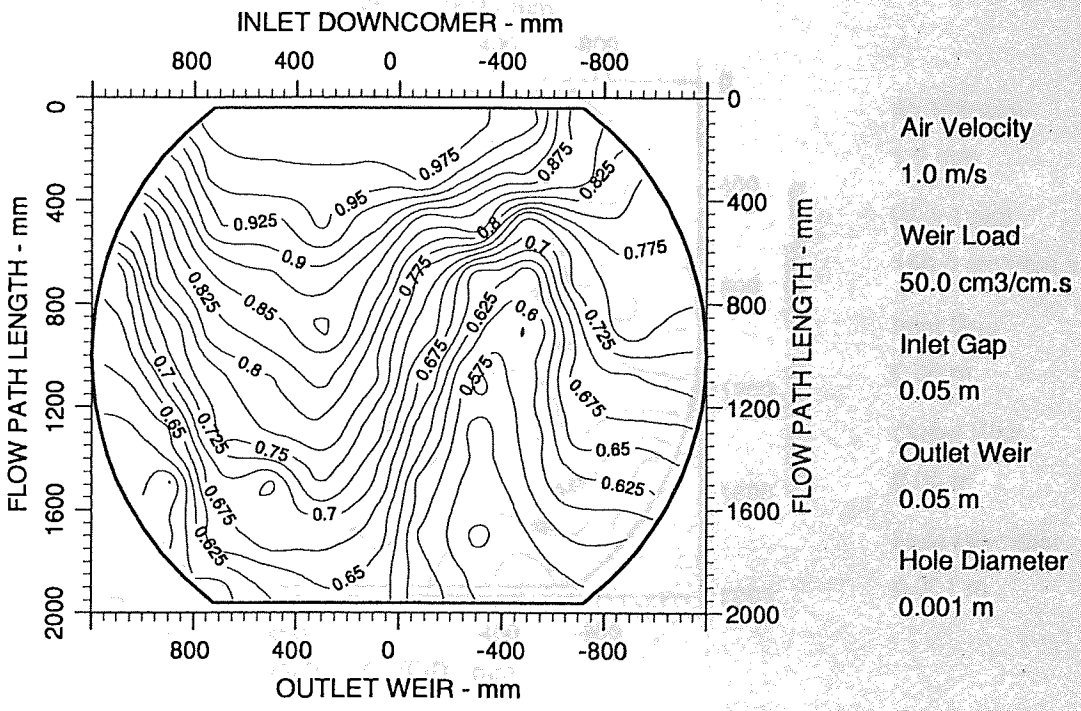

Figure A7.38 Two-dimensionl reduced temperature profiles for STR-1 tray

Emv/Eog 106/73 hCL 38

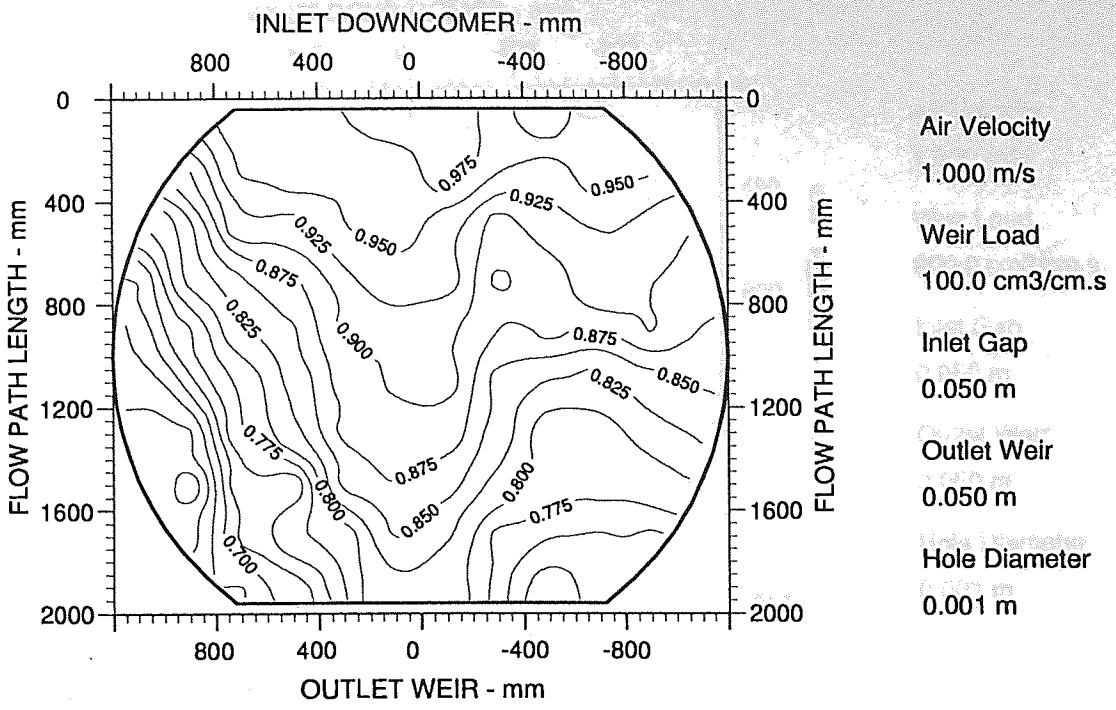

Figure A7.39 Two-dimensionl reduced temperature profiles for STR-1 tray
Emv/Eog 105/85 hCL 47

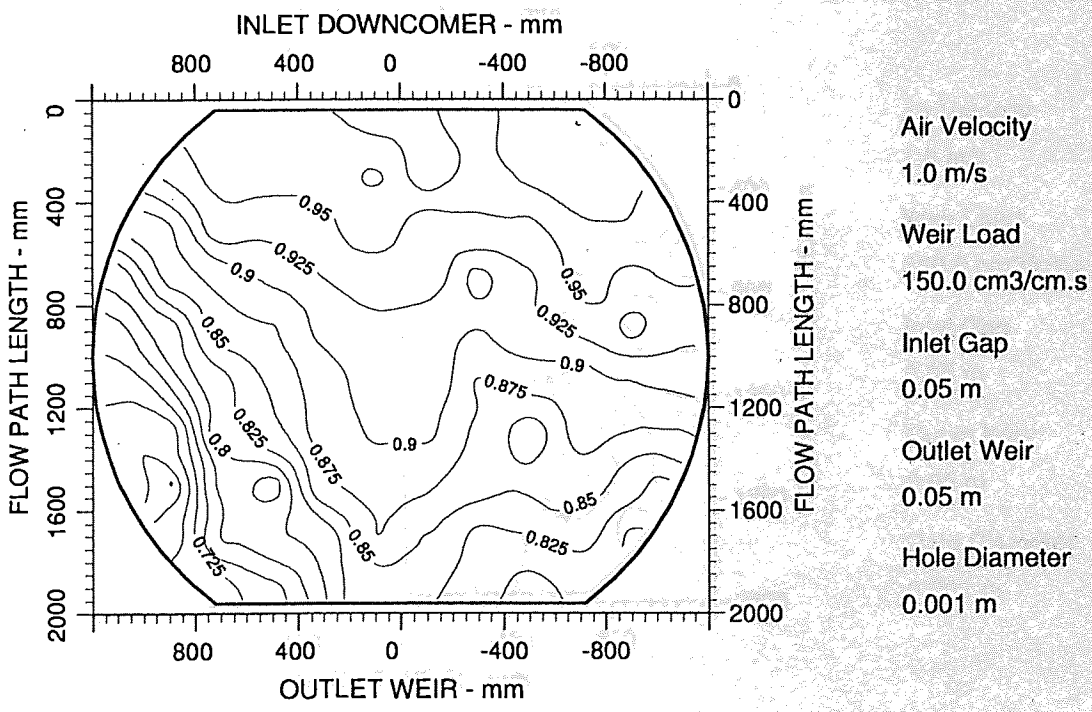

Figure A7.40 Two-dimensionl reduced temperature profiles for STR-1 tray
Emv/Eog 112/91 hCL 49

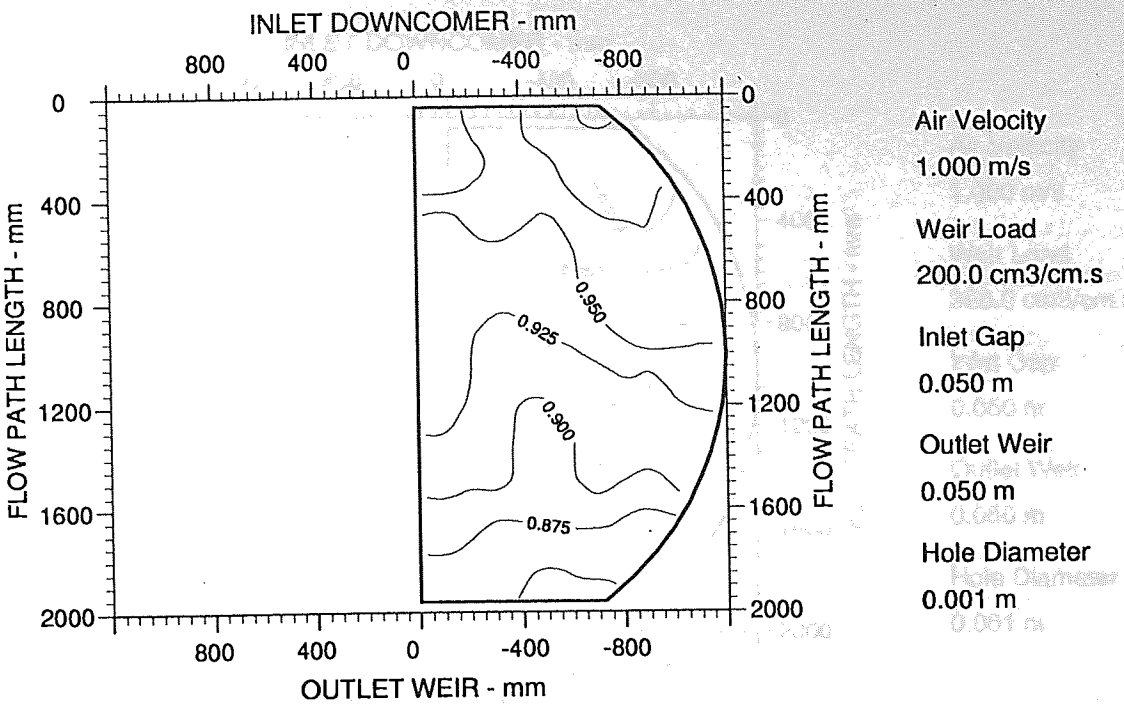

Figure A7.41 Two-dimensionl reduced temperature profiles for STR-1 tray
Emv/Eog 111/94 hCL 60

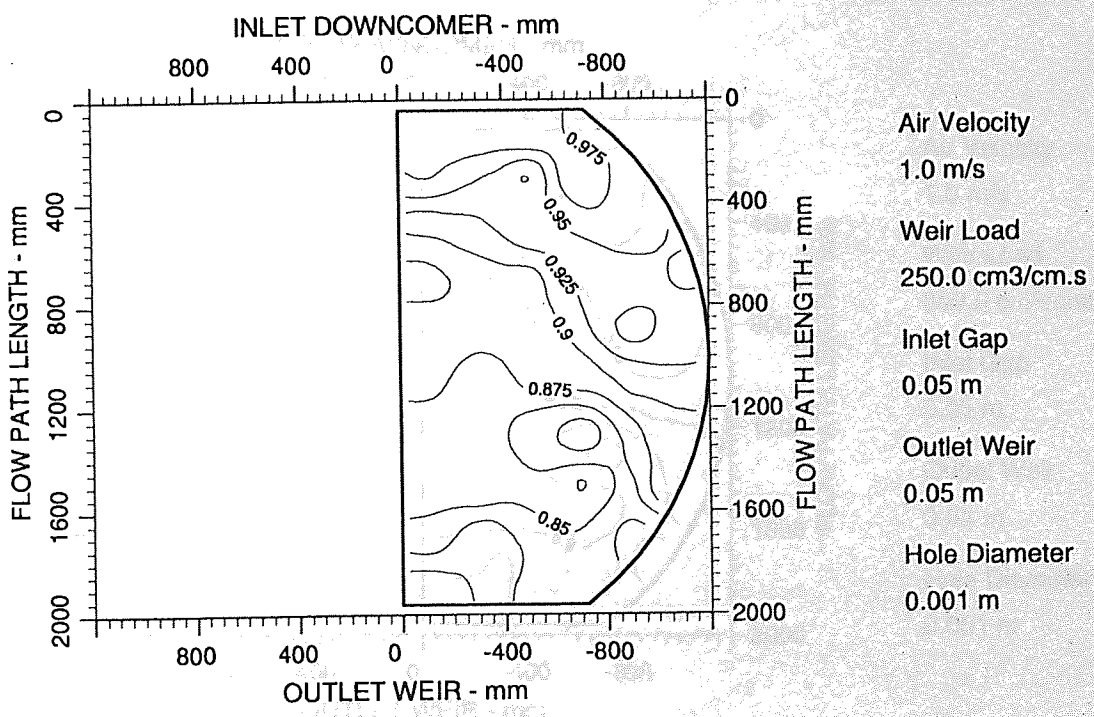

Figure A7.42 Two-dimensionl reduced temperature profiles for STR-1 tray
Emv/Eog 103/93 hCL

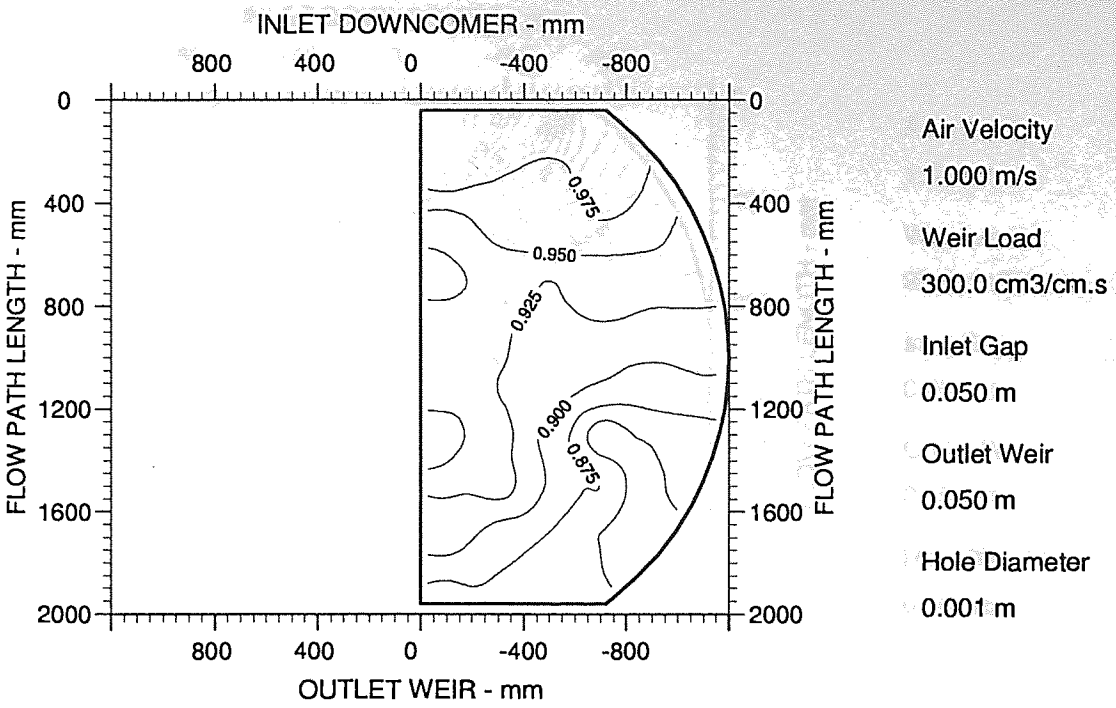

Figure A7.43 Two-dimensionl reduced temperature profiles for STR-1 tray Emv/Eog 102/95 hCL

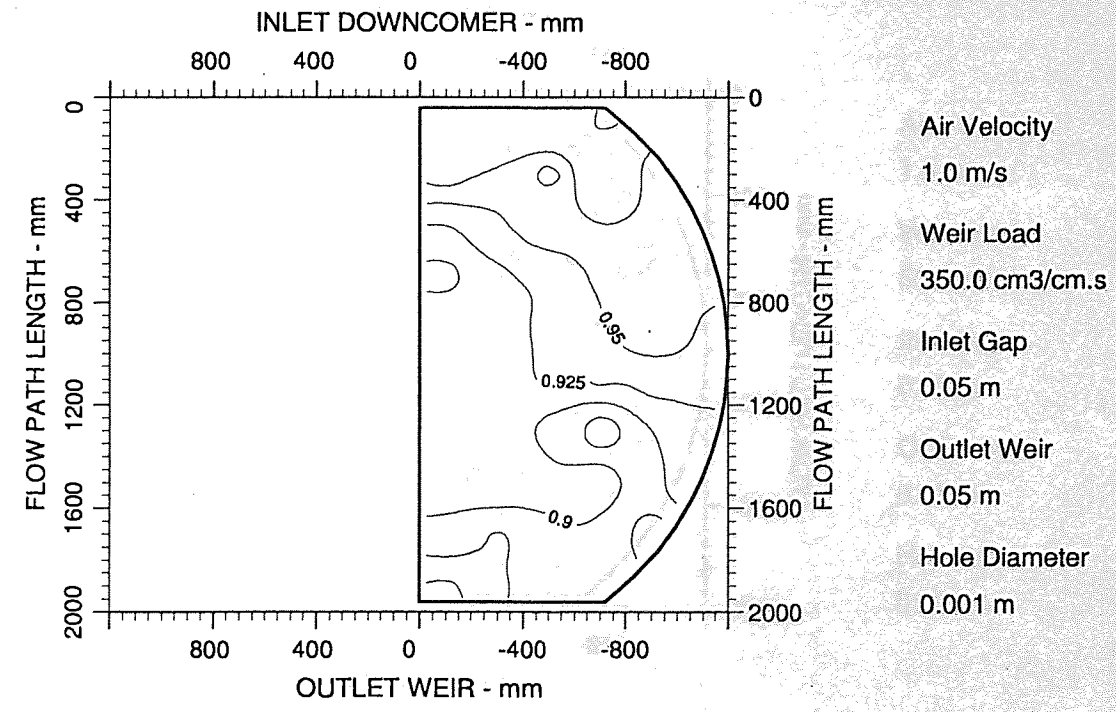

Figure A7.44 Two-dimensionl reduced temperature profiles for STR-1 tray Emv/Eog 104/96 hCL

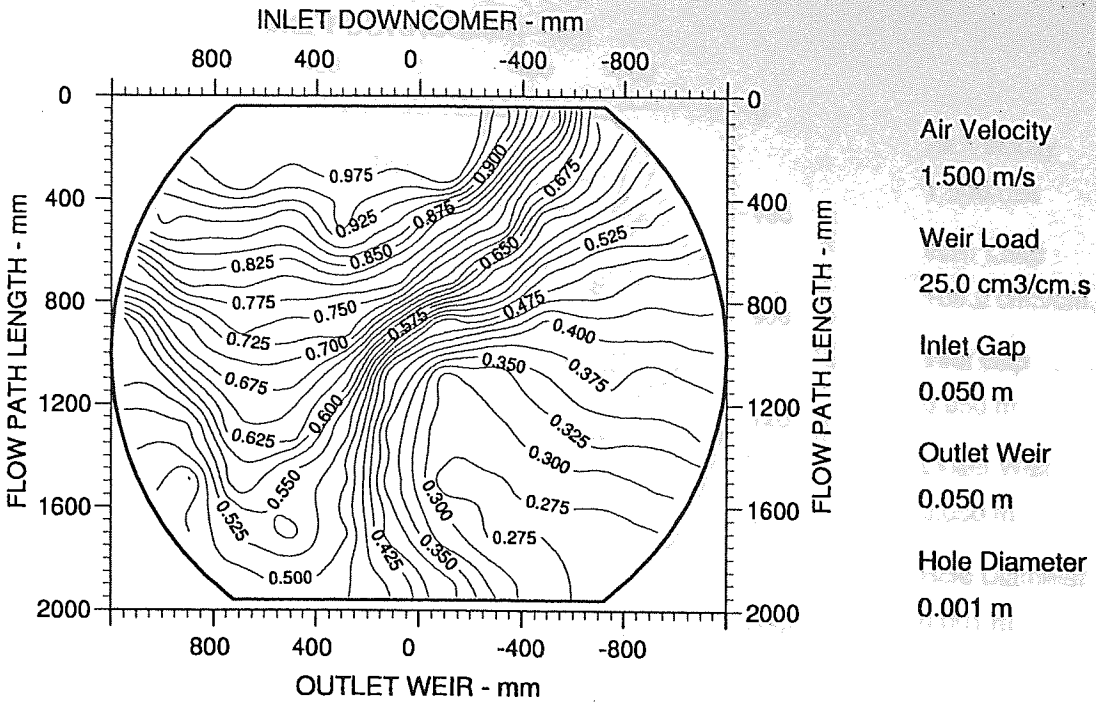

Figure A7.45 Two-dimensionl reduced temperature profiles for STR-1 tray

Emv/Eog 89/52 hCL 26

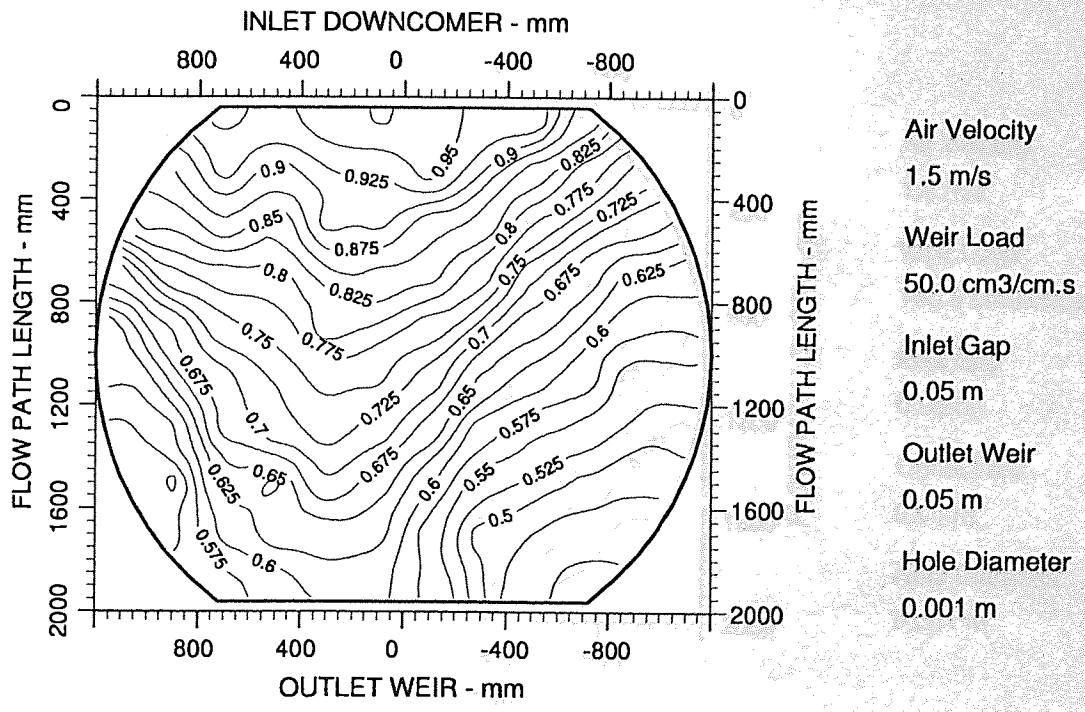

Figure A7.46 Two-dimensionl reduced temperature profiles for STR-1 tray

Emv/Eog 101/67 hCL 32

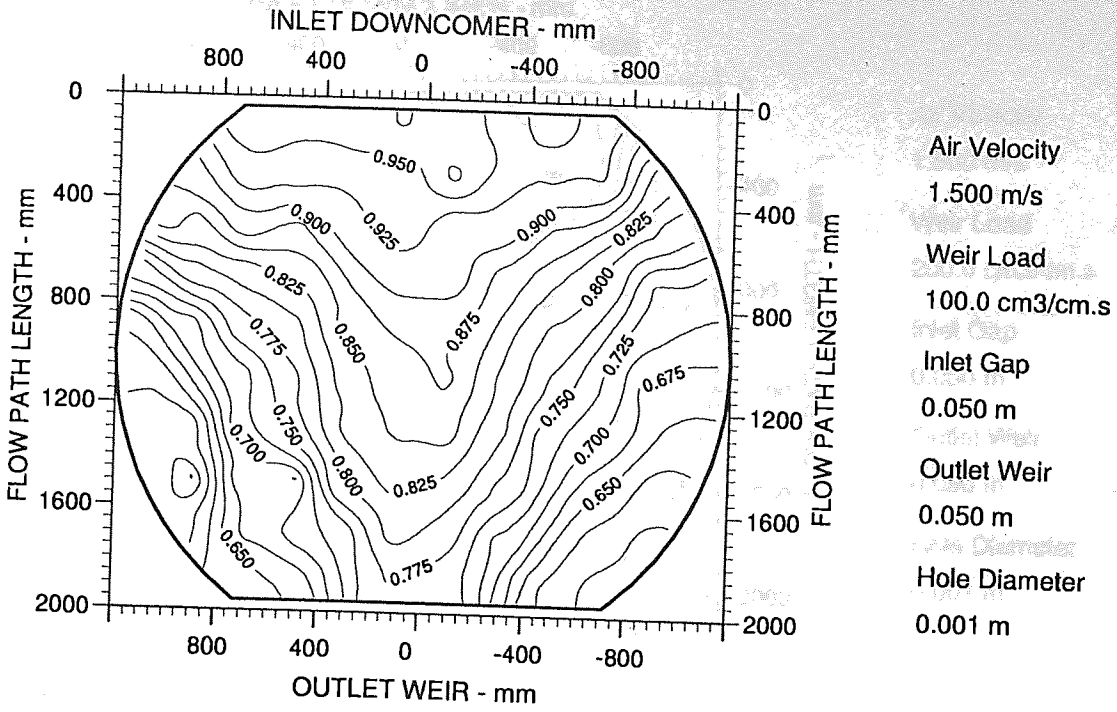

Figure A7.47 Two-dimensionl reduced temperature profiles for STR-1 tray
Emv/Eog 105/82 hCL 38

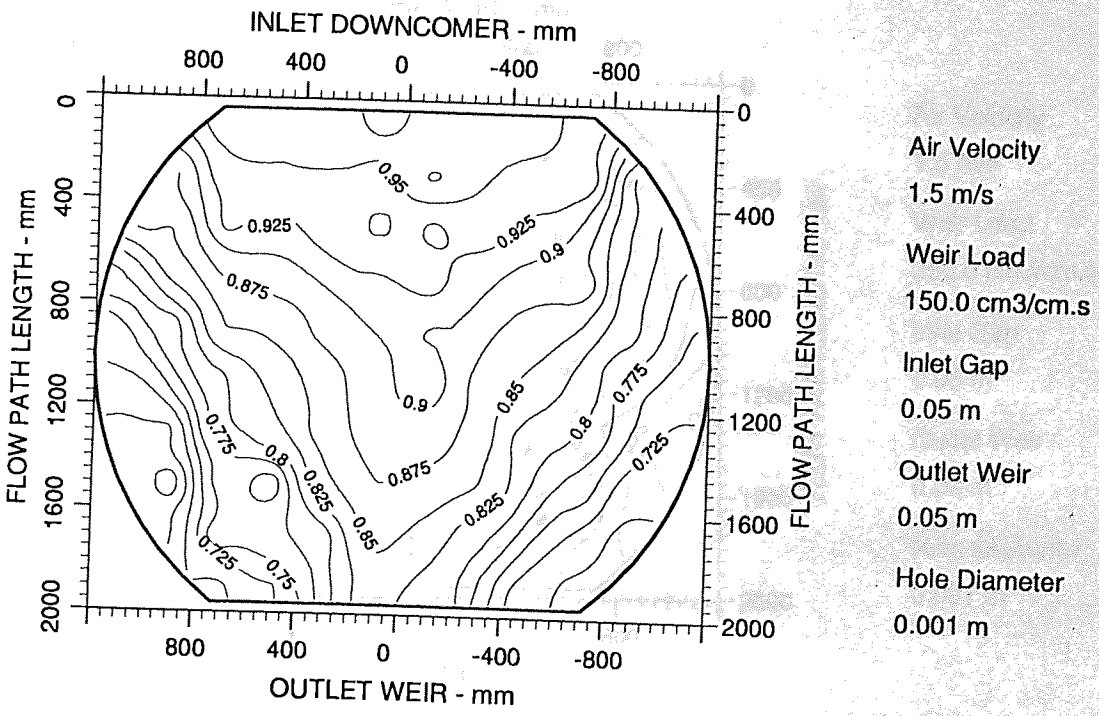

Figure A7.48 Two-dimensionl reduced temperature profiles for STR-1 tray
Emv/Eog 108/89 hCL 40

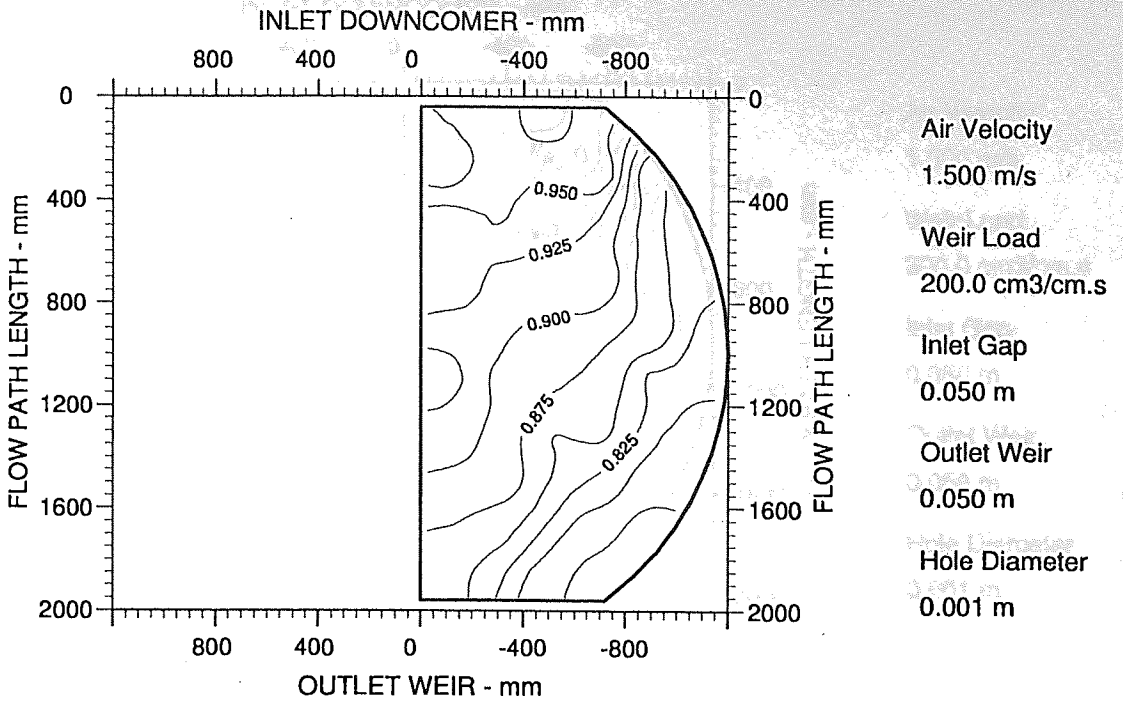

Figure A7.49 Two-dimensionl reduced temperature profiles for STR-1 tray
Emv/Eog 109/93 hCL 45

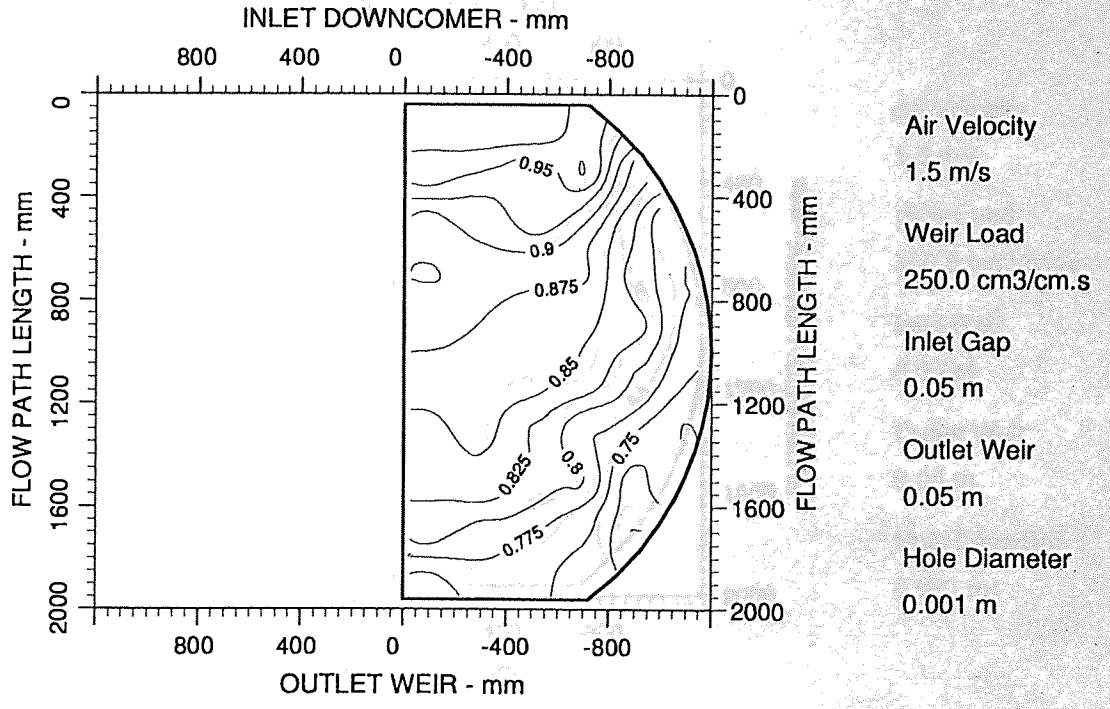

Figure A7.50 Two-dimensionl reduced temperature profiles for STR-1 tray
Emv/Eog 104/95 hCL 61

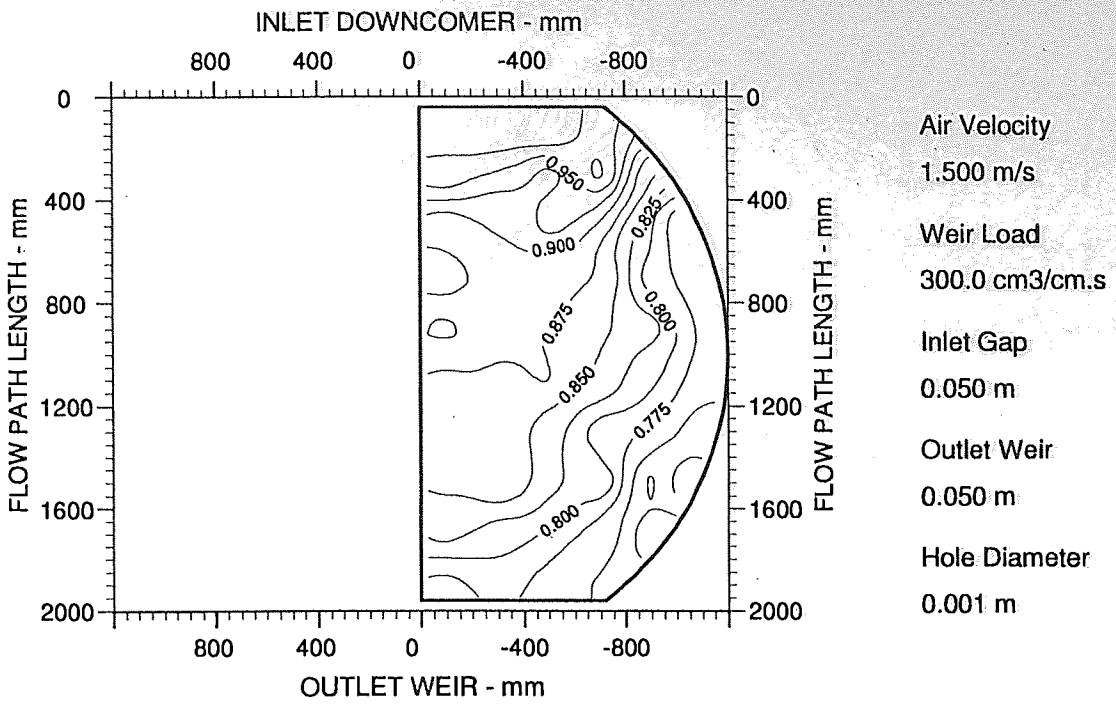

Figure A7.51 Two-dimensionl reduced temperature profiles for STR-1 tray
Emv/Eog 100/95 hCL 71

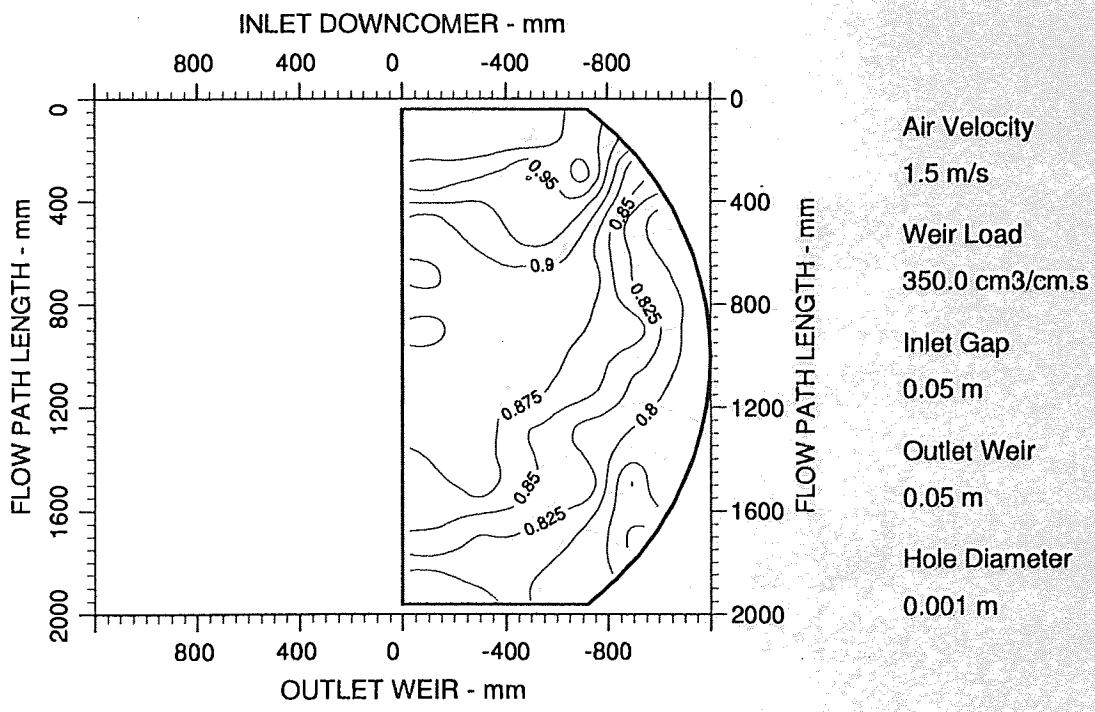

Figure A7.52 Two-dimensionl reduced temperature profiles for STR-1 tray
Emv/Eog 102/97 hCL 74

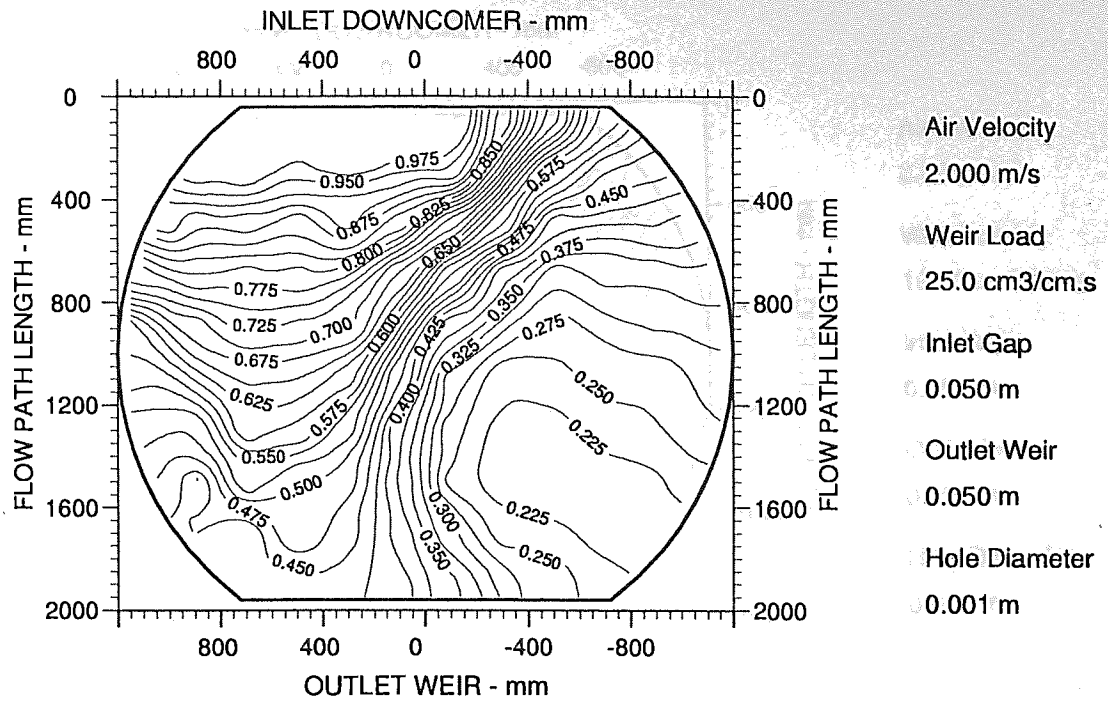

Figure A7.53 Two-dimensionl reduced temperature profiles for STR-1 tray

Emv/Eog 80/47 hCL 24

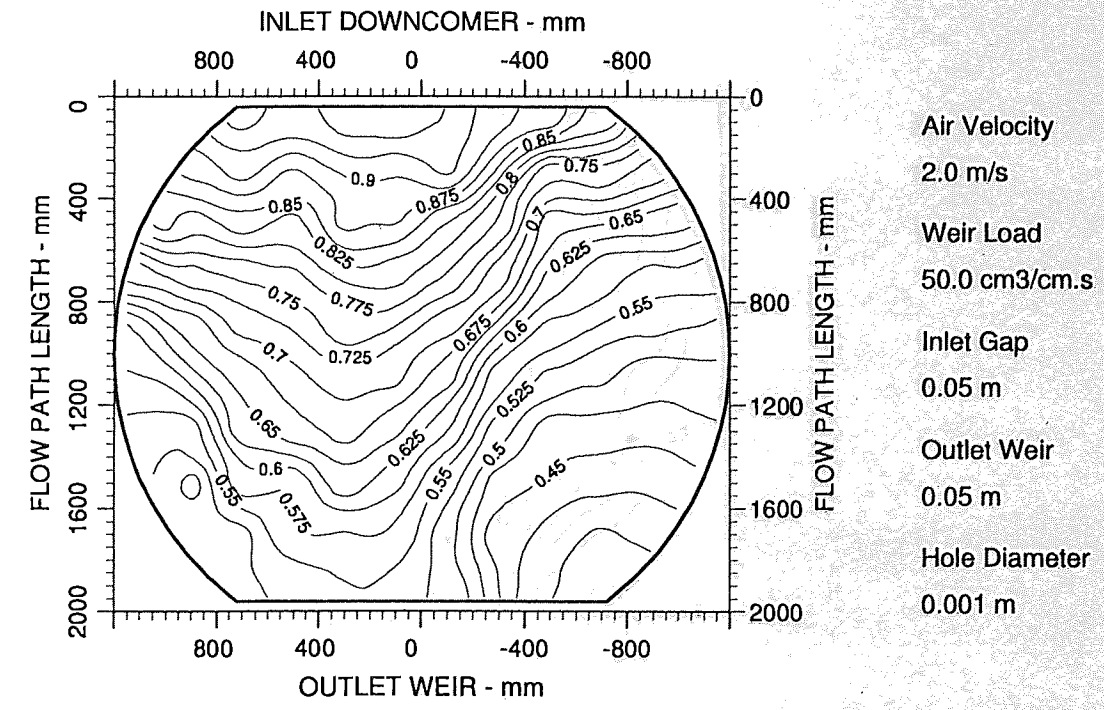

Figure A7.54 Two-dimensionl reduced temperature profiles for STR-1 tray

Emv/Eog 100/64 hCL 28

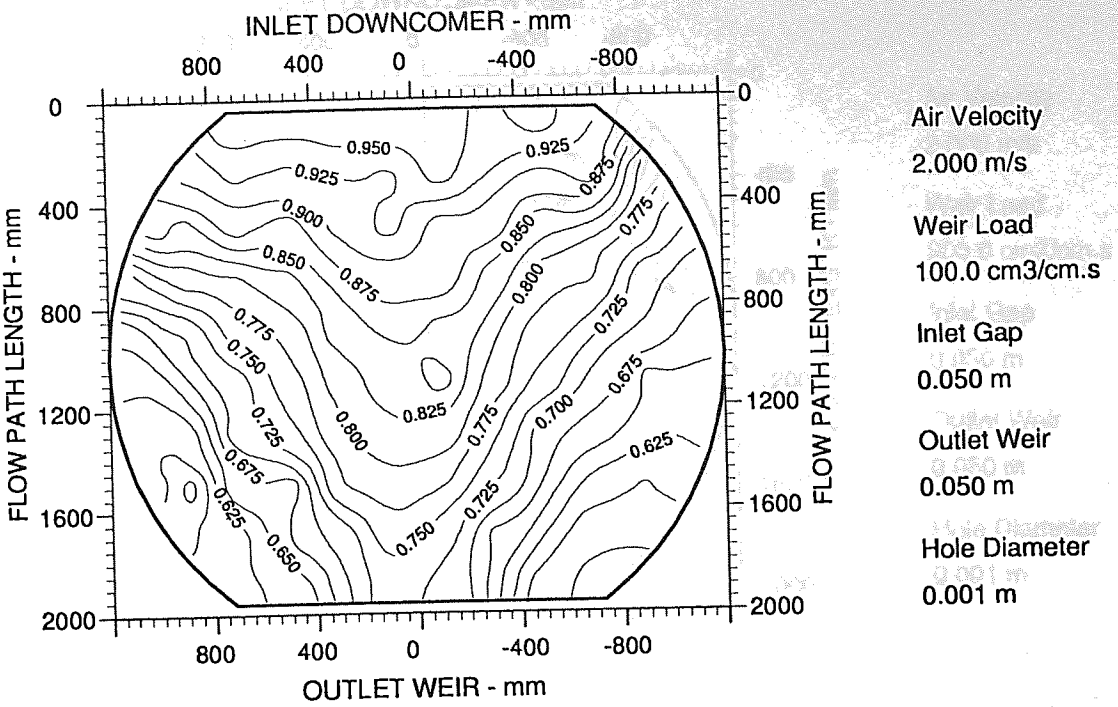

Figure A7.55 Two-dimensionl reduced temperature profiles for STR-1 tray

Emv/Eog 100/75 hCL 32

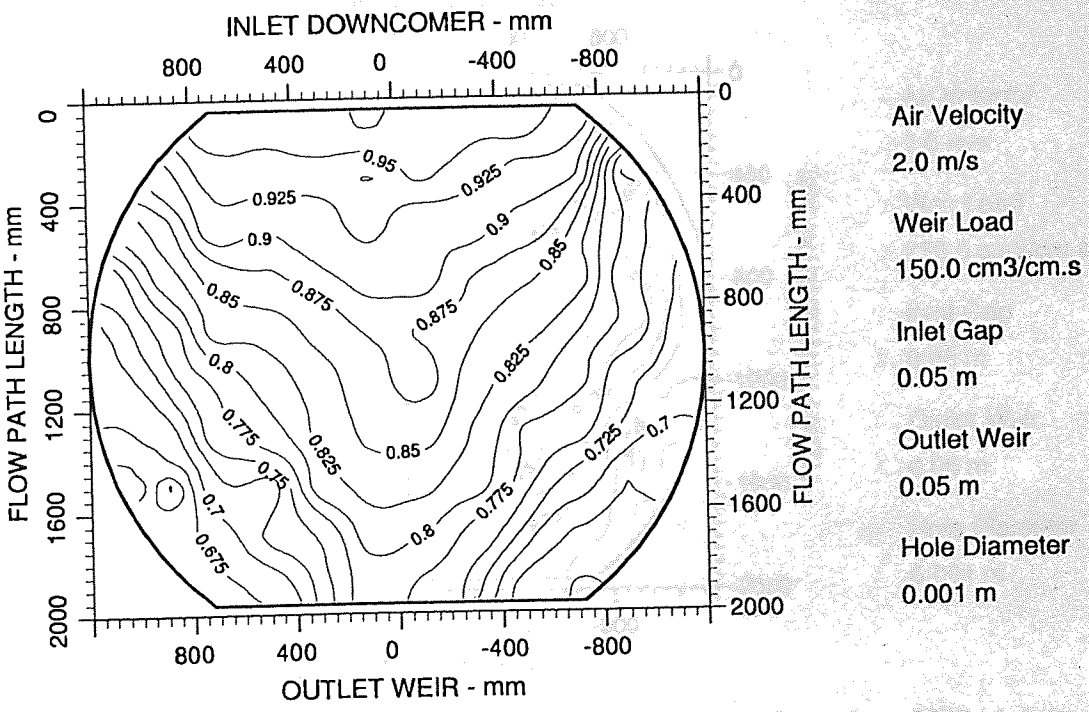

Figure A7.56 Two-dimensionl reduced temperature profiles for STR-1 tray

Emv/Eog 107/84 hCL 34

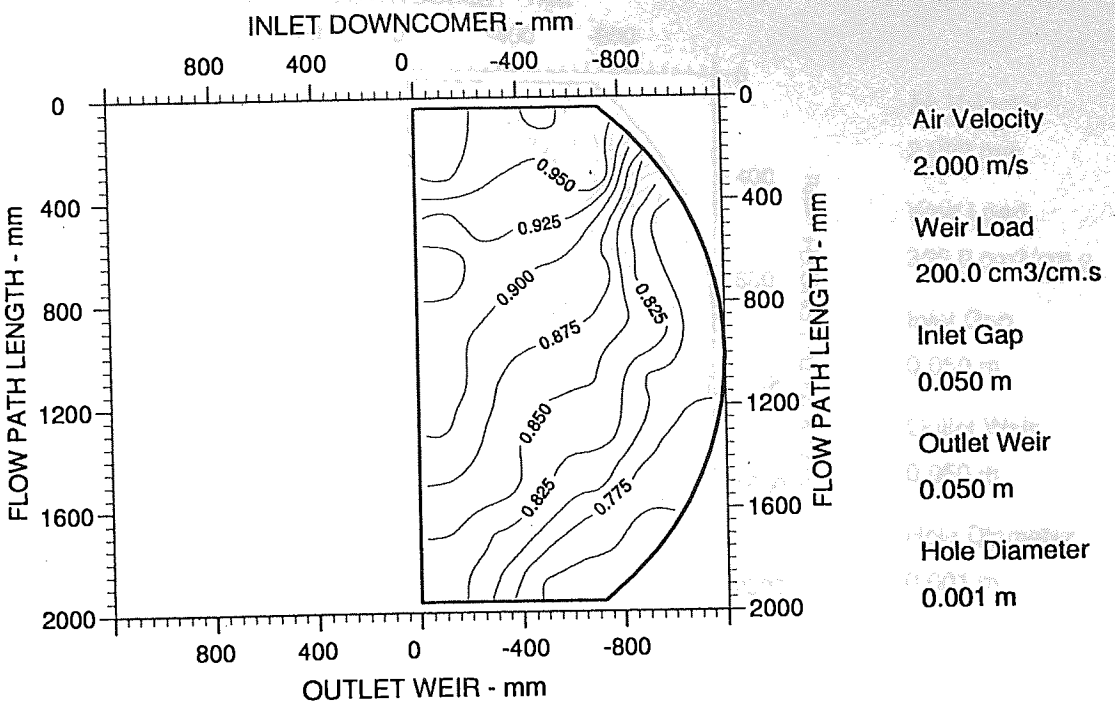

Figure A7.57 Two-dimensionl reduced temperature profiles for STR-1 tray

Emv/Eog 102/88 hCL 37

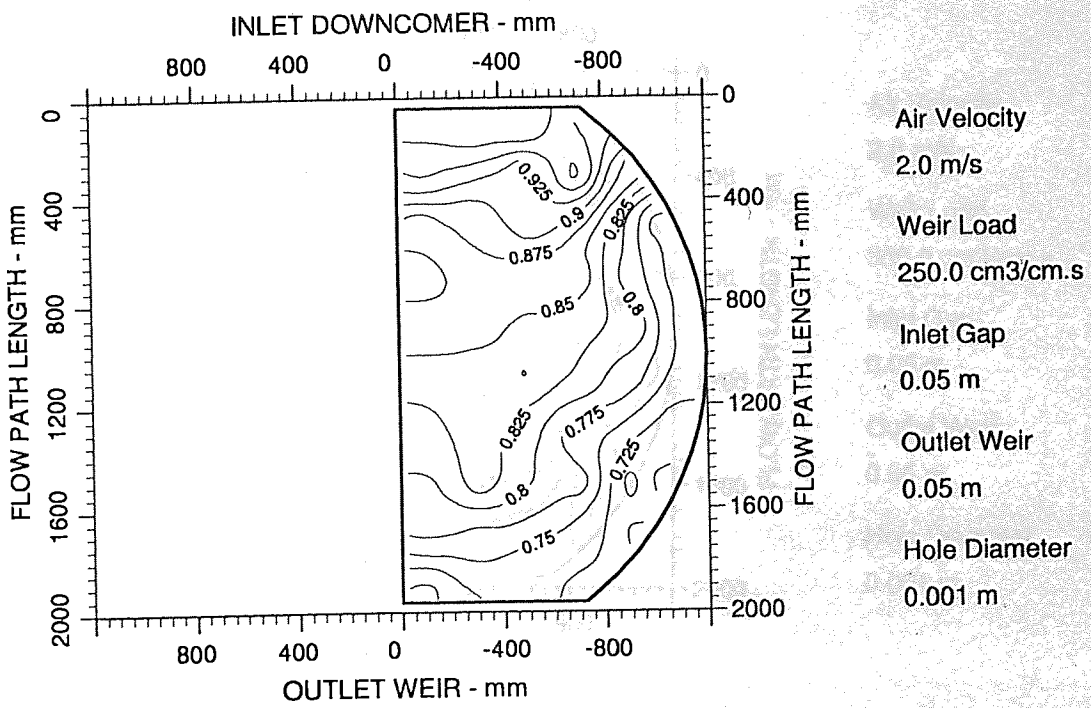

Figure A7.58 Two-dimensionl reduced temperature profiles for STR-1 tray

Emv/Eog 103/93 hCL 45

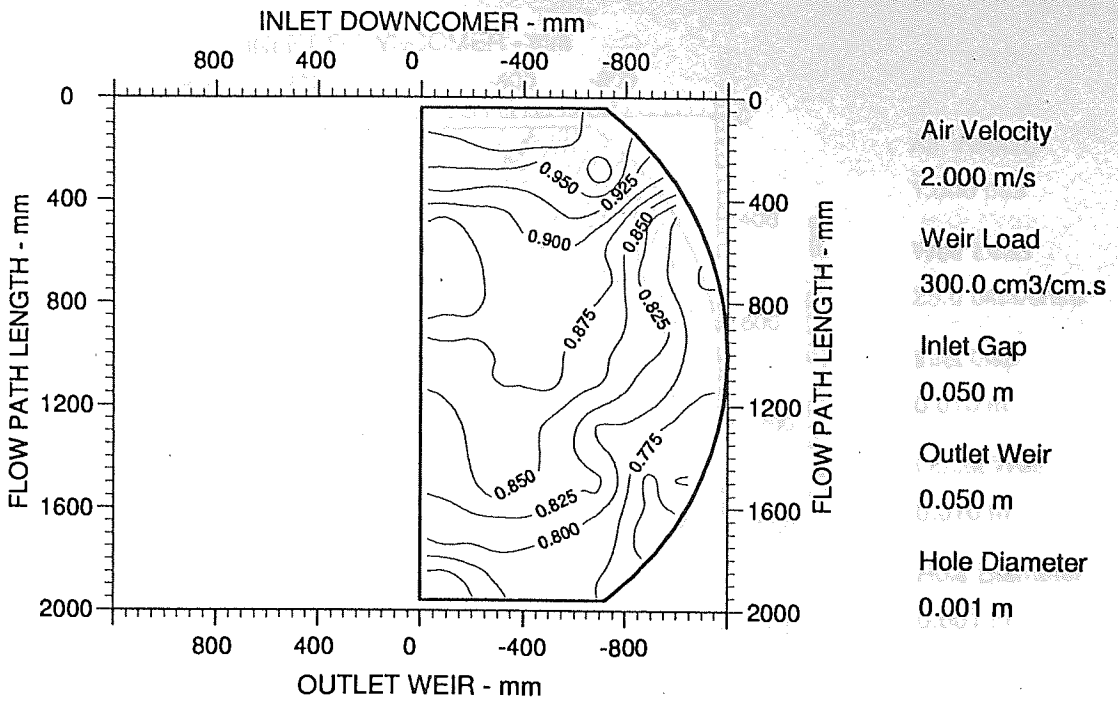

Figure A7.59 Two-dimensionl reduced temperature profiles for STR-1 tray
Emv/Eog 104/96 hCL 55

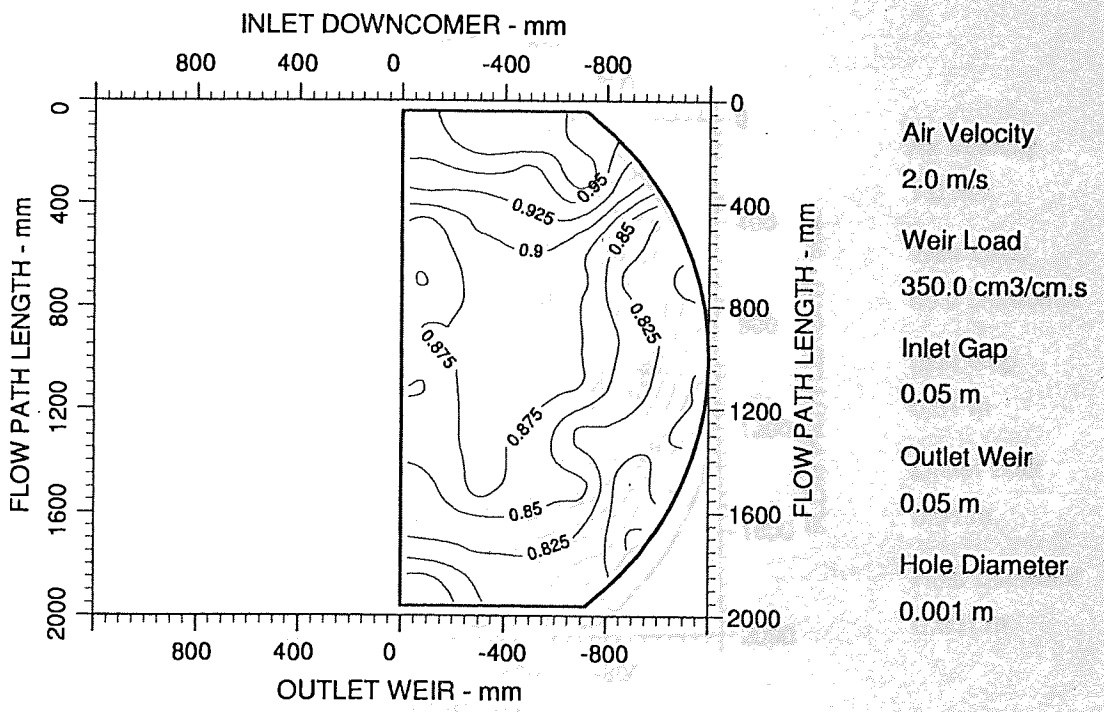

Figure A7.60 Two-dimensionl reduced temperature profiles for STR-1 tray
Emv/Eog 104/98 hCL 72

Appendix 8

Two-Dimensional Reduced Temperature Isotherm Displays for the ARC-1 Tray Cases

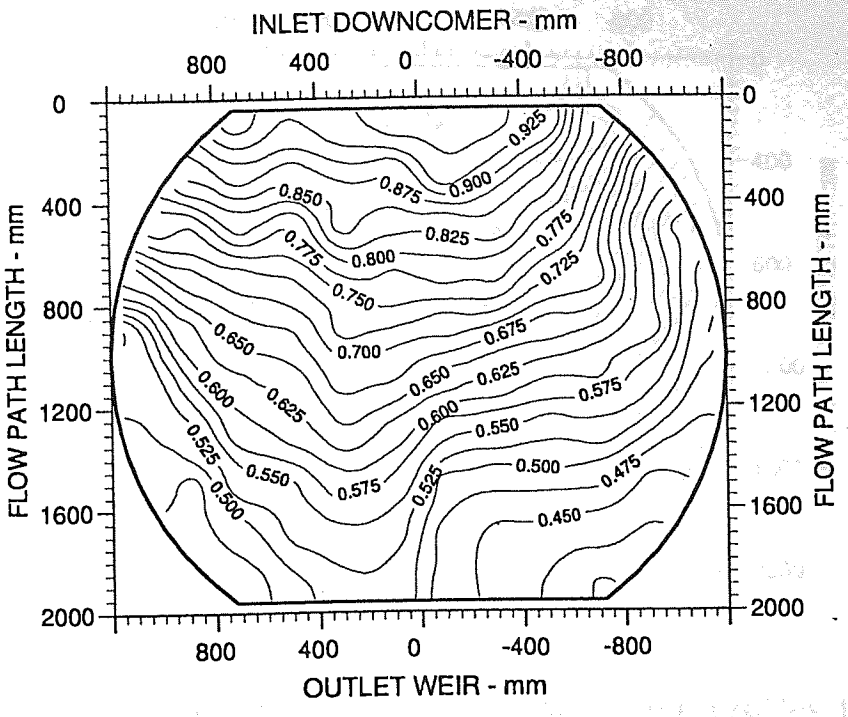

Figure A8.1 Two-dimensionl reduced temperature profiles for ARC-1 tray

Emv/Eog 97/57 hCL 24

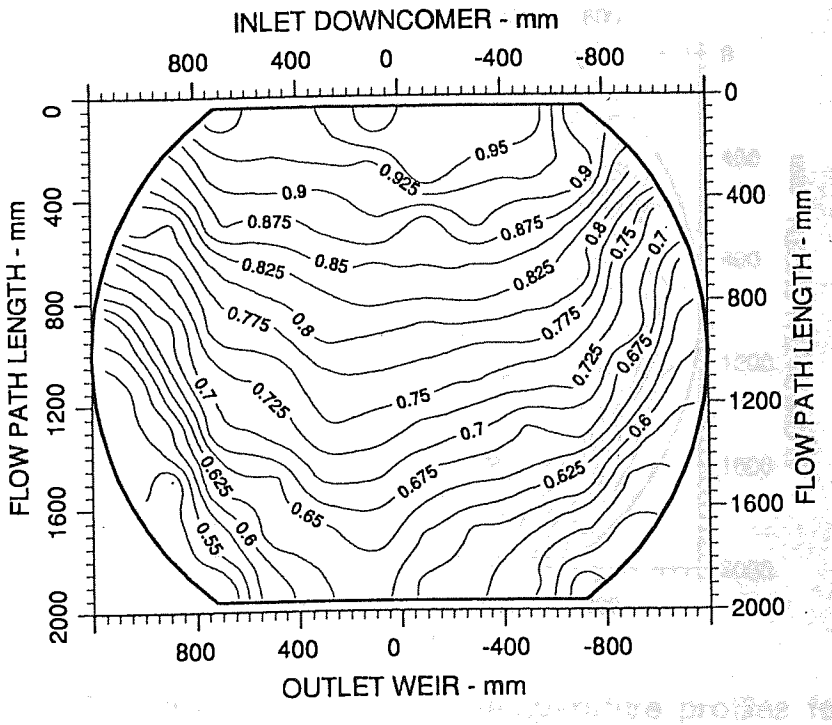

Figure A8.2 Two-dimensionl reduced temperature profiles for ARC-1 tray

Emv/Eog 107/72 hCL 28

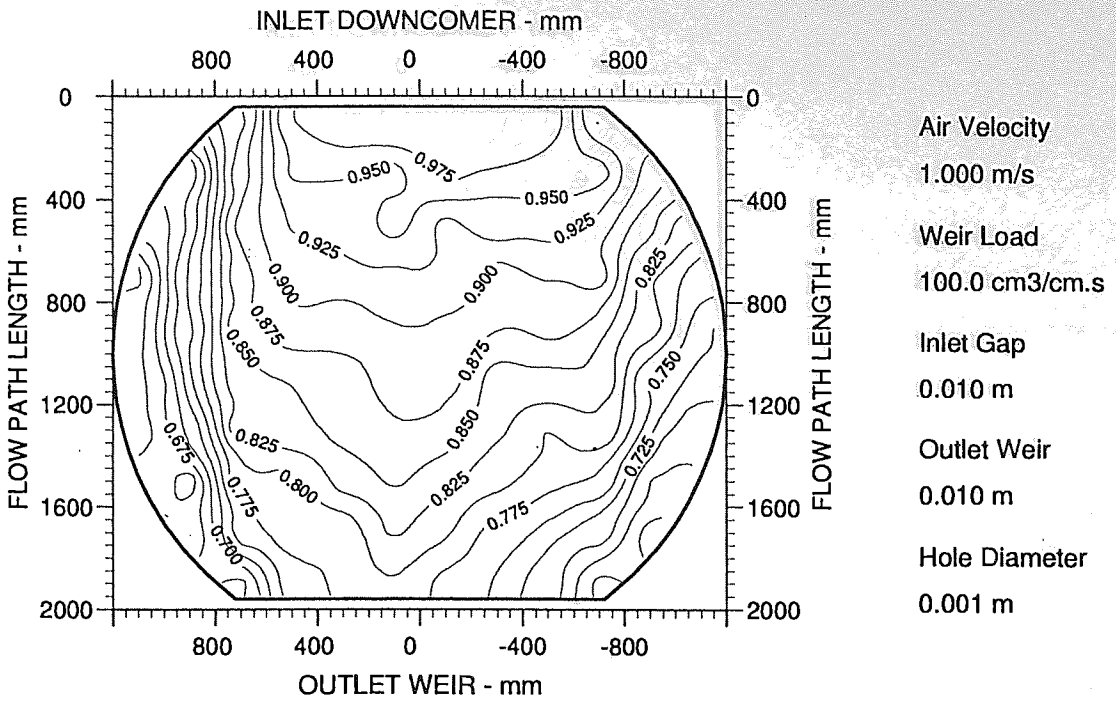

Figure A8.3 Two-dimensionl reduced temperature profiles for ARC-1 tray

Emv/Eog 98/81 hCL 32

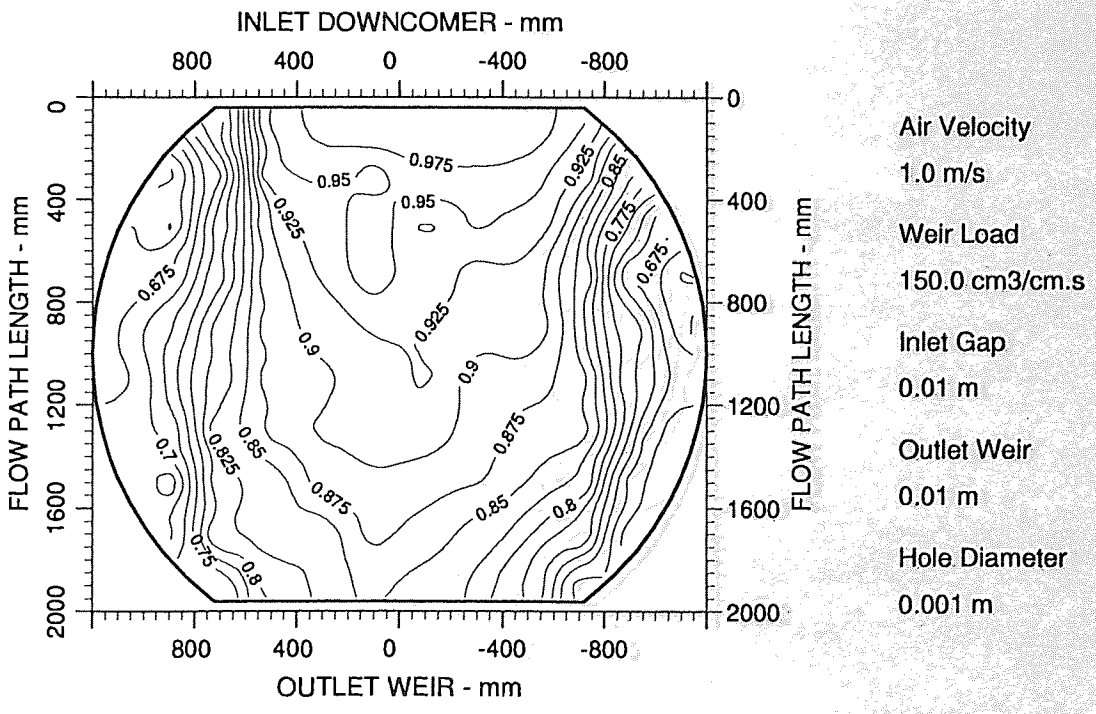

Figure A8.4 Two-dimensionl reduced temperature profiles for ARC-1 tray

Emv/Eog 101/90 hCL 34

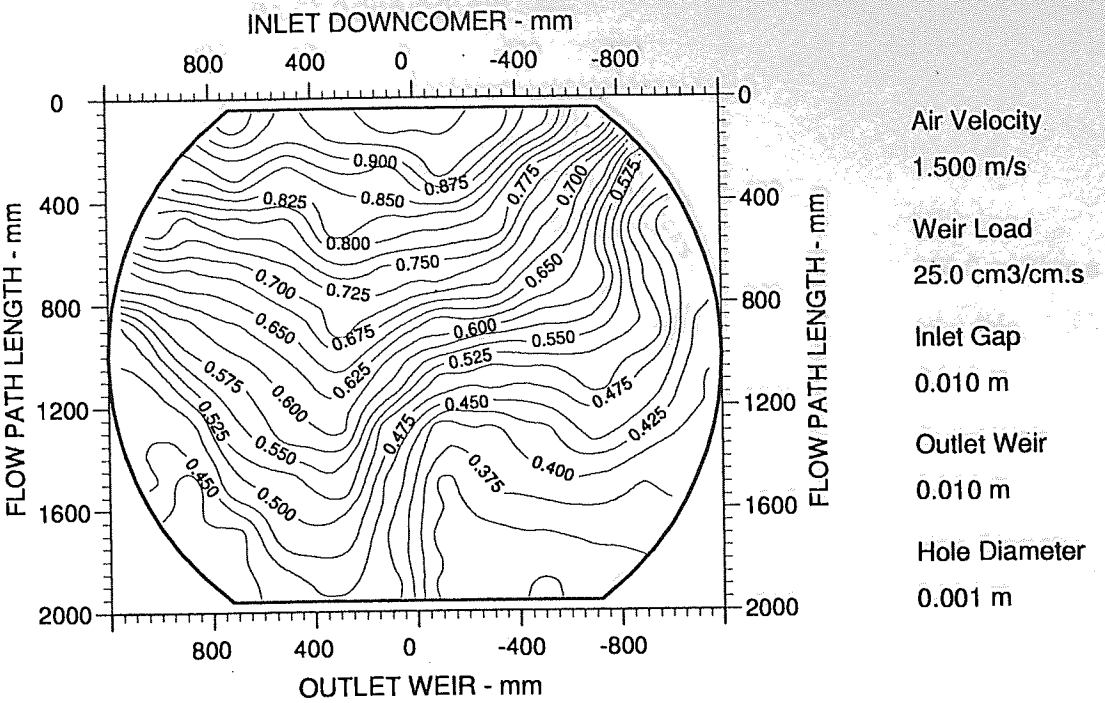

Figure A8.5 Two-dimensionl reduced temperature profiles for ARC-1 tray

Emv/Eog 86/50 hCL 21

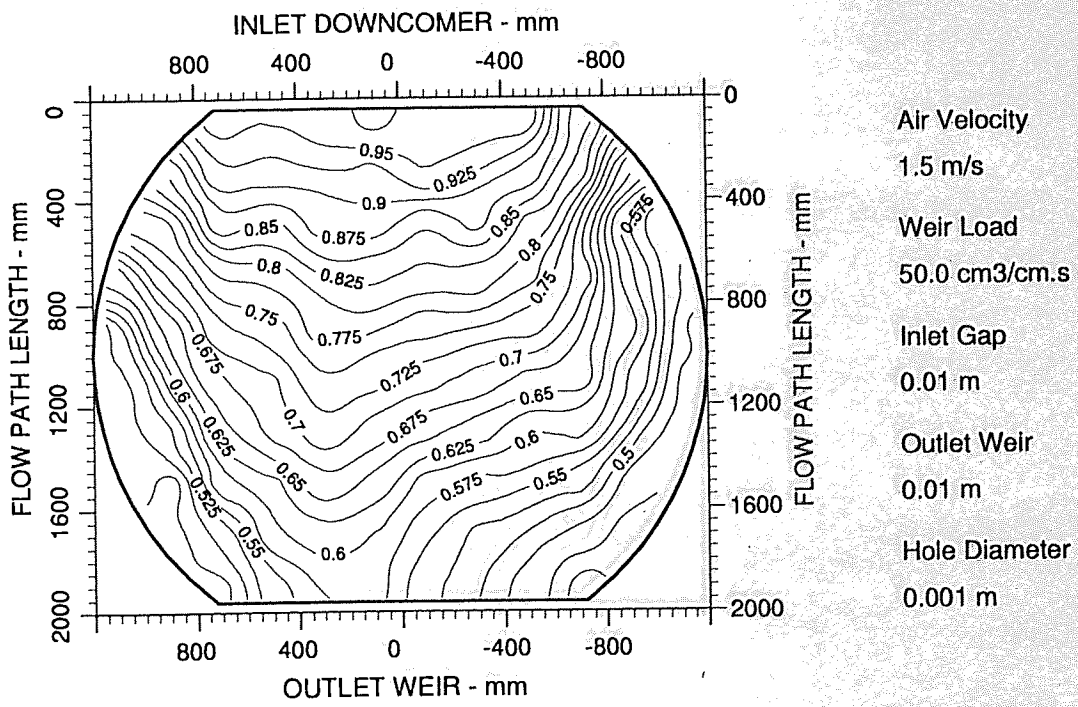

Figure A8.6 Two-dimensionl reduced temperature profiles for ARC-1 tray

Emv/Eog 99/64 hCL 24

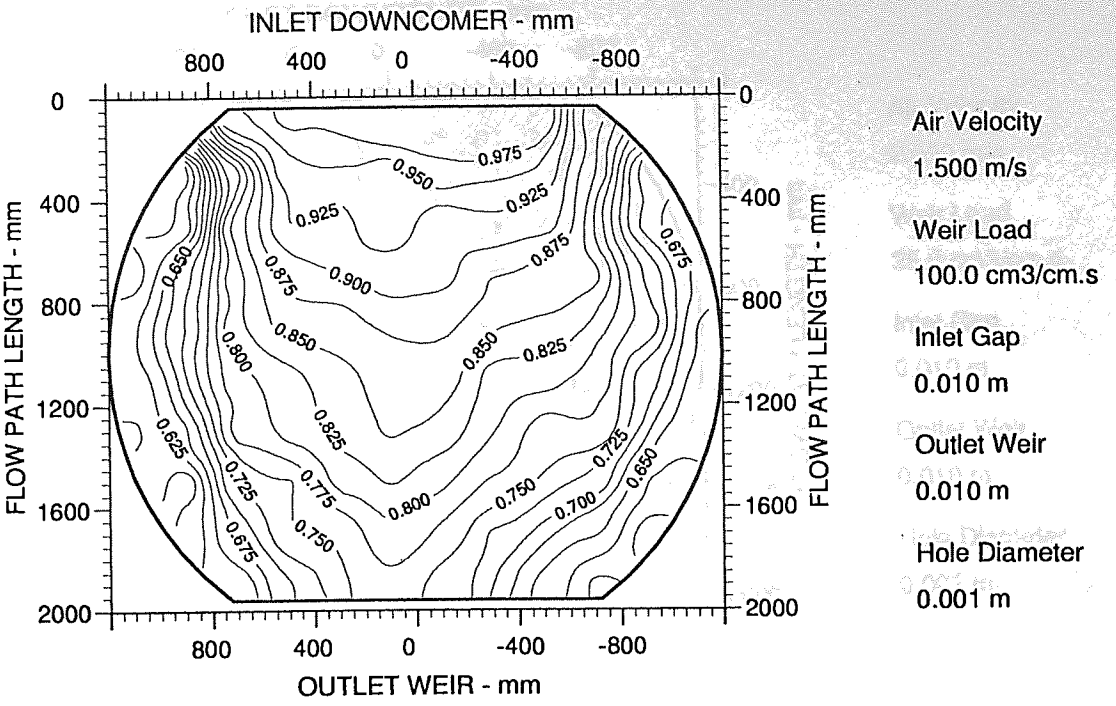

Figure A8.7 Two-dimensionl reduced temperature profiles for ARC-1 tray
Emv/Eog 91/74 hCL 27

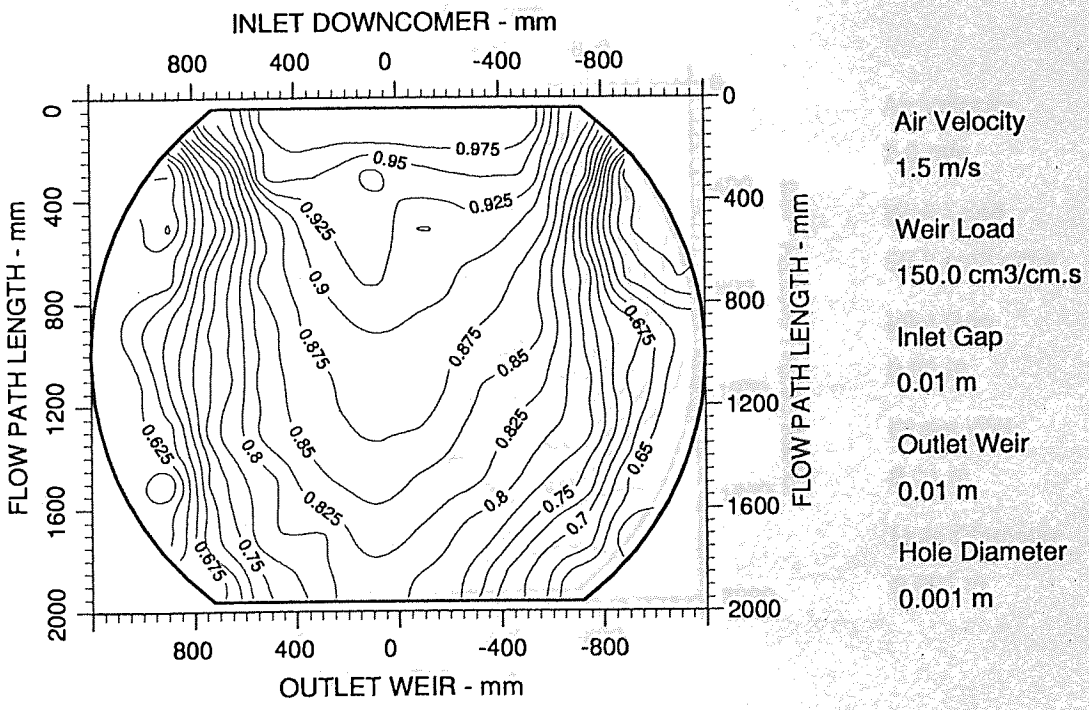

Figure A8.8 Two-dimensionl reduced temperature profiles for ARC-1 tray
Emv/Eog 96/84 hCL 32

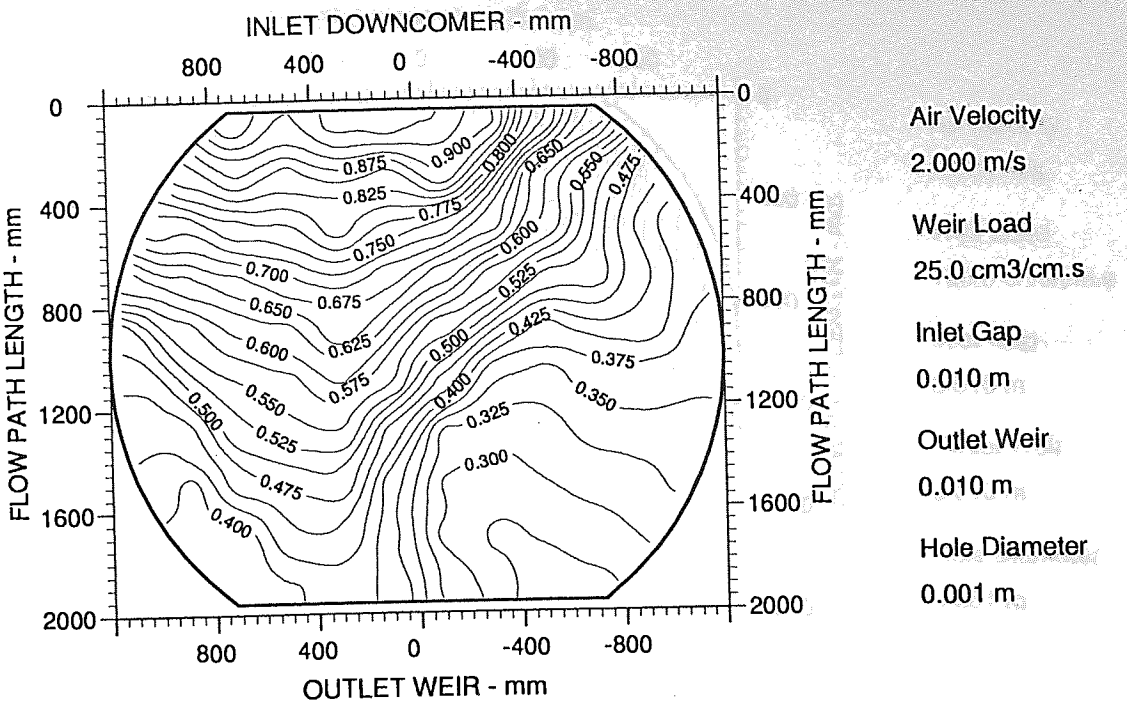

Figure A8.9 Two-dimensionl reduced temperature profiles for ARC-1 tray

Emv/Eog 82/45 hCL 19

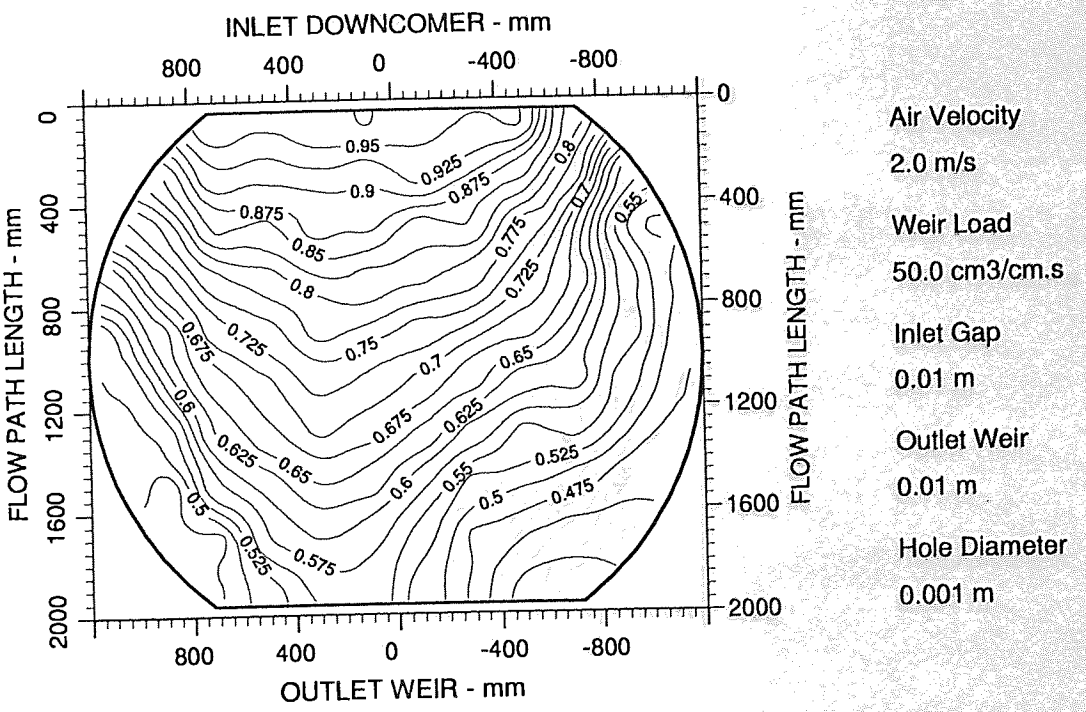

Figure A8.10 Two-dimensionl reduced temperature profiles for ARC-1 tray

Emv/Eog 85/56 hCL 20

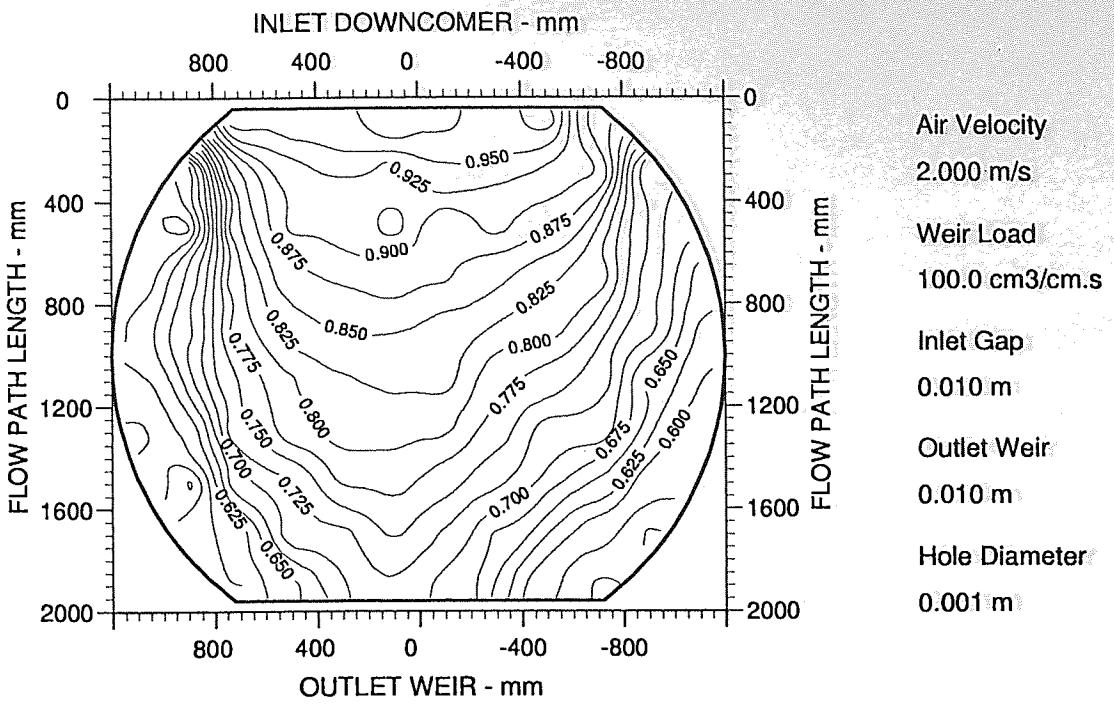

Figure A8.11 Two-dimensionl reduced temperature profiles for ARC-1 tray
Emv/Eog 89/70 hCL 24

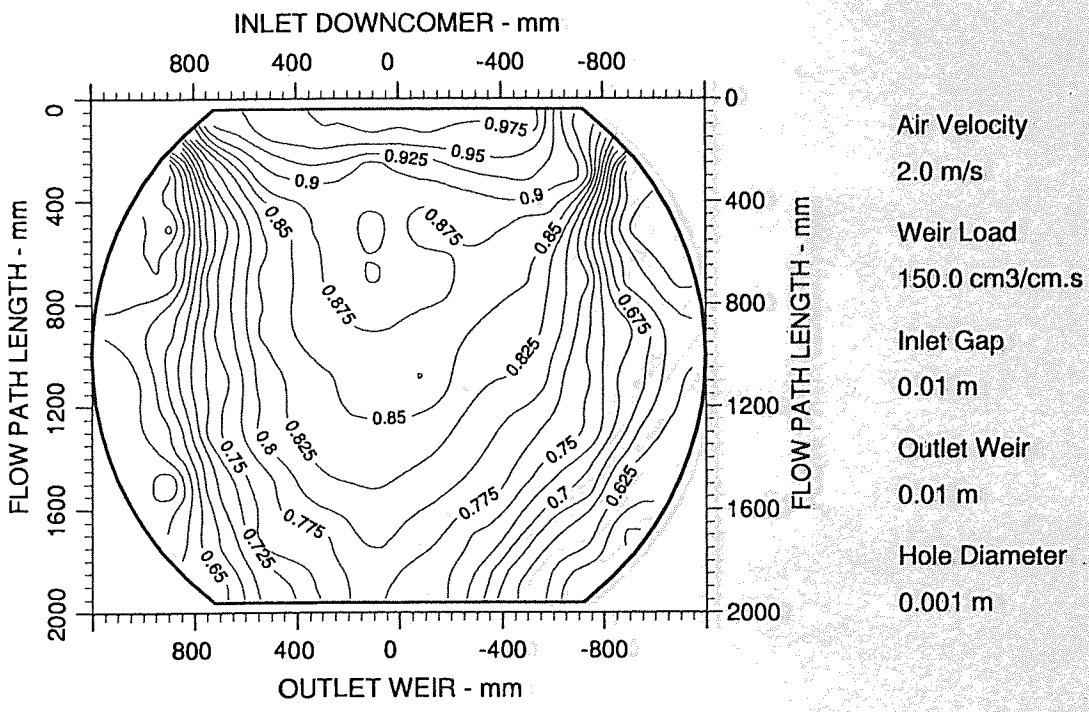

Figure A8.12 Two-dimensionl reduced temperature profiles for ARC-1 tray
Emv/Eog 96/81 hCL 24

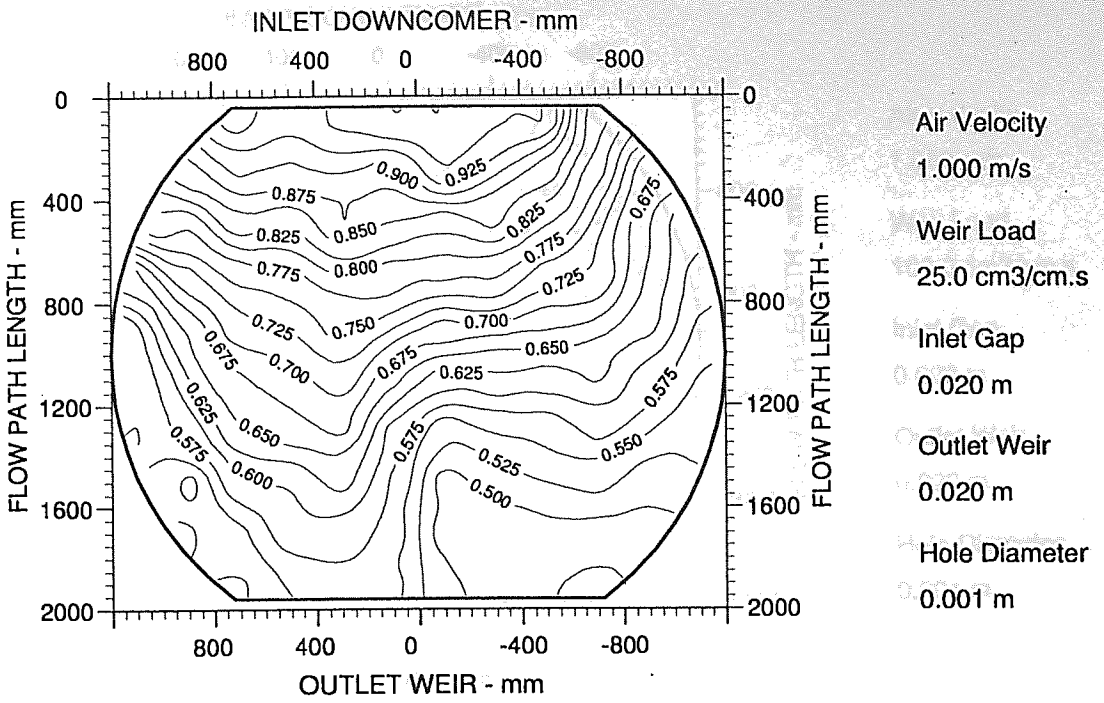

Figure A8.13 Two-dimensionl reduced temperature profiles for ARC-1 tray

Emv/Eog 87/54 hCL 25

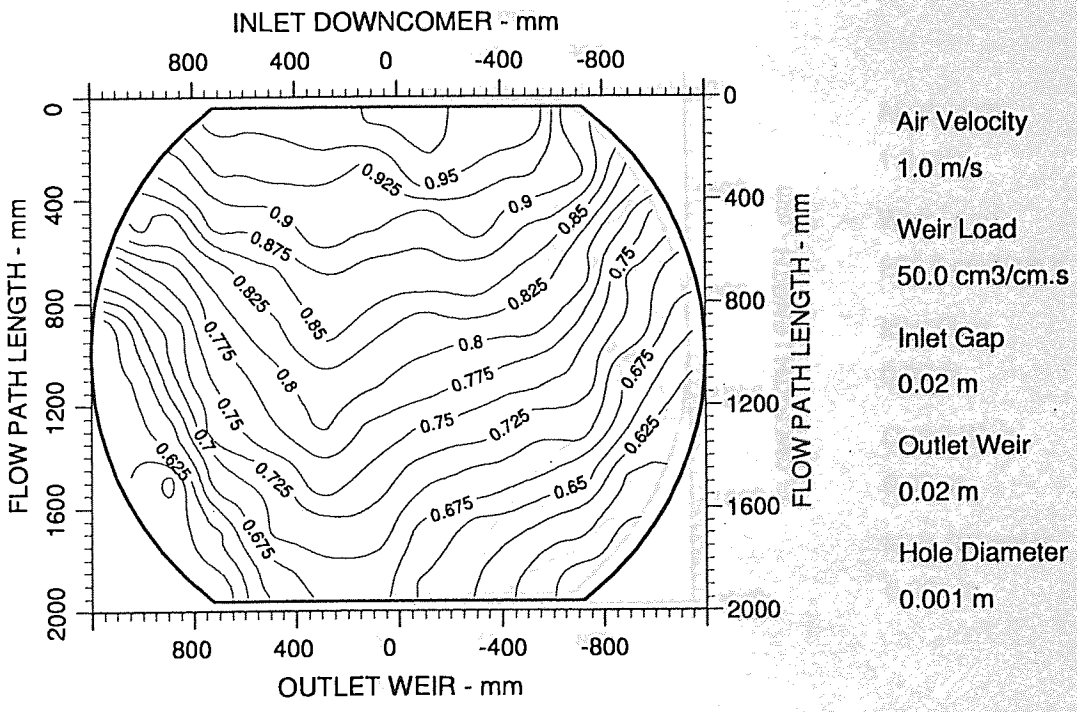

Figure A8.14 Two-dimensionl reduced temperature profiles for ARC-1 tray

Emv/Eog 98/69 hCL 30

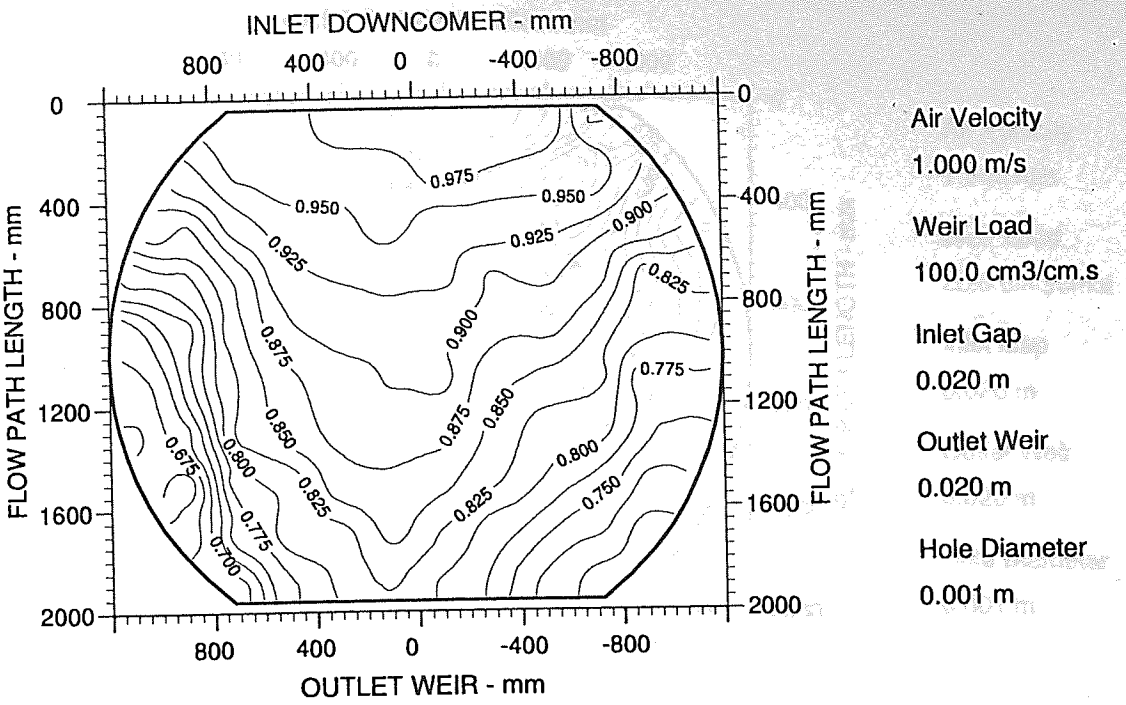

Figure A8.15 Two-dimensionl reduced temperature profiles for ARC-1 tray
Emv/Eog 100/80 hCL 35

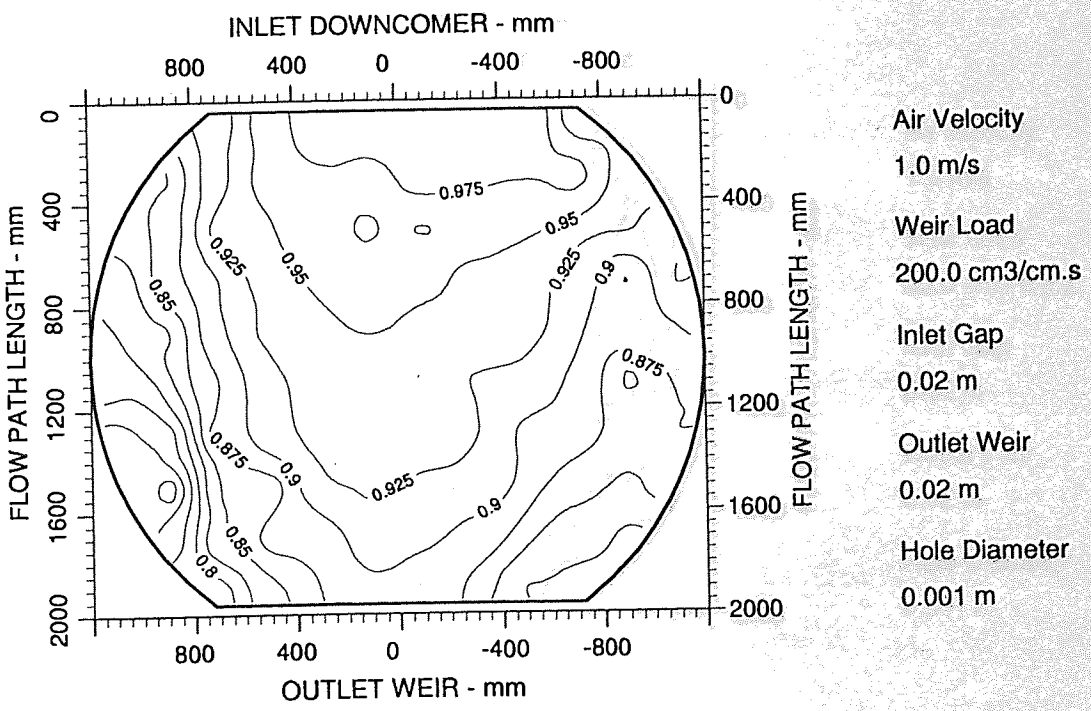

Figure A8.16 Two-dimensionl reduced temperature profiles for ARC-1 tray
Emv/Eog 103/92 hCL 44

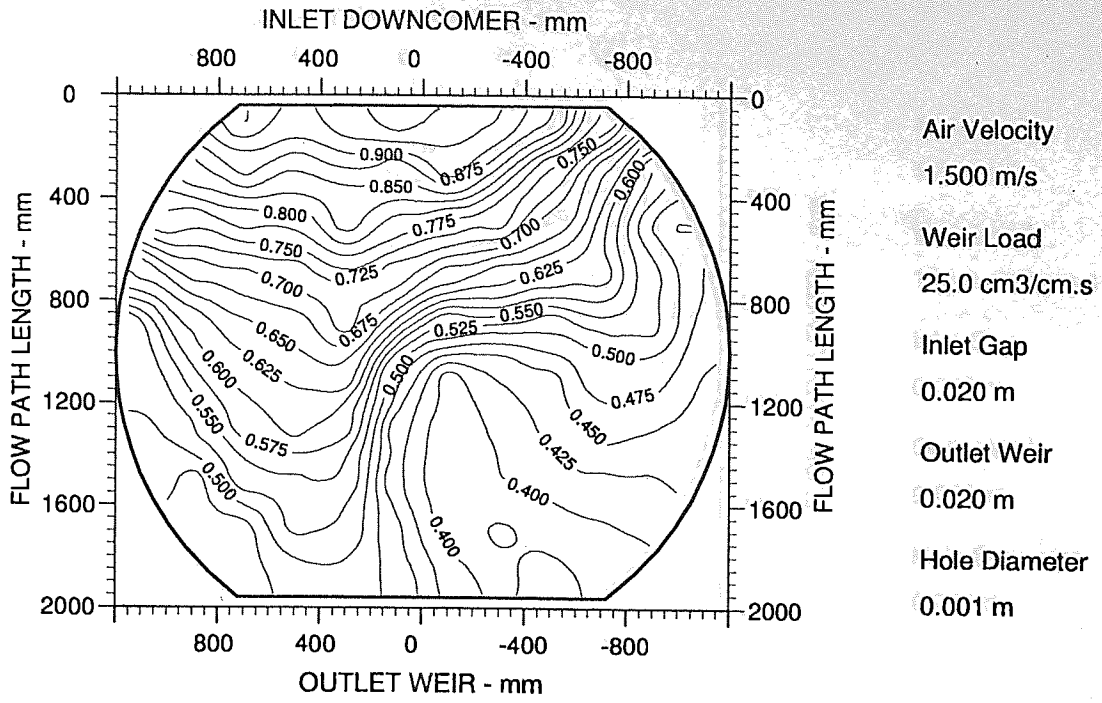

Figure A8.17 Two-dimensionl reduced temperature profiles for ARC-1 tray
Emv/Eog 84/50 hCL 24

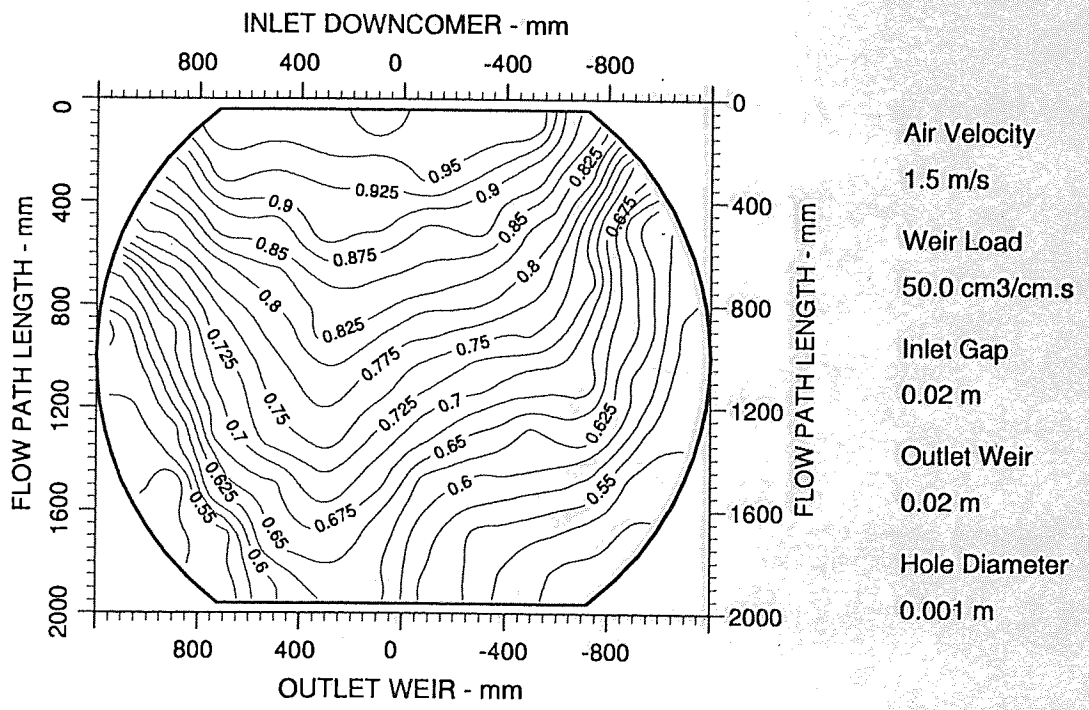

Figure A8.18 Two-dimensionl reduced temperature profiles for ARC-1 tray
Emv/Eog 89/61 hCL 28

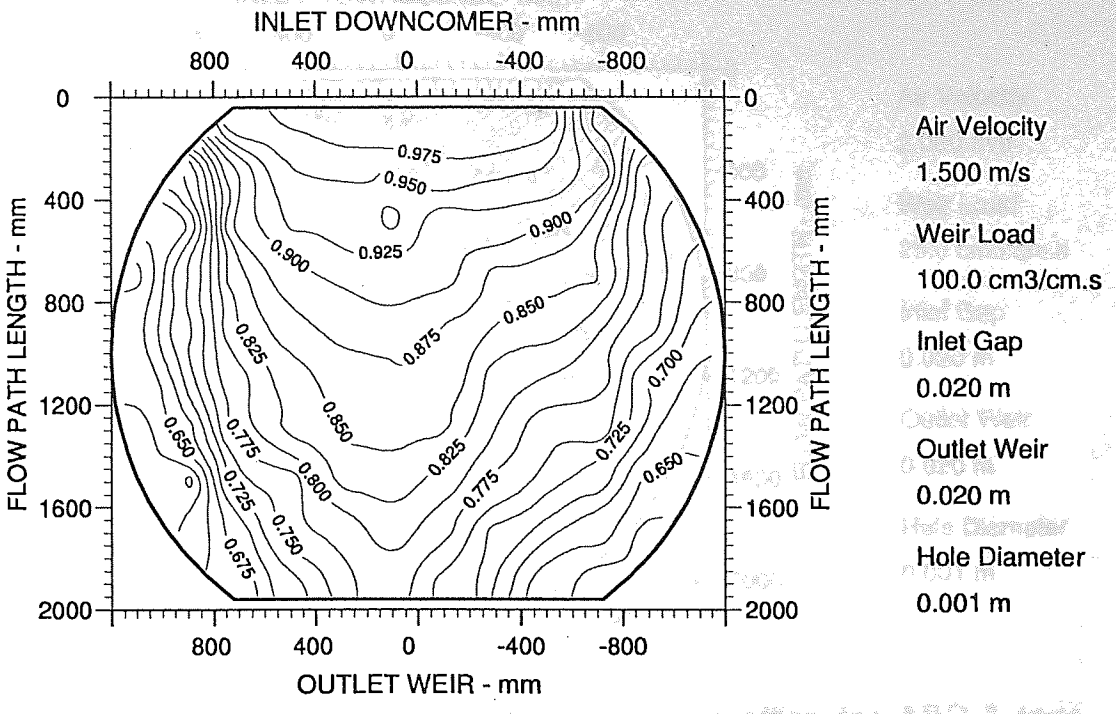

Figure A8.19 Two-dimensionl reduced temperature profiles for ARC-1 tray

Emv/Eog 95/76 hCL 33

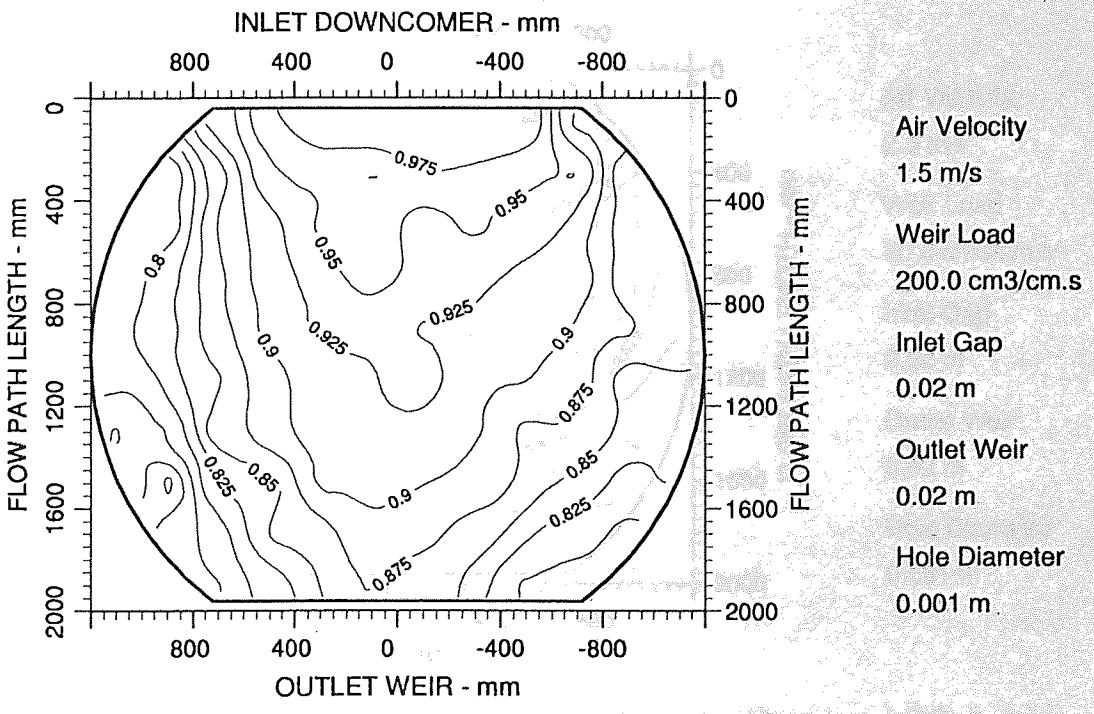

Figure A8.20 Two-dimensionl reduced temperature profiles for ARC-1 tray

Emv/Eog 93/83 hCL 42

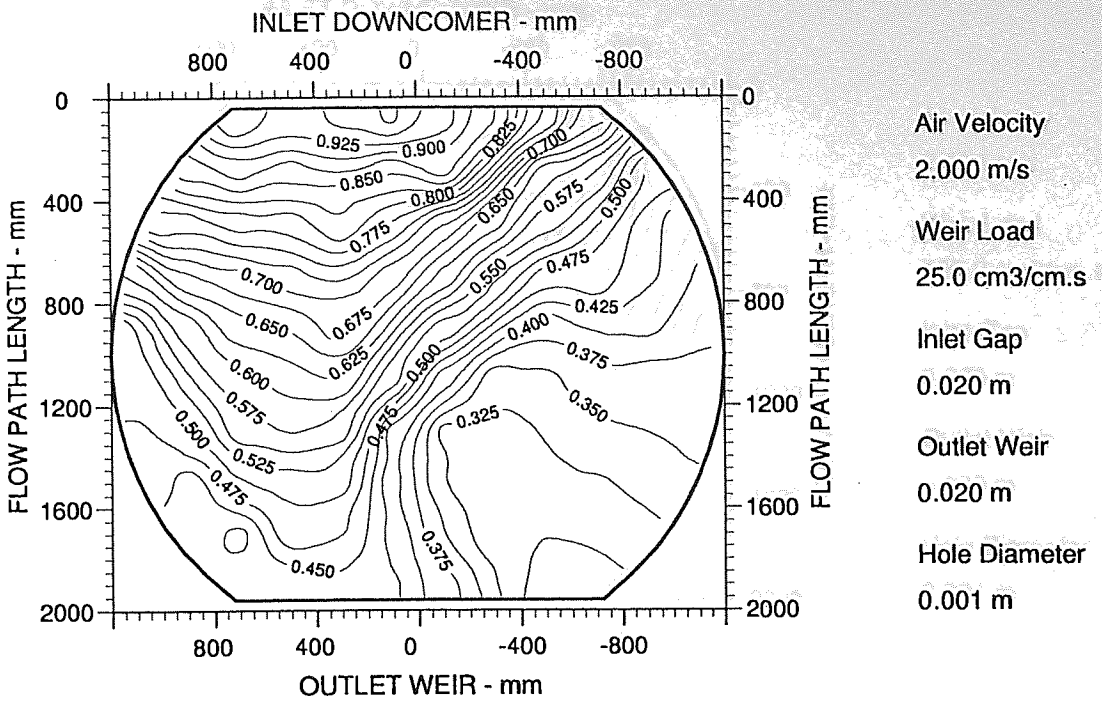

Figure A8.21 Two-dimensionl reduced temperature profiles for ARC-1 tray

Emv/Eog 80/47 hCL 20

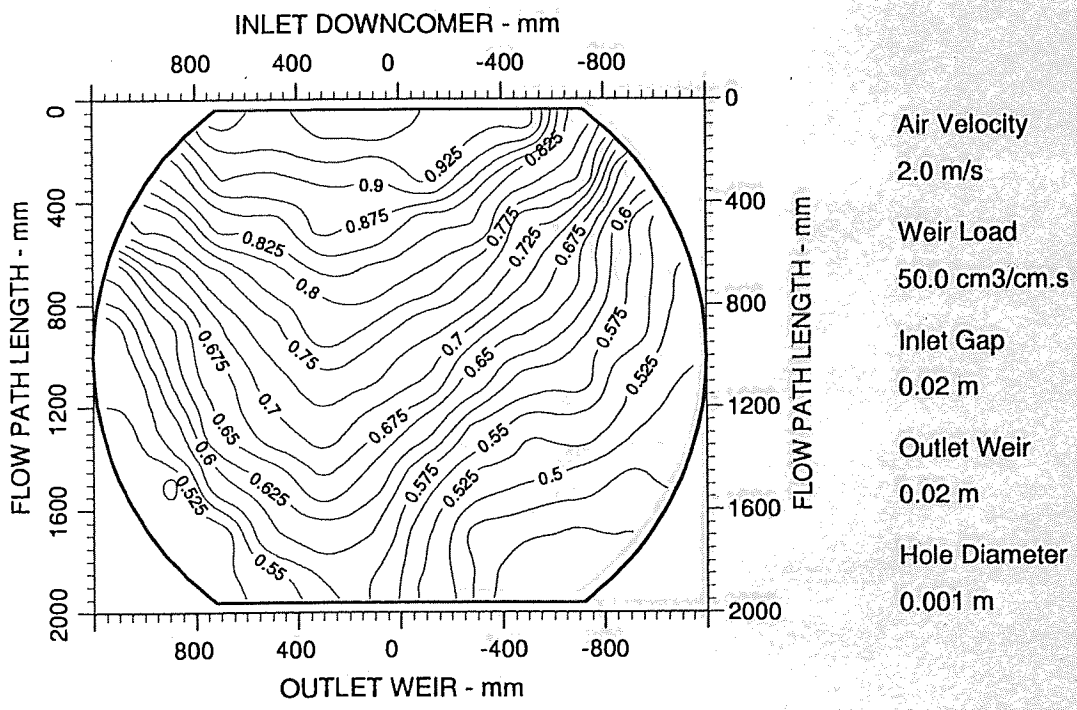

Figure A8.22 Two-dimensionl reduced temperature profiles for ARC-1 tray

Emv/Eog 91/59 hCL 22

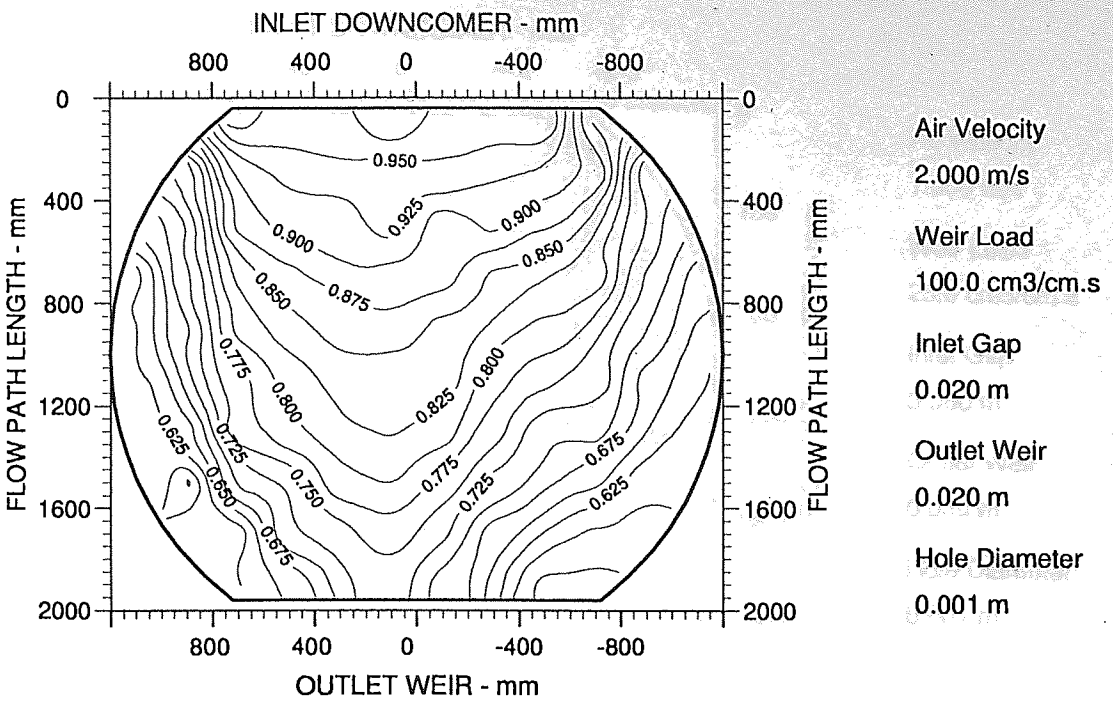

Figure A8.23 Two-dimensionl reduced temperature profiles for ARC-1 tray

Emv/Eog 95/73 hCL 25

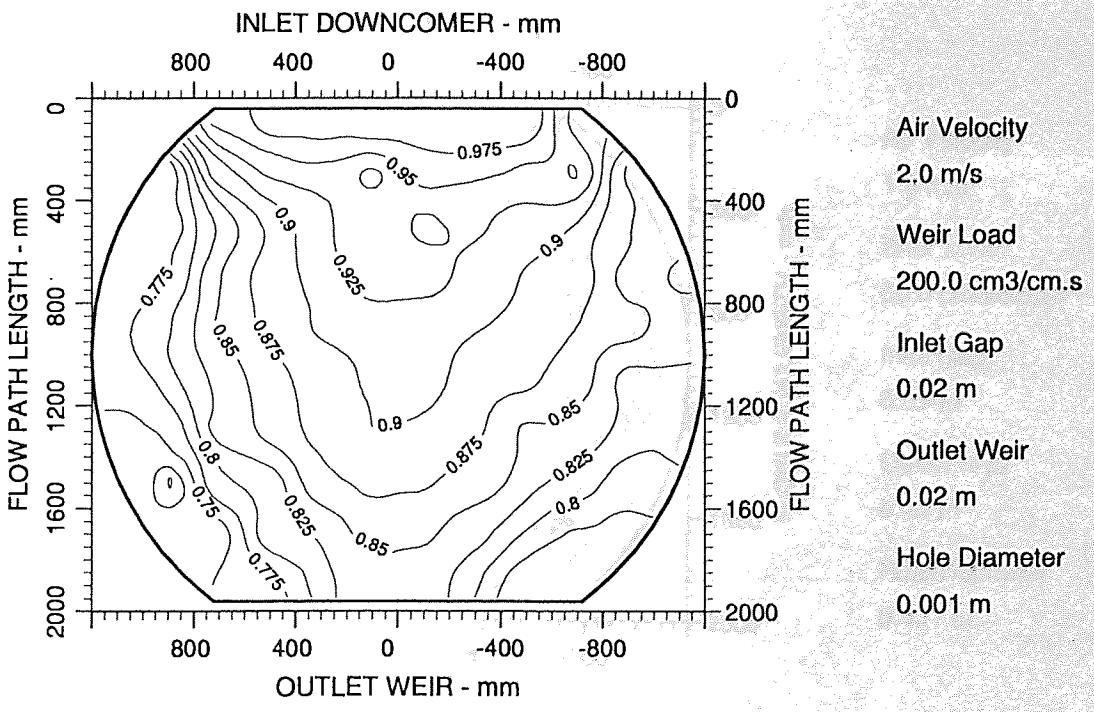

Figure A8.24 Two-dimensionl reduced temperature profiles for ARC-1 tray

Emv/Eog 93/81 hCL 34

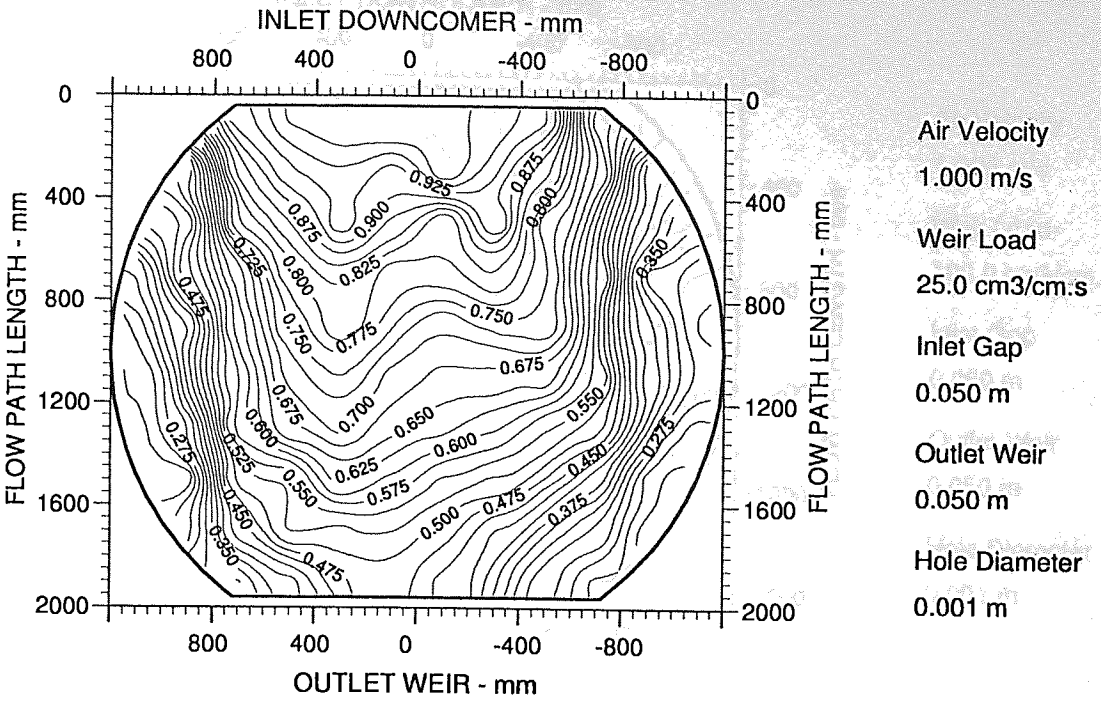

Figure A8.25 Two-dimensionl reduced temperature profiles for ARC-1 tray
Emv/Eog 89/50 hCL 35

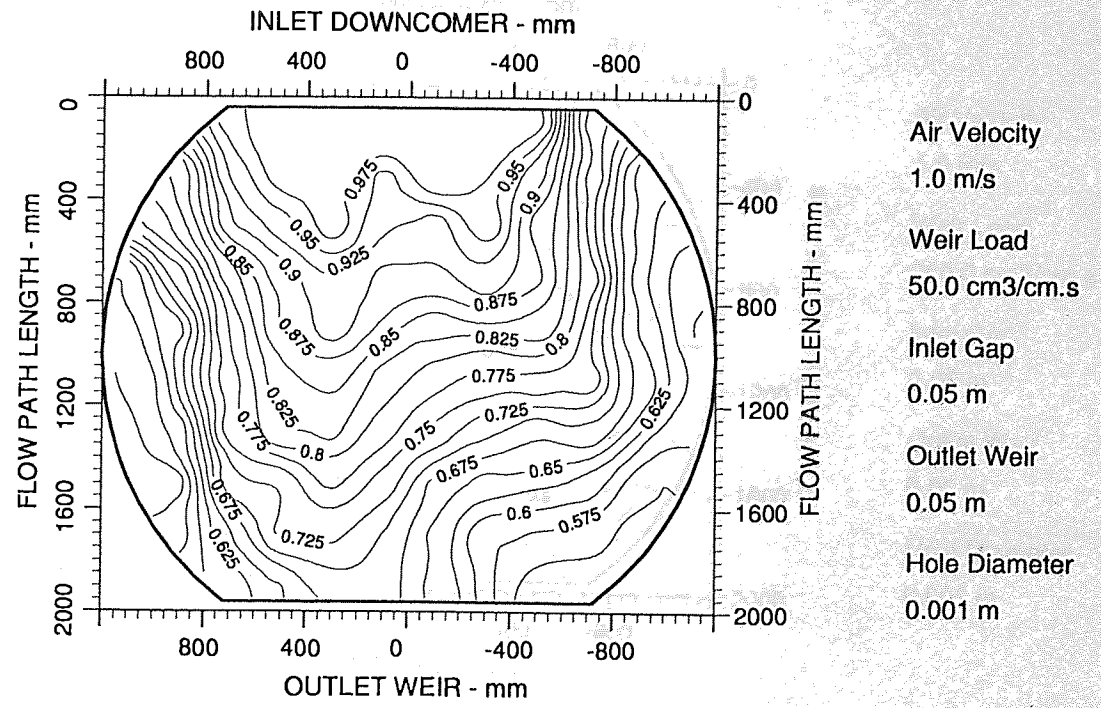

Figure A8.26 Two-dimensionl reduced temperature profiles for ARC-1 tray
Emv/Eog 97/74 hCL 40

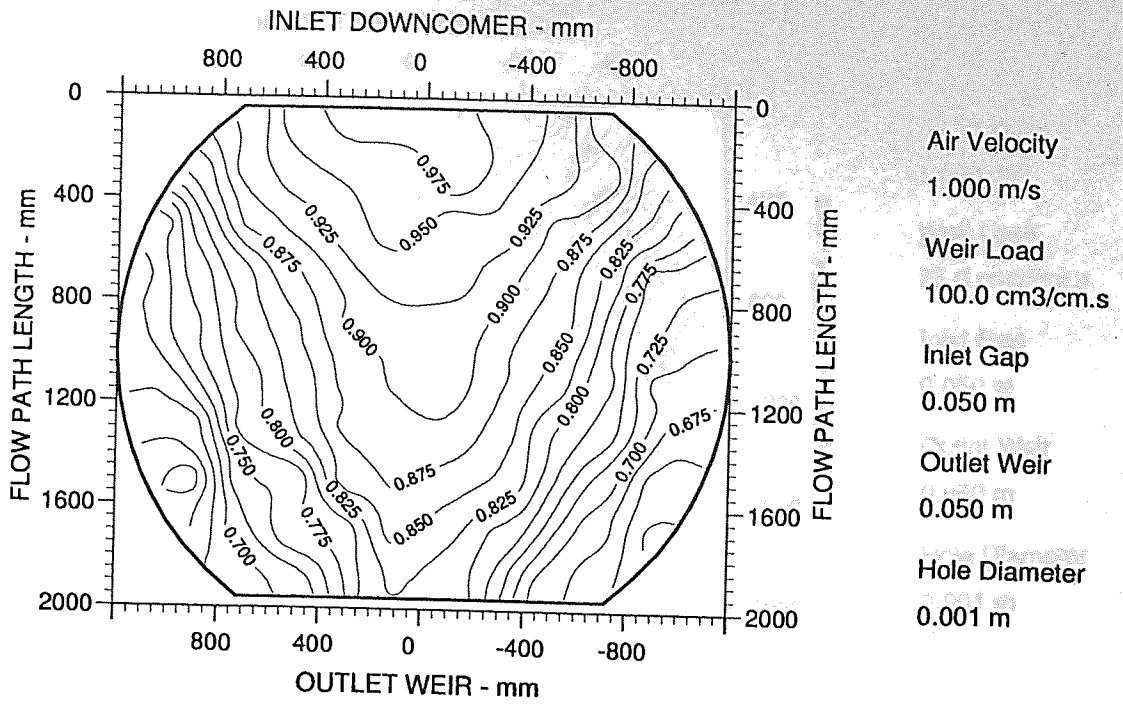

Figure A8.27 Two-dimensionl reduced temperature profiles for ARC-1 tray
Emv/Eog 106/88 hCL 48

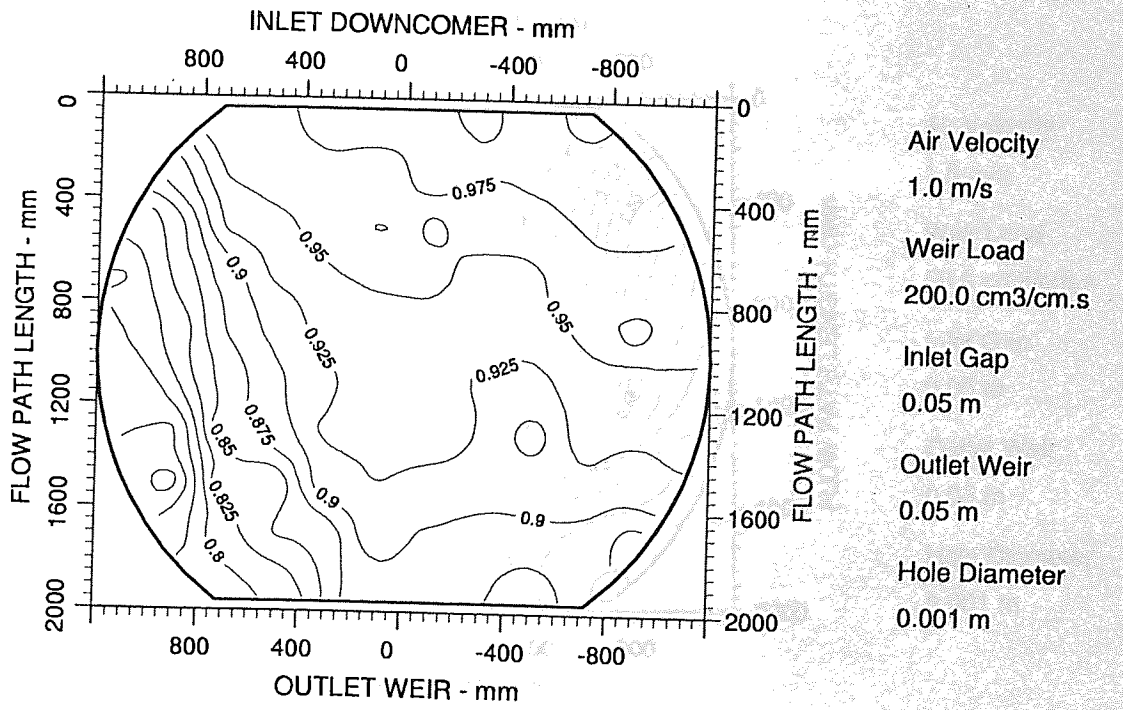

Figure A8.28 Two-dimensionl reduced temperature profiles for ARC-1 tray
Emv/Eog 104/94 hCL 62

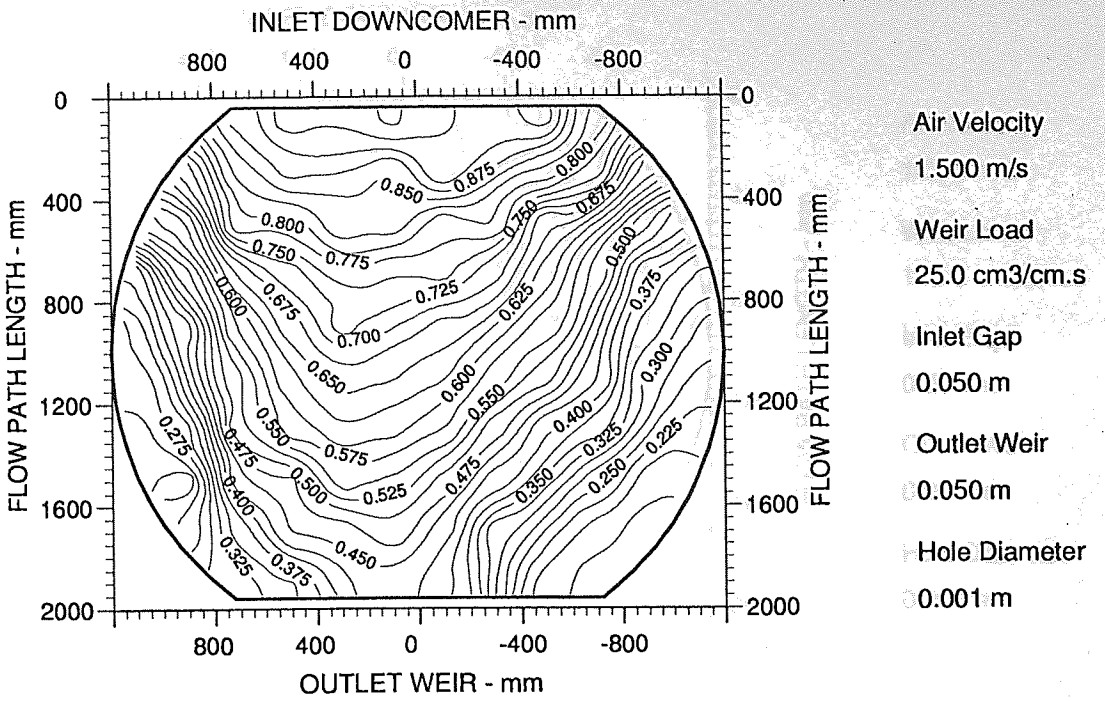

Figure A8.29 Two-dimensionl reduced temperature profiles for ARC-1 tray

Emv/Eog 87/44 hCL 33

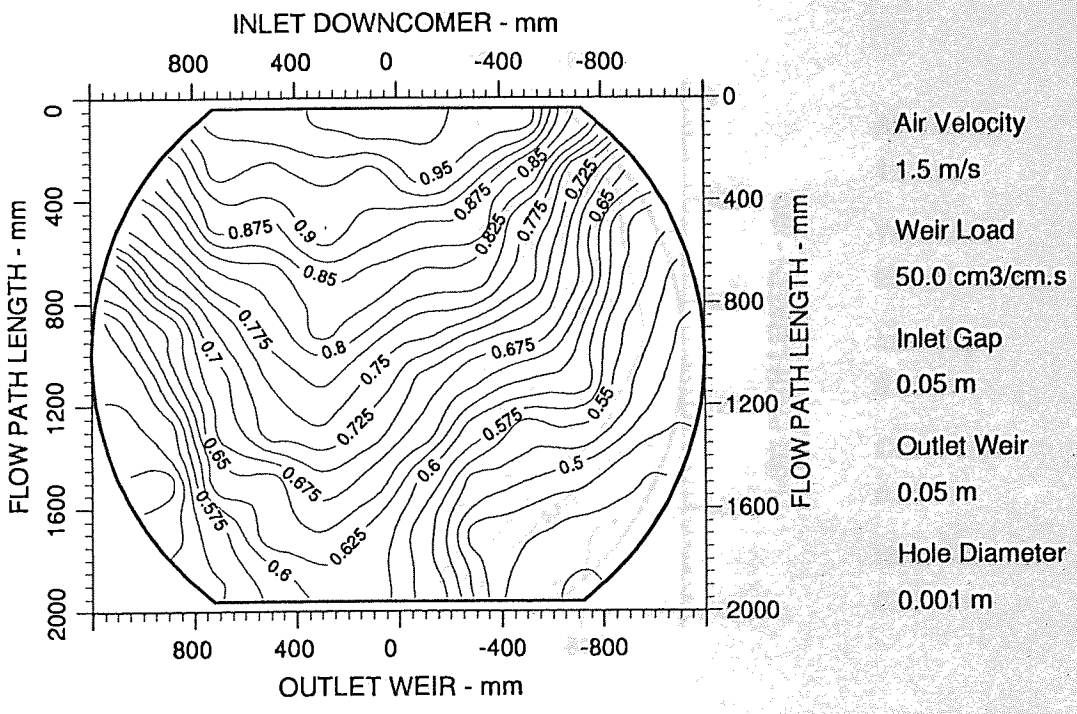

Figure A8.30 Two-dimensionl reduced temperature profiles for ARC-1 tray

Emv/Eog 94/68 hCL 38

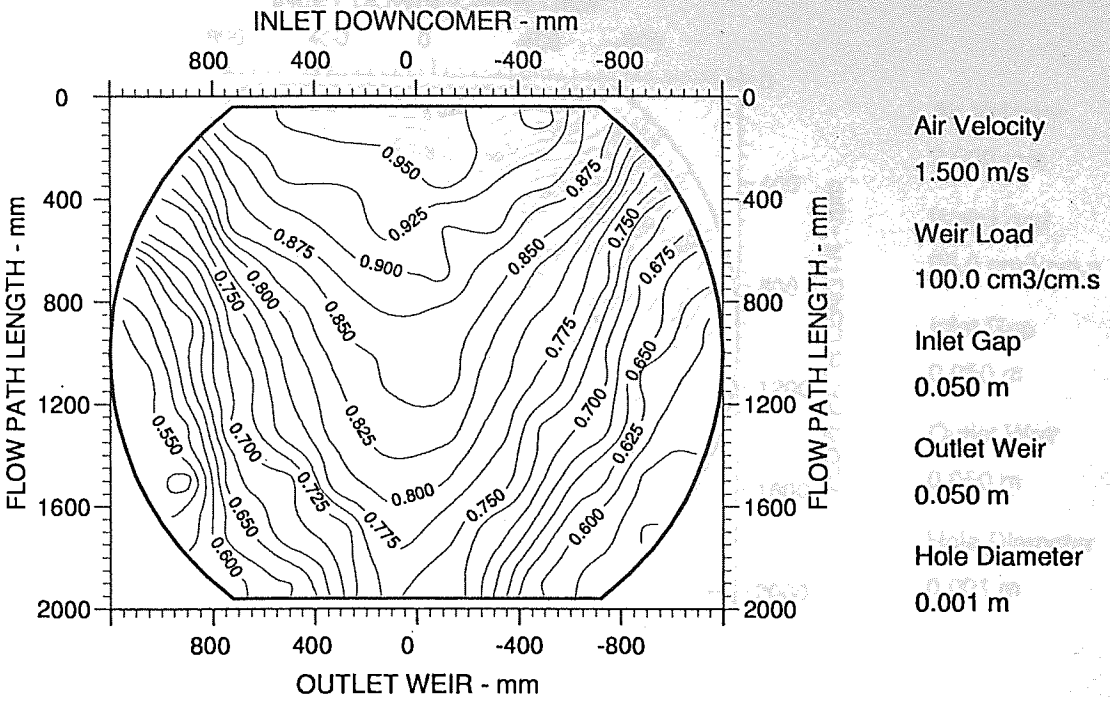

Figure A8.31 Two-dimensionl reduced temperature profiles for ARC-1 tray
Emv/Eog 108/84 hCL 42

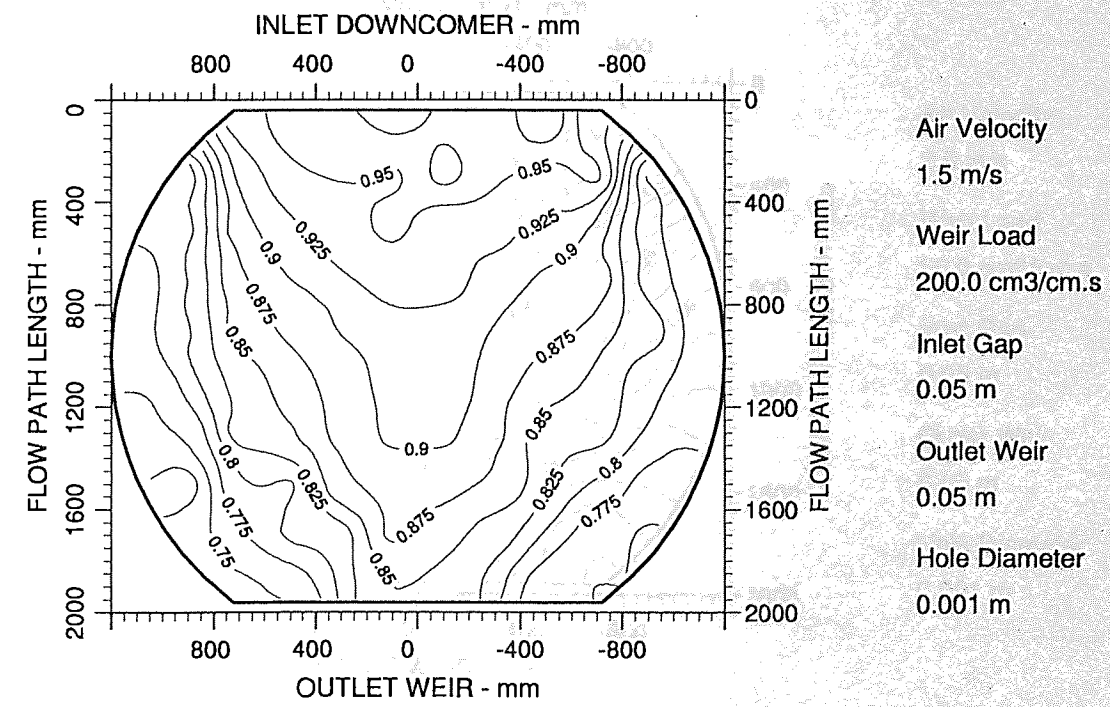

Figure A8.32 Two-dimensionl reduced temperature profiles for ARC-1 tray
Emv/Eog 109/92 hCL 53

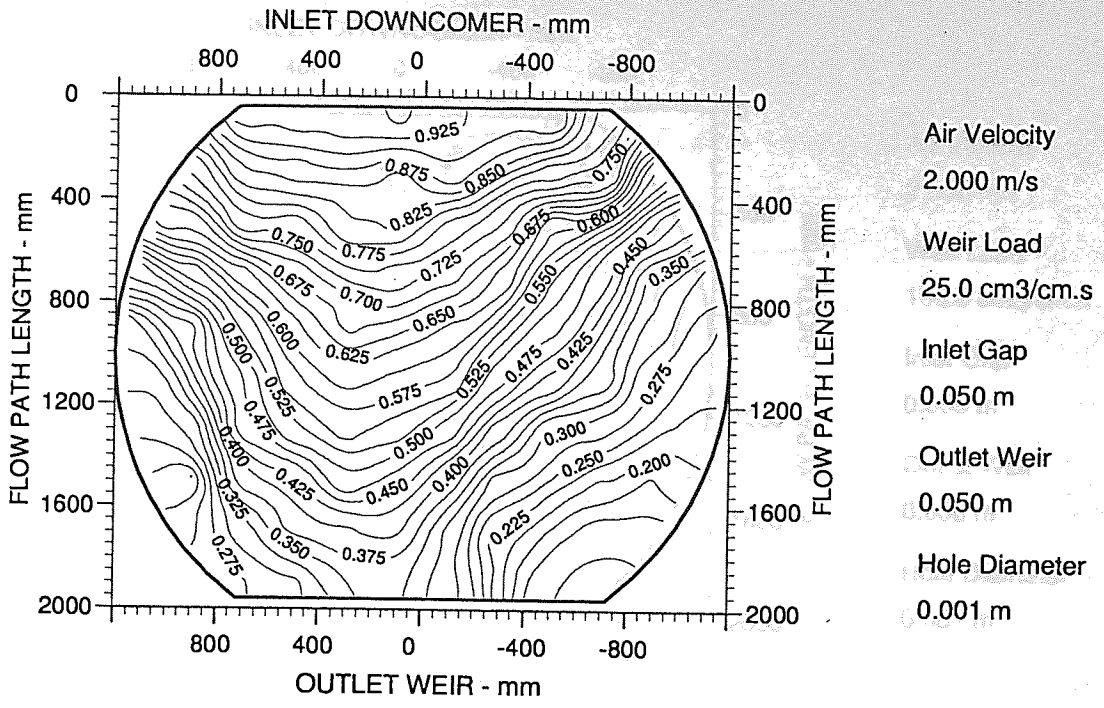

Figure A8.33 Two-dimensionl reduced temperature profiles for ARC-1 tray

Emv/Eog 96/42 hCL 25

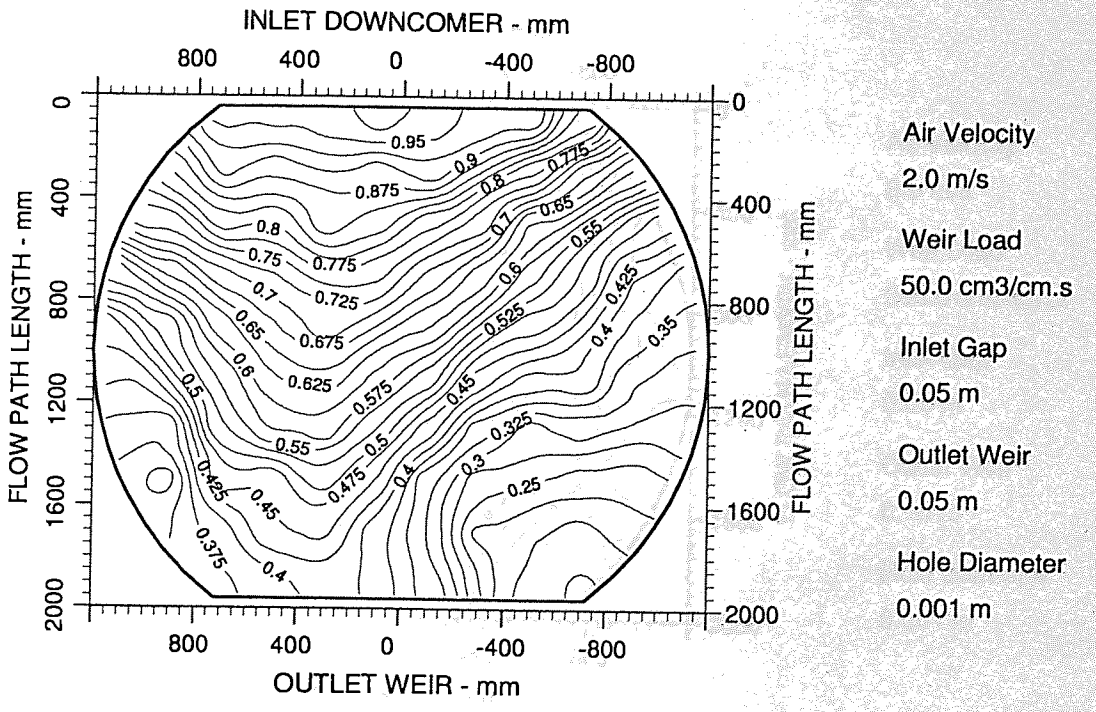

Figure A8.34 Two-dimensionl reduced temperature profiles for ARC-1 tray

Emv/Eog 98/59 hCL 28

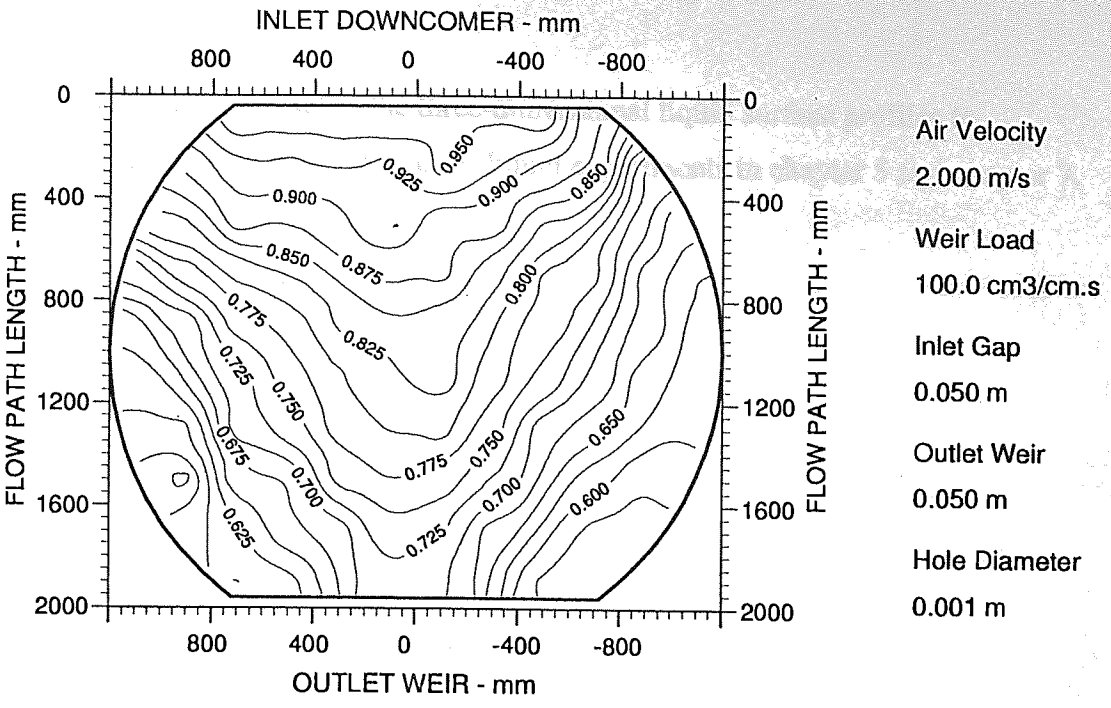

Figure A8.35 Two-dimensionl reduced temperature profiles for ARC-1 tray
Emv/Eog 97/74 hCL 32

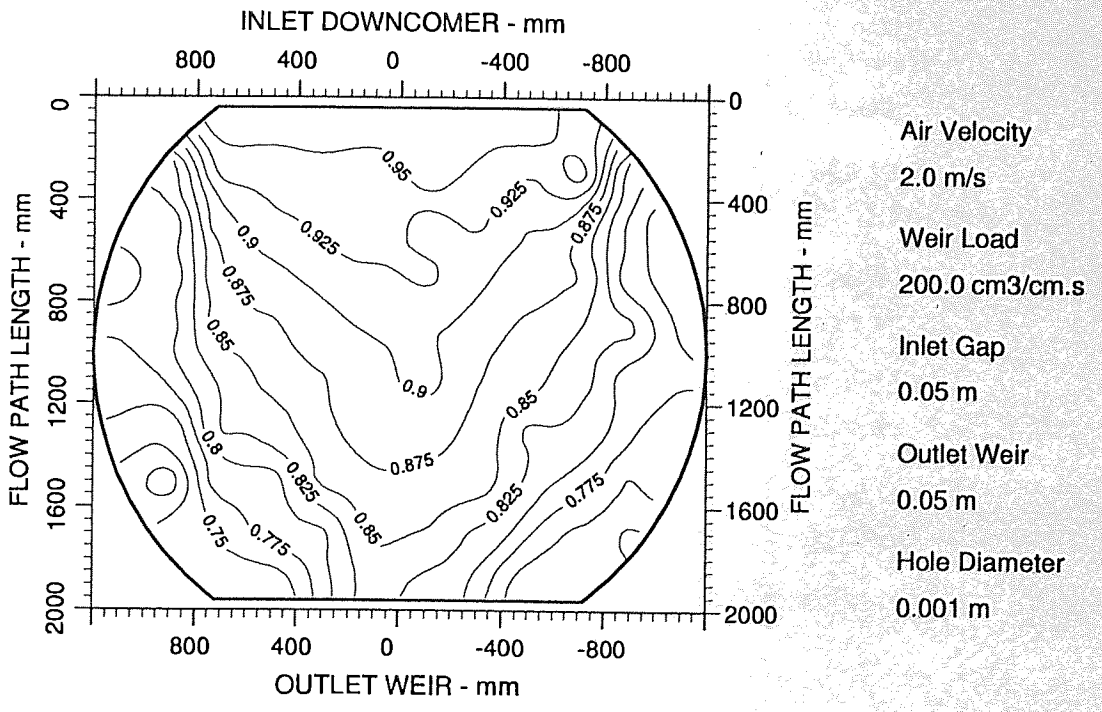

Figure A8.36 Two-dimensionl reduced temperature profiles for ARC-1 tray
Emv/Eog 102/88 hCL 39

Appendices 9-11
Three-Dimensional Liquid Head Surface Profiles
UMD, STR-1 and ARC-1 Tray Cases

The appendices contain a full set of the three-dimensional liquid surface profiles to complement the results of the height of clear liquid experiments in chapter 5 and chapter 7.

Appendices 9

Three-Dimensional Liquid Head Surface Profiles UMD Tray Cases

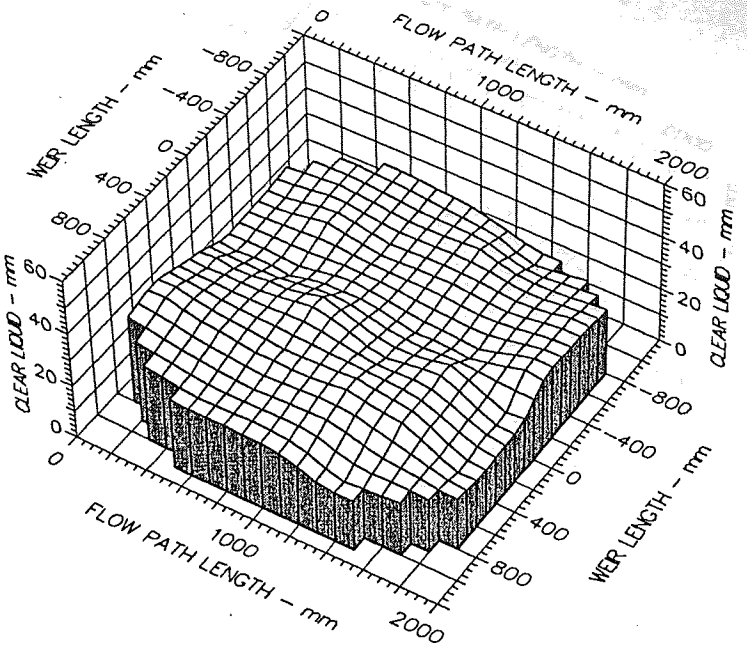

Air Velocity
1.000 m/s
Weir Load
50.0 cm3/cm.s
Inlet Gap
0.010 m
Outlet Weir
0.010 m
Hole Diameter
0.001 m

Figure A9.1 Surface of clear liquid hold-up for UMD tray
Mean hCL 26 Emg/Eog 101/72

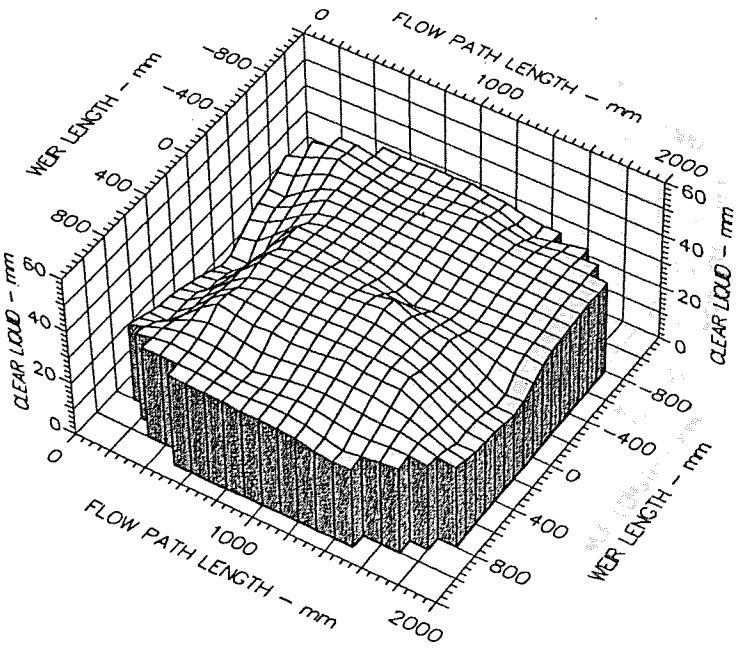

Air Velocity
1.0 m/s
Weir Load
150.0 cm3/cm.s
Inlet Gap
0.01 m
Outlet Weir
0.01 m
Hole Diameter
0.001 m

Figure A9.2 Surface of clear liquid hold-up for UMD tray
Mean hCL 34 Emg/Eog 97/90

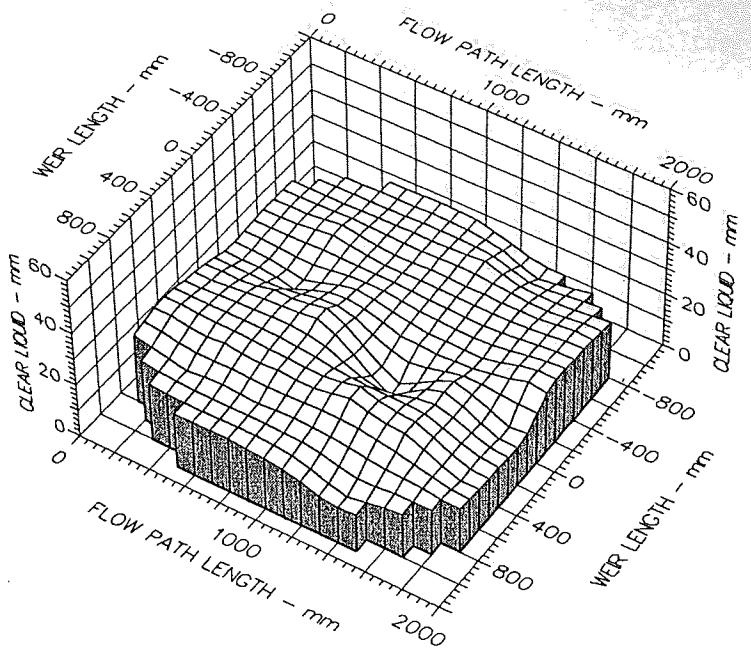

Air Velocity
1.500 m/s

Weir Load
50.0 cm3/cm.s

Inlet Gap
0.010 m

Outlet Weir
0.010 m

Hole Diameter
0.001 m

Figure A9.3 Surface of clear liquid hold-up for UMD tray
Mean hCL 22 Emg/Eog 99/64

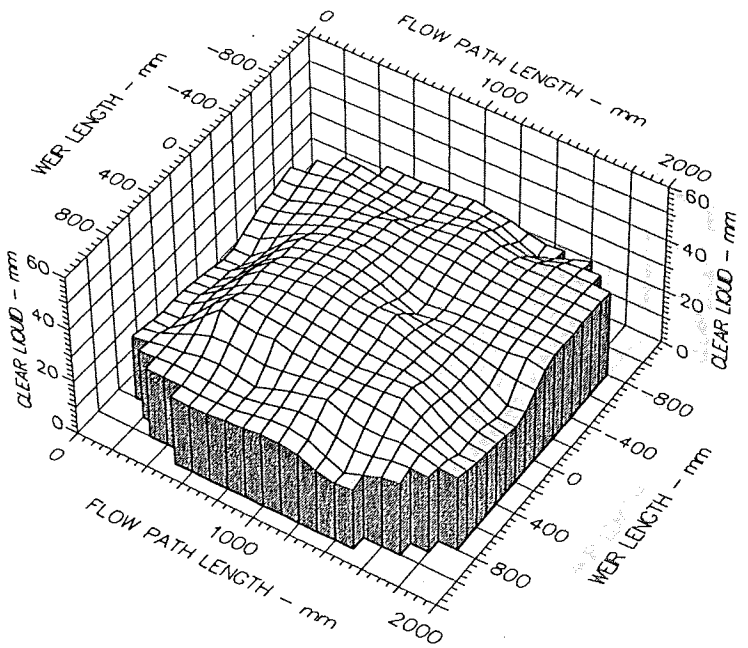

Air Velocity
1.5 m/s

Weir Load
150.0 cm3/cm.s

Inlet Gap
0.01 m

Outlet Weir
0.01 m

Hole Diameter
0.001 m

Figure A9.4 Surface of clear liquid hold-up for UMD tray
Mean hCL 31 Emg/Eog 94/84

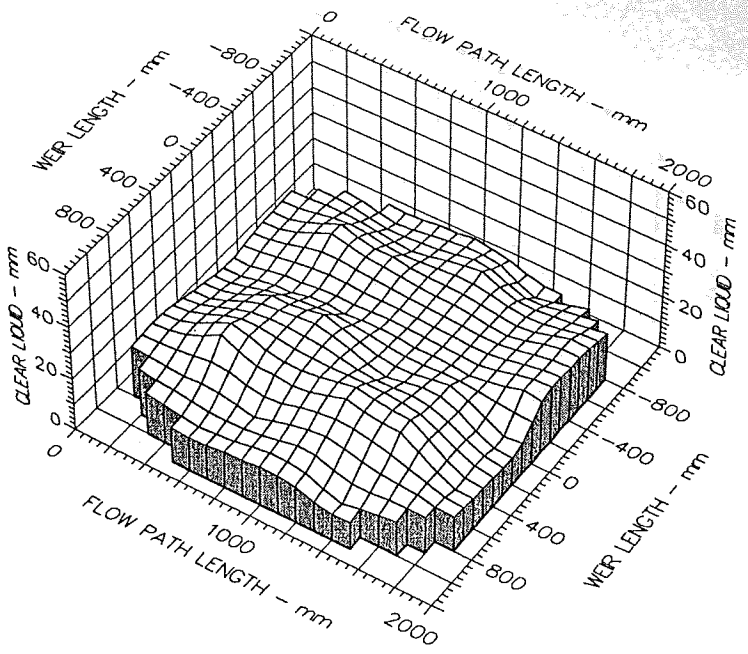

Air Velocity
2.000 m/s

Weir Load
50.0 cm3/cm.s

Inlet Gap
0.010 m

Outlet Weir
0.010 m

Hole Diameter
0.001 m

Figure A9.5 Surface of clear liquid hold-up for UMD tray
Mean hCL 19 Emg/Eog 91/57

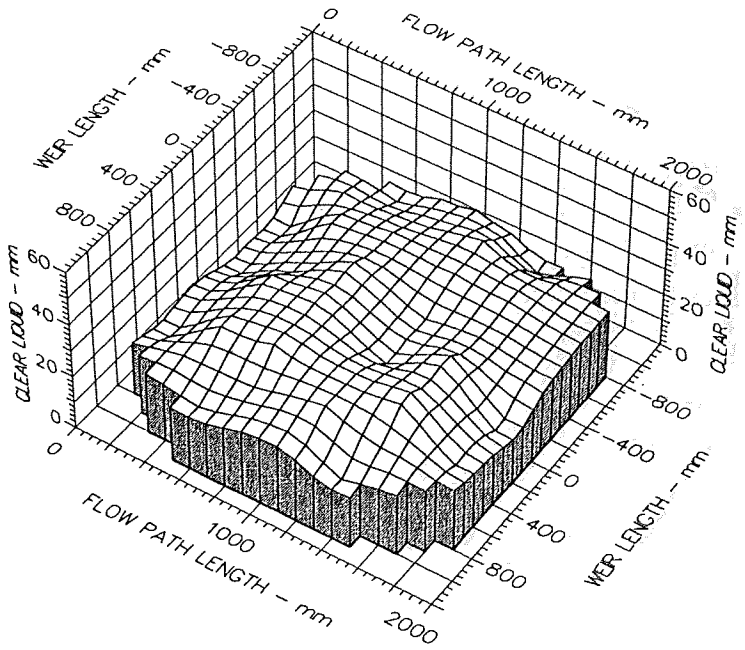

Air Velocity
2.0 m/s

Weir Load
150.0 cm3/cm.s

Inlet Gap
0.01 m

Outlet Weir
0.01 m

Hole Diameter
0.001 m

Figure A9.6 Surface of clear liquid hold-up for UMD tray
Mean hCL 26 Emg/Eog 94/81

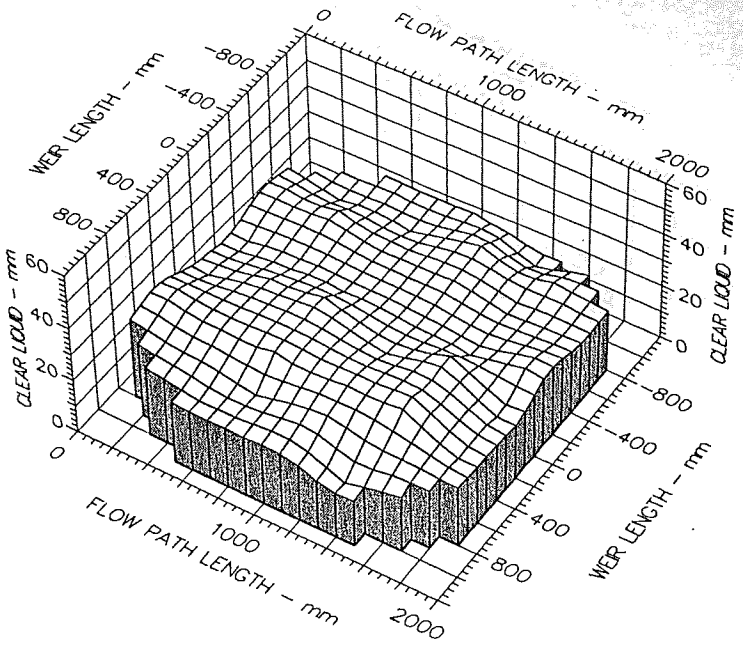

Air Velocity
1.500 m/s

Weir Load
50.0 cm3/cm.s

Inlet Gap
0.010 m

Outlet Weir
0.020 m

Hole Diameter
0.001 m

Figure A9.7 Surface of clear liquid hold-up for UMD tray
Mean hCL 26 Emg/Eog 99/68

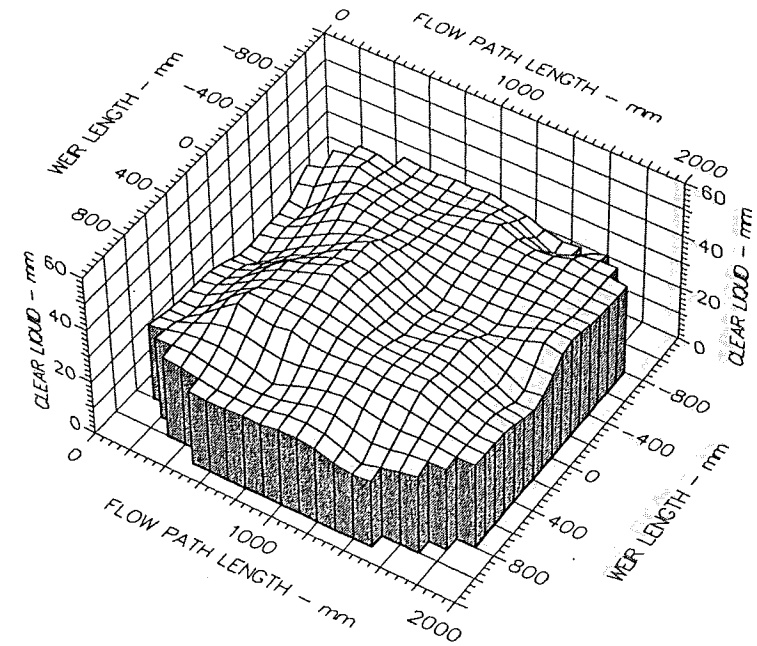

Air Velocity
1.5 m/s

Weir Load
150.0 cm3/cm.s

Inlet Gap
0.01 m

Outlet Weir
0.02 m

Hole Diameter
0.001 m

Figure A9.8 Surface of clear liquid hold-up for UMD tray
Mean hCL 33 Emg/Eog 92/84

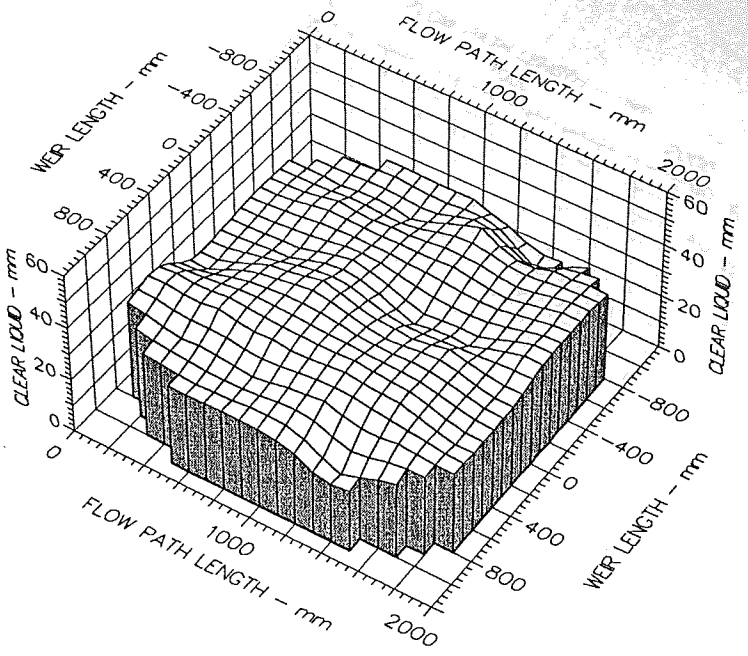

Air Velocity
1.500 m/s

Weir Load
50.0 cm3/cm.s

Inlet Gap
0.010 m

Outlet Weir
0.050 m

Hole Diameter
0.001 m

Figure A9.9 Surface of clear liquid hold-up for UMD tray
Mean hCL 33 Emg/Eog 107/71

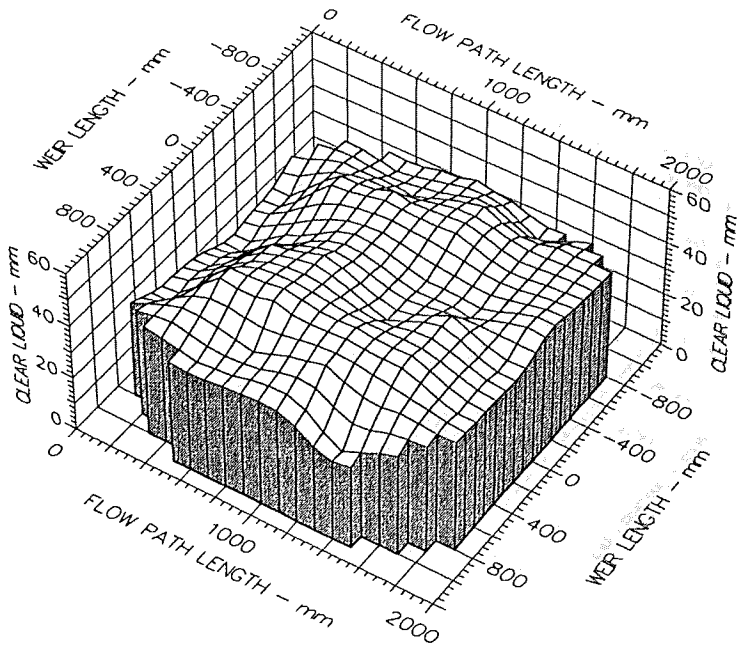

Air Velocity
1.5 m/s

Weir Load
150.0 cm3/cm.s

Inlet Gap
0.01 m

Outlet Weir
0.05 m

Hole Diameter
0.001 m

Figure A9.10 Surface of clear liquid hold-up for UMD tray
Mean hCL 41 Emg/Eog 100/90

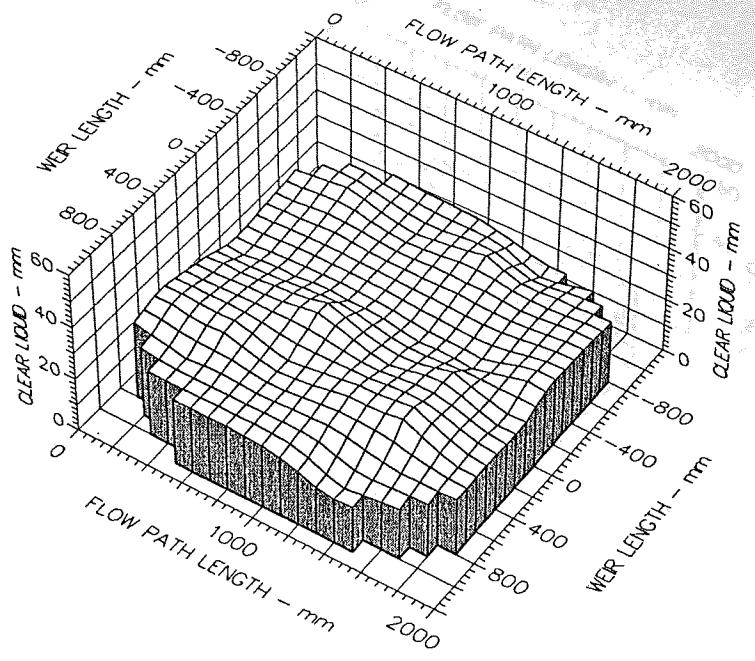

Air Velocity
1.500 m/s

Weir Load
50.0 cm3/cm.s

Inlet Gap
0.020 m

Outlet Weir
0.010 m

Hole Diameter
0.001 m

Figure A9.11 Surface of clear liquid hold-up for UMD tray
Mean hCL 25 Emg/Eog 84/58

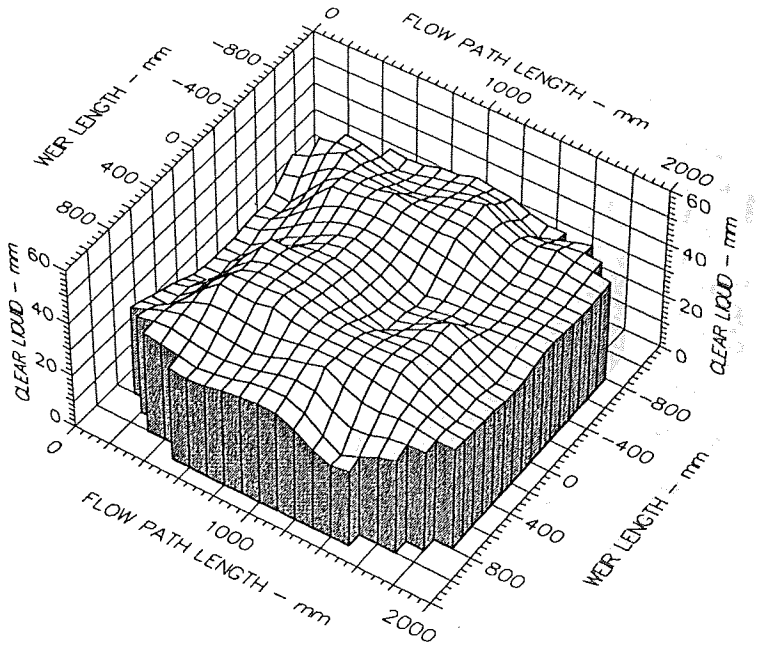

Air Velocity
1.5 m/s

Weir Load
200.0 cm3/cm.s

Inlet Gap
0.02 m

Outlet Weir
0.01 m

Hole Diameter
0.001 m

Figure A9.12 Surface of clear liquid hold-up for UMD tray
Mean hCL 38 Emg/Eog 93/83

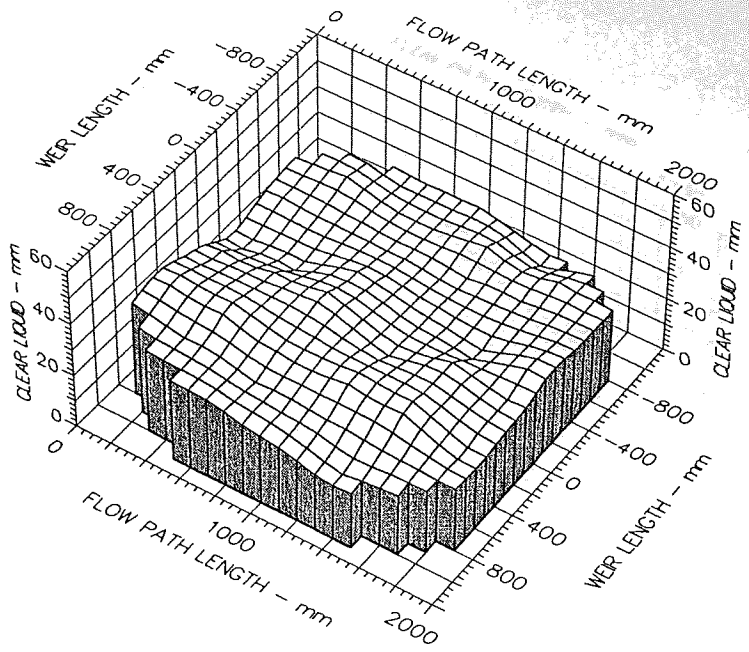

Air Velocity
1.000 m/s

Weir Load
50.0 cm3/cm.s

Inlet Gap
0.020 m

Outlet Weir
0.020 m

Hole Diameter
0.001 m

Figure A9.13 Surface of clear liquid hold-up for UMD tray
Mean hCL 28 Emg/Eog 94/68

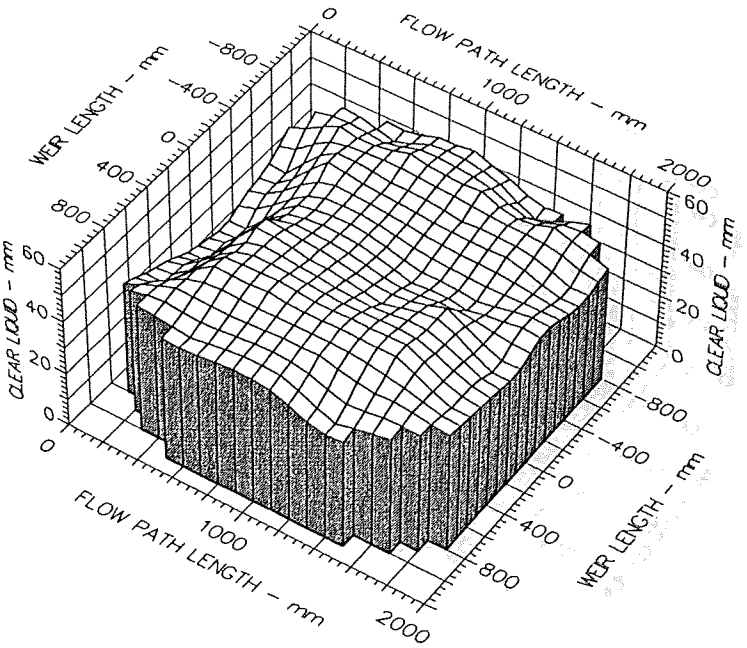

Air Velocity
1.0 m/s

Weir Load
200.0 cm3/cm.s

Inlet Gap
0.02 m

Outlet Weir
0.02 m

Hole Diameter
0.001 m

Figure A9.14 Surface of clear liquid hold-up for UMD tray
Mean hCL 45 Emg/Eog 104/94

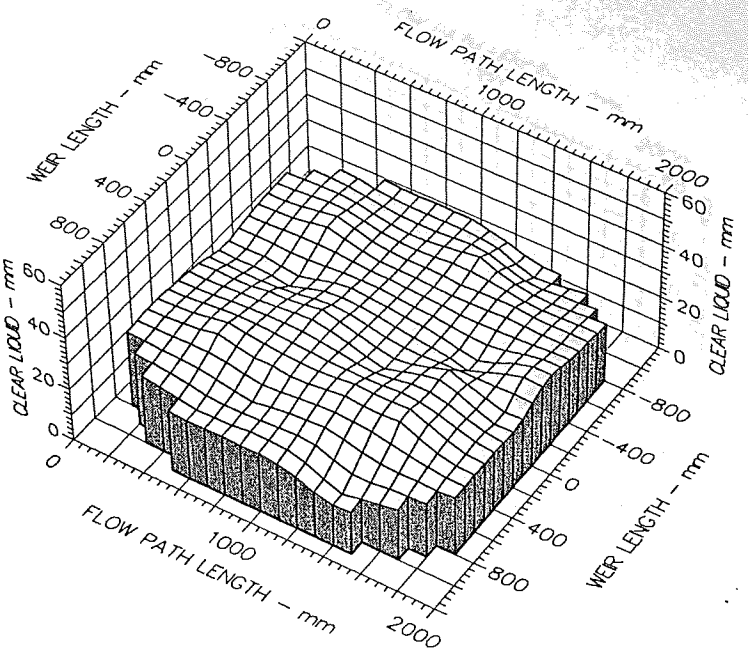

Air Velocity
1.500 m/s

Weir Load
50.0 cm3/cm.s

Inlet Gap
0.020 m

Outlet Weir
0.020 m

Hole Diameter
0.001 m

Figure A9.15 Surface of clear liquid hold-up for UMD tray
Mean hCL 26 Emg/Eog 94/62

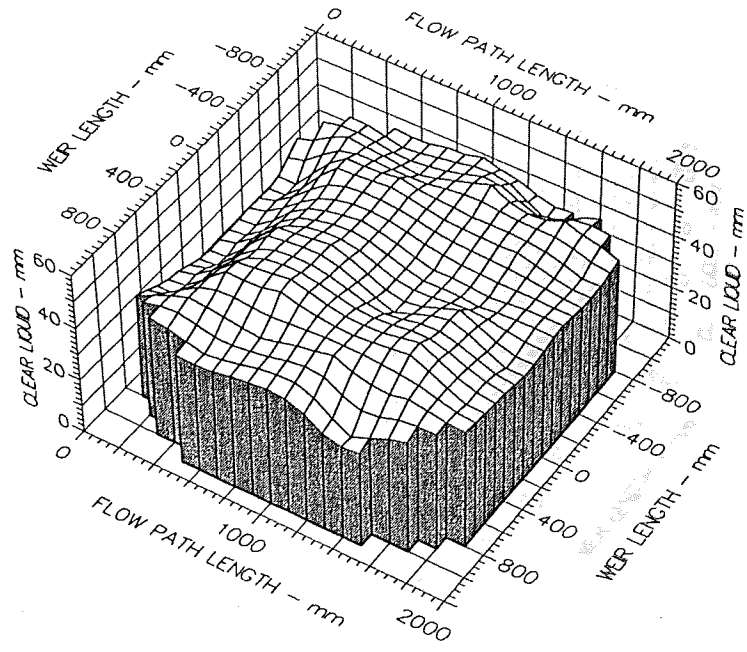

Air Velocity
1.5 m/s

Weir Load
200.0 cm3/cm.s

Inlet Gap
0.02 m

Outlet Weir
0.02 m

Hole Diameter
0.001 m

Figure A9.16 Surface of clear liquid hold-up for UMD tray
Mean hCL 44 Emg/Eog 92/85

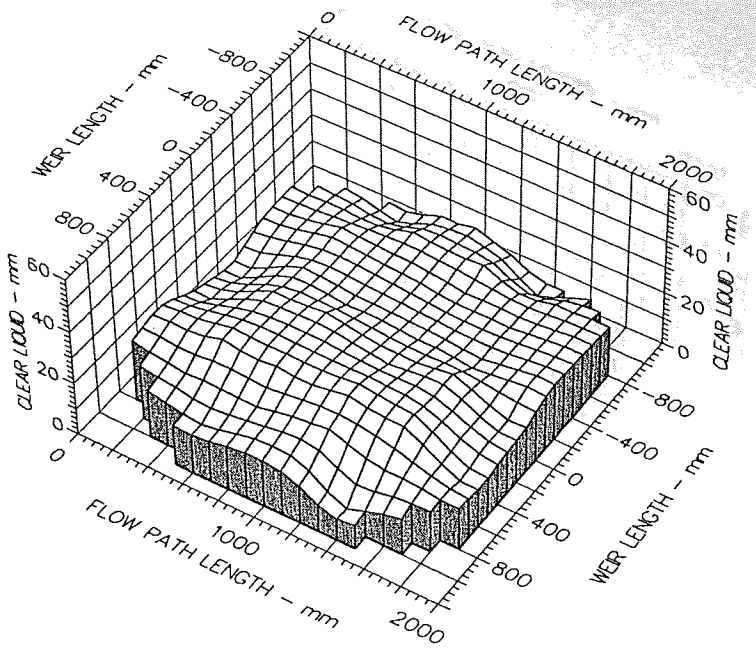

Air Velocity
2.000 m/s

Weir Load
50.0 cm3/cm.s

Inlet Gap
0.020 m

Outlet Weir
0.020 m

Hole Diameter
0.001 m

Figure A9.17 Surface of clear liquid hold-up for UMD tray
Mean hCL 21 Emg/Eog 94/60

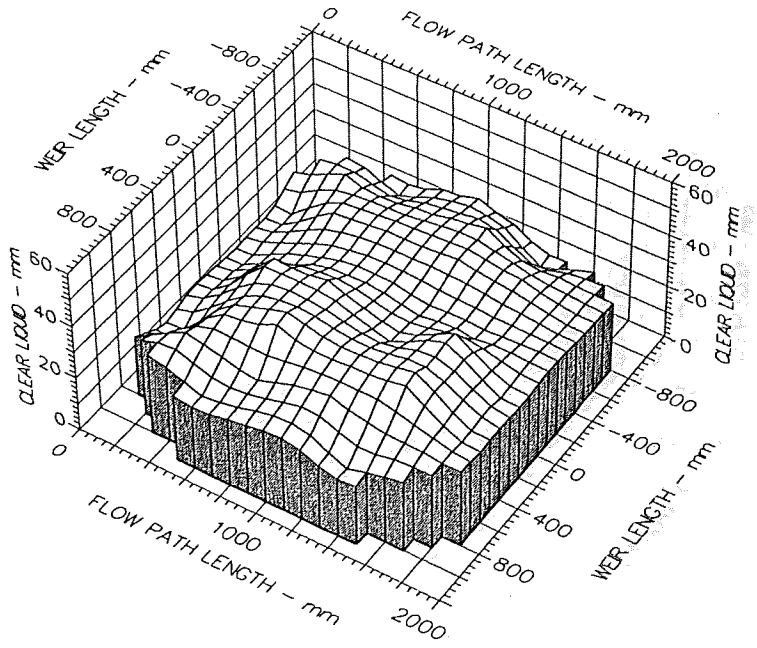

Air Velocity
2.0 m/s

Weir Load
200.0 cm3/cm.s

Inlet Gap
0.02 m

Outlet Weir
0.02 m

Hole Diameter
0.001 m

Figure A9.18 Surface of clear liquid hold-up for UMD tray
Mean hCL 30 Emg/Eog 97/84

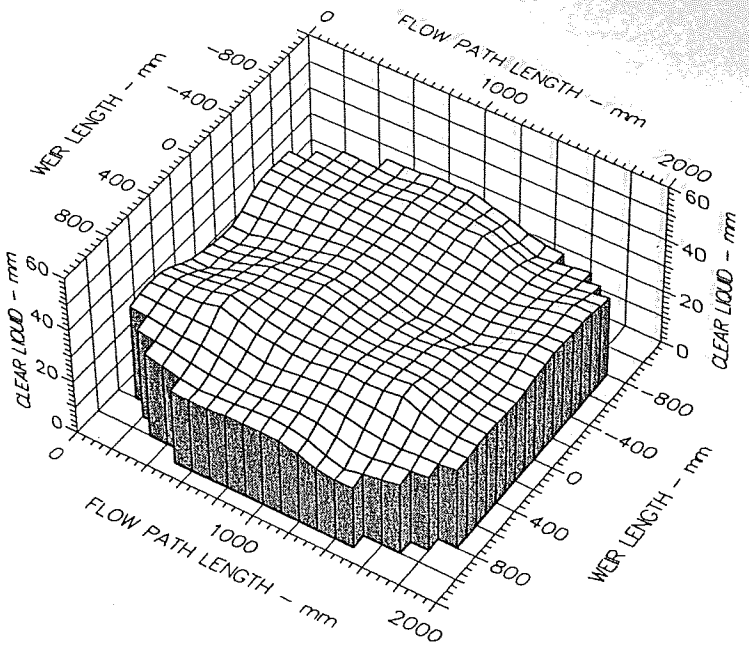

Air Velocity
1.500 m/s

Weir Load
50.0 cm3/cm.s

Inlet Gap
0.020 m

Outlet Weir
0.050 m

Hole Diameter
0.001 m

Figure A9.19 Surface of clear liquid hold-up for UMD tray
Mean hCL 32 Emg/Eog 104/70

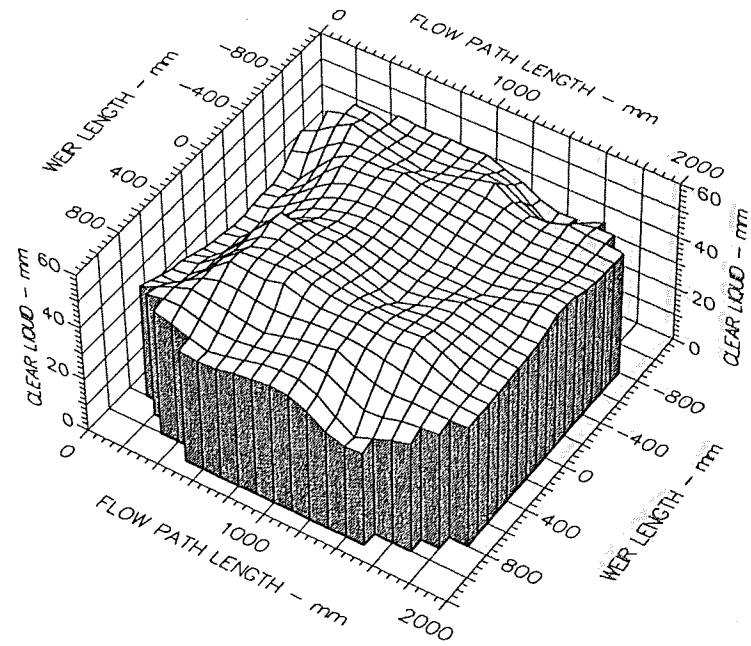

Air Velocity
1.5 m/s

Weir Load
200.0 cm3/cm.s

Inlet Gap
0.02 m

Outlet Weir
0.05 m

Hole Diameter
0.001 m

Figure A9.20 Surface of clear liquid hold-up for UMD tray
Mean hCL 47 Emg/Eog 98/87

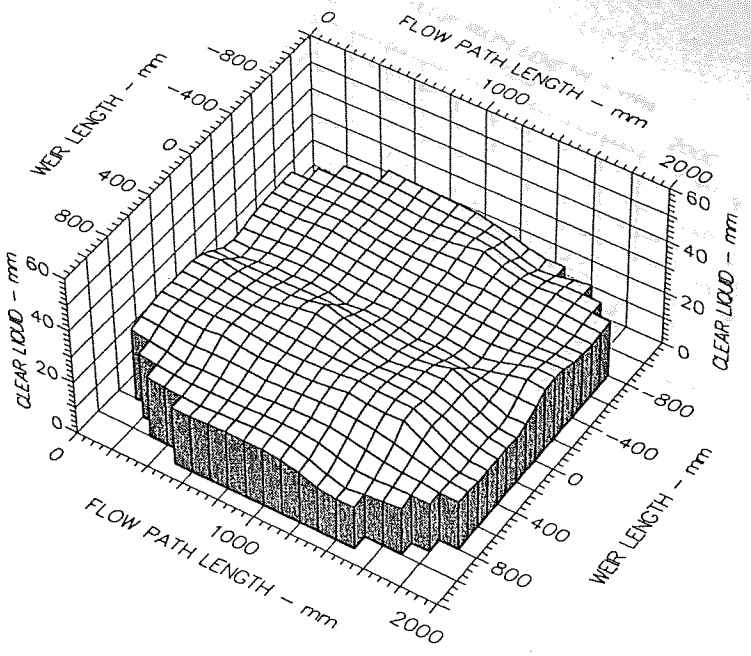

Air Velocity
1.500 m/s

Weir Load
50.0 cm3/cm.s

Inlet Gap
0.050 m

Outlet Weir
0.010 m

Hole Diameter
0.001 m

Figure A9.21 Surface of clear liquid hold-up for UMD tray
Mean hCL 24 Emg/Eog 85/57

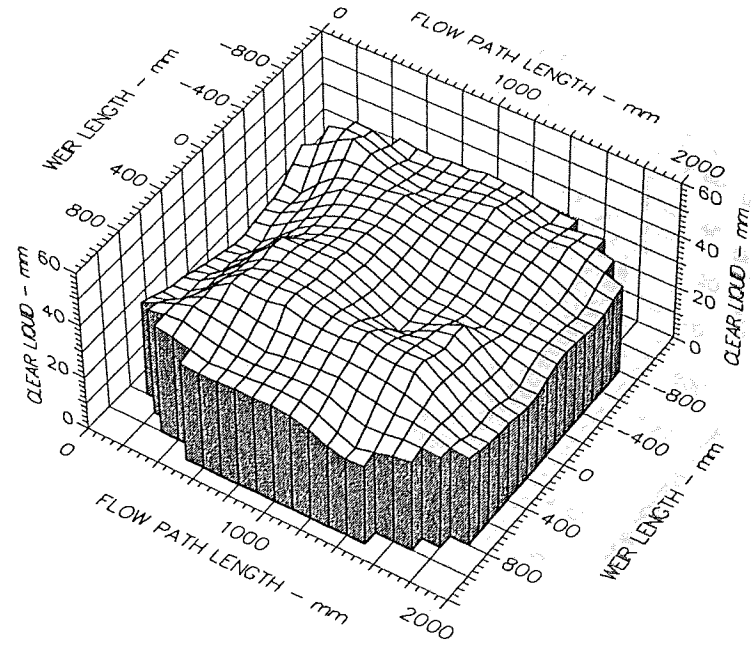

Air Velocity
1.5 m/s

Weir Load
200.0 cm3/cm.s

Inlet Gap
0.05 m

Outlet Weir
0.01 m

Hole Diameter
0.001 m

Figure A9.22 Surface of clear liquid hold-up for UMD tray
Mean hCL 38 Emg/Eog 103/90

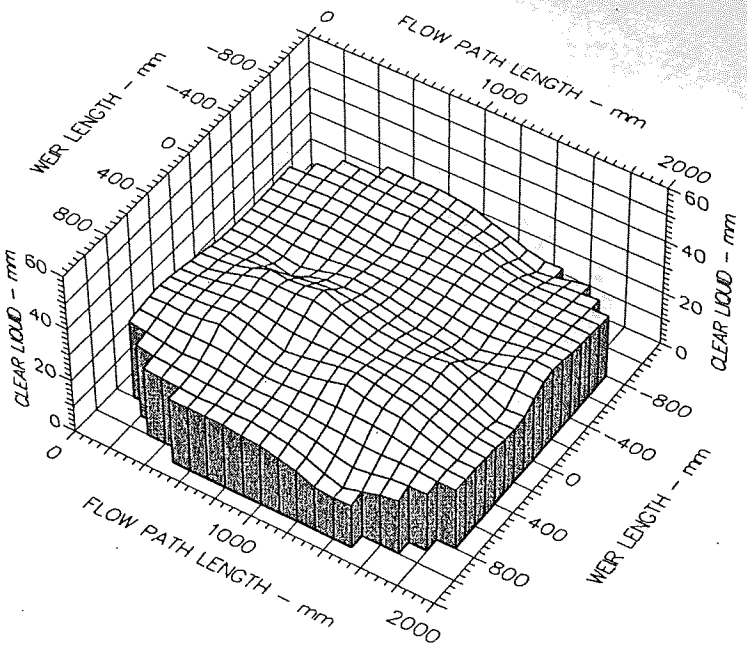

Air Velocity
1.500 m/s

Weir Load
50.0 cm3/cm.s

Inlet Gap
0.050 m

Outlet Weir
0.020 m

Hole Diameter
0.001 m

Figure A9.23 Surface of clear liquid hold-up for UMD tray
Mean hCL 26 Emg/Eog 90/59

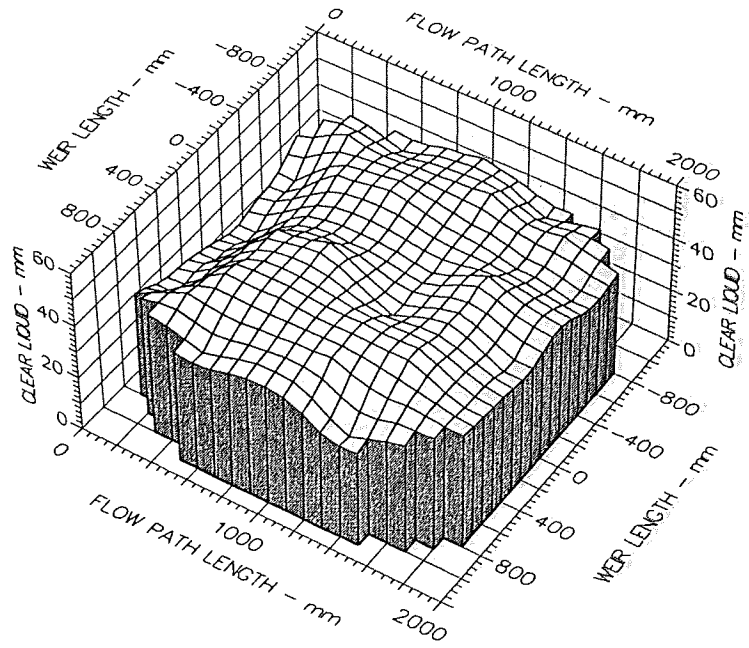

Air Velocity
1.5 m/s

Weir Load
200.0 cm3/cm.s

Inlet Gap
0.05 m

Outlet Weir
0.02 m

Hole Diameter
0.001 m

Figure A9.24 Surface of clear liquid hold-up for UMD tray
Mean hCL 44 Emg/Eog 102/87

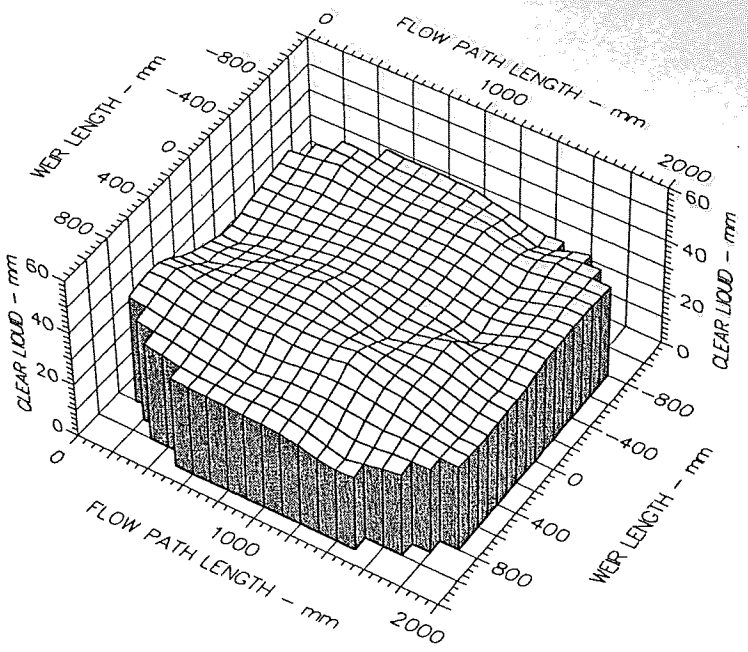

Air Velocity
1.000 m/s

Weir Load
50.0 cm3/cm.s

Inlet Gap
0.050 m

Outlet Weir
0.050 m

Hole Diameter
0.001 m

Figure A9.25 Surface of clear liquid hold-up for UMD tray
Mean hCL 34 Emg/Eog 96/73

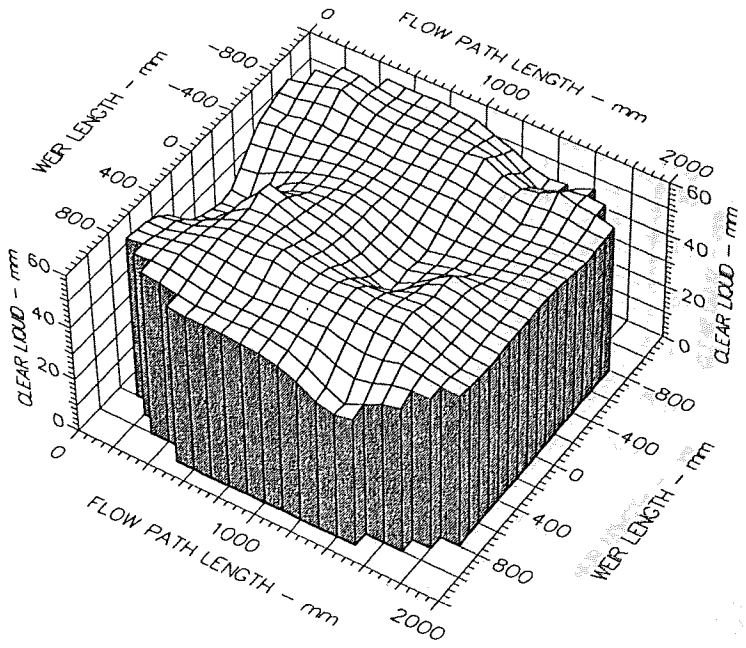

Air Velocity
1.0 m/s

Weir Load
200.0 cm3/cm.s

Inlet Gap
0.05 m

Outlet Weir
0.05 m

Hole Diameter
0.001 m

Figure A9.26 Surface of clear liquid hold-up for UMD tray
Mean hCL 57 Emg/Eog 105/94

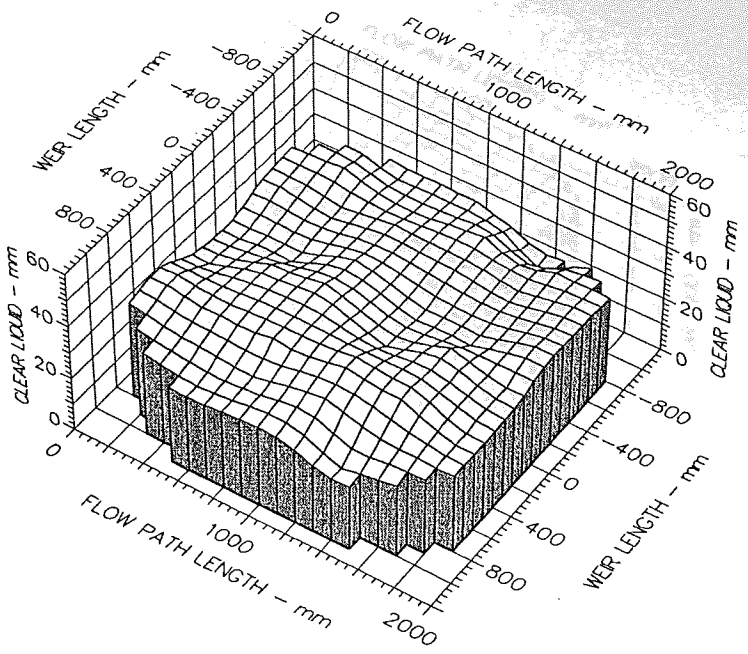

Air Velocity
1.500 m/s

Weir Load
50.0 cm3/cm.s

Inlet Gap
0.050 m

Outlet Weir
0.050 m

Hole Diameter
0.001 m

Figure A9.27 Surface of clear liquid hold-up for UMD tray
Mean hCL 33 Emg/Eog 92/67

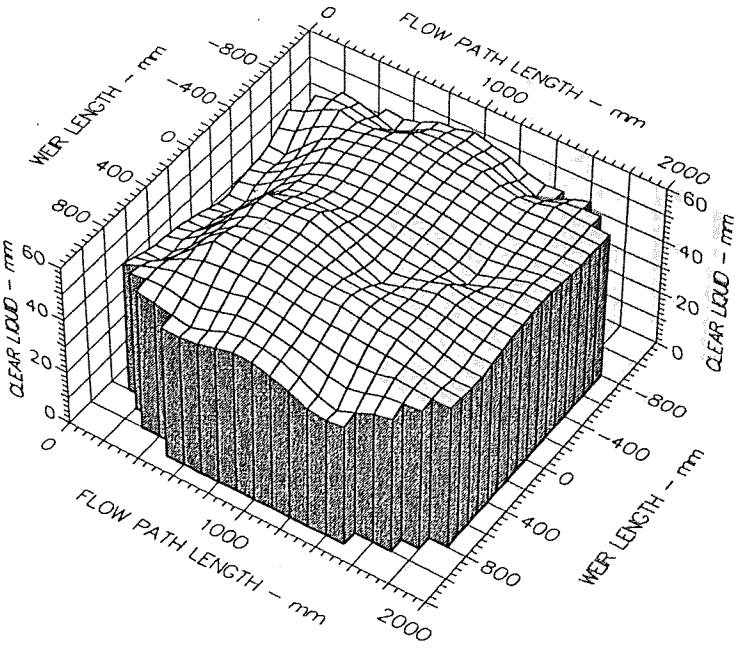

Air Velocity
1.5 m/s

Weir Load
200.0 cm3/cm.s

Inlet Gap
0.05 m

Outlet Weir
0.05 m

Hole Diameter
0.001 m

Figure A9.28 Surface of clear liquid hold-up for UMD tray
Mean hCL 54 Emg/Eog 105/93

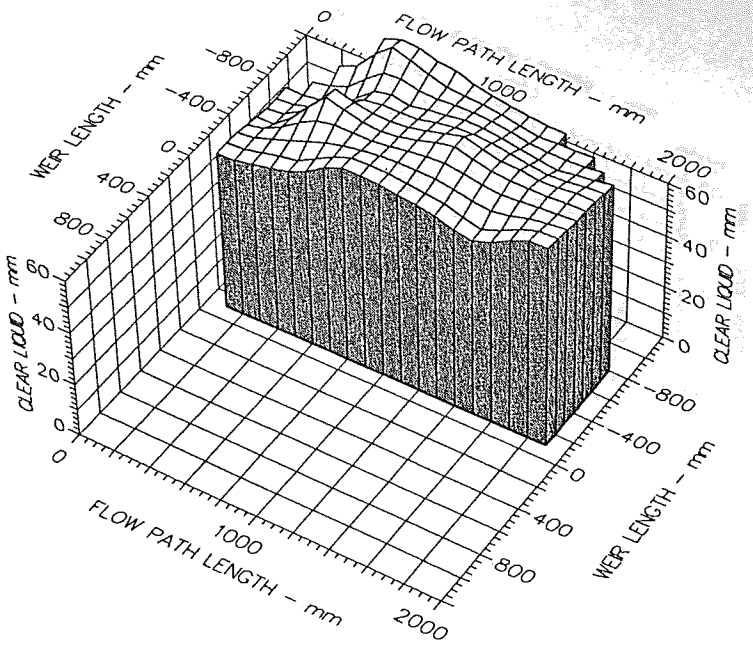

Air Velocity
1.500 m/s

Weir Load
300.0 cm3/cm.s

Inlet Gap
0.050 m

Outlet Weir
0.050 m

Hole Diameter
0.001 m

Figure A9.29 Surface of clear liquid hold-up for UMD tray
Mean hCL 70 Emg/Eog 99/95

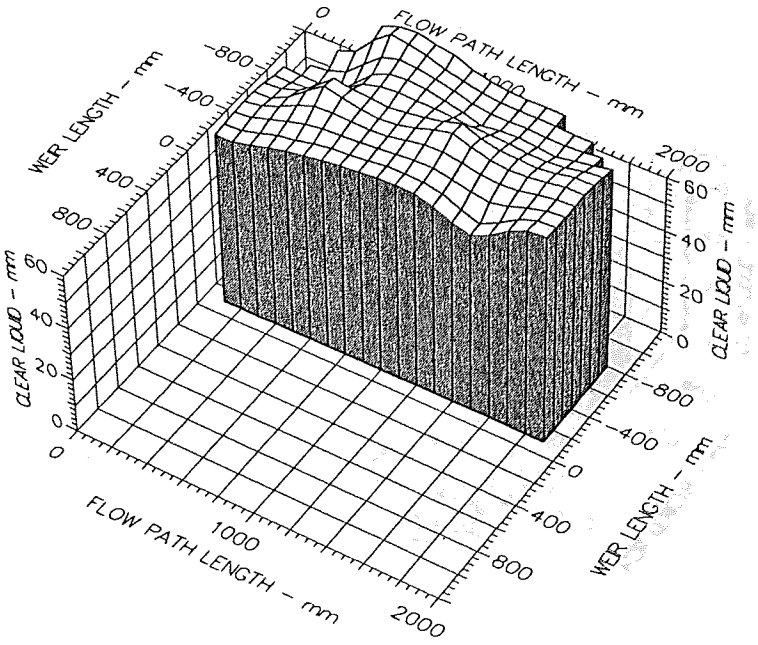

Air Velocity
1.5 m/s

Weir Load
350.0 cm3/cm.s

Inlet Gap
0.05 m

Outlet Weir
0.05 m

Hole Diameter
0.001 m

Figure A9.30 Surface of clear liquid hold-up for UMD tray
Mean hCL 73 Emg/Eog 101/97

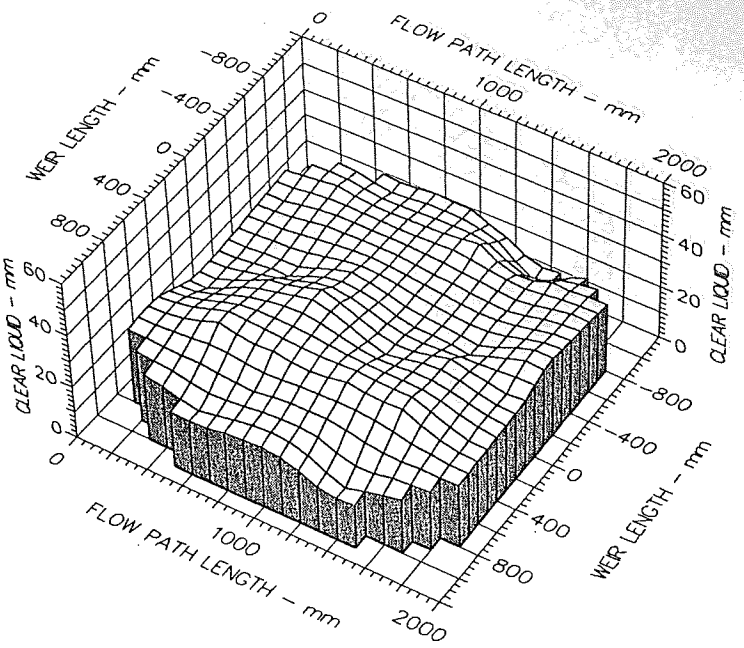

Air Velocity
2.000 m/s

Weir Load
50.0 cm3/cm.s

Inlet Gap
0.050 m

Outlet Weir
0.050 m

Hole Diameter
0.001 m

Figure A9.31 Surface of clear liquid hold-up for UMD tray
Mean hCL 27 Emg/Eog 90/64

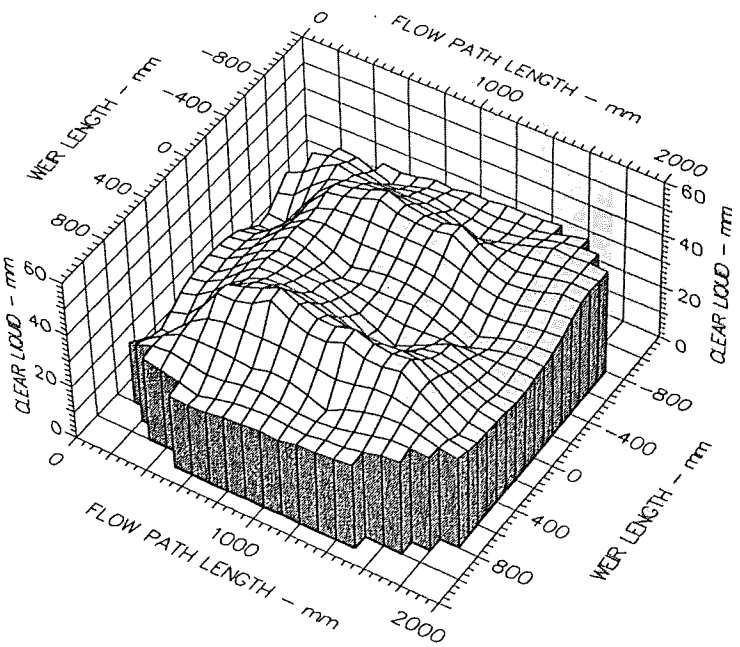

Air Velocity
2.0 m/s

Weir Load
200.0 cm3/cm.s

Inlet Gap
0.05 m

Outlet Weir
0.05 m

Hole Diameter
0.001 m

Figure A9.32 Surface of clear liquid hold-up for UMD tray
Mean hCL 35 Emg/Eog 101/88

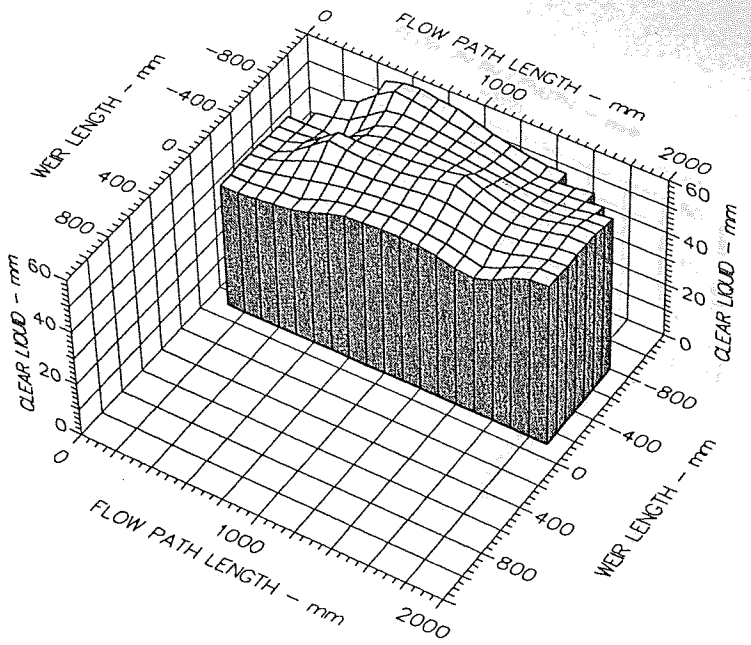

Air Velocity
2.000 m/s

Weir Load
300.0 cm3/cm.s

Inlet Gap
0.050 m

Outlet Weir
0.050 m

Hole Diameter
0.001 m

Figure A9.33 Surface of clear liquid hold-up for UMD tray
Mean hCL 55 Emg/Eog 102/94

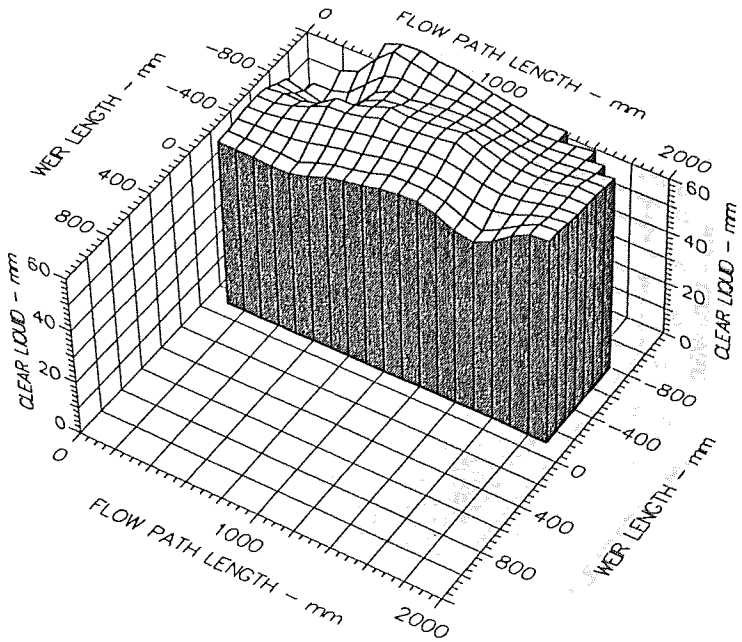

Air Velocity
2.0 m/s

Weir Load
350.0 cm3/cm.s

Inlet Gap
0.05 m

Outlet Weir
0.05 m

Hole Diameter
0.001 m

Figure A9.34 Surface of clear liquid hold-up for UMD tray
Mean hCL 70 Emg/Eog 103/97

Appendices 10

Three-Dimensional Liquid Head Surface Profiles STR-1Tray Cases

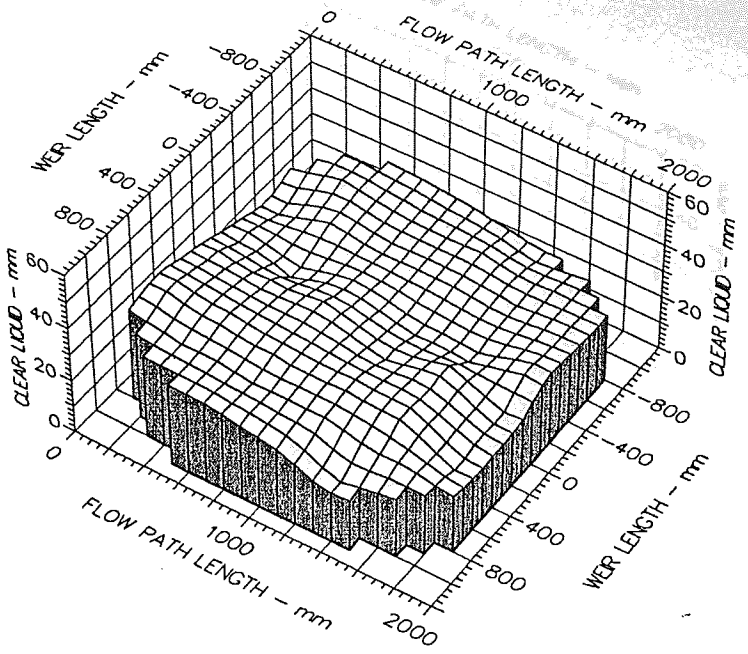

Air Velocity
1.000 m/s
Weir Load
50.0 cm3/cm.s
Inlet Gap
0.010 m
Outlet Weir
0.010 m
Hole Diameter
0.001 m

Figure A10.1 Surface of clear liquid hold-up for STR-1 tray
Mean hCL 27 Emg/Eog 109/72

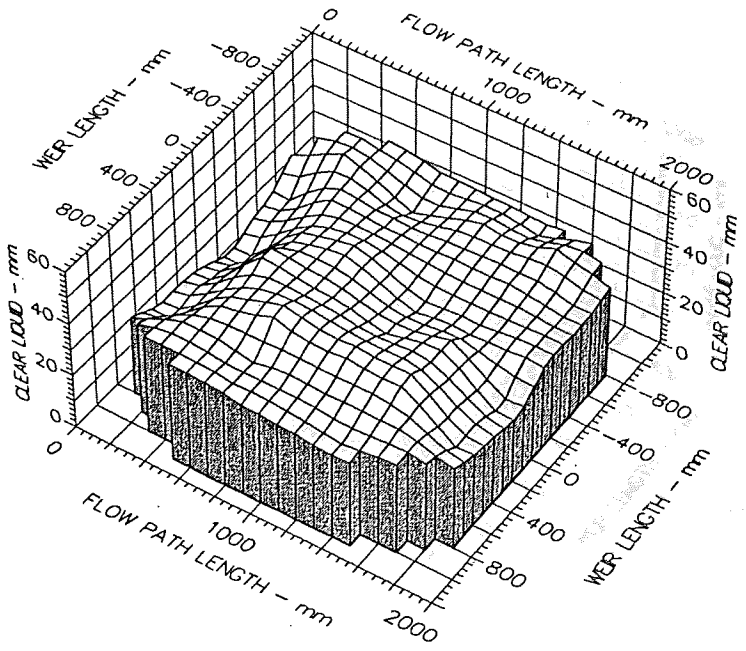

Air Velocity
1.0 m/s
Weir Load
150.0 cm3/cm.s
Inlet Gap
0.01 m
Outlet Weir
0.01 m
Hole Diameter
0.001 m

Figure A10.2 Surface of clear liquid hold-up for STR-1 tray
Mean hCL 34 Emg/Eog 98/90

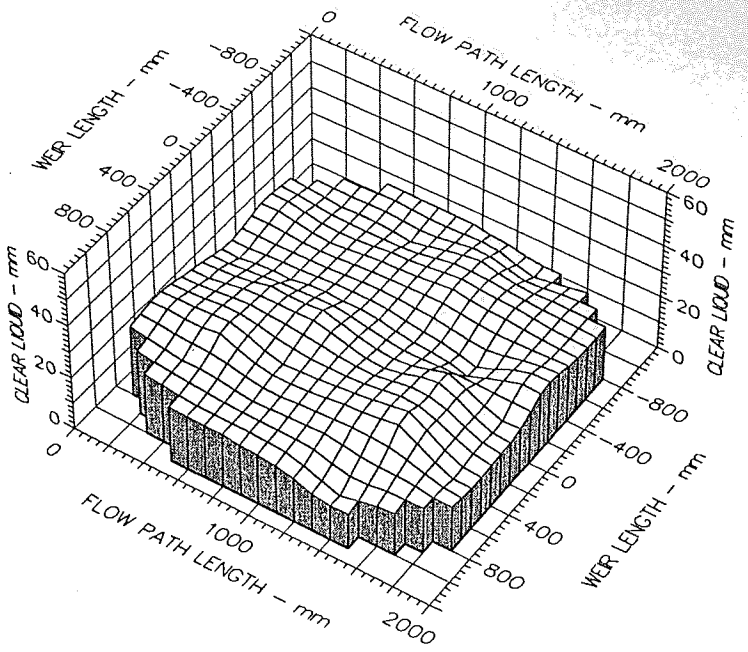

Air Velocity
1.500 m/s

Weir Load
50.0 cm3/cm.s

Inlet Gap
0.010 m

Outlet Weir
0.010 m

Hole Diameter
0.001 m

Figure A10.3 Surface of clear liquid hold-up for STR-1 tray
Mean hCL 22 Emg/Eog 99/63

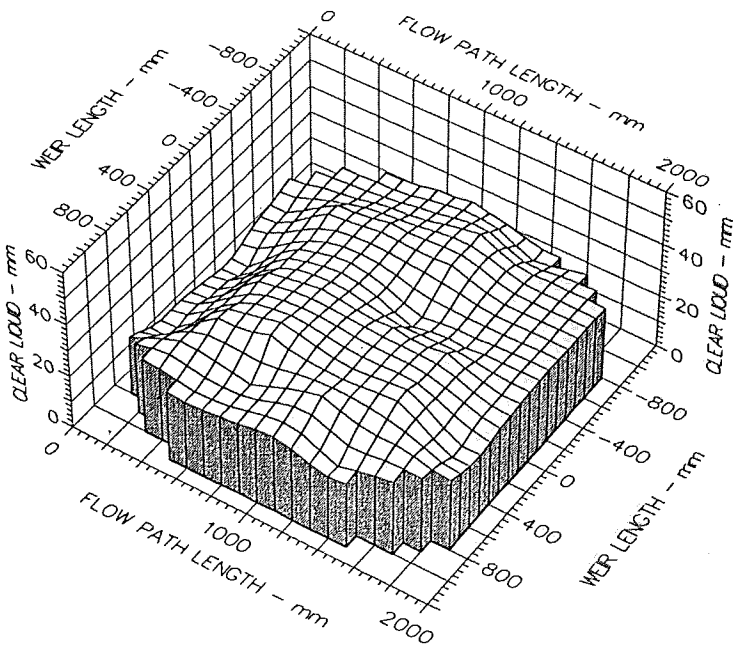

Air Velocity
1.5 m/s

Weir Load
150.0 cm3/cm.s

Inlet Gap
0.01 m

Outlet Weir
0.01 m

Hole Diameter
0.001 m

Figure A10.4 Surface of clear liquid hold-up for STR-1 tray
Mean hCL 29 Emg/Eog 93/83

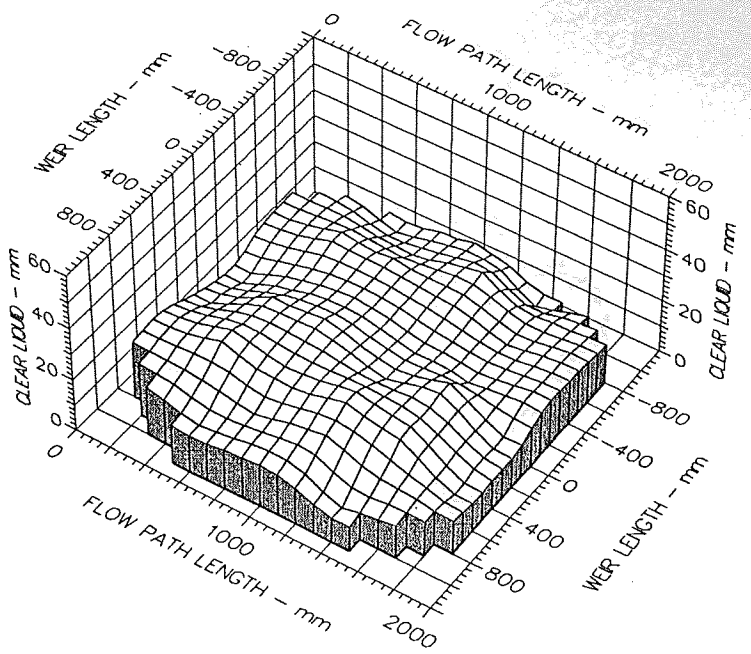

Air Velocity
2.000 m/s

Weir Load
50.0 cm3/cm.s

Inlet Gap
0.010 m

Outlet Weir
0.010 m

Hole Diameter
0.001 m

Figure A10.5 Surface of clear liquid hold-up for STR-1 tray
Mean hCL 18 Emg/Eog 88/55

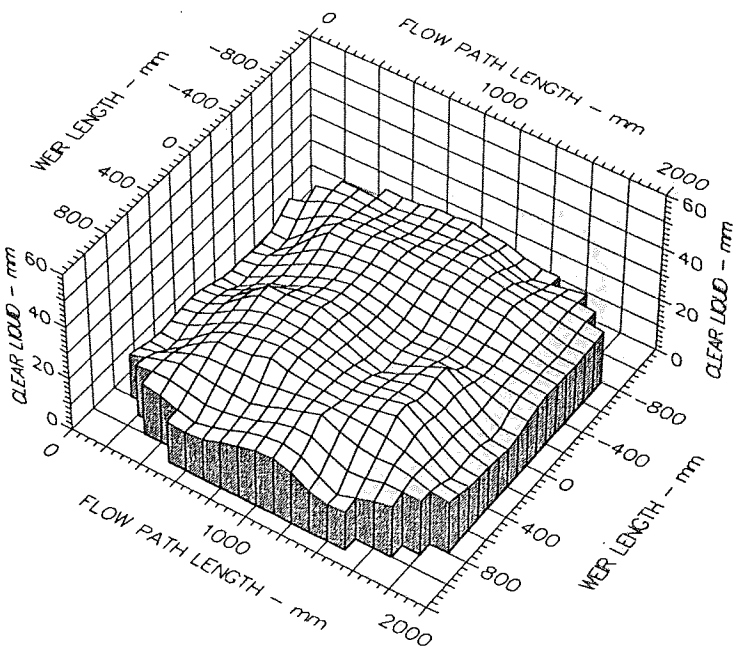

Air Velocity
2.0 m/s

Weir Load
150.0 cm3/cm.s

Inlet Gap
0.01 m

Outlet Weir
0.01 m

Hole Diameter
0.001 m

Figure A10.6 Surface of clear liquid hold-up for STR-1 tray
Mean hCL 22 Emg/Eog 94/79

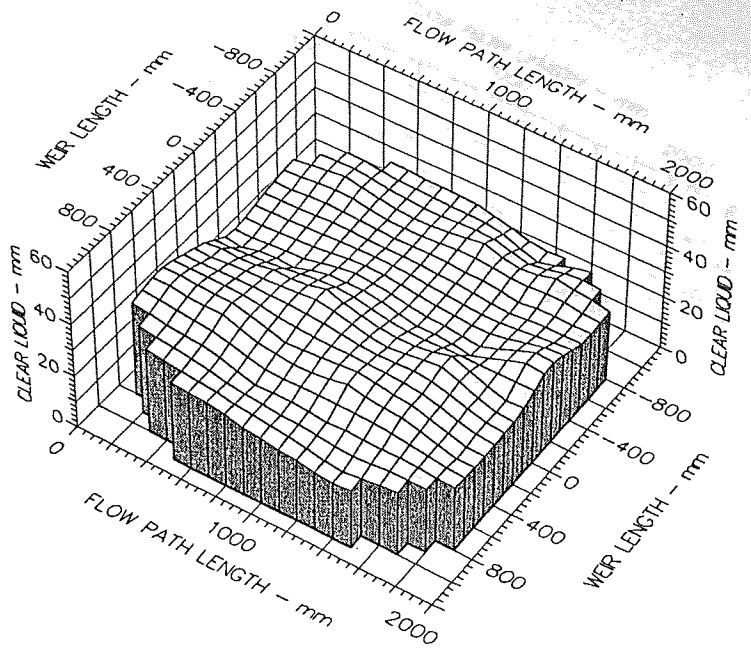

Air Velocity
1.000 m/s

Weir Load
50.0 cm3/cm.s

Inlet Gap
0.020 m

Outlet Weir
0.020 m

Hole Diameter
0.001 m

Figure A10.7 Surface of clear liquid hold-up for STR-1 tray
Mean hCL 29 Emg/Eog 103/70

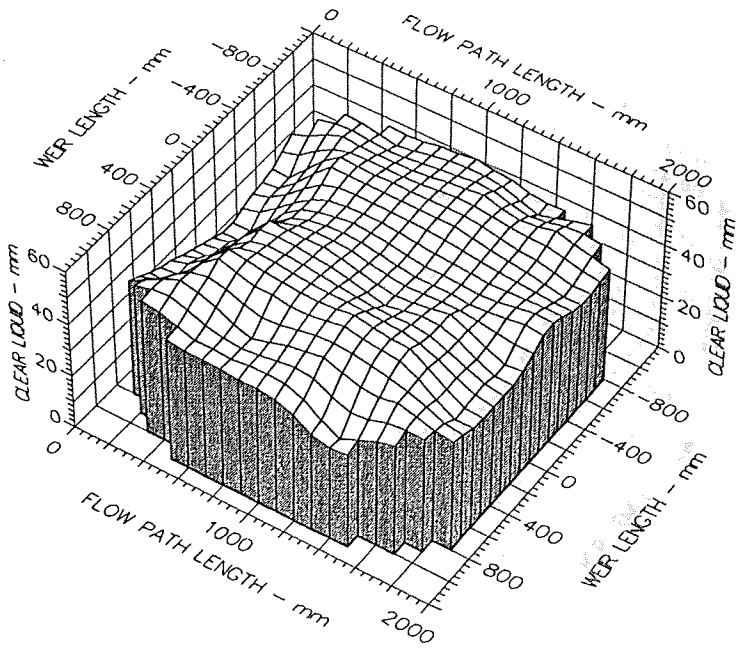

Air Velocity
1.0 m/s

Weir Load
200.0 cm3/cm.s

Inlet Gap
0.02 m

Outlet Weir
0.02 m

Hole Diameter
0.001 m

Figure A10.8 Surface of clear liquid hold-up for STR-1 tray
Mean hCL 46 Emg/Eog 102/90

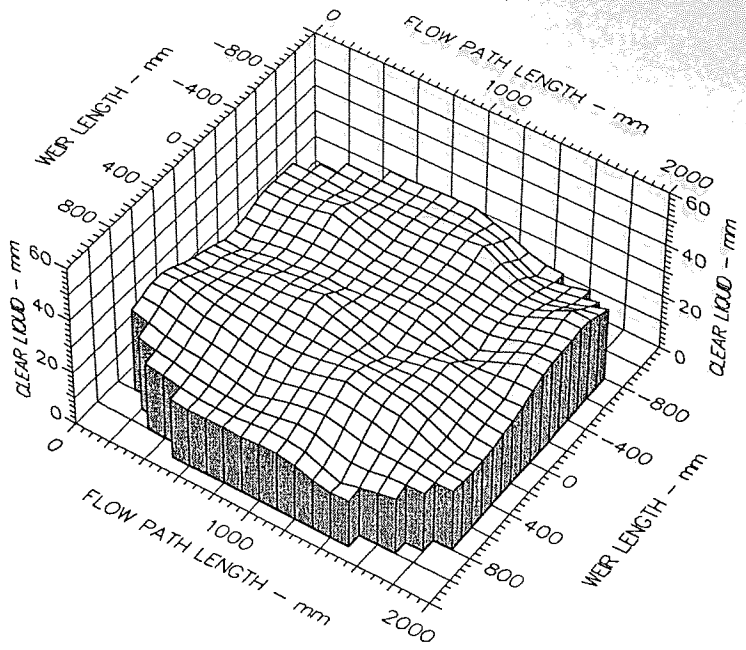

Air Velocity
1.500 m/s

Weir Load
50.0 cm3/cm.s

Inlet Gap
0.020 m

Outlet Weir
0.020 m

Hole Diameter
0.001 m

Figure A10.9 Surface of clear liquid hold-up for STR-1 tray
Mean hCL 27 Emg/Eog 88/60

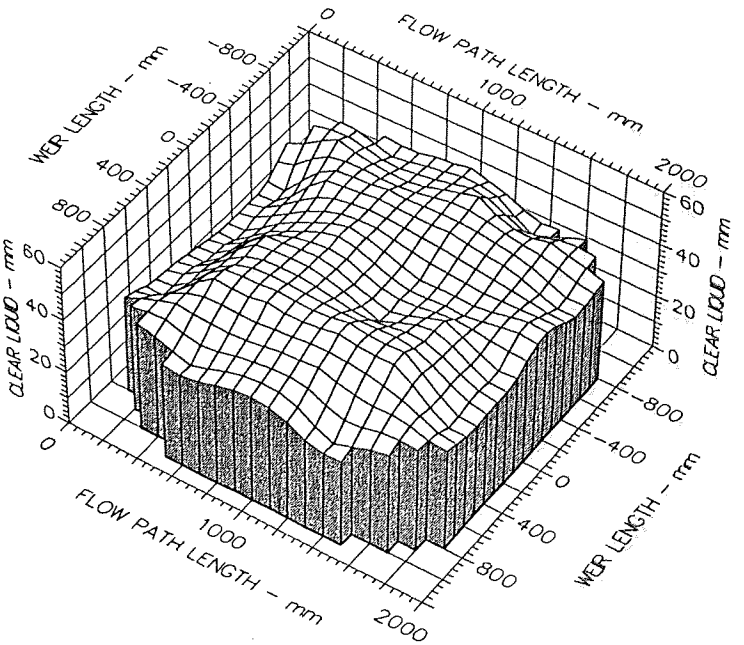

Air Velocity
1.5 m/s

Weir Load
200.0 cm3/cm.s

Inlet Gap
0.02 m

Outlet Weir
0.02 m

Hole Diameter
0.001 m

Figure A10.10 Surface of clear liquid hold-up for STR-1 tray
Mean hCL 41 Emg/Eog 98/86

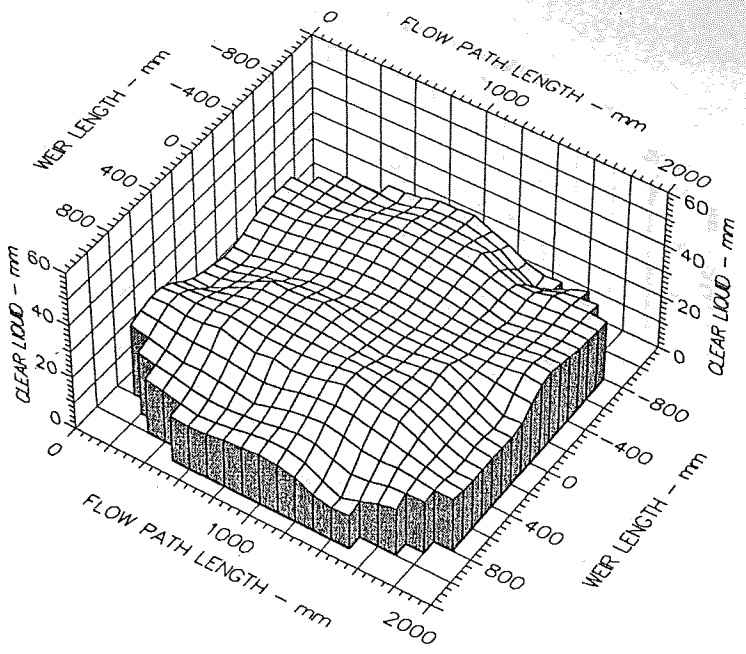

Air Velocity
2.000 m/s

Weir Load
50.0 cm3/cm.s

Inlet Gap
0.020 m

Outlet Weir
0.020 m

Hole Diameter
0.001 m

Figure A10.11 Surface of clear liquid hold-up for STR-1 tray
Mean hCL 24 Emg/Eog 92/59

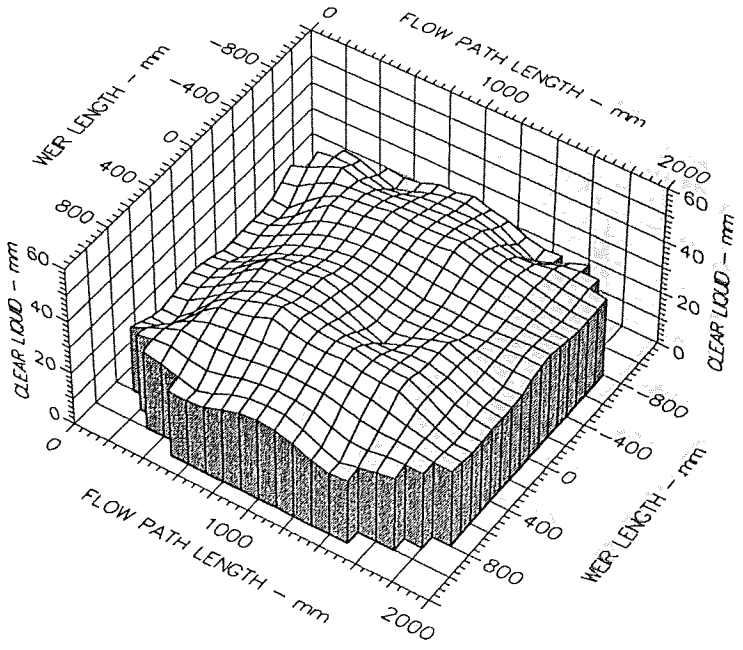

Air Velocity
2.0 m/s

Weir Load
200.0 cm3/cm.s

Inlet Gap
0.02 m

Outlet Weir
0.02 m

Hole Diameter
0.001 m

Figure A10.12 Surface of clear liquid hold-up for STR-1 tray
Mean hCL 32 Emg/Eog 101/85

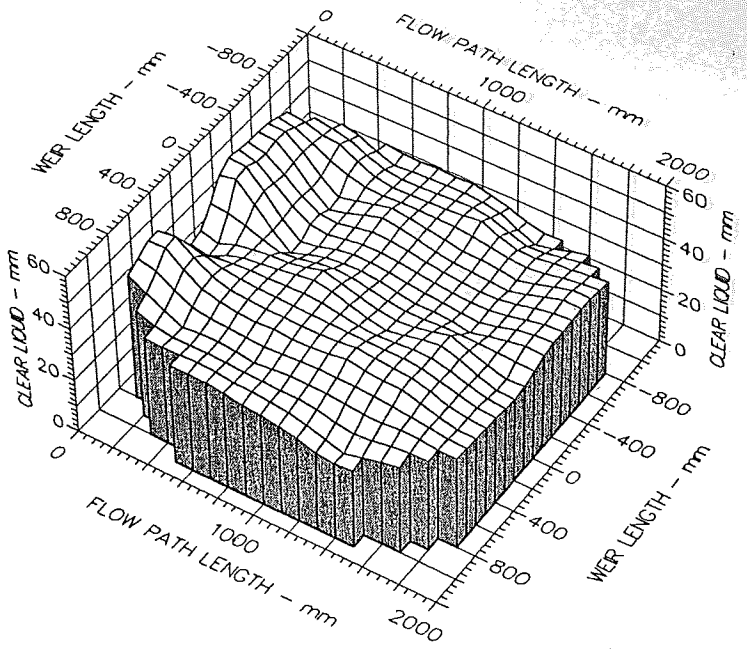

Air Velocity
1.000 m/s

Weir Load
50.0 cm3/cm.s

Inlet Gap
0.050 m

Outlet Weir
0.050 m

Hole Diameter
0.001 m

Figure A10.13 Surface of clear liquid hold-up for STR-1 tray
Mean hCL 38 Emg/Eog 106/73

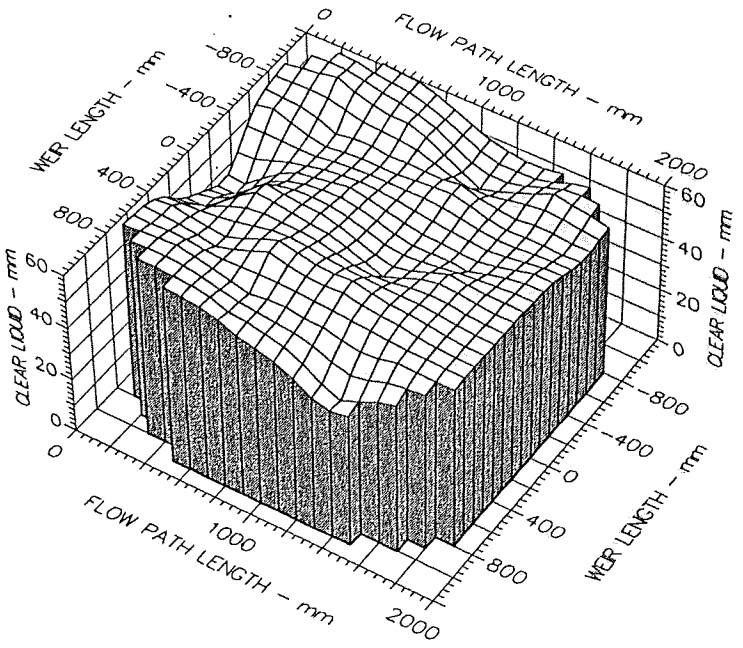

Air Velocity
1.0 m/s

Weir Load
200.0 cm3/cm.s

Inlet Gap
0.05 m

Outlet Weir
0.05 m

Hole Diameter
0.001 m

Figure A10.14 Surface of clear liquid hold-up for STR-1 tray
Mean hCL 60 Emg/Eog 111/94

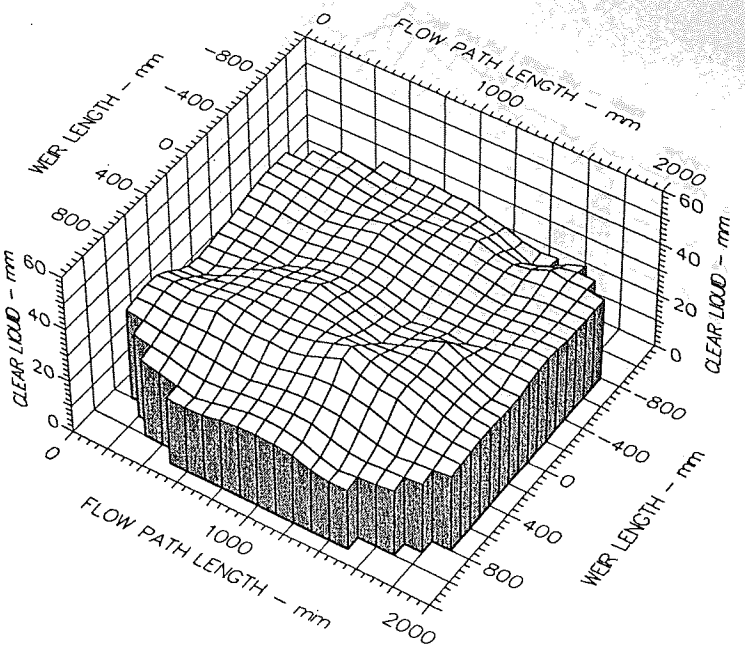

Air Velocity
1.500 m/s

Weir Load
50.0 cm3/cm.s

Inlet Gap
0.050 m

Outlet Weir
0.050 m

Hole Diameter
0.001 m

Figure A10.15 Surface of clear liquid hold-up for STR-1 tray
Mean hCL 32 Emg/Eog 101/67

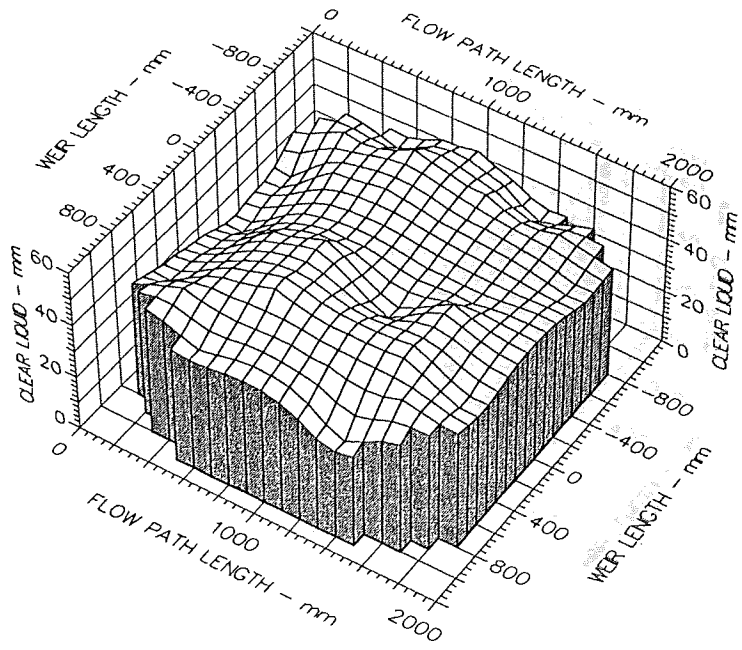

Air Velocity
1.5 m/s

Weir Load
200.0 cm3/cm.s

Inlet Gap
0.05 m

Outlet Weir
0.05 m

Hole Diameter
0.001 m

Figure A10.16 Surface of clear liquid hold-up for STR-1 tray
Mean hCL 45 Emg/Eog 109/93

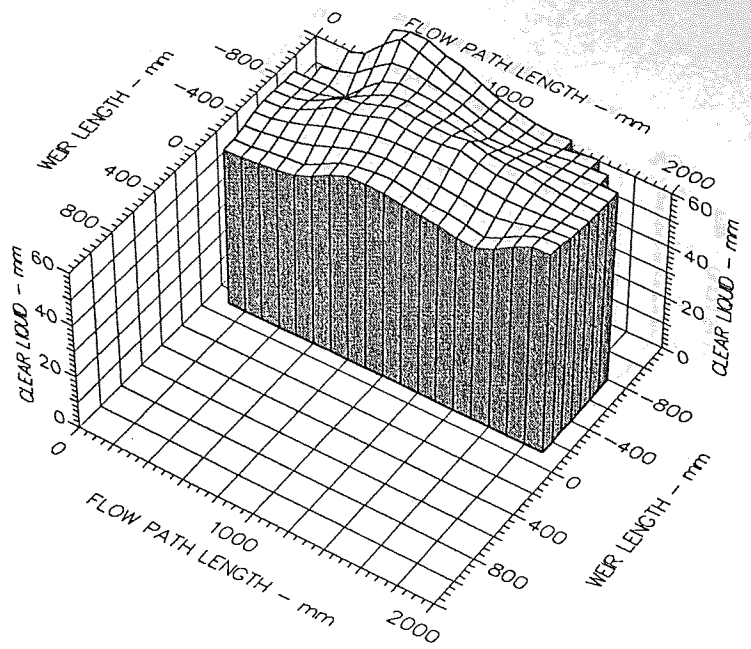

Air Velocity
1.500 m/s

Weir Load
300.0 cm3/cm.s

Inlet Gap
0.050 m

Outlet Weir
0.050 m

Hole Diameter
0.001 m

Figure A10.17 Surface of clear liquid hold-up for STR-1 tray
Mean hCL 71 Emg/Eog 100/95

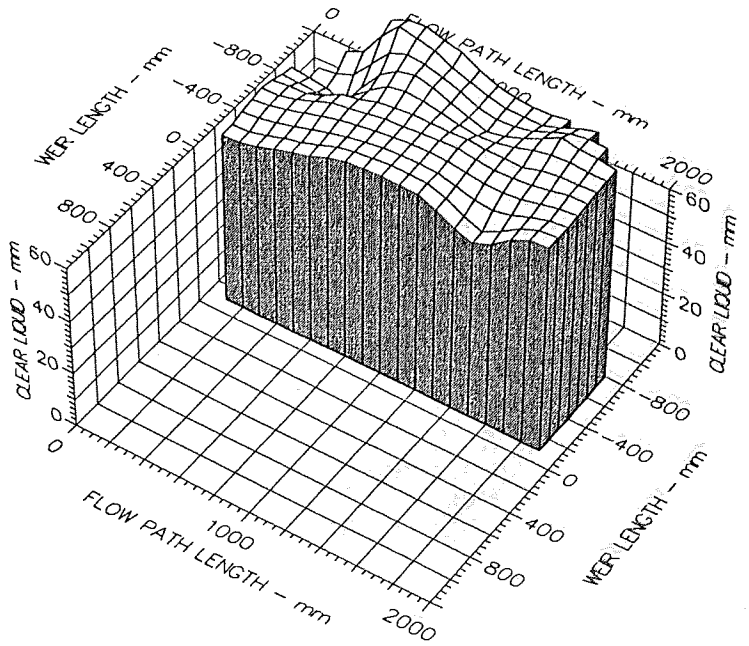

Air Velocity
1.5 m/s

Weir Load
350.0 cm3/cm.s

Inlet Gap
0.05 m

Outlet Weir
0.05 m

Hole Diameter
0.001 m

Figure A10.18 Surface of clear liquid hold-up for STR-1 tray
Mean hCL 74 Emg/Eog 102/97

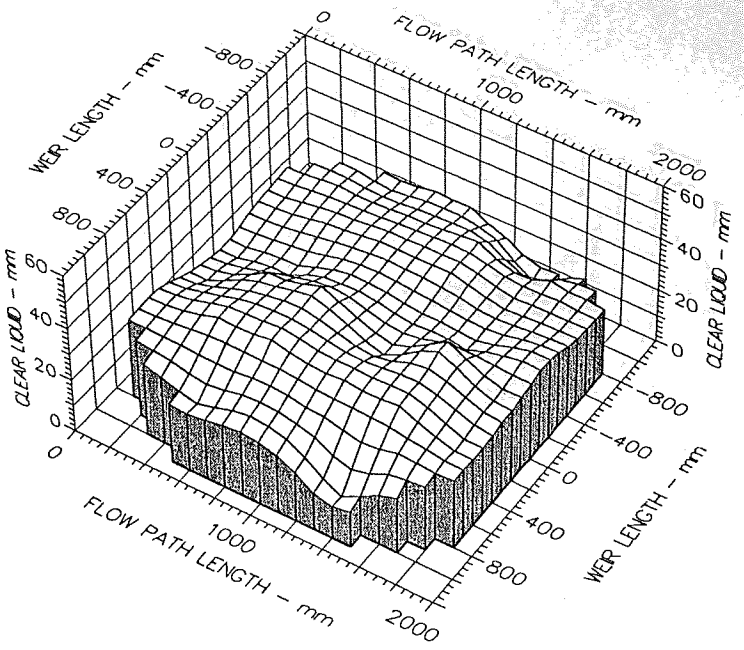

Air Velocity
2.000 m/s

Weir Load
50.0 cm3/cm.s

Inlet Gap
0.050 m

Outlet Weir
0.050 m

Hole Diameter
0.001 m

Figure A10.19 Surface of clear liquid hold-up for STR-1 tray
Mean hCL 28 Emg/Eog 100/64

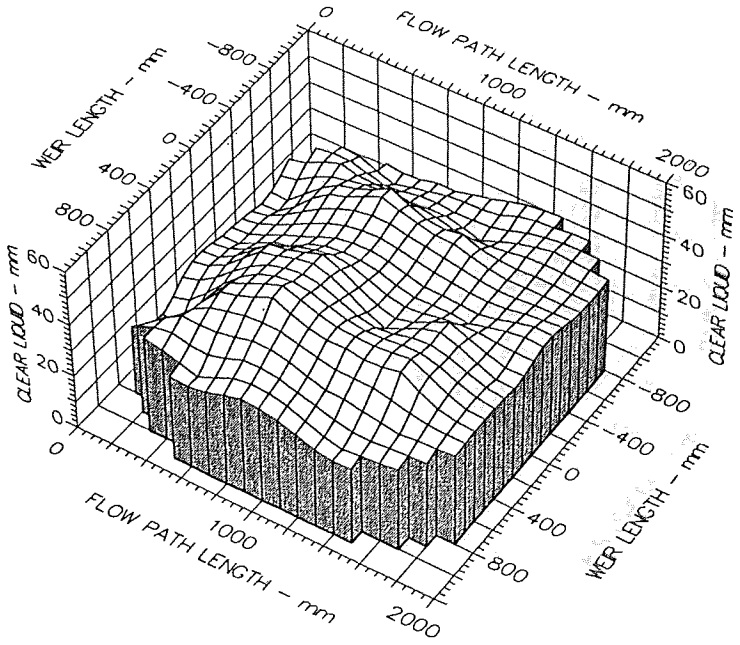

Air Velocity
2.0 m/s

Weir Load
200.0 cm3/cm.s

Inlet Gap
0.05 m

Outlet Weir
0.05 m

Hole Diameter
0.001 m

Figure A10.20 Surface of clear liquid hold-up for STR-1 tray
Mean hCL 37 Emg/Eog 102/88

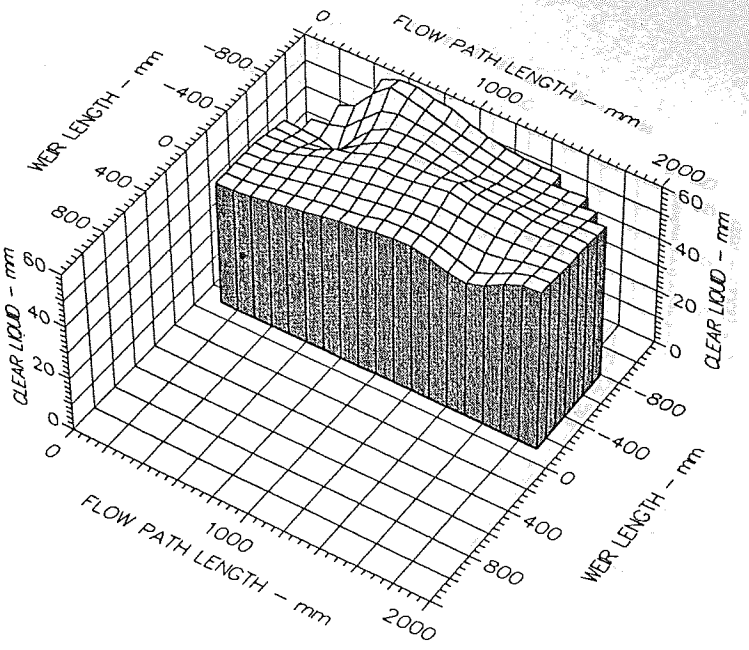

Air Velocity
2.000 m/s

Weir Load
300.0 cm3/cm.s

Inlet Gap
0.050 m

Outlet Weir
0.050 m

Hole Diameter
0.001 m

Figure A10.21 Surface of clear liquid hold-up for STR-1 tray
Mean hCL 55 Emg/Eog 104/96

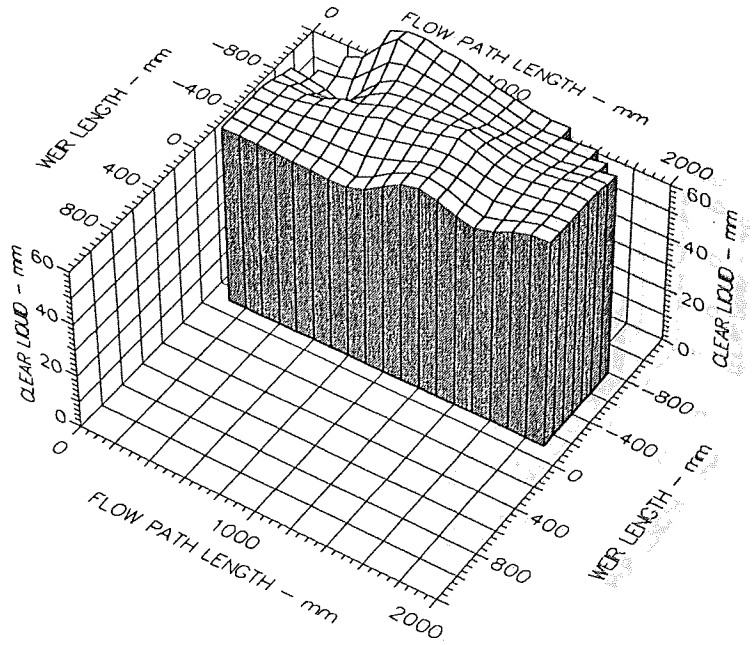

Air Velocity
2.0 m/s

Weir Load
350.0 cm3/cm.s

Inlet Gap
0.05 m

Outlet Weir
0.05 m

Hole Diameter
0.001 m

Figure A10.22 Surface of clear liquid hold-up for STR-1 tray
Mean hCL 72 Emg/Eog 104/98

Appendices 11

Three-Dimensional Liquid Head Surface Profiles ARC-1 Tray Cases

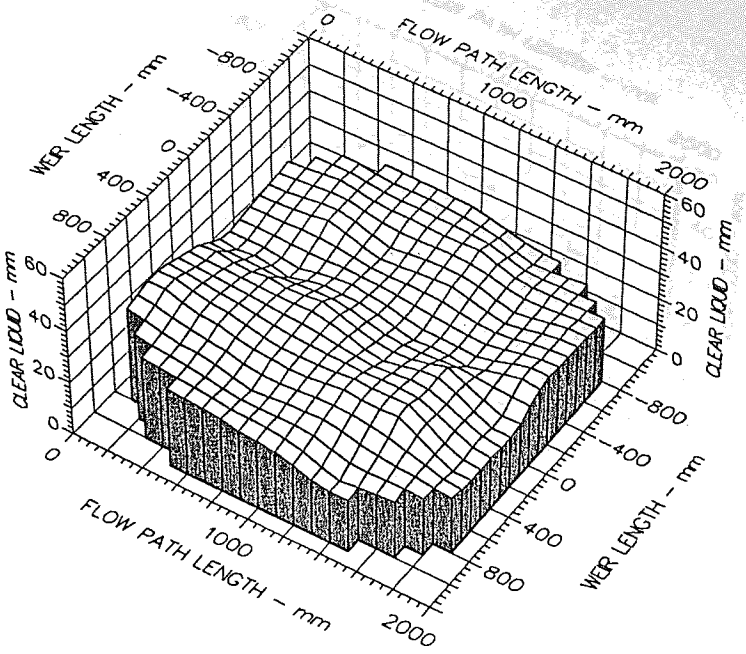

Air Velocity
1.000 m/s

Weir Load
50.0 cm3/cm.s

Inlet Gap
0.010 m

Outlet Weir
0.010 m

Hole Diameter
0.001 m

Figure A11.1 Surface of clear liquid hold-up for ARC-1 tray
Mean hCL 28 Emg/Eog 97/57

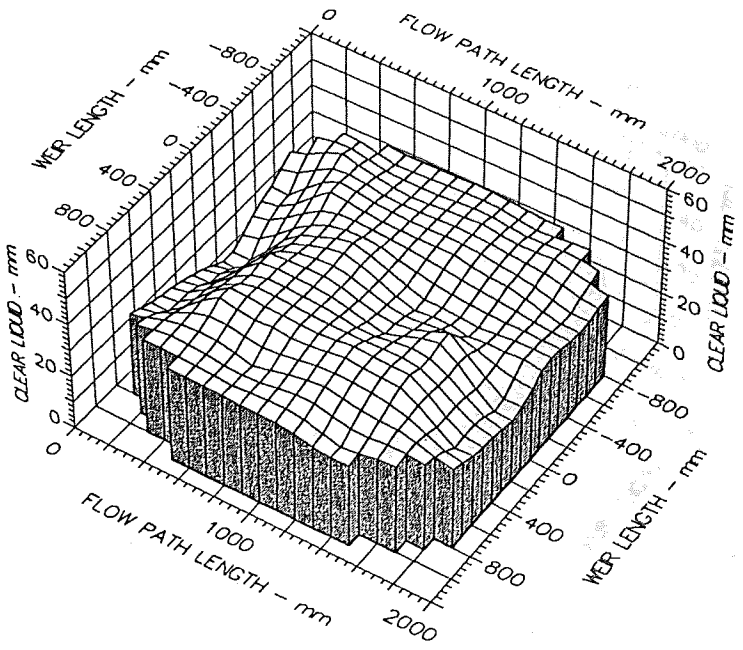

Air Velocity
1.0 m/s

Weir Load
150.0 cm3/cm.s

Inlet Gap
0.01 m

Outlet Weir
0.01 m

Hole Diameter
0.001 m

Figure A11.2 Surface of clear liquid hold-up for ARC-1 tray
Mean hCL 34 Emg/Eog 101/90

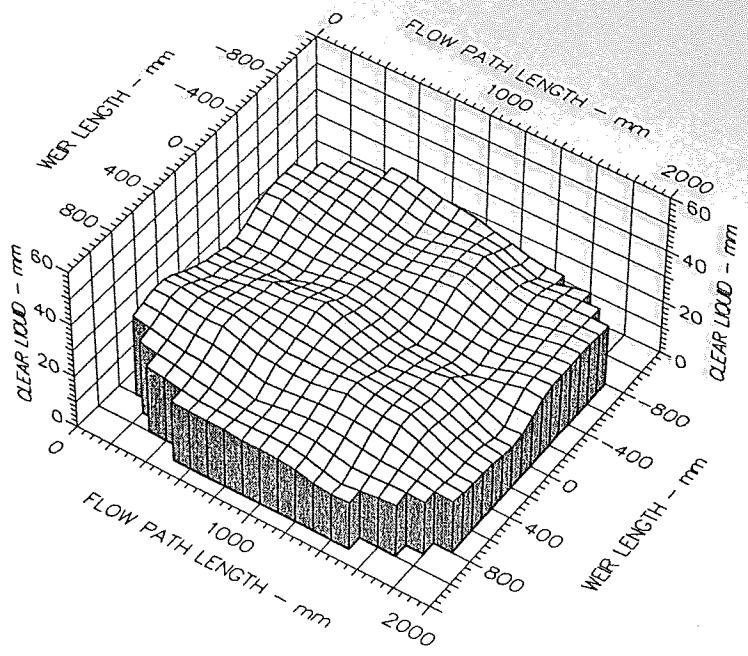

Air Velocity
1.500 m/s

Weir Load
50.0 cm3/cm.s

Inlet Gap
0.010 m

Outlet Weir
0.010 m

Hole Diameter
0.001 m

Figure A11.3 Surface of clear liquid hold-up for ARC-1 tray
Mean hCL 24 Emg/Eog 99/64

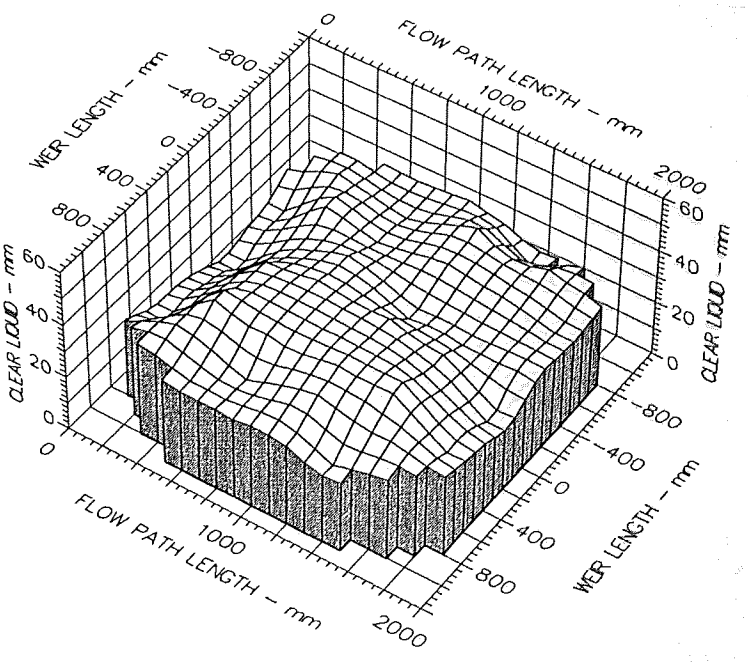

Air Velocity
1.5 m/s

Weir Load
150.0 cm3/cm.s

Inlet Gap
0.01 m

Outlet Weir
0.01 m

Hole Diameter
0.001 m

Figure A11.4 Surface of clear liquid hold-up for ARC-1 tray
Mean hCL 32 Emg/Eog 96/84

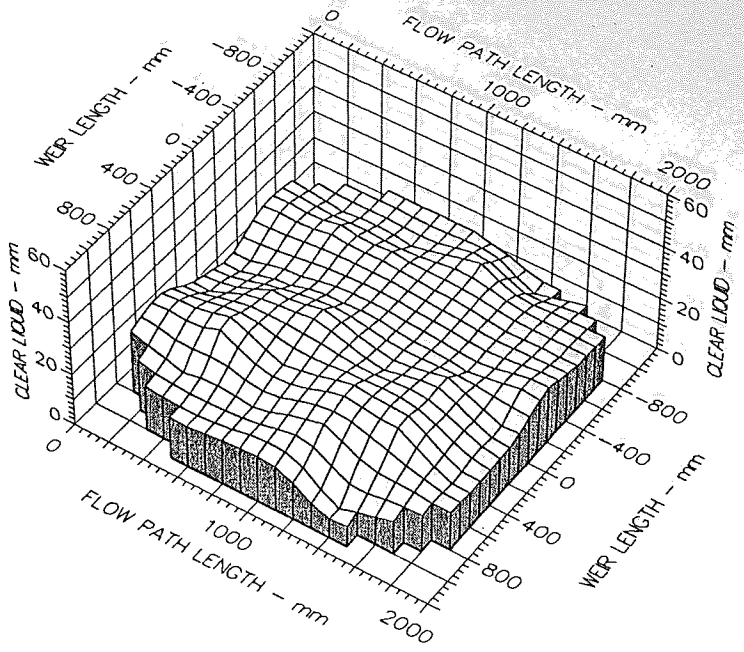

Air Velocity
2.000 m/s

Weir Load
50.0 cm3/cm.s

Inlet Gap
0.010 m

Outlet Weir
0.010 m

Hole Diameter
0.001 m

Figure A11.5 Surface of clear liquid hold-up for ARC-1 tray
Mean hCL 20 Emg/Eog 85/56

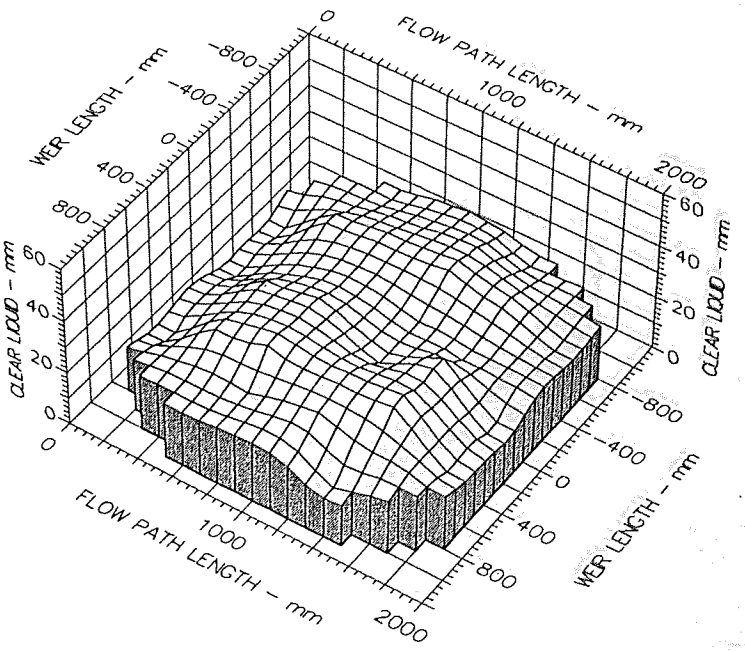

Air Velocity
2.0 m/s

Weir Load
150.0 cm3/cm.s

Inlet Gap
0.01 m

Outlet Weir
0.01 m

Hole Diameter
0.001 m

Figure A11.6 Surface of clear liquid hold-up for ARC-1 tray
Mean hCL 24 Emg/Eog 96/81

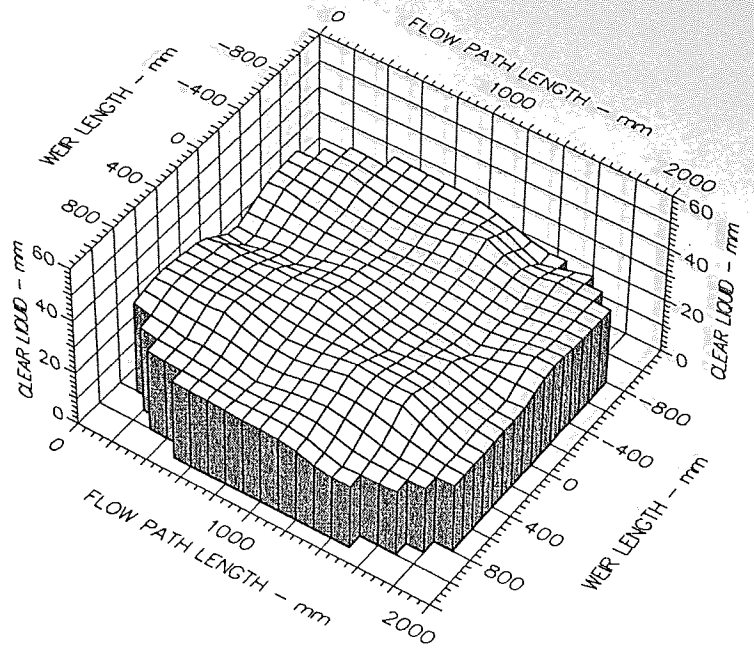

Air Velocity
1.000 m/s

Weir Load
50.0 cm3/cm.s

Inlet Gap
0.020 m

Outlet Weir
0.020 m

Hole Diameter
0.001 m

Figure A11.7 Surface of clear liquid hold-up for ARC-1 tray
Mean hCL 30 Emg/Eog 98/69

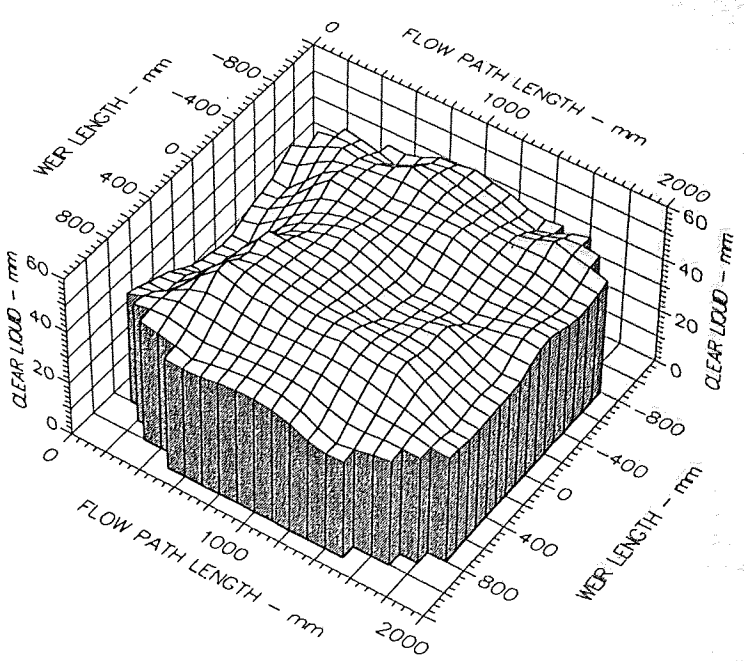

Air Velocity
1.0 m/s

Weir Load
200.0 cm3/cm.s

Inlet Gap
0.02 m

Outlet Weir
0.02 m

Hole Diameter
0.001 m

Figure A11.8 Surface of clear liquid hold-up for ARC-1 tray
Mean hCL 44 Emg/Eog 103/92

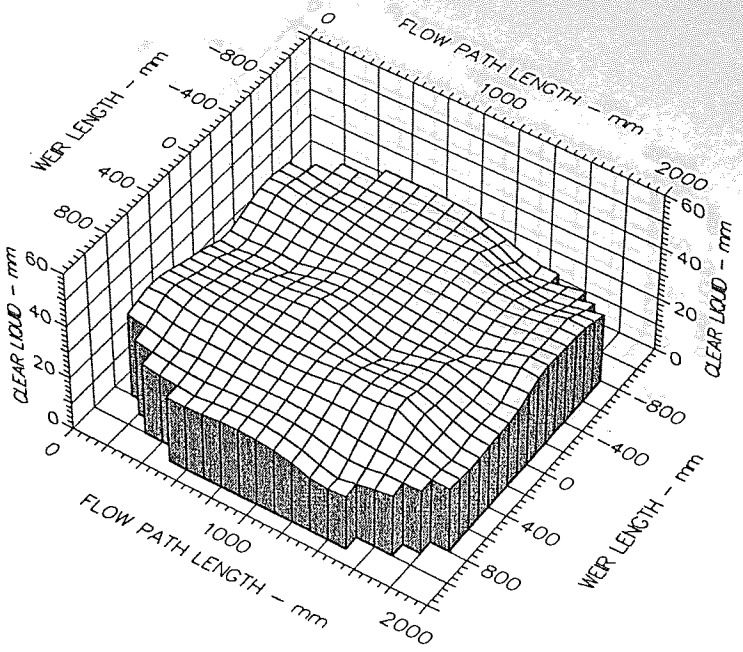

Air Velocity
1.500 m/s

Weir Load
50.0 cm3/cm.s

Inlet Gap
0.020 m

Outlet Weir
0.020 m

Hole Diameter
0.001 m

Figure A11.9 Surface of clear liquid hold-up for ARC-1 tray
Mean hCL 28 Emg/Eog 89/61

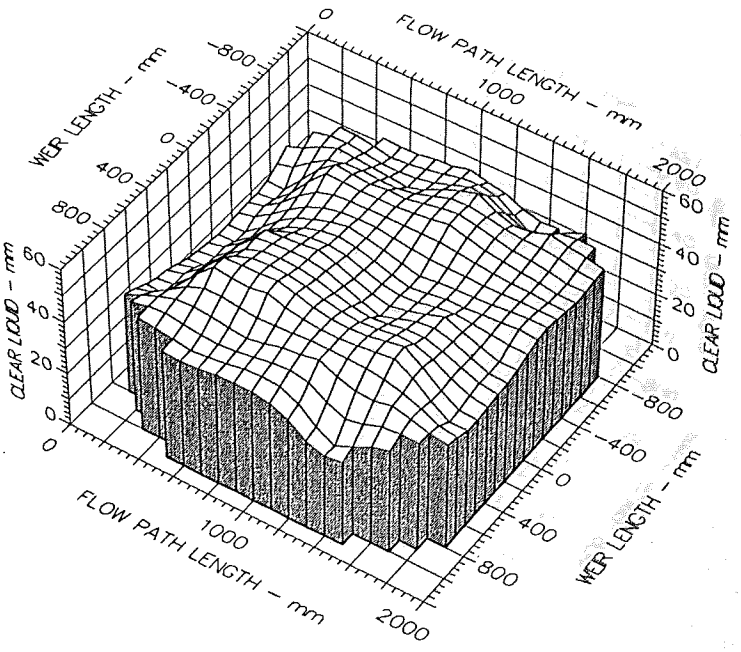

Air Velocity
1.5 m/s

Weir Load
200.0 cm3/cm.s

Inlet Gap
0.02 m

Outlet Weir
0.02 m

Hole Diameter
0.001 m

Figure A11.10 Surface of clear liquid hold-up for ARC-1 tray
Mean hCL 42 Emg/Eog 93/83

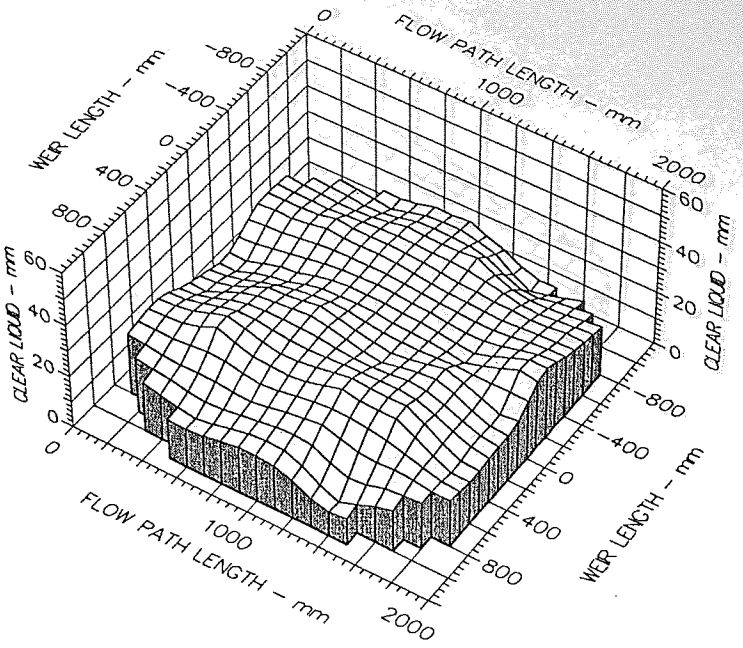

Air Velocity
2.000 m/s

Weir Load
50.0 cm3/cm.s

Inlet Gap
0.020 m

Outlet Weir
0.020 m

Hole Diameter
0.001 m

Figure A11.11 Surface of clear liquid hold-up for ARC-1 tray
Mean hCL 22 Emg/Eog 91/59

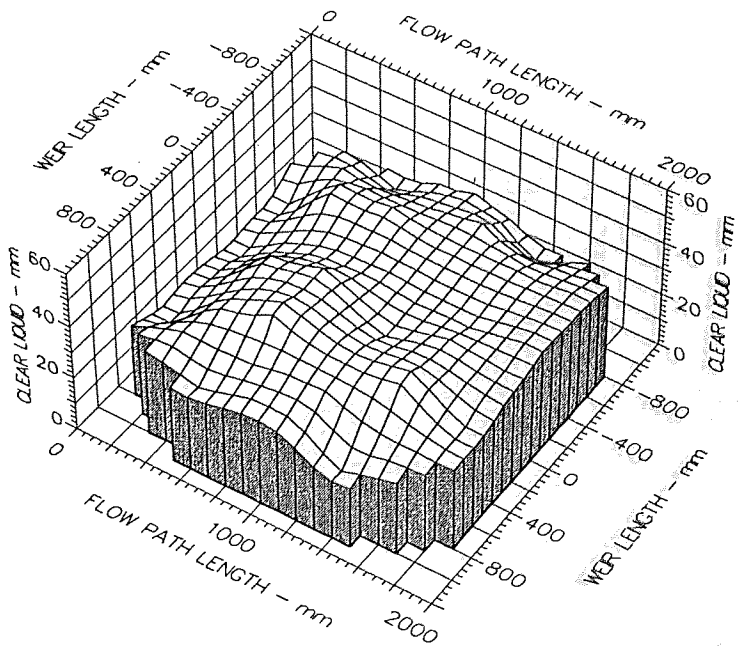

Air Velocity
2.0 m/s

Weir Load
200.0 cm3/cm.s

Inlet Gap
0.02 m

Outlet Weir
0.02 m

Hole Diameter
0.001 m

Figure A11.12 Surface of clear liquid hold-up for ARC-1 tray
Mean hCL 34 Emg/Eog 93/81

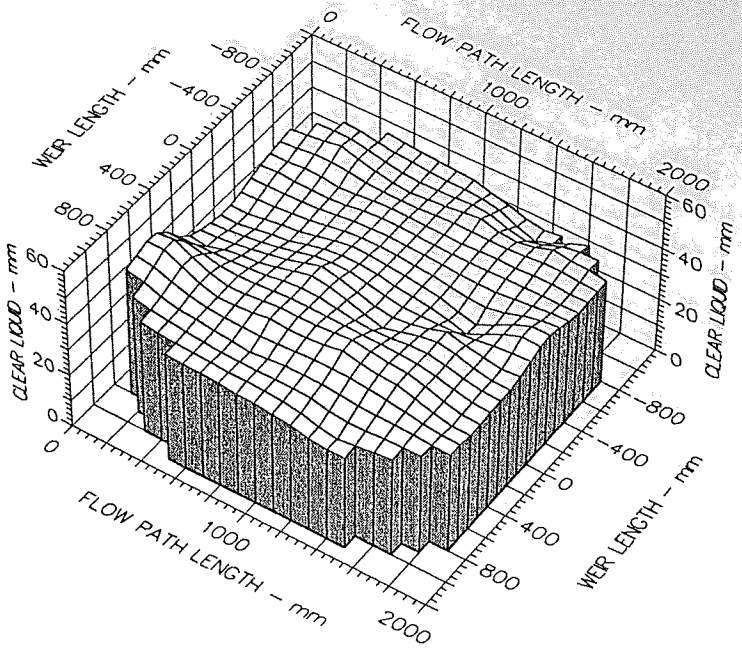

Air Velocity
1.000 m/s

Weir Load
50.0 cm3/cm.s

Inlet Gap
0.050 m

Outlet Weir
0.050 m

Hole Diameter
0.001 m

Figure A11.13 Surface of clear liquid hold-up for ARC-1 tray
Mean hCL 40 Emg/Eog 97/74

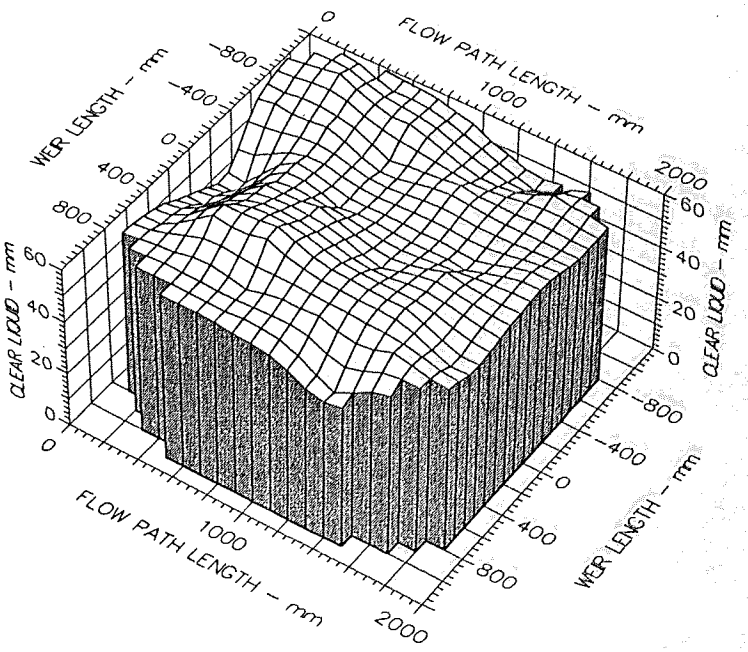

Air Velocity
1.0 m/s

Weir Load
200.0 cm3/cm.s

Inlet Gap
0.05 m

Outlet Weir
0.05 m

Hole Diameter
0.001 m

Figure A11.14 Surface of clear liquid hold-up for ARC-1 tray
Mean hCL 62 Emg/Eog 104/94

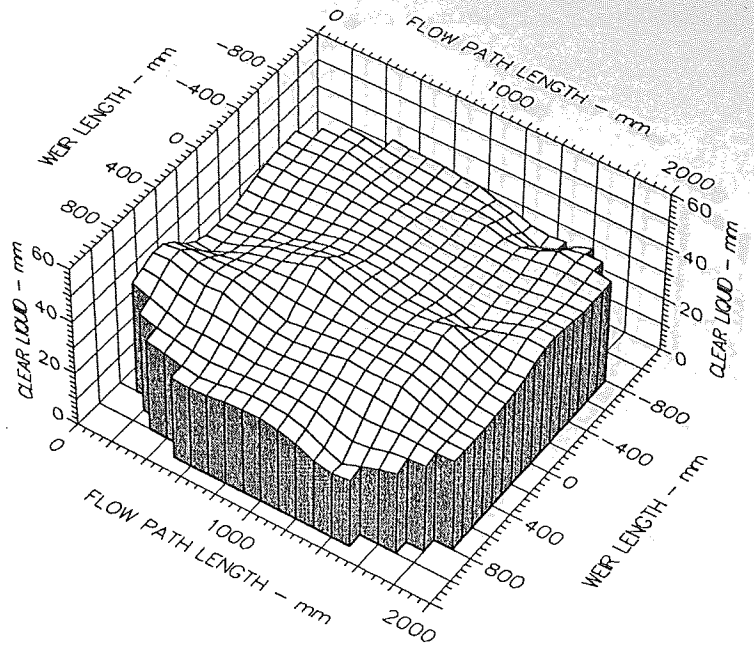

Air Velocity
1.500 m/s

Weir Load
50.0 cm3/cm.s

Inlet Gap
0.050 m

Outlet Weir
0.050 m

Hole Diameter
0.001 m

Figure A11.15 Surface of clear liquid hold-up for ARC-1 tray
Mean hCL 38 Emg/Eog 94/68

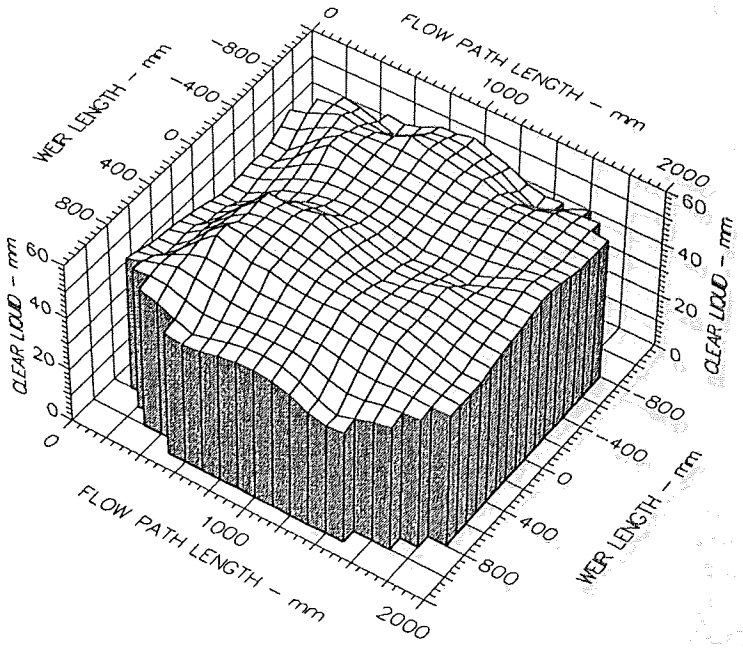

Air Velocity
1.5 m/s

Weir Load
200.0 cm3/cm.s

Inlet Gap
0.05 m

Outlet Weir
0.05 m

Hole Diameter
0.001 m

Figure A16.16 Surface of clear liquid hold-up for ARC-1 tray
Mean hCL 53 Emg/Eog 109/92

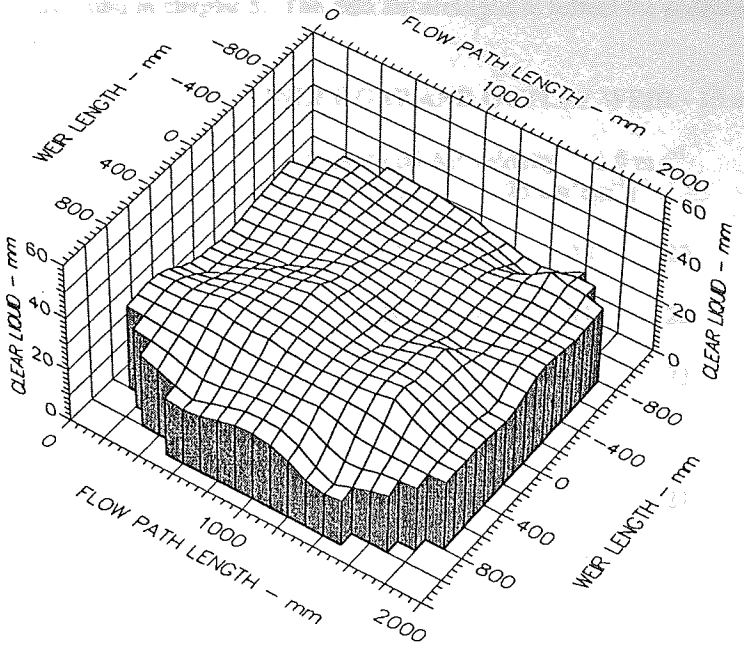

Air Velocity
2.000 m/s

Weir Load
50.0 cm3/cm.s

Inlet Gap
0.050 m

Outlet Weir
0.050 m

Hole Diameter
0.001 m

Figure A11.17 Surface of clear liquid hold-up for ARC-1 tray
Mean hCL 28 Emg/Eog 98/59

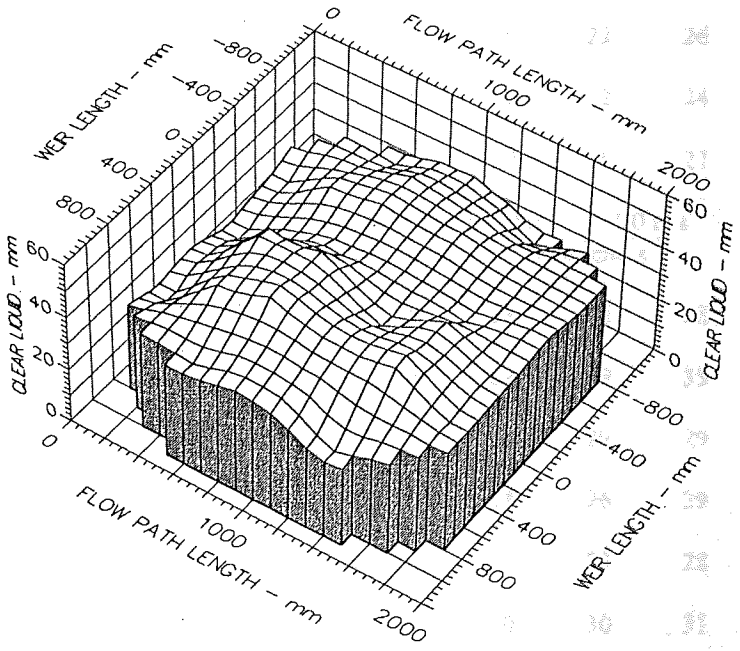

Air Velocity
2.0 m/s

Weir Load
200.0 cm3/cm.s

Inlet Gap
0.05 m

Outlet Weir
0.05 m

Hole Diameter
0.001 m

Figure A11.18 Surface of clear liquid hold-up for ARC-1 tray
Mean hCL 39 Emg/Eog 102/88

Appendices 12
Height of Clear Liquid Measurements for the UMD Tray Cases

Below are the values of the height of clear liquid (mm) measured over the 2.44 m diameter tray for the conditions as found in chapter 5. The data are arranged to reflect the positions of the thirty-six manometer points on the tray.

INLET GAP AND OUTLET WEIR - 10 mm

Superficial Air velocity 1.0 m s^{-1}
Weir Load 25 $cm^3cm^{-1}s^{-1}$

	30	25	23	23		
24					22	
	28	28	21	25		
21						20
	26	28	21	23	19	
24	25	22	18	23	22	
17						15
	24	23	19	21		
20					22	
	16	16	26	24		

Superficial Air velocity 1.0 m s^{-1}
Weir Load 50 $cm^3cm^{-1}s^{-1}$

	36	31	25	26		
30					29	
	32	31	24	29		
26						28
27	30	34	27	25	26	
28	31	26	23	26	27	
19						19
	28	29	22	24		
22					23	
	18	19	28	27		

Superficial Air velocity 1.0 m s^{-1}
Weir Load 75 $cm^3cm^{-1}s^{-1}$

	35	31	28	28		
32					33	
	36	32	29	33		
31						31
29	35	36	29	29	29	
30	34	28	26	29	31	
21						21
	33	31	23	28		
25					26	
	21	20	30	31		

Superficial Air velocity 1.0 m s^{-1}
Weir Load 100 $cm^3 cm^{-1} s^{-1}$

	31	31	23	28	
35					35
	39	37	31	37	
33					32
30	38	40	32	32	30
32	38	31	28	34	33
24					25
	36	34	27	30	
29					31
	23	23	32	30	

Superficial Air velocity 1.0 m s^{-1}
Weir Load 150 $cm^3 cm^{-1} s^{-1}$

	25	21	15	25	
36					38
	42	41	39	37	
35					33
33	40	42	38	36	34
37	41	44	32	36	37
30					29
	40	37	32	35	
35					35
	28	25	33	35	

Superficial Air velocity 1.5 m s^{-1}
Weir Load 25 $cm^3 cm^{-1} s^{-1}$

	24	22	18	22	
18					20
	22	23	18	20	
18					18
16	23	25	17	20	17
19	24	18	17	20	20
12					10
	23	21	17	17	
16					17
	14	15	23	22	

Superficial Air velocity 1.5 m s^{-1}
Weir Load 50 $cm^3 cm^{-1} s^{-1}$

	29	26	22	23	
22					22
	28	28	19	25	
21					22
22	27	30	25	22	23
22	29	12	20	22	24
14					15
	25	24	20	22	
19					20
	16	15	25	24	

Superficial Air velocity 1.5 m s^{-1}
Weir Load 75 $cm^3 cm^{-1} s^{-1}$

	26	22	18	24	
27					25
	33	31	23	33	
25					24
25	32	32	28	28	25
28	32	30	27	27	30
22					23
	31	31	26	26	
25					25
	19	17	27	26	

Superficial Air velocity 1.5 m s^{-1}
Weir Load 100 $cm^3 cm^{-1} s^{-1}$

	27	25	18	22	
28					27
	38	35	26	33	
26					28
27	34	33	35	28	27
30	34	31	29	29	30
19					19
	33	31	29	31	
25					27
	20	23	29	29	

Superficial Air velocity 1.5 m s^{-1}
Weir Load 150 $cm^3 cm^{-1} s^{-1}$

	22	21	18	24	
28					30
	40	38	35	31	
26					27
27	38	41	39	35	28
35	35	39	30	35	34
22					23
	37	33	32	33	
32					33
	25	22	33	33	

Superficial Air velocity 2.0 m s^{-1}
Weir Load 25 $cm^3 cm^{-1} s^{-1}$

	22	16	15	17	
18					17
	23	20	14	22	
15					15
14	21	23	21	19	15
19	25	18	17	17	20
8					9
	22	20	17	15	
12					11
	12	11	21	22	

Superficial Air velocity 2.0 m s^{-1}
Weir Load 50 $cm^3cm^{-1}s^{-1}$

	21	17	14	17		
18					18	
	30	25	17	25		
13						12
15	24	27	18	21	15	
21	28	19	18	19	20	
10						8
	25	22	17	16		
16					15	
	12	11	22	21		

Superficial Air velocity 2.0 m s^{-1}
Weir Load 75 $cm^3cm^{-1}s^{-1}$

	21	20	16	17		
22					21	
	30	25	20	27		
17						18
18	29	27	23	24	19	
26	29	20	21	25	25	
12						10
	27	27	18	18		
21					21	
	14	10	22	18		

Superficial Air velocity 2.0 m s^{-1}
Weir Load 100 $cm^3cm^{-1}s^{-1}$

	20	19	13	16		
20					21	
	32	26	23	29		
16						18
20	33	32	25	26	21	
27	31	22	22	26	26	
9						11
	29	28	22	22		
22					21	
	14	15	23	20		

Superficial Air velocity 2.0 m s^{-1}
Weir Load 150 $cm^3cm^{-1}s^{-1}$

	17	19	14	13		
25					25	
	32	32	24	28		
20						20
26	35	34	34	30	26	
32	32	23	24	30	31	
19						17
	35	33	27	29		
26					27	
	21	17	24	26		

INLET GAP AND OUTLET WEIR - 20 mm

Superficial Air velocity 1.0 m s^{-1}
Weir Load 25 $cm^3cm^{-1}s^{-1}$

	33	29	24	25		
26					27	
	31	30	22	28		
27						23
24	28	31	27	23	21	
25	27	25	21	24	25	
17						20
	28	30	20	20		
24					23	
	21	20	25	23		

Superficial Air velocity 1.0 m s^{-1}
Weir Load 50 $cm^3cm^{-1}s^{-1}$

	38	32	24	29		
32					32	
	37	33	25	28		
31						27
28	32	35	31	27	27	
27	33	27	26	25	30	
21						21
	32	31	23	26		
25					29	
	24	26	30	28		

Superficial Air velocity 1.0 m s^{-1}
Weir Load 100 $cm^3cm^{-1}s^{-1}$

	37	28	28	35		
37					36	
	40	40	33	36		
34						32
34	39	41	35	33	35	
37	40	33	30	36	38	
27						28
	37	37	28	34		
33					33	
	31	29	33	32		

Superficial Air velocity 1.0 m s^{-1}
Weir Load 150 $cm^3cm^{-1}s^{-1}$

	32	25	22	36		
41					37	
	44	44	39	40		
38						39
38	45	46	42	38	37	
43	44	34	32	39	41	
30						30
	42	41	33	36		
36					37	
	34	30	37	34		

Superficial Air velocity 1.0 m s^{-1}
Weir Load 200 $cm^3 cm^{-1} s^{-1}$

	37	30	27	33	
50					50
	54	53	46	51	
46					43
50	54	50	48	48	52
51	53	46	42	46	50
40					38
	53	51	41	46	
47					49
	43	40	45	40	

Superficial Air velocity 1.5 m s^{-1}
Weir Load 25 $cm^3 cm^{-1} s^{-1}$

	29	24	21	22	
24					24
	27	26	20	24	
22					22
24	25	27	21	22	23
28	29	22	21	23	26
14					16
	28	27	19	20	
20					18
	20	21	26	22	

Superficial Air velocity 1.5 m s^{-1}
Weir Load 50 $cm^3 cm^{-1} s^{-1}$

	30	28	24	27	
28					28
	33	29	22	30	
23					24
24	30	31	27	25	24
27	31	24	24	24	27
16					17
	31	30	20	25	
22					21
	23	22	28	24	

Superficial Air velocity 1.5 m s^{-1}
Weir Load 100 $cm^3 cm^{-1} s^{-1}$

	32	25	21	29	
34					33
	40	36	33	36	
32					33
31	39	39	32	34	31
35	38	34	31	36	36
23					22
	37	37	28	31	
31					32
	30	26	32	29	

Superficial Air velocity 1.5 m s^{-1}
Weir Load 150 $cm^3 cm^{-1} s^{-1}$

	28	22	20	21		
37					34	
	44	40	33	37		
31						30
35	43	43	38	37	36	
39	41	44	31	36	37	
25						25
	41	39	30	35		
34					35	
	30	27	35	31		

Superficial Air velocity 1.5 m s^{-1}
Weir Load 200 $cm^3 cm^{-1} s^{-1}$

	34	29	29	29		
48					46	
	53	50	45	49		
41						40
45	55	52	49	50	43	
51	50	42	42	46	51	
35						36
	53	49	41	46		
47					49	
	43	40	43	41		

Superficial Air velocity 2.0 m s^{-1}
Weir Load 25 $cm^3 cm^{-1} s^{-1}$

	21	17	13	17		
16					19	
	24	22	16	20		
13						11
15	23	28	22	19	15	
18	27	19	20	19	21	
7						5
	23	23	15	14		
15					17	
	15	13	19	19		

Superficial Air velocity 2.0 m s^{-1}
Weir Load 50 $cm^3 cm^{-1} s^{-1}$

	26	18	14	20		
20					20	
	29	27	24	24		
15						13
20	28	28	22	22	23	
24	29	24	21	19	22	
8						8
	27	26	19	19		
18					19	
	15	17	22	21		

Superficial Air velocity 2.0 m s^{-1}
Weir Load 100 $cm^3 cm^{-1} s^{-1}$

	22	20	17	19		
25					26	
	36	32	25	30		
17						17
24	35	33	26	29	25	
27	30	25	23	25	26	
13						15
	29	32	23	23		
22					25	
	16	18	25	21		

Superficial Air velocity 2.0 m s^{-1}
Weir Load 150 $cm^3 cm^{-1} s^{-1}$

	15	19	17	17		
29					31	
	36	33	26	35		
22						23
25	39	36	33	33	27	
32	34	24	25	29	31	
15						17
	33	32	23	27		
27					28	
	24	19	26	21		

Superficial Air velocity 2.0 m s^{-1}
Weir Load 200 $cm^3 cm^{-1} s^{-1}$

	16	19	17	17		
34					31	
	36	38	26	31		
24						21
28	42	38	31	33	30	
35	38	30	28	34	34	
22						17
	41	40	28	31		
30					27	
	28	28	29	27		

INLET GAP AND OUTLET WEIR - 50 mm

Superficial Air velocity 1.0 m s^{-1}
Weir Load 25 $cm^3cm^{-1}s^{-1}$

	38	32	30	33	
35					35
	38	36	28	33	
32					32
27	36	36	32	30	27
34	36	33	27	29	34
24					24
	36	35	29	28	
30					30
	30	28	35	31	

Superficial Air velocity 1.0 m s^{-1}
Weir Load 50 $cm^3cm^{-1}s^{-1}$

	43	33	28	32	
38					37
	40	38	32	33	
34					34
34	40	40	35	34	34
36	42	34	33	34	35
28					27
	38	39	29	30	
34					35
	32	33	36	36	

Superficial Air velocity 1.0 m s^{-1}
Weir Load 100 $cm^3cm^{-1}s^{-1}$

	68	32	29	56	
61					61
	48	44	40	40	
38					38
41	46	47	42	42	41
41	45	37	38	39	41
31					31
	45	43	37	39	
38					38
	37	37	43	39	

Superficial Air velocity 1.0 m s^{-1}
Weir Load 150 $cm^3cm^{-1}s^{-1}$

	49	33	29	67	
49					49
	52	50	45	39	
47					47
47	51	52	48	48	47
48	52	40	42	45	48
35					36
	50	49	40	42	
45					46
	43	44	50	45	

Superficial Air velocity 1.0 m s^{-1}
Weir Load 200 $cm^3 cm^{-1} s^{-1}$

	59	43	39	56	
64					64
	65	67	55	57	
59					59
60	66	60	59	57	60
61	64	49	49	57	61
47					47
	64	62	53	52	
60					60
	56	57	57	54	

Superficial Air velocity 1.5 m s^{-1}
Weir Load 25 $cm^3 cm^{-1} s^{-1}$

	36	29	28	29	
29					27
	32	32	25	26	
25					24
27	30	35	31	29	25
29	35	27	26	31	32
18					16
	34	34	24	25	
28					28
	28	26	33	30	

Superficial Air velocity 1.5 m s^{-1}
Weir Load 50 $cm^3 cm^{-1} s^{-1}$

	39	31	29	34	
33					36
	37	37	29	31	
29					30
31	38	39	36	34	31
36	40	31	29	33	34
24					21
	38	37	29	30	
30					33
	30	31	35	34	

Superficial Air velocity 1.5 m s^{-1}
Weir Load 100 $cm^3 cm^{-1} s^{-1}$

	42	30	28	31	
40					37
	44	42	34	40	
34					32
38	44	44	40	40	39
42	43	33	38	37	37
26					26
	43	42	34	35	
36					36
	37	33	43	37	

Superficial Air velocity 1.5 m s^{-1}
Weir Load 150 $cm^3 cm^{-1} s^{-1}$

	37	26	23	28		
43					45	
	46	45	40	42		
38						38
41	49	48	42	46	40	
42	45	45	38	41	42	
27						27
	45	45	37	41		
39					41	
	39	37	45	39		

Superficial Air velocity 1.5 m s^{-1}
Weir Load 200 $cm^3 cm^{-1} s^{-1}$

	45	42	37	40		
56					56	
	63	62	55	56		
49						47
59	63	64	57	59	59	
55	61	53	55	57	57	
44						46
	58	59	50	54		
55					56	
	53	56	57	55		

Superficial Air velocity 1.5 m s^{-1}
Weir Load 250 $cm^3 cm^{-1} s^{-1}$

		48	49		
				50	
		60	62		
					70
		59	67	63	
		62	64	55	
					59
		56	65		
				61	
		65	60		

Superficial Air velocity 1.5 m s^{-1}
Weir Load 300 $cm^3 cm^{-1} s^{-1}$

		60	58		
				57	
		64	77		
					79
		74	72	70	
		72	78	73	
					68
		67	74		
				69	
		76	74		

Superficial Air velocity 1.5 m s^{-1}
Weir Load 350 $cm^3cm^{-1}s^{-1}$

			65	66		
					61	
			70	79		
						82
			73	75	78	
			74	81	72	
						73
			67	76		
					72	
			78	78		

Superficial Air velocity 2.0 m s^{-1}
Weir Load 25 $cm^3cm^{-1}s^{-1}$

	25	20	19	23		
22					22	
	29	28	20	24		
17						18
22	29	33	25	26	20	
24	28	32	19	27	23	
6						10
	27	30	22	18		
20					20	
	20	22	25	25		

Superficial Air velocity 2.0 m s^{-1}
Weir Load 50 $cm^3cm^{-1}s^{-1}$

	30	23	23	25		
28					29	
	36	32	24	28		
21						24
26	34	37	31	28	27	
28	34	27	25	26	29	
16						13
	33	31	23	24		
24					26	
	25	26	31	28		

Superficial Air velocity 2.0 m s^{-1}
Weir Load 100 $cm^3cm^{-1}s^{-1}$

	20	26	22	16		
34					31	
	41	38	29	35		
23						24
35	41	42	33	35	33	
32	38	29	31	33	31	
21						23
	37	39	30	37		
31					34	
	29	29	35	29		

Superficial Air velocity 2.0 m s^{-1}
Weir Load 150 $cm^3cm^{-1}s^{-1}$

	16	25	22	13		
30					30	
	42	41	33	38		
22						24
37	49	37	31	41	37	
29	42	30	32	37	29	
30						32
	41	42	33	35		
34					35	
	32	33	27	34		

Superficial Air velocity 2.0 m s^{-1}
Weir Load 200 $cm^3cm^{-1}s^{-1}$

	16	25	25	16		
36					37	
	47	40	40	41		
27						27
35	54	39	32	47	36	
31	50	26	34	45	31	
32						32
	48	37	26	35		
39					39	
	32	30	32	40		

Superficial Air velocity 2.0 m s^{-1}
Weir Load 250 $cm^3cm^{-1}s^{-1}$

35	39		
		35	
42	56		
			61
44	51	49	
50	53	44	
			44
44	50		
		45	
48	47		

Superficial Air velocity 2.0 m s^{-1}
Weir Load 300 $cm^3cm^{-1}s^{-1}$

47	47		
		45	
49	60		
			62
55	59	59	
56	63	57	
			52
52	57		
		55	
61	61		

Superficial Air velocity 1.5 m s^{-1}
Weir Load 350 $cm^3 cm^{-1} s^{-1}$

63	65		
		53	
62	72		
			76
68	76	71	
72	78	73	
			67
65	72		
		70	
77	75		

Appendices 13
Height of Clear Liquid Measurements for the STR-1 Tray Cases

Below are the values of the height of clear liquid (mm) measured over the 2.44 m diameter tray for the conditions as found in chapter 7. The data are arranged to reflect the positions of the thirty-six manometer points on the tray.

INLET GAP AND OUTLET WEIR - 10 mm

Superficial Air velocity 1.0 m s^{-1}
Weir Load 25 $cm^3cm^{-1}s^{-1}$

	30	26	22	22		
26					24	
	31	28	18	21		
25						21
22	27	27	21	20	19	
22	27	20	19	22	24	
15						15
	25	25	18	19		
21					20	
	16	16	25	21		

Superficial Air velocity 1.0 m s^{-1}
Weir Load 50 $cm^3cm^{-1}s^{-1}$

	37	33	28	23		
31					31	
	34	31	23	29		
31						29
29	32	32	28	26	27	
29	31	26	23	26	27	
19						22
	30	30	22	24		
25					25	
	20	21	28	26		

Superficial Air velocity 1.0 m s^{-1}
Weir Load 75 $cm^3cm^{-1}s^{-1}$

	35	33	29	32		
33					34	
	38	35	29	33		
32						31
29	34	37	30	27	33	
29	35	31	27	28	30	
23						22
	34	32	25	27		
27					25	
	22	21	29	28		

Superficial Air velocity 1.0 m s^{-1}
Weir Load 100 $cm^3 cm^{-1} s^{-1}$

	34	29	25	32		
37					34	
	39	37	31	33		
35						30
35	38	39	34	31	29	
35	38	32	30	33	36	
25						25
	35	36	27	32		
31					31	
	24	21	32	30		

Superficial Air velocity 1.0 m s^{-1}
Weir Load 150 $cm^3 cm^{-1} s^{-1}$

	24	23	17	23		
38					40	
	39	42	36	37		
37						36
35	45	39	40	35	29	
36	42	34	30	35	37	
32						31
	41	38	31	35		
36					40	
	27	24	33	32		

Superficial Air velocity 1.5 m s^{-1}
Weir Load 25 $cm^3 cm^{-1} s^{-1}$

	28	29	20	23		
19					23	
	27	27	22	21		
19						18
16	21	29	24	21	18	
21	24	22	23	18	21	
11						11
	23	21	19	21		
17					17	
	13	17	23	22		

Superficial Air velocity 1.5 m s^{-1}
Weir Load 50 $cm^3 cm^{-1} s^{-1}$

	29	25	21	24		
24					20	
	30	28	22	21		
21						21
21	23	28	23	23	19	
22	25	22	20	25	24	
13						16
	28	27	16	23		
19					21	
	16	17	24	21		

Superficial Air velocity 1.5 m s^{-1}
Weir Load 75 $cm^3 cm^{-1} s^{-1}$

	24	23	17	22		
30					22	
	32	28	24	29		
23						21
25	33	30	26	28	24	
26	33	27	22	28	29	
18						18
	29	31	21	22		
22					23	
	17	14	24	23		

superficial Air velocity 1.5 m s^{-1}
Weir Load 100 $cm^3 cm^{-1} s^{-1}$

	24	24	18	20		
28					30	
	32	32	28	31		
27						27
25	34	34	30	28	24	
30	34	29	25	30	28	
18						16
	33	31	22	27		
25					26	
	19	17	24	23		

Superficial Air velocity 1.5 m s^{-1}
Weir Load 150 $cm^3 cm^{-1} s^{-1}$

	17	16	13	19		
31					25	
	35	33	30	32		
26						25
27	39	36	34	34	29	
36	34	34	25	34	34	
24						22
	36	34	27	28		
31					28	
	24	27	28	28		

Superficial Air velocity 2.0 m s^{-1}
Weir Load 25 $cm^3 cm^{-1} s^{-1}$

	20	17	12	17		
15					19	
	25	25	17	20		
12						13
13	19	23	22	18	13	
17	24	19	18	18	17	
5						7
	20	21	14	14		
14					13	
	11	12	18	17		

Superficial Air velocity 2.0 m s^{-1}
Weir Load 50 $cm^3cm^{-1}s^{-1}$

	23	16	12	18		
21					18	
	28	25	19	23		
14						10
17	23	26	22	22	15	
22	27	19	17	20	21	
9						6
	23	24	15	14		
15					14	
	11	12	18	17		

Superficial Air velocity 2.0 m s^{-1}
Weir Load 75 $cm^3cm^{-1}s^{-1}$

	20	17	12	14		
21					21	
	30	25	22	23		
16						14
19	27	26	22	21	20	
21	27	19	18	21	22	
9						8
	23	25	16	15		
18					17	
	11	11	16	16		

Superficial Air velocity 2.0 m s^{-1}
Weir Load 100 $cm^3cm^{-1}s^{-1}$

	19	15	12	16		
22					22	
	31	27	20	25		
16						16
20	33	30	24	26	20	
23	29	21	20	25	23	
9						12
	27	29	19	18		
17					20	
	13	11	20	18		

Superficial Air velocity 2.0 m s^{-1}
Weir Load 150 $cm^3cm^{-1}s^{-1}$

	13	15	10	9		
23					22	
	27	29	20	26		
15						19
21	31	30	27	28	23	
30	27	21	21	27	26	
14						16
	32	30	21	25		
24					22	
	17	15	20	19		

INLET GAP AND OUTLET WEIR - 20 mm

Superficial Air velocity 1.0 m s^{-1}
Weir Load 25 $cm^3 cm^{-1} s^{-1}$

	31	26	21	23	
25					25
	30	28	19	22	
25					21
24	26	29	23	21	22
22	28	21	21	23	23
16					15
	25	28	18	22	
22					23
	20	20	29	25	

Superficial Air velocity 1.0 m s^{-1}
Weir Load 50 $cm^3 cm^{-1} s^{-1}$

	38	33	25	28	
33					32
	37	34	26	29	
30					29
27	31	36	30	28	28
26	33	30	26	27	31
22					22
	30	33	24	25	
26					30
	24	25	32	26	

Superficial Air velocity 1.0 m s^{-1}
Weir Load 100 $cm^3 cm^{-1} s^{-1}$

	37	27	27	45	
39					39
	43	39	34	36	
32					33
35	39	41	37	33	35
35	40	36	33	37	35
27					29
	40	37	31	33	
32					35
	29	30	37	34	

Superficial Air velocity 1.0 m s^{-1}
Weir Load 150 $cm^3 cm^{-1} s^{-1}$

	35	28	24	30	
44					37
	49	45	41	44	
40					41
40	49	43	42	41	42
40	45	39	35	42	44
33					29
	43	43	35	40	
40					41
	33	32	41	39	

Superficial Air velocity 1.0 m s^{-1}
Weir Load 200 $cm^3 cm^{-1} s^{-1}$

	38	32	27	32	
54					47
	58	53	45	50	
46					42
45	54	52	49	49	46
51	55	46	45	49	49
35					40
	52	49	44	45	
47					48
	39	39	47	41	

Superficial Air velocity 1.5 m s^{-1}
Weir Load 25 $cm^3 cm^{-1} s^{-1}$

	29	27	21	21	
23					23
	25	27	18	24	
21					21
22	26	27	23	21	22
25	31	21	19	23	25
15					14
	29	27	20	20	
20					20
	20	22	26	23	

Superficial Air velocity 1.5 m s^{-1}
Weir Load 50 $cm^3 cm^{-1} s^{-1}$

	35	28	23	28	
27					26
	31	31	26	31	
22					25
22	29	33	27	26	27
28	33	26	28	26	29
17					16
	30	30	22	24	
24					21
	22	25	31	32	

Superficial Air velocity 1.5 m s^{-1}
Weir Load 100 $cm^3 cm^{-1} s^{-1}$

	27	24	19	29		
32					29	
	38	34	31	30		
29						30
30	38	39	34	31	28	
32	37	31	28	31	33	
21						22
	39	35	27	29		
28					28	
	24	24	34	28		

Superficial Air velocity 1.5 m s^{-1}
Weir Load 150 $cm^3 cm^{-1} s^{-1}$

	28	23	21	24		
34					35	
	45	39	35	36		
32						29
39	46	43	39	37	38	
40	41	43	31	39	41	
24						25
	44	40	33	36		
33					39	
	29	27	38	31		

Superficial Air velocity 1.5 m s^{-1}
Weir Load 200 $cm^3 cm^{-1} s^{-1}$

	32	29	26	26		
44					45	
	49	46	39	44		
35						37
43	50	47	47	46	41	
46	51	39	39	46	48	
32						32
	50	46	39	43		
42					43	
	35	36	43	36		

Superficial Air velocity 2.0 m s^{-1}
Weir Load 25 $cm^3 cm^{-1} s^{-1}$

	27	19	17	20		
20					21	
	26	24	19	25		
14						12
18	25	28	25	23	16	
25	29	21	22	20	23	
8						7
	26	26	20	17		
20					19	
	17	17	23	22		

Superficial Air velocity 2.0 m s^{-1}
Weir Load 50 $cm^3 cm^{-1} s^{-1}$

	31	21	18	23		
23					22	
	32	30	22	26		
17						20
20	30	31	25	28	27	
26	33	27	25	26	27	
12						12
	29	30	25	21		
22					23	
	19	19	28	24		

Superficial Air velocity 2.0 m s^{-1}
Weir Load 100 $cm^3 cm^{-1} s^{-1}$

	27	21	19	23		
27					28	
	39	33	29	36		
23						22
28	38	36	32	33	30	
31	32	28	28	30	29	
17						18
	36	34	26	28		
24					26	
	21	22	31	28		

Superficial Air velocity 2.0 m s^{-1}
Weir Load 150 $cm^3 cm^{-1} s^{-1}$

	21	22	18	19		
30					32	
	39	35	30	35		
23						23
28	42	38	33	35	31	
35	38	27	29	33	32	
24						18
	37	35	28	32		
29					33	
	23	22	32	28		

Superficial Air velocity 2.0 m s^{-1}
Weir Load 200 $cm^3 cm^{-1} s^{-1}$

	20	23	19	19		
34					34	
	38	37	30	34		
25						24
35	44	39	35	37	33	
36	41	30	31	38	34	
24						21
	39	37	31	34		
31					32	
	28	29	33	30		

INLET GAP AND OUTLET WEIR - 50 mm

Superficial Air velocity 1.0 m s^{-1}
Weir Load 25 $cm^3 cm^{-1} s^{-1}$

	40	34	29	33		
36					34	
	37	35	28	30		
31						31
32	35	38	33	29	30	
35	38	32	28	30	35	
27						24
	38	37	28	27		
29					34	
	31	31	36	31		

Superficial Air velocity 1.0 m s^{-1}
Weir Load 50 $cm^3 cm^{-1} s^{-1}$

	54	34	53	61		
37					44	
	42	40	32	33		
38						34
36	41	43	37	39	36	
37	42	36	34	34	38	
29						27
	40	40	32	32		
36					34	
	34	32	37	38		

Superficial Air velocity 1.0 m s^{-1}
Weir Load 100 $cm^3 cm^{-1} s^{-1}$

	67	49	65	76		
43					45	
	52	47	39	40		
43						44
44	51	52	46	46	48	
44	51	42	43	44	47	
35						35
	51	48	39	40		
47					43	
	42	42	46	43		

Superficial Air velocity 1.0 m s^{-1}
Weir Load 150 $cm^3 cm^{-1} s^{-1}$

	51	36	39	50		
53					53	
	55	50	46	49		
48						52
51	56	54	50	51	55	
53	56	44	45	49	50	
40						38
	54	54	44	46		
51					50	
	47	45	52	49		

Superficial Air velocity 1.0 m s^{-1}
Weir Load 200 $cm^3 cm^{-1} s^{-1}$

	65	52	45	63		
68					69	
	62	67	59	57		
67						65
62	70	64	62	58	63	
62	67	56	56	60	50	
49						52
	64	63	55	55		
61					60	
	61	61	60	55		

Superficial Air velocity 1.5 m s^{-1}
Weir Load 25 $cm^3 cm^{-1} s^{-1}$

	31	25	24	26		
30					23	
	33	31	21	23		
22						25
25	32	34	26	24	26	
30	33	25	23	28	30	
16						16
	31	31	21	22		
25					26	
	27	23	29	25		

Superficial Air velocity 1.5 m s^{-1}
Weir Load 50 $cm^3 cm^{-1} s^{-1}$

	37	27	29	33		
32					33	
	39	35	28	30		
25						29
30	37	39	33	34	30	
33	44	32	28	31	32	
23						21
	38	39	29	28		
27					33	
	31	30	33	31		

Superficial Air velocity 1.5 m s^{-1}
Weir Load 100 $cm^3 cm^{-1} s^{-1}$

	39	29	28	30		
41					37	
	47	41	34	39		
34						33
41	47	49	40	44	39	
43	45	37	35	41	40	
27						28
	46	45	37	38		
37					38	
	39	38	42	39		

Superficial Air velocity 1.5 m s^{-1}
Weir Load 150 $cm^3 cm^{-1} s^{-1}$

	34	28	27	27		
44					43	
	48	45	39	41		
38						40
41	55	48	43	47	44	
42	47	47	40	41	40	
30						28
	47	47	40	41		
39					42	
	40	40	44	41		

Superficial Air velocity 1.5 m s^{-1}
Weir Load 200 $cm^3 cm^{-1} s^{-1}$

	39	35	30	32		
51					48	
	50	48	43	47		
42						40
48	56	54	46	50	53	
47	51	40	43	46	48	
33						36
	52	52	43	44		
47					45	
	42	46	45	40		

Superficial Air velocity 1.5 m s^{-1}
Weir Load 250 $cm^3 cm^{-1} s^{-1}$

	36	37	
			41
	45	53	
			62
	49	58	59
	49	50	49
			45
	46	51	
			47
	54	50	

Superficial Air velocity 1.5 m s^{-1}
Weir Load 300 $cm^3 cm^{-1} s^{-1}$

	48	52	
			51
	50	61	
			71
	59	66	64
	57	66	59
			56
	54	63	
			60
	64	61	

Superficial Air velocity 1.5 m s^{-1}
Weir Load 350 $cm^3 cm^{-1} s^{-1}$

64 67
59
69 73
86
75 76 81
75 77 72
73
66 75
82
77 78

Superficial Air velocity 2.0 m s^{-1}
Weir Load 25 $cm^3 cm^{-1} s^{-1}$

31 22 21 24
28 23
29 30 22 23
18 20
23 31 34 24 26 25
23 30 24 21 28 21
13 10
30 30 25 22
20 25
25 23 28 26

Superficial Air velocity 2.0 m s^{-1}
Weir Load 50 $cm^3 cm^{-1} s^{-1}$

31 24 21 25
30 28
36 33 23 28
22 24
30 37 37 29 30 28
28 34 26 26 30 30
12 13
34 38 25 25
27 27
26 28 31 26

Superficial Air velocity 2.0 m s^{-1}
Weir Load 100 $cm^3 cm^{-1} s^{-1}$

26 26 22 26
38 33
44 39 30 35
27 24
35 42 44 33 38 32
32 40 29 30 32 33
21 21
39 42 29 31
31 34
31 30 35 31

Superficial Air velocity 2.0 m s^{-1}
Weir Load 150 $cm^3cm^{-1}s^{-1}$

	22	26	22	24		
38					30	
	41	40	27	36		
29						21
40	46	45	35	40	38	
36	40	34	33	38	30	
26						33
	43	42	32	35		
32					35	
	33	33	35	36		

Superficial Air velocity 2.0 m s^{-1}
Weir Load 200 $cm^3cm^{-1}s^{-1}$

	18	28	25	22		
40					35	
	44	43	33	38		
31						25
43	52	48	40	46	32	
37	45	35	35	40	29	
29						35
	46	44	34	35		
33					37	
	36	35	39	35		

Superficial Air velocity 2.0 m s^{-1}
Weir Load 250 $cm^3cm^{-1}s^{-1}$

34	36		
		35	
41	46		
			56
43	51	52	
48	51	46	
			41
44	47		
		44	
48	48		

Superficial Air velocity 2.0 m s^{-1}
Weir Load 300 $cm^3cm^{-1}s^{-1}$

47	47		
		41	
50	53		
			64
53	58	59	
56	61	55	
			53
51	59		
		55	
60	59		

Superficial Air velocity 2.0 m s^{-1}
Weir Load 350 $cm^3 cm^{-1} s^{-1}$

67	67	58	
66	71		81
65	76	76	
77	80	74	70
71	75	72	
78	78		

Appendices 14
Height of Clear Liquid Measurements for the ARC-1 Tray Cases

Below are the values of the height of clear liquid (mm) measured over the 2.44 m diameter tray for the conditions as found in chapter 7. The data are arranged to reflect the positions of the thirty-six manometer points on the tray.

INLET GAP AND OUTLET WEIR - 10 mm

Superficial Air velocity 1.0 m s^{-1}
Weir Load 25 $cm^3cm^{-1}s^{-1}$

	31	25	21	23	
26					26
	31	28	21	24	
24					22
25	26	30	23	19	19
25	29	23	20	24	24
18					17
	27	28	18	20	
22					24
	18	19	25	22	

Superficial Air velocity 1.0 m s^{-1}
Weir Load 50 $cm^3cm^{-1}s^{-1}$

	39	34	26	29	
32					32
	35	33	24	31	
30					29
27	31	33	27	25	29
29	32	26	22	27	29
20					22
	32	30	21	22	
24					24
	20	20	27	26	

Superficial Air velocity 1.0 m s^{-1}
Weir Load 100 $cm^3cm^{-1}s^{-1}$

	38	30	25	29	
34					33
	39	37	30	36	
35					31
32	37	39	34	32	35
34	39	33	29	34	36
25					26
	35	37	28	29	
29					31
	23	22	32	29	

Superficial Air velocity 1.0 m s^{-1}
Weir Load 150 $cm^3 cm^{-1} s^{-1}$

	27	22	15	25		
37					40	
	43	40	35	40		
36						34
34	41	40	41	37	35	
39	42	34	31	37	37	
31						33
	41	41	30	34		
36					36	
	27	24	32	29		

Superficial Air velocity 1.5 m s^{-1}
Weir Load 25 $cm^3 cm^{-1} s^{-1}$

	26	24	20	23		
20					20	
	29	23	18	23		
20						20
20	25	23	22	23	18	
20	30	22	20	17	21	
8						7
	27	26	17	21		
18					16	
	15	17	21	21		

Superficial Air velocity 1.5 m s^{-1}
Weir Load 50 $cm^3 cm^{-1} s^{-1}$

	34	26	22	29		
27					28	
	33	30	22	25		
23						28
22	28	32	26	23	22	
25	30	24	20	27	27	
18						17
	28	26	18	20		
22					23	
	19	16	24	24		

Superficial Air velocity 1.5 m s^{-1}
Weir Load 100 $cm^3 cm^{-1} s^{-1}$

	22	21	20	22		
30					31	
	37	34	32	34		
23						23
28	35	32	32	29	29	
31	34	28	28	31	32	
21						20
	28	25	25	27		
26					25	
	19	19	19	25		

Superficial Air velocity 1.5 m s^{-1}
Weir Load 150 $cm^3 cm^{-1} s^{-1}$

	24	22	16	20		
38					34	
	43	38	31	36		
31						29
	40	40	38	31	29	
38	41	39	30	36	38	
26						23
	41	35	30	33		
34					35	
	28	23	31	29		

Superficial Air velocity 2.0 m s^{-1}
Weir Load 25 $cm^3 cm^{-1} s^{-1}$

	29	19	18	18		
17					21	
	28	25	18	19		
15						16
15	20	25	23	20	17	
22	25	20	17	20	20	
12						10
	24	23	17	15		
16					14	
	14	14	19	18		

Superficial Air velocity 2.0 m s^{-1}
Weir Load 50 $cm^3 cm^{-1} s^{-1}$

	28	19	15	23		
18					18	
	31	26	19	24		
16						18
18	22	28	22	23	17	
25	28	21	20	21	23	
7						10
	26	25	18	18		
16					17	
	14	15	22	18		

Superficial Air velocity 2.0 m s^{-1}
Weir Load 100 $cm^3 cm^{-1} s^{-1}$

	19	18	14	17		
24					21	
	35	30	25	34		
18						19
23	32	33	46	26	25	
25	30	23	23	27	25	
13						15
	29	29	21	22		
22					21	
	14	15	23	16		

Superficial Air velocity 2.0 m s^{-1}
Weir Load 150 $cm^3 cm^{-1} s^{-1}$

	14	17	12	12		
22					22	
	30	29	23	28		
21						21
23	34	32	28	30	26	
29	32	23	23	32	29	
15						20
	34	32	22	27		
24					23	
	18	16	22	20		

INLET GAP AND OUTLET WEIR - 20 mm

Superficial Air velocity 1.0 m s^{-1}
Weir Load 25 $cm^3 cm^{-1} s^{-1}$

	32	29	24	26		
27					27	
	30	27	22	27		
27						26
25	29	30	26	23	22	
26	29	26	22	26	26	
19						16
	29	28	21	22		
23					26	
	21	23	28	28		

Superficial Air velocity 1.0 m s^{-1}
Weir Load 50 $cm^3 cm^{-1} s^{-1}$

	37	34	25	32		
31					33	
	37	34	27	29		
30						31
28	32	35	31	27	29	
32	36	29	27	29	33	
24						22
	35	31	25	26		
26					29	
	26	26	31	29		

Superficial Air velocity 1.0 m s^{-1}
Weir Load 100 $cm^3 cm^{-1} s^{-1}$

	36	29	28	33		
37					36	
	43	39	32	37		
35						35
37	41	40	35	33	35	
37	42	36	32	35	38	
27						29
	39	39	31	32		
33					36	
	29	30	36	34		

Superficial Air velocity 1.0 m s^{-1}
Weir Load 150 $cm^3 cm^{-1} s^{-1}$

	32	27	21	32		
45					44	
	47	44	39	44		
37						38
39	43	45	41	39	38	
40	44	36	35	40	43	
34						29
	40	41	35	36		
35					39	
	31	29	40	37		

Superficial Air velocity 1.0 m s^{-1}
Weir Load 200 $cm^3 cm^{-1} s^{-1}$

	38	29	26	32		
49					47	
	57	53	44	49		
42						39
47	53	51	51	47	52	
48	53	45	42	49	46	
37						39
	51	49	41	44		
43					49	
	39	40	46	41		

Superficial Air velocity 1.5 m s^{-1}
Weir Load 25 $cm^3 cm^{-1} s^{-1}$

	29	24	21	25		
24					24	
	31	29	23	22		
23						24
22	24	32	25	24	22	
24	29	23	22	26	25	
15						14
	29	27	21	22		
21					21	
	21	22	27	26		

Superficial Air velocity 1.5 m s^{-1}
Weir Load 50 $cm^3cm^{-1}s^{-1}$

	35	30	25	31		
28					27	
	33	31	25	29		
25						27
	28	31	33	29	27	27
	28	33	26	27	28	28
20						17
	34	31	25	27		
26					22	
	24	25	31	30		

Superficial Air velocity 1.5 m s^{-1}
Weir Load 100 $cm^3cm^{-1}s^{-1}$

	33	28	24	31		
33					34	
	43	40	35	32		
30						32
	30	40	40	35	30	29
	35	41	34	34	35	33
22						22
	34	34	34	35		
27					27	
	24	29	37	33		

Superficial Air velocity 1.5 m s^{-1}
Weir Load 150 $cm^3cm^{-1}s^{-1}$

	27	20	16	20		
33					32	
	44	40	32	36		
33						35
	31	40	44	37	34	34
	39	40	42	30	34	34
23						21
	38	36	32	31		
31					32	
	27	29	34	35		

Superficial Air velocity 1.5 m s^{-1}
Weir Load 200 $cm^3cm^{-1}s^{-1}$

	33	28	26	27		
46					42	
	54	49	41	47		
41						37
	44	54	50	47	46	39
	49	49	41	40	49	49
31						32
	52	47	42	44		
45					46	
	37	39	44	41		

Superficial Air velocity 2.0 m s^{-1}
Weir Load 25 $cm^3cm^{-1}s^{-1}$

	27	20	15	18		
19					22	
	30	25	18	20		
13						13
	16	22	28	27	19	19
	23	27	24	19	21	22
9						5
	25	27	23	16		
19					18	
	17	17	20	23		

Superficial Air velocity 2.0 m s^{-1}
Weir Load 50 $cm^3cm^{-1}s^{-1}$

	26	19	15	24		
21					21	
	32	27	20	26		
15						17
20	26	29	24	25	24	
24	30	23	23	22	24	
9						9
	29	27	20	21		
20					17	
	17	18	28	22		

Superficial Air velocity 2.0 m s^{-1}
Weir Load 100 $cm^3cm^{-1}s^{-1}$

	21	20	14	19		
26					26	
	34	29	26	30		
19						18
24	36	32	27	27	26	
27	33	25	26	27	25	
14						16
	30	32	25	24		
22					23	
	19	19	28	23		

Superficial Air velocity 2.0 m s^{-1}
Weir Load 150 $cm^3cm^{-1}s^{-1}$

	18	20	15	16		
29					30	
	35	31	25	31		
21						19
29	39	35	32	31	29	
31	35	25	28	32	29	
17						17
	34	33	26	29		
27					30	
	21	21	28	26		

Superficial Air velocity 2.0 m s^{-1}
Weir Load 200 $cm^3cm^{-1}s^{-1}$

	23	24	21	22		
35					35	
	39	40	32	40		
28						25
35	47	44	36	40	34	
38	40	34	35	37	38	
22						22
	43	39	35	37		
31					33	
	31	36	39	38		

INLET GAP AND OUTLET WEIR - 50 mm

Superficial Air velocity 1.0 m s^{-1}
Weir Load 25 $cm^3cm^{-1}s^{-1}$

	42	39	34	37		
38					36	
	40	36	31	35		
35						33
35	38	40	32	32	30	
36	42	35	33	33	35	
27						27
	39	39	30	33		
33					33	
	33	34	39	34		

Superficial Air velocity 1.0 m s^{-1}
Weir Load 50 $cm^3cm^{-1}s^{-1}$

	52	37	34	39		
43					44	
	43	40	37	38		
41						40
40	45	45	41	40	38	
41	46	38	38	39	41	
35						31
	43	43	33	39		
39					42	
	37	38	43	39		

Superficial Air velocity 1.0 m s^{-1}
Weir Load 100 $cm^3 cm^{-1} s^{-1}$

	75	37	33	63	
73					64
	52	49	41	43	
64					60
46	49	52	48	45	45
48	50	42	43	45	44
34					37
	49	49	39	41	
43					45
	41	43	49	47	

Superficial Air velocity 1.0 m s^{-1}
Weir Load 150 $cm^3 cm^{-1} s^{-1}$

	50	37	35	69	
82					79
	59	55	52	46	
72					72
52	58	55	50	50	52
50	56	45	44	50	51
39					37
	57	54	43	47	
51					48
	51	47	52	50	

Superficial Air velocity 1.0 m s^{-1}
Weir Load 200 $cm^3 cm^{-1} s^{-1}$

	60	52	45	65	
64					71
	74	66	63	65	
63					63
63	75	67	58	57	64
66	68	60	58	61	56
52					50
	67	65	57	59	
66					62
	59	62	63	59	

Superficial Air velocity 1.5 m s^{-1}
Weir Load 25 $cm^3 cm^{-1} s^{-1}$

	39	33	31	34	
33					32
	38	38	30	32	
28					29
30	35	36	33	32	30
34	39	36	30	32	35
23					22
	39	37	28	32	
31					34
	34	34	35	31	

Superficial Air velocity 1.5 m s^{-1}
Weir Load 50 $cm^3cm^{-1}s^{-1}$

47 34 34 39
36 41
45 42 37 40
31 37
35 39 48 41 39 36
37 42 42 39 37 38
25 28
42 45 35 36
35 41
35 37 42 39

Superficial Air velocity 1.5 m s^{-1}
Weir Load 100 $cm^3cm^{-1}s^{-1}$

47 33 29 38
45 42
49 47 40 43
36 36
45 51 50 44 42 44
44 50 40 40 43 45
29 32
50 47 37 39
38 44
40 41 48 44

Superficial Air velocity 1.5 m s^{-1}
Weir Load 150 $cm^3cm^{-1}s^{-1}$

46 32 28 33
44 49
53 49 41 44
41 44
49 55 52 47 47 44
46 51 53 42 47 46
33 32
51 49 42 45
45 47
46 43 48 44

Superficial Air velocity 1.5 m s^{-1}
Weir Load 200 $cm^3cm^{-1}s^{-1}$

47 44 40 41
57 54
65 62 50 57
46 45
53 61 63 54 54 58
54 59 54 50 53 54
42 42
57 58 50 55
51 54
51 55 58 54

Superficial Air velocity 2.0 m s^{-1}
Weir Load 25 $cm^3 cm^{-1} s^{-1}$

	27	23	22	26		
26					27	
	32	33	24	24		
17						21
21	28	35	27	28	23	
26	30	29	27	23	25	
11						13
	29	31	24	22		
23					30	
	23	25	29	25		

Superficial Air velocity 2.0 m s^{-1}
Weir Load 50 $cm^3 cm^{-1} s^{-1}$

	34	25	23	26		
31					30	
	37	33	26	29		
21						26
29	36	37	32	27	25	
31	34	30	28	29	25	
16						16
	37	36	27	28		
26					33	
	27	25	31	28		

Superficial Air velocity 2.0 m s^{-1}
Weir Load 100 $cm^3 cm^{-1} s^{-1}$

	34	26	23	27		
37					30	
	38	37	29	34		
27						25
33	41	40	32	37	33	
33	40	30	33	32	34	
19						22
	39	39	30	35		
28					34	
	32	32	36	32		

Superficial Air velocity 2.0 m s^{-1}
Weir Load 150 $cm^3 cm^{-1} s^{-1}$

	34	27	23	24		
38					30	
	43	44	32	39		
29						24
35	46	45	36	39	37	
37	42	33	36	38	31	
22						33
	42	41	34	35		
33					37	
	35	35	38	34		

Superficial Air velocity 2.0 m s^{-1}
Weir Load 200 $cm^3 cm^{-1} s^{-1}$

	29	31	26	29		
38					37	
	46	49	35	41		
35						34
43	52	49	39	44	43	
42	46	37	39	42	40	
29						29
	49	46	37	39		
38					38	
	38	39	41	38		